Return to Garbacz
SAT · NASA Hdqt.
DRA

CONTRACT NO. NAS5-9034

DESIGN STUDY REPORT FOR THE IMPROVED TOS (ITOS) SYSTEM

Volume II

Spacecraft Design

(NASA-CR-144816) DESIGN STUDY REPORT FOR THE IMPROVED TOS (ITOS) SYSTEM. VOLUME 2: SPACECRAFT DESIGN (Radio Corp. of America) 596 p
N76-78641
Unclas
00/98 15119

Prepared for the

GODDARD SPACE FLIGHT CENTER
NATIONAL AERONAUTICS AND SPACE ADMINISTRATION
WASHINGTON, D.C.

OCT 1976
RECEIVED
NASA STI FACILITY
INPUT BRANCH

By the

RCA
Astro-Electronics Division
Princeton, New Jersey

SEP 1975
RECEIVED
NASA STI FACILITY
INPUT BRANCH

AED R-3308

June 7, 1968

CONTRACT NO. NAS5-9034

DESIGN STUDY REPORT FOR THE IMPROVED TOS (ITOS) SYSTEM

Volume II

Spacecraft Design

Prepared for the

GODDARD SPACE FLIGHT CENTER
NATIONAL AERONAUTICS AND SPACE ADMINISTRATION
WASHINGTON, D.C.

By the

RCA
Astro-Electronics
Division
Princeton, New Jersey

AED R-3308

June 7, 1968

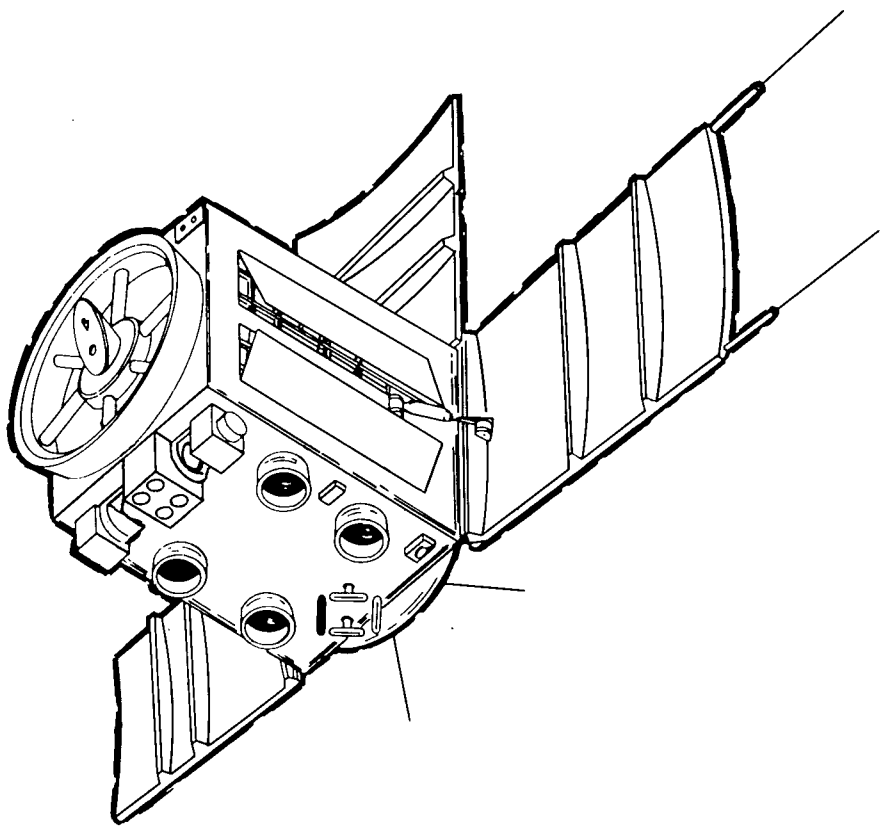

The ITOS Spacecraft

PREFACE

This report describes the system, spacecraft, and ground installation design, as well as related studies, for the Improved TOS (ITOS) meteorological satellite system. The ITOS design study program has been conducted by the Astro-Electronics Division of RCA for the Goddard Space Flight Center of the National Aeronautics and Space Administration (NASA), under Contract No. NAS5-9034.

This report is contained in three volumes, which describe the system design, the spacecraft design, and the ground equipment design, respectively. The third volume also contains appendices describing studies and analyses conducted in support of the ITOS design. Responses to NASA comments (File No. 17741, 28 February 1968) have been incorporated in this final document which supersedes the following preliminary reports prepared for GSFC-NASA under the design study program:

- "Design Study Report for the TIROS M System", Volumes I, II, and III; AED R-3116, dated February 15, 1967.
- "Design Study Report for the TIROS M System", Volumes I, II, and III; Review Draft, AED R-3188, dated June 1967.

Since the engineering cutoff date for this report (June 1967), several subsystem and component functions have been revised. A summary of these revisions is tabulated on the following pages to alert the reader to those areas in this document which do not reflect the current TIROS M/ITOS configurations. Descriptions of the final design configuration will be contained in the appropriate TIROS M and ITOS final engineering reports.

The reader is cautioned against use of nominal current, voltage, and time values contained in this report as discrete engineering parameter values. In all cases, the unit performance specification should be consulted for precise values and tolerances.

SUMMARY OF CURRENT DESIGN REVISIONS NOT COVERED IN THIS REPORT*

A. Mechanical and Structure Design (Volume II, Section II)

1. The spacecraft layout shown in this report does not reflect all the current modifications that have been made to accommodate the subsystem revisions itemized herein.

B. Vehicle Dynamics Subsystem (Volume II, Section IV)

1. The launch vehicle is a two-stage Delta N.
2. The earth-sky blanking techniques and scanning optics performance are improved.
3. The command modes for pitch sensing and backup modes for pitch control are expanded. Two pitch sensors and two roll sensors are provided.
4. Proportional QOMAC is unipolar.

C. Power Supply Subsystem (Volume II, Section V)

1. Each battery contains 23 cells.
2. The voltage regulator peak load capacity reflects spacecraft requirements.
3. The shunt limiter load capability is expanded and cut-in levels have been revised.
4. The preferred mode of operation for the scanning radiometer is now for both day and night operation; however, the power subsystem is not designed to accommodate this type of operation for a 6-month orbital life.

D. Primary Environmental Sensor Subsystems (Volume II, Section VI)

1. The scanning radiometer and APT data can be interleaved on the real time-link.
2. The APT format is 600 lines per frame rather than 800 lines.

*The revisions listed here are referenced by footnotes in the appropriate sections throughout this report.

3. The APT camera subsystem uses a separate wall and mesh vidicon.

4. The instantaneous field of view of the visible channel of the scanning radiometer is 2.8 milliradians rather than 5.3 milliradians.

5. The SR recorder drive system is servo-controlled.

E. Command Subsystem (Volume II, Section VIII)

1. Command capacity has been increased to 132 by a modification of the command coding.

2. An "AVCS run tape" command is provided.

3. Subsystem timing and control functions are modified, reflecting the changes noted herein.

4. Telemetry commands and beacon switching functions are modified, reflecting the latest requirements.

F. Communications Subsystem (Volume II, Section IX)

1. The beacon and command antenna is a single whip; associated coupling networks have been revised.

2. The S-band antenna is a turnstile, and associated coupling networks have been revised.

3. Two real-time antennas are employed, and associated coupling networks have been revised.

G. Command and Data Acquisition Stations (Volume III, Section III)

1. Secondary sensor signal processing is provided between the CDA tape recorder and the long lines.

TABLE OF CONTENTS

PART 1. INTRODUCTION

Section		Page
	PREFACE	iii
I	MISSION REQUIREMENTS	1-I-1
II	SYSTEM SUMMARY	1-II-1
	A. General	1-II-1
	B. Spacecraft	1-II-1
	C. Orbit	1-II-4
	D. Ground Complex	1-II-5

PART 2. SYSTEM FUNCTIONAL DESCRIPTION

I	SPACECRAFT	2-I-1
	A. Physical Description	2-I-1
	1. Configuration	2-I-1
	2. Central Equipment Module	2-I-1
	3. Solar Array	2-I-7
	4. Thermal Control	2-I-8
	5. Pitch Control Loop	2-I-8
	6. Separation Ring	2-I-10
	B. Launch Vehicle Compatibility	2-I-10
	C. Functional Description	2-I-14
	1. General	2-I-14
	2. Command Subsystem	2-I-17
	3. Primary Sensors	2-I-17
	a. Real-Time Data	2-I-17
	b. Stored Data	2-I-18
	4. Secondary Sensors	2-I-19
	5. Communications Subsystem	2-I-20
	a. S-Band Link	2-I-20
	b. Real-Time Link	2-I-20
	c. Command and Beacon Link	2-I-21
	6. Power Subsystem	2-I-22
	D. Subsystem Redundancy	2-I-22
	1. Operating Goals	2-I-22
	2. Alternate Modes of System Operation	2-I-23

TABLE OF CONTENTS (Continued)

Section		Page
II	SPACECRAFT/CDA STATION INTERFACE	2-II-1
	A. Command Link	2-II-1
	B. Beacon Link	2-II-2
	C. Real-Time Link	2-II-3
	D. S-Band Link	2-II-4
III	SPACECRAFT/APT GROUND STATION INTERFACE	2-III-1
IV	ORBIT CHARACTERISTICS	2-IV-1
	A. Sun-Synchronous Orbit	2-IV-1
	1. General	2-IV-1
	2. Sun-Synchronous Orbit Geometry	2-IV-1
	B. Operational Orbit Considerations	2-IV-7
	1. General	2-IV-7
	2. Orbit Inclination	2-IV-7
	3. Effect of Injection Error	2-IV-8
V	SENSOR COVERAGE	2-V-1
	A. Scene Illumination	2-V-1
	B. AVCS and APT Camera Parameters	2-V-5
	1. Field of View Projection	2-V-5
	2. Picture Coverage and Resolution	2-V-7
	C. SR Radiometry	2-V-10
	1. General	2-V-10
	2. Spectral Response	2-V-10
	3. Resolution	2-V-10
	4. SR Image Characteristics	2-V-14
VI	GROUND STATIONS	2-VI-1
	A. CDA Stations	2-VI-1
	B. TOS Operations Center (TOC)	2-VI-2
	C. TOS Evaluation Center/TIROS-TOS Checkout Center (TEC/TTCC)	2-VI-2
	D. Spacecraft Checkout Facilities	2-VI-3

TABLE OF CONTENTS (Continued)

PART 3. SYSTEM OPERATION

Section		Page
I	LAUNCH-TO-MISSION MODE EVENTS SEQUENCE	3-I-1
	A. Introduction	3-I-1
	B. Prelaunch Status of Spacecraft	3-I-1
	C. Launch and Orbit Injection	3-I-2
	D. Third-Stage Separation	3-I-3
	E. Satellite Despin, Verification of Pitch Loop Operation, and Nutation Damping	3-I-3
	F. Initial Orientation Maneuver and Solar Panel Deployment	3-I-5
	G. Maintenance of Mission Attitude	3-I-5
II	CAMERA, RADIOMETER, AND QOMAC PROGRAMMING	3-II-1
	A. General	3-II-1
	B. QOMAC Programming	3-II-1
	C. Camera Programming	3-II-2
	D. Radiometer Programming	3-II-2
	E. Radiometer Recorder Programming	3-II-2
III	GROUND STATION CONTACT TIME	3-III-1
	A. Command and Data Acquisition (CDA) Ground Stations	3-III-1
	B. Real-Time Readout APT Ground Stations	3-III-3
IV	USE OF REDUNDANCY	3-IV-1
	A. Philosophy of Redundancy	3-IV-1
	B. Subsystem Component Selectivity	3-IV-1
	1. AVCS Video Subsystem	3-IV-1
	2. SR Subsystem	3-IV-2
	3. Pitch Control Loop	3-IV-2
	4. Command Subsystem	3-IV-2
	C. SR Subsystem as a Backup for APT and AVCS	3-IV-3

TABLE OF CONTENTS (Continued)

PART 4. SPACECRAFT DESIGN

Section		Page
I	INTRODUCTION	4-I-1
II	MECHANICAL AND STRUCTURAL DESIGN	4-II-1
	A. General	4-II-1
	B. Design Concept	4-II-1
	1. General	4-II-1
	2. Mechanical Alignment	4-II-14
	3. Component Accessibility	4-II-15
	4. Interchangeability	4-II-15
	C. Major Structural Components	4-II-16
	1. Separation Ring	4-II-17
	2. Baseplate	4-II-17
	3. Equipment Panels	4-II-19
	4. Access Panels	4-II-20
	a. Earth-Oriented Panel	4-II-20
	b. Anti-Earth Side Panel	4-II-21
	5. Scanning Radiometer Mounting Plate	4-II-22
	6. Crossbrace Assembly and Thermal Fence	4-II-22
	7. Solar Array Structure and Deployment Mechanism	4-II-23
	8. Momentum and Attitude Control Coils	4-II-29
	9. Nutation Damper	4-II-31
	D. Fabrication and Assembly	4-II-31
	E. Spacecraft Balance, Weight Estimate, and Moment of Inertia	4-II-33
	1. Balance and Center of Gravity	4-II-33
	2. Spacecraft Weight Summary	4-II-33
	3. Moment of Inertia	4-II-38
	F. Stress Analysis	4-II-39
III	THERMAL DESIGN	4-III-1
	A. Objectives and Basic Requirements	4-III-1
	1. Thermal Design Concept	4-III-1
	2. Temperature Specifications	4-III-1
	a. Operational Mode	4-III-2
	b. Preoperational Mode	4-III-3
	c. Minimum Mission Requirements	4-III-3
	d. Active Thermal Controller Failure	4-III-3

TABLE OF CONTENTS (Continued)

Section		Page
	3. Power Specifications	4-III-6
	a. Operational Mode	4-III-6
	b. Preoperational Mode	4-III-6
	c. Growth Power	4-III-6
	B. Thermal Analysis	4-III-8
	1. Design Philosophy	4-III-8
	a. Adjustment of Spacecraft Temperature	4-III-9
	b. Orbital Heat Flux	4-III-10
	c. Internal Power Dissipation	4-III-11
	d. Failure Conditions	4-III-11
	2. Thermal Subsystem Design	4-III-11
	a. Thermal Fence	4-III-11
	b. Active Thermal Controller	4-III-16
	c. Baseplate Radiator	4-III-26
	C. Thermal Performance	4-III-28
	1. Analysis Model Description	4-III-28
	2. Preoperational Mode	4-III-28
	3. Operational and Failure Mission Modes	4-III-31
IV	VEHICLE DYNAMICS SUBSYSTEM	4-IV-1
	A. Subsystem Description	4-IV-1
	B. Initial Orientation Maneuver	4-IV-5
	1. Preseparation	4-IV-5
	2. Despin	4-IV-7
	3. Biased Flywheel Operation	4-IV-10
	4. Attitude Determination and Final Acquisition	4-IV-12
	C. Nutation Damping	4-IV-13
	1. General	4-IV-13
	2. Damper Caging	4-IV-14
	3. Basic Design	4-IV-15
	4. Time Constant	4-IV-16
	5. Weight Tradeoff	4-IV-16
	D. Attitude Sensing	4-IV-18
	1. General	4-IV-18
	2. Digital Solar Aspect Indicator	4-IV-19
	3. Acquisition Sensor	4-IV-19
	4. Operational Pitch and Attitude Sensors	4-IV-24
	a. General	4-IV-24
	b. Pitch Sensing	4-IV-27
	c. Alternate Pitch Sensing	4 IV-30
	d. Roll Sensing	4-IV-31

TABLE OF CONTENTS (Continued)

Section		Page
E.	Magnetic Attitude Control and Momentum Control	4-IV-33
1.	General	4-IV-33
2.	Coordinate System	4-IV-33
3.	Geomagnetic Field Equations	4-IV-35
4.	Quarter-Orbit Magnetic Attitude Control (QOMAC)	4-IV-36
5.	Proportional QOMAC	4-IV-37
6.	Magnetic Bias Control (MBC)	4-IV-44
7.	Momentum Control	4-IV-46
a.	Momentum Magnitude	4-IV-46
b.	Spin Momentum Change (T_{SPIN})	4-IV-47
c.	Procession Due to Momentum Correction (T_{PREC})	4-IV-48
F.	Pitch Control	4-IV-54
1.	General	4-IV-54
2.	Pitch Sensing	4-IV-57
3.	Servo Design	4-IV-59
4.	Component Description	4-IV-65
a.	General	4-IV-65
b.	Pulse Width Modulator (PWM) Error Detector	4-IV-67
c.	Compensation Amplifier	4-IV-70
d.	Gain Switching Circuit	4-IV-72
e.	Summing Amplifier	4-IV-72
f.	Power Amplifier	4-IV-72
g.	Torque Motor	4-IV-73
h.	Encoder	4-IV-74
i.	Encoder Electronics	4-IV-75
j.	DC-to-DC Converter	4-IV-76
k.	Sensor Threshold Amplifiers	4-IV-76
l.	Earth Blanking	4-IV-76
5.	Pitch Control Mechanical Design	4-IV-77
6.	Applicable Test Results	4-IV-81
a.	Brush Wear and Oil Leakage Rates	4-IV-81
b.	Bearing Wear	4-IV-84
G.	Accuracy Analysis	4-IV-86
1.	General	4-IV-86
2.	Pointing	4-IV-88
3.	Jitter	4-IV-96
H.	Systems Interfaces	4-IV-101
1.	Power	4-IV-101
2.	Command and Control	4-IV-101
3.	Telemetry	4-IV-101

TABLE OF CONTENTS (Continued)

Section		Page
V	POWER SUPPLY SUBSYSTEM	4-V-1
	A. Introduction	4-V-1
	B. Functional Description	4-V-7
	1. General	4-V-7
	2. Solar Array	4-V-10
	3. Batteries	4-V-13
	4. Series Voltage Regulators	4-V-13
	5. Charge Controllers	4-V-13
	6. Shunt Limiter	4-V-14
	7. System Protection	4-V-15
	C. Equipment Description	4-V-16
	1. Solar Array	4-V-16
	2. Batteries	4-V-20
	a. Mechanical	4-V-20
	b. Electrical	4-V-21
	c. System Considerations	4-V-22
	3. Power Supply Electronics	4-V-23
	a. General	4-V-23
	b. Charge Controllers	4-V-27
	c. Series Voltage Regulator	4-V-30
	d. Shunt Limiter	4-V-30
	D. System Analysis	4-V-32
	1. Tradeoff Studies	4-V-32
	a. Solar Array	4-V-32
	b. Power Conditioning Circuits	4-V-32
	c. Power Dissipation	4-V-37
	d. Battery Charging	4-V-40
	e. Current Telemetry Circuit Tradeoff Study	4-V-40
	2. End-of-Life Analysis	4-V-42
	3. Beginning-of-Life Analysis	4-V-51
	4. Preoperational Mode Analysis	4-V-53
	5. Analysis of Typical Performance	4-V-55
	a. Evaluation of ESSA 2 Data	4-V-55
	b. Typical ITOS Array Degradation	4-V-56
	6. Performance After Battery Failure	4-V-58
	a. Open Battery	4-V-58
	b. Shorted Battery Cells	4-V-60
	c. Reliability Analysis	4-V-60
	7. Fusing	4-V-63

Section		Page
	E. Power Dissipation	4-V-65
	1. General	4-V-65
	2. Initial Orientation Maneuver	4-V-66
	3. Operational Mode	4-V-67
	F. Telemetry Points	4-V-68
	1. General	4-V-68
	2. Battery Charge and Solar Array Current Telemetry	4-V-70
	3. Voltage Telemetry	4-V-72
	4. Temperature Telemetry	4-V-73
VI	PRIMARY ENVIRONMENTAL SENSOR SUBSYSTEMS	4-VI-1
	A. Introduction	4-VI-1
	B. AVCS Subsystem	4-VI-2
	1. General	4-VI-2
	2. Functional Description	4-VI-4
	a. Record Mode	4-VI-4
	b. Playback Mode	4-VI-11
	c. Direct Mode	4-VI-11
	3. AVCS Camera Sensor and Camera Electronics Assembly	4-VI-12
	a. General Description	4-VI-12
	b. Lens Assembly	4-VI-15
	c. AVCS Hybrid Vidicon	4-VI-15
	d. Video Clamp	4-VI-23
	e. Shading Correction	4-VI-28
	4. AVCS Tape Recorder	4-VI-34
	a. General	4-VI-34
	b. Tape Transport Assembly	4-VI-41
	c. Motor Drive Circuit	4-VI-43
	d. Video Signal Record and Playback Circuits	4-VI-43
	e. Flutter-and-Wow Record and Playback Circuit	4-VI-44
	C. Automatic Picture Transmission Subsystem	4-VI-45
	1. General	4-VI-45
	2. Functional Description	4-VI-45
	3. APT Subsystem and Spacecraft Interface Signals	4-VI-49
	4. APT Subsystem Characteristics	4-VI-50
	5. APT Subsystem Assemblies	4-VI-52
	D. Scanning Radiometer Subsystem	4-VI-52
	1. Introduction	4-VI-52
	2. Scanning Radiometer and Electronics	4-VI-57
	a. General	4-VI-57
	b. Scanning Radiometer	4-VI-63
	c. Scanning Radiometer Electronics	4-VI-67

TABLE OF CONTENTS (Continued)

Section		Page
	3. SR Processor	4-VI-69
	4. SR Recorders	4-VI-71
	a. General	4-VI-71
	b. Functional Description	4-VI-74
VII	SECONDARY SENSOR SUBSYSTEM	4-VII-1
	A. Introduction	4-VII-1
	B. Secondary Sensors	4-VII-1
	1. Solar Proton Monitor	4-VII-1
	2. Flat Plate Radiometer	4-VII-5
	C. Data Format Converter	4-VII-6
	1. General Description	4-VII-6
	2. Power Switching and Tape Recorder Controller	4-VII-6
	3. Input Data Processor	4-VII-7
	a. Data Format	4-VII-7
	b. SPM Data Processing	4-VII-8
	c. Clock Data Processing	4-VII-8
	d. FPR Data Processing	4-VII-9
	e. Time Code Processing	4-VII-9
	f. Digital Telemetry Processing	4-VII-9
	4. Output Data Processor	4-VII-11
	D. Incremental Tape Recorder	4-VII-11
	1. General Description	4-VII-11
	2. Tape Transport Assembly	4-VII-13
	a. Tape Drive	4-VII-14
	b. Tape Reel Subassembly	4-VII-14
	c. Record/Playback and Erase Head Subassembly	4-VII-15
	d. Tape Recorder Electronics	4-VII-15
	e. Packaging	4-VII-19
	f. Life Limiting Parts and Lubrication	4-VII-19
VIII	COMMAND SUBSYSTEM	4-VIII-1
	A. Function	4-VIII-1
	B. Design	4-VIII-7
	C. Subsystem Description	4-VIII-8
	1. Command Decoder	4-VIII-8
	a. General	4-VIII-8
	b. Inputs and Outputs	4-VIII-8
	c. Functional Operation	4-VIII-12
	d. Operation of Circuits	4-VIII-17

Section		Page
	2. Programmer	4-VIII-23
	a. General	4-VIII-23
	b. Functional Operation	4-VIII-24
	c. Programmer Interfaces	4-VIII-37
	3. Command Distribution Unit	4-VIII-41
	a. General	4-VIII-41
	b. Command Decoding	4-VIII-41
	c. Specific Decoding	4-VIII-42
	4. Dual Time Base Unit	4-VIII-57
	a. General	4-VIII-57
	b. Response to Commands	4-VIII-63
	c. Time Base Generator Description	4-VIII-63
	d. Time Code Generator Description	4-VIII-63
IX	COMMUNICATIONS SUBSYSTEM	4-IX-1
	A. Introduction	4-IX-1
	B. Command Receiver Link	4-IX-4
	1. General	4-IX-4
	2. Signal Characteristics	4-IX-4
	3. Command and Beacon Telemetry Antenna Subsystem	4-IX-6
	a. Antenna	4-IX-6
	b. Bandpass Filter, Notch Filter, and Hybrid	4-IX-15
	4. Dual Command Receiver	4-IX-16
	5. Subsystem Analysis and Link Calculation	4-IX-17
	a. Link Geometry and Path Loss	4-IX-17
	b. RF Power Margin Calculation	4-IX-17
	c. Receiver Bandwidth Requirements	4-IX-20
	C. Beacon and Telemetry Link	4-IX-30
	1. General	4-IX-30
	2. Signal Characteristics	4-IX-32
	a. Housekeeping Telemetry	4-IX-32
	b. Command Data Verification	4-IX-32
	c. Acquisition Sensor	4-IX-33
	d. Digital Solar Aspect Indicator	4-IX-33
	e. Roll Sensors	4-IX-34
	f. Pitch Sensor	4-IX-34
	g. Solar Proton Monitor	4-IX-34
	3. Link Components	4-IX-34
	a. Beacon Antenna	4-IX-34
	b. Beacon Transmitter Characteristics	4-IX-45

Section		Page
	c. Dual Subcarrier Oscillator	4-IX-46
	d. Signal Conditioner and Telemetry Commutators	4-IX-47
	4. Subsystem Analysis and Link Calculations	4-IX-48
	a. Receiver IF Bandwidth	4-IX-48
	b. Subcarrier Phase Deviations	4-IX-49
	c. Distortion Products	4-IX-52
	d. Link Calculation	4-IX-52
	e. Estimated Signal-to-Noise Degradation in Long Lines	4-IX-56
	5. Telemetry List	4-IX-58
D.	Real-Time Video Link	4-IX-65
	1. General	4-IX-65
	2. Video Signal Characteristics	4-IX-66
	a. APT Signals	4-IX-66
	b. SR Signals	4-IX-66
	3. Real-Time Transmitter	4-IX-68
	a. Video Coupler	4-IX-68
	b. Transmitter	4-IX-68
	4. Real-Time Antenna	4-IX-71
	5. Subsystem Analysis and Link Calculation	4-IX-75
	a. RF Link Calculation	4-IX-75
	b. Verification of RF Bandwidth Requirements	4-IX-76
	c. Real-Time Baseband Signal-to-Noise Ratio	4-IX-77
	d. Scanning Radiometer Baseband Signal-to-Noise Ratio	4-IX-79
	e. CDA Station Margins	4-IX-80
	f. Net Signal-to-Noise Ratio Including the Effect of Sensor Noise	4-IX-80
E.	Playback Video Link	4-IX-81
	1. General	4-IX-81
	2. Signal Characteristics	4-IX-83
	a. AVCS Signals	4-IX-83
	b. Scanning Radiometer Signals	4-IX-84
	c. Secondary Sensors	4-IX-85
	3. Dual Multiplexer	4-IX-86
	4. S-Band Transmitter	4-IX-88
	5. S-Band Antenna and Coupling Network	4-IX-89
	a. Requirements	4-IX-89
	b. Description of the Baseline S-Band Antenna and Coupling Network	4-IX-89
	c. Design Considerations	4-IX-92
	d. S-Band Antenna and Coupling Network Specifications	4-IX-93

Section		Page
	6. Subsystem Analysis and Link Calculation	4-IX-93
	a. RF Link Calculation	4-IX-93
	b. System Noise Temperature	4-IX-97
	c. Verification of RF Bandwidth Requirement	4-IX-97
	d. RF Deviation Allotments (Subcarrier Signal-to-Noise)	4-IX-98
	e. Baseband Signal-to-Noise Ratios	4-IX-99
X	SPACECRAFT TESTING	4-X-1
	A. ITOS Test Philosophy	4-X-1
	B. Unit and Subsystem Qualification Testing	4-X-2
	1. Test Philosophy	4-X-2
	2. Test Conditions	4-X-2
	a. Types of Tests	4-X-2
	b. Vibration Tests	4-X-2
	c. Thermal-Vacuum Tests	4-X-5
	3. Test Implementation	4-X-7
	a. Unit Testing	4-X-7
	b. Unit Combination Testing	4-X-7
	c. Subsystem Interface Testing	4-X-7
	C. Spacecraft Qualification Testing	4-X-8
	1. Test Philosophy	4-X-8
	2. Test Conditions	4-X-11
	a. Types of Tests	4-X-11
	b. Vibration Tests	4-X-11
	c. Thermal-Vacuum Tests	4-X-12
	3. Test Implementation	4-X-13
	a. General	4-X-13
	b. Flight Spacecraft Test and Calibration Plan	4-X-14
	D. Design Validity Testing	4-X-17
	1. General	4-X-17
	2. Thermal and RF Design Testing	4-X-18
	3. Mechanical and Electrical Design Testing	4-X-21

TABLE OF CONTENTS

PART 5. GROUND STATION EQUIPMENT

Section		Page
I	INTRODUCTION	5-I-1
II	COMMAND, PROGRAMMING, AND ANALYSIS CENTERS	5-II-1
	A. General	5-II-1
	B. TOS Operations Center	5-II-1
	1. Functions	5-II-1
	2. New Facilities	5-II-2
	a. Attitude Channel Selector	5-II-2
	b. Attitude Channel Discriminator	5-II-2
	c. Attitude Channel Calibrator	5-II-3
	d. Attitude Channel Chart Recorder	5-II-3
	e. Station Control	5-II-4
	f. Oscilloscope Display	5-II-4
	g. Location of New Equipment	5-II-4
	C. TOS Evaluation Center/TIROS-TOS Checkout Center (TEC/TTCC)	5-II-4
	1. Function	5-II-4
	2. New Facilities	5-II-4
	D. Data Processing and Analysis Facility	5-II-5
	1. Functions	5-II-5
	2. Data Inputs	5-II-5
	a. AVCS Data	5-II-5
	b. SR Data	5-II-6
	c. Secondary Sensor Data	5-II-7
	d. Beacon Data	5-II-7
	e. CDA Station Events	5-II-8
	3. Long Line Interface	5-II-8
III	COMMAND AND DATA ACQUISITION STATIONS	5-III-1
	A. General	5-III-1
	B. Data Acquisition Facilities	5-III-1
	C. Ground Station Redundancy	5-III-2
	D. RF Equipment	5-III-2
	1. Introduction	5-III-2
	2. Command Link	5-III-2
	3. Beacon Data Link	5-III-3
	4. Real-Time Link	5-III-4
	5. S-Band Link	5-III-4

TABLE OF CONTENTS (Continued)

Section		Page
	E. Video Equipment	5-III-5
	1. Introduction	5-III-5
	2. Demultiplexing	5-III-6
	3. Magnetic Tape Recorders	5-III-8
	4. Long Line Interface	5-III-13
	5. Secondary Sensor Data Transmission	5-III-13
	6. Video Display	5-III-16
	F. Command Equipment	5-III-17
	1. Introduction	5-III-17
	2. ITOS Command System	5-III-18
	3. Remote Commands	5-III-20
	G. Beacon Equipment	5-III-20
	1. Introduction	5-III-20
	2. Beacon Processing	5-III-22
	3. Beacon Display	5-III-23
	4. Long Line Interface	5-III-23
	H. Station Control	5-III-23
	1. Introduction	5-III-23
	2. Operating Procedure	5-III-25
	a. Spacecraft Contact	5-III-25
	b. Playback Data	5-III-29
	3. Station Events	5-III-29
	4. Chart Recorders	5-III-30
	a. Events Recorder	5-III-30
	b. Beacon Recorder	5-III-30
	c. Attitude Recorder	5-III-30
	5. Long Line Interface	5-III-30
	I. Mechanical Arrangement	5-III-32
IV	LONG LINES	5-IV-1
	A. Introduction	5-IV-1
	B. Channel Allocation	5-IV-1
	C. Long Line Utilization	5-IV-4
V	AED CHECKOUT FACILITY AND GROUND STATION	5-V-1
	A. General	5-V-1
	B. RF Signal Handling	5-V-1
	C. Video Display	5-V-1
	D. Secondary Sensor Data Processing	5-V-2
	E. Other System Modifications	5-V-2

TABLE OF CONTENTS (Continued)

Section		Page
VI	GO/NO-GO VAN	5-VI-1
VII	EQUIPMENT COMPLEMENT	5-VII-1
	A. CDA Stations	5-VII-1
	B. AED Ground Station	5-VII-2
	C. TOC and TEC/TTCC	5-VII-3
	D. GO/NO-GO Van	5-VII-4
	E. AED Checkout Facility	5-VII-5

APPENDICES

APPENDIX A.	EVALUATION OF THE ITOS RADIATION ENVIRONMENT	A-1
	1. Introduction	A-1
	2. Tolerances Obtained by "Hardening" to a 1965 Environment	A-1
	a. Approach to the Problem	A-1
	b. Ionization Damage Effects in Transistors - The Ionization Damage Profile	A-2
	c. The Dose Margin Chart	A-5
	d. Bulk Damage Effects in Transistors	A-9
	e. Damage Effects in Solar Cells	A-9
	3. Application of the Dose Margin Chart to ITOS Electronic Systems	A-12
	a. Constant Dose Tolerance Factor Hardening Technique	A-12
	b. Minimum Permissible Threshold Dose Hardening Technique	A-16
	c. Minimum Dose Thresholds Based on Recommended Dose Tolerance Factors Using a Modified 1968 Environment	A-17
	4. Vulnerability to Damage from Nuclear Explosions	A-18
	5. Conclusions	A-26
APPENDIX B.	ATTITUDE DETERMINATION	B-1
	1. General	B-1
	2. Mathematical Description of Sensor Subsystem	B-1
	3. Instantaneous Attitude Determination	B-1
	a. Single Half-Vee Method of Roll Angle Determination	B-2
	b. Comparative Methods of Roll Angle Determination	B-3
	4. Error Analysis	B-4
	5. Statistical Processing	B-7

TABLE OF CONTENTS (Continued)

Section		Page
APPENDIX C.	DISTURBANCE ANALYSIS	C-1
	1. Residual Magnetic Dipoles	C-1
	2. Solar Torques	C-6
	3. Magnetic Hysteresis Losses	C-16
	4. Eddy Current Losses	C-17
	5. Gravity Gradient	C-17
	6. Internal Rotating Components	C-18
APPENDIX D.	SIMULATION OF YO-YO DEVELOPMENT	D-1
APPENDIX E.	MATHEMATICAL ANALYSIS OF THE LIQUID-FILLED NUTATION DAMPER	E-1
APPENDIX F.	SYSTEM PERFORMANCE AT VARIOUS SUN ANGLES	F-1
	1. Sensor Performance at Small to Large Sun Angles	F-1
	2. Operation of Power Supply Subsystem at Large Sun Angles	F-4
APPENDIX G.	SYSTEM PERFORMANCE IN ELLIPTICAL ORBIT	G-1
	1. Sensor Pointing Offsets	G-1
	2. Attitude and Momentum Control Performance	G-2
	a. Measurement Accuracy of Attitude Determination	G-2
	b. Torquing Rates	G-4
	c. Drag Effects	G-4
	3. Elliptical Orbit Perigee and Apogee versus Picture Size	G-9
	4. Radiation Damage Analysis for an Elliptical Orbit	G-11
	a. The Elliptical Orbit Problem	G-11
	b. Elliptical Orbit Particle Flux Determination	G-12
	c. Radiation Damage Estimates for Six-Month and One-Year Missions	G-16
	d. Effect of the Radiation Environment on Transistors	G-18
	e. Effect of Radiation Environment on the Solar Array	G-19
APPENDIX H.	ITOS EXTENDED MISSION MODE TEMPERATURE PREDICTIONS	H-1
	1. General	H-1
	2. Predicted Flight Temperatures for Small-to-Large Sun Angles at an Orbit Altitude of 775 Nautical Miles	H-2
	3. Predicted Flight Temperatures for Normal Operating Sun Angles at Orbiting Altitudes of 600 and 900 Nautical Miles.	H-2

LIST OF ILLUSTRATIONS

Figure		Page
	The ITOS Spacecraft	ii
	PART 1. INTRODUCTION	
1-I-1	The ITOS Spacecraft, Identification of External Features	1-I-2
1-II-1	The ITOS System	1-II-2
1-II-2	Orbit Coverage of the ITOS Satellite	1-II-5
	PART 2. SYSTEM FUNCTIONAL DESCRIPTION	
2-I-1	ITOS Spacecraft Orientation	2-I-2
2-I-2	ITOS Spacecraft in Operational Mode Showing Sensor Fields of View	2-I-3
2-I-3	ITOS Spacecraft Component Layout	2-I-5
2-I-4	Panel 5 of the Central Equipment Module (Exterior View)	2-I-9
2-I-5	ITOS Spacecraft Launch Configuration (Side View)	2-I-11
2-I-6	Bottom of ITOS Spacecraft in Launch Configuration	2-I-13
2-I-7	ITOS Spacecraft Block Diagram	2-I-15
2-IV-1	Seasonal Variations in Illumination for an Afternoon Sun-Synchronous Orbit	2-IV-2
2-IV-2	Geometry of the Sun-Synchronous Orbit	2-IV-4
2-IV-3	Definition of Sun (Gamma) Angle	2-IV-5
2-IV-4	Seasonal Variation of Sun Angle for Various O'Clock Angles	2-IV-6
2-IV-5	Altitude Versus Inclination for Sun-Synchronous Orbits	2-IV-7
2-IV-6	Nodal Drift Rate vs Inclination Error	2-IV-9
2-IV-7	Nodal Drift Rate vs Mean Height Error	2-IV-9
2-V-1A	Polar Stereographic Projection of Northern Hemisphere Showing Ground Station Contact Boundaries for the ITOS Spacecraft	2-V-2
2-V-1B	Solar Elevation Contours for ITOS Satellite at Winter and Summer Solstices	2-V-3
2-V-1C	Camera and SR Coverage for ITOS	2-V-4
2-V-2	Camera Field of View for Orbit at 775-Nautical-Mile Altitude	2-V-6
2-V-3	Camera Coverage as a Function of Altitude and Camera Field of View	2-V-8
2-V-4	Effect of Orbit Altitude on Period and Longitude Difference Between Passes	2-V-9
2-V-5	Typical Scanning Radiometer Transfer Function	2-V-11
2-V-6	Orbit Geometry for Scanning Radiometer	2-V-13
2-V-7	SR Direct Readout Coverage Format	2-V-15

LIST OF ILLUSTRATIONS (Continued)

Figure		Page
	PART 3. SYSTEM OPERATION	
3-II-1	AVCS and APT Camera Cycle Timing Diagram	3-II-3
3-II-2	Scanning Radiometer Recorder Timing Diagram	3-II-6
3-III-1	Ground Contact Boundaries for Wallops Island and Alaska CDA Stations	3-III-2
3-III-2	CDA Station Contact Time	3-III-3
3-III-3	Ground Station Contact Times for a 26-Earth-Revolution Sequence	3-III-5
	PART 4. SPACECRAFT DESIGN	
4-I-1	ITOS Spacecraft, Block Diagram	4-I-3
4-II-1	The TIROS M Spacecraft	4-II-2
4-II-2	Baseplate Assembly	4-II-3
4-II-3	Equipment-Carrying Panel	4-II-5
4-II-4	Earth-Oriented Access Panel	4-II-7
4-II-5	Anti-Earth Access Panel	4-II-9
4-II-6	Top Assembly (Panel V)	4-II-11
4-II-7	ITOS Basic Structure (Without Solar Panels and Antenna), Shown Mounted on Separation Ring	4-II-12
4-II-8	ITOS Basic Structure, Showing Panel Access Ports (Cutouts) and Hinged AVCS Equipment Panel Opened	4-II-13
4-II-9	Spacecraft Component-Integration Configuration	4-II-13
4-II-10	Cross Section of Equipment-Panel Edge Member	4-II-19
4-II-11	Thermal Fence Assembly Configuration	4-II-24
4-II-12	Solar Panel, Mechanical Configuration	4-II-25
4-II-13	Solar-Panel Hydraulic Actuator	4-II-28
4-II-14	Deployment of Solar Panel	4-II-30
4-II-15	ITOS Spacecraft Configuration, Simplified Diagram	4-II-38
4-III-1	Thermal Control Fence	4-III-2
4-III-2	Range of Injection Sun Angles Versus O'Clock Angle for Various Launch Times	4-III-4
4-III-3	Eclipse Times for Various Launch Windows	4-III-5
4-III-4	Spacecraft Operational Electrical Heat Dissipation Characteristics	4-III-7
4-III-5	Spacecraft Injection Mode Electrical Heat Dissipation Characteristics	4-III-7
4-III-6	22-Node Analytical Thermal Model	4-III-8

Figure		Page
4-III-7	Energy Absorbed by a Three-Fin Fence with a Polished Aluminum Reflector	4-III-15
4-III-8	Thermal Fence Temperature Distribution for a 30-Degree Sun Angle	4-III-17
4-III-9	Thermal Fence Temperature Distribution for a 60-Degree Sun Angle	4-III-18
4-III-10	Thermal Fence Temperature Variation	4-III-19
4-III-11	Net Heat Exchange Between Thermal Fence Plate and 20°C Spacecraft	4-III-20
4-III-12	Baseplate Temperature as a Function of Radiator Variables for a 30-Degree Sun Angle	4-III-21
4-III-13	Baseplate Temperature as a Function of Radiator Variables for a 60-Degree Sun Angle	4-III-22
4-III-14	Active Thermal Controller (Actual Control)	4-III-25
4-III-15	Active Thermal Controller Performance Characteristics	4-III-26
4-III-16	Preoperational Mode Temperatures for 38-Degree Sun Angle and 88-Percent Sun Time	4-III-29
4-III-17	Preoperational Mode Temperatures for 60-Degree Sun Angle and 73-Percent Sun Time	4-III-30
4-III-18	Average Equipment Panel Temperatures for 38-Degree Orbit Angle Injection Case and 150-Degree Sun Angle	4-III-31
4-III-19	ITOS Operational Temperature of APT Equipment Panel Versus Flap Angle	4-III-33
4-III-20	ITOS Operational Temperature of AVCS Equipment Panel Versus Flap Angle	4-III-33
4-III-21	Average Temperature Versus Bias Setting of Active Thermal Controller Flap for Minimum Power of 50 Watts at 60-Degree Orbit Angle at End of Life	4-III-35
4-IV-1	Vehicle Dynamics Subsystem, Simplified Block Diagram	4-IV-3
4-IV-2	Effects of Initial Spacecraft Nutation	4-IV-9
4-IV-3	Acquisition Operating Range After Despin	4-IV-9
4-IV-4	Stability Criteria	4-IV-11
4-IV-5	Operating Regions of Attitude Sensors	4-IV-13
4-IV-6	Liquid-Filled Nutation Damper	4-IV-16
4-IV-7	Optimization Curve for Dynamic Mass	4-IV-18
4-IV-8	Digital Solar Aspect Indicator, Scan Geometry	4-IV-20
4-IV-9	Digital Solar Aspect Indicator, Functional Diagram	4-IV-21
4-IV-10	Acquisition Sensor, Scan Geometry	4-IV-22
4-IV-11	Infrared Bolometer	4-IV-23
4-IV-12	Acquisition Sensor Electronics, Block Diagram	4-IV-25
4-IV-13	Attitude Sensor Mirror Assembly, Functional Diagram	4-IV-25
4-IV-14	Pitch and Roll Sensor Electronics, Block Diagram	4-IV-26

LIST OF ILLUSTRATIONS (Continued)

Figure		Page
4-IV-15	Attitude Sensor Scan Geometry	4-IV-28
4-IV-16	Pitch Offset Versus Orbit Eccentricity	4-IV-29
4-IV-17	Sensor Electronics Measured Signal Response	4-IV-29
4-IV-18	Horizon Sensor Half Earth Angles	4-IV-31
4-IV-19	Roll Sensor, Pitch Angle Error	4-IV-32
4-IV-20	Orbital Coordinates	4-IV-34
4-IV-21	Spacecraft Coordinates and Attitude Angles	4-IV-34
4-IV-22	Dipole Moment Program for Proportional QOMAC	4-IV-39
4-IV-23	Relative Precession Rate and Attitude Change for Proportional QOMAC Torquing	4-IV-41
4-IV-24	Momentum Vector Attitude Drift	4-IV-43
4-IV-25	Momentum Change Versus Torquing Period	4-IV-50
4-IV-26	Attitude Change Versus Torquing Period	4-IV-52
4-IV-27	Phase Angles for Momentum Coil Commutation	4-IV-53
4-IV-28	Operational Block Diagram of Pitch-Axis Control Loop	4-IV-56
4-IV-29	Horizon Sensors, Torque Motors, and Encoder	4-IV-58
4-IV-30	Geometry of Horizon Pulse and Reference Index Pulse	4-IV-60
4-IV-31	Open-Loop Frequency Response of Pitch Control Loop (Fine Gain Case)	4-IV-63
4-IV-32	Open-Loop Frequency Response of Pitch Axis Control Loop (Coarse Gain Case)	4-IV-64
4-IV-33	Open-Loop Frequency Response of Tachometer Loop	4-IV-66
4-IV-34	Error Detection	4-IV-71
4-IV-35	Operational Amplifier, Simplified Schematic Diagram	4-IV-71
4-IV-36	Gain Switching Circuit, Block Diagram	4-IV-73
4-IV-37	Torque and Speed Characteristics at Power Amplifier Voltage for Inland Torque Motor of -24 Volts	4-IV-75
4-IV-38	Oil Loss Rate Versus Housing Temperature	4-IV-80
4-IV-39	Silver-Graphite Brushes Before and After Tests	4-IV-83
4-IV-40	Spacecraft Reference Coordinates	4-IV-87
4-IV-41	Half-Cone Nutation Due to Flywheel Unbalance	4-IV-91
4-V-1	Power Supply Subsystem, Load Profile	4-V-4
4-V-2	Power Supply Subsystem, Block Diagram	4-V-11
4-V-3	Solar Panel, Block Diagram	4-V-17
4-V-4	Solar Panel Output Characteristics at Beginning of Life	4-V-18
4-V-5	Solar Panel, Outline Drawing	4-V-18
4-V-6	Battery, Schematic Diagram	4-V-21
4-V-7	Battery Voltage Versus State of Charge	4-V-22
4-V-8	Battery Charge Discharge Profiles	4-V-24
4-V-9	Power Supply Electronics, Block Diagram	4-V-25
4-V-10	Regions of Normal Charge Controller Operation	4-V-28
4-V-11	Charge Controller Functional Diagram, Region I	4-V-28
4-V-12	Charge Controller Functional Diagram, Region II	4-V-29

Figure		Page
4-V-13	Battery Charging Voltage Limits Versus Temperature	4-V-31
4-V-14	Battery Dissipation (Continuous Overcharge) Versus Temperature	4-V-31
4-V-15	Solar Array Configuration Comparison	4-V-33
4-V-16	Direct Energy Transfer System, Block Diagram	4-V-34
4-V-17	Power Supply Current Versus Regulated Load Voltage Deviations	4-V-36
4-V-18	Comparison of Output Impedances of Power Conditioning Systems	4-V-38
4-V-19	ITOS Solar Cell Output Curve at End of Life	4-V-45
4-V-20	Solar Panel Temperature Versus Time in Sunlight at End of Life	4-V-46
4-V-21	Daytime Average Array Current Available and Average Required Versus Sun Angle at End of Life	4-V-47
4-V-22	Power Supply Subsystem Voltages and Currents at a 45-Degree Sun Angle at End of Life	4-V-48
4-V-23	ITOS Nickel Cadmium Battery, End-of-Discharge Voltage Versus Battery Charge-Discharge Cycles	4-V-50
4-V-24	Average Available Array Current and Average Shunt Limiter Current Versus Sun Angle for Beginning-of-Life Conditions	4-V-52
4-V-25	Power Supply Subsystem Voltages and Currents for 45-Degree Sun Angle at Beginning of Life	4-V-53
4-V-26	Solar Array Output and Load Demands Versus Sun Angle During Initial Orientation Maneuver	4-V-54
4-V-27	Solar Array Output During Initial Maneuver (Solar Panels Folded)	4-V-55
4-V-28	Typical ITOS Daytime Average Solar Array Output and Load Current Requirements	4-V-57
4-V-29	ITOS Eclipse Time Versus Sun Angle	4-V-59
4-V-30	Picofuse Time-Current Curves at 25°C	4-V-65
4-V-31	Baseplate Component Temperature Versus Sun Angle During Initial Orientation Maneuver	4-V-66
4-V-32	Baseplate Power Dissipation Versus Sun Angle During Initial Orientation Maneuver	4-V-67
4-V-33	Baseplate Power Dissipation Versus Sun Angle During Operational Mode	4-V-68
4-V-34	Battery Charge and Solar Array Current Telemetry Circuit, Schematic Diagram	4-V-71
4-V-35	Typical Voltage Telemetry Circuit, Schematic Diagram	4-V-73
4-V-36	Regulated Bus Voltage Telemetry Circuit, Schematic Diagram	4-V-74
4-V-37	Temperature Telemetry Circuit, Schematic Diagram	4-V-74
4-VI-1	AVCS Subsystem, Block Diagram	4-VI-3
4-VI-2	AVCS Subsystem, Timing Diagram	4-VI-5
4-VI-3	Operation of the Double-Bladed Focal Plane Shutter	4-VI-8
4-VI-4	Composite Video Signal	4-VI-10

LIST OF ILLUSTRATIONS (Continued)

Figure		Page
4-VI-5	AVCS Camera Sensor and Electronics, Modified Block Diagram	4-VI-13
4-VI-6	Hybrid Vidicon Tube	4-VI-18
4-VI-7	Equivalent Circuit of Vidicon Target, Schematic	4-VI-21
4-VI-8	Vidicon Signal Sequence Diagram	4-VI-22
4-VI-9	Video Clamp, Block Diagram	4-VI-24
4-VI-10	Video Signal With No Incident Light	4-VI-25
4-VI-11	Dark Current Pedestal	4-VI-25
4-VI-12	Vidicon Dark Current Sampling, Simplified Schematic	4-VI-26
4-VI-13	Clamp Circuit, Partial Schematic	4-VI-27
4-VI-14	Dark Current Sampling, Timing and Sequencing Diagram	4-VI-28
4-VI-15	Shading Correction Circuit, Block Diagram	4-VI-29
4-VI-16	Vertical Shading Components	4-VI-31
4-VI-17	Video Modulator Operation, Simplified Schematic	4-VI-32
4-VI-18	AVCS Tape Recorder Record/Playback Electronics, Block Diagram	4-VI-35
4-VI-19	AVCS Tape Recorder Drive and Control, Block Diagram	4-VI-36
4-VI-20	APT Subsystem, Block Diagram (One of Two Redundant Cameras)	4-VI-46
4-VI-21	APT Subsystem, Timing and Sequencing Diagram	4-VI-47
4-VI-22	Scanning Radiometer Subsystem, Block Diagram	4-VI-54
4-VI-23	SR Scan Projection	4-VI-55
4-VI-24	Scanning Radiometer and Electronics	4-VI-57
4-VI-25	IR and Visible Channel Signals	4-VI-58
4-VI-26	Scanning Radiometer Coverage (Altitude: 775 Nautical Miles)	4-VI-60
4-VI-27	Radiometer Scan Geometry	4-VI-62
4-VI-28	Orbital Conditions for Direct Radiometer Sun Scanning	4-VI-62
4-VI-29	Scanning Radiometer Block Diagram	4-VI-64
4-VI-30	Earth Atmosphere Radiation Absorption Bands	4-VI-65
4-VI-31	Typical IR Radiance Transfer Curve	4-VI-66
4-VI-32	Visible Channel Transfer Characteristics	4-VI-68
4-VI-33	SR Processor Block Diagram	4-VI-72
4-VI-34	SR Recorder Block Diagram	4-VI-75
4-VI-35	Power Converter Block Diagram	4-VI-81
4-VII-1	Secondary Sensor Subsystem, Block Diagram	4-VII-2
4-VII-2	Solar Proton Monitor, Detector Location Diagram	4-VII-4
4-VII-3	Tape Transport Mechanism, Simplified Diagram	4-VII-13
4-VII-4	Incremental Tape Recorder Electronics, Block Diagram	4-VII-16
4-VII-5	Stepper Drive Signal Phasing	4-VII-17
4-VIII-1	Command Subsystem, Block Diagram	4-VIII-3
4-VIII-2	Command Sequence Timing and Data Format	4-VIII-13
4-VIII-3	Command Decoder, Block Diagram	4-VIII-15

Figure		Page
4-VIII-4	Programmer, Block Diagram	4-VIII-27
4-VIII-5	Camera and Scanning Radiometer, Timing Diagram	4-VIII-31
4-VIII-6	AVCS and APT Camera Control, Timing Diagram	4-VIII-32
4-VIII-7	Proportional QOMAC Cycle	4-VIII-37
4-VIII-8	AVCS Camera Selection Circuits	4-VIII-43
4-VIII-9	AVCS Tape Recorder Selection Circuits	4-VIII-44
4-VIII-10	S-Band Transmitter and Multiplexer Selection Circuits	4-VIII-45
4-VIII-11	APT Camera Selection Circuit	4-VIII-47
4-VIII-12	SR Selection Circuits	4-VIII-48
4-VIII-13	SR Motor Selection Circuits	4-VIII-49
4-VIII-14	SR Visible and IR Channel Selection Circuits	4-VIII-50
4-VIII-15	SR Visible and IR Channel Calibration Selection Circuits	4-VIII-51
4-VIII-16	SR Recorder Selection Circuits	4-VIII-53
4-VIII-17	RT Transmitter Selection Circuits	4-VIII-55
4-VIII-18	Programmer Selection Circuits	4-VIII-56
4-VIII-19	TBU Selection Circuits	4-VIII-57
4-VIII-20	Beacon Selection Circuits	4-VIII-58
4-VIII-21	Telemetry Commutator Selection Circuits	4-VIII-59
4-VIII-22	Acquisition Mode Telemetry Selection Circuits	4-VIII-61
4-VIII-23	Time Base Generator, Block Diagram	4-VIII-64
4-VIII-24	Time Base Generator, Typical Interface Circuits	4-VIII-65
4-VIII-25	Time Code Generator, Block Diagram	4-VIII-67
4-VIII-26	Data Format of the RZ (Three-Level) Output of the Time Code Generator	4-VIII-68
4-IX-1	ITOS Ground Station Configuration	4-IX-3
4-IX-2	Command and Beacon Telemetry Link, Block Diagram	4-IX-5
4-IX-3	Quadrupole Command Antenna Contour Pattern, Solar Panels Folded (Linear Horizontal Transmission, Scale Factor 2.5:1, 371 MHz, 3-db Isotropic Level)	4-IX-9
4-IX-4	Quadrupole Command Antenna Contour Pattern Solar Panels Deployed (Horizontal Transmission; Scale Factor 2.5:1, 371 MHz, 6-db Isotropic Level, Preliminary Data)	4-IX-11
4-IX-5	Relation of the ITOS Spacecraft to the Spherical Coordinate System as Used in Antenna Pattern Measurements	4-IX-13
4-IX-6	Cosmic Noise Temperature Versus Frequency	4-IX-27
4-IX-7	Block Diagram of the Beacon/Telemetry Link	4-IX-31
4-IX-8	Beacon Antenna Pattern, Solar Panels Stowed (Vertical Polarization, Scale Factor 2.5:1, 342 MHz, 2.7-db Reference Level)	4-IX-37
4-IX-9	Beacon Antenna Pattern, Solar Panels Deployed (Vertical Polarization, Scale Factor 2.5:1, 342 MHz, 2.7-db Reference Level)	4-IX-39

Figure		Page
4-IX-10	Beacon Antenna Pattern, Solar Panels Deployed (Vertical Polarization, Scale Factor 2.5:1, 342 MHz, 3-db Reference Level)	4-IX-41
4-IX-11	Beacon Antenna Pattern, Solar Panels Deployed (Horizontal Polarization, Scale Factor 2.5:1, 342 MHz, 3-db Reference Level)	4-IX-43
4-IX-12	Composite Subcarrier Spectrum of Demodulated Beacon and Telemetry Baseband	4-IX-52
4-IX-13	Real-Time Transmission Link, Block Diagram	4-IX-67
4-IX-14	Real-Time IR and Visible Channel Output Signals from SR Processor	4-IX-69
4-IX-15	Real-Time Transmitter, Block Diagram	4-IX-70
4-IX-16	Baseline Real-Time Video Link Antenna	4-IX-72
4-IX-17	Real-Time Antenna Gain (Right-Circular Polarization, Scale Factor 2.5:1, 344 MHz, Preliminary Data)	4-IX-73
4-IX-18	Playback Video Link, Block Diagram	4-IX-82
4-IX-19	Dual Multiplexer, Basic Signal Interfaces	4-IX-87
4-IX-20	S-Band Antenna Radiation Pattern	4-IX-89
4-IX-21	Baseline-S-Band Antenna for ITOS	4-IX-91
4-IX-22	Baseline Coupling Network for S-Band Antenna Printed on a Stripline Board	4-IX-92
4-X-1	Spacecraft Test Sequence Diagram	4-X-3
4-X-2	Preliminary Flight Spacecraft Test and Calibration Plan	4-X-9
4-X-3	Preliminary Design Verification Test Program	4-X-19
	PART 5. GROUND STATION EQUIPMENT	
5-I-1	The ITOS System	5-I-2
5-III-1	Data Handling at CDA Stations, Block Diagram	5-III-7
5-III-2	ITOS Demultiplexer, Modified Block Diagram	5-III-9
5-III-3	Command Word Format	5-III-19
5-III-4	Beacon Data Handling, Block Diagram	5-III-21
5-III-5	Ground Processing of AVCS Signal, Modified Block Diagram	5-III-26
5-III-6	Ground Processing of Scanning Radiometer Signal, Modified Block Diagram	5-III-27
5-III-7	Ground Processing of Secondary Sensor Signals, Modified Block Diagram	5-III-28
5-IV-1	TOS Wideband Communications System	5-IV-2
5-IV-2	TOS Wideband Channel Allocations	5-IV-3
5-IV-3	Long Line Transmission Time for One and Two Orbits	5-IV-4

LIST OF ILLUSTRATIONS (Continued)

Figure		Page
A-1	Comparison of Ionization Damage Profile TOS Orbit	A-3
A-2	ITOS Dose Margin Referred to 1968 Environment for Ionization Damage	A-6
A-3	Comparison of Bulk Damage Profiles TOS Orbit	A-10
A-4	ITOS Dose Margin Referred to 1968 Environment for Bulk Damage	A-11
A-5	Limiting Threshold Doses for 1968 Environment Dose Tolerance Factor = 3 Ionization Damage	A-15
A-6	Proposed Minimum Threshold Ionization Doses in 1968 Environment	A-19
A-7	Proposed Minimum Threshold Bulk Damage Doses in 1968 Environment	A-20
A-8	ITOS Shielding Requirements for 1962 Environment Ionization Damage	A-22
A-9	ITOS Protection Against Bulk Damage from Nuclear Burst Effects	A-25
B-1	Attitude and Orbit Geometry	B-9
C-1	Planar Array	C-7
C-2	Canted Array	C-7
C-3	Dimensional Analysis of Planar Array	C-9
C-4	Dimensional Analysis of Canted Array	C-9
C-5	Relative Power versus Sun Angle Rotation about Spin Axis (β)	C-15
C-6	Nutation Cone Angles Due to Transverse Momentum	C-19
D-1	Yo-Yo Analysis Geometry	D-2
E-1	Spacecraft Nutation about Total Momentum Vector	E-3
E-2	Coupling Factor versus Damper Parameters	E-4
F-1	Seasonal Variation of Sun Angle for Various O'Clock Angles	F-2
F-2	Illumination Geometry on Celestial Sphere	F-3
G-1	Pitch Offset Versus Orbit Eccentricity, Showing Distance Ratio r_p/r_a	G-2
G-2	Momentum Change Versus Torquing Period	G-5
G-3	Ground Contact Pattern, Perigee at 65 Degrees North	G-6
G-4	Time in View, Perigee at 65 Degrees North	G-6
G-5	Ground Contact Times for 26 Revolutions, Perigee at 65 Degrees North	G-7
G-6	Ground Contact Pattern, Apogee at 65 Degrees North	G-8
G-7	Time in View, Apogee at 65 Degrees North	G-8

LIST OF ILLUSTRATIONS (Continued)

Figure		Page
G-8	Ground Contact Times for 26 Revolutions, Apogee at 65 Degrees North	G-10
G-9	Relationship of Elliptical Orbit to the Radiation Belt	G-13
H-1	Structure Thermal Model for 127-Body Analysis	H-4
H-2	Component Thermal Model for 127-Body Analysis	H-5
H-3	Predicted Flight Temperatures for Baseplate Equipment: Nodes 1 through 5	H-6
H-4	Predicted Flight Temperatures for Baseplate Equipment: Nodes 14 and 6 through 9	H-7
H-5	Predicted Flight Temperatures for Baseplate Equipment: Nodes 10 through 13	H-8
H-6	Predicted Flight Temperatures for Baseplate Equipment: Nodes 15 through 20	H-9
H-7	Predicted Flight Temperatures for APT Panel Equipment: Nodes 21 through 29	H-10
H-8	Predicted Flight Temperatures for AVCS Panel Equipment: Nodes 40 and 30 through 36	H-11
H-9	Predicted Flight Temperatures for AVCS Panel Equipment: Nodes 41, 42, and 37 through 39	H-12
H-10	Predicted Active Thermal Control Flap Angle Characteristics	H-13

LIST OF TABLES

Table		Page
	PART 2. SYSTEM FUNCTIONAL DESCRIPTION	
2-I-1.	Spacecraft Subsystem Complement	2-I-24
2-II-1	Command Link Characteristics	2-II-1
2-II-2	Beacon Link Characteristics	2-II-2
2-II-3	Real-Time Link Characteristics	2-II-3
2-II-4	S-Band Link Characteristics	2-II-4
2-III-1	Spacecraft/APT Ground Station Data Link Characteristics	2-III-1
	PART 4. SPACECRAFT DESIGN	
4-II-1	Estimated Weight of ITOS Spacecraft	4-II-34
4-II-2	Stress Critical Margins of Safety for Spacecraft Structure	4-II-40
4-II-3	Stress Critical Margins of Safety for Solar Panels	4-II-42
4-III-1	Radiator Area Values for Constant 20° Temperature of Side and Baseplate	4-III-24
4-III-2	60-Degree Orbit Angle Injection Case Transient Temperature Study at 30-Degree Sun Angle	4-III-32
4-III-3	Component Mounting Surface Temperatures During Operational Mode	4-III-34
4-III-4	Component Mounting Surface Temperatures for ATC Flap Failure Cases	4-III-35
4-IV-1	Damper Time Constants during Various Modes	4-IV-17
4-IV-2	ITOS QOMAC Coil Parameters	4-IV-37
4-IV-3	ITOS MBC Coil Operating Parameters	4-IV-45
4-IV-4	ITOS MBC Coil Physical Parameters	4-IV-49
4-IV-5	ITOS Momentum Coil Parameters	4-IV-49
4-IV-6	Pitch Axis Control Loop Electronic Specifications	4-IV-68
4-IV-7	Pitch Axis Control Loop Power Requirements	4-IV-70
4-IV-8	Thermal Vacuum Tests Since October 13, 1964 (No Component Failures)	4-IV-85
4-IV-9	Random Roll Error Contributions	4-IV-93
4-IV-10	Bias Roll Error Contributions	4-IV-93
4-IV-11	Principal-Point Maximum Roll Error Contributions	4-IV-94
4-IV-12	Pitch Error Contributions	4-IV-95
4-IV-13	Initial Orientation Maneuver	4-IV-102
4-IV-14	Operational Power Requirements	4-IV-102

LIST OF TABLES (Continued)

Table		Page
4-V-1	Power Supply Subsystem Loads for One Orbit	4-V-2
4-V-2	Power Supply Subsystem	4-V-5
4-V-3	Power Supply Subsystem Loads During Preoperational Mode	4-V-6
4-V-4	Summary of ITOS Power Supply Subsystem Parameters	4-V-8
4-V-5	Solar Cell Characteristics	4-V-19
4-V-6	Solar Panel Weight Breakdown	4-V-20
4-V-7	Estimated Power Dissipation in the ITOS Spacecraft	4-V-38
4-V-8	Alternative Methods of Reducing Power Dissipation	4-V-39
4-V-9	Comparison of Magnetic Amplifier and DC Amplifier Current Telemetry	4-V-41
4-V-10	Computer Program Input Data for Worst-Case End-of-Life Analysis	4-V-43
4-V-11	Required Mission for ITOS Batteries	4-V-49
4-V-12	Changes in Computer Program Data for Beginning-of-Life Analysis	4-V-51
4-V-13	Steady-State Array Temperatures During Initial Orientation Maneuver	4-V-54
4-V-14	Probability of Battery Survival (For 6 Months and 1 Year)	4-V-62
4-V-15	Power Supply Subsystem Telemetry List	4-V-69
4-VI-1	AVCS Camera and Electronics Characteristics	4-VI-16
4-VI-2	AVCS Camera and Electronics and Spacecraft Interface Signals	4-VI-17
4-VI-3	AVCS Tape Recorder Characteristics	4-VI-37
4-VI-4	AVCS Tape Recorder and Spacecraft Interface Signals	4-VI-39
4-VI-5	APT Subsystem and Spacecraft Interface Signals	4-VI-50
4-VI-6	APT Subsystem Characteristics	4-VI-51
4-VI-7	Scanning Radiometer Subsystem Parameters	4-VI-53
4-VI-8	SR Processor Input and Output Functions	4-VI-69
4-VI-9	SR Recorder Characteristics	4-VI-73
4-VII-1	Solar Proton Monitor, Detector Characteristics	4-VII-3
4-VII-2	DFC Output Characteristics	4-VII-7
4-VII-3	Data Frame Format	4-VII-8
4-VII-4	Digital Telemetry Points	4-VII-10
4-VII-5	Characteristics of Voltage Controlled Oscillators	4-VII-12
4-VIII-1	ITOS Commands	4-VIII-4
4-VIII-2	Format of T_o Word	4-VIII-24
4-VIII-3	Format of Rephasing Word	4-VIII-25
4-VIII-4	Format of the QOMAC Program Word	4-VIII-30

LIST OF TABLES (Continued)

Table		Page
4-IX-1	Summary of ITOS Communications Links	4-IX-2
4-IX-2	Command Receiver Specifications	4-IX-16
4-IX-3	Path Losses as a Function of Elevation Angle for the 148-MHz Command Link	4-IX-18
4-IX-4	Worst-Case Link Calculation	4-IX-19
4-IX-5	Command Link RF Margin Computation for Three Different Antennas	4-IX-20
4-IX-6	Interference Levels at the Command Receiver Port	4-IX-24
4-IX-7	Subcarrier-to-Noise Ratios at RF Power Threshold	4-IX-29
4-IX-8	Beacon Transmitter-Characteristics	4-IX-45
4-IX-9	Dual SCO Assembly Characteristics	4-IX-46
4-IX-10	Telemetry Commutator Characteristics	4-IX-48
4-IX-11	CDA Ground Station Parameters (Beacon Reception)	4-IX-52
4-IX-12	Subcarrier Noise Power Computations	4-IX-53
4-IX-13	Summary of Link Calculations	4-IX-54
4-IX-14	Worst-Case Link Calculation for 3.9-kHz Channel	4-IX-55
4-IX-15	Worst-Case Link Calculation for 2.3-kHz Channel	4-IX-56
4-IX-16	Link Calculation for Carrier Tracking	4-IX-57
4-IX-17	S/N Contribution by the Long Lines	4-IX-58
4-IX-18	Assignment of Telemetry Points for ITOS	4-IX-58
4-IX-19	Baseline Antenna Characteristics	4-IX-71
4-IX-20	Real-Time Link Parameters (Field Stations)	4-IX-76
4-IX-21	S-Band Transmitter Specifications	4-IX-90
4-IX-22	S-Band Antenna Specifications	4-IX-94
4-IX-23	Coupling Network Specifications	4-IX-95
4-IX-24	Worst-Case S-Band Link Calculation	4-IX-95
4-IX-25	Variation of RF Margin with Elevation and Nadir Angles	4-IX-96
4-IX-26	RF Deviation Allotment; Subcarrier Signal-to-Noise Due to Line Along	4-IX-99
4-IX-27	Secondary Sensors Channel Characteristics	4-IX-102
4-X-1	Unit and Subsystem Vibration Test Conditions	4-X-5
4-X-2	Unit and Subsystem Thermal Vacuum Test Conditions	4-X-6
4-X-3	Camera and AVCS Tape Recorder Thermal Vacuum Test Conditions	4-X-6
4-X-4	Spacecraft Sinusoidal Vibration Test Conditions	4-X-11
4-X-5	Spacecraft Random Vibration Test Conditions	4-X-12
4-X-6	Spacecraft Thermal Vacuum Test Conditions	4-X-13

LIST OF TABLES (Continued)

Table		Page
	PART 5. GROUND STATION EQUIPMENT	
5-II-1	Long Line Subgroups	5-II-8
5-III-1	Control and Indicator Interface	5-III-3
5-III-2	Composite Subcarrier Signals	5-III-8
5-III-3	Track Allocations for Recorders A and B	5-III-12
5-III-4	Track Allocations for Recorders C and D	5-III-12
5-III-5	Signal Demodulator Characteristics	5-III-16
5-IV-1	Characteristics of TOS Wideband Data Channels	5-IV-3
5-VII-1	Equipment at the CDA Stations	5-VII-1
5-VII-2	Equipment at the AED Ground Station	5-VII-2
5-VII-3	Equipment at TOC and TEC/ITCC	5-VII-3
5-VII-4	Equipment in the GO/NO-GO Van	5-VII-4
5-VII-5	Equipment at AED Checkout Facility	5-VII-5
A-1	Estimates of Solar Array Degradation	A-13
C-1	Summary of Disturbances and Effects	C-2
C-2	Planar Array with No Compensating-Vanes	C-12
C-3	Solar Pressure Precession Rates for Canted and Vane Compensated Arrays	C-12
C-4	Normalized Average Energy per Orbit	C-16
C-5	Transverse Momentum Disturbances	C-21
F-1	Picture-Taking Capability and Sun Angle	F-4
G-1	Sensor Scan of Illuminated Earth as a Function of Zenith Angle and Sun Angle	G-3
G-2	Particle Flux Per Day for an Elliptical Orbit	G-15
G-3	ITOS Radiation Environment Comparison	G-17
G-4	ITOS Comparison of Dose Levels	G-19
G-5	Transistor Beta Loss Comparison	G-20

PART 4

SPACECRAFT DESIGN

SECTION I

INTRODUCTION

The Improved TOS (ITOS) spacecraft comprises eight functional subsystems. The relationships of the subsystems and their major components are shown in the block diagram in Figure 4-I-1. The AVCS, APT, and scanning radiometer subsystems, which are the primary environmental sensors, are discussed in Section VI of this part. The vehicle dynamics subsystem, the power supply subsystem, the secondary sensor subsystem, the command subsystem, and the communications subsystem are treated are Sections IV, V, VII, VIII, and IX. Beacon and telemetry functions as well as all RF functions are included in the communications subsystem. The structure of the spacecraft and its thermal control are discussed separately in Sections II and III, respectively, preceding the subsystem discussions. The spacecraft testing program is discussed in Section X.

The ITOS spacecraft differs markedly in appearance from previous TOS and TIROS spacecraft. The structure is a rectangular prism, with the subsystem components mounted on the baseplate and on the interior surfaces of two of the sides. The solar array consists of three panels folded at launch and deployed after the spacecraft has achieved orbit. The AVCS cameras, the APT cameras, and the scanning radiometers are located so that their fields of view are on the earthward side of the spacecraft. The secondary sensors are located so that the flat plate radiometer views the earth during orbital operation and the sensing elements of the solar proton monitor view open space. A momentum flywheel is mounted on the exterior surface of the baseplate. A "thermal fence" and a quadripole command and beacon antenna are located on the side of the spacecraft opposite the baseplate. The thermal fence is a variable absorptivity device that regulates the absorption of solar energy as a function of sun angle. Active thermal controllers are mounted on the exterior of the component mounting panels, a four-element S-band remote data antenna is located on the earthward side of the spacecraft, and a two-element real-time data antenna is attached to one of the solar panels.

The vehicle dynamics subsystem makes use of the TOS-proved techniques of magnetic bias control and quarter-orbit magnetic attitude torquing and incorporates a speed-controlled momentum flywheel to achieve the pitch control required for earth orientation of the primary environmental sensors. The "yo-yo" technique of despinning the spacecraft is used. Attitude sensing is accomplished by an acquisition horizon sensor, a digital solar aspect indicator, a pitch horizon sensor, and two roll horizon sensors. Liquid dampers are used to reduce spacecraft nutation. The power supply subsystem is similar to the TOS power supply subsystem, but has a greater capacity so that it can handle the increased demands of the three primary data subsystems. A greater solar cell area is created by an array of cells mounted on three deployable panels.

The APT and AVCS primary environmental sensor subsystems are very similar individually to the TOS APT and AVCS subsystems, with revised timing to provide 11 pictures from one of the APT cameras and 11 pictures from one of the AVCS cameras during the daylight portion of the orbit. Continuous infrared mapping is obtained during the nighttime portion of the orbit by the scanning radiometer (SR) subsystem. The APT and SR data are transmitted in real time for reception by APT ground stations around the world. SR data is also recorded in the satellite and transmitted with recorded AVCS data to CDA ground stations. The SR subsystem also produces a visible output, and either the visible or infrared output can be substituted for the APT output during subpoint daylight operations.

The secondary environmental sensors include the flat plate radiometer for obtaining earth heat balance data and the solar proton monitor for sensing proton flux levels at the satellite altitude. Secondary sensor data is recorded on an incremental tape recorder and played back for transmission to the CDA ground stations.

The command subsystem for ITOS is nearly identical to the TOS subsystem. However, it has an increased command capacity since the ITOS spacecraft has a greater number of functions than TOS. The communications subsystem consists of four data links which handle (1) commands transmitted to the satellite, (2) real-time environmental data transmitted from the satellite, (3) remote environmental data transmitted from the satellite, and (4) telemetry data transmitted from the satellite. The command, real-time, and beacon telemetry links have their counterparts in the TOS communications links, while the S-band

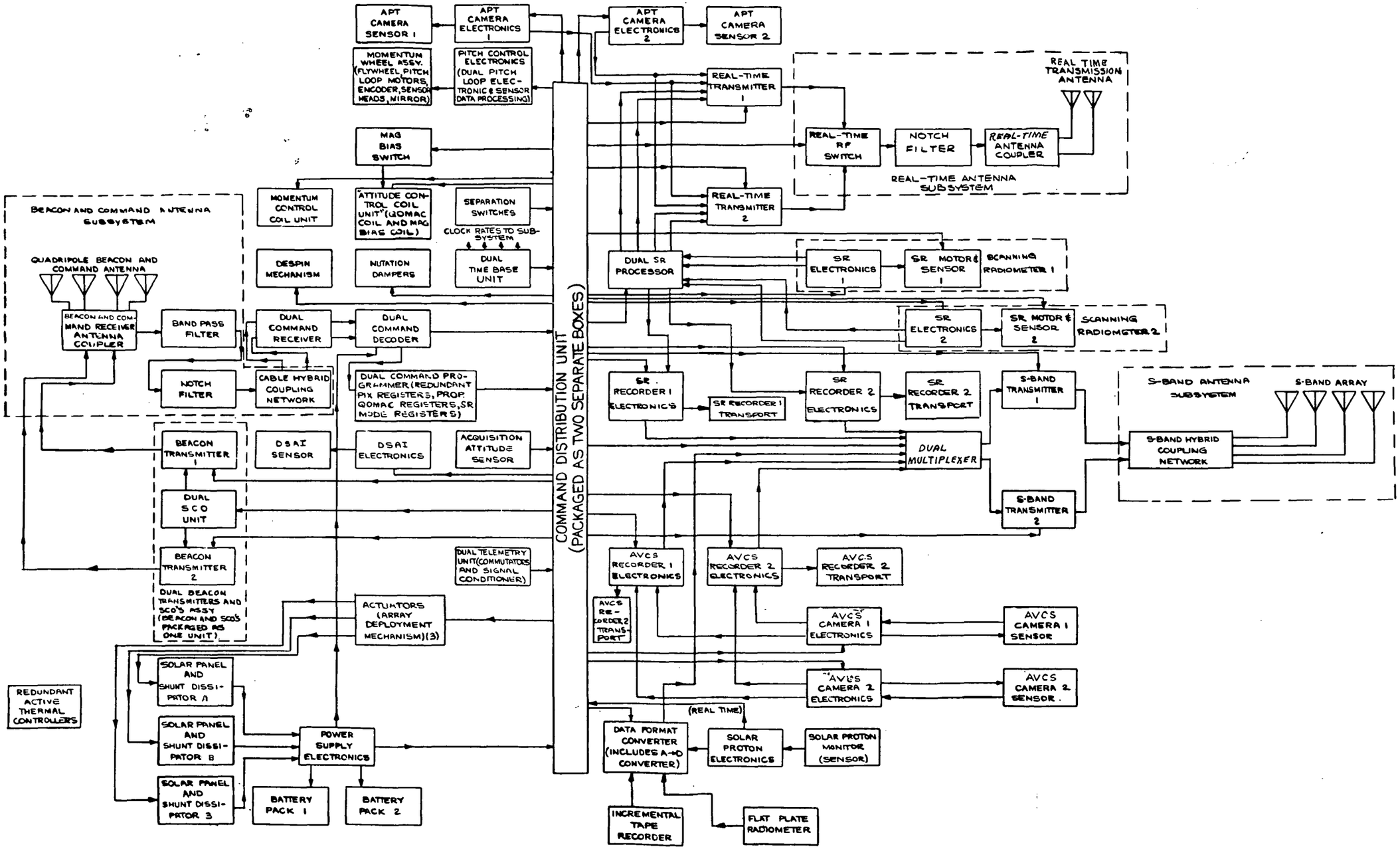

Figure 4-I-1. ITOS Spacecraft, Block Diagram

playback data link is new. The quadripole command and beacon antenna is similar to the TOS antenna, although the pattern is altered by the new spacecraft configuration. Both the remote data link antenna and the real-time data link antenna designs are new.

The ITOS spacecraft tests are conducted on four levels, with parallel testing of the primary environmental sensor subsystems. This plan assures standard performance at each stage of spacecraft subsystem assembly, integration, environmental exposure, and calibration.

SECTION II

MECHANICAL AND STRUCTURAL DESIGN*

A. GENERAL

As described in Part 2, the ITOS spacecraft (Figure 4-II-1) employs a boxlike structure, three sides of which are used to support most of the electronic equipment and sensors (see Figure 2-I-3 of Part 2). These component-carrying structural members are the baseplate and the two equipment panels (panels 2 and 4). The mechanical configurations of the baseplate assembly and one of the equipment panels are shown in Figure 4-II-2 and 4-II-3, respectively. The equipment panels are attached at their bottom edge to the baseplate and along their vertical edges to the structural earth-oriented and anti-earth access panels (panels 1 and 3) to form a box-like configuration, with the top of the structure stabilized by crossbraces. (See Figures 4-II-4, 4-II-5 and 4-II-6). The thermal fence and yo-yo despin mechanism are mounted to the top crossbracing.

The spacecraft structure is mounted on a separation ring (see Figures 2-I-5 and 4-II-7) which mates with the launch vehicle third-stage attach fitting. Three identical curved solar panels (see Figure 4-II-1) are hinged along the top edges of the equipment panels and the anti-earth access panel. All main structural components, with the exception of the solar panels, utilize a skin-and-stringer type design and are fabricated from riveted sheet aluminum. The solar panels are fabricated from bonded honeycomb material with three sheet metal reinforcing channels bonded to the panel underside (concave side).

B. DESIGN CONCEPT

1. General

In the mechanical design of the ITOS spacecraft, a major design goal was to provide a structure that would serve as a general equipment bus. This has been achieved in that the structure will accommodate a variable array of electronic and sensor equipment without

*Refer to Summary of Current Design Revisions Not Covered in this Report, following the Preface, for a brief description of revisions made since the cut-off date for this report.

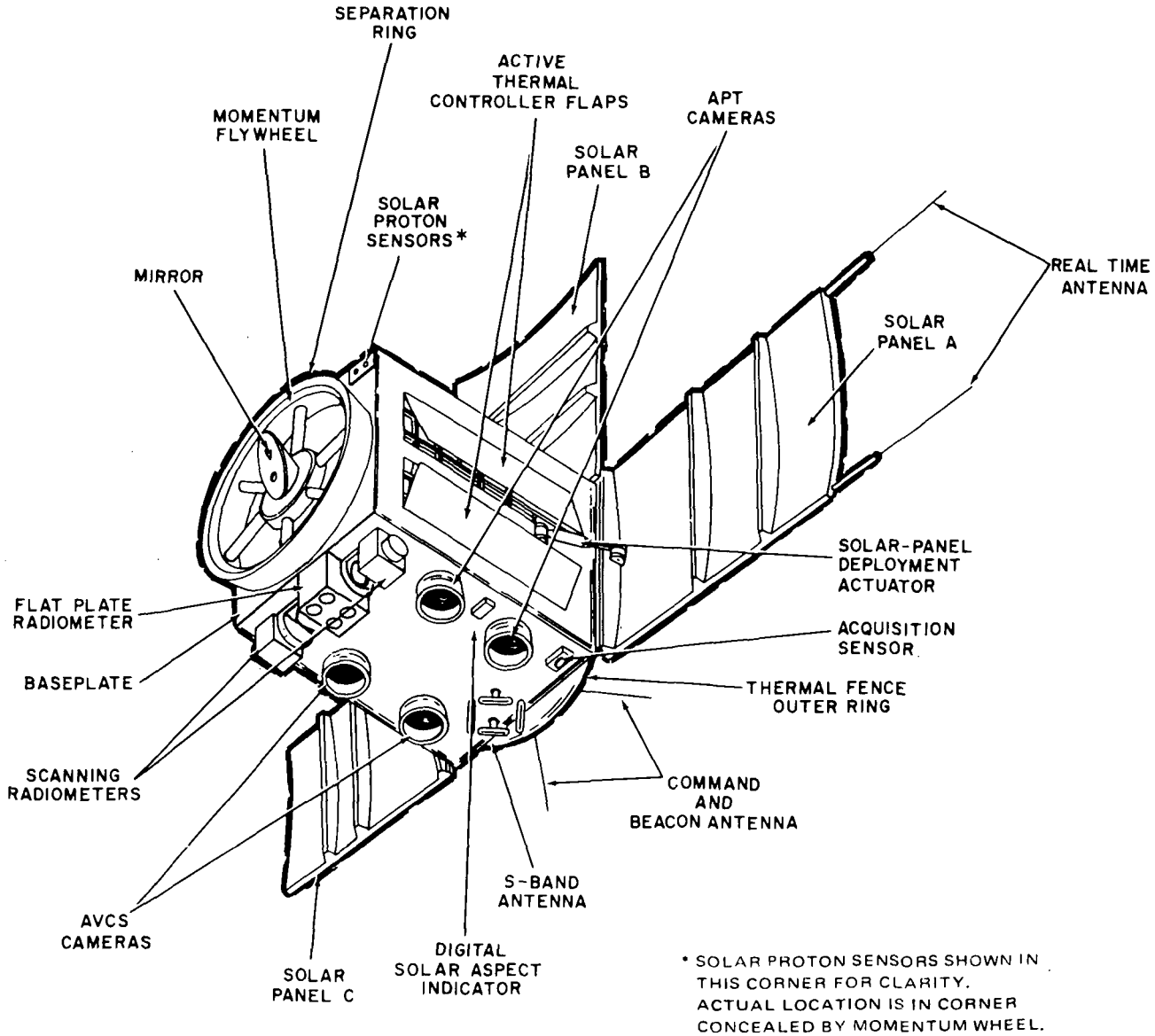

Figure 4-II-1. The ITOS Spacecraft

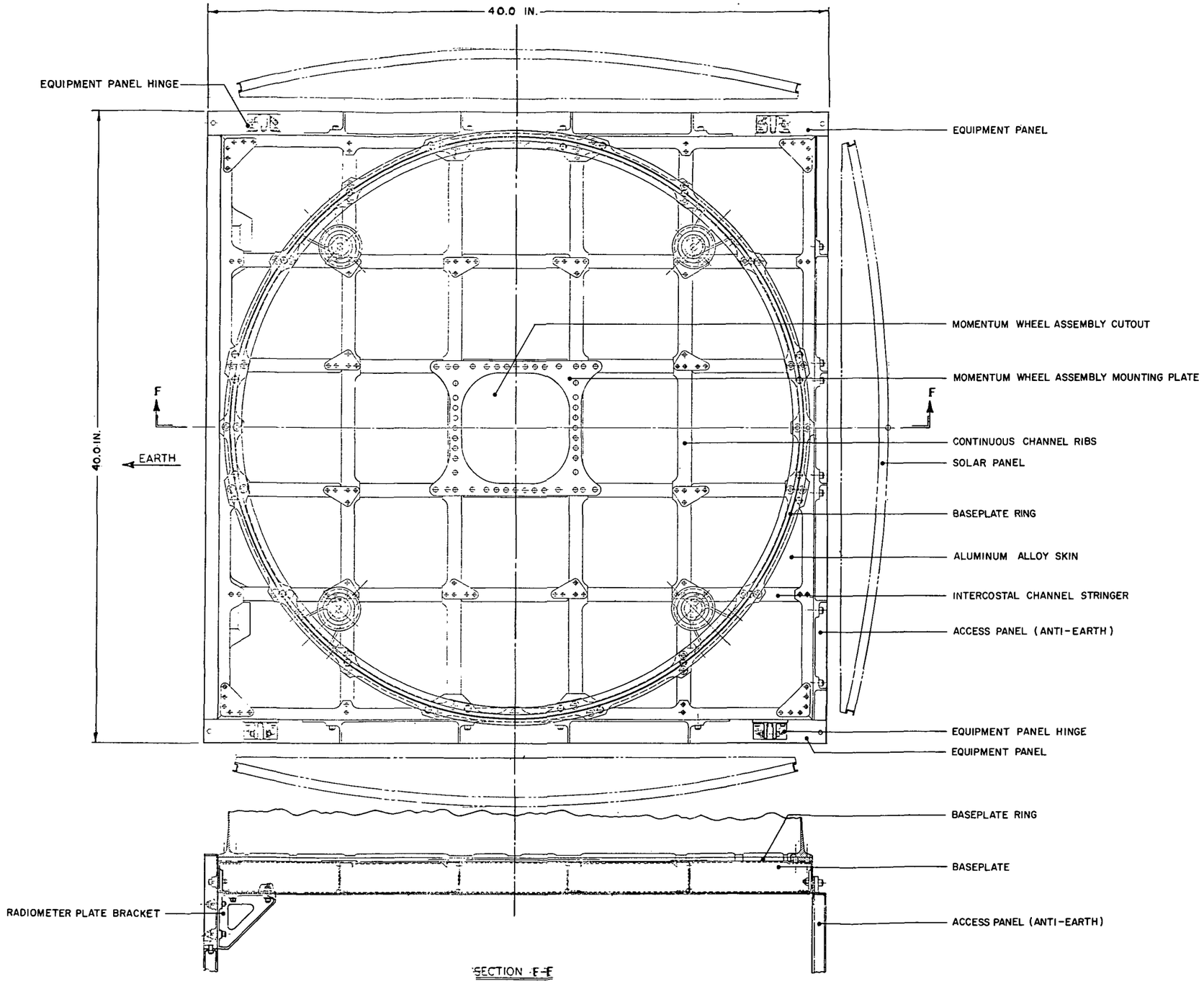

Figure 4-II-2. Baseplate Assembly

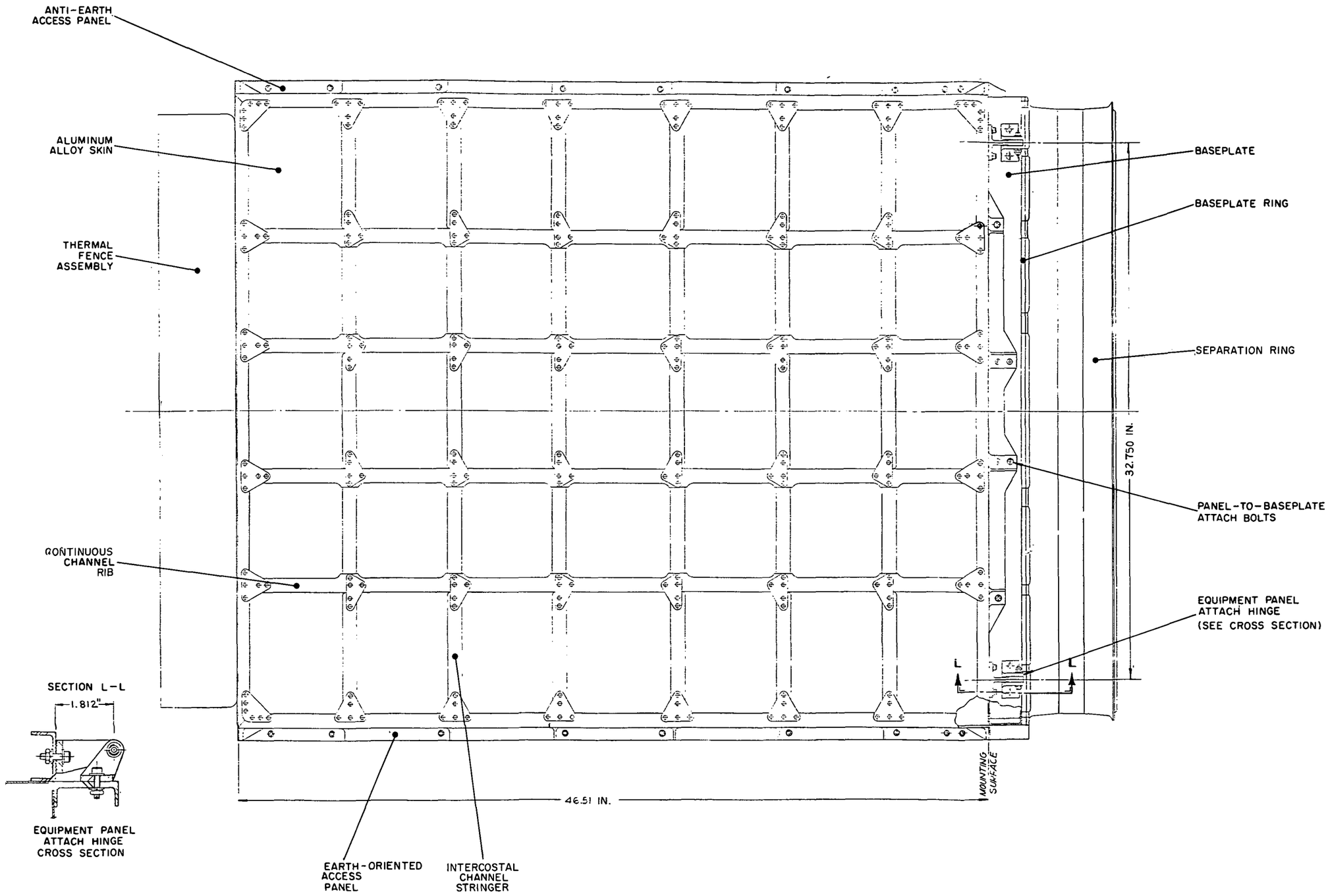

Figure 4-II-3. Equipment-Carrying Panel

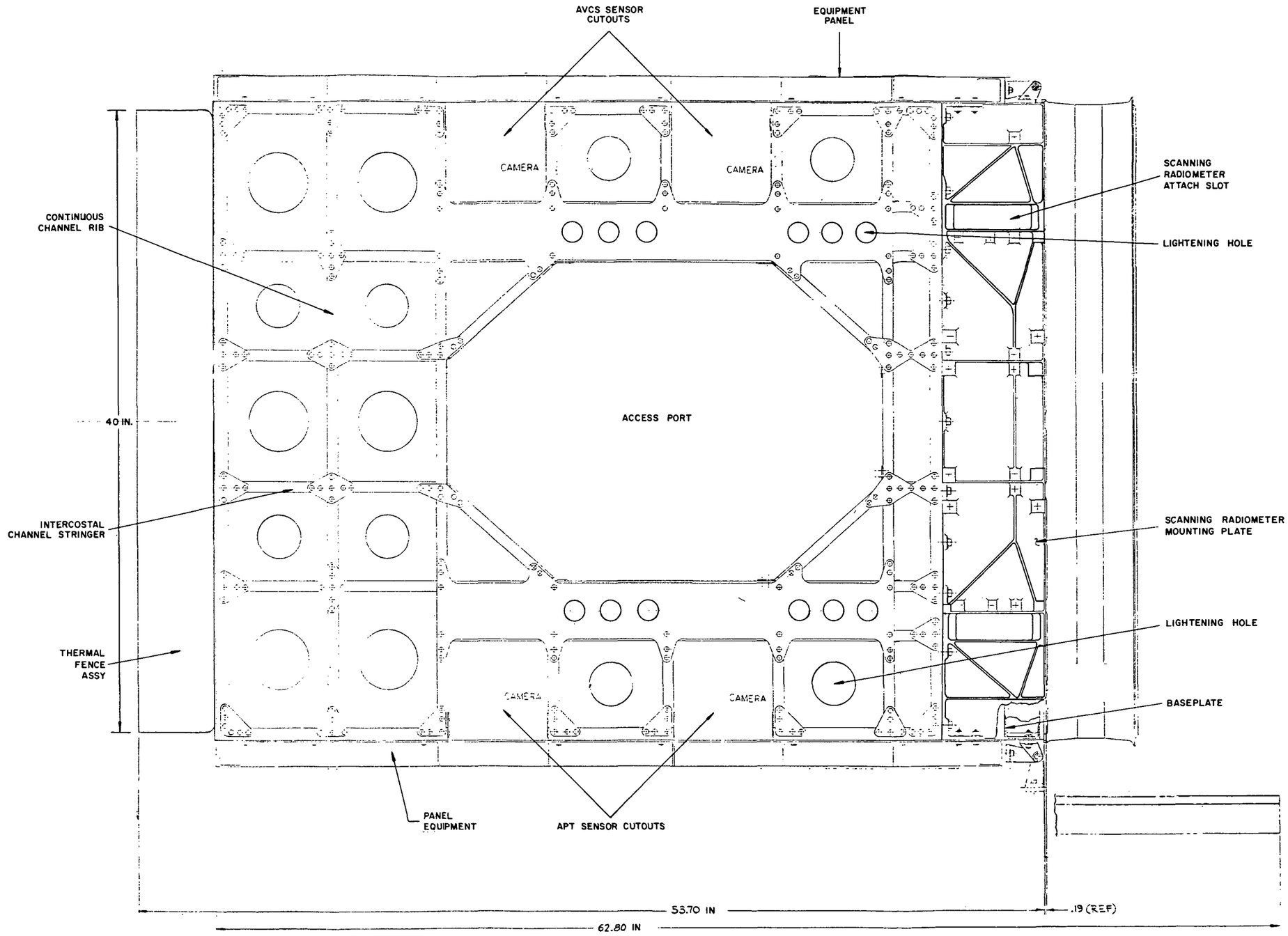

Figure 4-II-4. Earth-Oriented Access Panel

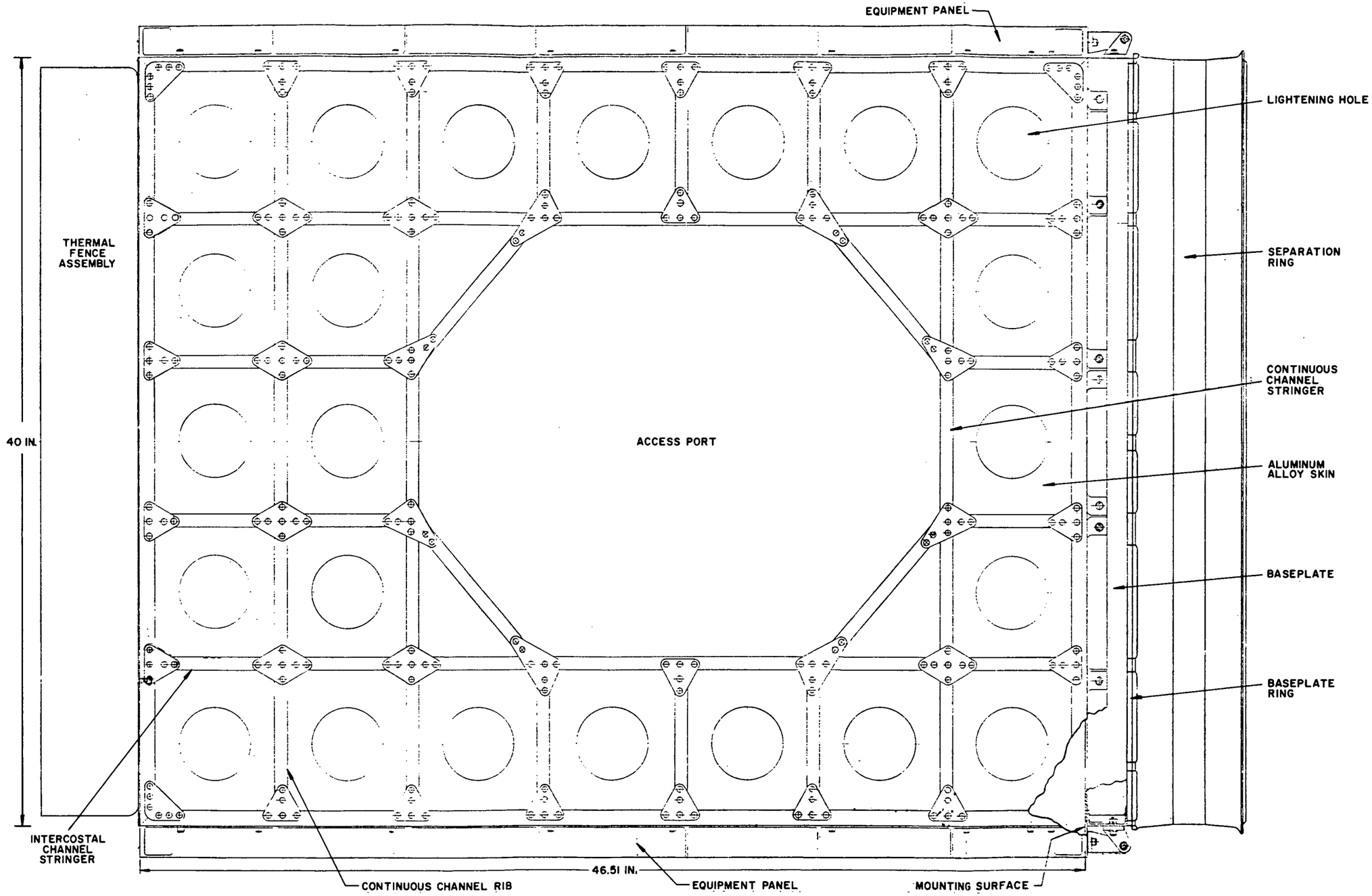

Figure 4-II-5. Anti-Earth Access Panel

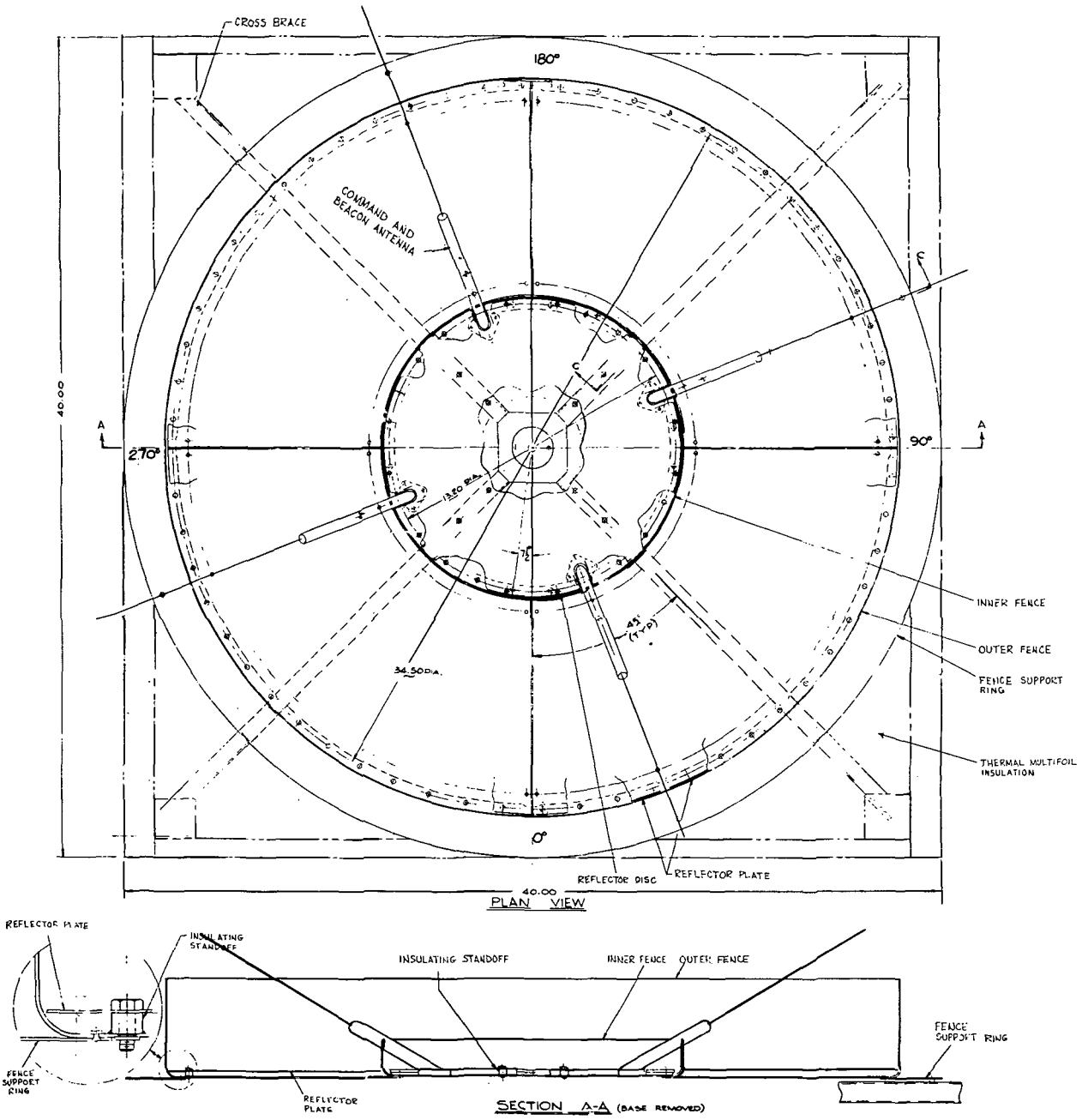

Figure 4-II-6. Top Assembly (Panel V)

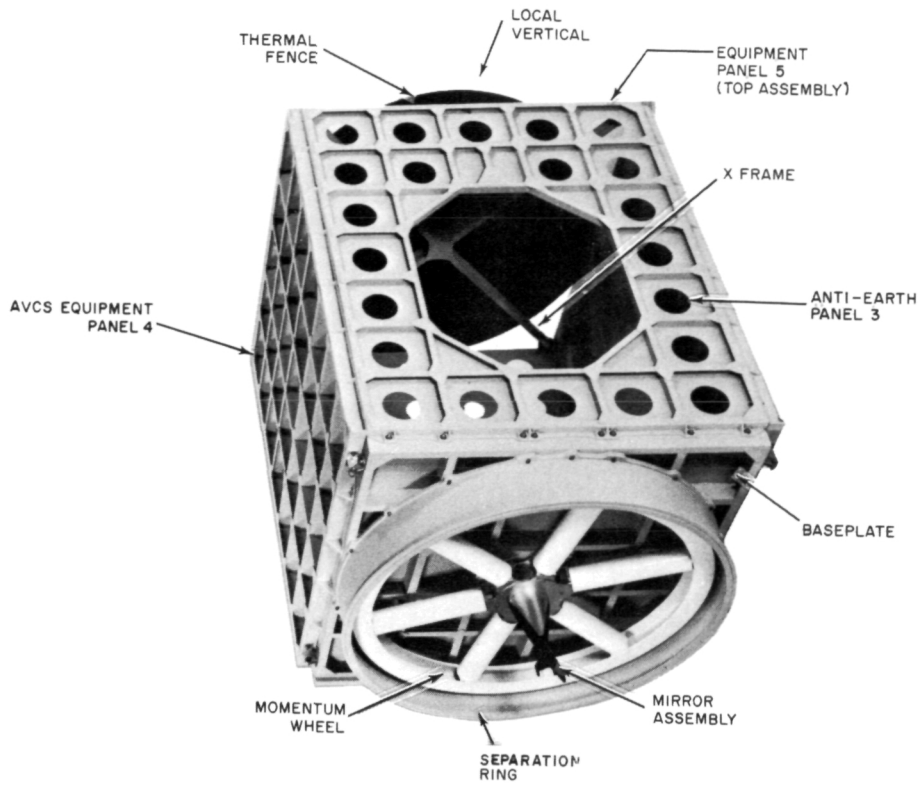

Figure 4-II-7. ITOS Basic Structure (Without Solar Panels and Antenna), Shown Mounted on Separation Ring

major modification. Accessibility during spacecraft integration is maximized by hinging the equipment-carrying panels to the baseplate. The equipment panels can be folded down into a coplanar arrangement with the baseplate so that integration of the electronic components can be performed on a totally flat and easily accessible work area. (See Figures 4-II-8 and 4-II-9.) The numerous components and subsystems can be electrically tested in this "open-spacecraft" configuration. When the structure is in the assembled configuration, the large cutouts in the access panels permit component replacement or repair without disassembly of the structure.

The ITOS spacecraft is capable of supporting a total weight of 720 pounds. The design of the structure is based on the assumptions that uniformly distributed static loads will be applied to the equipment panels and the baseplate, and that each equipment panel will carry 30 percent of the total component weight, while the baseplate will support 40 percent. During the design study phase, the primary loads induced in the structure by the critical sinusoidal and random vibrations encountered during the launch phase were analyzed; the secondary or

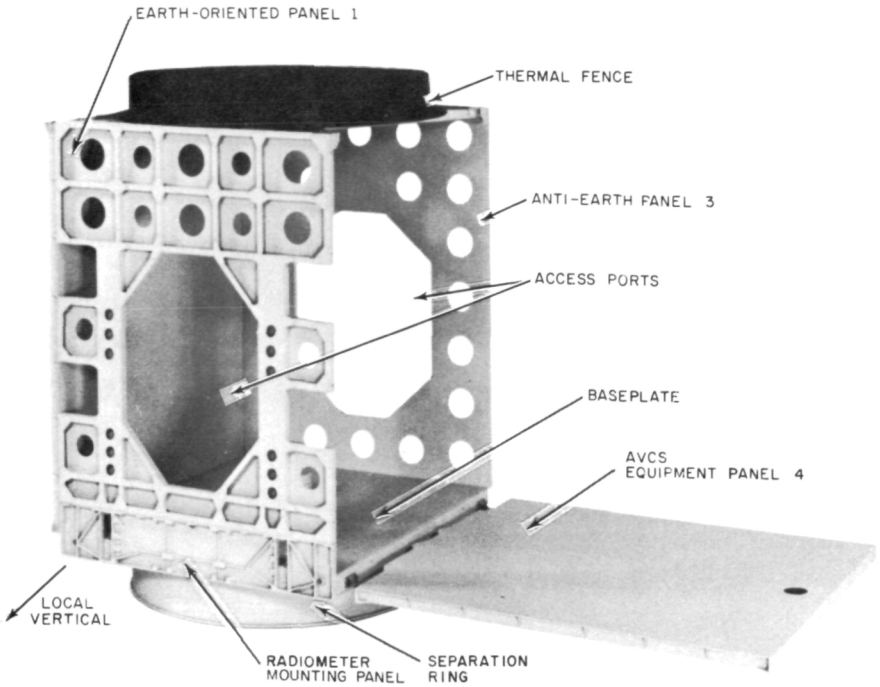

Figure 4-II-8. ITOS Basic Structure, Showing Panel Access Ports (Cutouts) and Hinged AVCS Equipment Panel Opened

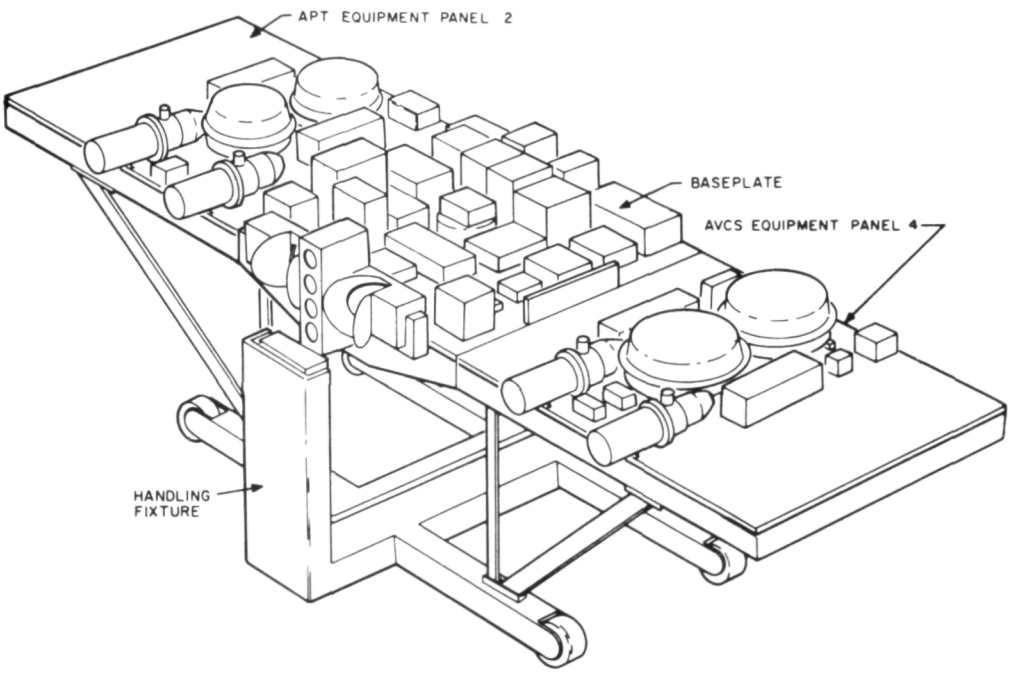

Figure 4-II-9. Spacecraft Component Integration Configuration

local loads induced in the structure by the loading of the actual subsystem configuration during vibration will be investigated when that configuration has been finalized. High local stresses induced by component loading will require that reinforcing brackets be added to the underside of the basic structure. The actual number, sizes, and locations of these brackets will be unique for each spacecraft mission.

2. Mechanical Alignment

The main structural components, such as the baseplate, the equipment panels, and the access panels, are designed to achieve and maintain squareness and parallelism of the structure. Accurate fixture jigs achieve the necessary tolerances of the assembled structure, and the use of body-bound bolts maintains the repeatability of alignment. There is no weight penalty for this alignment control feature.

A small annular ring, the baseplate ring (see Figure 4-II-2), is permanently fastened to the rib structure of the baseplate to provide an interface for attaching the spacecraft to the separation ring.

Final machining of the baseplate ring after attachment to the baseplate and the use of close-tolerance bolts at the interface of the baseplate ring and the separation ring achieve and maintain control of the alignment of the spacecraft with the launch vehicle. The mating surface of the baseplate ring will be perpendicular to the spin (pitch) axis within 0.01 degree, and flat to 0.005 inch TIR.* The upper and lower mating surfaces of the separation ring will be parallel and flat within 0.005 inch TIR.

The mounting plate for the momentum wheel assembly will be machined perpendicular to the pitch axis within 0.05 degree and flat to 0.005 inch TIR. This maintains the total non-perpendicularity from the separation ring mating surface to the mounting surface of the momentum wheel assembly within the 0.1 degree of the system requirement for alignment. The lower mating surface of the separation ring can therefore be used as a reference surface for momentum wheel assembly and camera sensor alignment procedures when the separation ring is bolted to the baseplate ring.

---

* TIR - Total indicator runout.

Close control of the camera and sensor mounting surfaces (to 0.03 inch TIR) will minimize the number of shims required for the final alignment of the cameras and sensors. The use of body-bound bolts, to join the major assemblies of the structure, will maintain alignment during environmental tests and the launch environment.

3. Component Accessibility

The method of integrating electronic components into the spacecraft structure was discussed previously and is illustrated in Figure 4-II-9. As shown in Figures 4-II-3 and 4-II-8, the equipment panels are equipped with removable hinges for attaching to the baseplate and, when in the folded-down position, are coplanar with the baseplate. The integration and initial electrical testing of subsystems are performed while the structure is in this configuration, with excellent accessibility provided to all subsystem components during these operations. When the structure is assembled to its final configuration with all side panels in place, access to the interior of the spacecraft is provided through the large central cutout in the earth-oriented and anti-earth access panels. The access holes are approximately 27 by 25.5 inches in the anti-earth panel and 18.5 by 26.5 inches in the earth-oriented panel, and are thus large enough so that the electronic equipment can be repaired or removed from the spacecraft without disassembly of the structure. (Two men can reach into the assembled spacecraft at the same time through the two access panels.) Since no subsystem component will be more than 20 inches from the access holes, inspection during environmental tests can be made without disturbing the spacecraft structure.

The nutation dampers and momentum control coil are mounted on the exterior of the equipment panels, and accessibility to these elements will be no problem; however, in the completely assembled spacecraft, the solar panels would have to be deployed and the thermal blanket removed if inspection of the nutation damper were required.

4. Interchangeability

Two approaches to the application of interchangeability to the ITOS structure were considered. One approach was to make all major assemblies of the structure interchangeable. Due to cost, design, and fabrication considerations, and electronic component failure

possibilities and possible extensive physical damage to major structural assemblies, a compromise philosophy of interchangeability was adopted.

The equipment panels (panels 2 and 4) were designed for interchangeability because most of the primary data equipment is located on these panels. Experience has shown that technical difficulties are more probable with primary data electronic equipment than with the electronic equipment of support subsystems. A failure within electronic equipment mounted to one of the equipment panels might dictate that it would be more economical, from a schedule standpoint, to replace a complete panel with its full complement of electronic components than to repair or replace the individual failed electronic unit. For much the same reason, each solar panel is made identical and, therefore, interchangeable.

The thermal fence is also interchangeable since all crossbraces (panel 5), on which the thermal fence is mounted, are jig-drilled with the same fixture. Other major structural assemblies, such as the baseplate, access panels, separation ring, and crossbrace assembly, are interchangeable with minimum rework. If necessary, a baseplate or access panel replacement could be accomplished by placing it in the structure assembly and drilling the required mounting holes for the equipment panels using the accurate jig and fixtures.

The means and methods of providing interchangeability are discussed in more detail in Paragraph D, Fabrication and Assembly.

C. MAJOR STRUCTURAL COMPONENTS

The major structural components of the ITOS spacecraft are the baseplate, equipment panels (2), access panels (2), and the top crossbracing structure. These components are illustrated in Figures 4-II-2 through 4-II-6. In addition, the separation ring (for mating the spacecraft to the launch vehicle third-stage attach fitting) performs an auxiliary structural function in that most of the structural loads encountered during the launch phase are applied to this ring, which remains attached to the spacecraft after third-stage separation.

1. Separation Ring

The separation ring forms an interstage between the spacecraft baseplate and the launch vehicle third-stage attach fitting, as shown in the spacecraft compatibility diagram, Figure 2-I-5 of Part 2. The ring will be fabricated from a forged ring of type 7075-T73 aluminum alloy and then machined to final dimensions of approximately 38 inches outside diameter, 35.5 inches inside diameter, and 4.5 inches high. Type 7075-T73 aluminum was chosen to provide minimum weight since this material is 50 percent stronger in tensile yield strength than 6061-T6 aluminum and therefore permits a thinner cross section to be used. The separation ring design has no pilot diameter on the baseplate ring flange. Analysis has shown that the pilot diameter section would not withstand the shear loads imposed by the launch environment; to increase the section strength, more weight would be needed, and, therefore, from a weight economics standpoint, another means of carrying the shear load was necessary. In the present design, the shear loads will be carried by high strength, close tolerance bolts that join the baseplate ring to the separation ring. Alignment and concentricity control of the separation ring is also maintained by these bolts.

The outer wall of the cylindrical portion of the separation ring has a double taper. (See Figure 4-II-3.) The wall is thickest at the flanges and thinnest at the midpoint between the flanges. The taper is a compromise between weight and the stiffness that is necessary in the flange areas. The straight inner wall of the cylinder provides a convenient mounting for the four separation spring support assemblies and spring pad brackets and the separation switches. When attached to the baseplate, the separation ring will allow removal of the momentum wheel if the separation switch brackets and spring pad brackets are removed.

2. Baseplate

The baseplate assembly (Figure 4-II-2) is fabricated from sheet metal and machined components. The edge members of the baseplate are four machined 2024-T4 aluminum channels, with 0.09-inch-thick web and flanges. Bosses are located in the bolt-clamping areas, and machined clips are used to tie continuous channel ribs and intercostal channel stringers. The edge channels are joined together at the corners with type 6061-T6 aluminum

angle clips. The mounting plate for the momentum wheel assembly is machined from 0.19-inch-thick 2024-T4 aluminum plate and is riveted to the continuous channel ribs and intercostal channel stringers.

All continuous channel ribs are fabricated from 0.05-inch-thick, type 2024-0 aluminum and then heat-treated to the T4 condition. All intercostal channel stringers are fabricated from 0.05-inch-thick, type 7075-0 aluminum and then heat-treated to T6 condition. This procedure allows these parts to be fabricated while the material is easily workable and then maximum strength capabilities can be achieved through solution heat treatment and aging. The skin is 0.05-inch-thick, type 2024-T4 aluminum. The main gussets are 0.08-inch-thick, 7076-T6 aluminum, which is black anodized on the equipment mounting side for thermal reasons.

In the design of the baseplate, the continuous channel ribs are oriented in one direction and are continuous between the equipment panel mounting (edge) channels of the baseplate. This design aids thermal conductivity from the baseplate to the equipment panels since it reduces the number of joints between the electronic equipment located on the baseplate and the active thermal controllers located on the equipment panels. The continuous ribs also provide more efficient support for the equipment panels and momentum wheel assembly, which is the heaviest unit on the baseplate. The intercostal channel stringers are riveted between the continuous channel ribs and run perpendicular to them. Angle clips of the same material are used at the joint because bending the intercostal end 90 degrees to form a riveting area may cause rib distortion.

The baseplate skin is riveted to the edge channels, ribs, and intercostal stringers. The skin and intercostal stringers will be countersunk to accept the flathead rivets and provide a flat (within 0.03 inch TIR) surface for mounting electronic equipment. Gussets are riveted at all intersections of structural members of the baseplate on the lower side. A ring which joins the separation ring to the baseplate is riveted to the ribs, intercostals, and edge members.

3. Equipment Panels

The equipment mounting panels (panels 2 and 4), like the baseplate, are fabricated from sheet metal and have machined components around their parameters. Continuous ribs and intercostal stringers make up an "egg-crate" portion within the edge members, and the skin serves as the mounting surface for electronic equipment. The edge members are machined, with 0. 09-inch-thick web and flange, from type 2024-T4 aluminum. A cross section of these members is shown in Figure 4-II-10.

The continuous ribs are formed from 0. 04-inch, type 2024-0 aluminum and are solution-heat-treated and then precipitation-hardened to the T6 condition. The intercostal stringers are forms of type 7075-0 aluminum, heat-treated to the T6 condition, as are the clips that tie the intercostal stringers to the ribs. The ribs are continuous and oriented vertically and are riveted to the upper and lower edge channels. This orientation provides a better thermal path than an arrangement of the ribs in a horizontal direction. The ribs are located to join the baseplate at the same location as the baseplate ribs to provide continuous stress-load paths to the separation ring. Intercostal members are located between the ribs and are perpendicular to them. The intercostal stringers are riveted directly to the ribs at one end and are tied to the adjacent rib at the other end by angle clips. This procedure reduces the possibility of causing rib distortion during riveting. The pitch of the ribs and intercostal stringers on the equipment panels and the baseplate was selected to provide the strongest structure for the least weight within the space and equipment constraints and still allow reasonable accessibility to attach component reinforcing brackets.

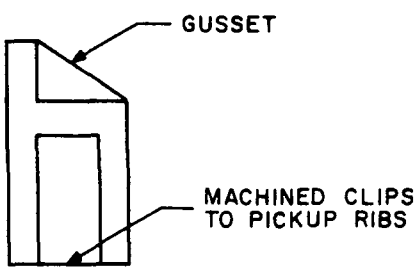

Figure 4-II-10. Cross Section of Equipment Panel Edge Member

The skin of the equipment panels is 0.04-inch-thick, type 2024-T4 aluminum, black anodized on the inside surface for thermal reasons and riveted to the ribs, intercostal stringers, and edge channels using flathead rivets. The skin and structural members are either countersunk or dimpled, depending on the section thickness, to recess the rivet heads below the surface of the skin and provide a flat (within 0.03 inch TIR) surface for mounting electrical equipment.

Gussets of 0.08-inch-thick, type 2024-T4 aluminum are riveted to each intersection of ribs, intercostal stringers, and edge members to provide section continuity on the rib side of the panels.

4. Access Panels

a. Earth-Oriented Panel

The earth-oriented access panel (Figure 4-II-4) has the same construction as the baseplate and equipment panels; it has machined channels around the perimeter of the panel and a system of sheet metal ribs and intercostal stringers within the area bounded by the edge channels. A sheet metal skin covers the interior structural area.

The edge channels are machined from type 2024-T4 aluminum bar stock. The web of the channels is 0.09 inch thick and the flanges are 0.06 inch thick. The bottom channel will interface with the radiometer mounting plate using close tolerance bolts.

The ribs and the intercostal stringers are formed from type 2024-0 aluminum, and then solution-heat-treated, quenched, and age-hardened to the T4 condition. Rib and intercostal stringers are 0.03, 0.04, or 0.06 inch thick, depending upon local strength requirements. Unlike the baseplate and equipment panels, the ribs of the earth-oriented access panel are not consistent in the direction of orientation due to sensor view requirements and a large access cutout. Three ribs are directed horizontally and two short ribs run vertically along the two vertical edges of the access cutout. These ribs are tied together by a system of intercostal stringers and edge members which are perpendicular to the ribs. Clips are again used at one end of each intercostal stringer to reduce the possibility of distortion during fabrication.

The skin is fabricated from 0.03-inch-thick, type 2024-T4 aluminum with a black anodize surface on the side opposite the ribs. The earth-oriented access panel is not designed to support equipment but, rather, is designed for minimum weight and maximum access to the interior of the spacecraft. Roundhead rivets are used to join the skin to the edge channel rib assembly. Gussets of type 2024-T4 aluminum, 0.05 and 0.8 inch thick, are placed at most of the intersections of ribs, edge members, and intercostal stringers; intersections that do not have gussets are along each vertical side of the access cutout. These areas are supported by large shear plates riveted to the ribs which compensate for the loss of strength due to the camera cutouts. These plates are fabricated from 0.05-inch-thick, type 2024-T4 aluminum. The plates have lightening holes where strength is not necessary.

Large aircraft-type lightening holes with formed lips are used in the skin. These holes are centrally located between rib and intercostal intersections to reduce the panel weight without jeopardizing panel strength.

The access cutout is basically a rectangle with gusseted corners. The gussets are formed by the skin and a rib-type member at each corner. Small standard gussets carry the stress load from the corner rib to the main structural ribs. The camera sensor slots in the access panel are specifically located for the ITOS mission. The configuration can change as the number and location of the cameras and sensors change for different missions; however, the basic design concept of this member will probably remain the same.

b. Anti-Earth Side Panel

The anti-earth access panel (Figure 4-II-5) construction closely resembles that of the earth-oriented access panel. The access cutout centrally located in the panel is larger than the cutout in the earth-oriented panel but does not have cutouts for camera sensors along the vertical edges.

The channels that form the panel edges are the same as the edges of the earth-oriented panel, with the exception of the bottom channel whose cross section is a "J" section. This extra flange provides a surface for bolts to join the panel to the baseplate.

The ribs and intercostal stringers are fabricated by the same methods and from the same material used on the earth-oriented panel. Material thickness of these members is 0.03 or 0.06 inch, depending on local strength requirements.

Again, this access panel is not designed to support electronic equipment but, rather, is designed for minimum weight and maximum access to the interior of the spacecraft. Roundhead rivets join the skin to the edge channel assembly.

The skin consists of two separate sheets of type 2024-T4 aluminum, with an overlap joint between the two pieces. The lower and upper pieces are 0.04 and 0.03 inch thick, respectively. The two-piece skin provides maximum shear strength on the lower portion where it is required and preserves the minimum weight concept in the upper area. Both areas are black anodized on the side opposite the ribs.

Gussets of type 2024-T4 aluminum, either 0.04 or 0.08 inch thick, are used to provide maximum strength, where necessary, and minimum weight, where possible. As in the earth-oriented panel, lightening holes are provided in the skin where possible, to provide a maximum strength, minimum weight panel.

5. Scanning Radiometer Mounting Plate

The radiometer plate, shown in Figure 4-II-4, is different in form from the other assemblies of the structure. This plate, which is the mounting and support structure for the two scanning radiometers and the flat plate radiometer, is machined from type ZK60A-T5 magnesium. The design is predicated on maximum strength and minimum weight, which are accomplished through the liberal use of machined ribs and minimum rib cross section.

6. Crossbrace Assembly and Thermal Fence

The crossbrace assembly (see Figure 4-II-6) is located at the top of the structure (panel 5). This assembly stabilizes the top of the spacecraft structure, supports the thermal fence, and provides a location for the spacecraft dual despin mechanism. The dual despin mechanism is mounted on the thermal fence with the cables wrapped around the circumference.

To further support the despin mechanisms, an angle brace is installed from the X-frame under the dual mechanism to the earth-oriented access panel for one mechanism and to the anti-earth access panel for the other.

The X-frame portion of the crossbrace is fabricated from 0.04-inch-thick, type 7075-0 aluminum sheet, which is formed into a channel and then heat-treated to the T6 condition. The shape of the beam is designed for uniform strength.

The corner fittings are machined from type 2024-T4 aluminum, with flanges to join them to the X-frame beams. The center of the X-frame, where the two channels intersect, is strengthened on the top and bottom with 0.08-inch-thick, type 2024-T4 aluminum gussets, which are riveted to the channels. The upper plate has studs to fasten a shaft for checking spacecraft runout from the separation plane.

The thermal fence assembly is fabricated from type 6061-T0 aluminum alloy and consists of two spun cup-like fences (4.81 inches high) and a flat fence support ring. As shown in Figures 4-II-6 and 4-II-11, the inner fence (14.7-inch diameter) is riveted to the outer fence (36-inch diameter) at 24 equispaced locations, and the outer fence is riveted at 60 equispaced locations to the flat fence support ring. The concentric fence configuration is then mounted on the structural crossbraces by 24 insulating standoffs. The spun edge of the outer fence is slotted in 8 places to relieve thermal stresses. ALZAK reflective surfaces are mounted inside the inner and outer cups by insulating standoffs, with insulation placed between the reflecting surfaces and the base of the cups. Note that the command and beacon antenna protrudes through notches in the wall of the inner fence and is supported and thermally insulated by grommet-type inserts on the base of the inner cup.

7. Solar Array Structure and Deployment Mechanism

The solar array consists of three identical curved solar panels, 36.38 inches wide (measured on the chord of the 75.61-inch radius of curvature) by 63.8 inches long. (See Figure 4-II-12.) The solar panels are a sandwich-type construction, consisting of an aluminum honeycomb core with aluminum foil facing sheets. This design provides high torsional stiffness and high natural frequency, combined with low inertia and low weight. The convex side of the panel has one continuous face for the mounting of solar cells; the concave face has

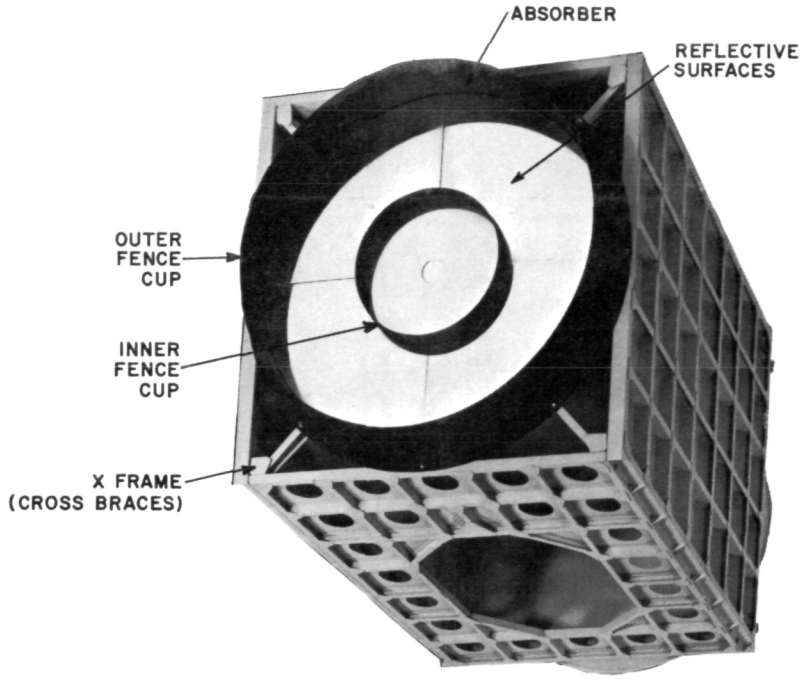

A. ITOS Structure Top View, Showing Thermal Fence Assembly

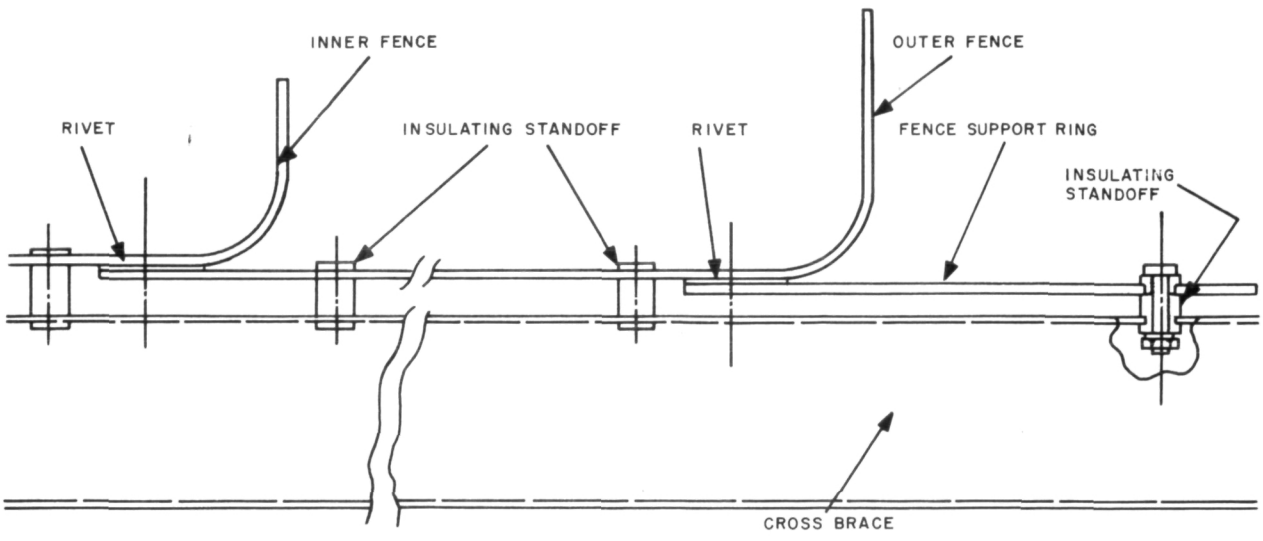

B. Thermal Fence Assembly Mounting Technique, Detailed

Figure 4-II-11. Thermal Fence Assembly Configuration

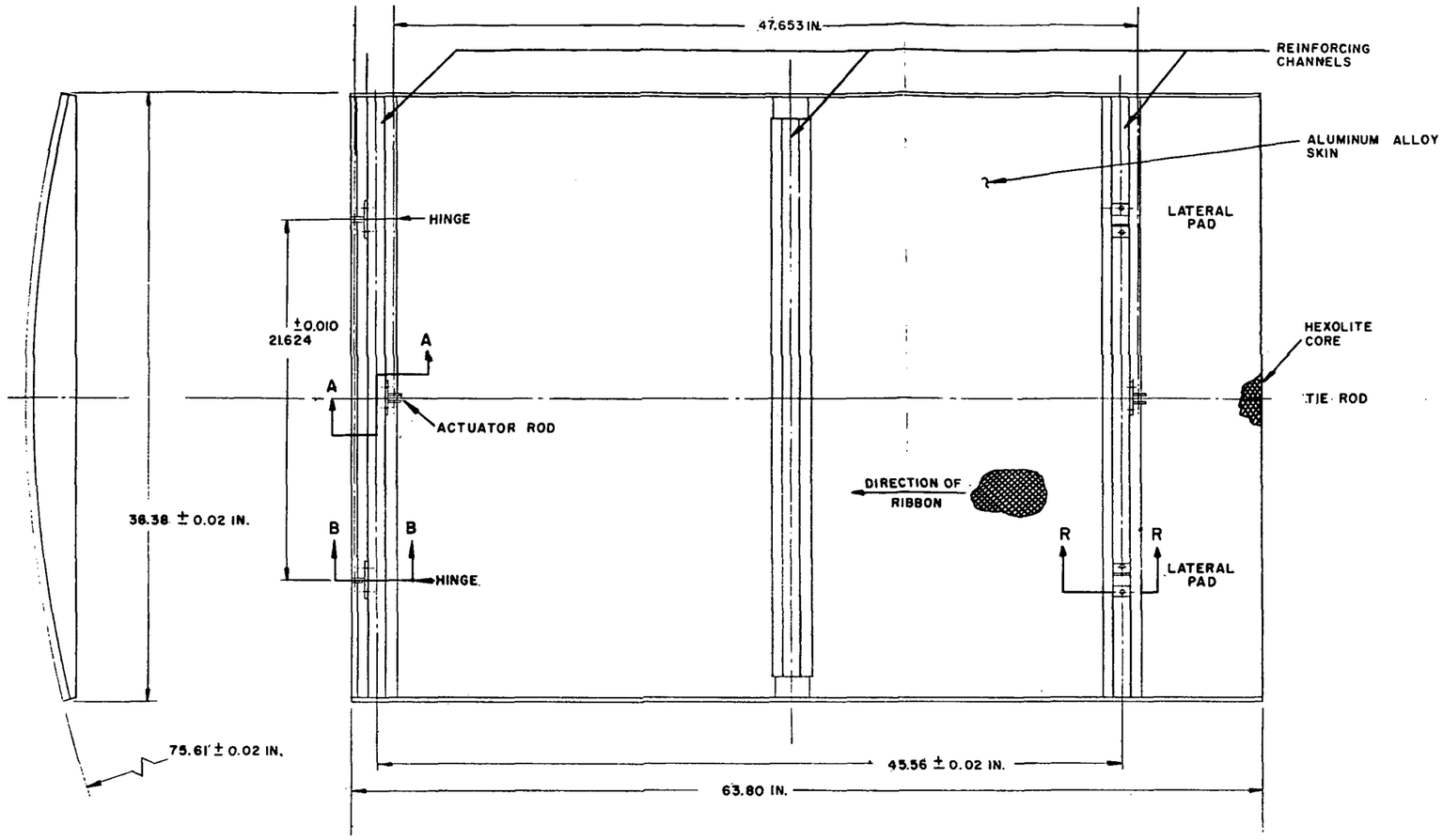

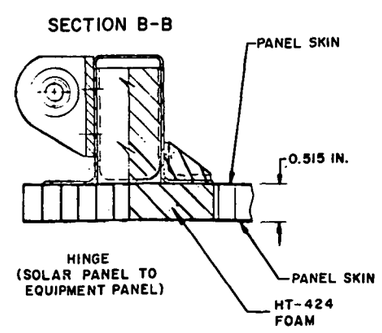

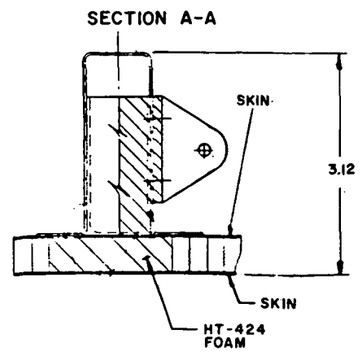

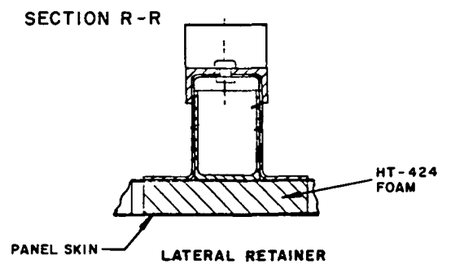

Figure 4-II-12. Solar Panel, Mechanical Configuration

three reinforcing channels (hat sections) bonded to it. In addition to their structural function, these hat sections serve as mounting surfaces for the array isolation diodes and shunt dissipators. Formed C-channel members are bonded to the long edges of the panel and serve as a closeout structure. Both ends of the panel have a honeycomb core with the last cell compressed to obtain a proper surface for subsequent operations. Type HT-424 foam, an epoxy-phenolic material which foams-in-place upon reaching a temperature of 330°F, is then introduced on the cut honeycomb core to delocalize stress.

Three adhesives were selected for use on the ITOS solar panel structure. Type FM-1000 adhesive is used for bonding the honeycomb core to the aluminum skin. Type M-688/CH-16 was chosen as the adhesive for bonding the three structural reinforcing channels to the honeycomb skin, while type HT-424 foam adhesive is used as the bonding agent between the honeycomb core and the edge-closure structural members. These adhesives have received a thorough evaluation and were used on the solar panels of the Lunar Orbiter spacecraft. Two hinges mounted to the inboard (top) reinforcing channel attach each solar panel to the equipment module along the top edges of the spacecraft (panels 2, 3, and 4) and permit the solar panel to be stowed in the launch configuration. A hydraulic actuator is attached to the center of the same reinforcing channel. This unit is a spring/hydraulically-damped device (see Figure 4-II-13) which deploys the solar array from its stowed position to its operating position.

Two other secondary restraints are also employed. Two vibration snubbers are located at the outer edges of the center reinforcing channel and interface with screw jacks on the spacecraft structure. A set of pads on the outboard (bottom) reinforcing channel restrain the lateral movement of the solar panels and also interface with the structure through screw jacks. The pads and jacks are angled from a line normal to a panel reinforcing channel and the structure so that the intersections of the lines of force of the two jacks meet at a point inside the structure. This produces a two-directional stabilizing effect on the panels; the third-direction stabilization is provided by the hinges and hinge pins.

Two additional interfaces associated with the deployment mechanism exist between the solar panel and the spacecraft. A clevis fitting to accept the deployment actuator is located in the center of the top reinforcing channel. A restraining link is attached to a clevis fitting

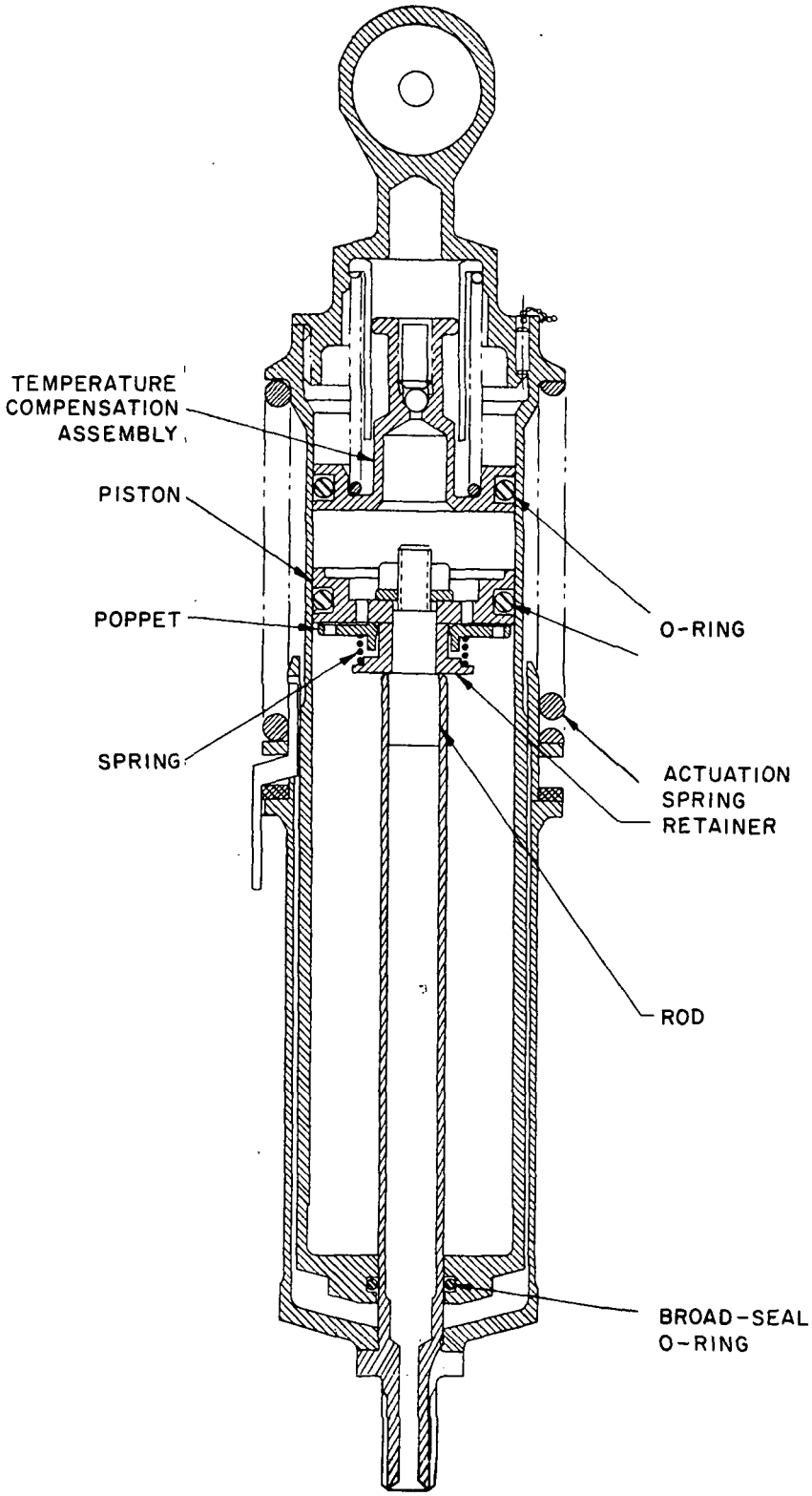

Figure 4-II-13. Solar Panel Hydraulic Actuator

on the bottom reinforcing channel. All rotating interfaces between the solar panel, spacecraft panel, and the deployment mechanism are through Teflon-lined spherical bearings, which allow for up to 10-degree angular build-up between the solar panel and its interfaces.

Deployment of the solar panels from their stowed position along the spacecraft module is initiated by the actuation of pyrotechnic pin puller devices which are located on the spacecraft structure. (See Figure 4-II-14.) Upon ground command to deploy the solar array, the pin pullers release the top edge of the solar panels and the actuators rotate the solar panels 90 degrees to their deployed position. Built-in latches in the actuator lock each panel in the deployed position.

8. Momentum and Attitude Control Coils

The momentum coil is fastened to the ribs of the AVCS equipment panel, beneath the thermal blanket, while the attitude control coil is mounted to the underside of the baseplate on the outside of the baseplate ring (see Figure 2-I-3). The concepts used in the mechanical design of the momentum and attitude control coils are identical, although the finished sizes and cross-sectional shapes differ due to specific size, position, and electrical requirements.

Each coil is wound within a preformed, epoxy-impregnated, glass-cloth channel having the specified coil dimensions. As each layer of wire is completed, a coating of epoxy resin is brushed over the layer; this process continues until the entire winding operation is completed. The resulting assembly results in a coil (or coils) embedded in a continuous epoxy matrix, with the glass channel forming an integral protective shell on three sides of the coil.

The free ends of the coil windings are soldered to connections on an epoxy terminal board which is bonded to the coil assembly. All such exposed connections will be epoxy-coated to prevent subsequent damage to the coil wires. A second set of terminals will be provided for external spacecraft connection.

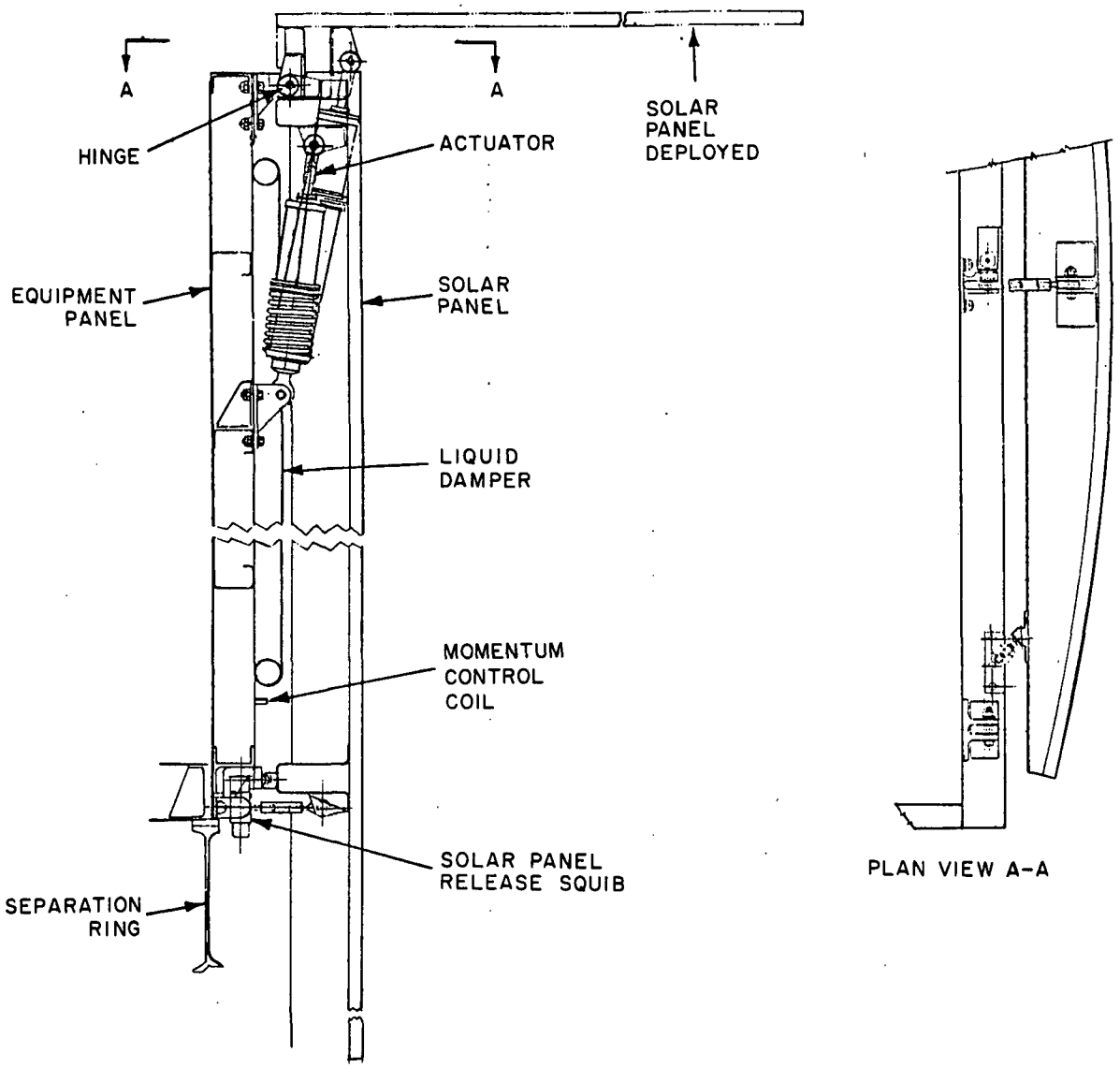

Figure 4-II-14. Deployment of Solar Panel

9. Nutation Damper

The two nutation dampers are fastened to the outside of each equipment panel, beneath the thermal blanket (see Figure 2-I-3). The nutation dampers are fabricated from type 5052-0 aluminum alloy drawn tubing having a 1.00-inch outside diameter and 0.035-inch wall thickness. The assembly will approximate a rectangle with rounded corners, having a short filling tube perpendicular to the rectangular plane and located in the center of one of the shorter sides. A normally closed, explosively actuated valve will be placed in the shorter side adjacent to the filling tube. Joints between the main tube and valve and between the main tube and filling tube will be made using 37-degree flared aluminum tube fittings. Prior to filling the assembled tubing with silicone fluid, all joints will be leak tested using helium and a mass spectrometer.

D. FABRICATION AND ASSEMBLY

In keeping with the philosophy of providing structural alignment and interchangeability, fabrication and assembly procedures were considered. Tolerances on dimensions, squareness, parallelism, and the flatness of mating and mounting surfaces, which are difficult to maintain on large sheet metal assemblies, will be achieved by the use of accurate jigs and fixtures.

The base of the structure has a short ring (baseplate ring) permanently attached, which mates to the separation ring. After fabrication of the baseplate, the baseplate ring will be final-machined using the skin of the baseplate as a reference surface. This method eliminates distortions in riveting the ring to the baseplate and assures parallelism between the baseplate skin and the mounting surface for the baseplate ring. The mounting plate for the momentum wheel assembly will also be final-machined during the same operation, ensuring that an accurate reference between the baseplate ring and the momentum flywheel assembly is maintained. After machining, the baseplate-ring-to-separation-ring mating holes will be jig-drilled. Close tolerance, high strength bolts will be used to provide alignment and concentricity control and to carry shear loads.

The radiometer mounting plate makes up the lower portion of the earth-oriented access panel and must be the same width. Close tolerance bolts are used to join the mounting plate

to the panel. The bolt holes are jig-drilled and reamed for the bolts to ensure re-alignment of these structural parts should they require disassembly and also to provide good shear strength at the joint between the panel and the mounting plate.

Assembly of the baseplate and the access panels is performed first. The earth-oriented access panel and the baseplate are jig-drilled from a single jig. The holes are then reamed to final size for shoulder bolts, and the panel is joined to the baseplate. The anti-earth access panel is next joined to the baseplate in the same manner. Due to a different mounting-hole pattern in the anti-earth panel (earth-oriented panel mounting holes are located in the radiometer mounting plate), a different drill jig or a combination jig is necessary.

Once the access panels are joined to the baseplate, bolt holes for the equipment panels can be drilled. The baseplate/access panel subassembly is clamped or fixtured to present as square a configuration as possible for drilling. A drill jig is then used to drill the bolt holes in the baseplate and along the edges of the access panels. Using the other side of the same jig, matching holes are drilled in the first equipment panel. The same procedure is then used for drilling the mating bolt holes in the second equipment panel using the same jig. The bolt holes are then reamed to final size and shoulder bolts are installed, thus completing the major assembly of the structure. Shoulder bolts are used for two reasons; they allow for good alignment control and perform a shear function at the joint between adjacent panels and between the panels and the baseplate.

The crossbrace of panel 5 is the last structural assembly integrated into the structure. The four corner pieces are installed first and may have to be shimmed to correct any non-perpendicularity between panels. Non-perpendicularity could occur even though the structure is fabricated within specified tolerances and is not detrimental to the function of the structure. Once each corner piece is joined to the structure, the crossbrace is fitted, drilled, and riveted to the corner pieces, and the thermal fence is then assembled to the crossbrace. The screw holes for this assembly will be spotted from the crossbrace. Standard hardware will be used to join the crossbrace corner fittings to the panels and to attach the thermal fence.

After structure assembly, hinges will be attached to the lower edges of equipment panels, one hinge at each side of each equipment panel (see Figure 4-II-3); the other half of the hinge will be attached to the baseplate. These hinges permit the equipment panels to be lowered from their assembled position to a horizontal position for testing or replacement of components mounted on these panels without requiring complete disassembly of the structure.

The three solar panels can then be joined to the structure. A fixture and drill jig must be provided to locate the hinges on the solar panels and the structure. The fixture controls the position of the interface between the halves of the hinges rather than the mounting holes for the hinges.

E. SPACECRAFT BALANCE, WEIGHT ESTIMATE, AND MOMENT OF INERTIA

1. Balance and Center of Gravity

The ITOS spacecraft is essentially balanced for the component layout as shown in Figure 2-I-3 of Part 2, with the spacecraft center of gravity located 21.56 inches from the separation plane. This will, of course, be subject to continuous minor revision as subsystem mechanical parameters are finalized and the spacecraft main electrical harness is defined.

2. Spacecraft Weight Summary

A detailed weight summary of the ITOS spacecraft is presented in Table 4-II-1. The total estimated spacecraft weight, including the separation ring, is 673.5 pounds.

TABLE 4-II-1. ESTIMATED WEIGHT OF ITOS SPACECRAFT

Group and Component	Estimated Weight (pounds)	
	Component	Group
STRUCTURE		109.9
Baseplate	22.5	
Equipment Panels (2)	40.1	
Earth-Oriented Panel	10.4	
Anti-Earth Panel	8.8	
Hardware	3.5	
Separation Ring	12.7	
Subsystem Brackets	9.1	
SR Mounting Plate	1.9	
Despin Mechanism Support Brackets	0.9	
SOLAR ARRAY		56.5
Panel Structures (3)	30.6	
Cells Wiring and Adhesive	18.0	
Deployment Mechanism	4.2	
Locking Mechanism and Pin Puller	1.9	
Panel Hinges and Bolts	0.6	
Panel Bumpers and Snubbers	1.2	
THERMAL		27.5
Insulation	5.0	
Fence and Crossbrace	15.5	
Active Thermal Controller	7.0	
Temperature Sensors	0.2	
CAMERA SUBSYSTEM		74.4
AVCS Cameras (2)	18.0	
AVCS Electronics (2)	12.0	
APT Cameras (2)	25.4	
APT Electronics (2)	19.0	

TABLE 4-II-1. ESTIMATED WEIGHT OF ITOS SPACECRAFT (Continued)

Group and Component	Estimated Weight (pounds)	
	Component	Group
RECORDERS		74.9
Recorder Mounting Brackets	2.5	
AVCS Recorders (2)	24.5	
SR Recorders (2)	24.5	
SR Recorder Electronics (2)	12.2	
AVCS Recorder Electronics (2)	11.2	
COMMUNICATIONS		42.0
Dual Command Receiver	2.6	
Beacon Transmitter and Dual SCO	3.4	
Dual S-Band Transmitter	11.9	
Real-Time Transmitters (2)	4.3	
Dual Multiplexer	11.8	
Signal Conditioner and Dual TLM Comm.	8.0	
ANTENNA EQUIPMENT		13.7
Notch Filter (137 MHz)	0.1	
Beacon Cabling	2.0	
Hybrid Coupler	0.4	
Beacon Antenna	0.8	
Beacon Antenna Coupler	2.3	
Bandpass Filter (148 MHz)	0.3	
S-Band Array, Coupler and Ground Plate S-Band Cabling S-Band Loads	3.3	
Real-Time Antenna and Deploy. Mech.	1.2	
Real-Time Antenna Coupler	0.4	

TABLE 4-II-1. ESTIMATED WEIGHT OF ITOS SPACECRAFT (Continued)

Group and Component	Estimated Weight (pounds)	
	Component	Group
ANTENNA EQUIPMENT (Continued)		
RF Switch, Relay (cables & fittings)	0.9	
RF Cables	1.7	
Notch Filter (148 MHz)	0.3	
DYNAMIC CONTROL		72.9
Momentum Wheel Assembly	38.0	
Pitch Control Electronics	6.5	
Attitude Control Coil	2.6	
Momentum Control Coil	1.0	
Nutation Dampers (2)	14.1	
Magnetic Bias Switch	0.7	
Despin Mechanism (yo-yo less weights)	3.5	
Despin Mechanism Weights	4.0	
Digital Solar Aspect Sensor	1.7	
Acquisition Attitude Sensor	0.8	
COMMAND SUBSYSTEM		35.7
Dual Decoder	7.0	
CDU A	5.4	
CDU B	7.1	
Dual Programmer	9.5	
Dual Time Base Unit	6.7	
POWER SUPPLY (except solar array)		47.6
Batteries (2)	29.0	
Power Supply Electronics	10.2	
External Shunt Dissipators	8.4	

TABLE 4-II-1. ESTIMATED WEIGHT OF ITOS SPACECRAFT (Continued)

Group and Component	Estimated Weight (pounds)	
	Component	Group
RADIOMETERS		44.5
Scanning Radiometers (2)	24.4	
SR Electronics	14.0	
Dual SR Processor	5.6	
Sun Shields	0.5	
EXPERIMENT EQUIPMENT		26.6
Flat Plate Radiometer	6.0	
Incremental Recorder	5.3	
Solar Proton Sensors	2.6	
Solar Proton Electronics	4.4	
Data Format Converter	8.3	
MISCELLANEOUS		47.1
Trimming Magnets and Brackets	1.0	
Separation Switches and Brackets	1.1	
Balance Weights	6.5	
Harness	35.0	
Ground Plate	0.5	
Component Mounting and Hardware	3.0	
TOTAL SPACECRAFT WEIGHT		673.5

3. Moment of Inertia

For the present component layout configuration of the ITOS spacecraft (Figure 2-I-3), the moments of inertia of the spacecraft in the launch configuration are as follows (see Figure 4-II-15):

$$I_{x-x} = 293,659 \text{ lb-in}^2$$

$$I_{y-y} = 323,875 \text{ lb-in}^2$$

$$I_{z-z} = 254,090 \text{ lb-in}^2$$

$$I_{MAX} = 325,167 \text{ lb-in}^2$$

The maximum moment of inertia (I_{MAX}) occurs in the XY plane at an angle of 0.1618 radians from the X-axis.

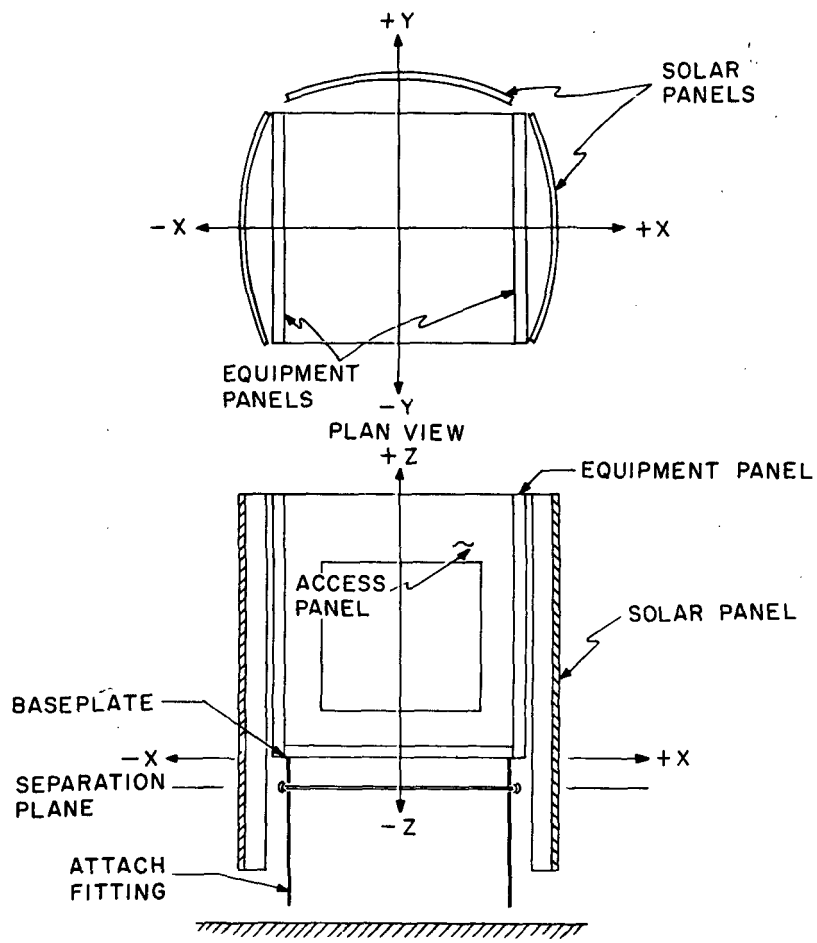

Figure 4-II-15. ITOS Spacecraft Configuration, Simplified Diagram

F. STRESS ANALYSIS

A detailed stress analysis will be included as a special design report to be submitted at a later date. For this reason, only a brief summary of stress critical margins of safety will be presented here. In the stress analysis report, a complete tabulation of design loading cases and the critical margins of safety will be given. Currently, continuing stress analyses are being performed as part of a general weight reduction program; therefore, preliminary stress critical margins of safety are summarized in Tables 4-II-2 and 4-II-3, where margin of safety (MS) $= \frac{\text{Allowable Stress}}{(\text{Actual Stress})\ (\text{Factor of Safety})} - 1$. Being essentially a closed box, the load paths within the spacecraft structure are straightforward; each side panel provides edge support to the adjacent sides. Vertical loading in the side panels is applied directly to and reacted upon at four points on the separation ring tangent to the edges of the baseplate. Baseplate loads are uniformly applied to and reacted upon by the separation ring.

The use of annular access ports on the earth and anti-earth panels (Figures 4-II-4 and 4-II-5), as opposed to the V-braces originally proposed, provides edge stiffening for the equipment-carrying panels and results in a more rigid overall structure. The access panels act as shear webs under lateral loading cases in transmitting loads from the vertical edges of the equipment panels into the separation ring. Local loads in the equipment panels are carried to the edges by the network of channel ribbing on the outer surface.

In line with the "equipment bus" design concept, analysis to this point has assumed a uniform distribution of subsystem weight, for which the "waffle" gridding panel construction is ideal in that it provides maximum flexibility in equipment location. More detailed analysis will be performed to determine the extent of local interrib bracketry required to provide structurally adequate equipment mounting points.

To provide sufficient clearance between the solar panels and the attach fitting, a curved solar panel design was selected which also results in a considerably increased panel stiffness. This approach permits a stress-limited rather than deflection-limited design of the solar panels, and thus a reduction in the thickness and weight of the panel substrate over a flat panel design is realized.

TABLE 4-II-2. STRESS CRITICAL MARGINS OF SAFETY FOR SPACECRAFT STRUCTURE

Item	Critical Condition	Type of Stress	Margin of Safety
BASEPLATE			
Rib	Z excit. panel reson.	Bending-crippling	0.27
Intercostal	Z excit. panel reson.	Rivet bear. at splice	0.17
Equip. Channel	X excit. S/C reson.	Bending yield	0.09
Radiometer	Y excit. S/C reson.	Bending yield	0.03
Rear Channel	Y excit. S/C reson.	Bending yield	0.06
Edge Channel	Y excit. S/C reson.	Bearing yield	0.58
EQUIPMENT PANEL			
Internal Channel	X excit. panel reson.	Bending-crippling	0.05
Internal Channel	X excit. panel reson.	Rivet bear. at splice	0.01
Vertical Channel	X excit. S/C reson.	Axial-buckling	0.32
Skin	Y excit. S/C reson.	Shear buckling	0.00
Top Channel	X excit. panel reson.	Bending-fatigue	0.43
FRONT PANEL			
Channel	X excit. S/C reson.	Bending-crippling	0.33
Skin	X excit. S/C reson.	Shear buckling	0.06
Skin	X excit. S/C reson.	Rivet bear. yield	0.12
Channel	Y excit. S/C reson.	Bending-crippling	0.11
Channel	Y excit. S/C reson.	Attachments	0.18
Channel	Z excit. radiometer load	Bending-fatigue	0.08
RADIOMETER PANEL			
Plate	Y excit. S/C reson.	Bending-fatigue	0.23

TABLE 4-II-2. STRESS CRITICAL MARGINS OF SAFETY FOR SPACECRAFT STRUCTURE (Continued)

Item	Critical Condition	Type of Stress	Margin of Safety
BACK PANEL			
Intercostal	X excit. S/C reson.	Bending-axial cripp.	0.31
Rib	Y excit. S/C reson.	Bending-fatigue	0.06
Brace	Y excit. S/C reson.	Attachments	0.06
Skim	Y excit. S/C reson.	Shear buckling	0.40
SEPARATION RING			
Adapter	Lateral excit. S/C reson.	Buckling at center	0.41
	Lateral excit. S/C reson.	Fatigue near Vee clamp	0.09
	Lateral excit. S/C reson.	Fatigue near baseplate	0.09
	Lateral excit. S/C reson.	Fatigue upper flange	0.09
CROSS-BRACE			
Channels	Z excit. panel reson.	Bending-fatigue	0.37
Splice at Center	Z excit. panel reson.	Rivet bear. yield	0.08
End Attachment	Z excit. panel reson.	Rivet bear. yield	0.30

TABLE 4-II-3. STRESS CRITICAL MARGINS OF SAFETY FOR SOLAR PANELS

Item	Critical Condition	Type of Stress	Margin of Safety
HONEYCOMB			
Honeycomb Penel	X excit. solar panel reson. (unsnubbed, with antenna)	Bending	0.44
HINGE BRACKET			
Shear Pin	Z excit. S/C reson.	Bending	0.68
STOP FITTING			
Hat Section, Top Skin	Y excit. S/C reson.	Bending	0.33
Core Stress Under Stop Fitting	Y excit. S/C reson.	Compressive	0.78
DAMPER ASSEMBLY			
Hat Section, Rivet	X excit. S/C reson.	Bearing	0.25
Hat Section, Rivet	X excit. S/C reson.	Shear	0.74

SECTION III

THERMAL DESIGN

A. OBJECTIVES AND BASIC REQUIREMENTS

1. Thermal Design Concept

Since ITOS is three-axis stabilized and is geometrically complex, it requires a more sophisticated method of thermal control than the previous TIROS and TOS satellites; the design concept selected involves fixed thermal control surfaces in conjunction with active thermal control surfaces. The ITOS basic structure is covered with multilayer insulation blankets except for the temperature-control surfaces and the primary sensor openings. The control surfaces comprise (1) the top of the spacecraft, on which a variable absorptivity device called a "thermal fence" is mounted, as shown in Figure 4-III-1; (2) the baseplate, which constitutes a fixed radiator; and (3) a variable radiator area, with two temperature-actuated flaps on each of the two side equipment panels.

The basic objective in developing this thermal control concept has been to achieve an overall measure of control passively by means of the thermal fence and a more exact control for enhanced subsystem performance through the use of the temperature actuated flaps. This approach ensures not only a favorable temperature environment for the electronic equipment during the preoperational and operational mission phases but also a capacity to accommodate spacecraft growth in terms of higher power and more precise temperature control.

2. Temperature Specifications

With the exception of certain external components, the spacecraft subsystems will be environmentally tested in accordance with the TOS subsystem specification, RCA specification 1750920. Although the flight subsystems are tested to the specification limits (-10 to 55°C), they may not be required to operate over the entire temperature range; in fact, some are only required to survive the limits. Listed below are the component mounting surface temperature control requirements during several modes of operation.

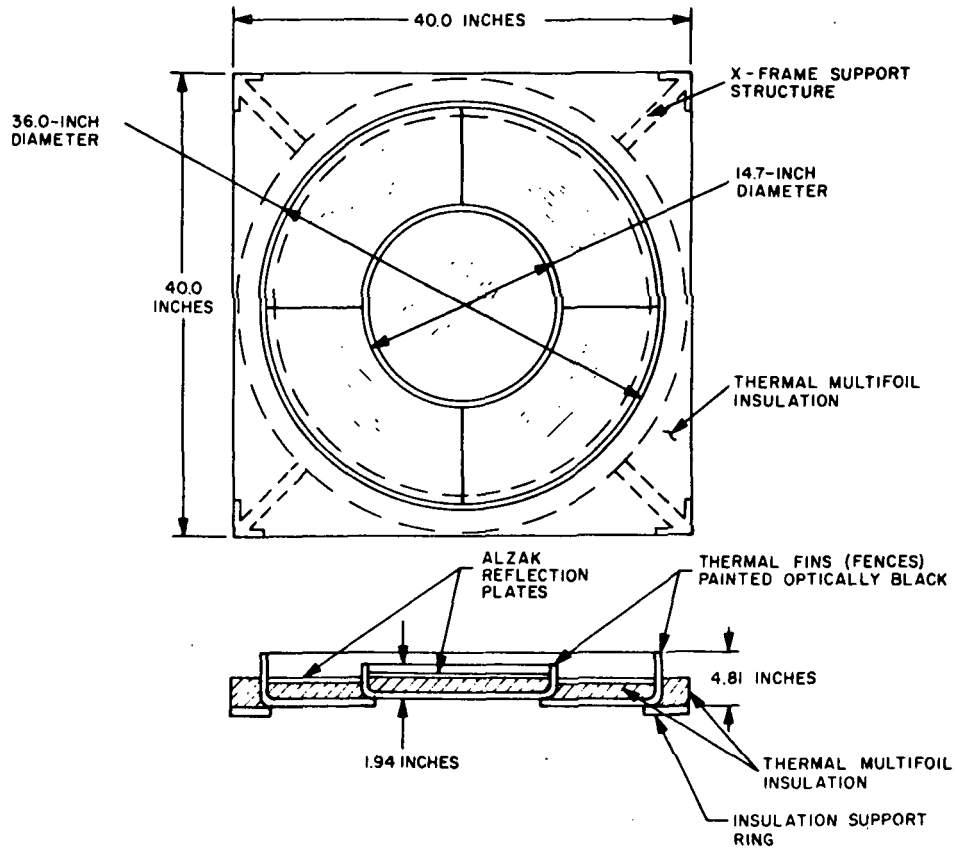

Figure 4-III-1. Thermal Control Fence

a. Operational Mode

The ITOS orbit (at 775 nautical miles) and spacecraft relationships are defined in Part 2 of this report. To account for orbit errors, launch delay, and seasonal effects, a range of sun angles (γ)* from 30 to 60 degrees must be accommodated.

The solar panels lie in the orbital plane, and the spacecraft rotates at one revolution per orbit. The spin axis is maintained normal to the orbit plane, and γ is essentially constant over one orbit.

Temperature design limits for the operational mission mode (30- to 60-degree sun angle, 100- to 73-percent suntime) are as follows:

Component	Temperature (°C) Max	Min
Battery Mounting	30	10
Camera Mounting (Desired)	30	5
Other Subsystem Mounting	35	5

*Angle between orbit normal and sun line.

b. Preoperational Mode

During the initial orientation phase of the preoperational mode the solar panels are in the folded position, and the spacecraft is spinning at a rate sufficient to achieve thermal averaging of the folded solar panels. The range of possible injection sun angles is shown in Figure 4-III-2 as a function of the o'clock angle (the angle between the ascending node and the projection of the true sun vector on the equatorial plane) and the time of year. Launch windows for morning and afternoon orbits are also shown. The curves are based on TOS A (ESSA 3) data and are probably slightly conservative for the proposed Improved TOS/Delta M booster. To account for the possibility of large coning angles subsequent to despin, a range of sun angles from 35 to 145 degrees has been selected for design purposes. This is 30 degrees in excess of the range shown in Figure 4-III-2. Eclipse times associated with the launch windows are shown in Figure 4-III-3. The range of sun angles depends on the percent orbit suntime; however, for preliminary purposes, it is assumed that the complete range from 35 to 145 degrees can occur in every orbit up to 88-percent suntime.

The design limit for the temperature of the subsystem mounting during the preoperational mode is -5 to 45°C.

c. Minimum Mission Requirements

A worst-case minimum standby load of 50 watts is assumed to occur at a 60-degree sun angle and at the end-of-mission-life (EOL). The thermal control system should maintain a temperature level above 0°C for this condition. This minimum power level encompasses all the probable required mission failure mode levels (i.e., both APT cameras and transmitter off; one solar array panel not unfolded; APT, SR, and one battery off; etc.).

d. Active Thermal Controller Failure

The design goal is to provide a component mounting temperature range of 0 to 40°C for a failure of two flaps of the active thermal controller subsystem. The worst case is considered to be a failure of two flaps on the same side.

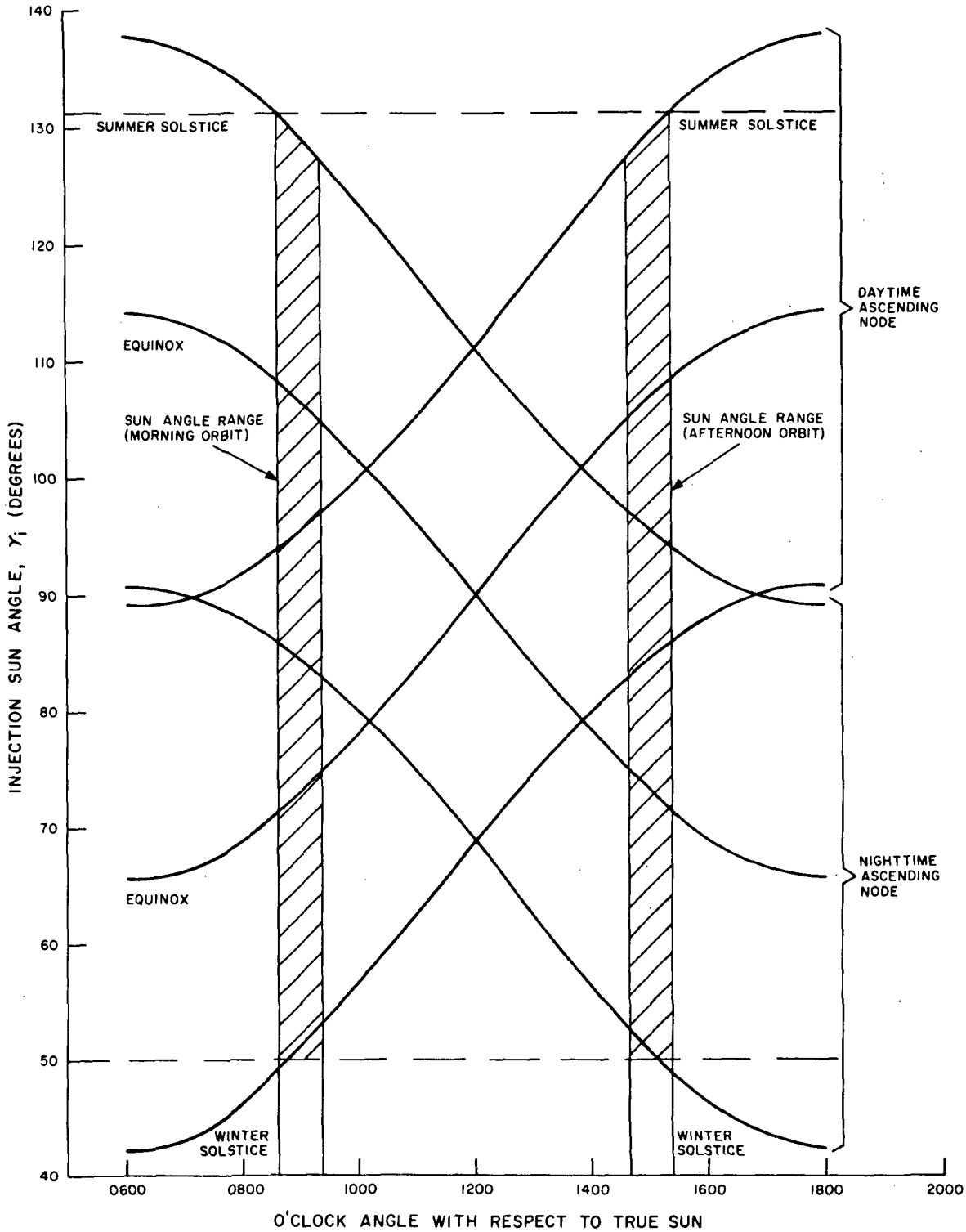

Figure 4-III-2. Range of Injection Sun Angles Versus O'Clock Angle for Various Launch Times

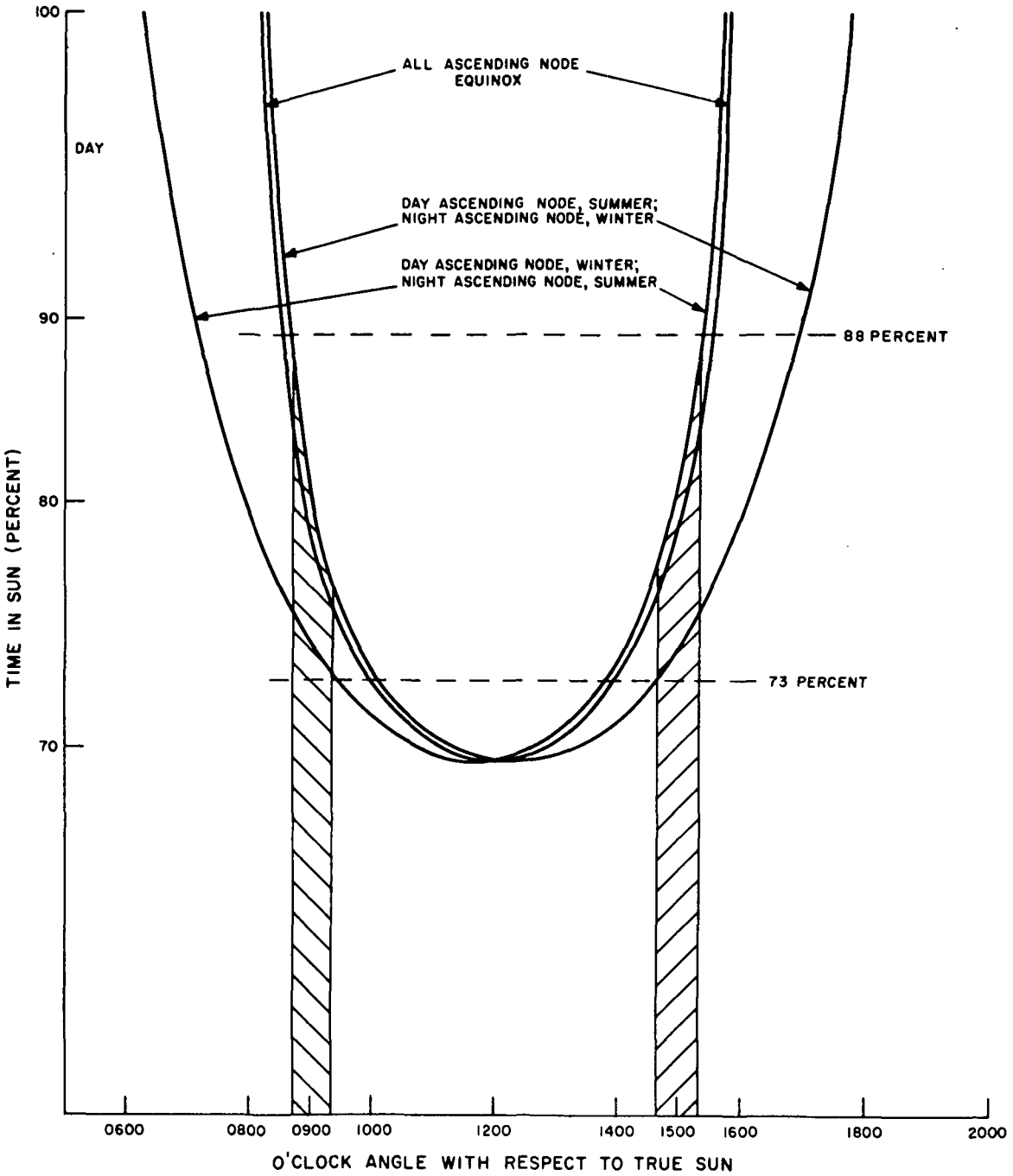

Figure 4-III-3. Eclipse Times for Various Launch Windows

3. Power Specifications

a. Operational Mode

The range of electrical power dissipation of the equipment and the distribution of this power within ITOS, in the operational (full load) mode, are shown in Figure 4-III-4, excluding the shunt limiter dissipation since this unit is mounted externally. Variations occur only on the baseplate where the batteries and power-supply electronics are located. Variations of solar array power with orbit angle are included as well as degradation with mission life. The power dissipation limiting values are: (1) 165 watts at a 30-degree sun angle and beginning-of-life (BOL) and (2) 110 watts at a 60-degree sun angle and end of life (EOL).

b. Preoperational Mode

The electrical power dissipation as a function of injection sun angle is given in Figure 4-III-5 for maximum and minimum suntime orbits and with QOMAC operating. It should be noted that the values depend on the rate of battery charge which, in turn, is a function of the battery temperature; therefore, interpolation is required to obtain the final power on the baseplate. For the preliminary analysis the applicable values are those shown in Figure 4-III-5, which include taper charge function.

c. Growth Power

To accommodate future system capability, provision is made to allow for additional sensors by providing a power growth of 10 watts per side panel. This added power is available at beginning-of-life and is to be accounted for in meeting the mission mode temperature specification of 5 to 35°C at the component mounting surface.

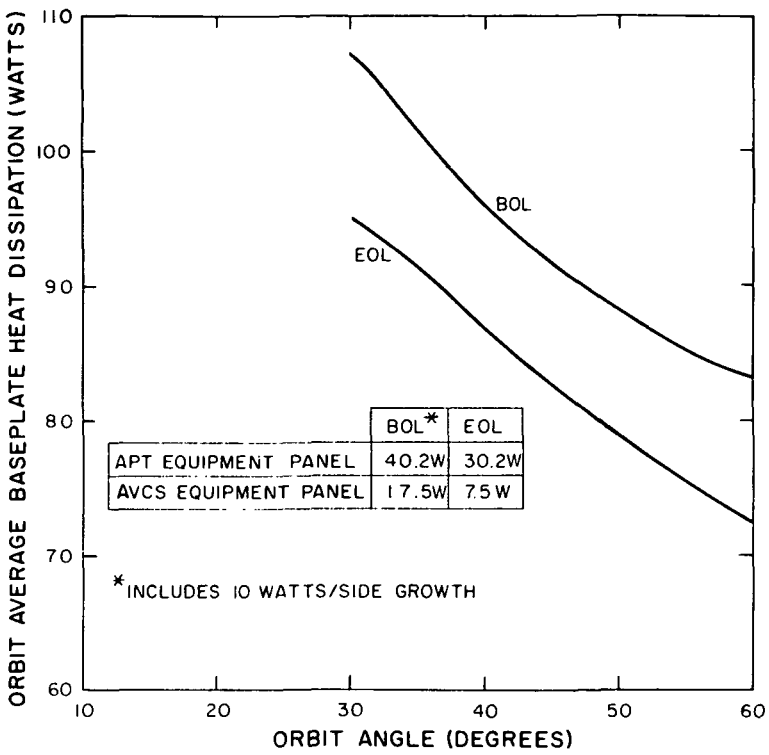

Figure 4-III-4. Spacecraft Operational Electrical Heat Dissipation Characteristics

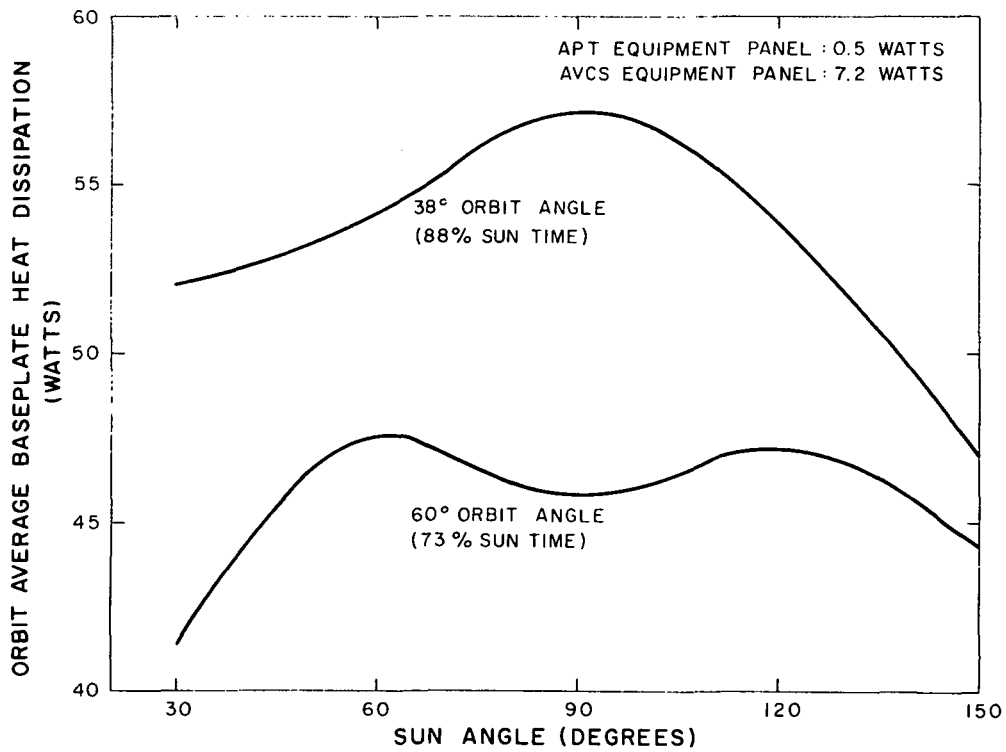

Figure 4-III-5. Spacecraft Injection Mode Electrical Heat Dissipation Characteristics

B. THERMAL ANALYSIS

1. Design Philosophy

The total spacecraft may be represented by the following parts:

- The thermal fence,
- The two side equipment panels, which have temperature-controlled external radiator areas,
- The baseplate, which has an external fixed radiator area,
- The three curved solar panels, and
- The earth-viewing panel and the panel opposite, which are covered externally with insulation blankets.

This basic model, described above, was divided into a 22-node analytical model, as shown in Figure 4-III-6, and used to investigate the thermal behavior. Each of the 22 nodes was

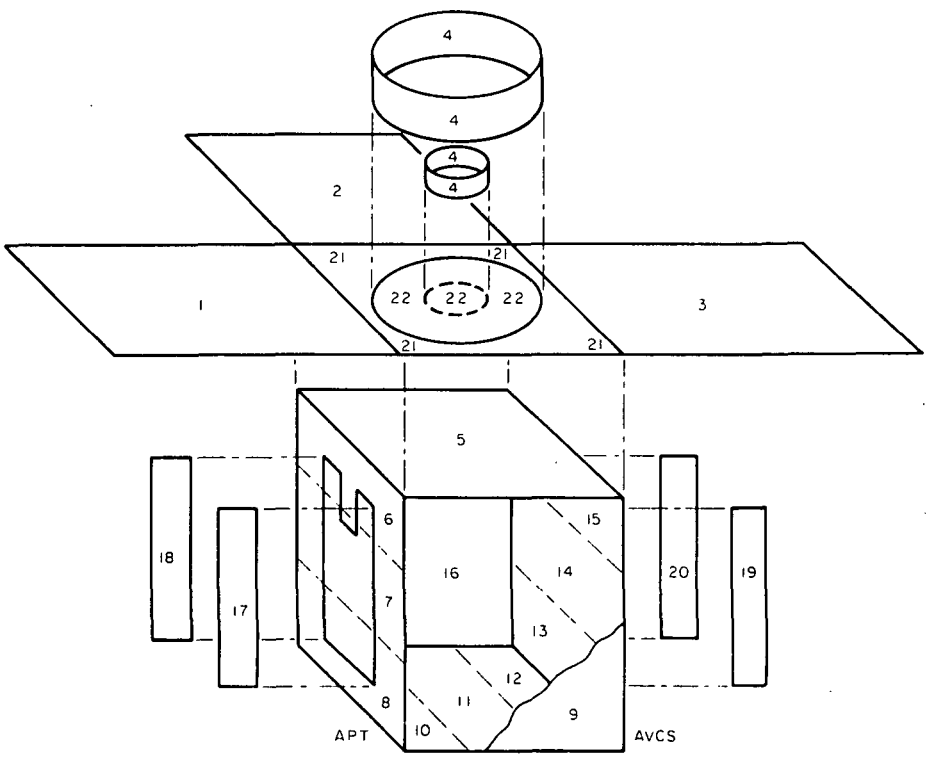

Figure 4-III-6. 22-Node Analytical Thermal Model

assumed to be isothermal during the studies (e.g., the baseplate was broken into three nodes, with the total power dissipation of the baseplate-mounted components at each of these nodes uniformly distributed). Orbital average temperatures were computed for the operational and preoperational mode conditions. Some exceptions to this basic model were necessary. For example, a 70-node model of the thermal fence was studied to determine its performance. For this case, the spacecraft itself (excluding the fence) was approximated by 3 nodes of the 70-node total (the two equipment sides and the baseplate). From this detailed fence analysis, effective thermal parameters were obtained such that a 4-node fence could be accurately used in the 22-node model. Also a solar simulation test was conducted at JPL on a full-scale model of the fence to verify both the functional ability of the thermal fence and the accuracy of the analytical technique.

a. Adjustment of Spacecraft Temperature

Since the spacecraft is thermally coupled to the fence plate by radiative heat transfer only, adjustment of the spacecraft temperature level to the desired values can be achieved by two methods. The radiative coupling between the plate and the spacecraft can be adjusted downward by insulating part of the plate area. The second adjustment method is to change the effective external radiator size of the spacecraft equipment panels, which is easily accomplished by adding or removing thermal insulation from the external surfaces. This second method has been utilized during the design studies; the coupling between the fence plate and the spacecraft interior has been left unaltered at its maximum value.

When the spacecraft is operational, two worst-case conditions occur. In a 30-degree sun angle, beginning-of-life orbit, maximum total internal power dissipation (165 watts) occurs primarily due to battery system overcharging. The total amount of heat absorbed by an equipment panel inner surface consists of the heat dissipated by the equipment plus the net radiant heat absorbed from the thermal fence and the other panels viewed by the sun. This total amount of heat is reflected to space from the equipment panel and baseplate radiators; the radiator size establishes the temperature level of the panel.

In a 60-degree sun angle, end-of-life orbit, minimum operational power dissipation (110 watts) occurs due to a reduced battery system dissipation. Again, the total heat absorbed is that dissipated by the equipment plus the net heat absorbed from the thermal fence and the other panels viewed by the sun. The amount of energy absorbed by the fence at this sun angle is higher than that absorbed at a lower sun angle. Hence, the net heat exchange between the fence and the spacecraft increases, compensating for the decrease in internal power dissipation. If the increase in heat transfer from the fence to the spacecraft were 55 watts over the 30- to 60-degree orbital range, there would be no temperature change of the structure since the power dissipation decrease from 165 to 110 watts would be exactly balanced.

b. Orbital Heat Flux

Externally incident heat flux consists of direct solar energy, earth-emitted infrared energy, and earth-reflected solar energy (albedo). These values were computed for operational modes for each of the exposed spacecraft surfaces as a function of the orbit parameters and the 1-revolution-per-orbit spacecraft orientation relative to the earth. For the pre-operational mode, the spinning spacecraft configuration was evaluated for each orbital condition; this data was then orbit-averaged in order to be compatible with the analysis model.

Direct solar illumination of the spacecraft surfaces was determined using a computer program which accounts for solar blockage by any intervening surfaces (such as blockage of the spacecraft side by a solar panel). The program also describes the boundary on the surface in question between solar illuminated area and shadowed area. This is necessary since a given surface may have more than one solar absorptance property. An example of this is the spacecraft equipment side panel, which has a thermal insulation blanket in some areas and a thermal radiator surface in another area. Seasonal variations of solar constant were taken into account.

Earth infrared and albedo flux were also obtained using established thermal computer programs. Since the programs do not automatically account for surface blockage, engineering judgments were applied in each specific blockage situation and a correction factor was applied. The value of the albedo constant used in the computations was 0.36.

c. Internal Power Dissipation

The spacecraft power profiles have been described previously in Paragraph A. 3. The numbers used for the thermal analysis represent selected worst-case values for each mode examined and may not necessarily match the actual forecast power. This approach often penalizes the thermal design, but if acceptable solutions are obtained for worst-case values, then greater confidence is obtained in the thermal design.

d. Failure Conditions

To accommodate, within the thermal design, for component power failure and/or active controller failures, provision for a fixed bias radiator is incorporated. No override of the actuator is provided; however, an optimization between side radiator, baseplate radiator, and bias will allow some degree of control.

2. Thermal Subsystem Design

a. Thermal Fence

(1) Description

As stated previously, gross thermal control of the spacecraft is achieved by utilizing a device called the thermal control fence (see Figure 4-III-1) which provides variable solar absorptance with changing solar incidence angle. The fence assembly consists of the following members:

- Fins and Plate — The basic construction of the fence consists of an assembly of spun right-angle cups riveted together concentrically. The vertical sections of the cups are called the fence fins. The horizontal riveted portion is called the fence plate. The fins and plate surfaces are thermally finished with an optically black paint (such as 3M Black Velvet) so that the solar absorptance (α) and infrared thermal emittance (ϵ) values approach unity. The spun construction eliminates thermal joints between the fins and the plate.

- Support Frame — The fence is riveted to an "X" configuration channel support frame at the surface opposed to the fins. The riveted connections contain low conductivity insulation spacers which minimize conduction heat transfer between the plate and the support frame. The support frame is joined to the upper surface of the spacecraft at the four corners via bolted T-sections.

- Plate Insulation — At the outside surface of the fence (the fin side), a multifoil insulation blanket is placed over the plate in the areas within the fins. The blanket is constructed by alternating layers of double-sided aluminized mylar (H-film for high temperature use) and a glass microfiber spacer material. Many alternating layers are placed together to form the insulation blanket. Typical values of effective emmitance (ϵ_e) through the insulation blanket of 0.005 have been measured using 20 alternating layer units. The insulation on the external surfaces of the spacecraft structure is constructed in a similar manner.

- Reflector Plate — Thin metal plates are placed over the top of the insulation in the areas within the fins. The reflector plates are supported from the fence plate via insulation spacer posts which minimize conduction heat transfer between the two bodies. The plate insulation blanket minimizes radiant heat transfer between the two bodies; therefore, the reflector plate is thermally isolated from the fence plate and is thermally coupled by radiation heat transfer only to the fence fins and to space.

- On the external surface of the reflector plate a highly reflective mirror-like property is desired. Several types of surfaces have been studied including deposited vaporized aluminum, polished aluminum plate, second-surface quartz mirrors, and ALZAK aluminum (Alcoa trade name). In general, a high specular solar reflectivity was sought, which all of the investigated materials exhibited. However, the infrared thermal emittance varies from approximately 0.05 for the vaporized aluminum to greater than 0.80 for the second-surface mirror, and studies have shown that the higher emittance materials result in improved fence performance. Since

the second-surface mirror is extremely expensive, difficult to apply, and subject to breakage, a compromise selection of the ALZAK aluminum was made. ALZAK is a commercially fabricated, high purity aluminum which is highly polished. A thin coating of transparent anodize is applied over the polished surface, which protects the surface and does not significantly reduce the specularity of solar reflectance of the polished aluminum. The coating is opaque to infrared energy, resulting in the desired high surface emittance. The emittance and absorptance values are $\epsilon = 0.62$ and $\alpha = 0.14$. A detailed evaluation of the ALZAK is currently being conducted, including determination of its radiation damage resistance while exposed to the space environment.

- Insulation Support Ring — A circular metal ring 40 inches in diameter is riveted to the outer fence plate. This ring supports an insulation blanket covering the top of the spacecraft outside the largest fin diameter (the transition area between the circular fence fin and the square spacecraft top). In addition, the insulation support ring becomes simply a thermal extension of the fence plate, thereby increasing the plate area viewing the inside of the spacecraft to a 40-inch diameter circle. The support ring is finished with an optically black paint (3M Black Velvet). The support ring does not touch the spacecraft at its outer edge and is therefore thermally coupled only to the fence plate and the spacecraft interior.

- Beacon and Command Antenna — The beacon antenna, consisting of four dipole elements, is supported from the fence plate. Thermal isolation between the antenna elements and the fence plate is achieved by use of fiberglass insulation spacers at the interface. Shadowing and blockage effects on the fence due to the antenna are minor.

(2) Theory of the Thermal Fence

At a given solar angle of incidence, solar energy is received at the exposed, black fin surface of the fence from two sources; namely, by direct illumination and by indirect reflection from the reflector plate. The reflector plate surface is of high specular

reflectance so that a considerable amount of indirect reflected solar energy may reach the fin. At an angle of incidence of 90 degrees (γ, the angle between the spin axis and the solar vector, is 0 degrees; the solar vector is perpendicular to the reflector plate and parallel to the fins), zero direct solar energy is received by the fin for a perfectly collimated sun, since no fin area is projected to the source. Also, zero indirect solar energy is received by the fin since the perfectly collimated solar flux strikes the reflector plate normally and is reflected back to space. (For this to be exactly correct, the reflector plate must be perfectly flat and perfectly specular.) Thus, for an ideal situation at γ equals 0 degrees, zero solar energy is received by the fin surface.

As the sun angle increases, a different situation occurs. Both direct and indirect solar energy are received by the fin surface. The total amount of solar energy received by the fin continues to increase with increasing γ until a critical angle, γ_c, is reached. At the γ_c position, energy absorbed due to the combined effect of directly projected fin area and effective reflector projected area is maximum, and a further increase in γ causes the energy absorbed to decrease. The thermal fence design selected has a maximum input angle, γ_c, of slightly greater than 60 degrees. This condition was achieved by selecting the geometric relationship of the number of fins, the fin diameter, and the fin height. Thus, a plot of total solar energy incident on the fin surfaces as a function of γ would begin at zero, increase in an approximate sine-curve function to a maximum at γ_c, and then drop sharply at angles greater than γ_c in direct proportion to the solar projected fin area. At γ equal to 90 degrees, only the cylindrical outside surface of the largest diameter fin receives solar input.

In addition to the solar energy flux, an element on a fin surface receives infrared thermal energy from two sources, from the reflector plate and from the other fin elements; this energy can be relatively large quantity for certain situations. Figure 4-III-7 indicates the relative contribution of direct and reflected solar and infrared energy absorbed by a typical thermal fence.

Upon absorption of the incident energy, a major portion is immediately radiated away from the fin element. The remainder is conducted to the adjacent fin elements and to the fence plate, which is normally at a lower temperature than the fin. The fence plate is the primary

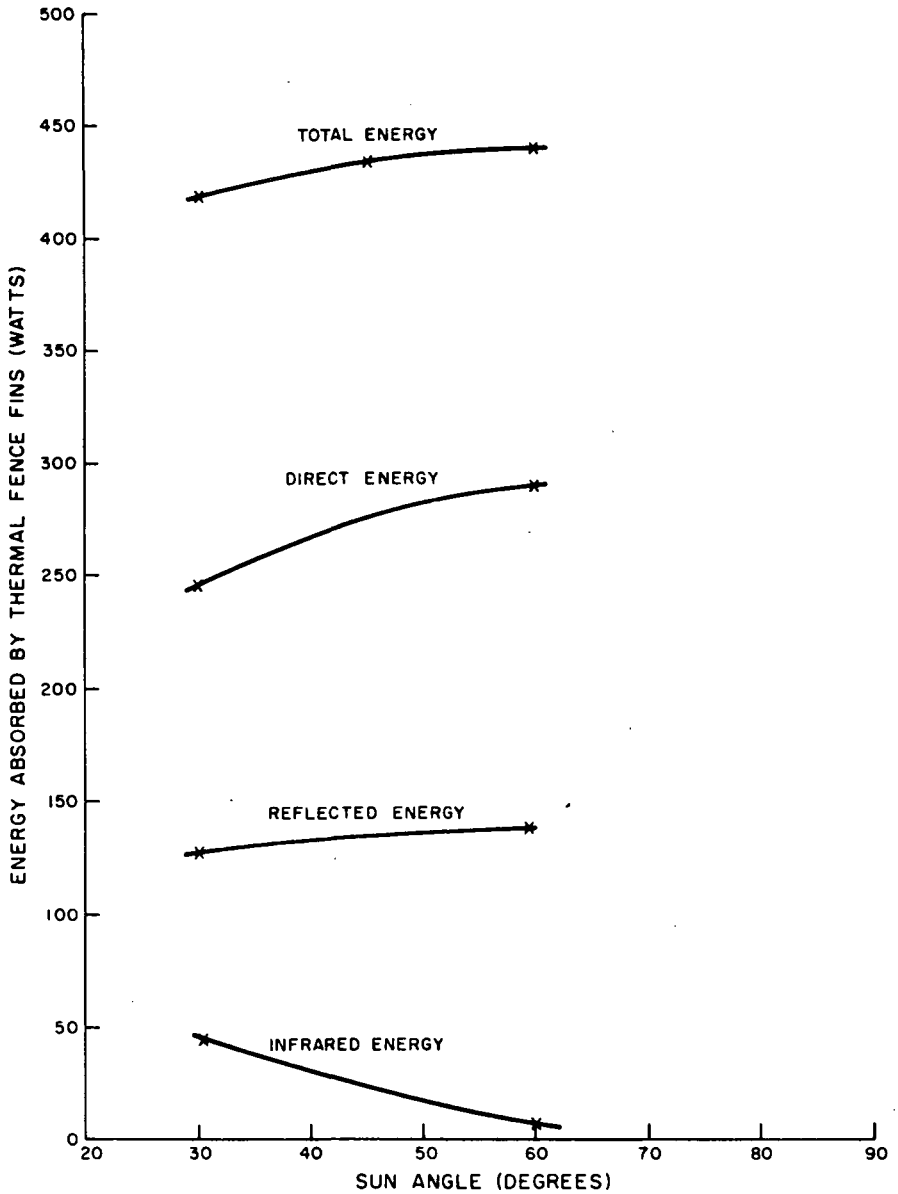

Figure 4-III-7. Energy Absorbed by a Three-Fin Fence with a Polished Aluminum Reflector

part of the assembly which controls the spacecraft temperature, since an observer stationed inside the spacecraft can "see" only the fence plate. Fin-absorbed energy flowing on a net basis into the plate is balanced with the amount of radiant energy exchanged between the fence plate and the spacecraft interior. The fins are distributed relative to the plate in a configuration that helps achieve a relatively uniform plate temperature. In addition, the plate is sufficiently thick to aid distribution of heat input from the fins. Therefore, even though relatively large thermal gradients occur on the fence fins and reflector plate, the fence plate itself approaches an isothermal condition. Figures 4-III-8 and 4-III-9 show typical thermal fence temperature distributions.

(3) Thermal Fence Test

Since a device of this nature has not been used in other space vehicles and has been only reported on a theoretical basis, it was decided to test a full-scale model of the thermal fence under solar simulated conditions. A test was performed at JPL on a two-ring fence design with ALZAK as the reflective surface.

Results of this test were very favorable, in that they matched the predicted temperature values closely. The thermal fence plate was within 2°C of predicted values; and although the values for fins and reflector panels did not agree quite as well; the plate temperature is the determining value. Figure 4-III-10 illustrates the predicted and test values for the two-ring design.

Since the thermal fence is only radiatively coupled to the spacecraft by means of the fence plate, it is desirable to maintain this fence plate at a reasonable uniform temperature. As this was the case in the JPL test, a computation of the net heat exchanged between a 20°C spacecraft and the fence plate was made. The results of these computations and test results are given in Figure 4-III-11.

b. Active Thermal Controller

(1) Selection of Radiation Area

Refinement of thermal control performance is achieved by using temperature-controlled flaps, as previously noted. The performance achievable with varying radiator area is reviewed herein.

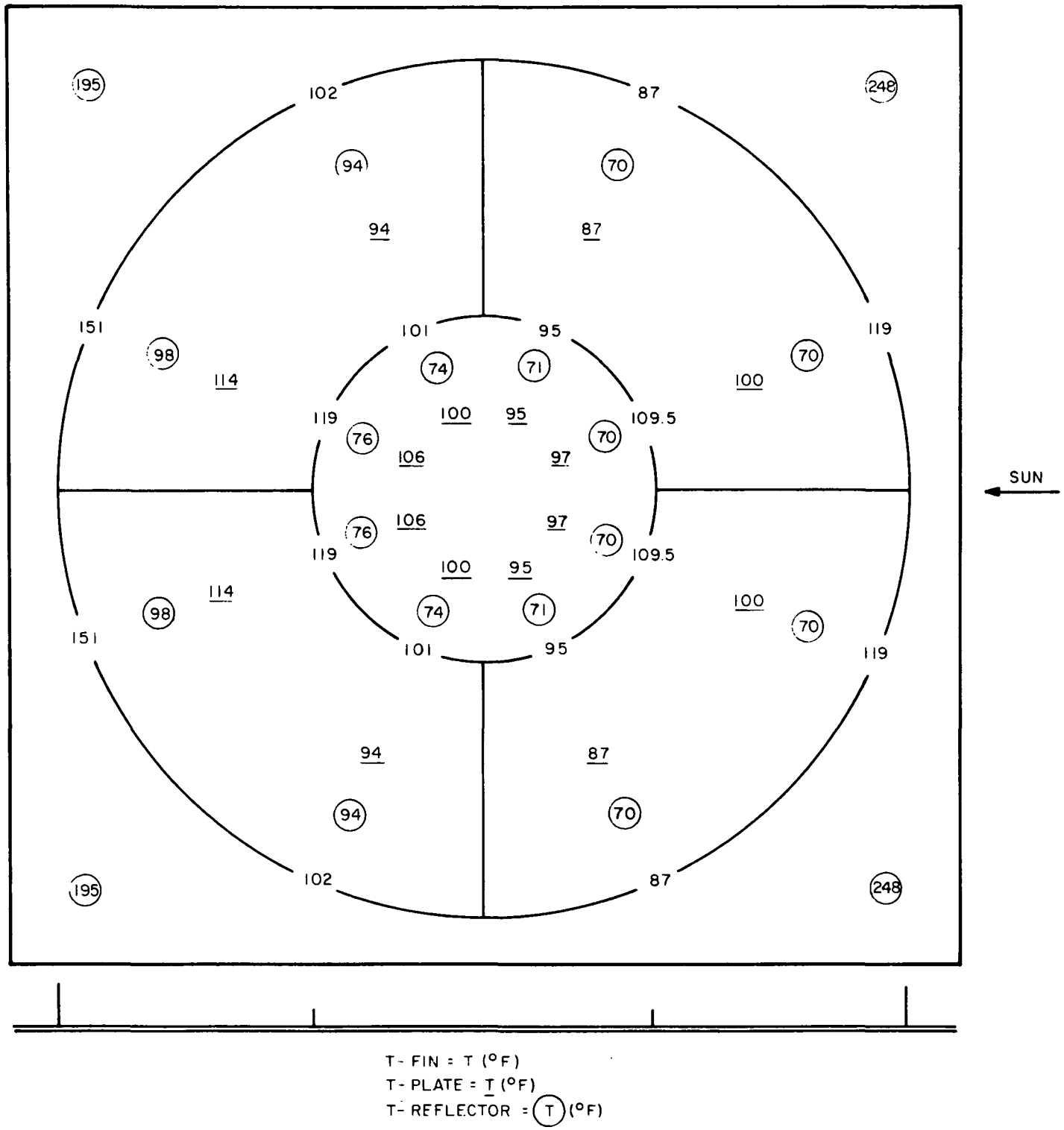

Figure 4-III-8. Thermal Fence Temperature Distribution for a 30-Degree Sun Angle

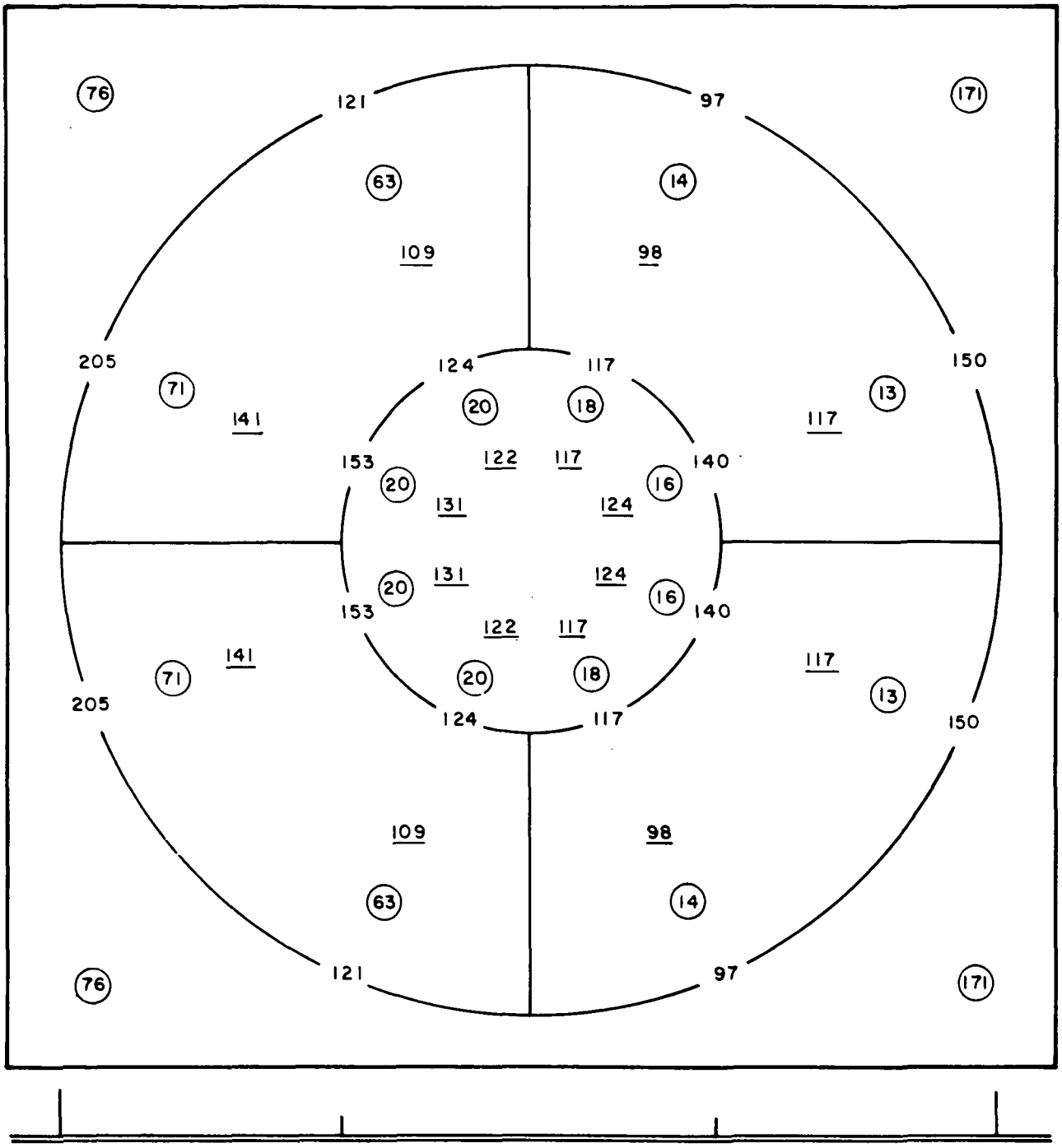

Figure 4-III-9. Thermal Fence Temperature Distribution for a 60-Degree Sun Angle

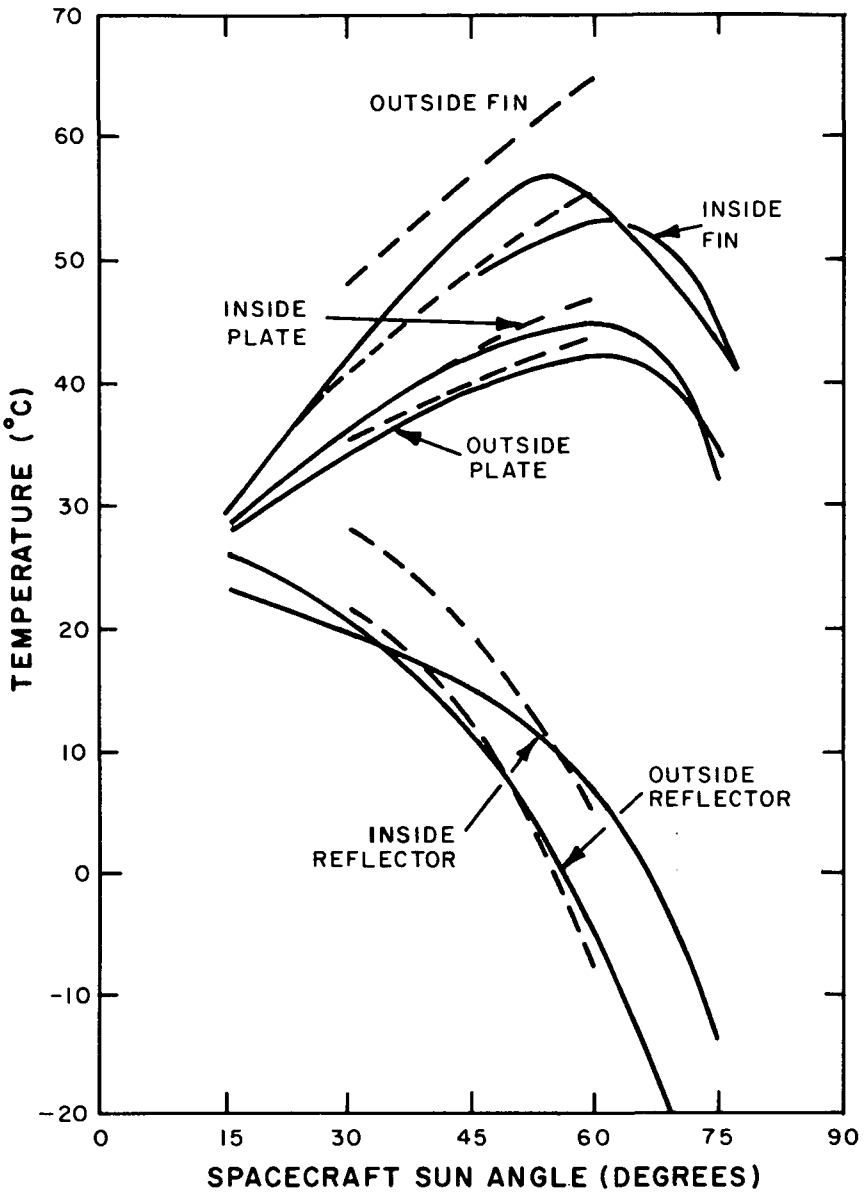

Figure 4-III-10. Thermal Fence Temperature Variation

The temperature levels of the spacecraft can be adjusted by selection of the proper radiator size and distribution on the equipment panels and baseplate. Figures 4-III-12 and 4-III-13 show the importance of such selections. These curves apply only to a three-ring fence design; however, they are included here for illustration of radiator size effect on the thermal balance. The ratio of the baseplate radiator to the total radiator area is shown. The total radiator area is the sum of the baseplate area plus the two equal side-radiator values. The solid curves represent the baseplate temperature isotherms, while

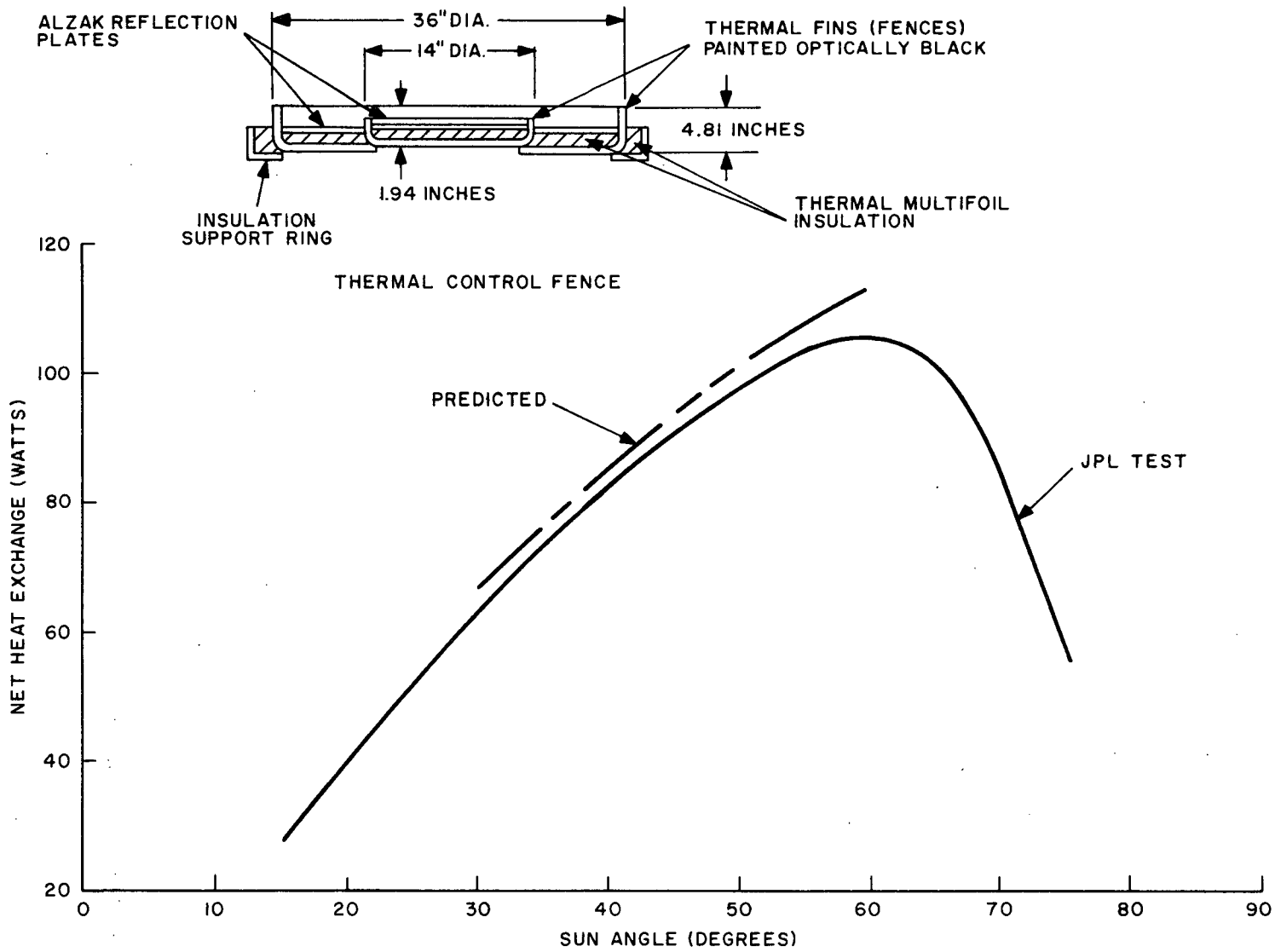

Figure 4-III-11. Net Heat Exchange Between Thermal Fence Plate and 20°C Spacecraft

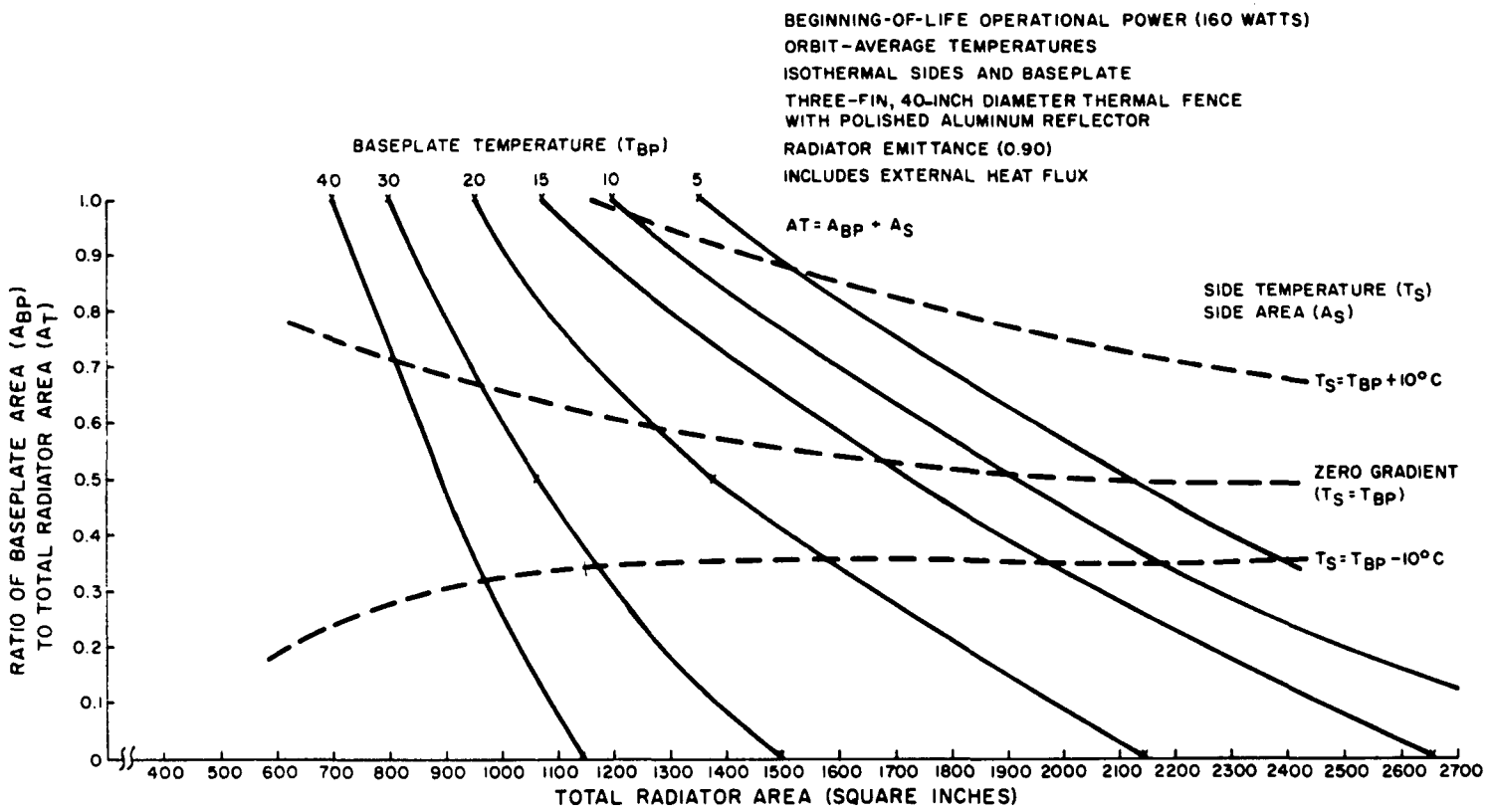

Figure 4-III-12. Baseplate Temperature as a Function of Radiator Variables for a 30-Degree Sun Angle

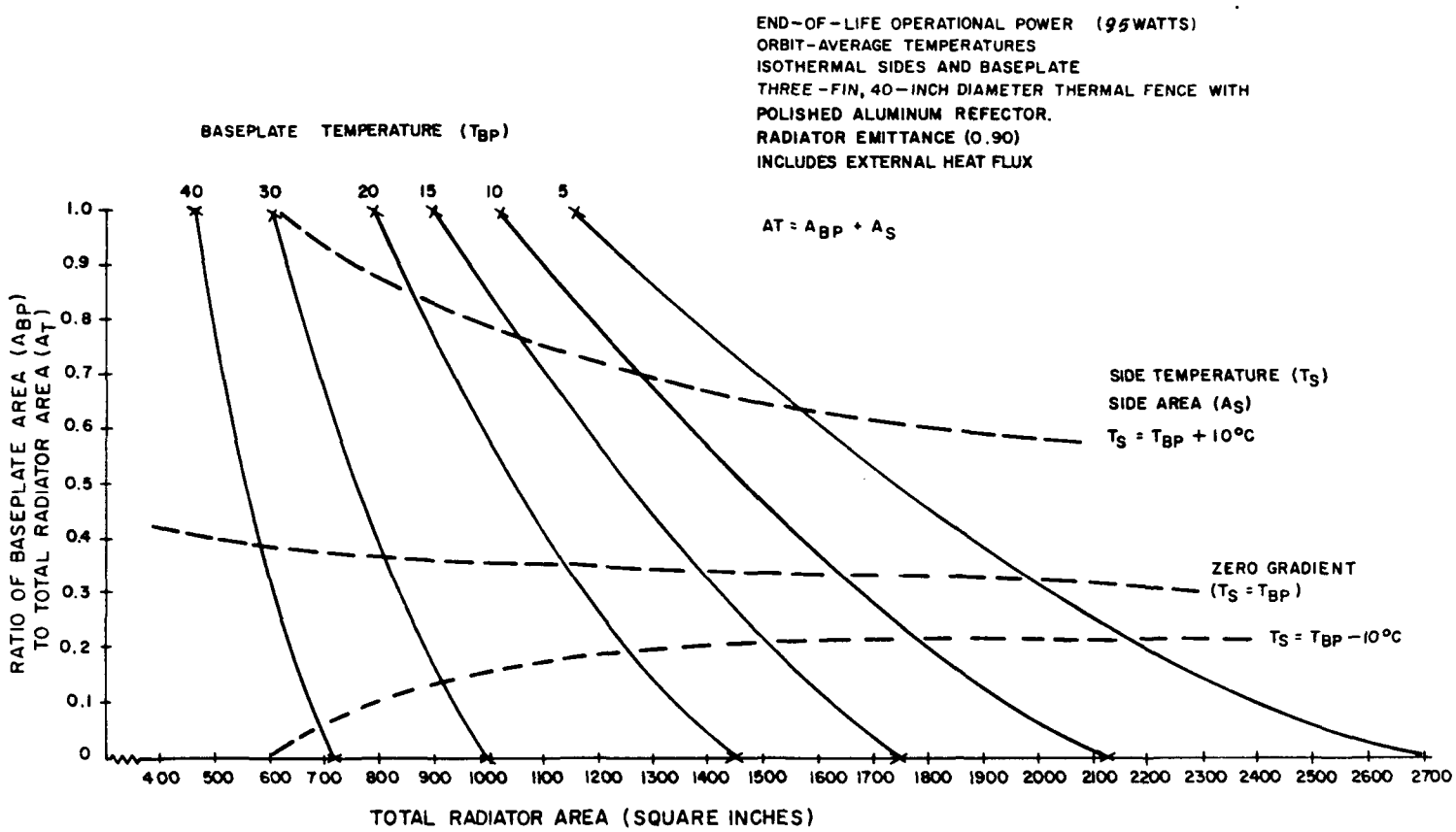

Figure 4-III-13. Baseplate Temperature as a Function of Radiator Variables for a 60-Degree Sun Angle

the dashed curves show the difference between the side temperature and the baseplate temperature. Of particular interest is the side temperature curve labeled "zero gradient". This line indicates those radiator relationships that result in equal side and baseplate temperatures. An example may best explain the significance of the curves. If a baseplate and side temperature of 20°C is desired at a 30-degree sun angle, Figure 4-III-12 indicates that the radiator relationship must be such that the total area must be 1270 square inches, and the ratio of the baseplate area to the total area must be 0.59. From these values the baseplate area must be 750 square inches, and each side area must be 260 square inches. In Figure 4-III-13, for a 60-degree sun angle, these radiator areas result in a baseplate temperature of 13°C and a side temperature of 20°C.

While equal side and baseplate temperatures could be achieved for the 30-degree orbit case, a 7°C temperature gradient occurs at the 60-degree orbit case for a fixed radiator distribution. If the same total radiator area were utilized with a distribution of $A_S = 400$ in^2, $A_{BP} = 470$ in^2, and $A_{BP/AT} = 470/1270 = 0.37$, the resulting temperatures would be as follows:

	Temperature (°C)	
Area	30-Degree Orbit	60-Degree Orbit
Baseplate	26	17
Side	17	17

From this new example, an entirely new set of temperatures has been obtained, the gradient at the 60-degree orbit condition has been eliminated, but a reversed 9°C gradient now occurs at the 30-degree orbit condition. Proper selection of the total area and the radiator distribution becomes important if particular temperature gradient values are desired.

Figures 4-III-12 and 4-III-13 show the wide range of radiator combinations that maintain the temperatures within the range of 10 to 30°C. However, the wide range of solutions are considerably reduced when the preoperational mode is considered. Generally, the results of the preoperational mode studies require that the baseplate radiator area be confined to a relatively narrow range of values and that the side radiator areas viewing the solar panels be relatively large.

(2) Control of Radiation Area

An obvious consequence of the foregoing discussion is that if the radiator area values were allowed to vary, almost any desired temperature distribution could be achieved. For example, if constant side and baseplate temperatures of 20°C were desired for the 30- and 60-degree operational conditions, the values from Figures 4-III-12 and 4-III-13 would be given in Table 4-III-1.

TABLE 4-III-1. RADIATOR AREA VALUES FOR CONSTANT 20° TEMPERATURE OF SIDE AND BASEPLATE

Orbital Condition	T_{BP}	T_S	A_{BP}	A_S	A_T	A_{BP}/A_T
30-Degree Orbit, BOL	20°C	20°C	750 in^2	260 in^2	1270 in^2	0.59
60-Degree Orbit, EOL	20°C	20°C	400 in^2	375 in^2	1150 in^2	0.35

Therefore, if means were provided to vary the baseplate area by 350 square inches and each side area by 115 square inches, a constant 20°C temperature would be achieved. To accomplish this variation, an active thermal control system can be employed. The active control system does not change area, but rather, varies the effective emittance of the fixed radiator area to achieve the same effect. Typical effective emittance controllers include rotating louvers, sliding vanes, and iris-type devices. In each case the effective emittance change is the result of covering part of the high emittance radiator surface (0.9) with a variable position, low emittance surface (0.005 to 0.2). Since radiant heat rejection from a radiator is a function of the area emissivity (AE) product, the weighted area emissivity products of the high and low emittance materials give the desired effect.

(3) Method of Active Area Control

While placement problems preclude the use of an active controller on the ITOS baseplate (the ideal case), active area control is provided by a pair of variable radiator surfaces, one on each of the two side panels. Currently, the radiators provide a maximum area of approximately 450 square inches on each of the two equipment panels. Of this 450 square inches of area, 150 square inches are continuously exposed to the external environment. This provides a bias area that is available in case of a failure of the active controller

in the closed position. In the operational mode, the exposure of each radiating surface is controlled by two flaps whose angles with respect to the side panels are a function of the spacecraft temperature. Figure 4-III-14 illustrates the fluid actuation mechanism that provides an angular range of 0 to 90 degrees for a 0.6-inch linear motion over a 20°C temperature differential. Prior to achieving the operational mode, the controlling flaps expose as much of the side radiating surface as possible.

The essential elements of the system are the flaps, an actuator, and a sensing element. The flaps consist of a reinforced "picture-frame" structure, filled with a multilayer insulation. Because a maximum side radiator area must be exposed during launch, and to maximize the efficiency during both the preoperational and operational modes, the flaps are designed with a single fold and a 5-inch bias. When the solar panels are deployed, the active thermal control flaps unfold to expose the radiator area of 450 square inches partially. In their folded positions during launch, the flaps are retained by the panels and expose the entire 450-square-inch radiator area.

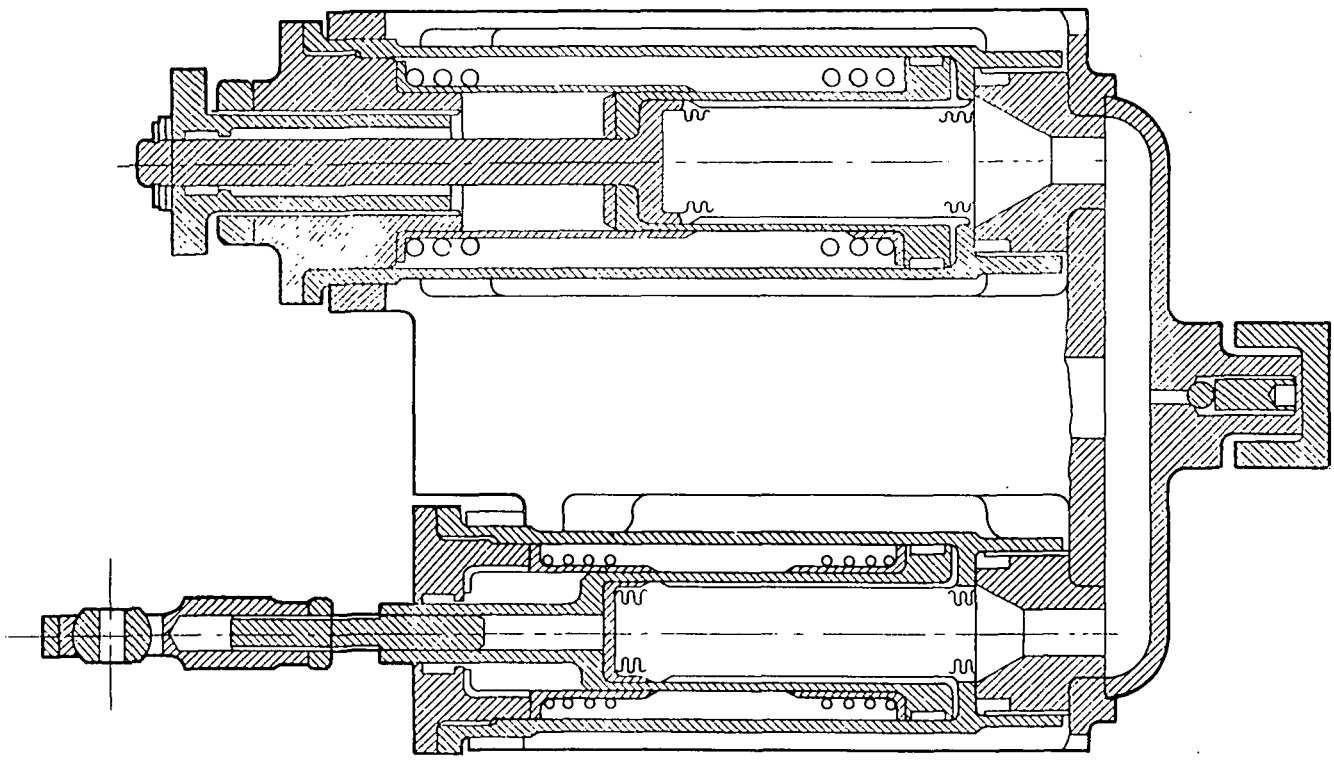

Figure 4-III-14. Active Thermal Controller

The positioning actuator for the system is a fluid-driven bellows whose linear travel is converted to angular position through a drive linkage. This linkage also compensates in some degree for the nonlinear emittance versus flap angle characteristic such that the resulting effective radiating area as a function of spacecraft temperature will approximate a linear function.

The sensing element is a fluid of predetermined volume and known thermal expansion coefficient. This sensing fluid changes volume which results in linear expansion or contraction of the actuator. Figure 4-III-15 presents the effective radiator area as a function of the flap angle provided by this position actuator.

c. Baseplate Radiator

(1) Preoperational Mode Considerations

Preoperational mode conditions impose severe thermal restraints. The side radiators can view only the folded solar panels during injection. A temperature range of

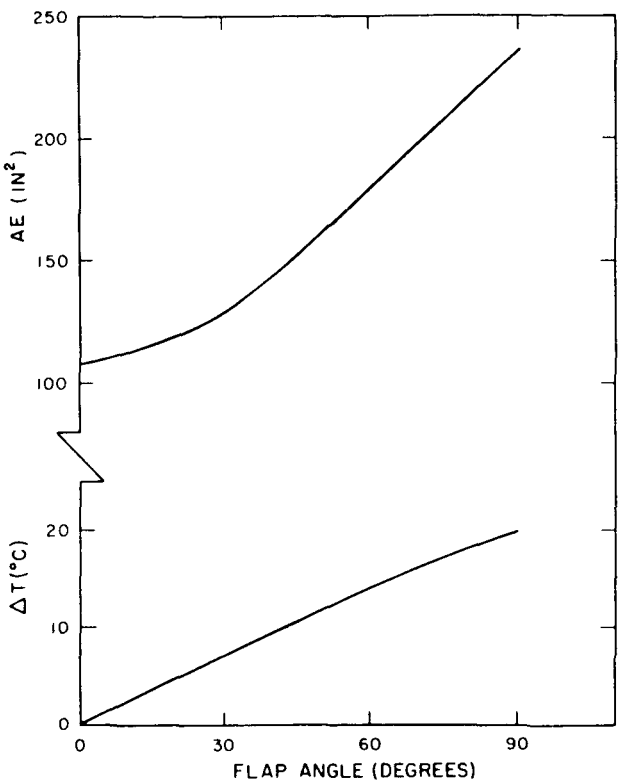

Figure 4-III-15. Active Thermal Controller Performance Characteristics

-5 to 45°C was specified as the goal for the baseplate and side surfaces for the preoperational situations. A worst-case analysis was performed where steady-state orbital average temperatures were computed for a sun angle range from 30 to 150 degrees and for 88- and 73-percent suntime orbits. Curves similar to those of Figures 4-III-12 and 4-III-13 were developed for each of the preoperational conditions. The key information developed from this analysis is as follows:

- The temperature adjustment afforded by radiator location is lost since the side radiators are blocked by the folded solar panels.
- The area variation of the side radiator has a small effect upon the spacecraft temperature as compared to an area variation of the baseplate surface which views cold space.
- The effective thermal control by the thermal fence is lost at sun angles greater than 90 degrees since the thermal fence is not illuminated by the sun. A relatively large heat loss from the fence occurs at these high sun angles, resulting in low temperature values.
- The total radiator area is considerably reduced with the side radiators blocked. Thus, at sun angles near the fence critical angle (approximately 60 degrees), high temperatures result since the fence is absorbing a large amount of energy relative to the total radiator size.
- A sun angle of 90 degrees generally results in the coldest temperature levels. The primary source of heat input is the warm solar panels viewed by the side radiators. (Minimum load power was used for all preoperational mode calculations. See Figure 4-III-5.)

Design restrictions during the preoperational mode call for a 24-hour period prior to start of the maneuver to the operational mode. This allows for a transient period to maintain the equipment within the -5 to 45°C temperature limit. Proper sizing of the baseplate radiator and the thermal time constant of the components can be utilized to meet these limits.

C. THERMAL PERFORMANCE

1. Analysis Model Description

The system for which temperature data is reported herein has the following features:

- A two-fin thermal fence with an outside fin diameter of 36 inches. The reflector plate material is ALZAK.
- A fixed baseplate-radiator area of 610 square inches.
- Side radiator areas which assume the following fixed area positions:
  - (1) Both active control systems in completely open flap position (A_S = 450 in^2);
  - (2) Both active control systems in completely closed flap position (A_S = 150 in^2); or
  - (3) Both active control louvers in the fully open position under the solar panels during preoperational mode (A_S = 450 in^2).
- Black side radiator (α = 0.97, ϵ = 0.895) and gray baseplate radiator (α = 0.45, ϵ = 0.87).
- Power dissipation profiles as specified in Paragraph A.3 of this section.

2. Preoperational Mode

Figures 4-III-16 and 4-III-17 illustrate the thermal performance of the selected design for two preoperational orbits. Steady-state temperature values were computed for the complete spacecraft sun angle range of 30 to 150 degrees. For the required range of 35 to 145 degrees, the figures show an overall worst-case steady-state envelope for the baseplate of from -2°C (at γ = 90°, 73-percent suntime orbit) to +34°C (at γ = 145°, 88-percent suntime orbit). The side equipment panels have an overall worst-case envelope from -4°C (at γ =.120°, 73-percent suntime orbit) to 29°C (at γ = 60°, 88-percent suntime orbit). Thus, bounding of the steady-state temperatures within -5 to 45°C has been achieved with the selected configuration.

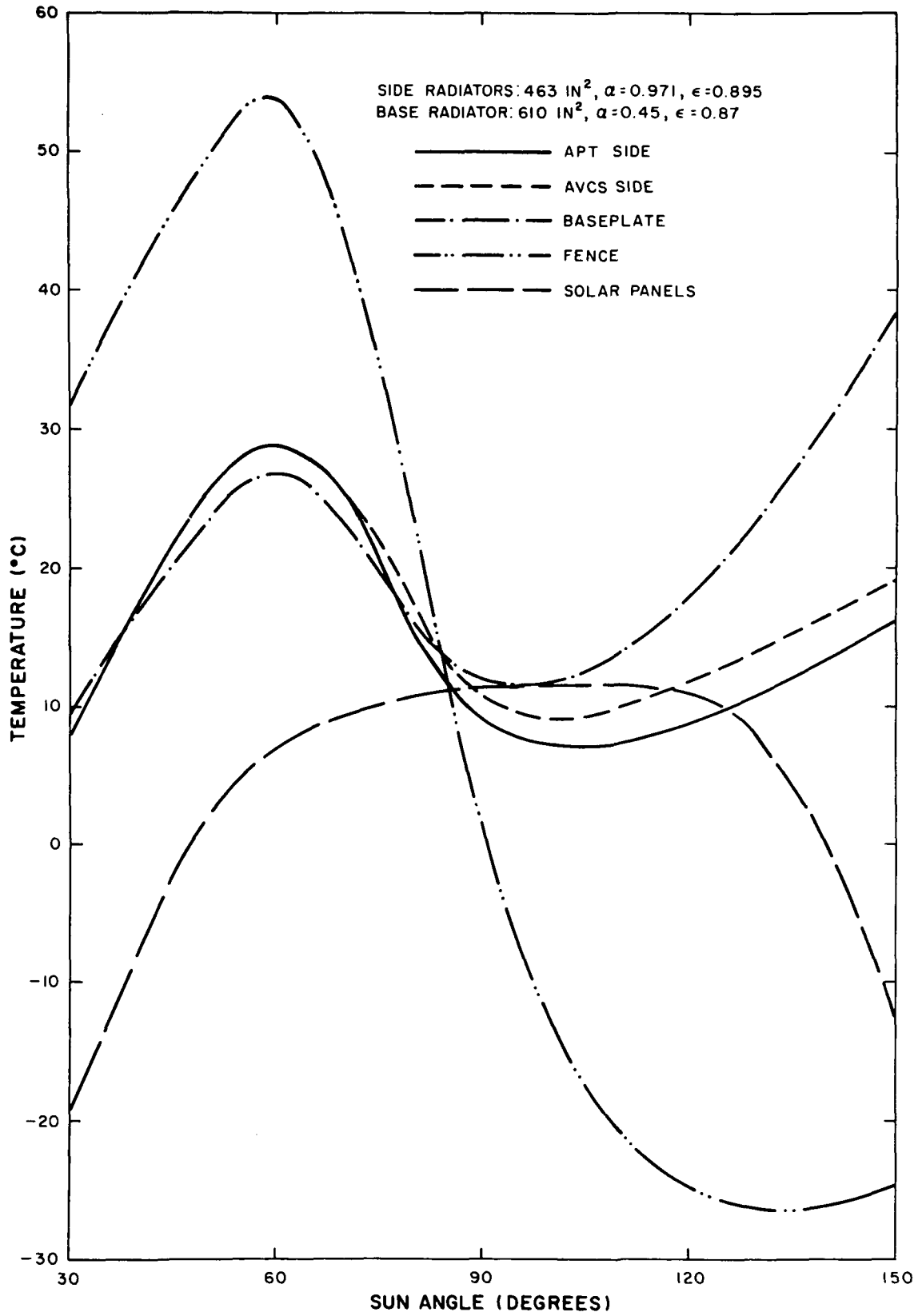

Figure 4-III-16. Preoperational Mode Temperatures for 38-Degree Sun Angle and 88-Percent Suntime

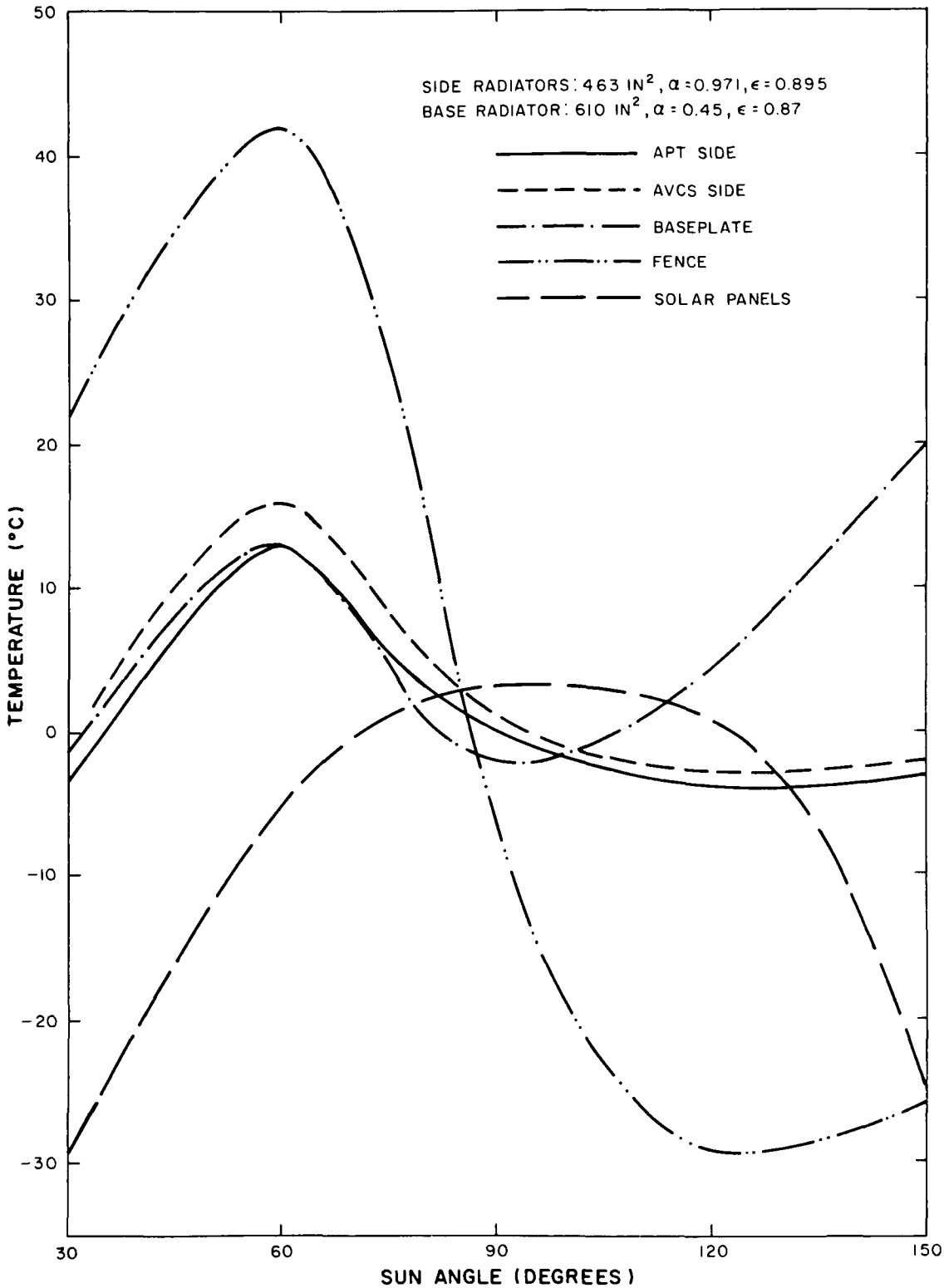

Figure 4-III-17. Preoperational Mode Temperatures for 60-Degree Sun Angle and 73-Percent Suntime

Figure 4-III-18 shows preoperational mode steady-state equipment panel temperatures for a 38-degree orbit angle and 150-degree sun angle.

Since the above figures are for steady-state conditions, a transient computation of preoperational mode temperatures for a 24-hour period after injection was made for the cold condition only (at $\gamma = 30°$, 73-percent suntime orbit). The results of the transient analysis given in Table 4-III-2 indicate a larger margin than steady-state temperatures.

3. Operational and Failure Mission Modes

Figures 4-III-19 and 4-III-20 illustrate the orbit average temperature range achieved for the selected design. Power dissipation values assume a growth of 10 watts per side panel at 30 degrees BOL (maximum condition) and no growth at 60 degrees EOL (minimum condition).

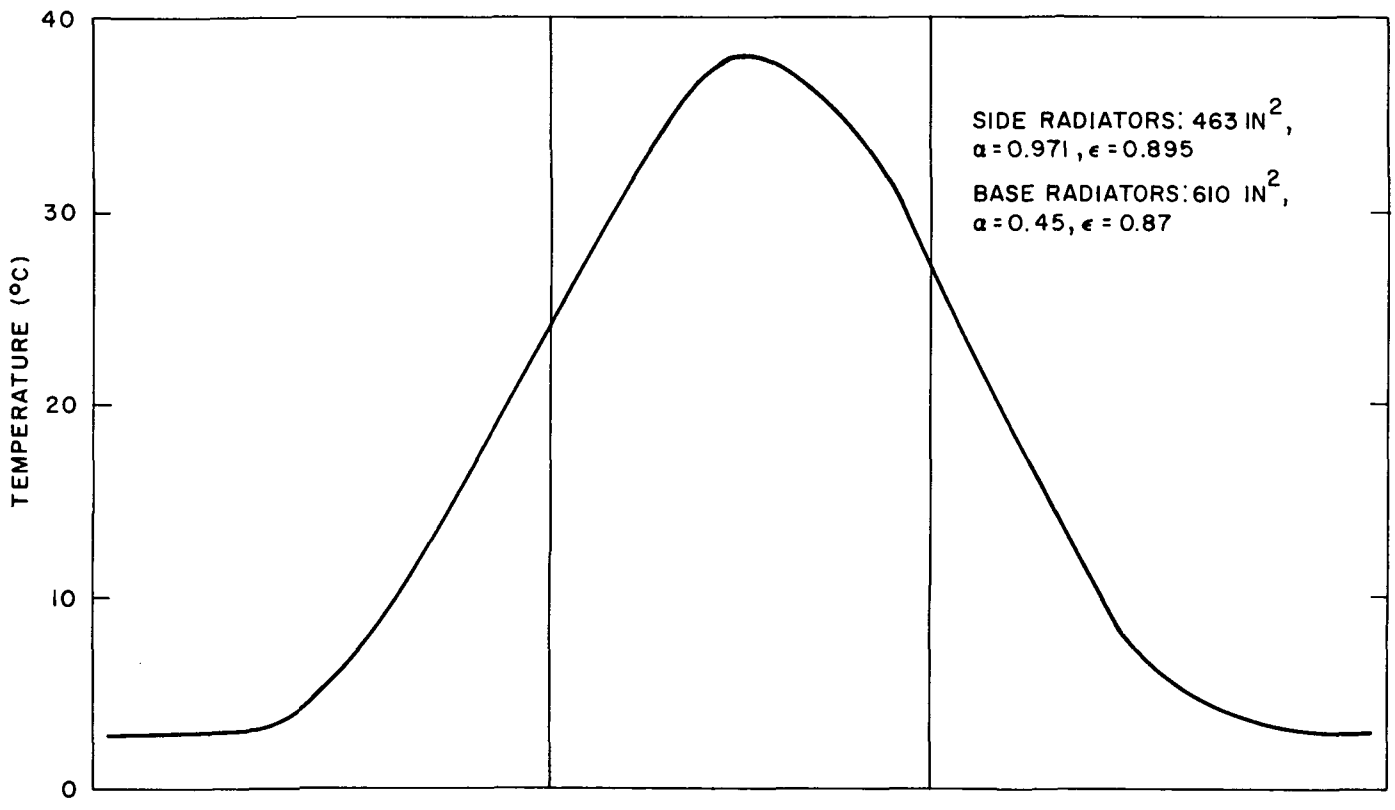

Figure 4-III-18. Average Equipment Panel Temperatures for 38-Degree Orbit Angle Injection Case and 150-Degree Sun Angle

TABLE 4-III-2. 60-DEGREE ORBIT ANGLE INJECTION CASE TRANSIENT TEMPERATURE STUDY AT 30-DEGREE SUN ANGLE

Location	Temperature (°C)		
	24 Hours After Launch (minimum)	Steady-State (minimum)	Steady-State (orbit average)
Solar Panels	-62.0 to -42.3	-62.7 to -43.3	-30 to -25
Fence	-22.3	-23.7	-21
Top	-12.6	-14.4	-16
APT Side	-0.4 to 0	-3.8 to -2.5	-4 to 0
Baseplate	-0.8 to 6.0	-3.1 to 2.1	-3 to 2
AVCS Side	1.1 to 2.2	-2.4 to -0.6	-2 to 0
Nonequip. Panels	1.2 to 3.9	-1.7 to 0.9	1 to 2
ATC Flaps	-47.5	-48.3	-25
ALZAK	-41.4	-41.8	-11
Top Corners	-73.9	-74.3	-74

Figures 4-III-19 and 4-III-20 give the temperatures of the equipment panels over the entire 0- to 90-degree flap angle range as well as the limits of the temperature gradients on the side panels. Combining the results of the analysis gives the mean temperatures of the component mounting surfaces during the operational mode, as shown in Table 4-III-3 for flap angles of 83 degrees at beginning of life and 64 (APT) and 61 (AVCS) degrees for end of life.

Table 4-III-3 indicates that the design specification of 5 to 35°C for the component mounting surfaces is easily met with the proposed thermal design configuration. Also, it should be noted that the active thermal controlled flaps provide a maximum component mounting temperature variation of 10°C. This is well within the specified differential for the

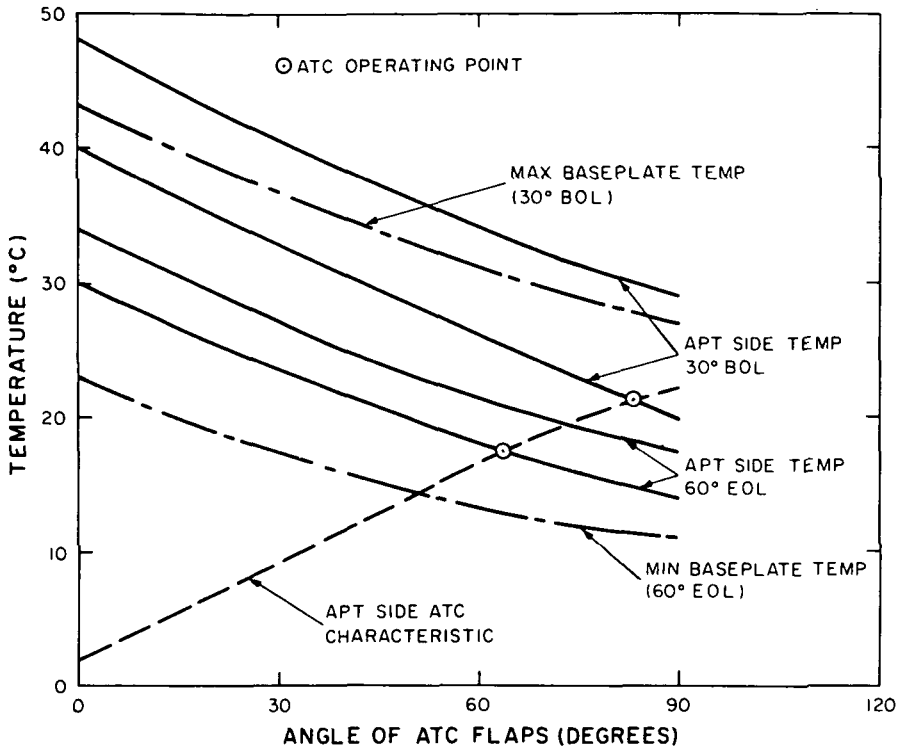

Figure 4-III-19. ITOS Operational Temperature of APT Equipment Panel Versus Flap Angle

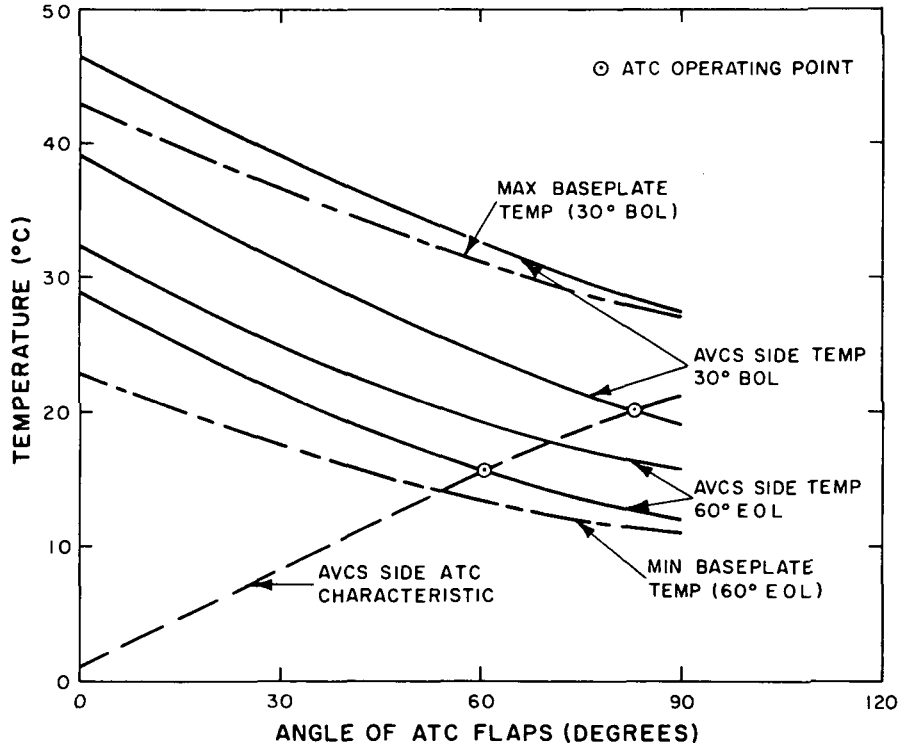

Figure 4-III-20. ITOS Operational Temperature of AVCS Equipment Panel Versus Flap Angle

TABLE 4-III-3. COMPONENT MOUNTING SURFACE TEMPERATURES DURING OPERATIONAL MODE

Location of Measurement	Temperature (°C)	
	30 Degrees, BOL*	60 Degrees, EOL**
Fence	47	43
Component Mounting Surfaces		
APT Side	24	19
Baseplate	26	16
AVCS Side	23	17

*APT and AVCS flap angles, 83 degrees.

**APT flap angle, 64 degrees; AVCS flap angle, 61 degrees.

30- to 60-degree operational orbits. The only other criterion to be met is the failure mode temperature specification of 0 to 40°C.

Two types of failure were considered, a failure of component subsystems resulting in a lower power dissipation level (50 watts minimum, all on the baseplate) and a failure of both flaps on one side. Figures 4-III-19 and 4-III-20 show the resulting temperatures for all the flaps failing either open (90-degree angle) or closed (0-degree angle). The resultant mean temperatures for such failures are listed in Table 4-III-4 along with the temperatures for failures with one side open and the other closed. These results indicate that even for the more severe failure (all flaps failed), the temperature range specification of 0 to 40°C for the component mounting surfaces is almost met.

For a power failure of the component subsystems, the flaps would go to the closed position depending on the level of reduced wattage. In the extreme, all the flaps would be closed and the component mounting temperature and power dissipation would be dependent on the bias area. Figure 4-III-21 shows the average temperature of the equipment mounting surface versus the bias setting for 50 watts dissipation on the baseplate and no dissipation on the side panels. This curve illustrates that to meet the temperature specification of 0°C the bias could be

TABLE 4-III-4. COMPONENT MOUNTING SURFACE TEMPERATURES FOR ATC FLAP FAILURE CASES

Location of Measurement	Temperatures (°C)		
	30 Degrees, BOL		60 Degrees, EOL
	APT Side Closed, AVCS Side Open	Both Sides Closed	Both Sides Open
Fence	50	53	42
Component Mounting Surfaces			
APT Side	35	43	16
Baseplate	32	40	14
AVCS Side	28	42	14

larger than the 5 inches selected for this configuration and the power level could go below 50 watts.

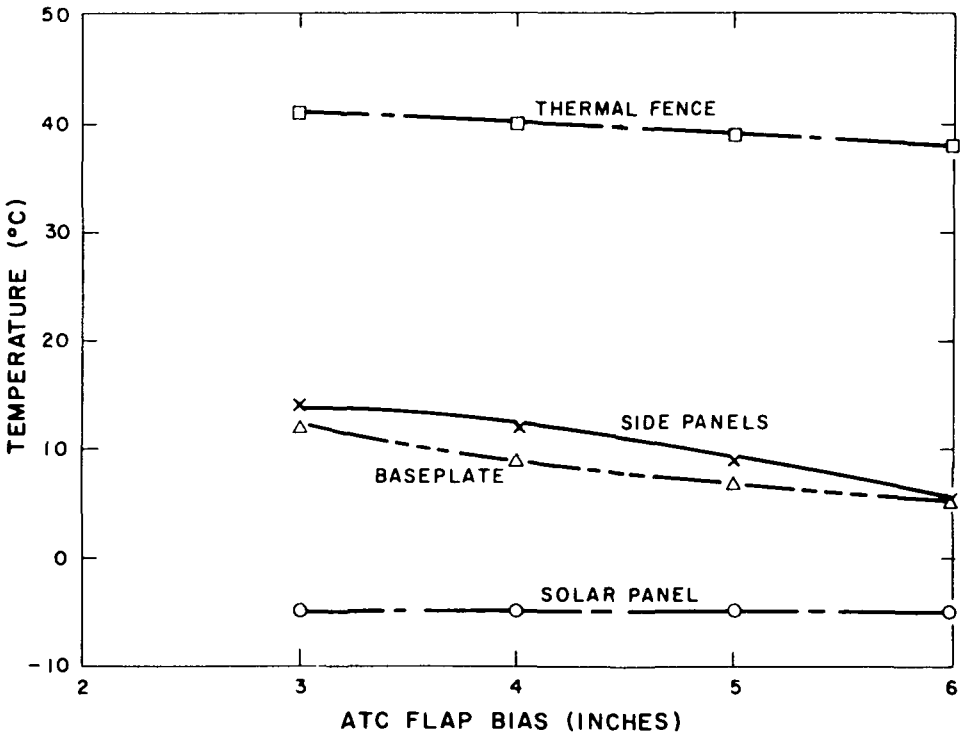

Figure 4-III-21. Average Temperature Versus Bias Setting of Active Thermal Controller Flap for Minimum Power of 50 Watts at 60-Degree Orbit Angle at End of Life

SECTION IV

VEHICLE DYNAMICS SUBSYSTEM*

A. SUBSYSTEM DESCRIPTION

The attitude control performance requirements for ITOS are largely dictated by the pointing and stability of the multiple primary sensor configuration and by the rates of satellite and orbital plane motion. Optimum orientation for such a multiple sensor platform is continuous earth orientation. The unique coupling of a despun platform, through bearings, to a spinning flywheel is the simplest method of meeting the primary sensor requirements while maintaining all the desirable dynamics of a spin stabilized spacecraft.

The ITOS dynamics subsystem enables the satellite to align the roll, yaw, and pitch axes with a rotating set of coordinates consisting of the local horizontal, local vertical, and orbit normal. (See Figure 2-I-1.) The subsystem will:

- Despin the spacecraft from the initial spin rate of the spacecraft third-stage combination to a nominal spin rate,
- Dynamically stabilize the despun satellite,
- Damp the nutation of the satellite to a half-cone angle of less than 0.3 degree,
- Precess the spacecraft until the momentum vector is nominally aligned with the orbit normal,
- Adjust the total momentum to within ±10 percent of the nominal design value of 200 inch-pound-seconds,
- Align and maintain the attitude about the pitch axis to ±1 degree about an earth reference, and
- Align and maintain the momentum vector to within ±1 degree about the orbit normal.

---

*Refer to Summary of Current Design Revisions Not Covered in this Report, following the Preface, for a brief description of revisions made since the cut-off date for this report.

This subsystem is designed to operate continuously in the space environment for at least 1 year. The major functional elements of the subsystem are shown in the block diagram in Figure 4-IV-1. The subsystem consists in part of a redundant pitch control loop, functionally redundant roll axes control coils (QOMAC and MBC), redundant momentum control coils, redundant nutation dampers, and a despin mechanism.

In orbit operation, motion about the pitch axis is controlled by a flywheel and torque motor, utilizing error signals from the pitch horizon sensor and the shaft encoder. Either of the redundant roll horizon sensors can be switched into the pitch loop if the orthogonal pitch horizon sensor becomes inoperative. These horizon sensors derive their scanning from a mirror mounted on the flywheel. The pitch loop can be commanded into either of two modes. The open-loop mode causes the flywheel to rotate at a fixed speed for dynamic stability. The equipment module is not despun and oriented to the earth. The closed-loop mode causes the wheel to rotate at a speed that will despin the equipment module to 1 revolution per orbit and establish its proper pitch orientation. The pitch control loop is capable of performing this orientation maneuver within 5 minutes after the closed-loop command is received, assuming the spacecraft momentum is within ±10 percent of the nominal design value. If the momentum is not within the specified limits, redundant magnetic coils can be activated to correct the total spin axis momentum.

In addition to pitch axis control, the subsystem provides roll and yaw axis control by ground command. This is accomplished by utilizing the torques developed by the interaction of the earth's magnetic field with controlled dipole moments generated within the spacecraft. The controlled dipole moments are generated by the same type of magnetic coils flown successfully on the TOS spacecraft. The magnetic bias control (MBC) coil, controlled by the magnetic bias switch, generates a continuous dipole and is used to cancel the spin axis component (rotation about the pitch axis) of the spacecraft residual dipole as well as to provide the torque necessary to precess the spin axis at the orbital regression rate of 1 degree per day. The quarter-orbit magnetic attitude control (QOMAC) coil provides controlled precession of the spin axis through quarter-orbit polarity reversal of its spin axis dipole moment. Two QOMAC modes of operation are provided. The high torque QOMAC mode electrically parallels the MBC and QOMAC coils so that high precession rates can be

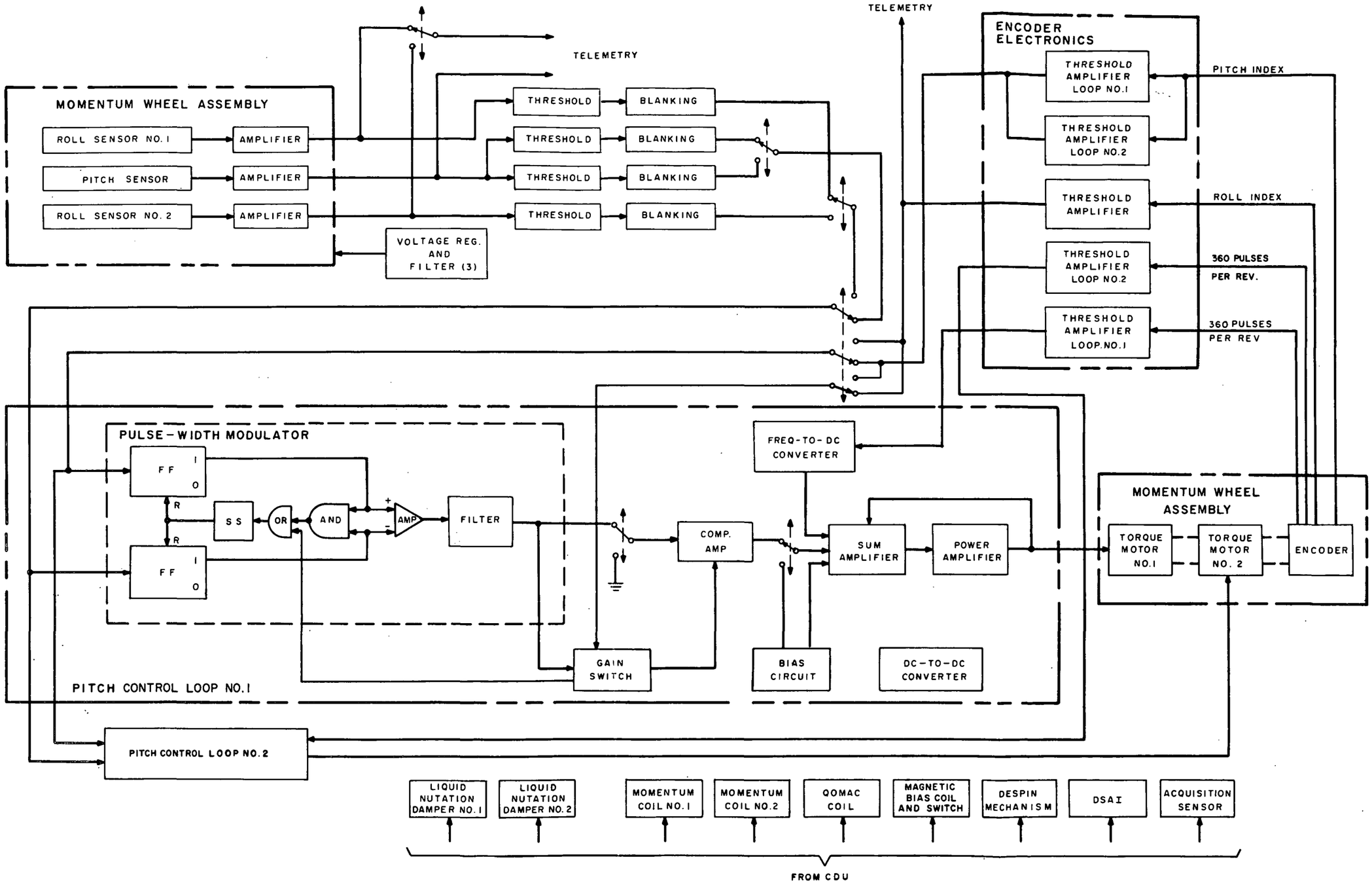

Figure 4-IV-1. Vehicle Dynamics Subsystem, Simplified Block Diagram

achieved for the initial orientation maneuver which positions the spacecraft pitch axis perpendicular to the orbit plane. The low torque QOMAC mode is used to provide minor corrections to mission mode spin axis drifts.

Spin axis nutation is controlled by liquid dampers similar to those flown on the TOS spacecraft. Nutation will result from the following disturbances: (1) operation of the on-board equipment that contains momentum along a transverse axis, (2) operation of the separation and despin equipment, (3) operation of the magnetic control components, and (4) bombardment by micrometeorites. The liquid-filled nutation dampers will be "caged" until the spacecraft is stabilized by the flywheel operating in the open-loop mode, because of a dynamically unfavorable spacecraft inertia ratio. They will be uncaged by ground command.

The yo-yo mechanism will despin the satellite after separation from the third stage and will reduce the system momentum to near the nominal operational value.

The spacecraft is equipped with sensors to provide continuous attitude information for all spacecraft attitudes. During the initial orientation maneuver, the flywheel-mounted attitude sensors may not be scanning the earth when the spacecraft is over the ground station. Attitude information, however, will be obtained from an attitude acquisition infrared horizon sensor and a digital solar aspect indicator (DSAI) mounted on the spinning equipment module.

B. INITIAL ORIENTATION MANEUVER

1. Preseparation

The initial orientation maneuver consists of the events required to alter the attitude and momentum of the spacecraft from third-stage separation to operational three-axis earth-oriented control. The maximum time for the entire sequence is 2 days. ITOS, with the third stage, has an inertia distribution dynamically equivalent to that of a rod spinning about its longitudinal axis. The spin rate is sufficient to prevent significant nutation during the short interval prior to separation. Douglas Aircraft Corporation (DAC) defines the maximum coning angle of ITOS and the third stage (TE-364) as 2 degrees, half angle, based on the records of Surveyor I and a recent Air Force flight.

The sequence of events which represents the initial orientation maneuver is presented as follows:

- Third stage and spacecraft spin up to between 81 and 99 rpm (momentum axis nominally pointing south).
- Third stage and spacecraft achieve injection velocity.
- Third stage and spacecraft separate approximately 10 minutes after spin up (separation velocity greater than or equal to 5 feet per second). Yo-yo time delay begins.
- Spacecraft despins to 1.0 rpm by releasing yo-yo's, nominally 20 seconds after separation; then power is applied to the tachometer loop for the torque motor for open-loop operation (controlled by redundant separation switches and timers).
- Torque motor rotates the momentum wheel at 60 rpm with respect to the main body of the spacecraft.
- When ground station contact is next established, the spacecraft telemeters attitude and torque motor data to the CDA station.
- Liquid dampers "uncage" by ground command.
- High torque QOMAC begins by ground command.
- Spacecraft attitude is measured until mission orientation is achieved.
- Solar panels deploy by ground command.
- Control loop for the torque motor switches to closed-loop operation by ground command. Under control of the electronic loop, momentum wheel speed is nominally 150 rpm.
- Momentum coils correct the satellite momentum by ground command, as required.

Prior to separation, the third-stage/satellite combination is spun up to 90 rpm, with the resulting momentum vector pointing toward the southern hemisphere. During the period from spin up to separation (minimum of 9 minutes), approximately 30 seconds are used for third-stage burning; the remainder of the time is used primarily for decay of the solid motor "chuffing".

2. Despin

When separating from the third stage, the following inertia changes take place:

Axis	Inertia (lb-in-sec^2) Third Stage/ ITOS (before separation)	ITOS (after separation)
Pitch (spin)	660	625
Roll	1796	678
Yaw	1859	735

Since the spin rates remain essentially unchanged during the short time required for separation, the maximum 2-degree nutation angle defined for the combination will reduce to about 1.0 degree for the separated ITOS, due to the above inertia changes. Allowing for an additional transverse rate of 3 degrees per second (DAC figure) as the result of tolerances pertaining to the four separation springs, a maximum initial nutation angle of 1.4 degrees can be expected prior to despin. While the third stage and spacecraft are separating at a minimum rate of 5 feet per second, no provision can be made for passive damping of the nutation in preparation for yo-yo despin. Unlike earlier TIROS and TOS spacecraft, ITOS exhibits an unfavorable inertia distribution even after spacecraft separation. To minimize the tendency of the spacecraft to spin about the axis of maximum inertia (yaw), the liquid-filled nutation dampers are initially caged.

The despin of the ITOS spacecraft was analyzed by digital computer simulation. The parameters which governed the analysis are presented below (further analysis is presented in Appendix D of this report).

Parameter	Value
Initial Spacecraft Spin Rate	90 rpm ± 10 percent
Initial Momentum	5900 in-lb-sec ± 10 percent
Flywheel Momentum at 90 rpm	120 in-lb-sec
Initial Nominal Body Momentum	5780 in-lb-sec
Operational Momentum	200 in-lb-sec

Parameter	Value
Desired Body Momentum After Despin	60 in-lb-sec
Despin Ratio	96.5:1
Number of Cable Wraps	Two per cable
Nominal Yo-Yo Weight	2.0 pounds, each
Nominal Despin Time	1.5 seconds

The digital computer simulation of the ITOS mechanical (yo-yo) despin shows that initial nutation angles imposed by the third stage can grow by more than an order of magnitude, as illustrated in Figure 4-IV-2. The momentum remaining in the spacecraft at the conclusion of the despin phase will be displaced from the original total momentum by the final half-cone nutation angle. The nominal maximum sun angle between the spin axis and the sun line can grow from 120 degrees to about 140 degrees, depending on the initial conditions.

The desired body momentum along the spin axis after despin is 60 inch-pound-seconds, since 120 inch-pound-seconds of the operational momentum is already stored in the flywheel. The 3σ tolerance for the 60-inch-pound-second body momentum is ±24-inch-pound-seconds, when the following tolerances are applied:

Cable Length:	±0.25 inch
Yo-Yo Weight:	±1.5 grams
Center-of-Mass to Cable Attachment:	±0.125 inch
Pitch Moment of Inertia:	±0.5 percent

In addition, a 10-percent tolerance of the initial 90-rpm rate reflects as the same percentage into the operational momentum; i.e., ±18 inch-pound-seconds; or a worst-case tolerance for 0 initial nutation of ±42 inch-pound-seconds (±23.3 percent). As shown in Figure 4-IV-3, the upper limit of momentum tolerance will increase as a function of the initial nutation angle.

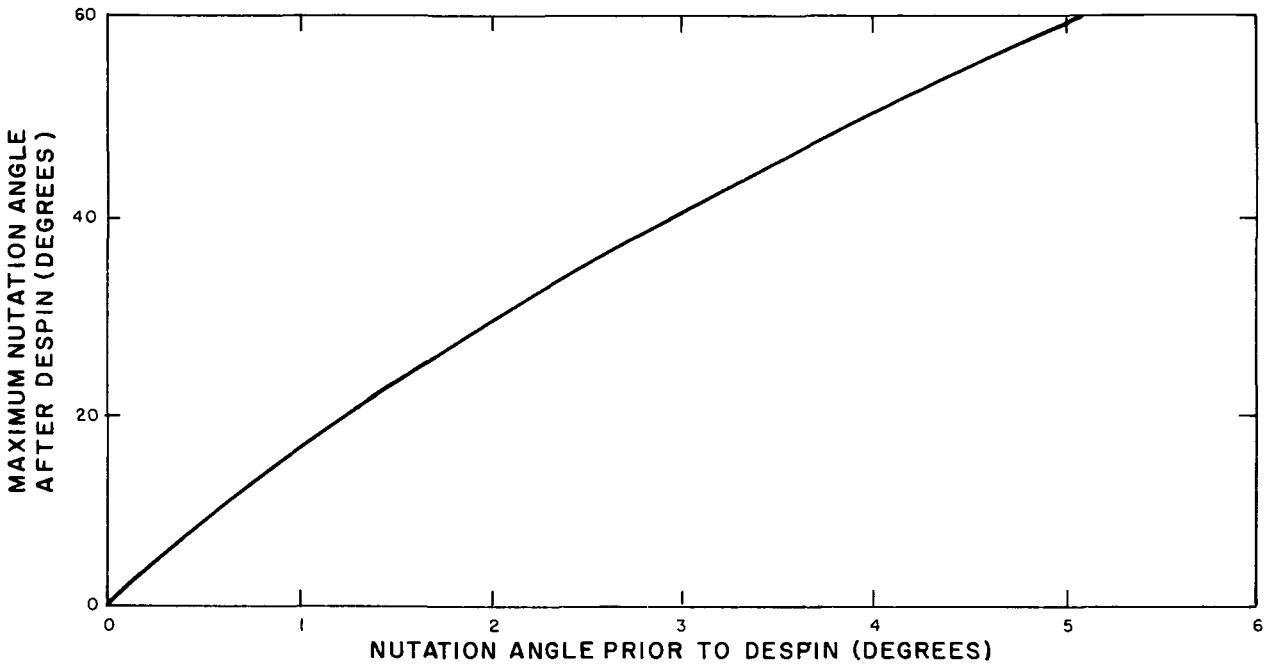

Figure 4-IV-2. Effects of Initial Spacecraft Nutation

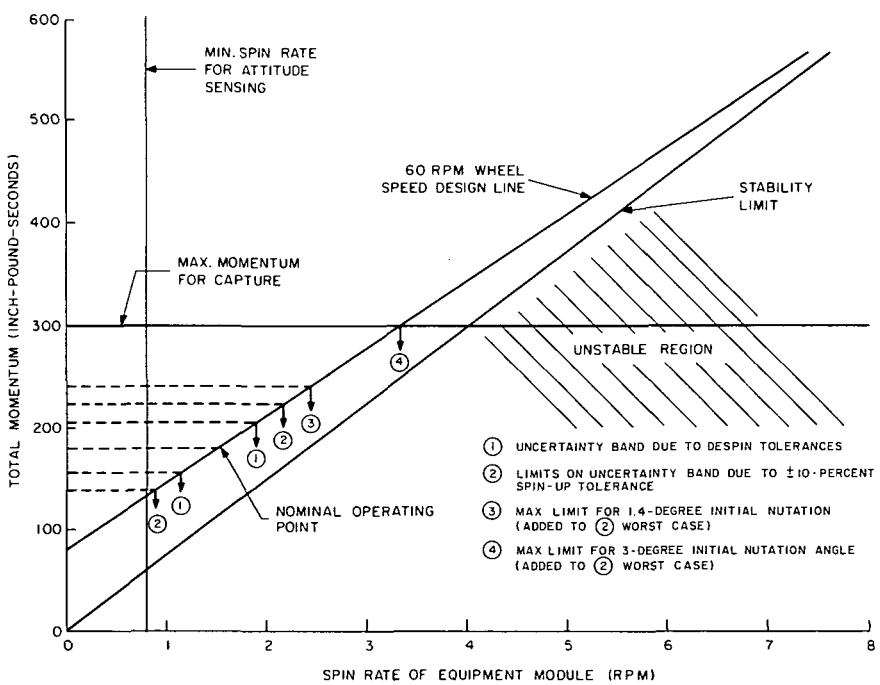

Figure 4-IV-3. Acquisition Operating Range After Despin

3. Biased Flywheel Operation

After despin, it is necessary to establish a gyroscopically stable spacecraft configuration. Such stability can be achieved if the following equation is satisfied.*

$$\omega_3 (I_3 - I_1) + \omega_f I_f > O$$

where

ω_3 is the spacecraft spin rate about the pitch axis,

ω_f is the flywheel spin rate,

I_3 is the spacecraft moment of inertia about the spin axis,

I_1 is the spacecraft moment of inertia about the transverse axis, and

I_f is the flywheel moment of inertia.

This criterion is based on the following assumptions: (1) roll inertia equals yaw inertia; i.e., body of revolution; (2) damper on despun body; (3) H cos Θ equals $I_3\omega_3$ plus $I_f\omega_f$, and H sin Θ equals $I_1\omega_1$; (4) 2E equals $I_3\omega_3^2$ plus $I_1\omega_1^2$ plus $I_f\omega_f^2$; and (5) ω_f minus ω_3 equals a constant,

where:

H is the total momentum,

Θ is the half-cone nutation angle,

E is the total spacecraft energy, and

ω_1 is the spacecraft spin rate about the transverse axis.

The first assumption implies that the moment of inertia about the roll axis, as a principal axis, is equal in magnitude to that about the yaw axis, as a principal axis. This will not be so in the case of ITOS but the effect of the actual inertia distribution is expected to be small. No proof of this statement is presently furnished because the manipulation of the

*Radio Corporation of America, Astro-Electronics Division, Flywheel Stabilized Magnetically Torqued Attitude Control System for Meteorological Satellites Study Program, Final Report, Contract NAS5-3886, Princeton, N.J., December 4, 1964.

Euler equations with actual moment of inertia values require a computer simulation which will be conducted during a subsequent phase of this program. For the unequal transverse moments of inertia of ITOS, the maximum value is used in order to arrive at the conservative stability limits shown in Figures 4-IV-3 and 4-IV-4. Assumptions 2, 3, and 4 are definitions applicable to the system. Closed-loop operation of the flywheel corresponds to assumption 5. Deviations in this constant speed differential can be adjusted with the momentum control by ground command once three-axis control is established.

Figures 4-IV-3 and 4-IV-4 show that a flywheel speed of 60 rpm provides an adequate stability margin for the range of expected momentum subsequent to yo-yo despin. Therefore, after the release of the yo-yo weights, power will be applied to the pitch loop, which is preset for open-loop operation, and to the torque motor. Then, using the beacon and telemetry subsystem, the despin and flywheel rotation can be verified at a ground. Acquisition sensor data will be indicative of satellite spin rate, and an index pulse and pitch horizon sensor data will be a measure of the wheel rate, relative to the spacecraft. In addition, roll sensor data (backup) may be commanded for further analysis.

After determining yo-yo despin and flywheel operation, the caging valves blocking the passages of the liquid-filled nutation dampers are released by ground command.

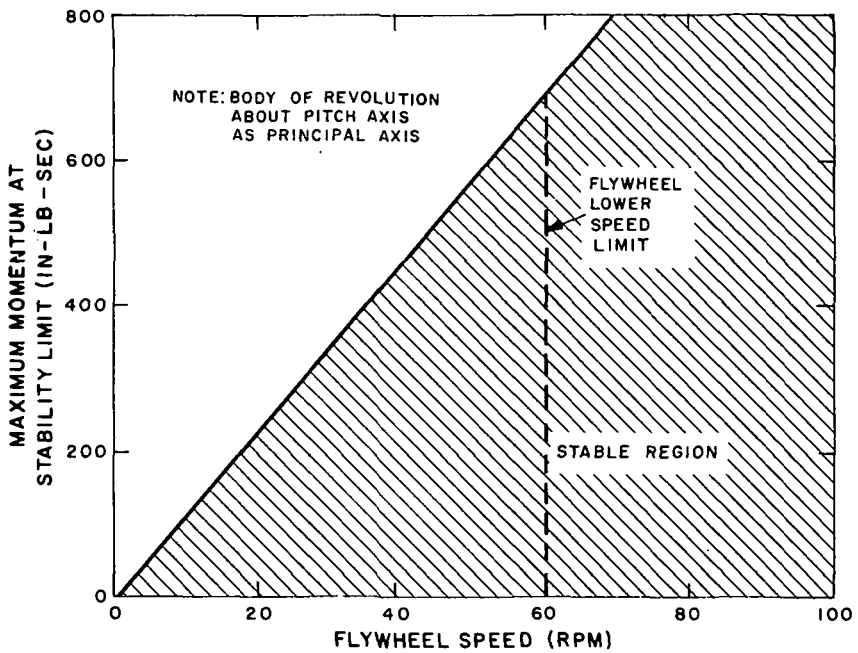

Figure 4-IV-4. Stability Criteria

4. Attitude Determination and Final Acquisition

The spacecraft attitude is determined by monitoring the output from the various sensors on board the spacecraft; i.e., the DSAI and the pitch, acquisition, and roll horizon sensors. The operating regions of the acquisition and roll sensors are shown in Figure 4-IV-5. The initial attitude or nominal injection orientation of ITOS faces the flywheel axis approximately toward geographic north. As a result, the roll attitude sensors and pitch horizon sensor will generally not face earthward while orbiting over the northern hemisphere. However, an acquisition sensor is mounted on the spacecraft body; its scanning is achieved by the spacecraft spinning at the relatively slow rates of 1 to 3 rpm. This sensor can be defined as a "half-Vee" configuration similar to the TIROS or TOS design. The combination of the digital solar aspect indicator and the acquisition sensor permits determination of spacecraft attitude during the initial maneuver; i.e., during reorientation of the spacecraft momentum vector towards alignment with the orbit normal.*

After the spacecraft attitude has been determined, quarter-orbit magnetic torquing, as in the TOS satellites, precesses the momentum vector from an essentially in-orbit-plane orientation to an orientation perpendicular to the orbit plane. During this maneuver, conducted at a rate of about 10 degrees per orbit, the attitude of the spacecraft will initially be determined by the acquisition sensor and DSAI data. As the operational attitude is approached, the roll sensors can be used for attitude determination.

Once the initial orientation maneuver has been completed, the solar panels are deployed by ground command, and the torque motor control loop is switched to the flight configuration. The flywheel spin rate will change to approximately 150 rpm. The control loop operation is now synchronized with respect to the earth's horizon; this involves phase locking the sky-earth pulse of the pitch horizon sensor to an index pulse.

---

*A detailed discussion of this attitude determination method, presently used on TOS, is contained in the following report: Radio Corporation of America, Astro-Electronics Division, Design Study Report on the TIROS-Wheel Spacecraft With an APT Camera, Contract NAS5-3344, Princeton, N.J., November 15, 1963.

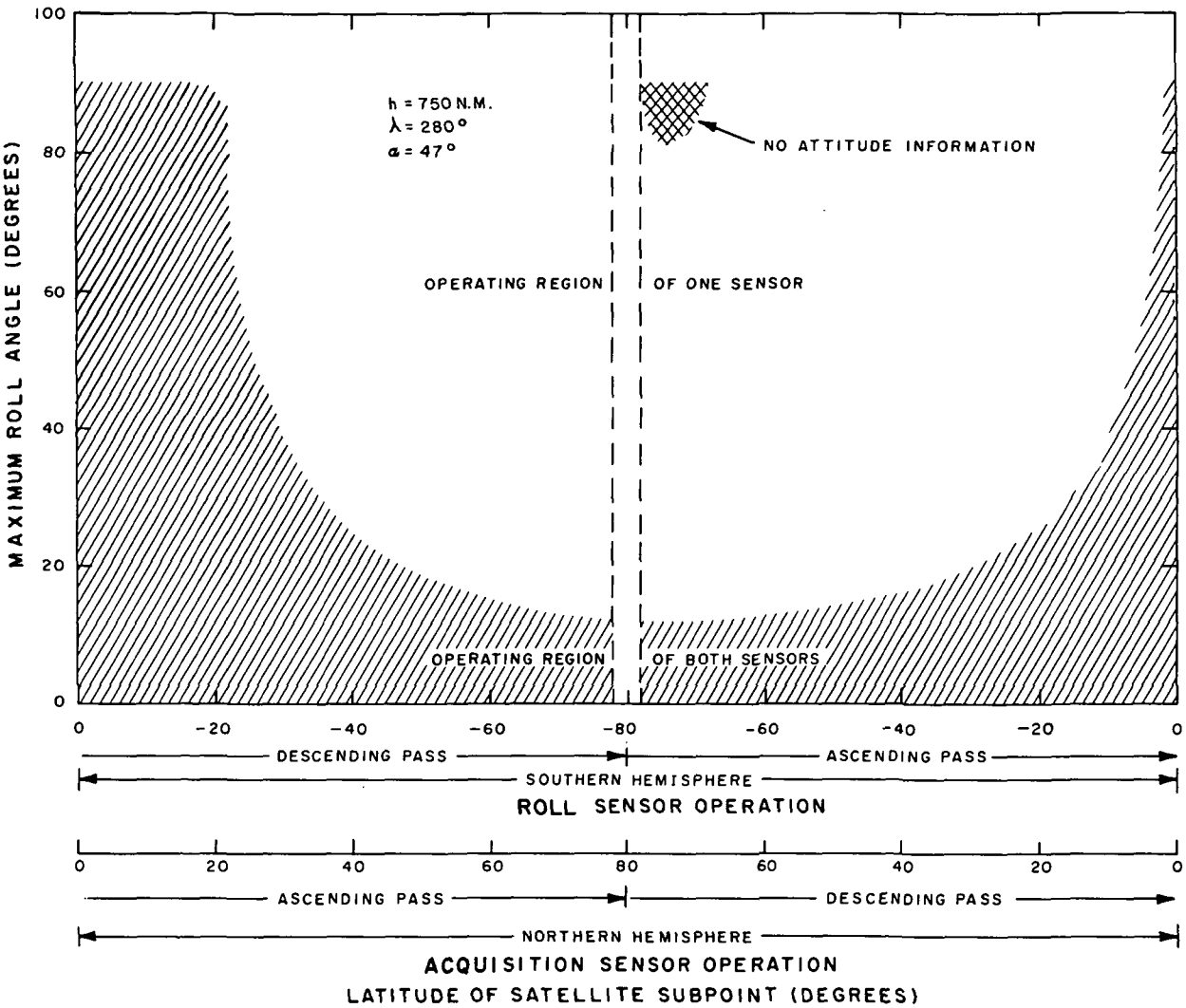

Figure 4-IV-5. Operating Regions of Attitude Sensors

Should the total spacecraft momentum deviate from the design value of 200 inch-pound-seconds, magnetic momentum control can be activated by ground commands. The torque motor control loop is designed to compensate for momentum variations along the pitch axis.

C. NUTATION DAMPING

1. General

Nutation occurs when the angular momentum vector and spin vector are not colinear. The spin vector then "cones" about the momentum vector at a rate determined by the inertia

characteristics and the spin rates of the spacecraft and the flywheel. This motion must be kept to a minimum since it results in a primary sensor pointing error. Redundant dampers in the spacecraft provide an effective and simple method for reducing nutation angles to near 0. *

The optimum liquid damper is a toroid completely filled with silicon oil and mounted so that the plane of the toroid is parallel to the spin axis. During nutation of the vehicle, transverse angular accelerations excite the oil, causing it to move relative to the damper tube walls. Kinetic energy is transferred to thermal energy through the viscous drag of the fluid. This loss of energy transfers momentum from the transverse axis to the spin axis of the spacecraft, thereby decreasing the nutation. This one-way transfer of energy continues as long as the fluid maintains its Newtonian viscosity characteristics. Thus, for no energy input to the spacecraft, the damper action continues as the nutation cone angle approaches 0.

2. Damper Caging

For ITOS, the dampers are initially caged since the transverse axis moment of inertia is greater than that of the spin (pitch) axis. After separation from the third stage, and until the flywheel motor is energized, the spacecraft operates in a dynamically unstable mode. Approximately 8 seconds after separation, the despin mechanism is released and stability is restored by rotating the flywheel at 60 rpm. In the unlikely event that the redundant firing circuits for the despin mechanism malfunction, 1.5 hours could elapse before a ground station could command despin. Since internal energy losses tend to rotate a spinning body about its maximum moment of inertia axis, the nutation damper, the largest source of energy loss, must be caged. Each nutation damper will have a restrictor valve placed in its line to inhibit relative fluid motion, thereby eliminating this source of energy loss. The restrictor valves will be opened by ground command.

---

*A complete analysis of the dynamic action of these dampers is presented in the following report: Radio Corporation of America, Astro-Electronics Division, Flywheel Stabilized, Magnetically Torqued Attitude Control System for Meteorological Satellites Study Program, Final Report, Contract NAS5-3886, Princeton, N.J., December 4, 1964.

3. Basic Design

a. Mathematical Analysis

A mathematical analysis of the dampers is given in Appendix E of this report. The analysis yields the following equation for computing the damper time constant:

$$\tau = \frac{I_2}{F\ I_d\ \dot{\phi}}$$

where:

τ is the time constant,

I_2 is the transverse moment of inertia,

F is the coupling factor,

I_d is the damper moment of inertia, and

$\dot{\phi}$ is the nutation rate.

b. Mechanical Configuration

As shown in Figure 4-IV-6, the ITOS nutation damper is not an optimum toroid. Each damper is mounted inside the spacecraft, on opposite sides of the equipment module, with the plane of the dampers parallel to the spin axis. Each damper contains an expansion chamber to act as a void trap for gasses and to allow room for thermal expansion of the fluid. The entire assembly is fabricated from aluminum tubing with an outside diameter of 1.0 inch and a 0.035-inch wall thickness. The fluid is a low viscosity silicone oil (Dow Corning, type 200).

The restrictor valve seals the entire inside diameter of the tubing; when open it provides an unrestricted opening equal to the nominal internal cross-sectional area of the tubing. The combined weight of the two nutation dampers is estimated at 14.1 pounds; they have a damping time constant of 68 minutes.

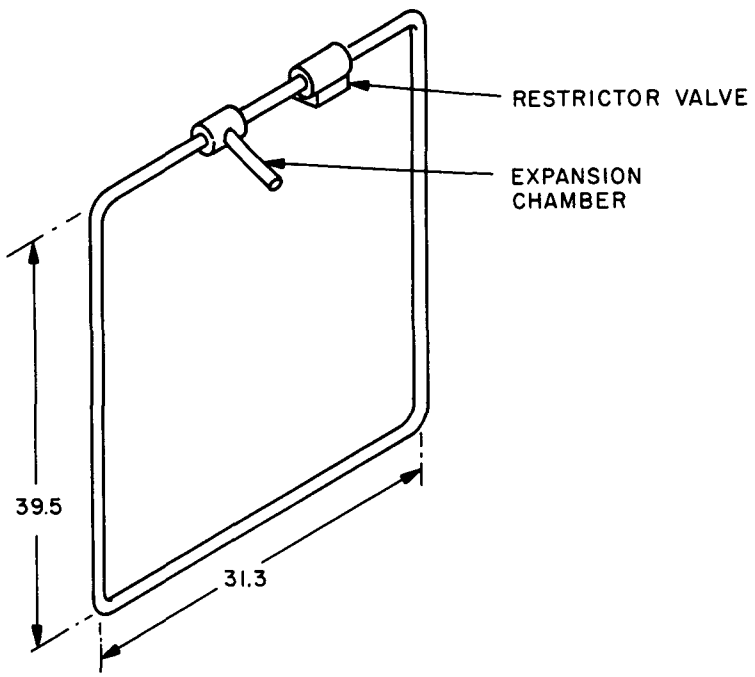

Figure 4-IV-6. Liquid-Filled Nutation Damper

4. Time Constant

Table 4-IV-1 presents a summary of the spacecraft and nutation damper parameters during various dynamic modes. During modes 1 and 2 the need for damper caging is apparent if nutation angle build-up is to be eliminated.

5. Weight Tradeoff

To determine the optimum mission mode angular momentum of the stabilization subsystem, and to minimize the total mass of this subsystem, the concept of "dynamic mass" has been established. The dynamic mass has been defined* as the sum of the mass of the flywheel and the mass of the liquid in the damper assembly, or expressed mathematically:

$$M = \left(\frac{1}{R_f^2\ \omega_f}\right) H + \left(\frac{I_2\ \sqrt{I_1\ I_2}}{F\ R_d^2\ \tau}\right) \frac{1}{H}$$

*"Monthly Progress Report No. 2; Flywheel Stabilized Magnetically Torqued Attitude Control System for Meteorological Satellites", dated August 10, 1964 (Contract No. NAS5-3886).

where:

M is the dynamic mass,

H is the angular momentum,

R_f is the flywheel radius of gyration (17.25 inches),

R_d is the effective radius of gyration of the two nutation dampers (20.4 inches),

ω_f is the flywheel angular velocity (15.7 radians per second),

F is the damper coupling factor (0.16),

I_1 is the maximum transverse moment of inertia of satellite (1015 in-lb-sec),

I_2 is the minimum transverse moment of inertia of satellite (892 in-lb-sec), and

τ is the effective time constant of the two liquid dampers (68 minutes).

TABLE 4-IV-1. DAMPER TIME CONSTANTS DURING VARIOUS MODES

Parameter	Dynamic Mode*				
	1**	2**	3†	4†	5†
Time Duration (sec)	9 Min	10	1-2 Days	600	-
Total Momentum (in-lb-sec)	6400	5900	200	200	200
Nutation Freq (rad/sec)	+7.3	+9.2	-0.09	-0.08	-0.21
Damper Coupling Factor	0.02	0.02	0.10	0.08	0.16
Time Constant (min)	-	-	61	136	68
Time Constant†† (min)	180	18.5	61	136	68

*Mode:
1. Last-stage ignition to spacecraft separation;
2. Spacecraft separation to despin;
3. Flywheel speed at 60 rpm;
4. Flywheel speed at 60 rpm,solar panels deployed; and
5. Mission mode.

**Damper caged in modes 1 and 2 (dynamically unstable in modes 1 and 2).

†Damper dynamically stable in modes 3, 4, and 5.

††Values represent dampers not caged.

The dynamic mass and momentum are shown in Figure 4-IV-7 where a system angular momentum of 150 inch-pound-seconds yield a mass of 20.2 pounds. A system angular momentum of 200 inch-pound-seconds has been chosen, since a 33-percent increase in the dynamic stiffness can be obtained for a negligible increase in the dynamic mass.

D. ATTITUDE SENSING

1. General

ITOS utilizes the following sensors for attitude and pitch determination:

- One digital solar aspect indicator (DSAI),
- One acquisition horizon sensor,
- One pitch horizon sensor, and
- Two roll horizon sensors.

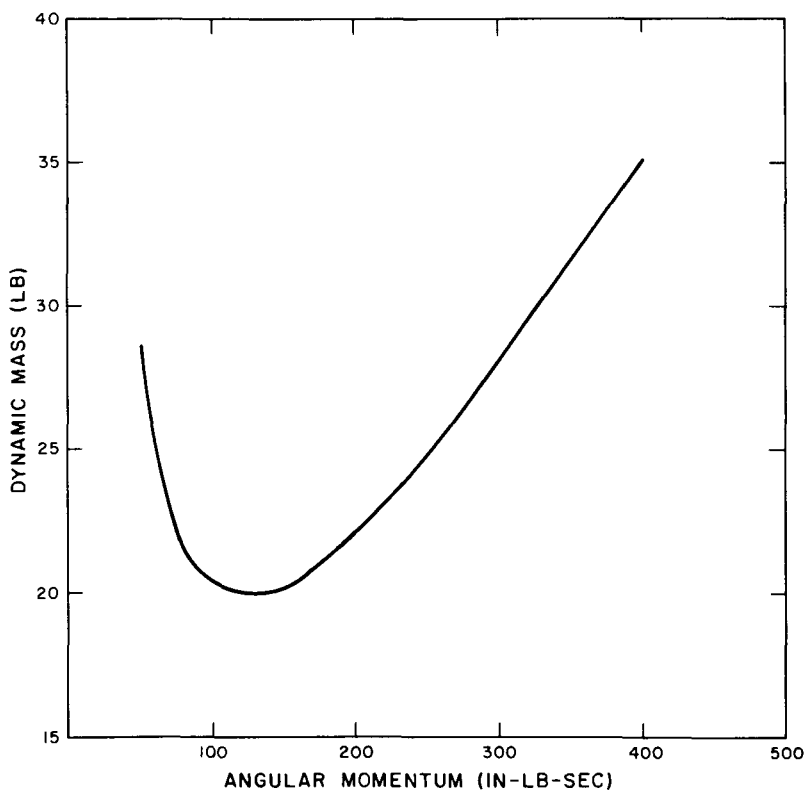

Figure 4-IV-7. Optimization Curve for Dynamic Mass

The digital solar aspect indicator and the acquisition sensor are utilized during the initial orientation maneuver and prior to pitch lock-on. They derive their scanning from the body spin of the spacecraft. Subsequent to the initial orientation maneuver, sensing is accomplished by the three (pitch and roll) infrared sensors which describe a space plane or cone by viewing a scanning mirror which is integral with the momentum wheel. In case of malfunction of the pitch sensor, one of the two roll sensors can be utilized for pitch backup.

2. Digital Solar Aspect Indicator

The digital solar aspect indicator, which has been space-proved on TOS flights, is used to determine the angle between the vehicle-sun line and the flywheel spin axis during the initial orientation maneuver (see Figure 4-IV-8). The indicator has an entrance slit with a field of view of 128 degrees. As the spacecraft rotates, the 128-degree beam generates a solid angle of approximately 3π steradians about the satellite's spin axis. As illustrated in Figure 4-IV-9, the sunlight that falls upon the entrance slit strikes a reticle that has a seven-bit Gray-coded pattern screen. Seven photocells are positioned behind the Gray-coded pattern, and, depending on the angle of incidence of the sun rays, from zero to seven photocells are illuminated. The signal output of the seven cells is amplified, stored, and updated. When a trigger pulse is received from a command photocell, the stored data is read out serially. The digital solar aspect indicator has a resolution of 1.0 degree and an accuracy of ± 0.5 degree.

3. Acquisition Sensor

The acquisition sensor, which is mounted on the main body of the spacecraft, is used during the initial orientation maneuver of the spacecraft. As the spacecraft rotates, the sensor field of view generates a cone having a half-apex angle of 47 degrees and a centerline coincident with the flywheel axis (see Figure 4-IV-10).

The acquisition sensor comprises a germanium-immersed bolometer and a 1-inch germanium lens system, as shown in Figure 4-IV-11. The bolometer consists of two thermistors, an active thermistor which is exposed to incident radiation and a compensating thermistor which is shielded from radiation and senses only the ambient temperature changes. The two thermistors form part of a bridge circuit across which is applied a DC bias. When the incident

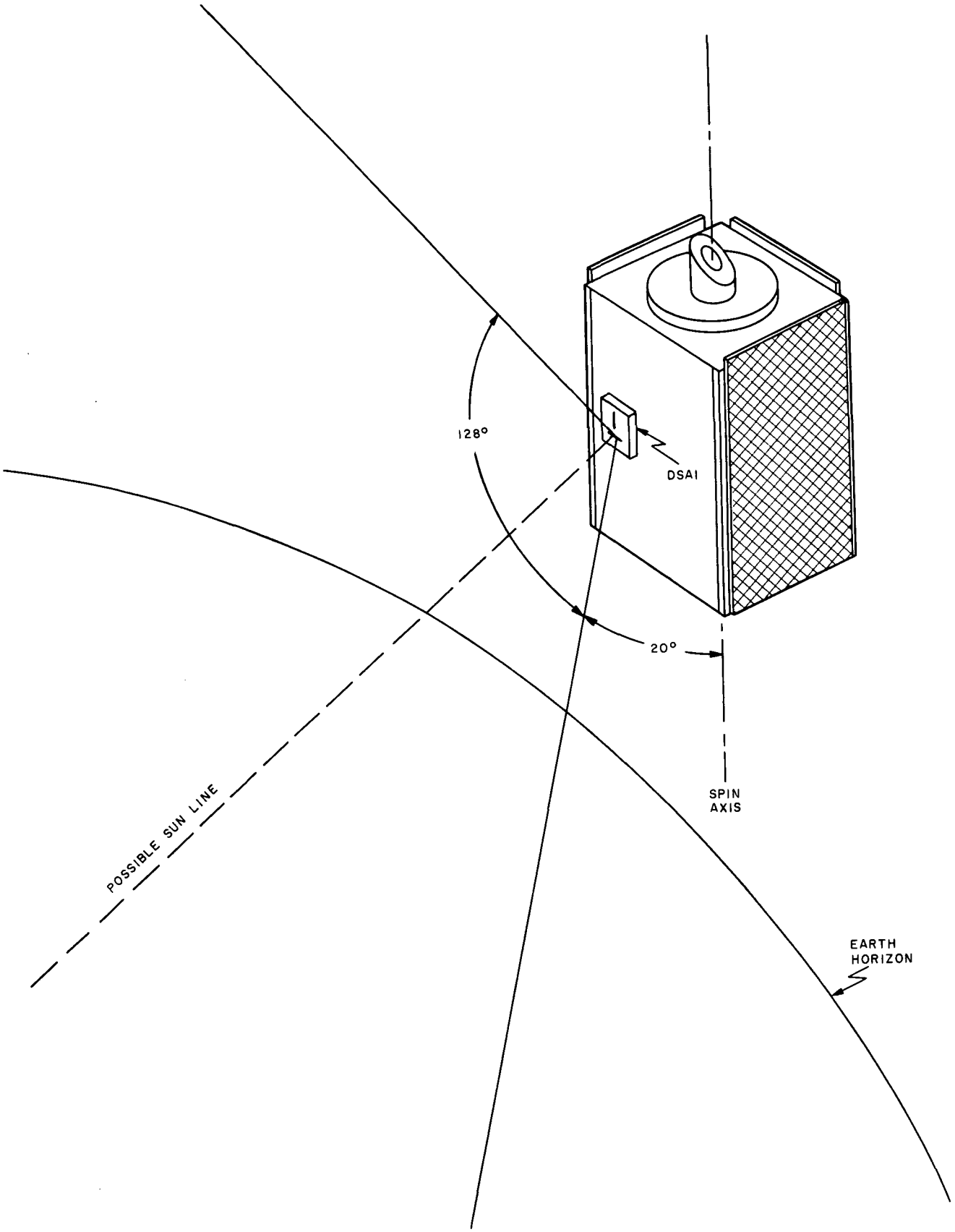

Figure 4-IV-8. Digital Solar Aspect Indicator, Scan Geometry

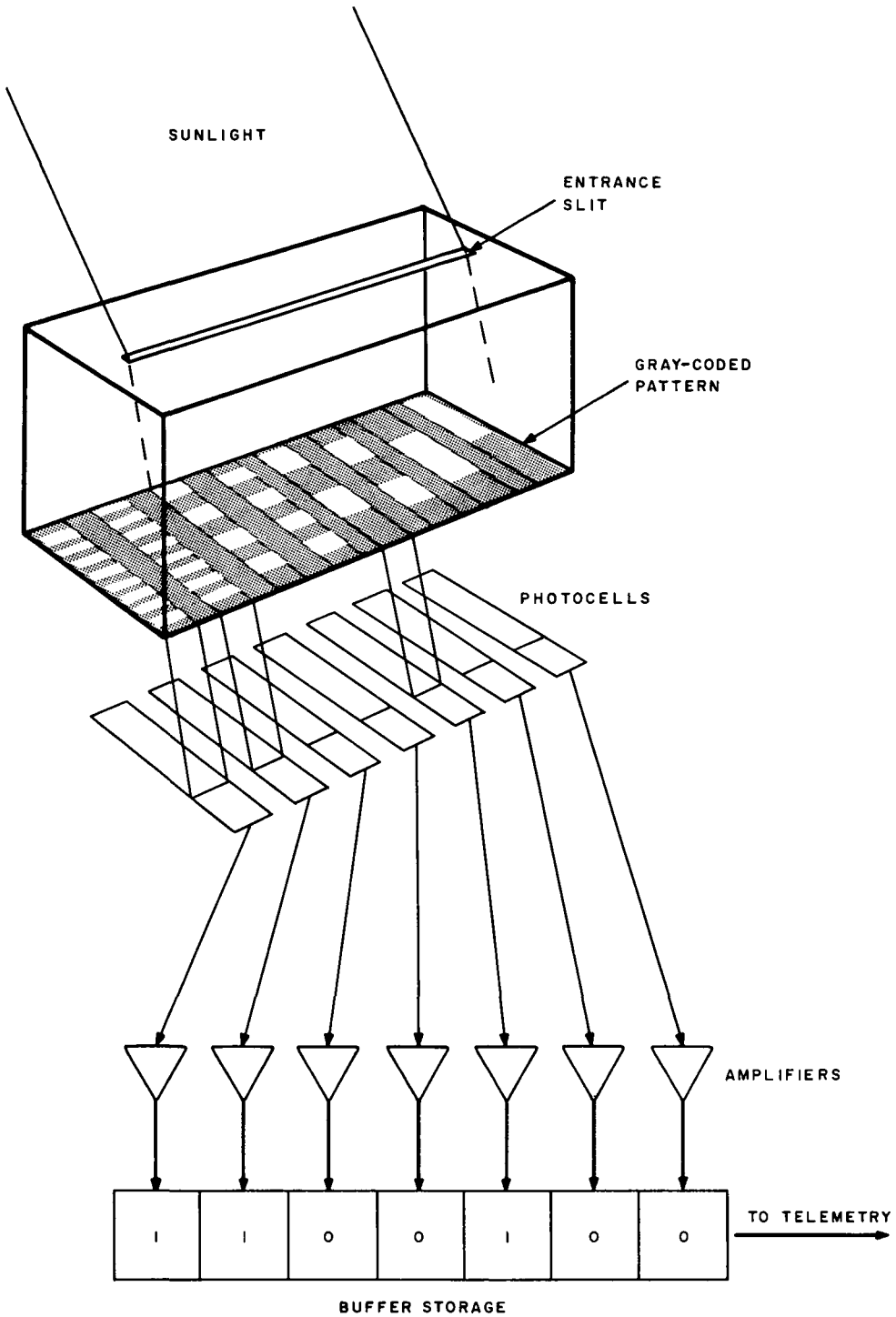

Figure 4-IV-9. Digital Solar Aspect Indicator, Functional Diagram

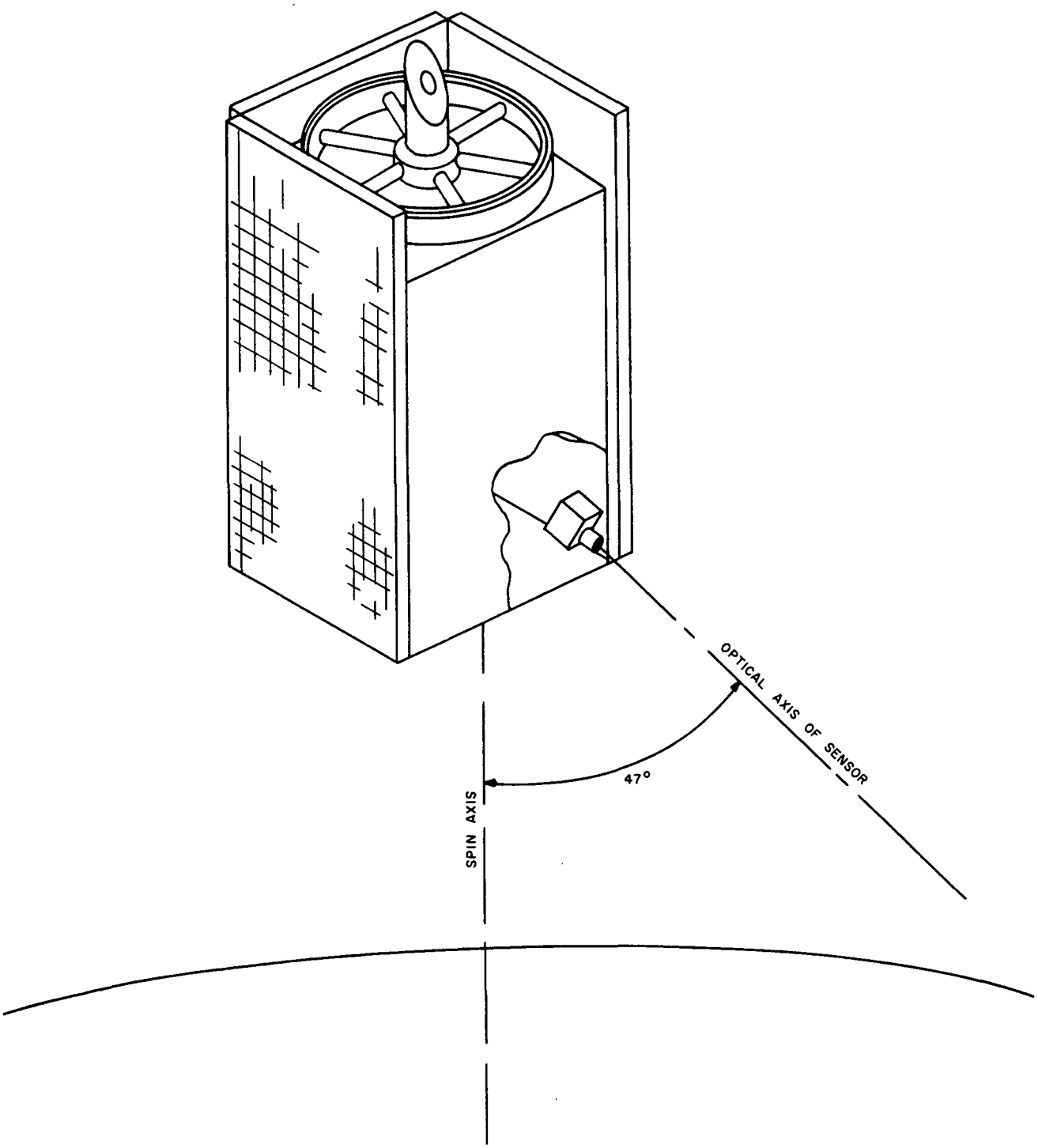

Figure 4-IV-10. Acquisition Sensor, Scan Geometry

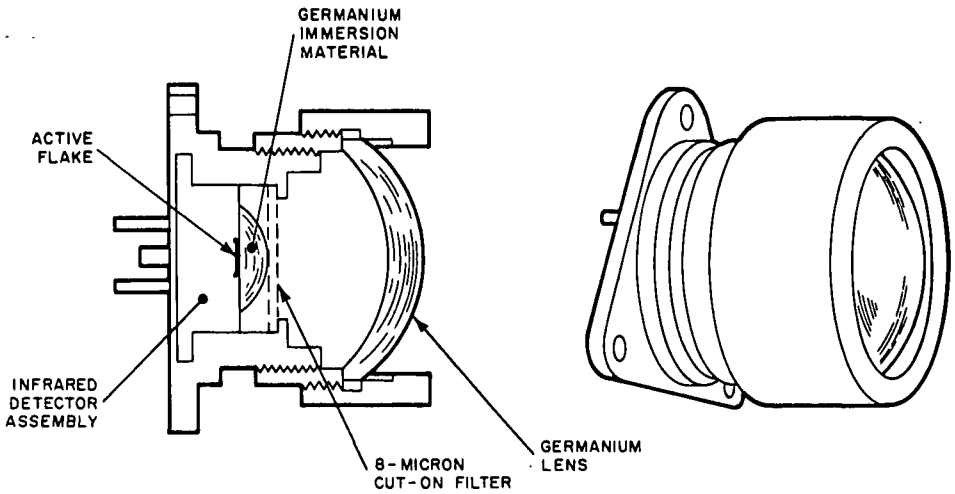

Figure 4-IV-11. Infrared Bolometer

radiation is focused onto the active thermistor, its temperature rises. This change in temperature results in a change of thermistor resistance, which affects the bridge balance and results in a voltage output at the junction of the thermistors. This voltage has two components: (1) a DC component due to the mismatch of the resistance and (2) an AC component due to the change in radiation levels at the earth horizon crossover.

The resistance of each thermistor is approximately 1.40×10^5 ohms at 25°C. The change in resistance that generates a signal equal to system noise level is less than 0.15 ohm. Since the matching of thermistors is not within 1 percent of their resistance values, at times the DC signal may exceed the AC signal level by a factor of 10^4. Furthermore, the matching of thermistor resistances is not constant, but shifts with changes in ambient temperature. Since only the AC signal is of interest, the bolometer output is capacitively coupled to the preamplifier. This is equivalent to differentiating the AC component while effectively blocking the DC component.

During its operation, the scan plane of this sensor intercepts the sun, thereby increasing the sensor recovery time. Since a long recovery time would interfere with the generation of horizon crossing signals, the sun effect is reduced by inclusion of an 8-micron cut-on filter which attenuates the solar radiation incident upon the bolometer. This filter has previously been used in the TIROS and TOS programs.

The sensor electronics consists of a preamplifier and a filter regulator (see Figure 4-IV-12). The electronics package is a flight-proved, RCA design that has been modified to provide a bandwidth from 1 to 50 Hz and a telemetry peak-to-rms signal-to-noise ratio of approximately 43 db (assuming a 280°K source that is scanned at 1 rpm at a grazing angle of 49.6 degrees). The preamplifier incorporates the following: a capacitor coupled input and DC coupled transistor stages throughout, a high impedance, low noise field-effect transistor input stage, a DC bias loop that provides bias point stabilization, and two separate negative feedback loops which maintain stable gain and dynamic characteristics.

The primary function of the regulator is to act as an ultra-low-frequency rejection filter. The circuit is designed to reduce supply line ripple in the frequency range from 0.1 to 15 Hz. An active filter is included in the design to provide additional filtering for the bolometer bias supply in the bandpass of the amplifier.

4. Operational Pitch and Attitude Sensors

a. General

The pitch and roll bolometers are identical to the acquisition bolometer described in Paragraph D.3, but with smaller time constants. As shown in Figure 4-IV-13, the three bolometers are mounted in a fixed position and are aligned parallel to the spin axis. A mirror assembly, comprising a 45-degree pitch mirror and a 23.5-degree roll mirror, is fixed to the momentum wheel shaft and reflects the bolometer fields of view. The two mirror surfaces, which are oriented 180 degrees of wheel rotation apart, have an aluminized finish and are protected with a silicone monoxide coating. Because of the mirror reflection, the pitch sensor look angle is perpendicular to the spin axis, while the roll sensor look angle is inclined by 47 degrees to the same axis.

The sensor electronics associated with the pitch and roll bolometers consist of a preamplifier, filter, regulator, and threshold amplifier (see Figure 4-IV-14). The electronics are a flight-proved, RCA design modified to provide a bandwidth of approximately 15 to 160 Hz. The preamplifier and filter are located adjacent to the associated bolometers and are mounted on the same plate. The regulator and threshold amplifier are located in the pitch loop electronics package.

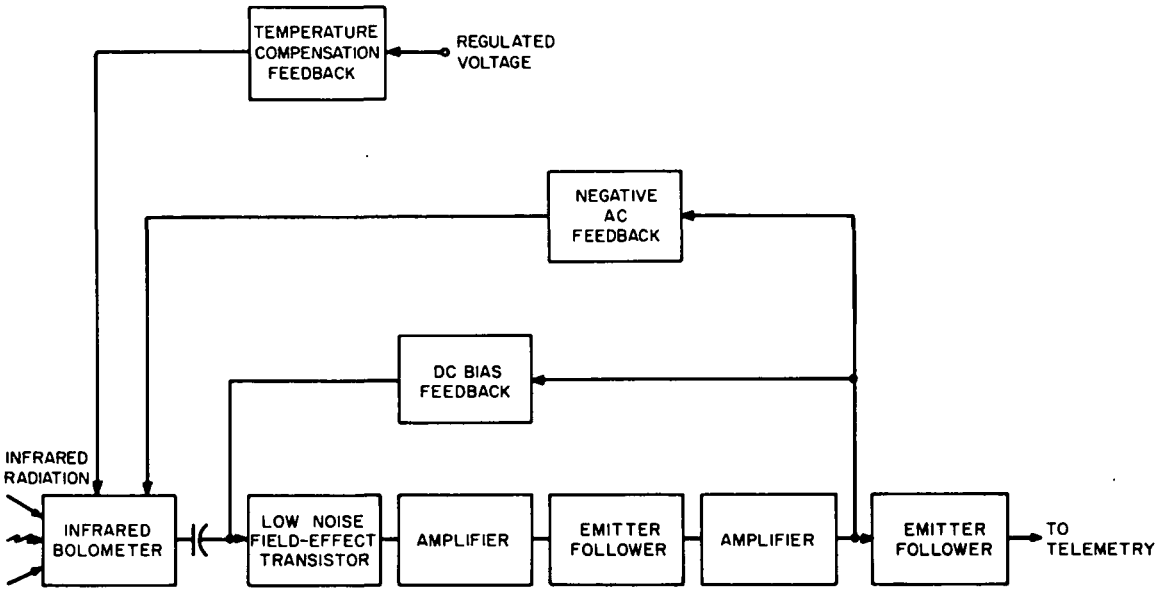

Figure 4-IV-12. Acquisition Sensor Electronics, Block Diagram

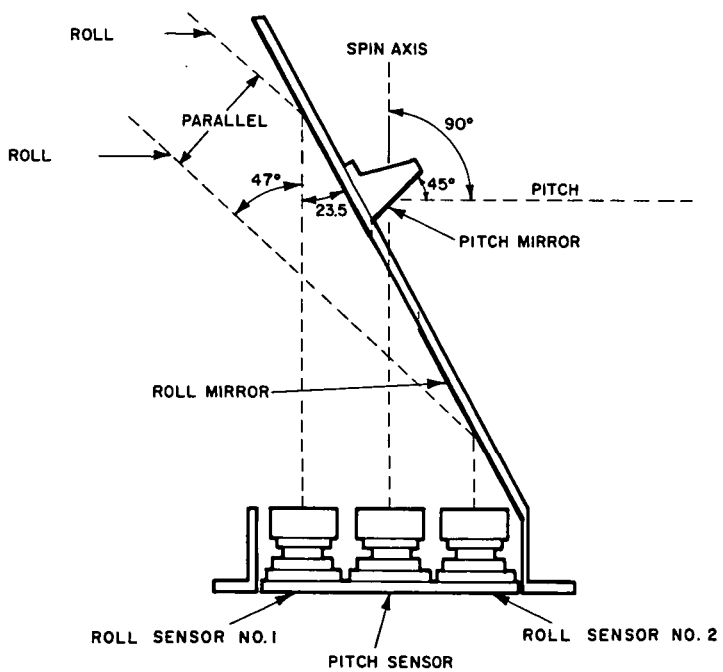

Figure 4-IV-13. Attitude Sensor Mirror Assembly, Functional Diagram

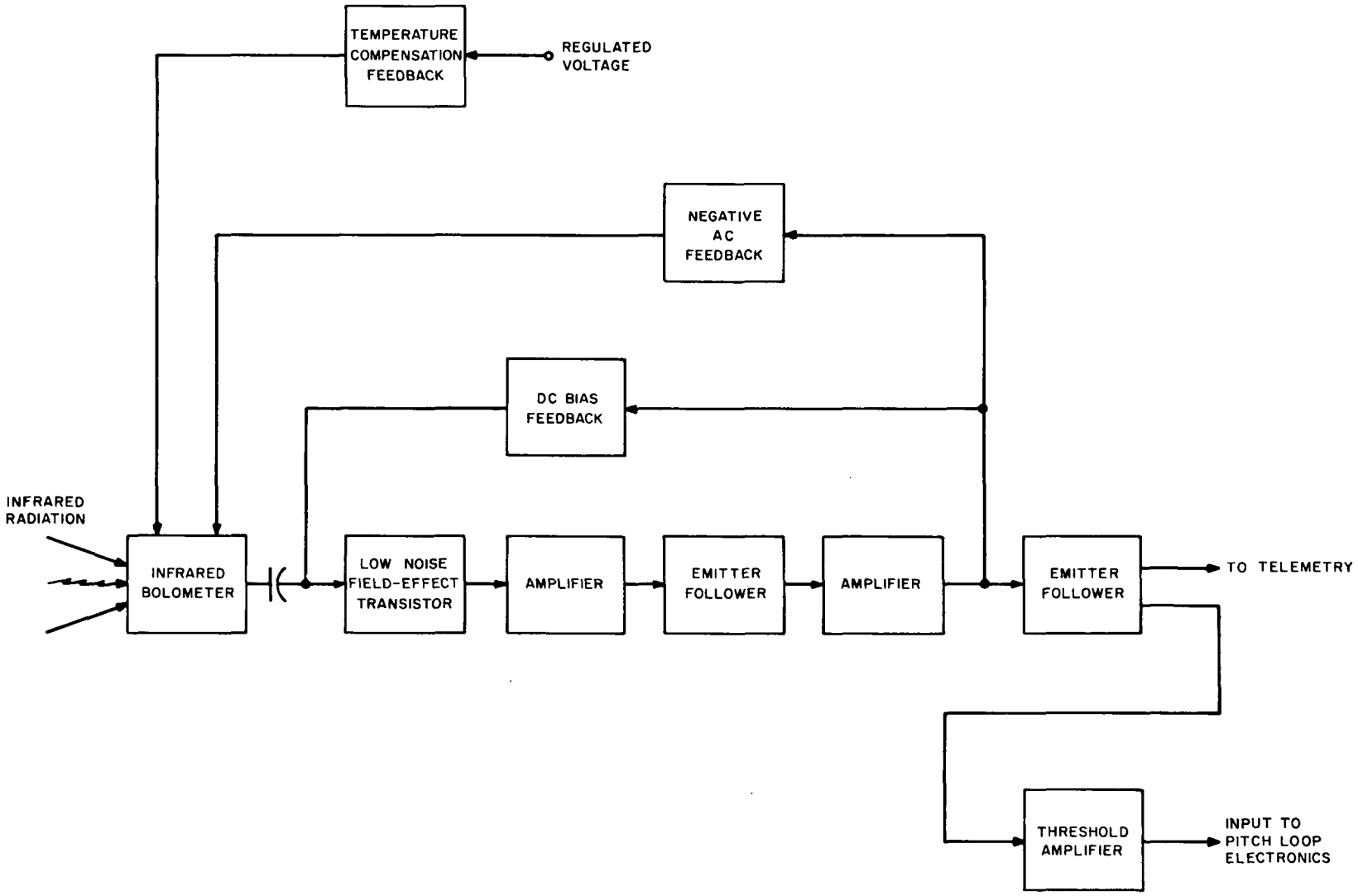

Figure 4-IV-14. Pitch and Roll Sensor Electronics, Block Diagram

When the momentum wheel is rotating, the pitch sensor field of view generates a plane perpendicular to the spin axis, while each roll sensor field of view generates a symmetrical cone about the spin axis (see Figure 4-IV-15). In the mission attitude, the field of view of each sensor intercepts the earth once for each revolution of the wheel. The bolometers respond to the radiance change between cold space and the earth, thus producing the horizon intercept data necessary for determining attitude and pitch reference.

b. Pitch Sensing

The pitch control loop utilizes a pulse from the pitch sensor, which references the position of the momentum wheel to the earth horizon, and an index pulse, which relates the position of the momentum wheel to the spacecraft structure. Generation of the index pulse is discussed in Paragraph F.

The accuracy of sensing the pitch attitude depends primarily on the uncertainties of locating the infrared horizon. Since the earth-space horizon transition is contaminated by noise from preceding earth and cloud temperature variations, only the space-earth transition is used for pitch determination. The 3σ limit of the pitch sensing uncertainty band due to the ill-defined horizon is shown in Figure 4-IV-16, which is a plot of maximum angular offset versus orbit eccentricity.

Since a 200°K horizon is caused by high level cloud cover, the actual infrared horizon appears slightly sooner in a sky-earth scan. This causes the 200°K curve to occur slightly earlier in time, when referred to the spacecraft index pulse, and thus causes a time difference between the 280 and 200°K earth horizons. To avoid false triggering from earth noise subsequent to the space-earth transition, the sensor output is blanked for a portion of the scan (225 milliseconds). Experiments were performed using a 16- to 160-Hz bandpass preamplifier and a bolometer with a 3.0-millisecond basic time constant. Figure 4-IV-17 shows plots of preamplifier signal level versus time for 200 and 280°K horizons. For a signal-to-peak-noise ratio of 10 to 1, the time displacement is 1.25 milliseconds (or 1.12 degrees).

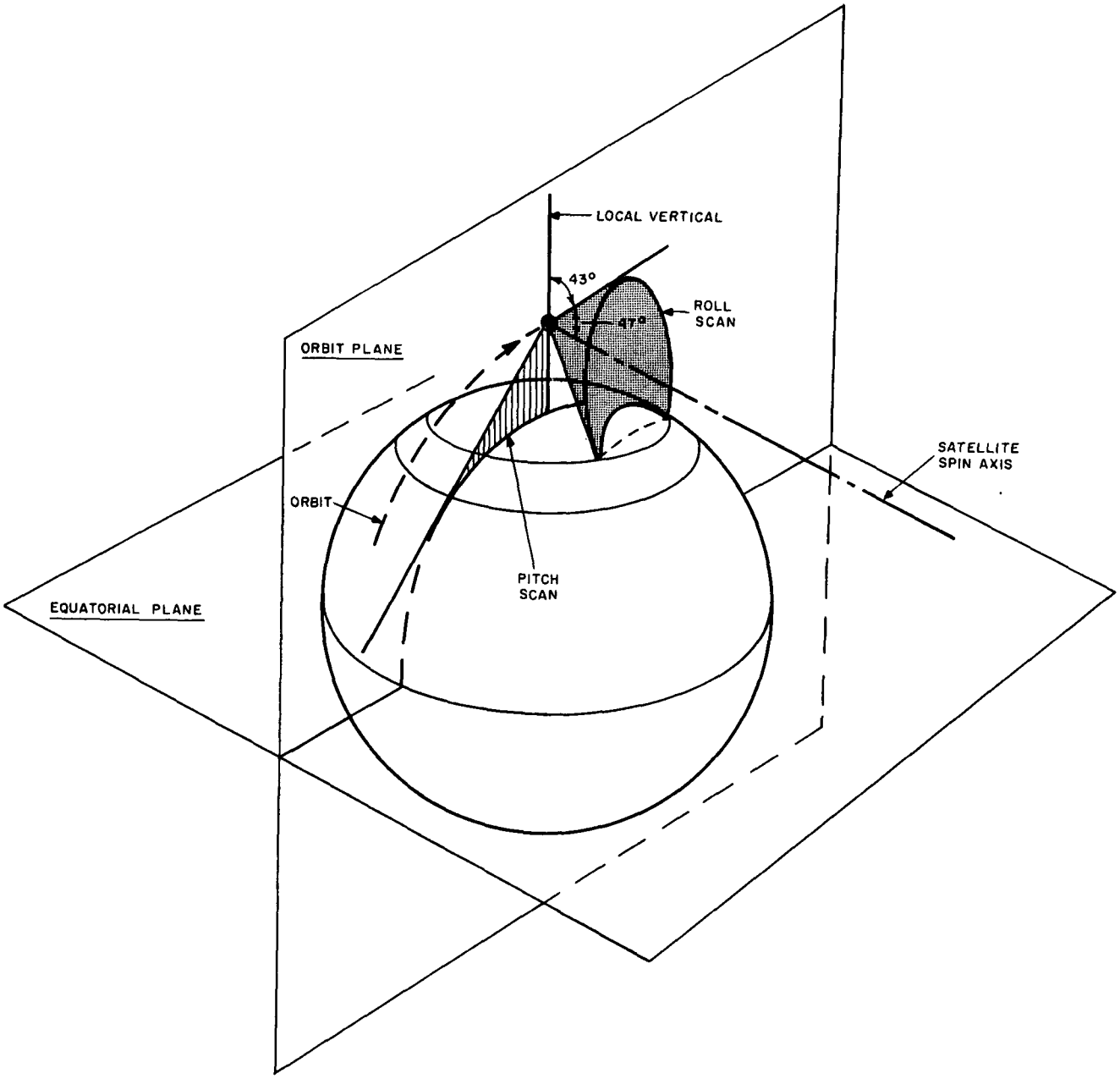

Figure 4-IV-15. Attitude Sensor Scan Geometry

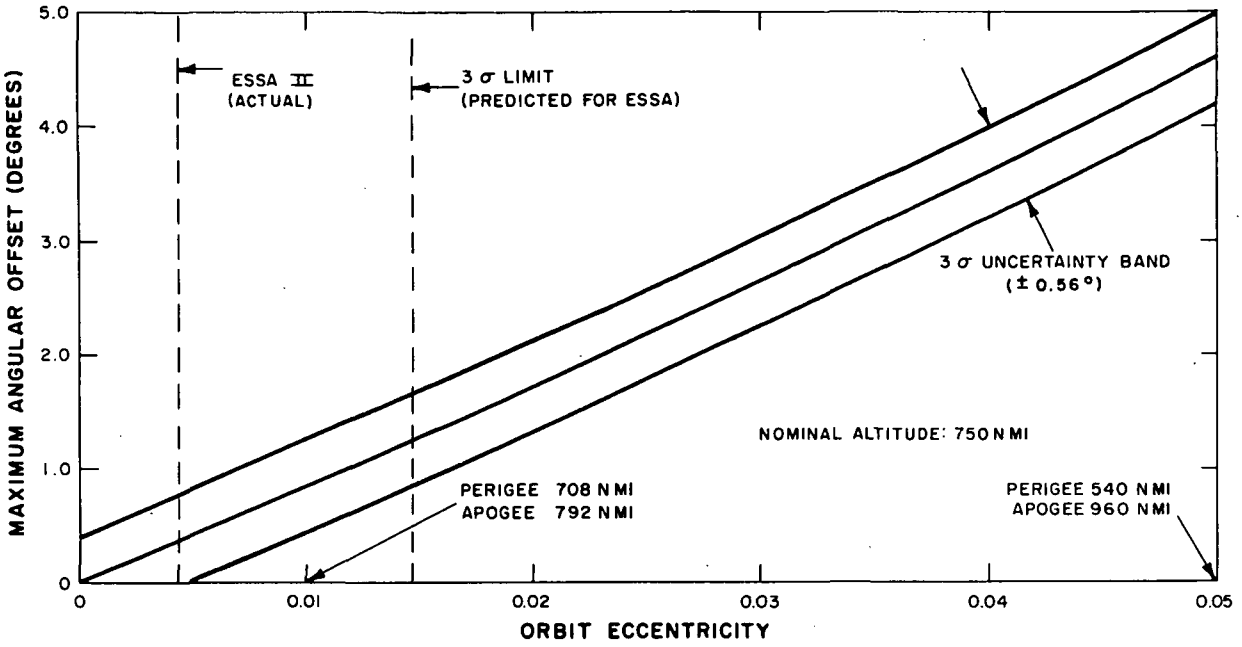

Figure 4-IV-16. Pitch Offset Versus Orbit Eccentricity

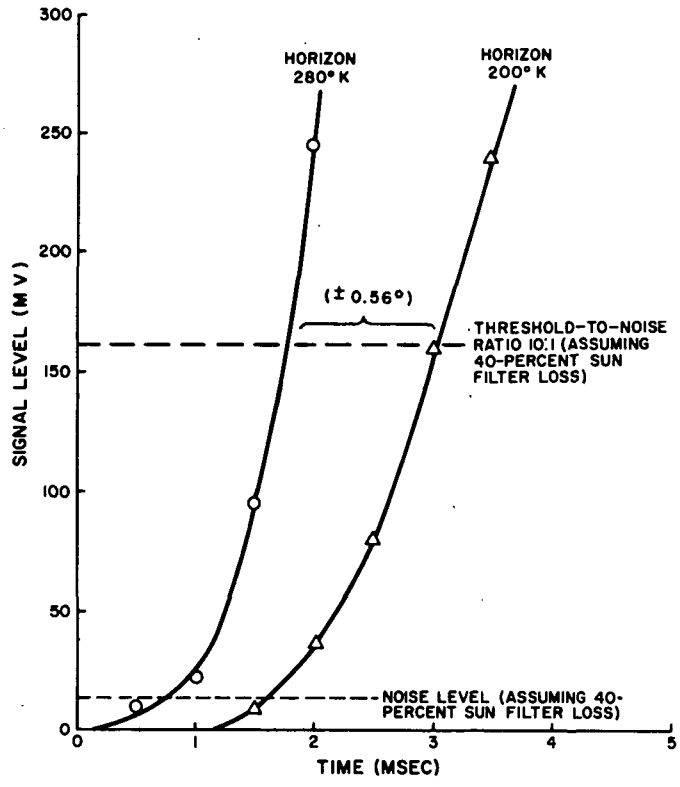

Figure 4-IV-17. Sensor Electronics Measured Signal Response

The above 3.0-millisecond bolometer has been selected for ITOS in view of the following: (1) satisfactory experimental data when using peaking techniques, (2) previous experience in working with this bolometer, (3) adding bias source circuitry not presently available but necessary for a faster time constant bolometer, and (4) possibility of increased noise levels due to the added bias source.

Utilizing the horizon crossing transition as a reference for local vertical assumes a circular orbit of known altitude. An elliptical orbit would cause an angular pitch offset from the nominal. The maximum value of pitch offset, which is plotted in Figure 4-IV-16, occurs at the perigee of the orbit. While the 3σ limit for orbit eccentricity for ITOS has not yet been established, the 3σ limit predicted for ESSA II and the actual eccentricity given in Figure 4-IV-16 are intended to serve as a guide.

The effects of changes in mirror assembly temperatures on the sensor accuracy were given consideration. The mirror is tied thermally to the flywheel and, therefore, can be expected to have a negligible temperature change during one rotation. Since the bolometers are always looking at the surface of the mirror and since the mirror temperature (and, therefore, the radiant energy from the mirror to the bolometer) will be constant during one spin period, the AC-coupled bolometer electronics will see only changes in the radiant energy due to horizon crossings, with no noticeable signal due to mirror temperature changes.

c. Alternate Pitch Sensing

In case of failure of the primary pitch sensor, either of the two roll sensors can be used as an alternate. However, the space-earth transition of the roll sensor lags that of the pitch sensor by 16.5 degrees of mirror rotation. This is due to the earth curvature and to the 43-degree angle between the pitch and roll scan patterns as shown in Figure 4-IV-15. In addition, the roll and pitch mirror surfaces are 180 degrees out of phase; thus, the total angular lag between the space-earth transitions is 196.5 degrees. When a roll sensor is used for pitch sensing, the index pulse generated by the magnetic encoder is shifted by the same lag angle of 196.5 degrees.

The roll offset error causes some deterioration in the determination of the local vertical (see Figure 4-IV-18). In addition, when a roll sensor is used for pitch control, a roll attitude error causes a sinusoidal pitch oscillation at a rate equal to the orbital frequency. The peak magnitude of such oscillations as a function of roll attitude error is shown in Figure 4-IV-19. In the vicinity of 0 roll angle, the sensitivity of pitch with respect to roll is 1.5 degrees per degree of roll for either of the two backup sensors. The 3σ limit of pitch sensing when using either roll sensor is ±0.61 degree. The roll sensors are also blanked for 225 milliseconds to eliminate false triggering in the pitch loop.

d. Roll Sensing

The horizon crossing data generated by either of the two roll sensors is telemetered to a CDA station where it is processed to produce the required error correction commands.

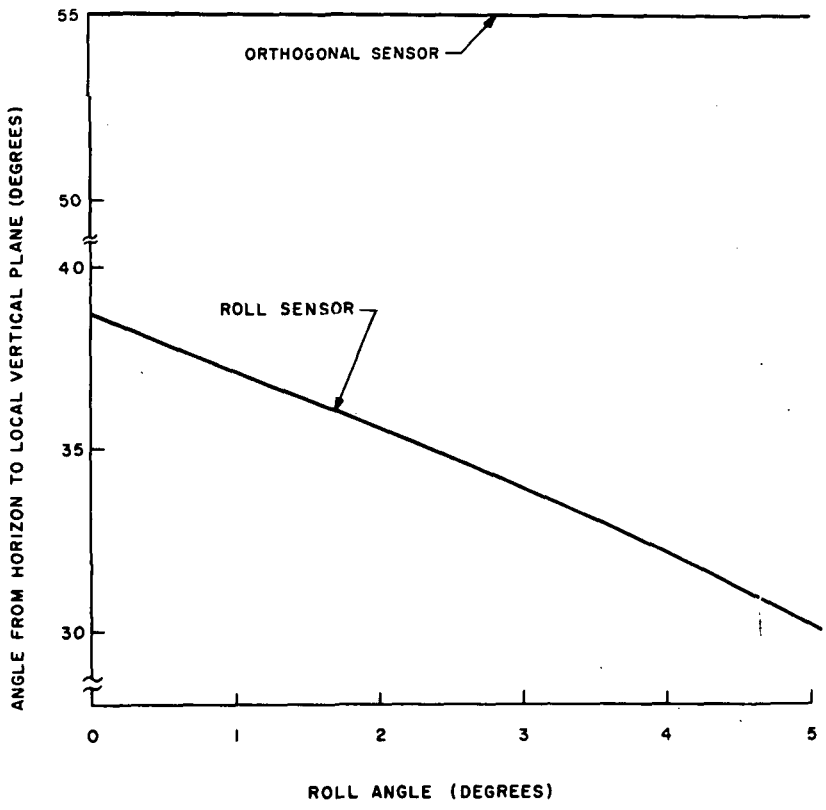

Figure 4-IV-18. Horizon Sensor Half Earth Angles

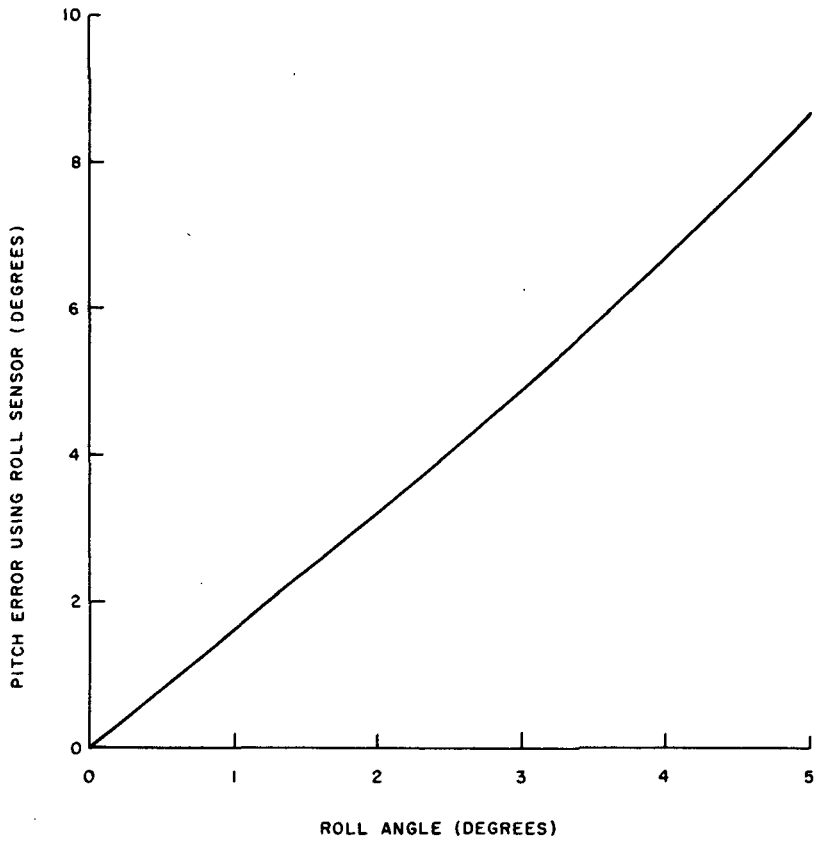

Figure 4-IV-19. Roll Sensor, Pitch Angle Error

In normal roll operation, the preamplifier provides an analog signal which produces a telemetry link peak-signal-to-rms-noise level of approximately 37 db. This value is specified for a spin rate of 150 rpm, a horizon temperature of 280°K, and a grazing angle of 49.6 degrees. The telemetry data is subsequently processed to compute the error corrections required for maintaining proper attitude and spin control.

Since the geometry of the roll sensor scan is essentially a half-Vee scan, satellite ephemeris information is required for attitude determination. If a hybrid technique of combining half-Vee data with pitch data is employed, the ephemeris data is not required. A comparison of these techniques is presented in Appendix E. As discussed in further detail in Appendix B, the accuracy of roll determination depends on the method of data reduction at the ground station and the amount of data utilized. Under all circumstances, however, it appears feasible to limit the 3σ scatter in instantaneous roll measurement to about 0.51 degree random plus a bias offset of no more than 0.26 degree.

E. MAGNETIC ATTITUDE CONTROL AND MOMENTUM CONTROL

1. General

The magnetic attitude control and momentum control systems have two basic functions: (1) to perform the initial orientation maneuver and to keep the spacecraft momentum vector aligned with the orbit normal and (2) to control the total momentum of the satellite so that it is always in the dynamic range of the pitch control loop.

The magnetic attitude control system is basically the same as that used on the TOS spacecraft and is based on the experience acquired during the operation of the TOS and the earlier TIROS spacecraft. Roll control is maintained by quarter-orbit magnetic attitude control (QOMAC), with similar coils and the same techniques as used on the TOS program. A magnetic bias control (MBC) coil nulls the residual spacecraft magnetic spin axis dipole and induces the required 1-degree-per-day precession rate for orbit regression correction.

The magnetic momentum control system of the spacecraft is similar to the spin control techniques used on TOS spacecraft. Coils similar to the magnetic spin control (MASC) coils are used. The basic change in the operation of the coils is that current communication is not required due to the fact that the spacecraft (and thus the coils) is not spinning.

2. Coordinate System

To describe the various controls, orbital geometry, magnetic fields, and related topics covered in this discussion, appropriate coordinate systems must be defined. A set of unit vectors, $\hat{\ell}$, $\hat{b}$, and $\hat{n}$, is used in describing roll control. A second set, $\hat{r}$, $\hat{t}$, and $\hat{n}$, is required for description of momentum control. As shown in Figure 4-IV-20, $\hat{n}$ is the orbit normal, $\hat{\ell}$, is along the ascending node, $\hat{b}$ is perpendicular to $\hat{n}$ and $\hat{\ell}$, $\hat{r}$ is along the radius vector from the center of the earth to the spacecraft, and $\hat{t}$ is along the spacecraft velocity vector. The $\hat{r}$, $\hat{t}$, and $\hat{n}$ set rotates with respect to the $\hat{\ell}$, $\hat{b}$, and $\hat{n}$ set once per orbit; the rotation angle, β, is the orbit anomaly angle measured from the ascending node.

The spacecraft coordinate system, $\hat{1}$, $\hat{2}$, and $\hat{3}$, and the attitude angles in the $\hat{r}$, $\hat{t}$, and $\hat{n}$ system are shown in Figure 4-IV-21. The momentum vector of the spacecraft is along the

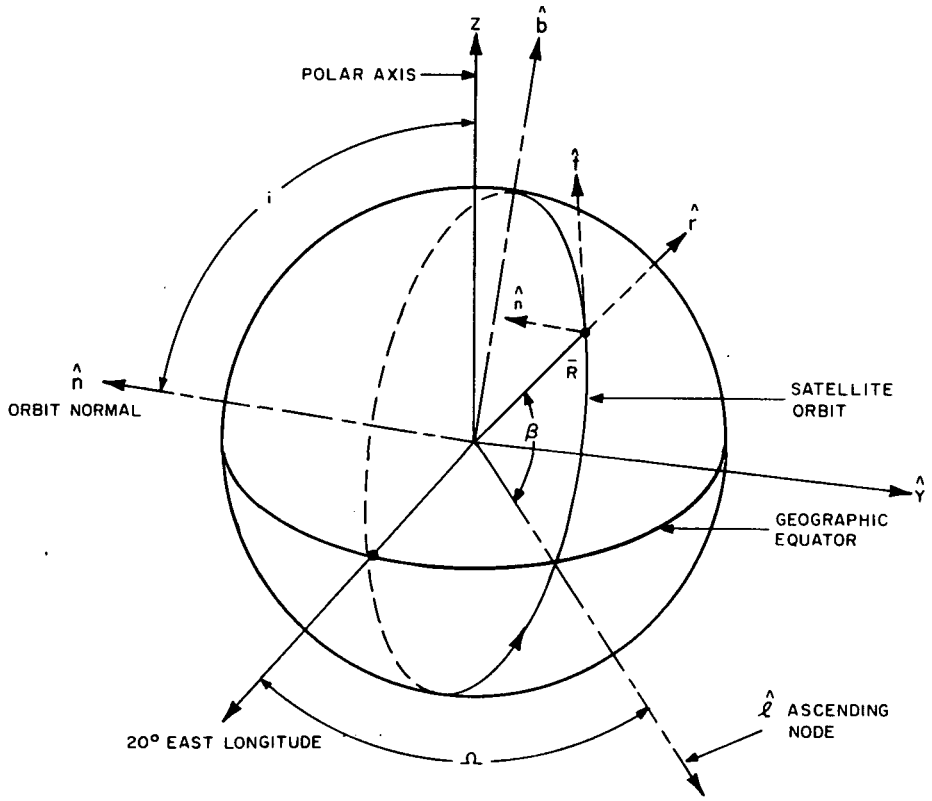

Figure 4-IV-20. Orbital Coordinates

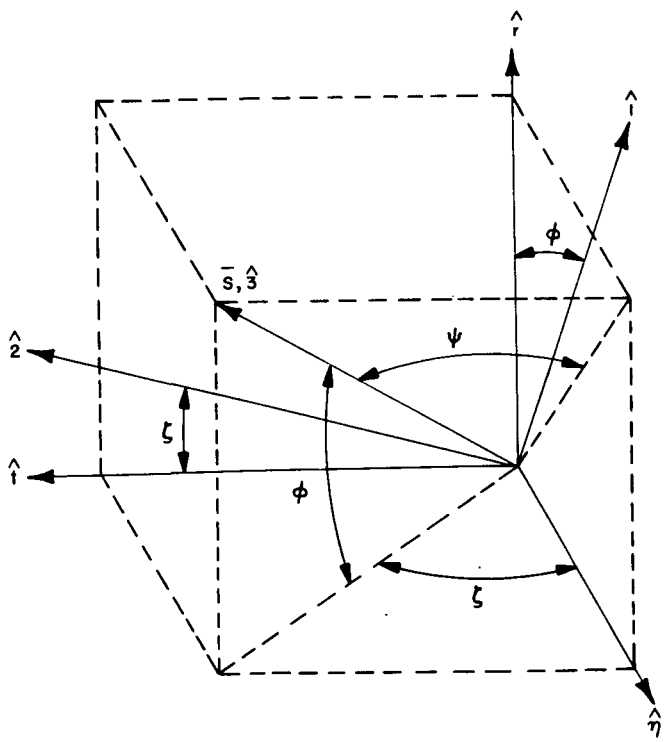

Figure 4-IV-21. Spacecraft Coordinates and Attitude Angles

$\hat{3}$ axis and should be directed along the orbit normal. Normally, the pitch axis is along the $\hat{n}$ axis, the yaw axis is along the $\hat{r}$ axis, and the roll axis is along the $\hat{t}$ axis. The roll angle, ϕ, measured by the horizon sensors is the angle between the spin vector, $\hat{3}$, and the local horizontal plane; this angle is cyclic over an orbit due to the gyroscopic stiffness of the spacecraft. Attitude information is obtained from knowledge of the maximum roll angle, ϕ_{max}, and the point in the orbit of its occurrence.

3. Geomagnetic Field Equations

The earth's magnetic field equations have been derived and discussed on many earlier programs, including TOS. The results are the following field equations, in the $\hat{\ell}$, $\hat{b}$, and $\hat{n}$ coordinate system:

$$B_\ell = \frac{K}{R^3}\left[3/2\,(\cos i \sin i_m \cos\Omega - \sin i \cos i_m)\sin 2\beta + 3/2 \sin i_m \sin\Omega \cos 2\beta + 1/2 \sin i_m \sin\Omega\right],$$

$$B_b = \frac{K}{R^3}\left[-3/2\,(\cos i \sin i_m \cos\Omega - \sin i \cos i_m)\cos 2\beta + 3/2 \sin i_m \sin\Omega \sin 2\beta + 1/2\,(\cos i \sin i_m \cos\Omega - \sin i \cos i_m\right], \text{ and}$$

$$B_n = \frac{K}{R^3}\,(\cos i \cos i_m + \sin i \sin i_m \cos\Omega). \qquad (4\text{-IV-1})$$

In the preceding equation:

B_ℓ, B_b, and B_n are the earth's magnetic field components in the $\hat{\ell}$, $\hat{b}$, and $\hat{n}$ coordinate system,

K is the geomagnetic dipole moment constant,

R is the orbit radius,

i is the orbit inclination,

i_m is the earth's magnetic dipole inclination, and

Ω describes the location of the ascending node with respect to the intersection of the geographic and geomagnetic equators.

For a three-axis stabilized spacecraft, the equations need to be expressed in the $\hat{r}$, $\hat{t}$, and $\hat{n}$ system. This is obtained by a rotation around $\hat{n}$ through the angle β. The resulting equations are:

$$B_r = \frac{2K}{R^3}\left[(\cos i \sin i_m \cos \Omega - \sin i \cos i_m)\sin\beta + \sin i_m \sin\Omega \cos\beta\right],$$

$$B_t = \frac{K}{R^3}\left[-(\cos i \sin i_m \cos \Omega - \sin i \cos i_m)\cos\beta + \sin i_m \sin\Omega \sin\beta\right], \text{ and}$$

$$B_n = \frac{K}{R^3}(\cos i \cos i_m + \sin i \sin i_m \cos\Omega). \qquad (4\text{-IV-2})$$

4. Quarter-Orbit Magnetic Attitude Control (QOMAC)

The QOMAC coil is mounted in the spacecraft so that its dipole vector is aligned with the spin axis. The positive moment, M_Q, of the QOMAC coil is taken in the positive direction of the angular momentum:

$$\overline{M}_Q = \pm M_Q \hat{3}. \qquad (4\text{-IV-3})$$

It has been shown that the precessional motion of the spin axis at any instant will be directed negatively about the direction of the earth's magnetic field at that instant.

The magnitude of the average precession rate* (ω_{PQ}) at the completion of one QOMAC torque cycle is:

$$\omega_{PQ} = \frac{3KM_Q}{\pi R^3 H} \sin i, \qquad (4\text{-IV-4})$$

where H is the total spacecraft momentum.

*Radio Corporation of America, Astro-Electronics Division, Design Report for the TIROS Operational Satellite (TOS) System, Contract NAS 5-3173, Princeton, N.J., December 30, 1964.

Table 4-IV-2 gives the parameters of the ITOS QOMAC coil. For a system momentum of 200-inch-pound-seconds, the low torque precession rate is 0.56 degree per torque cycle or 1.12 degrees per orbit.

TABLE 4-IV-2. ITOS QOMAC COIL PARAMETERS

Parameters	Value
Dipole Moment	4 ampere-turn-meters^2
Type	Center-tapped
Number of Turns	178 per half
Wire Gage	31 AWG
Wire Resistance	380 ohms
Series Resistor	435 ohms
Current	30 ma (at 24.5 volts)
Power	0.75 watts
Weight	0.50 pound

5. Proportional QOMAC

The normal QOMAC cycle consists of quarter-orbit reversals of current in the coil starting at a certain time measured from the ascending node. For the dipole moment of 4 ampere-turns-meters^2, a precession rate of 0.56 degree per torque cycle is obtained. As shown in Appendix C, the precession rate due to solar torques at a sun angle of 45 degrees is 1.41 degrees per day or 0.056 degree per half orbit. This error could be corrected with normal QOMAC and would require a QOMAC cycle every five orbits. However, a proportional QOMAC programmer has been added which will operate continuously to torque the satellite at approximately 0.056 degree per half orbit. Then, normal QOMAC will have to be initiated only once or twice a week to correct errors due to other sources of disturbance and to correct any possible accumulation of small errors from the proportional QOMAC operations. This would also enhance the accuracy of attitude determination.

The normal QOMAC operations, including the initial orientation maneuver, would be accomplished in this programmer in the same manner as on TOS.

The proportional QOMAC programmer for ITOS is able to set the full quarter-orbit period of QOMAC torquing from 25.6 to 34.1 minutes (nominally 28.5 minutes). The programmer can also set the QOMAC pulse width from 16 seconds to 11 minutes. Any fraction of the maximum precession available from proportional QOMAC can be programmed; however, accuracy may be lost in establishing the direction of the precession vector if less than 20 percent of the full quarter-orbit QOMAC cycle is used.

The programmed cycle repeats itself every half orbit until commanded to stop. The need to stop and start the recycling is a function of the resolution of the quarter-orbit period (±2 seconds) and, thus, the amount of drift of the switching point. An updated program could be retransmitted to return the switching point to the original point in the orbit. Updating may be needed once every day or two; if not updated, the original program will continue.

Figure 4-IV-22 shows the relationship between a typical dipole moment program of one cycle of proportional QOMAC operation (shaded area) and one cycle of conventional QOMAC torquing. To establish the desired relationships, the general precession equations are averaged over an orbit but with limits pertinent to the proportional QOMAC conditions; this yields:

$$\bar{\tilde{\omega}}_p = \frac{-M_Q}{n \pi H} \left[\int_{\beta_s + \pi/2(1-n)}^{\beta_s + \pi/2} \bar{B}\, d\beta \; - \int_{\beta_s + \pi/2}^{\beta_s + \pi/2(1+n)} \bar{B}\, d\beta \right] \quad 0 < n \leq 1 \qquad (4\text{-IV-5})$$

where ω_p is the average precession rate due to proportional QOMAC, and B is the earth's magnetic field strength; or, in the $\hat{\ell}$, $\hat{b}$, and $\hat{n}$ coordinate system:

$$(\tilde{\omega}_p)_{\ell} = \frac{3 K M_Q \sin i}{2 R^3 H n \pi} (1 - \cos n \pi) \cos 2\beta_s,$$

$$(\tilde{\omega}_p)_b = \frac{3\,K\,M_Q \sin i}{2\,R^3\,H\,n\,\pi} (1 - \cos n\,\pi) \sin 2\beta_s, \text{ and}$$

$$(\tilde{\omega}_p)_n = 0. \qquad (4\text{-IV-6})$$

As in conventional QOMAC operation, the $\hat{n}$ component of the precession vector is 0.

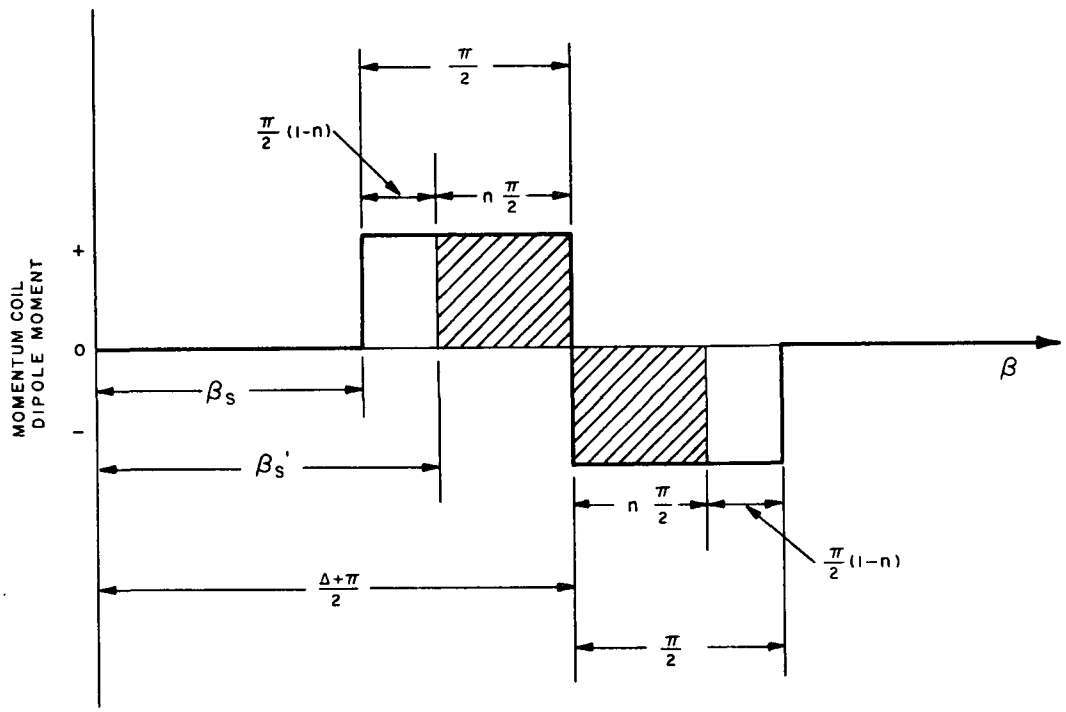

Figure 4-IV-22. Dipole Moment Program for Proportional QOMAC

Hence, the precession axis lies in the orbital plane. The average precession motion occurs about an axis which is at an angle Λ to the ascending node and is given by:

$$\tan \Lambda = \frac{(\tilde{\omega}_p)_b}{(\tilde{\omega}_p)_\ell} = \tan 2\beta_s. \qquad (4\text{-IV-7})$$

The start angle, β_s', for proportional QOMAC is:

$$\beta_s' = \frac{\Lambda + \pi (1 - n)}{2}, \qquad (4\text{-IV-8})$$

and the switching point occurs at:

$$\beta = \frac{\Lambda + \pi}{2} .$$

The magnitude of the average precession rate is as follows:

$$\left| \tilde{\omega}_P \right| = \frac{3 K M_Q \sin i}{2 \pi R^3 H n} (1 - \cos n \pi). \qquad (4\text{-IV-9})$$

This may be compared with Equation 4-IV-4 to determine the value of n for the required fraction of the maximum available torque. Figure 4-IV-23 shows the normalized relationship of the average precession rate during torquing and attitude change versus the fraction of a normal QOMAC cycle. It can be seen that as the period of torquing is reduced, the decrease in attitude change is first gradual and then more rapid. This is due to the fact that as the torquing duration is shortened, the average precession rate during torquing increases at first to a value higher than that for conventional QOMAC. However, because the rate increase is not sufficient to offset the decrease in torquing time, the net attitude change brought about by proportional QOMAC is always less than the conventional QOMAC change.

To obtain the required 0.056 degree per cycle, or 0.1 of full QOMAC, it can be seen for Figure 4-IV-23 that n should be 0.2. The torquing interval for each polarity is then 1/20 of an orbit instead of the normal one quarter orbit.

As described in Appendix C, the direction of the orbit-averaged precession axis due to solar torques is approximately along the $\hat{\ell}$ axis. The precession axis will be somewhat above or below the $\hat{\ell}$ axis, depending on the time of the year. By selecting angle Λ for the proportional QOMAC precession axis to be 180 degrees from the solar torque axis, solar torque cancellation can be achieved. For example, if the precession is along the $-\hat{\ell}$ axis, the required precession from QOMAC should be along the $+\hat{\ell}$ axis. Thus, angle Λ would

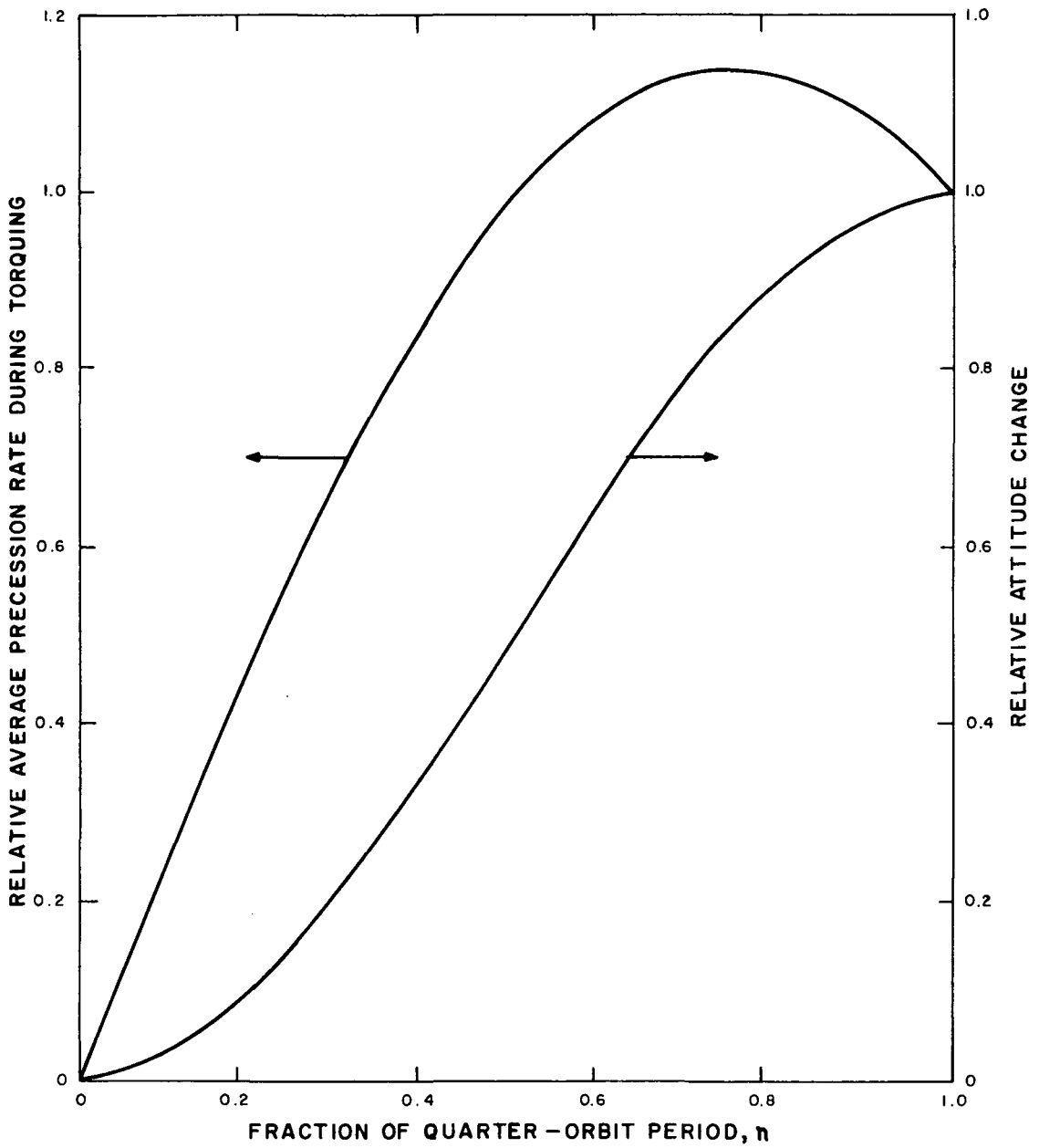

Figure 4-IV-23. Relative Precession Rate and Attitude Change for Proportional QOMAC Torquing

be 0, and the switching point would be at $\frac{\pi}{2}$, or approximately over the poles. This angle will shift very slowly over the year and can be plotted against time. Every few weeks, the new angle can be substituted in the program and transmitted during one of the times the proportional QOMAC programmer is being updated. In this manner, the effects of the solar torque can be removed with a minimum amount of effort at the ground stations and with no calculations required once the initial postlaunch observation has established the magnitude of the solar torque precession.

Two attitude maneuvers were programmed on a digital computer which simulates the torques present. The first simulation was made with no correcting torques. The disturbing torques simulated would be the solar torques, gravity gradient torques, and the effects of the residual dipole along the spin axis. The following data were used as inputs:

Momentum:	200 inch-pound-seconds
Spin moment of inertia:	818 inch-pound-seconds^2
Transverse moment of inertia:	863 inch-pound-seconds^2
Altitude:	750 nautical miles
Inclination:	101.4 degrees
East longitude of ascending node on first orbit:	0 degree
Total continuous dipole moment along spin axis:	0.522 atm^2
Solar torque:	6.2×10^{-3} inch-pound
Sun angle:	35 degrees from $\hat{n}$ in the $\hat{\ell}$, $\hat{n}$ plane

Figure 4-IV-24 shows the computer results with nominal drift. The nominal drift of the momentum axis over 75 orbits (6 days) would yield a maximum attitude error at this time of 7.9 degrees. The precession vector would be approximately along the $+\hat{\ell}$ axis. Thus the precession vector produced by proportional QOMAC should be along the $-\hat{\ell}$ axis. The precessing needed per orbit would be approximately 0.105 degree or 0.0938 of that produced by normal QOMAC. From Figure 4-IV-23 the value of n to be used would be 0.195.

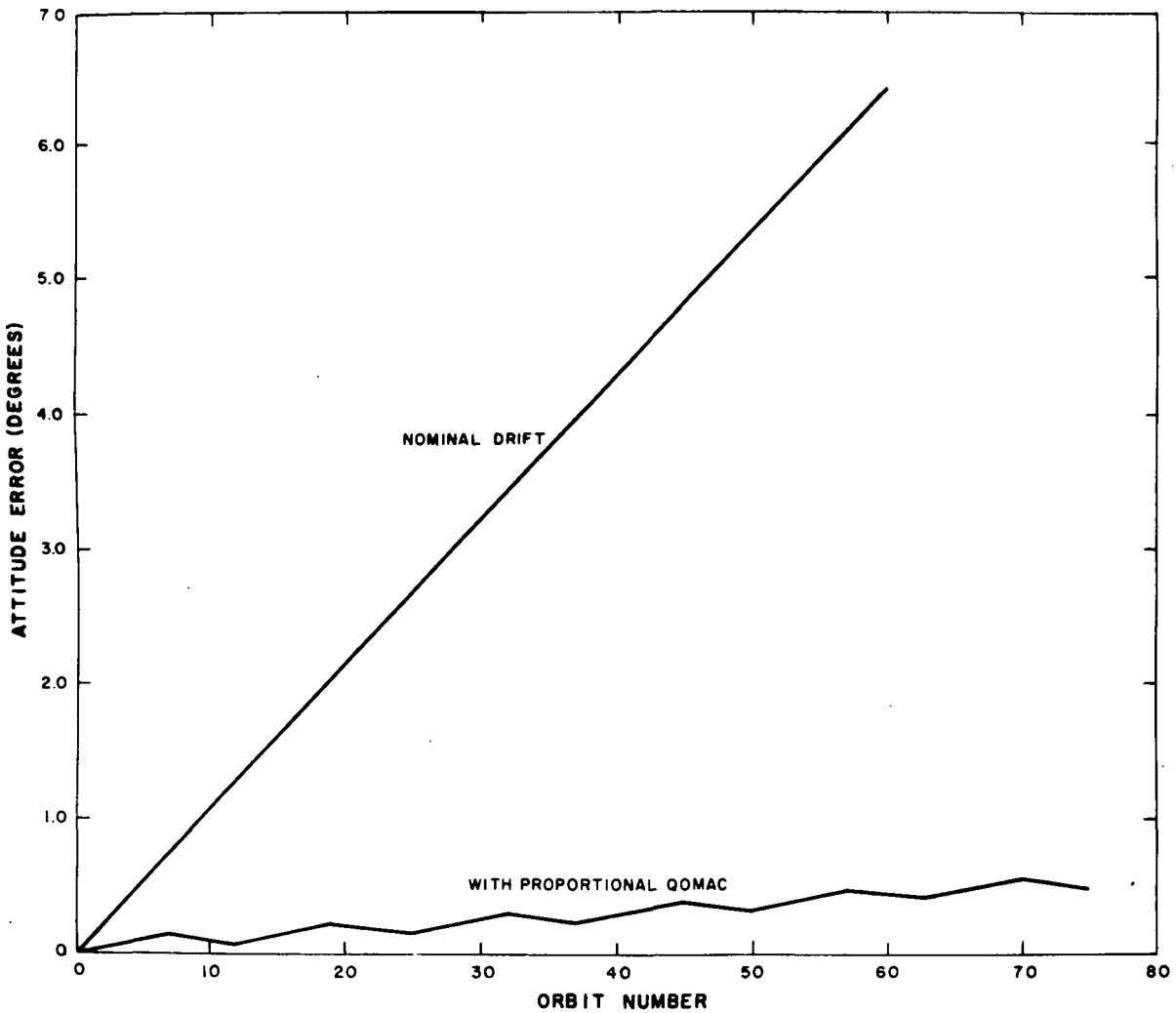

Figure 4-IV-24. Momentum Vector Attitude Drift

The start angles would be 162.4 and 342.4 degrees with the dipole switching at 180 and 360 degrees.

Figure 4-IV-24 also shows the computer results with the proportional QOMAC superimposed on the first torques. These results show a maximum attitude error after 75 orbits of 0.49 degree. The oscillation shown is due to the effects of the canted dipole. Although the first choice is quite acceptable, a finer choice of n based on these results would make the total drift even less.

The proportional QOMAC approach for cancellation of attitude drift due to solar pressure torques was selected by RCA because of its inherent design simplicity and demonstrated satisfactory performance. Additional solutions to this problem, such as canted solar panels or additional compensating vanes on the solar panels, were investigated. The results of these investigations are presented in detail in Appendix C.

6. Magnetic Bias Control (MBC)

The MBC coil provides a continuous dipole to offset the residual magnetic dipole of the spacecraft along the spin axis. Additional coil current is selected by ground command to generate a torque that corrects attitude changes due to orbital regression; i.e., approximately a 1-degree-per-day precession rate. The MBC coil is wound on the same structure as the QOMAC coil; its dipole moment, M_{MB}, is aligned with the QOMAC coil dipole, as follows:

$$M_{MB} = M_{MB}\,\hat{3}. \qquad (4\text{-IV-}10)$$

The magnitude of the precession rate, ω_{PMB}, is approximately

$$\omega_{P\,MB} = \frac{K\,M_{MB}}{2\,R^3\,H}\,. \qquad (4\text{-IV-}11)$$

Table 4-IV-3 gives the electromagnetic parameters of the MBC coil for each MBC switch position. The maximum dipole moment of 31.6 atm^2 is used in parallel with the QOMAC coil during the high torque mode of the initial orientation maneuver. The precession rate

is determined from Equation 4-IV-4. For a system momentum of 200 inch-pound-seconds and a total high torque QOMAC dipole moment of 35.6 atm^2, the precession rate is 5.0 degrees per torque cycle or 10.0 degrees per orbit. The dipole moment of 8 atm^2 is developed in the MBC coil so that it can be used as a backup for the QOMAC coil in the low torque mode. The dipole moment granularity between switch positions of 0.1 atm^2 gives a worst-case drift rate of 0.189 degree per day. The maximum range of dipole moments can produce a controlled attitude change of from -3.4 to +3.4 degrees per day. The physical parameters of the MBC coil are presented in Table 4-IV-4.

TABLE 4-IV-3. ITOS MBC COIL OPERATING PARAMETERS

Switch Position	Current (ma)	Power (watts)	Total Resistance (ohms)	Dipole Moment (atm^2)
1	1.1	0.027	22,200	0.2
2	2.2	0.054	11,100	0.4
3	3.2	0.078	7,650	0.6
4	4.3	0.105	5,700	0.8
5	5.4	0.132	4,530	1.0
6	6.5	0.159	3,760	1.2
7	7.5	0.184	3,250	1.4
8	8.6	0.210	2,850	1.6
9	9.7	0.238	2,520	1.8
10	43	1.05	570	8
11	170	4.17	144	31.6
12,0	OFF	-	-	0.0

The switching arrangement for the MBC coil is essentially the same as on the TOS spacecraft except that the coil polarity is reversed through a DPDT relay rather than with a center-tapped coil; this change was made to reduce the weight of the coil by a factor of two. In the low torque QOMAC mode, the MBC coil polarity is controlled from the CDU, and the power is routed through the switch resistors. In the high torque QOMAC mode, the MBC polarity is controlled by a set of QOMAC programmer drivers, and the power is applied from the -24.5-volt source on position 11 of the magnetic bias switch.

7. MOMENTUM CONTROL

a. Momentum Magnitude

The total momentum of the spacecraft must be controlled between specified limits around the nominal design point to keep within the dynamic range of the pitch control loop. Magnetic pitch axis momentum control produces a torque collinear with the momentum axis. This may be obtained by positioning the plane of each coil parallel to the flywheel axis; two momentum coils are mounted in this way in ITOS. Any momentum change will be transferred directly to a change in spin rate of the flywheel through the pitch control loop.

Considering a coil with its dipole moment, M_{MM}, in the $\hat{1}$, $\hat{2}$ plane at an angle of γ from the $\hat{1}$ axis, the magnetic dipole moment is as follows:

$$\overline{M}_{MM} = M_{MM} (\cos \gamma \hat{1} + \sin \gamma \hat{2}). \qquad (4\text{-IV-12})$$

The interaction of this moment with the earth's magnetic field produces two torques: one, T_{SPIN}, changes the magnitude of the momentum and the other, T_{PREC}, has the undesirable effect of changing the direction of the momentum vector. These torques are:

$$\overline{T}_{SPIN} = M_{MM} (B_2 \cos \gamma - B_1 \sin \gamma) \hat{3} \quad \text{and}$$

$$\overline{T}_{PREC} = M_{MM} (B_3 \sin \gamma \hat{1} - B_3 \cos \gamma 2). \qquad (4\text{-IV-13})$$

The $\hat{1}$, $\hat{2}$, and $\hat{3}$ coordinate axes are nominally aligned with the $\hat{r}$, $\hat{t}$, and $\hat{n}$ axes, and thus, for small attitude error angles:

$$B_1 = B_r,$$

$$B_2 = B_t, \text{ and}$$

$$B_3 = B_n$$

where B_1, B_2, and B_3 are the earth's magnetic field components in the $\hat{1}$, $\hat{2}$, and $\hat{3}$ coordinate system.

As can be seen from the field equations (4-IV-1), over some torquing interval, $\Delta\beta$, the average magnitude of B_r is twice that of B_t. To take advantage of this, the angle between the momentum coil dipole moment and the $\hat{1}$ axis is made 90 degrees; i.e., the positive dipole moment lies along the $\hat{2}$ axis, or nominally along the spacecraft velocity vector $\hat{t}$. The torque equations are then:

$$\bar{T}_{SPIN} = -M_{MM} B_1 \hat{3} \text{ and}$$

$$\bar{T}_{PREC} = M_{MM} B_3 \hat{1}. \qquad (4\text{-IV-}14)$$

b. Spin Momentum Change (T_{SPIN})

The torque along the momentun axis, T_{SPIN}, is the desired torque which will change the magnitude of the total spacecraft momentum. When Equations 4-IV-2 and 4-IV-14 are analyzed in terms of B_r and B_1, they yield a 0 average torque over an entire orbit. Therefore, the coil moment should only be applied over a partial orbit, specifically limited to the real-time acquisition by the ground stations. The average torque, $\tilde{T}_{SPIN}$, over some interval, β_s to β_f, is as follows:

$$\tilde{T}_{SPIN} = \frac{-2M_{MM}K}{(\beta_f-\beta_s) R^3} \left[-(\cos i \sin i_m \cos \Omega - \sin i \cos i_m)(\cos \beta_f - \cos \beta_s) \right.$$

$$\left. + \sin i_m \sin \Omega (\sin \beta_f - \sin \beta_s) \right]. \qquad (4\text{-IV-}15)$$

With the pitch control loop in the closed-loop mode, a momentum change will cause a direct change in the flywheel spin rate as follows:

$$T_{SPIN} = \frac{d}{dt} H = I_f \frac{d}{dt} \omega_f. \qquad (4\text{-IV-16})$$

where I_f is the flywheel moment of inertia and ω_f is the flywheel spin rate. Thus, the average spin torque acting over an interval Δt changes the flywheel spin rate as follows:

$$\Delta\omega_f = \frac{\Delta t}{I_f} \tilde{T}_{SPIN}. \qquad (4\text{-IV-17})$$

The parameters of each momentum coil are given in Table 4-IV-5.

Polarity reversals of the momentum coils are made through a DPDT relay as in the MBC coil. The spin rate change for one coil as a function of the torquing period is given in Figure 4-IV-25. This figure assumes a nominal 750-nautical-mile altitude, sun-synchronous orbit, and several ascending nodes. A spin rate change is determined by the difference between the final and initial $\Delta\omega_f$ corresponding to a given torquing period. The most efficient area of operation is near the north pole ($\beta = 90°$). As an example, if the torquing interval was from 60 to 107.05 degrees (corresponding to a 15-minute pass), the spin rate change would be 1.81 rpm for the case of a 200-degree east longitude ascending node. If both momentum coils were used, the change would be twice this amount. From Figure 4-IV-25, a torquing interval of some predetermined length starting at some point in the ground station contact circle can be established to give the required momentum (spin rate) change within specified limits.

c. Procession Due to Momentum Correction (T_{PREC})

The torque along the $\hat{1}$ axis, T_{PREC}, is an undesired torque which will change the direction of the mementum vector or precess the spacecraft. The torque equation is

$$\bar{T}_{PREC} = M_{MM} B_s \hat{1} = \frac{M_{MM} K}{R^3} \left[\cos i \cos i_m + \sin i \sin i_m \cos \Omega \right] \hat{1}. \qquad (4\text{-IV-18})$$

TABLE 4-IV-4. ITOS MBC COIL PHYSICAL PARAMETERS

Parameter	Value
Type	Single coil
Number of Turns	251
Wire Gage	25 AWG
Wire Resistance	132 ohms
Weight	2.1 pounds

TABLE 4-IV-5. ITOS MOMENTUM COIL PARAMETERS

Parameter	Value
Dipole Moment	10 atm^2
Type	Single coil
Number of Turns	160
Wire Gage	30 AWG
Wire Resistance	314 ohms
Series Resistor	12 ohms
Current	75 ma
Power	1.8 watts
Weight	0.5 pound

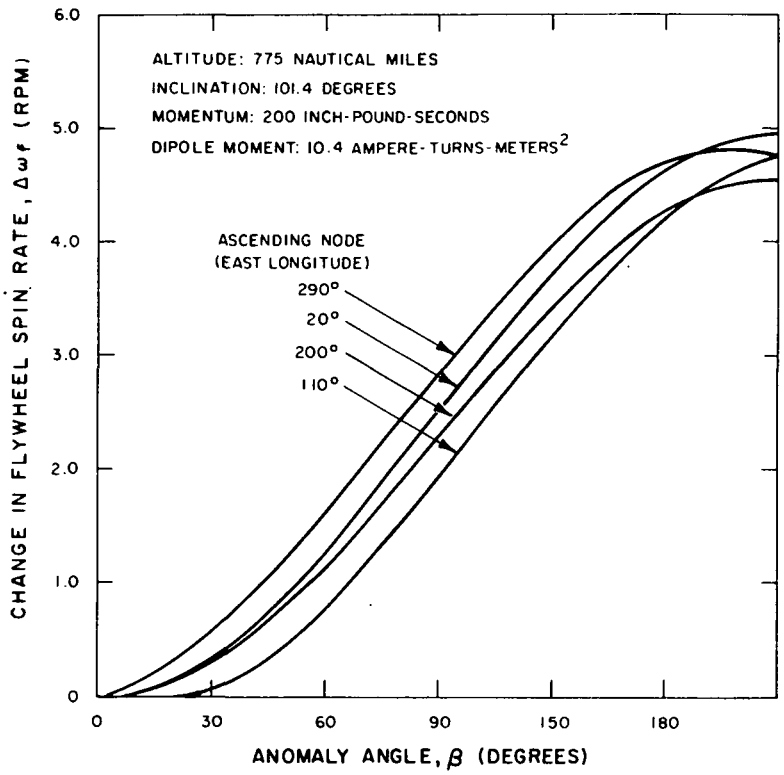

Figure 4-IV-25. Momentum Change Versus Torquing Period

The precession torque is a constant (for a given ascending node); hence the attitude change generated is a function of the time the momentum coil is turned on. The precession rate is a constant along the $\hat{2}$ axis, but this axis is rotating in the orbit fixed $\hat{\ell}$, $\hat{b}$, and $\hat{n}$ coordinate system. The precession torque in the fixed coordinate system is as follows:

$$T_{PREC} = M_{MM} B_s (\cos\beta\,\hat{\ell} + \sin\beta\,\hat{b}). \qquad (4\text{-IV-19})$$

Taking the average torque over the torquing interval, β_s to β_f, yields:

$$\tilde{T}_{PREC} = \frac{M_{MM} K}{(\beta_f - \beta_s) R^3} (\cos i \cos i_m + \sin i \sin i_m \cos\Omega)$$

$$\left[(\sin\beta_f - \sin\beta_s)\hat{\ell} - (\cos\beta_f - \cos\beta_s)\,\hat{b} \right]. \qquad (4\text{-IV-20})$$

The absolute value of the angular change, $\Delta\phi$, produced during the torquing time, Δt, is:

$$\left|\Delta\phi\right| \simeq \left|\tilde{T}_{PREC} \frac{\Delta t}{H}\right|. \qquad (4\text{-IV-}21)$$

A graph of this angular change is shown in Figure 4-IV-26 as a function of the orbit angle; curves are plotted for several ascending nodes. The attitude error generated is the difference in value between the final and initial $\Delta\phi$ angles, corresponding to the torquing interval. For the example cited earlier of an ascending node of 200 degrees east longitude and a torquing interval of from 60 to 107.5 degrees (for a 1.81-rpm change in flywheel speed), the error generated in attitude would be 0.11 degree. For an ascending node of 20 degrees east longitude, no attitude change would be produced regardless of the torquing period. Thus, a judicious choice of the orbit for momentum changes will keep the effects of attitude error to a minimum.

If both momentum coils are used for momentum corrections, the attitude change will be twice that shown in Figure 4-IV-26 for the same torquing interval. For the same momentum change, however, the coils would have to be on for only half the time required for one coil.

If the momentum must be changed while the spacecraft body is spinning, the momentum coil can be commutated manually from the ground stations instead of automatically within the spacecraft as in TOS. Torquing can only be accomplished while the satellite is in contact with the ground station; hence, the dipole switch phasing can be optimized with respect to the magnetic field experienced over the ground station. The average dipole direction should be normal to the magnetic field component, $\overline{\beta}_{\ell b}$. Figure 4-IV-27 shows the angles used to determine the commutation point. The dipole should be switched to

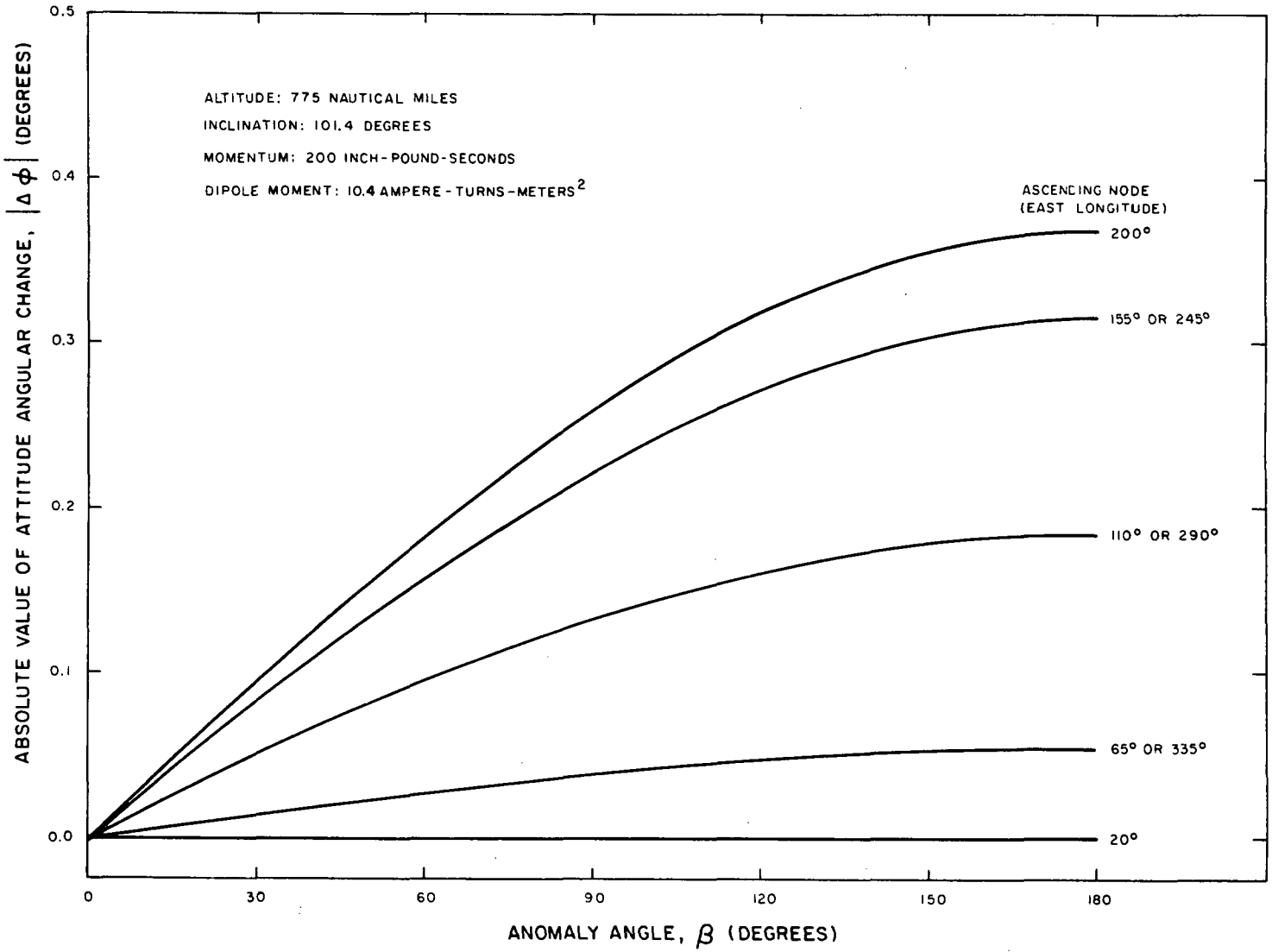

Figure 4-IV-26. Attitude Change Versus Torquing Period

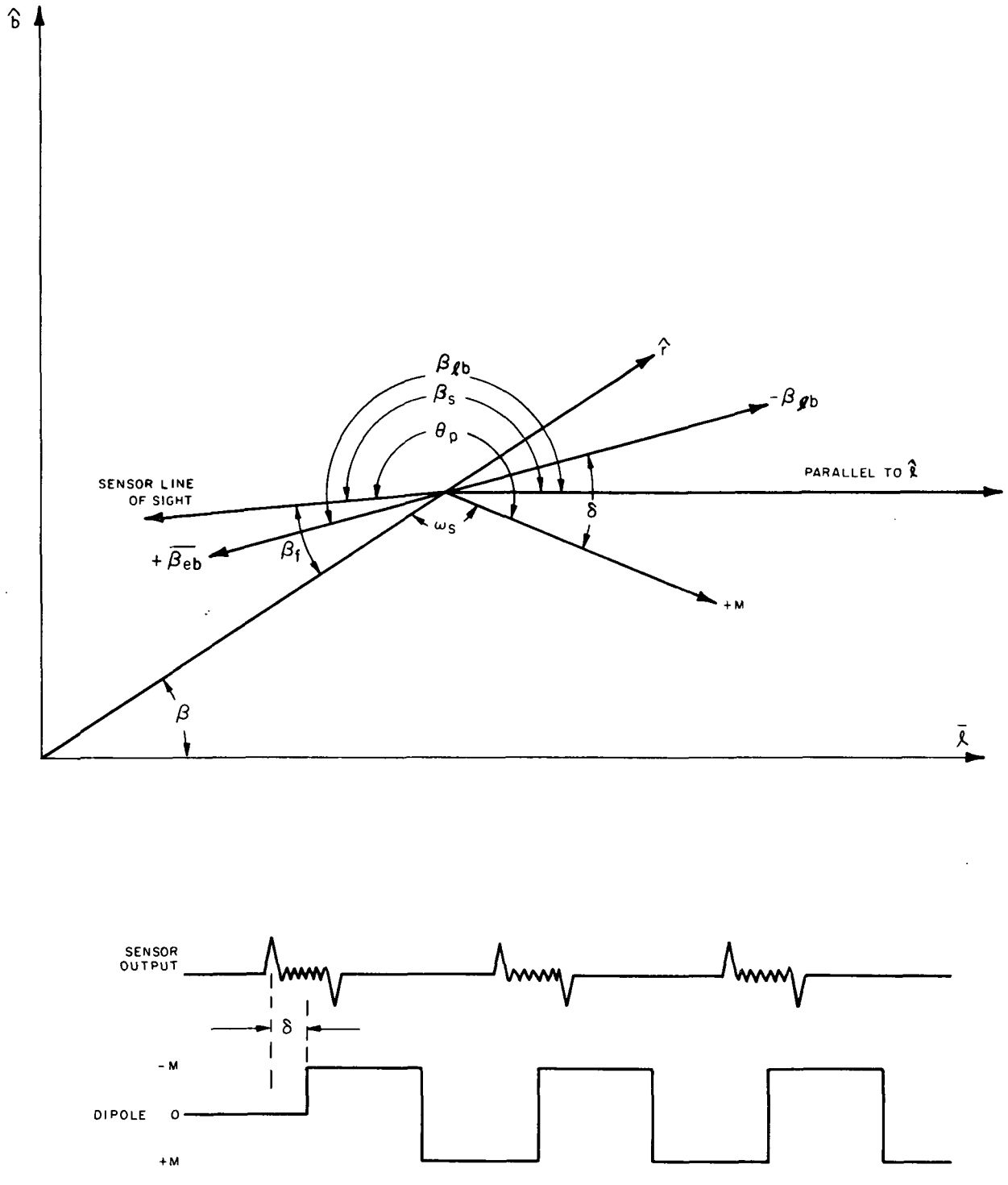

Figure 4-IV-27. Phase Angles for Momentum Coil Commutation

$-M_{MM}$ when it is aligned with $-\bar{\beta}_{\ell b}$ for a reduction in total momentum. The angle $\beta_{\ell b}$ is determined by:

$$\beta_{\ell b} = \tan^{-1} \frac{B_b}{B_\ell}$$

$$= \tan^{-1} \left[\frac{-3/2 \, (\cos i \sin i_m \cos \Omega - \sin i \cos i_m) \cos 2\beta}{3/2 \, (\cos i \sin i_m \cos \Omega - \sin i \cos i_m) \sin 2\beta} \right.$$

$$\left. \frac{+ \, 3/2 \sin i_m \sin \Omega \sin 2\beta + 1/2 \, (\cos i \sin i_m \cos \Omega - \sin i \cos i_m)}{+ \, 3/2 \sin i_m \sin \Omega \cos 2\beta + 1/2 \sin i_m \sin \Omega} \right] . \quad (4\text{-IV-22})$$

The commands to switch the dipole are transmitted at angles of δ and $\delta + 180$ degrees from the reception of the acquisition sensor pulse, and

$$\delta = \beta_{\ell b} - \beta + \beta_E + \theta_p \quad (4\text{-IV-23})$$

where:

θ_p is the fixed angle from the coil normal to the sensor line of sight and

β_E is the half-earth intercept angle for the acquisition sensor.

Angle $\beta_{\ell b}$ can be calculated for the range of β angles covering the ground station contact circle. Thus, an average value of angle δ, for a ground station, can be determined; this will make the ground commutation of the momentum coil relatively simple. The level of momentum change that can be achieved in a pass is approximately $2/\pi$ of that obtained with the nonspinning coil.

F. PITCH CONTROL

1. General

The pitch axis control loop maintains the spacecraft body in the desired orientation about the pitch axis with respect to an earth reference. In the absence of roll errors, this

consists of aligning the yaw axis with the local vertical throughout the orbit. Pitch axis control is commanded into operation after the initial orientation maneuver.

The satellite is controlled about the pitch axis by means of momentum transfer between the flywheel and the body. Momentum is transferred with a DC torque motor which couples the flywheel to the body. The torque motor is controlled by a reference voltage developed when a sky-earth horizon pulse is compared with a reference index pulse produced by a shaft encoder. Normally the pitch horizon sensor generates a horizon pulse for each rotation of the flywheel during the sky-earth transition. The reference index pulse is produced by a variable reluctance pickoff coil passing a reference point fixed in the body. For the particular orbit altitude, this reference point is geometrically positioned so that the horizon pulse and the index pulse are time coincident when there is a 0 pitch error. An operational block diagram of the pitch axis control loop is shown in Figure 4-IV-28.

Two redundant pitch axis control loops are provided on ITOS. The pitch horizon sensor is redundant by virtue of the backup roll horizon sensors. One of the three sensors may be used upon command to produce the torque motor voltage. Either of the torque motors with its corresponding electronic channel will be selected by ground command.

The position error detector, which detects deviation of the body axis from the local vertical, uses pulse width modulation (PWM) to measure the time difference between the horizon pulse and the index pulse. An error signal is produced of constant amplitude and variable pulse width; the width of the error signal is proportional to the angular error. The signal is shaped to an amplitude-modulated voltage by filtering (smoothing circuit). Subsequently, this voltage is compensated by frequency sensitive networks (compensation amplifier) and applied to the speed control loop. The voltages from the fixed-speed bias and the compensated-position error circuits are compared, in a summing amplifier, with a rate signal proportional to the relative rotational speed between flywheel and body. This latter rate signal is generated by a magnetic pulse encoder mounted integrally with the drive motor and generating 360 equally spaced pulses per revolution. The pulses are converted to a DC voltage by means of a frequency-to-DC converter and are smoothed by a simple lag circuit. The sum of the bias, error, and rate signals is applied through a power amplifier

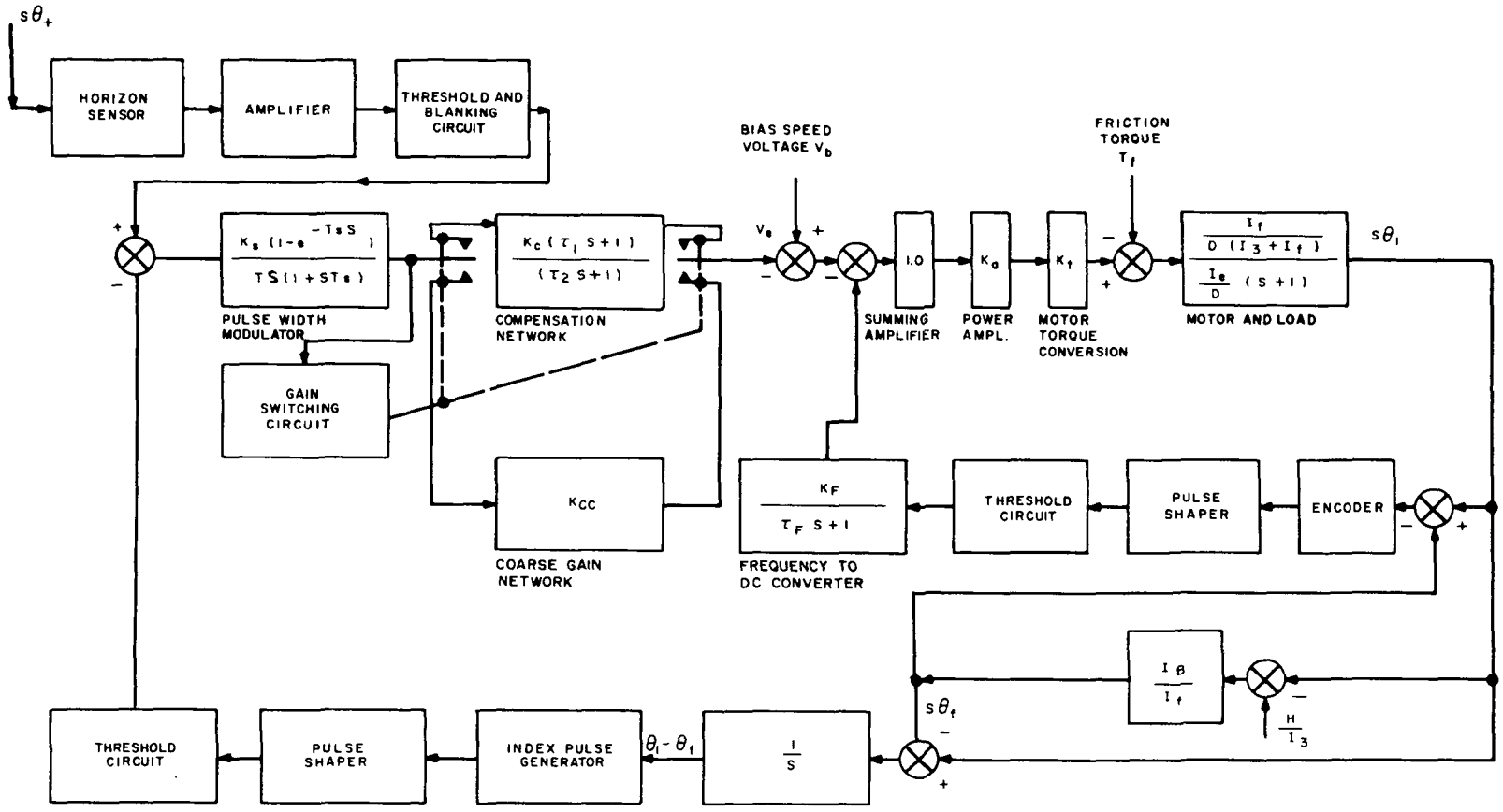

Figure 4-IV-28. Operational Block Diagram of Pitch Axis Control Loop

to the armature of the DC torque motor. Finally, motor action transfers momentum between the flywheel and the body, thus reducing the pitch position error toward a value of 0.

During the initial pitch acquisition, the pitch error may be large enough to saturate the amplifiers. Under these conditions the effective loop gain would be reduced and the tachometer loop time constant would be increased, leading to a possibility of control instability. To eliminate this condition, a two-mode control system is utilized. The compensation amplifier gain is switched to a low value (coarse gain mode) when the position error exceeds a value that would normally cause the unstable condition. Ensuring stability by loop gain reduction under all expected conditions will also result in larger pointing errors for momentum deviations from the nominal momentum of 200 inch-pound-seconds. When the pitch error is reduced to a nominal value of 15 degrees (final determination will be made by analog computer study), the system is automatically switched to the high (fine) gain control mode. For stability reasons, the compensation provided by the frequency sensitive network of the compensation amplifier is not utilized for the coarse gain mode; i.e., for the larger position errors possible during the initial pitch acquisition.

2. Pitch Sensing

The pitch control error detector requires input pulses from an earth horizon sensor and a reference index associated with the flywheel and the spacecraft body. Any deviation of the two pulses from coincidence generates an error signal which adjusts the speed of the torque motor. To obtain horizon information, one of three sensors shown in the block diagram of Figure 4-IV-1 and the mechanical layout of Figure 4-IV-29 will be used. The optical axis of each sensor is parallel to the flywheel spin axis.

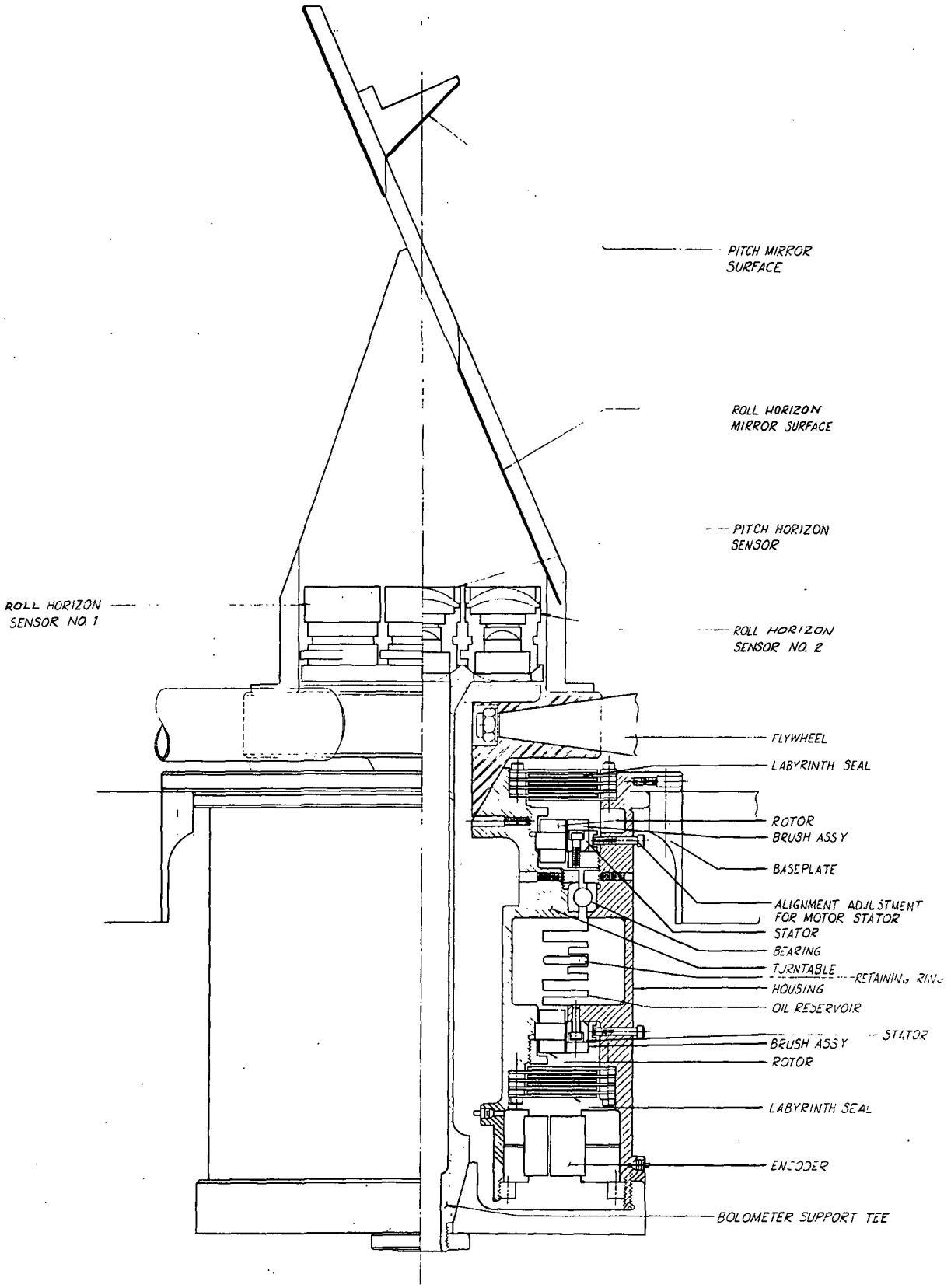

Figure 4-IV-29. Horizon Sensors, Torque Motors, and Encoder

The sky-earth pulse obtained from the pitch horizon sensor is phase-compared to a magnetically generated index pulse from the encoder. Figure 4-IV-30 illustrates the applicable geometry for either the primary horizon sensor (pitch) or backup horizon sensor (roll) with a corresponding encoder reference pulse. The line of sight of the primary sensor axis (camera, SR) is offset from the pitch horizon sensor by the half-earth angle, as defined by the orbit altitude at the instant of index pulse occurrence. Before launching, the encoder stator is positioned such that the required transition sensed by the horizon sensor coincides with the magnetic index pulse, as required for the anticipated altitude; this is achieved by manually rotating the entire electromechanical pitch loop assembly relative to the spacecraft body.

3. Servo Design

The pitch axis control block diagram in Figure 4-IV-28 has an open-loop transfer function for the fine gain mode as follows:

$$G(S) = \frac{1-e^{-TS}}{ST\,(1+ST_3)} \left(\frac{K_s K_c}{S}\right) \left(\frac{1+T_1 S}{1+T_2 S}\right) \left(\frac{I_F}{I_F + I_3}\right) \left(\frac{\frac{K_t K_a}{D}}{1+\frac{K_a K_f K_t}{D}}\right) \left(\frac{1}{1+\frac{\frac{I_e S}{D}}{\left(1+\frac{K_a K_f K_t}{D}\right)}}\right) \qquad (4\text{-IV-}24)$$

where:

T is the sampling period (nominal 0.4 second),

K_s is the modulator DC gain (1.27 volts per radian),

K_c is the compensation amplifier fine gain (53.6 volts per volt),

K_{cc} is the compensation amplifier coarse gain (2.45 volts per volt),

T_1 is the small-error compensation amplifier lead (16.67 seconds),

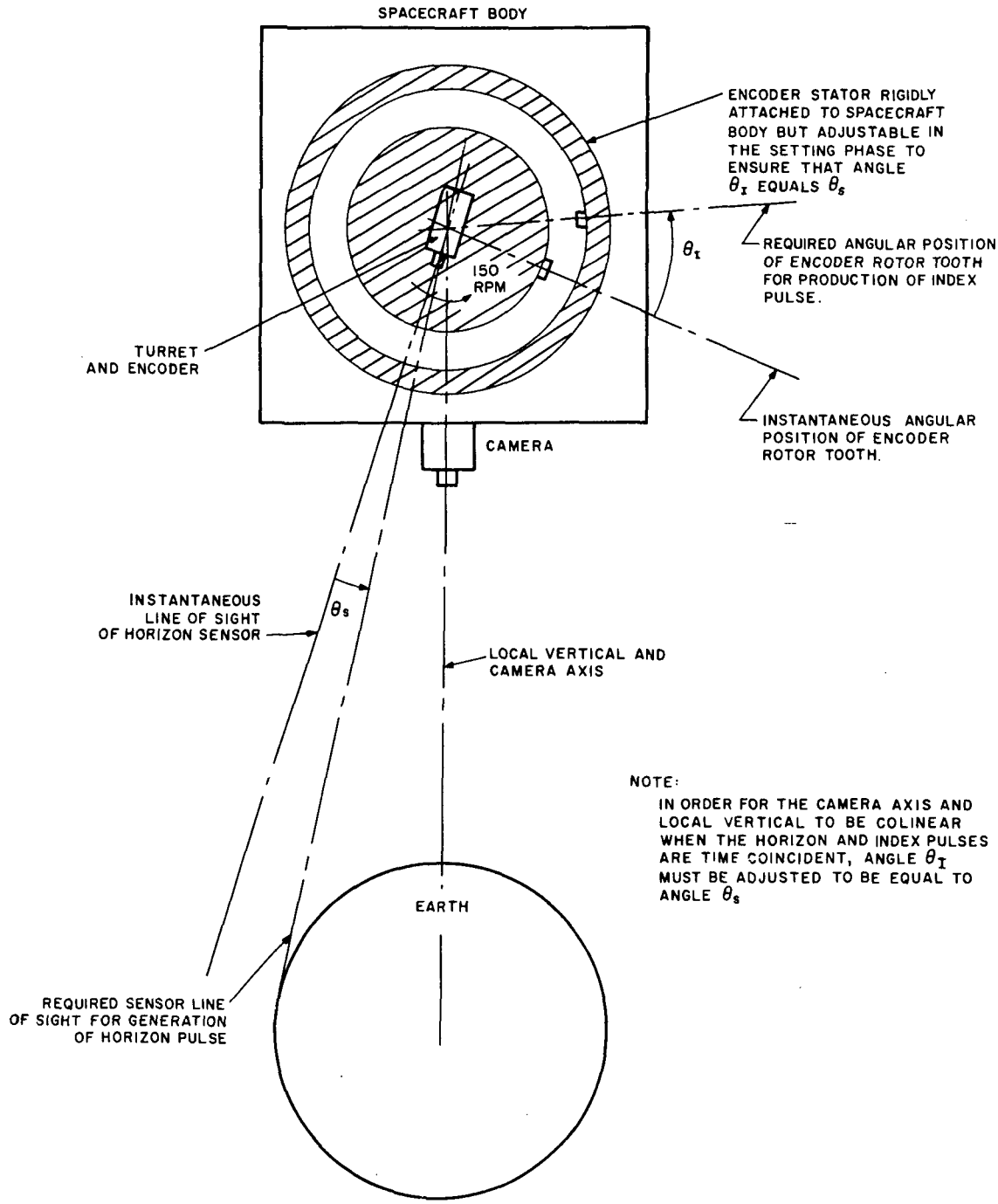

Figure 4-IV-30. Geometry of Horizon Pulse and Reference Index Pulse

T_2 is the small error compensation amplifier lag (417 seconds),

I_f is the flywheel moment of inertia (12.6 inch-pound-seconds^2),

I_3 is the body moment of inertia about the pitch axis (800 inch-pound-seconds^2),

$I_e = \frac{I_f I_3}{I_f + I_3} = 12.6$ inch-pound-seconds^2,

K_t is the motor torque constant (3.27 ounce-inches per volt),

K_a is the power amplifier gain (82 volts per volt),

K_f is the tachometer feedback gain (0.276 volt per radian per second),

D is the motor damping, equivalent to back emf (2.42 ounce-inches per radian per second),

H is the nominal momentum (200 inch-pound-seconds),

T_f is the friction torque, two motors (20 ounce-inches),

V_f is the motor viscous function (0.134 ounce-inches per radian per second),

θ_s is the error region for fine gain (±15 degrees),

T_3 is the PWM smoothing lag (0.8 second), and

$\omega_{f\ NOM.}$ is the nominal wheel speed (150 rpm).

The PWM error detector transfer function is

$$G(S)_{PWM} = \frac{1 - e^{-TS}}{ST} . \qquad (4\text{-IV-}25)$$

The above equation is an approximation derived from sampled data theory. For sinusoidal analysis purposes, this transfer function can be expressed as follows:

$$G(j\omega)_{PWM} = \frac{\sin\frac{\omega T}{2}\; e^{\frac{-j\omega T}{2}}}{\frac{\omega T}{2}} . \qquad (4\text{-IV-}26)$$

And, since the sampling period T will always be small compared with ω,

$$G(j\omega)_{PWM} = e^{\frac{-j\omega T}{2}} . \qquad (4\text{-IV-}27)$$

According to the tradeoff in the dynamic mass of the flywheel and the nutation damper (see Figure 4-IV-7), the nominal momentum stored within the flywheel is defined as 200 inch-pound-seconds. For the 17.5-inch radius of gyration achievable within the envelope limits of the attach fitting, and the nominal spin rate of 150 rpm, the inertia ratio between vehicle pitch and flywheel is about 63. The selected, nominal wheel speed is not only conducive to low brush wear and good commutation but also compatible with the attitude sensing scanning requirements and reasonable sampling rates. Within the above constraints, it is desirable to minimize the pitch position offset for this Class I servo loop resulting from momentum deviations. Selecting a velocity gain as:

$$K_V = \frac{K_s K_c K_T K_a}{D\left(1 + \left(\frac{K_j K_T K_F}{D}\right)\right)} \frac{I_f}{I_f + I_1} = 4 \qquad (4\text{-IV-}28)$$

will limit the pitch offset to 0.363 degree for the sizable momentum deviation of 10 percent from the nominal 200-inch-pound-second value.

Figures 4-IV-31 and 4-IV-32 are the open-loop Bode plots of the position loop for both fine gain and coarse gain cases. The figures indicate the need for the coarse gain region by

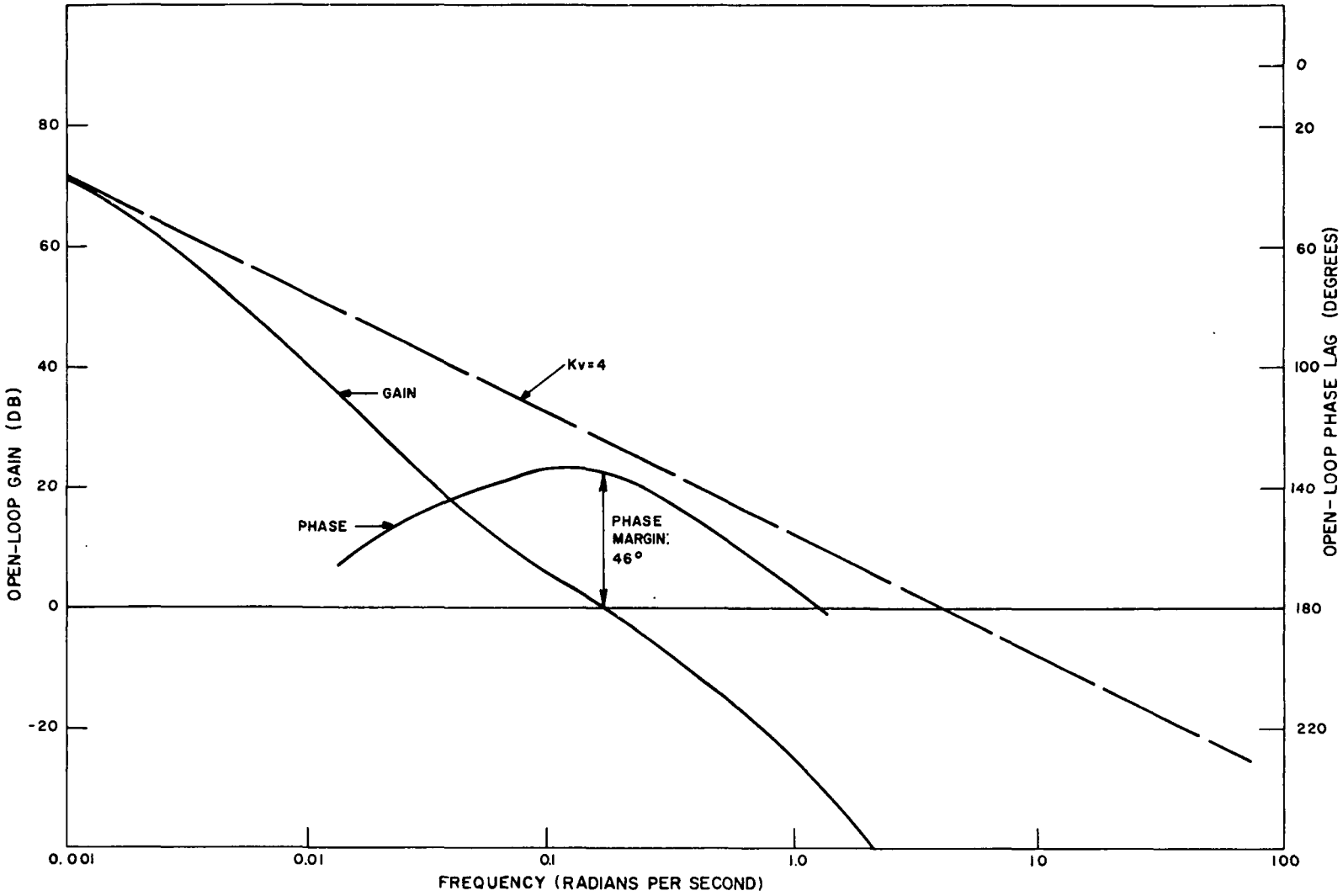

Figure 4-IV-31. Open-Loop Frequency Response of Pitch Control Loop (Fine Gain Case)

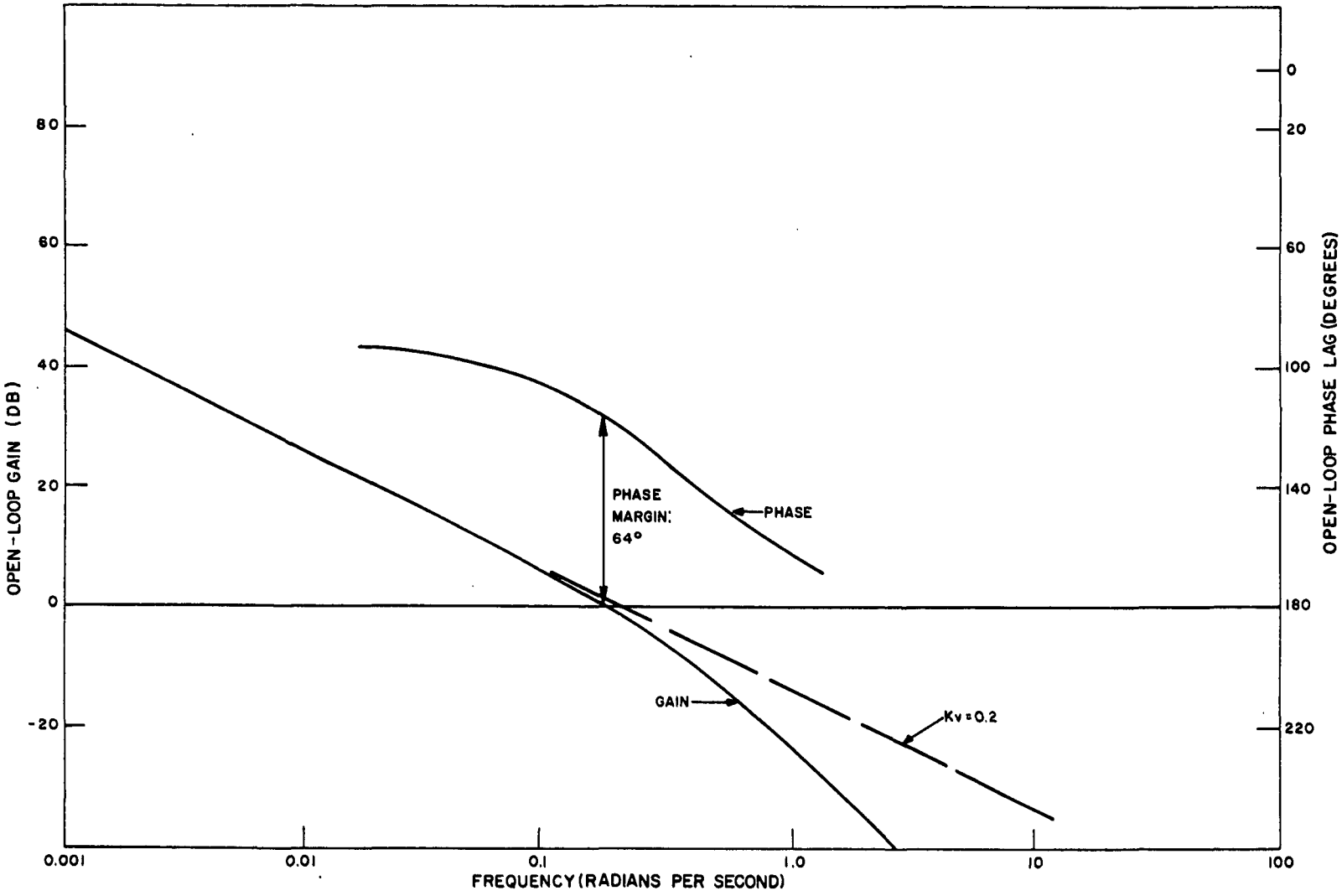

Figure 4-IV-32. Open-Loop Frequency Response of Pitch Axis Control Loop (Coarse Gain Case)

virtue of the system being adequately stable in its linear range, but the phase margin of the fine gain curve would suffer severely if the loop gain were to decrease due to amplifier saturation.

It should be observed that the crossover frequency occurs at about 0.2 radian per second for both fine gain and coarse gain cases, or nearly two orders of magnitude below the nominal sampling frequency of 15.7 radians per second. The PWM can be represented in simplified fashion as indicated above, and a PWM smoothing network with a time constant in the vicinity of the sampling frequency has little effect on the system stability. The open-loop Bode plot of the tachometer loop is shown in Figure 4-IV-33.

The gain switching circuit reduces the loop gain (compensation amplifier) and removes the lag-lead compensation network in the presence of large pitch errors, which are expected during the initial pitch acquisition and might recur during recovery from unexpectedly large disturbances. Without such switching, amplifier saturations would result in a highly under-damped system. The described servo is scheduled for analog computer study during the next phase of this program. Therefore, the stipulated coarse gain, the PWM smoothing time constant, and the fine-to-coarse gain switch point are subject to some modification based on computer results; the suggested values of these three parameters are based on studies of similar control circuitry. In any case, for momentum offsets of ±10 percent, the servo is always expected to capture within 6 minutes.

4. Component Description

a. General

The pitch axis control loop consists of the following components:

- Pulse width modulator (PWM) error detector,
- Compensation amplifier,
- Gain switching circuit,
- Summing amplifier,

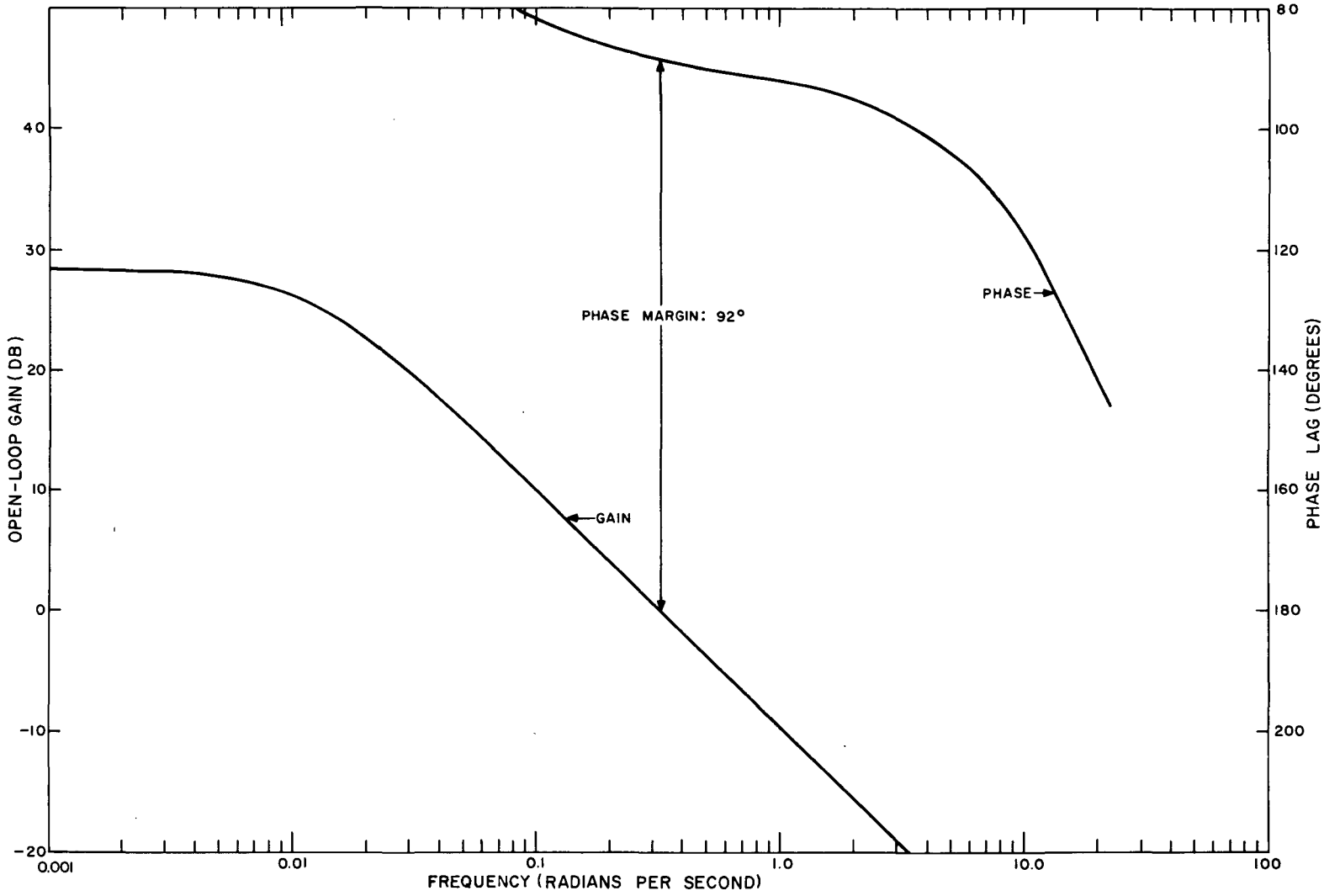

Figure 4-IV-33. Open-Loop Frequency Response of Tachometer Loop

- Power amplifier,
- Torque motor ,
- Encoder,
- Encoder electronics ,
- Frequency-to-DC converter,
- DC-to-DC converter,
- Roll and pitch sensors,
- Sensor threshold amplifiers, and
- Blanking circuits.

The sensors and sensor amplifiers are discussed in Paragraph D. A general functional description of the remaining components follows. The entire pitch axis control loop is shown in Figure 4-IV-1. Table 4-IV-6 lists the tentative electronic specifications for these components; Table 4-IV-7 lists the power requirements.

b. Pulse Width Modulator (PWM) Error Detector

The block diagram of the PWM error detector is shown in Figure 4-IV-1. The leading edge of the horizon sensor pulse and its corresponding index pulse from the encoder set their respective control flip-flops. The outputs of the flip-flops are applied to a difference amplifier which provides a bipolar output error pulse. The duration of the error pulse is proportional to the difference in time between the two input pulses. The polarity of the error pulse is determined by the order of occurrence of the input pulses, corresponding to a plus or minus pitch error. The error pulse is filtered through an R-C circuit to provide an average DC level.

After both flip-flops are set, the output of the AND gate is delayed and resets the two flip-flops, which are then ready to accept the next input pulses. Should the flip-flops not be reset, the second index pulse, which is "OR'ed" with the output of the AND gate in the fine-gain mode, will reset them. The error measurement characteristics are shown in

TABLE 4-IV-6. PITCH-AXIS CONTROL LOOP ELECTRONIC SPECIFICATIONS

Component	Characteristic	Specification
Pulse Width Modulator	Input pulse	> 2 volts
	Input pulse duration	> 10 μ seconds
	Input impedance	> 7 kilohms
	Output impedance	< 15 kilohms
	Gain	1.27 volts/radian
	Smoothing time constant	0.8 second
	Supply voltage	-24.5, -15, and +15 volts
Compensation Amplifier	Coarse gain	2.45
	Fine gain	53.6
	Input impedance	>40 kilohms
	Output impedance	<100 ohms
	Supply voltage	+15 and -15 volts
Gain Switching Circuit	Input impedance	>40 kilohms
	Load capacity	0.33 volt error (15°)
	Supply voltage	-24.5, -15, and +15 volts
Summing Amplifier	Gain	9.65
	Input impedance	>50 kilohms
	Output impedance	<500 ohms
	Supply voltage	-15 and +15 volts
Power Amplifier	Gain	10
	Input impedance	>100 kilohms
	Switch point	50 ohms
	Supply voltage	-26 to -36 volts

TABLE 4-IV-6. PITCH-AXIS CONTROL LOOP ELECTRONIC SPECIFICATIONS (Continued)

Component	Characteristic	Specification
Encoder Electronics	Input impedance	>100 kilohms
	Index pulse amplitude	>2 volts
	Index pulse output impedance	1000 ohms
	Pulse amplitude	30 volts, p-p
	Supply voltage	+15 and -15 volts
Frequency-to-DC Converter	Sensitivity	0.276 volts/rad/sec
	Smoothing time constant	0.05 second
	Ripple	≤100 mv, p-p, at 900 Hz
	Input impedance	>100 kilohms
	Output impedance	<10 kilohms
	Supply voltage	-24.5 volts ±1 percent
DC-to-DC Converter	Output voltages	+15 and -15 volts
	Efficiency	>75 percent at 2.8-watt load
	Supply voltage	-24.5 volts ± 1 percent
Blanking Circuits	Blanking time (pitch sensor)	225 msec± 10 percent
	Blanking time (roll sensor)	225 msec ±10 percent
	Input impedance	>7 kilohms
	Output impedance	<1 kilohm
	Input pulse duration	>10 μseconds
	Supply voltage	-15 and +15 volts

TABLE 4-IV-7. PITCH-AXIS CONTROL LOOP POWER REQUIREMENTS

Component	Power
Pitch Loop Electronics (based on 75-percent DC-to-DC converter efficiency)	100 ma at -24.5 volts
Power Amplifier and Motor (20 ounce-inch friction torque)	227 ma at -26 to -36 volts
Horizon Sensors (1 pitch and 2 roll/yaw)	18 ma at -24.5 volts

Figure 4-IV-34. As the analog error decreases, the pulse width error decreases correspondingly. The equivalent error after smoothing is a satisfactory linearization of the analog error.

c. Compensation Amplifier

The compensation amplifier is a high gain DC operational amplifier to generate transfer characteristics. The operational amplifier circuit is shown in Figure 4-IV-35. The summing point voltage for this circuit, as defined in Figure 4-IV-35 can be expressed as:

$$e_P = \frac{e_o}{K} \simeq \frac{e_1 Z_B}{Z_A + Z_B} - \left[\frac{e_o Z_2 Z_3 + e_2 Z_3 Z_f + e_3 Z_2 Z_f}{Z_2 Z_3 + Z_f (Z_2 + Z_3)} \right]. \qquad (4\text{-IV-}29)$$

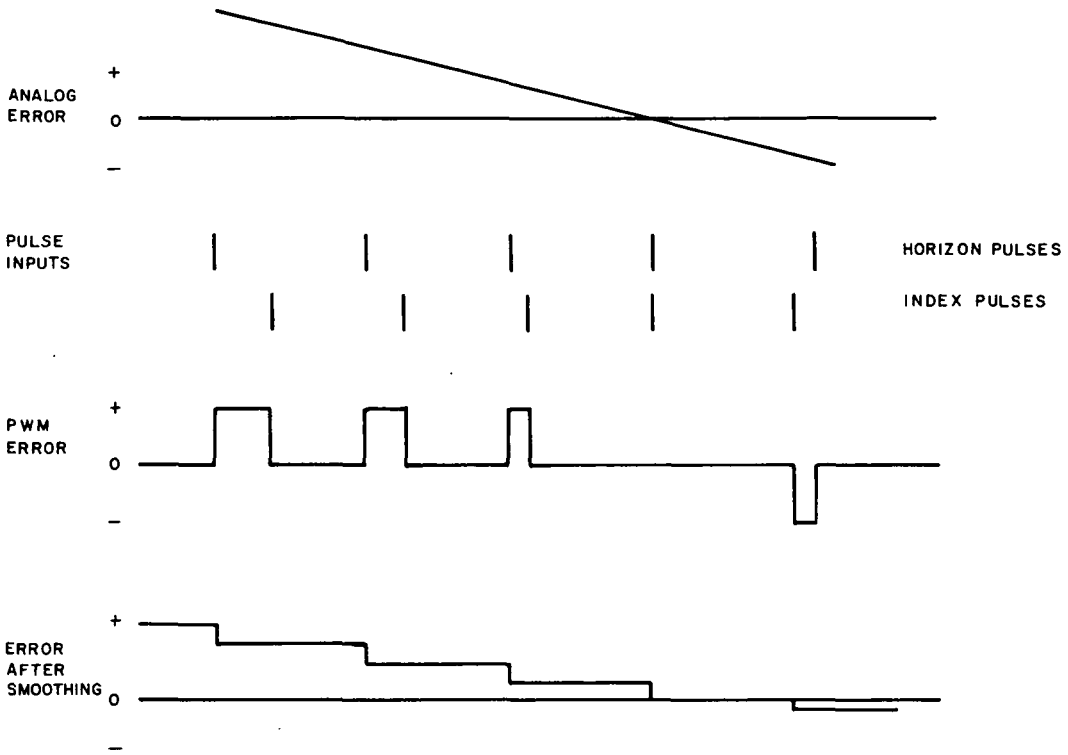

Figure 4-IV-34. Error Detection

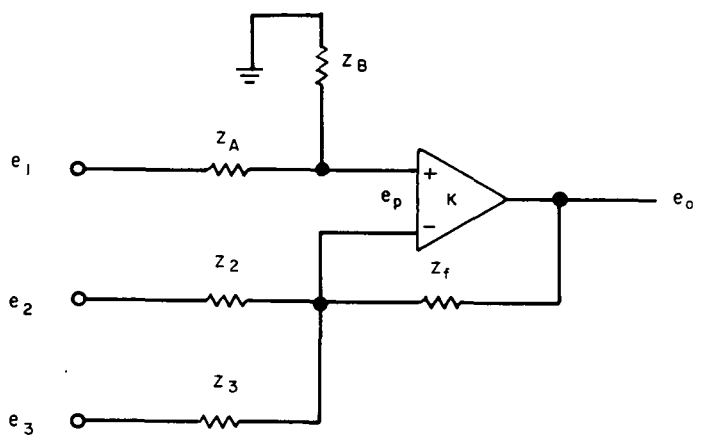

Figure 4-IV-35. Operational Amplifier, Simplified Schematic Diagram

This equation assumes that the input impedance is large and the output impedance is small. For very large values of amplifier gain, the output of the amplifier is

$$e_o = \frac{e_1 Z_B}{Z_A + Z_B} \left[1 + \frac{Z_f}{\left(\frac{Z_2 Z_3}{Z_2 + Z_3} \right)} \right] - \frac{e_2 Z_f}{Z_2} - \frac{e_3 Z_f}{Z_3} . \qquad (4\text{-IV-}30)$$

The compensation amplifier provides signal gain and phase compensation to the smoothed PWM error signal.

d. Gain Switching Circuit

A block diagram of the gain switching circuit is shown in Figure 4-IV-36. This circuit consists of a differential amplifier that produces the absolute value of the smoothed error signal, a filter, a threshold circuit, and a relay driver. When the error exceeds a preset value, the relay driver is activated, switching the gain and phase characteristics in the compensation amplifier.

e. Summing Amplifier

The summing amplifier, as shown in Figure 4-IV-1, is a high gain DC operational amplifier which sums the motor bias voltage, the frequency-to-DC converter output, and the compensated error signal. In the open-loop mode, the compensated error signal is removed and replaced by a second bias voltage to run the motor at a constant speed of 60 rpm.

f. Power Amplifier

The power amplifier, as shown in Figure 4-IV-1, extends the dynamic range of the summing amplifier to the full extent of the unregulated -24.5-volt power supply, and it serves as an efficient power interface between the summing amplifier and the torque motor.

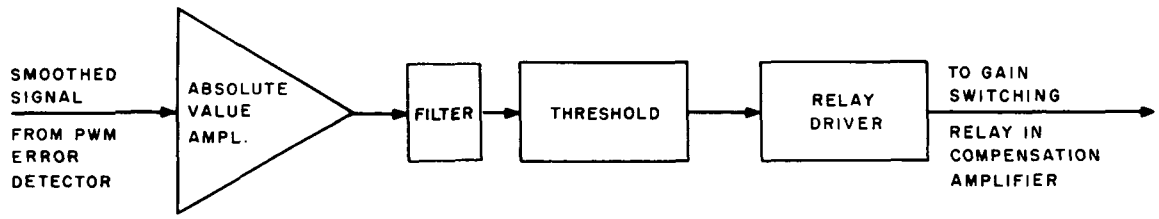

Figure 4-IV-36. Gain Switching Circuit, Block Diagram

g. Torque Motor

The following criteria were applied in the selection of a torque motor for the pitch axis control loop:

1. The inside diameter of the motor has to be large enough to provide proper support and installation of the pitch and roll horizon sensors. This permits the use of mirror-scanned horizon sensors and eliminates the need of sensor slip rings.

2. The motor operates from the -26- to -36-volt unregulated power supply to avoid the inefficiencies associated with DC-to-DC power conversions.

3. The motor must be capable of supplying 20 ounce-inches of steady-state friction torque (due to bearing friction, brush friction, and magnetic drag), and it must have an adequate reserve capability to allow capture for a ±40-percent momentum change from the despin value.

4. The motor must be a direct drive pancake-type unit to eliminate any gearing requirements.

The Inland model T-4411-D DC torquer or its equivalent was selected for the redundant configuration shown in Figure 4-IV-29. For the minimum available unregulated supply voltage of 24 volts (allowing 2 volts for power amplifier drop), the torque and speed characteristics shown in Figure 4-IV-37 satisfies 2 and 3. The sensor layout in Figure 4-IV-29 satisfies criterion 1; criterion 4 is also apparent from this figure. The motor exclusive of the power amplifier requires 3.44 watts at the design point.

Before the brush-type torque motor was selected, special attention was focused on the proper and reliable operation of the armature brushes throughout the life of the mission. Testing conducted by RCA under thermal vacuum conditions with both carbon and 50/50 silver graphite brushes has adequately demonstrated, during the last 2 years, proper and reliable operation. Both bearing and brushes will operate in an oil vapor atmosphere of dioctyl adipate, a low vapor pressure synthetic lubricant, stored within the momentum wheel assembly. It is of interest to note that the motor manufacturer experienced significantly higher silver graphite wear rates under standard atmospheric conditions. Therefore, it appears that from the standpoint of brush wear, the lubrication provided for the ITOS design in vacuum conditions is superior to that used under standard atmospheric conditions.

h. Encoder

The encoder is a three-track variable reluctance transducer with permanent magnets. The unit has full peripheral sensors that minimize the effects of shaft misalignment and mounting eccentricities. One of the tracks provides 360 pulses per revolution for rate feedback around the motor. This signal is generated with 360 teeth on the rotor and two full-perimeter magnetic pickoffs on the stator. The other two tracks consist of a suitable tooth pattern on the rotor and full-perimeter magnetic pickoffs on the stator; these tracks

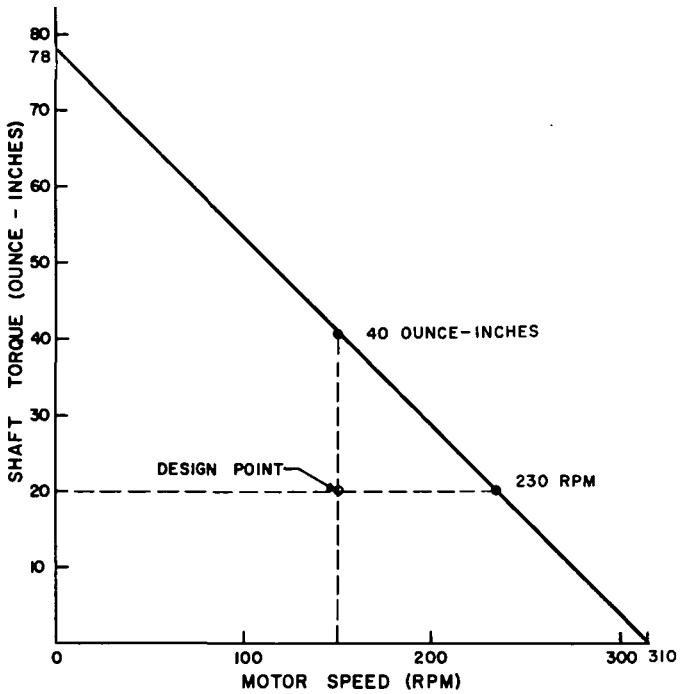

Figure 4-IV-37. Torque and Speed Characteristics at Power Amplifier Voltage for Inland Torque Motor of -24 Volts

produce the desired index pulses spaced 196.5 degrees apart. The first index pulse is used with the pitch horizon sensor; the second index pulse is used with either of the two side-looking roll horizon sensors, in the backup mode. The outputs from the encoder are low level signals which require amplification and processing before they can be utilized in the pitch control loop.

i. Encoder Electronics

A block diagram of the encoder electronics is shown in Figure 4-IV-1. The four sinusoidal output signals (the two lines of 360 pulses per revolution, the pitch index pulse, and the roll index pulse) from the encoder are each amplified by a threshold amplifier from the zero crossings and shaped by a Schmitt trigger to produce sharp pulses. The final pulse widths are determined by the pulse width of the encoder signal and the threshold level.

j. DC-to-DC Converter

The DC-to-DC converter consists of a transistorized, saturable reactor multivibrator, a coupling transformer, and an output rectifying circuit. The input voltage to the converter is -24.5 volts DC ±1 percent; the nominal output voltages are +15 and -15 volts DC. A 3-percent tolerance on output voltage is maintained for loads of 20 to 100 milliamperes on each output tap with a minimum overall conversion efficiency of 75 percent, at these current levels.

k. Sensor Threshold Amplifiers

The threshold level of the sensors will be set 10 to 1 above the zero-to-peak noise. This corresponds to a level of 160 millivolts. The threshold amplifier following the horizon sensor is essentially a Schmitt trigger circuit, set to switch at a 160-millivolt input. For a sky-earth horizon crossing at the lowest expected temperatures, the input is sufficiently high to exceed the threshold. This threshold network is connected at the output of each of the three horizon sensors. Two sets of electronics follow the pitch horizon sensor, the circuits being selected by ground command.

l. Earth Blanking

As the horizon sensors scan the earth, the varying temperatures of the earth can cause fluctuations in the bolometer output. From previous experience, it is reasonable to assume that during the earth time, many pulses will be produced that will trigger the threshold circuit. To keep these earth pulses from interfering with the pitch-axis-control-loop electronics, earth blanking of the sensor outputs is included.

Each horizon sensor output triggers a single-shot multivibrator with a pulse width of 225 milliseconds. At the nominal 150-rpm wheel speed, this corresponds to 200 degrees. For higher wheel speeds, this pulse covers a greater angle. The allowable speed range is 60 to 225 rpm to ensure complete earth blanking and to ensure against blanking out the next true horizon pulse. The wheel speed will not be below 60 rpm for spacecraft stability reasons and the torque motor control loop will saturate at 230 rpm. Thus, the 225-millisecond blanking time is sufficient for the expected conditions.

5. Pitch Control Mechanical Design

The pitch control electromechanical assembly is a single unit consisting of an outer fixed housing and an inner rotating turntable, each shaped to mount and retain the following essential parts: (1) encoder, (2) labyrinth seals, (3) redundant torque motors, (4) stored oil, (5) flywheel, (6) mirror, and (7) bolometers and bolometer electronics. The turntable assembly is supported by the external housing through a single bearing as shown in Figure 4-IV-29.

The assembly resorts to a single bearing rather than two spaced bearings for support of a rotating shaft for the following reasons:

- The single bearing has less friction than two bearings.
- The single bearing allows visible assembly control over the concentricity of the motors. If two bearings were used they would require adequate axial spacing to give a reasonable base, requiring motor mounting between bearings. With the necessary assembly tolerances, such an arrangement introduces greater concentricity tolerances.
- The single bearing shortens the assembly and this compactness saves weight.
- The single bearing can perform all the requirements of the system satisfactorily.

The Conrad four-point contact ball bearing is the Kaydon KD45XP with selected diametral clearance between 0.0010 and 0.0015 inch.

The shake (along spin axis) is 0.0016 to 0.0024 inch. Maximum shake and maximum diametral clearance are not simultaneously additive. Cone angle, self alignment (tilt) with maximum diametral displacement is 0.0182 to 0.0256 degree.

The bearing allowable load values based on a standard usable Brinelling value are:

Radial load: 12,400 pounds;
Thrust load: 30,800 pounds; and
Moment: 31,000 inch-pounds.

Calculations show that an adverse differential temperature across the bearing races of 29°F will just eliminate the minimum diametral clearance of 0.0010 inch. Normally at this temperature differential bearing binding would commence. Selecting a temperature safety factor of 2.0 established a maximum desirable race temperature differential of 14.5°F.

A thermal investigation of the entire assembly shows a favorable differential of 7.6°C (14°F) to be the maximum gradient expected. This favorable gradient will cause an increase in bearing clearances and, together with the self-aligning angle increases, the gradient can cause a delta change in the encoder gap of 0.000735 inch. By geometry all other gaps are affected less.

To fully control gaps, clearances, and tolerances the bearing is to be matched to its titanium housing bores by measuring the bearing dimension and adding a small predetermined clearance for the housing bore dimension.

The bearing races and balls are of SAE52100 steel which shows excellent oxidation resistance up to 250°F. This plus an oil film will preclude any corrosion of the bearing during storage.

Each motor consists of three separate parts: a two segment brush assembly, an armature, and a stator. Radial self-locking screws (see Figure 4-IV-29) align the rotor and stator to the bearing rotational center. This system is preferred to the use of a fixed pilot for alignment precision.

The encoder is installed at the top of the assembly. Both the rotating part and the fixed part of this magnetic transducer are shown mounted through adaptors which allow flexibility to accommodate the exact dimensions of the encoder.

An oil reservoir composed of Nylasint stores 42 grams of lubricant, or about one third by volume. Lubrication is achieved by low pressure vaporization of the oil in the closed housing. The vapor is able to lubricate the motor brushes and bearings. The synthetic lubricant is dioctyl adipate, dibasic-acid ester. Selection of this lubricant for ITOS is based on its successful performance during thermal vacuum tests.

Associated with the oil vapor pressure is a labyrinth-type sealing system. The leak rate of this labyrinth controls the life of the lubrication. The labyrinth seals are constructed of stacks of magnesium sheets of the proper diameter and thickness so that the rotating sheets have a nominal 0.02-inch clearance and thus no rubbing contact and zero associated friction. Experience has shown this construction to be satisfactory.

The theoretical lubricant loss rate through the two labyrinth seals can be predicted for the applicable free molecular flow regime as follows:*

$$W = \left[0.0583 \; P \left(\frac{M}{T} \right)^{1/2} A \right] f \qquad \text{(4-IV-31)}$$

where:

W is the oil loss rate (grams per second),
P is the vapor pressure (mm Hg),
M is the molecular weight of the oil,
T is the oil temperature ($^{\circ}$K),
A is the aperture area (cm^2), and
f is the transmission probability of molecular flow.

The transmission probability is a function of the seal-length-to-clearance ratio and of the number of directional changes from the inner cavity to the outer environment. Each of the two labyrinth seals consists of 14 consecutive L-shaped segments. For dioctyl adipate (molecular weight: 370), the loss rate is illustrated in Figure 4-IV-38. Based on test

* W.A. Salmon and C.M. Apt, "A Lubrication System for Space Vehicles", Automotive Engineering Congress Paper 632E, January 1963, and D. Santeler, "Vacuum Technology", International Science and Technology, No. 13, January 1963, pp. 46-54.

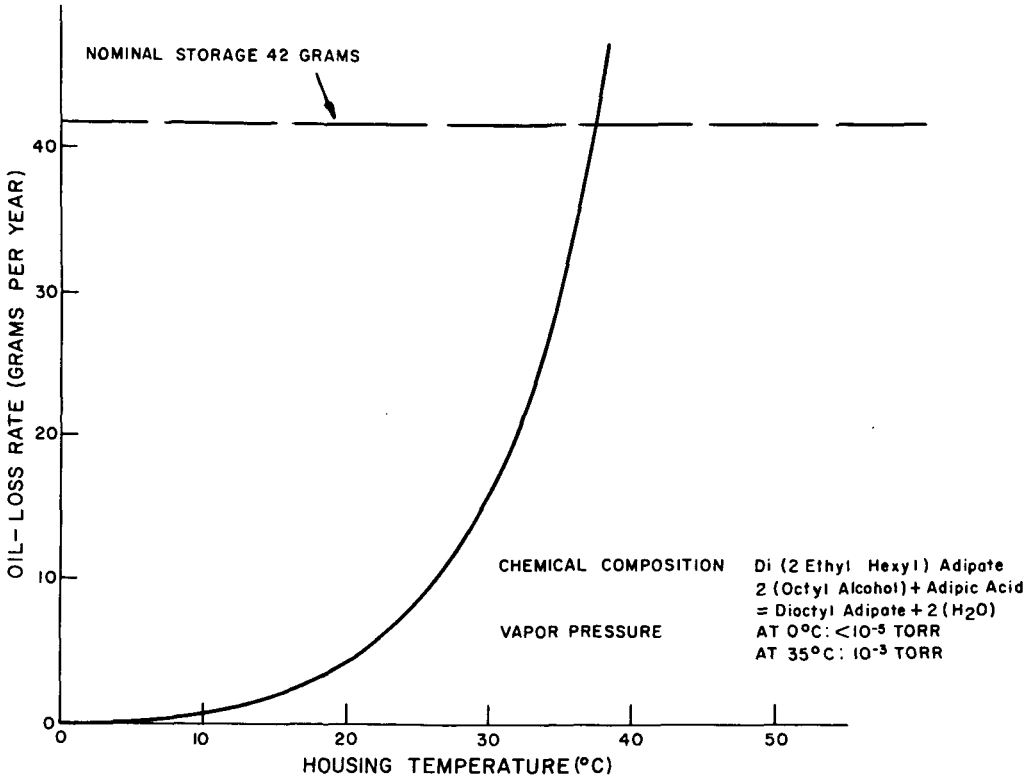

Figure 4-IV-38. Oil-Loss Rate Versus Housing Temperature

results, this theoretical prediction is conservative by a factor ranging from about 2:1 to 4:1.

Three bolometers, as shown in Figure 4-IV-29, are mounted on a support tee which extends through the rotating platform to a fixture point. Electronics for preamplifying the bolometer signals are mounted on the platform adjacent to the bolometers. A shimming technique for the bolometers aligns the optical axes.

A continuous rim spoked flywheel is attached to the rotating platform. The outside diameter of the flywheel is selected to just clear the inside of the marman clamp, extending from the baseplate section of the satellite. When the four separation spring, mushroom-shaped, pushoff pads are removed from the adapter, the pitch axis control assembly, complete with flywheel, is inserted and attached to the baseplate.

Attached to the flywheel hub is the sensor mirror assembly, a small 45-degree mirror (pitch mirror surface) that reflects its signal to the centerline bolometer through a hole in the large mirror. The roll mirror reflects its signal to either of the redundant roll bolometers. Each mirror uses 6061-T3 aluminum alloy as a structural base on which a pure aluminum surface finish is vacuum deposited and overcoated with silicon monoxide. Prior to the final finish, nickel electroplating and physical surfacing is performed as required.

The lower end of the roll mirror shown in Figure 4-IV-29 is a flat plate cantilever. Centrifugal force from rotation at 150 rpm will cause deflection of the mirror. Calculations show a local change in the mirror angle, from the installed flat mirror, as approximately 2 minutes of arc at the extreme tip and 1 minute of arc at 0.6 inch from the tip, a position corresponding to the centerline line of sight of roll bolometer no. 2. Even though reflections double these angles, such changes are insignificant.

6. Applicable Test Results

a. Brush Wear and Oil Leakage Rates

(1) Test Description

The motor used to drive the ITOS flywheel is the Inland model T-4411D. An Inland T-4411E motor, which is similar to this motor except that the stator winding resistance is 52 ohms compared with the T-4411D motor resistance of 32 ohms, has been subjected to continuous running for 44,000 hours (6 months) at a nominal speed of 150 rpm under thermal vacuum conditions. The test was conducted using 50/50 silver graphite brushes without adjuvants, with the motor in a labyrinth-sealed housing containing a vapor of dioctyl adipate, the lubricant to be used for ITOS. The entire subassembly was placed in a thermal vacuum chamber; the speed was controlled by a phase lock, position control loop similar to the ITOS pitch control.

The conditions prevalent for more than 90 percent of the time are listed below. For the remainder of the time, the ambient temperature and pressure varied between these and room conditions.

Ambient pressure: 3×10^{-7} to 9×10^{-7} torr

Oil vapor pressure within housing: $<10^{-5}$ torr

Housing temperature: $0^{\circ}C$

Wheel speed: 150 rpm

Motor current: 0.085 ampere (equivalent to 12 ounce-inches of torque)

(2) Brush Wear Rate

At the end of the test, each of the four brushes had traveled 46.6 million feet. Photographs showing one of the brushes before and after the test are shown in Figure 4-IV-39.

The following brush wear was measured:

Brush A (in tension)	0.53×10^{-3} inch
Brush B (in compression)	1.06×10^{-3} inch
Brush C (in tension)	0.99×10^{-3} inch
Brush D (in compression)	1.70×10^{-3} inch

Taking the worst case (brush D) and adding the three-sigma optical measurement tolerance of 0.66×10^{-3} inch gives a maximum wear rate of 0.051×10^{-3} inch per million feet of travel. For ITOS, the friction torque will be about 20 ounce-inches, for which a drive current of 0.192 ampere is required; this is about double the test current. (The armature resistance for ITOS is 32 ohms.) It is possible that future tests with the ITOS motor will show somewhat higher wear rates. For a standard brush thickness of 0.05 inch, the above maximum wear rate is equivalent to a brush half-life (at 150 rpm) of 5.4 years at 85 milliamperes.

(3) Oil Leakage Rate

By weighing the motor assembly before and after the 6-month vacuum test, it was found that the oil loss was 0.79 gram from the reservoir containing approximately 60

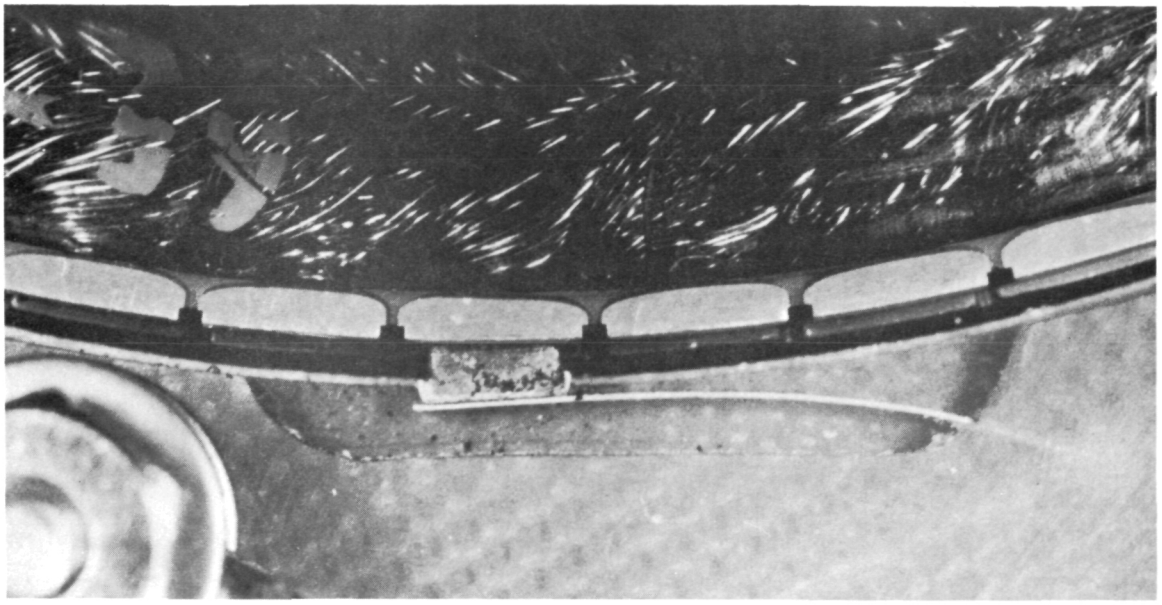

AT COMMENCEMENT OF TEST

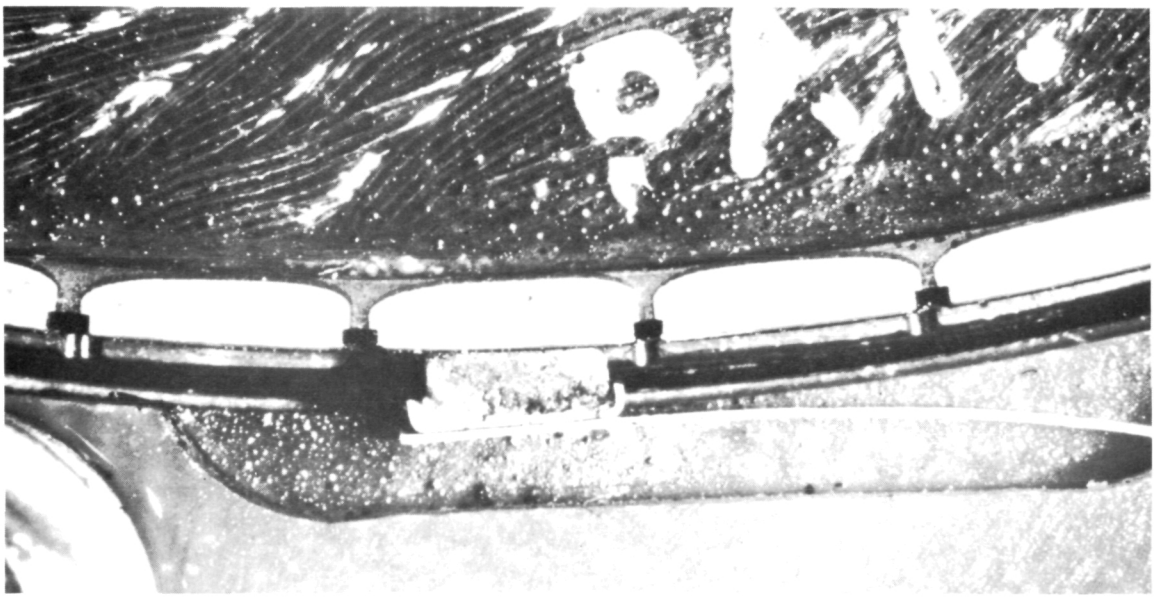

AT COMPLETION OF TEST

Figure 4-IV-39. Silver Graphite Brushes Before and After Tests

grams, compared with a predicted loss of 2.56 grams. The actual loss was less than one third of that predicted. The equation used to predict the loss was the same as that for the calculation of the ITOS loss rate. This seems to indicate that the predicted loss rate for ITOS is high. The difference between the actual and predicted losses is due to a constant in the equation which, derived from statistical evidence, scales the molecular flow loss rate to take into account a 90-degree bend in a seal. The labyrinth seal used in the test had 14 such bends, and the constant appeared in the loss rate equation raised to the 14th power. However, in order for the theoretical loss rate to be out by a factor of 3, it is only necessary for the factor to be in error by 8 percent, which is very possible.

Table 4-IV-8 summarizes data for the 6-month vacuum test and similar tests of shorter duration performed since October 1964. Although these tests were conducted for projects other than ITOS, the data is relevant since all the motors were running in labyrinth-sealed chambers containing a lubricant vapor of dioctyl adipate. The table shows that whenever measurements were taken, the brush wear and lubricant loss rates were considerably lower than the rates predicted by calculation. Also, visual examination of the commutators and brushes after all the tests showed insignificant amounts of deposit build-up.

The safe limits for brush thickness and lubricant reservoir contents for the ITOS subsystem have been devised by calculating the brush wear rates and lubricant loss.

Statistical evidence then, based on the test results, indicates that the brush thickness and oil reservoir supply will be more than adequate for an extended mission life.

b. Bearing Wear

At the completion of the 6-month continuous test, the single Fafnir model 555K bearing supporting the assembly was removed from the housing after the brush wear and lubrication loss measurements had been made. A dial gage was then used to measure the

TABLE 4-IV-8. THERMAL VACUUM TESTS SINCE OCTOBER 13, 1964 (NO COMPONENT FAILURES)

Date	Motor (Inland DC Torquer)	Brush Material	Temp. Range (°F)	Speed (rpm)	Motor Cavity Pressure Range (torr)	Current Range (ma)	Brush-Wear Rate mils/10^6ft.		Dioctyl Adipate Loss		Motor Travel	
							Measured Average	Prediction for Standard Atmosphere	Measured (grams)	Predicted by Calculation (grams)	Revs x 10^6	Feet x 10^6
10/13/64-11/16/64	2157 (640 Ohms)	Carbon	15 to 120	15	< 10^{-5} to 10^{-3}	8.5	*	0.71	*	-	0.73	0.36
11/17/64-1/26/65	2157 (640 Ohms)	Carbon	43 to 75	150	< 10^{-5} to 10^{-3}	8.5	*	0.71	*	-	10.5	5.2
11/9/65 - 12/23/65	2157E	Carbon	14 to 120	150	< 10^{-5} to 2×10^{-4}	70	*	0.10	0.9	2.1	9.1	4.5
2/7/66-2/23/66	4411E	Carbon	13 to 122	150	< 10^{-5} to 2.5×10^{-3}	65 to 150	0.22	0.86	0.75	3.3	3.5	4.0
2/24/66-3/24/66	4411E	50/50 Silver-Graphite	12 to 122	150	< 10^{-5} to 3.7×10^{-3}	64 to 130	0.127	0.406	2.5	4.8	6.1	6.9
4/4/66 - 10/5/66	4411E	50/50 Silver-Graphite	32 to 70	152	< 10^{-5} to 2.4×10^{-3}	60 to 90 (Trans. to 250)	0.023	0.35	0.79	2.56	40.5	46.6
										Total	70.4	67.6

* Data not available.

Total Time: 373 days

Note: Ambient pressures maintained in chamber are temperature dependent.

bearing self-aligning angle and total radial play. The figures derived compared with the manufacturer's specifications and are as follows:

	Self-Aligning Angle (degree)	Radial Play (inch)
Measurements After 6-Month Test	±0.0745	0.0005
Manufacturer's Specification	±0.06 to 0.08	0.00065 to 0.00092

These figures supported by microscopic inspection of the unit led to the conclusion that no visible wear had occurred on the bearing.

G. ACCURACY ANALYSIS

1. General

The attitude of ITOS is defined with respect to the rotating coordinates $\hat{n}$ (orbit normal) and $\hat{r}$ (local vertical), as shown in Figure 4-IV-40. The discussion on measurement and control accuracy which follows is based on the availability of accurate ephemeris data to define the motion of these coordinates.

The attitude performance specification requires ±1.0 degree uncertainty in the body axes position with respect to the orbit normal and local vertical at any instant. Since leading edge triggering of the pitch axis control loop is required, it is clear that orbit variations due to eccentricities cannot be removed without a priori knowledge. The worst-case variation of the earth's included angle for an orbit eccentricity of 0.01 would result in an apparent shift of 0.9 degree in local vertical. Therefore, all reference to the pitch error, Θ, will be to the nominal local vertical as defined by the nominal circular orbit geometry. It is further assumed that no attempt will be made to track the motion of the true local vertical with respect to that defined by the nominal geometry for any elliptical orbit within the specified tolerances. However, a small constant offset, resulting from a fixed altitude error can be removed by changing the nominal system momentum. An offset resulting from orbit parameter deviations is not included in any discussion dealing with attitude errors.

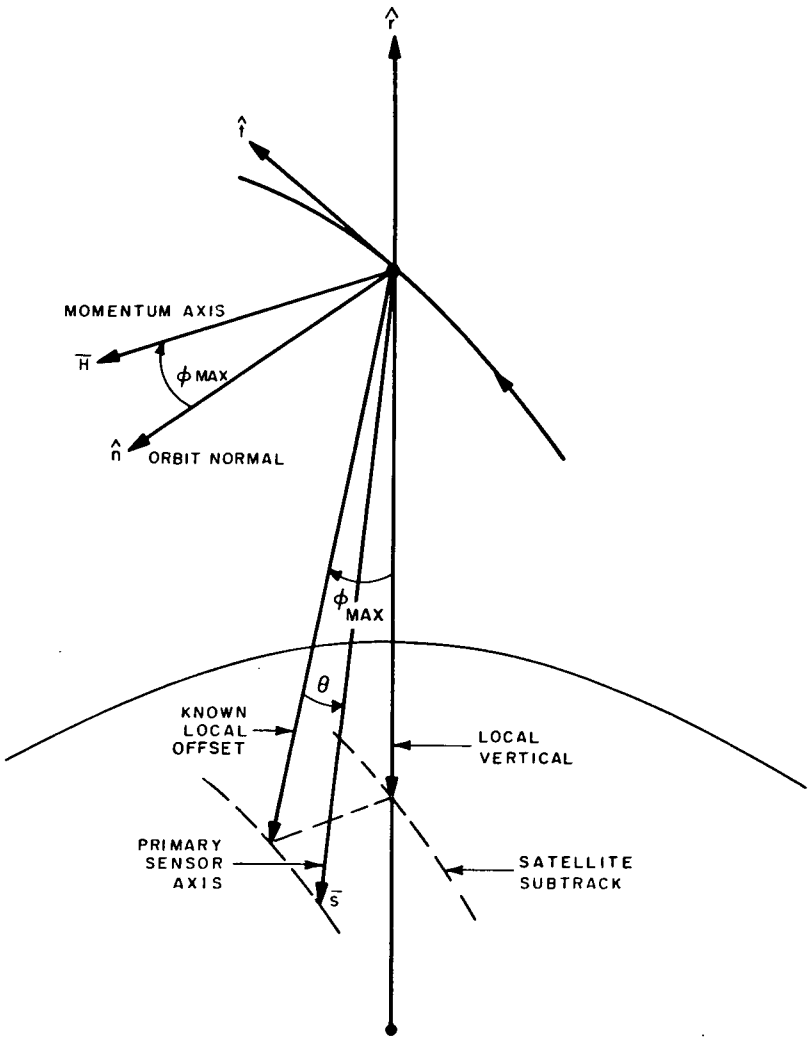

Figure 4-IV-40. Spacecraft Reference Coordinates

2. Pointing

The attitude deviations to be considered are as follows:

ϕ_{max} is the angle between the spacecraft momentum vector, $\overline{H}$, and the orbit normal, $\hat{n}$; also called maximum roll angle.

Θ is the angle between the primary sensor axis and the known local offset, also called pitch error.

Θ_1, ϕ_1 is the misalignment between the pitch axis horizon sensor optical line of sight and the flywheel spin axis.

Θ_2, ϕ_2 is the misalignment between the roll axis horizon sensor optical line of sight and the flywheel spin axis.

Θ_3, ϕ_3 is the misalignment between the pitch mirror normal and the flywheel spin axis.

Θ_4, ϕ_4 is the misalignment between the roll mirror normal and the flywheel spin axis.

Θ_5, ϕ_5 is the misalignment between the mounting surface of the pitch axis horizon sensor and the flywheel spin axis.

Θ_6, ϕ_6 is the misalignment between the flywheel spin axis and the angular momentum axis due to tape recorder operation (or other transverse momentum devices).

Θ_7, ϕ_7 is the misalignment between the flywheel spin axis and the angular momentum axis due to the principal moment of inertia misalignment.

Θ_8, ϕ_8 is the misalignment between the flywheel spin axis and the angular momentum axis due to flywheel unbalance.

Θ_9, ϕ_9 is the misalignment between the flywheel spin axis and the nominal pitch axis due to bearing free motion.

Θ_{10}, ϕ_{10} is the measurement error in determining the alignment of the spin axis with respect to the local horizontal plane due to:

a. Radiance changes,
b. Noise,
c. Horizon gradient variations, or
d. Ground data processing.

Θ_{11}, ϕ_{11} is the measurement error in determining the line of sight between the satellite and the sky-earth intercept with respect to:

a. Radiance changes,
b. Noise,
c. Horizon gradient variations,
d. Threshold level variations, or
e. Sensor gain changes.

Θ_{12}, ϕ_{12} is the measurement error introduced by the pitch axis servo loop with respect to:

a. Bias speed drift,
b. Torque load changes,
c. Momentum changes, or
d. Gain changes.

Θ_{13}, ϕ_{13} is the cyclic deviation between the orbit normal and the angular momentum vector due to:

a. Residual magnetic dipole changes,
b. Solar torque variations, or
c. Gravity gradient effects.

The tolerances assigned to the deviations with subscripts 1, 3, 4, and 5 are based on static measurements using a variety of surface plates, theodolites, and shims. The basis for the deviation with subscript 2 is the sensor profile in terms of the half-power points, as

referenced to the mechanical horizon sensor alignment; the horizon sensors are adjusted using shims.

Angular deviations designated by subscripts 6 and 7 relate to the amount of uncompensated momentum of the various tape recorders in combination with the intended duty cycle pertaining to AVCS and SR equipment and to other momentum deviations.

Angular deviations identified with subscript 8 can be determined from the equation for the angular shift between the flywheel spin axis and the nominal pitch axis due to mass unbalance in the flywheel, as follows:

$$\phi_8 = \frac{\rho}{\left[Z \left(\frac{I_T - I_{fT}}{mZ^2} \right)^2 + 1 \right]^{1/2}} .$$

The unknowns are derived from Figure 4-IV-41. A 0.003-inch distance from the flywheel center of mass to the flywheel spin axis results in a half-cone angle of 1.3×10^{-4} degrees for a 16-inch offset from the center of mass of the spacecraft to the center of rotation of the flywheel. Such a balance is readily obtainable for the 15-pound wheel to be utilized.

The torque motor bearing has an angular misalignment of 0.023 degree, resulting in the applicable coning angle pertaining to subscript 9.

As a result of cross-coupling between roll and pitch axes (when using the roll horizon sensors in the backup mode for pitch measurement), deviations with subscripts 2, 6, 7, 8, and 9 result in pitch tolerances as indicated in Tables 4-IV-9 through 4-IV-12.

The tolerances pertaining to subscript 10 are defined by the instantaneous roll random tolerance as 0.507 degree; this value can readily be reduced by short-term averaging (4 seconds, i.e., 10 samples) to 0.160 degree.

The instantaneous pitch measurement capability is related to the 10:1 ratio of threshold to zero-to-peak noise and is a function of earth radiance changes and other pertinent parameters associated with subscript 11. Using the backup horizon sensor results in a somewhat

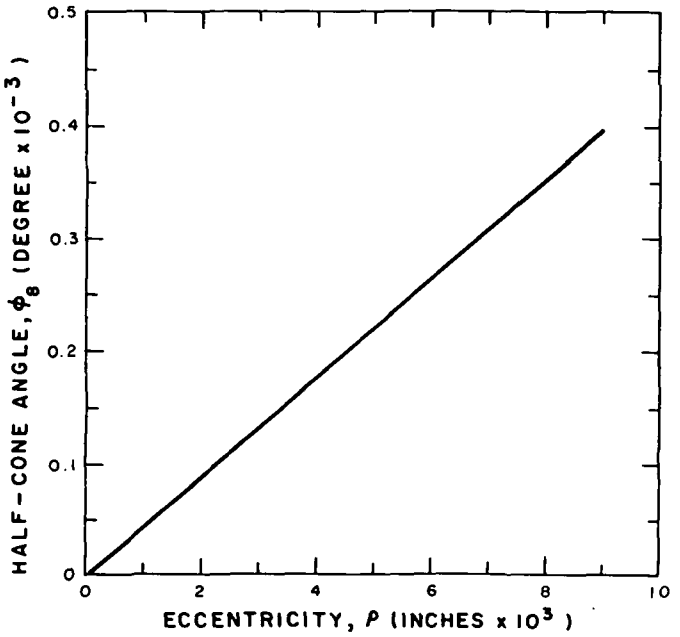

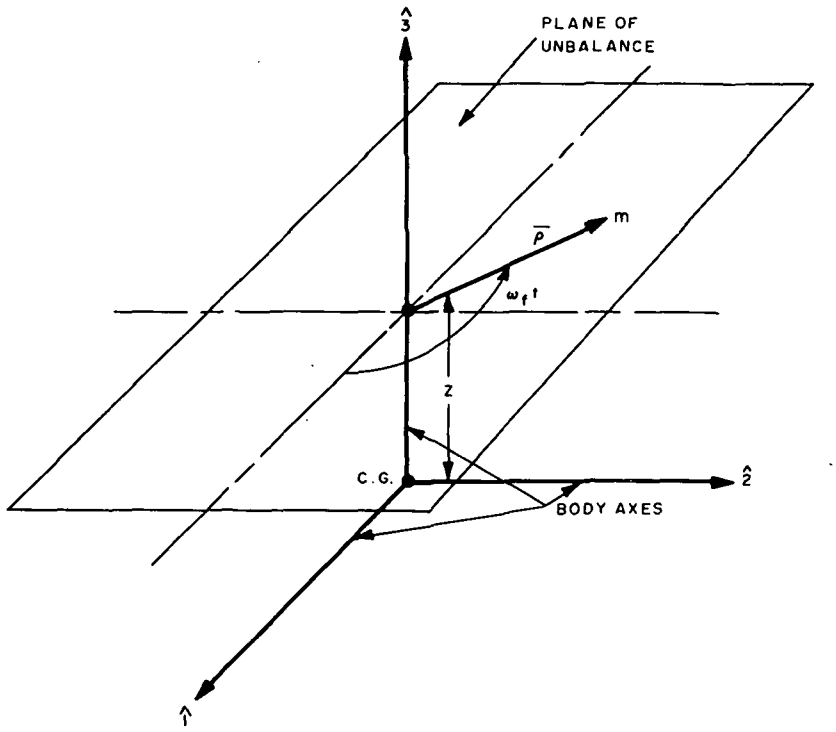

Figure 4-IV-41. Half-Cone Nutation Due to Flywheel Unbalance

increased pitch tolerance due to the effects of the altered grazing angles. In either case, noise effects are not included since the pitch axis servo loop will nullify this effect by inherent filtering action.

Attitude deviations designated by subscript 12 represent the pitch offset due to changes in servo gains and bias drifts primarily induced by thermal effects. Although these shifts can be corrected with an adjustment in momentum, these tolerances are included for the sake of completeness.

As indicated in the disturbance analysis summary (Appendix C), attitude deviations can be anticipated due to residual dipoles, solar torques, gravity gradient torques, and momentum offsets (e.g., eddy current losses and hysteresis losses). These tolerances are considered for variations represented by subscript 13.

The attitude deviations are summarized in Tables 4-IV-9 through 4-IV-12. As indicated in Tables 4-IV-10, some of the tolerances cause a random scatter for roll (ϕ) determination, during a nominal 10-minute measurement pass; other deviations have a definite biasing effect on the roll angle. The largest contribution to the random uncertainty in nominal roll measurement results from the horizon sensor tolerances; averaging 10 samples (4 seconds of data) for each measurement point will naturally reduce this random scatter. The 3σ random roll tolerance due to all causes listed in Table 4-IV-9 results in a maximum roll attitude uncertainty by least square fit as stipulated in Appendix B. The principal-point maximum roll error is a function of this least square fit uncertainty and a number of other factors as shown in Table 4-IV-11. Random factors due to various coning motions, primary sensor mounting uncertainties, and a maximum roll least square scatter are combined by root-sum-square (rss).

Unless precessional motion due to the residual spin axis uncompensated magnetic dipole and the solar torque is rectified by calibration, this motion must be included in the attitude uncertainty. Precession motion that causes roll errors due to solar torque is essentially about the line of nodes ($\pm\hat{\ell}$), and precession due to residual magnetism is about a line in the orbit plane perpendicular to the nodes ($\pm\hat{b}$). Table 4-IV-11 combines these two drifts vectorially. The use of proportional QOMAC would result in a much smaller ripple, as

TABLE 4-IV-9. RANDOM ROLL ERROR CONTRIBUTIONS*

Description (best slope fit)	Roll Error (degrees)	
	Single Sample	10 Samples (4-second average)
Flywheel Unbalance	0.0015	0.0006
Bearing Free Motion	0.028	0.009
Roll Horizon Sensor (noise and ground data processing)	0.507	0.160
Tape Recorder (transverse) Momentum (worst-case)	0.140	0.140
3σ Tolerance	0.526	0.212

*High frequency with respect to 10 minutes of roll determination.

TABLE 4-IV-10. BIAS ROLL ERROR CONTRIBUTIONS*

Description (best slope fit)	Roll Error (degrees)
Roll Sensor Misalignment	0.0784
Roll Mirror Misalignment	0.157
Principal Moment of Inertia Misalignment	0.0104
Roll Horizon Sensor Variation (IR horizon, earth radius)	0.192
3σ Tolerance	0.26

*During 10 minutes of roll determination.

TABLE 4-IV-11. PRINCIPAL-POINT MAXIMUM ROLL-ERROR CONTRIBUTIONS

Item No.	Description	Maximum Roll Error (degrees)	
1	Least square fit of 10 minutes of random data, maximum error for single sample	0.663	(0.267)*
2	Primary sensor mounting surface misalignment	0.100	
3	Tape recorder (transverse) momentum	0.140	
4	Principal moment of inertia misalignment	0.0104	
5	Flywheel unbalance	0.002	
6	Cyclic solar torque	0.024	
7	Gravity gradient torque	0.043	
8	Roll/yaw residual dipole (1 atm^2 transverse)	0.037	
9	3σ rss (Items 1 to 8)	0.69	(0.318)*
10	Residual magnetic dipole (attitude in four orbits) 0.1 atm^2	0.060	
11	Solar torque Three standard QOMAC cycles per day	0.280	(0.060)**
12	Vector addition of items 10 and 11	0.286	(0.085)**
13	Bias roll error	0.260	
	Maximum roll error (Items 9, 12, and 13)		
	Maximum principle point error		
	Single sample:		
	Standard QOMAC	1.24	
	Proportional QOMAC	1.04	
	10 averaged samples:		
	Standard QOMAC	0.86	
	Proportional QOMAC	0.66	

*Maximum error for 10 averaged samples.
**Proportional QOMAC.

TABLE 4-IV-12. PITCH-ERROR CONTRIBUTIONS

Description	Pitch Error (degrees)	
	Pitch Sensor	Backup Sensor (roll sensor)
Roll Sensor Misalignment	-	0.118
Pitch Index Pulse Alignment Uncertainty	0.100	-
Roll Index Pulse Alignment Uncertainty	-	0.247
Principal Moment of Inertia Misalignment	Negligible	0.0156
Maximum Roll Error (10 samples):		
Three Standard QOMAC Cycles per Day	-	1.14
Proportional QOMAC	-	0.99
Pitch Horizon Sensor Variation (10:1 Threshold-to-noise ratio)	0.56	0.611
Pitch Axis Servo Loop Tolerances	0.182	0.182
Residual Magnetic Dipole Variation (attitude)	Negligible	0.0555
Residual Magnetic Dipole Variation (momentum)	0.012	0.012
Solar Torque:		
Three Standard QOMAC Cycles Per Day	Negligible	0.420
Proportional QOMAC	Negligible	0.0908
Gravity Gradient Torque	Negligible	0.0645
Hysteresis and Eddy Current Decay (1-percent momentum offset)	0.045	0.045
3σ Principal Point Error:		
Standard QOMAC	0.60	1.4
Proportional QOMAC	0.60	1.2

discussed in paragraph 4-IV-E-5. Adding the rss scatter, the precessional drifts, and the biasing effect on the roll angle will result in the maximum principal point roll deviation, as shown in Table 4-IV-11.

The principal point tolerance due to pitch attitude uncertainties is shown in Table 4-IV-12. Utilizing the roll sensors as backup for pitch determination deteriorates the pitch error because of static cross-coupling effects between the pitch and roll axes. Noise has no influence on the accuracy of pitch control because the servo bandwidth shows a crossover of only 0.15 radian per second.

Sensor pointing offsets due to elliptical orbits are analyzed in Appendix G, which also covers the effects of elliptical orbits on attitude and momentum performance.

In summary, the tabulations show that the principal point uncertainty about the roll or yaw axis is ±0.66 degree with proportional QOMAC and 10-sample averaging, whereas the primary pitch axis horizon sensor assures a tolerance about the pitch axis of ±0.60 degree. This is compatible with the specification requirements.

3. Jitter

Jitter about the pitch axis is estimated to be less than 0.003 degree per second. The sources from which this value was computed are described in the following paragraphs.

Motor commutator ripple (W_{P1}):

$$W_{P1} = \frac{T_{d1}}{I_3 \omega_{d1}} = 0.405 \times 10^{-5} \text{ degree per second}$$

where:

T_{d1} is the torque disturbance (1 ounce-inch),

I_3 is the body moment of inertia in the pitch axis (800 pound-inch-second^2), and

ω_{d1} is the ripple torque disturbance frequency (1115 radians per second at 150-rpm motor speed).

Motor "once around" torque (W_{p2}):

$$W_{p2} = \frac{T_{d2}}{I_3 \omega_{d2}} = 0.291 \times 10^{-3} \text{ degree per second}$$

where:

T_{d2} is the torque disturbance (1 ounce-inch), and

ω_{d2} is the torque disturbance frequency (15.7 radians per second at 150-rpm motor speed).

Tachometer ripple (W_{pt}):

$$W_{pt} = \frac{E_f K_a K_t}{I_3 \omega_{dt}\left[\left(\frac{L_a}{R_a}\ \omega_{dt}\right)^2 + 1\right]^{1/2}} = 0.136 \times 10^{-5} \text{ degree per second}$$

where:

E_f is the tachometer ripple voltage (±0.12 volt),

K_a is the power amplifier gain (82 volts per volt),

K_t is the motor torque constant (3.27 ounce-inches per volt),

L_a is the motor inductance (19.6×10^{-3} henry),

R_a is the motor winding resistance (32.1 ohms), and

ω_{dt} is the disturbance frequency (4020 radians per second at 150 rpm).

PWM error detector ripple (W_{pD}):

$$W_{pD} = \frac{2 \pi K_v \tau_1 t_o^2}{\tau_s \tau_m \tau_2} = 2.9 \times 10^{-5} \text{ degree per second}$$

where:

K_v is the system velocity gain (4),

τ_1 is the compensation lead time constant (16.7 seconds),

τ_2 is the compensation lag time constant (417 seconds),

τ_s is the smoothing time constant (0.8 second),

τ_m is the motor loop time constant (3 seconds), and

t_o is the pulse width (1.1×10^{-3} second for a one position error at 150 rpm).

Orbit ellipticity (W_{pe}):

$$W_{pe} = \frac{\epsilon R_e}{R_o^2 - R_e^2} \qquad \omega_o = 1.12 \times 10^{-3} \text{ degree per second}$$

where:

R_e is the earth's radius (3444 nautical miles),

R_o is the nominal circular orbit radius (4194 nautical miles),

ω_o is the nominal orbital rate (9.23×10^{-4} radian per second), and

ϵ is the orbit ellipticity (0.0147; 3σ limit for ESSA).

Deadband oscillations (W_{pd})

Jitter due to deadband oscillations produces a system resolution of 0.002 degree with state-of-the-art components as follows:

$$W_{pd} = A\omega_n = 0.32 \times 10^{-3} \text{ degree per second}$$

where:

A is the system resolution (2×10^{-3} degree) and

ω_n is the system natural frequency (0.16 radian per second).

Radiance variations (W_{pr})

Jitter due to radiance variations will be associated with the sensor error on any three sucessive sky-earth pulses with a tolerance of +0.2 to -0.2 degree in the worst-case. This can be expressed as:

$$W_{pr} = \Delta\Theta \frac{2\pi}{2TG\left(\frac{1}{2T}\right)} = 0.506 \times 10^{-3} \text{ degree per second}$$

Where:

T is the sampling period (0.4 second),

$\Delta\Theta$ is the angular error (0.2 degree), and

$G\left(\frac{1}{2T}\right)$ is the pitch servo gain at the half-sampling frequency (1/3100).

Bias speed variation (W_{ps})

The bias speed will change due to varying temperature effects on the reference voltage. For a 1°C change in temperature, a 0.1-percent change in bias voltage is anticipated as a tolerance. For a maximum linear temperature change of 5°C per quarter orbit, the speed change for this period will be 0.5 percent. In terms of change in body rate, this results in

$$\Delta W_3 \approx \frac{\Delta W_f}{I_3/I_f} = 0.072 \text{ degree per second}$$

where:

ΔW_3 is the equivalent change in body rate,

I_f is the flywheel moment of inertia (12.75 pound-inch-seconds^2), and

ΔW_f is the equivalent change in flywheel spin rate.

To reduce this change in body rate to zero, the pitch position error will be

$$\Delta\Theta = \frac{\Delta W_3}{K_v} = 0.018 \text{ degree.}$$

For 1700 seconds per quarter orbit, the resulting jitter is

$$W_{ps} = \frac{0.018 \text{ degrees}}{1700 \text{ seconds}} = 1.06 \times 10^{-5} \text{ degree per second.}$$

Jitter about the roll axis for a free body rotation of the satellite without disturbance can be assumed to be zero under the action of the liquid-filled nutation damper. However, there are two sources of internal disturbances that produce undesired motion about the spacecraft roll and yaw axes, namely, the tape recorders and the flywheel.

As shown in the discussion on disturbances (Appendix C), maximum coning due to tape recorder operation can reach a maximum half angle of 0.140 degree. The jitter is

$$W_{T_t} = 0.140\ \dot{\Psi} = 0.035 \text{ degree per second,}$$

where $\dot{\Psi}$ is the nutation frequency (0.25 radian per second).

Similarly, flywheel unbalance results in a half-cone angle of 1.3×10^{-4} degree. Jitter due to this can be expressed as:

$$W_{T_f} = 1.3 \times 10^{-4}\ \omega_f = 2 \times 10^{-3} \text{ degree per second,}$$

where ω_f is the flywheel spin rate (150 rpm).

The 3σ roll jitter is 0.035 degree per second which is an rss value for the above two jitter rates as uncorrelated values.

H. SYSTEMS INTERFACES

1. Power

The power for this subsystem will be supplied at -26 to -36 volts unregulated and -24.5 volts regulated from the spacecraft power supply. Other voltages used in the pitch axis control loop will be derived in a DC-to-DC converter operating from the -24.5-volt supply. Table 4-IV-13 gives the power requirements during the initial orientation maneuver or during recovery from a large transient; Table 4-IV-14 gives the power requirements for the operational mode once the initial orientation is completed.

2. Command and Control

All required switching will be routed through the ITOS command distribution unit (CDU). The required commands and their functions are given in Section 4-VIII.

3. Telemetry

All telemetry data will be routed to the ITOS signal conditioner. All points in the pitch axis control loop will be conditioned to assure compatibility with the spacecraft telemetry subsystem voltage and impedance requirements. The required telemetry points are given in Section 4-IX.

TABLE 4-IV-13. INITIAL ORIENTATION MANEUVER

Item	Power at -24.5 Volts	Operation Time	Watt-Minutes
High Torque Mode, QOMAC and MBC Coils	4.95 watts	10 orbits max - 1136 minutes	5610
Low Torque Mode, QOMAC Coil	0.75 watts	1 orbit - 113.6 minutes	85
Momentum Coil	3.6 watts	2 to 3 orbits - partial 45 minutes	162
Pitch Axis Control Loop*	22.3 watts peak	5 minutes, max	111.5
	8.4 watts	10 orbits - 1136 minutes	9450
Total		10 orbits, max	15,418.5
*Power from both regulated (-24.5 volts) and unregulated (-26 volts) supplies.			

TABLE 4-IV-14. OPERATIONAL POWER REQUIREMENTS

Item	Power at -24.5 Volts	Operation Time	Equivalent Continuous Drain
Pitch Axis Control Loop*	8.4 watts	Continuous	8.4 watts
Magnetic Bias Coil	0.027 to 0.238 watts	Continuous	0.027 to 0.238 watt
Momentum Coil	1.8 watts per coil	**	**
QOMAC Coil	0.75 watts	1/5 orbit/orbit (23 minutes)	0.15 watt
Total (Continuous maximum)			8.79 watts
*Power from both regulated (-24.5 volts) and unregulated (-26 volts) supplies. **As required for adjustment.			

SECTION V

POWER SUPPLY SUBSYSTEM*

A. INTRODUCTION

The ITOS power supply subsystem is a solar cell rechargeable battery subsystem which delivers a regulated output of -24.5 volts ±1 percent and an unregulated output of -26 to -36 volts. The output voltages are maintained within their limits when, in addition to the steady-state loads, the subsystem is subjected to 10-ampere transient loads of less than 1-millisecond duration with rise and fall times of no less than 200 microseconds.

The spacecraft loads for one orbit are listed in Table 4-V-1. Command loads are not included as part of the design load, since they do not occur regularly during each orbit and since they have a negligible effect over a long-term average period.

The values given in Table 4-V-1 represent, in general, the upper specification limits for the loads. The significant loading on each orbit represents the following spacecraft operation:

- Scanning radiometer data recorded and transmitted during earth night.
- Eleven AVCS pictures taken and recorded during earth day.
- Eleven APT pictures taken and transmitted during earth day.
- An 8-minute readout of AVCS and radiometer picture information and secondary sensor data via the S-band transmission link.

For design purposes, the definition of the operational load as it applies to establishing the criteria for end-of-life conditions excludes the beacon and dual subcarrier oscillator loads. The beacons and the digital telemetry system may be turned off during the operational life of the satellite if signals indicate that the array output is not sufficient to permit recharging of the batteries.

*Refer to Summary of Current Design Revisions Not Covered in this Report, following the Preface, for a brief description of revisions made since the cut-off date for this report.

TABLE 4-V-1. POWER SUPPLY SUBSYSTEM LOADS FOR ONE ORBIT

Equipment	Note	Night (ma)	Day (ma)	AVCS Pictures (ma)	Readout (ma)	Comment
Magnetic Bias Switch		6	6	6	6	
QOMAC		30	30			11.5 minutes each time
Momentum Wheel Assembly	1	196	196	196	196	
Pitch Control Electronics		131	131	131	131	
Roll or Pitch Sensors		12	12	12	12	
Dual SCO		24	24	24	24	Assumed off at end of life (6 months)
Beacon Transmitter		85	85	85	85	
Commutated TLM Signal Conditioner					200	On for 24 seconds
S-Band Transmitter	1				2000	On for 8 minutes
Multiplexer					60	
Real Time Transmitter		735	735	735	735	
Dual Command Receiver						36 at -23v; load included in decoder load
Dual Programmer		90	90	90	90	
Dual Time Base Unit		75	75	75	75	
Dual Decoder	1	140	140	140	225	
Data Format Converter		87	87	87	182	182 for 1 minute
APT Camera	2		735	735/ 940		940 for 8 seconds after each AVCS picture
AVCS Camera	2	4	110	400	4	

TABLE 4-V-1. POWER SUPPLY SUBSYSTEM LOADS FOR ONE ORBIT (Continued)

Equipment	Note	Night (ma)	Day (ma)	AVCS Pictures (ma)	Readout (ma)	Comment
AVCS Recorder		15	15	670	565	Readout load on for 2 minutes; 670 for 10.25 seconds per picture
SR Processor		60			60	
Scanning Radiometer	1	20	20	20	20	
Scanning Radiometer		430	280	280	430	On for 8 minutes
Scanning Radiometer Recorder		545	30	30	585	
Solar Proton Monitor		61	61	61	61	
Incremental Tape Recorder		94	94	94	94/ 150	150 for 1 minute
Flat Plate Radiometer		40	40	40	40	
TOTALS	3	2850	2966	Note 5	Note 5	
	4	2880	2966			

Notes:
1. Power is supplied from the unregulated bus (-26 to -36 volts).
2. The shutter pulse load is on the shutter bus.
3. Without QOMAC loads.
4. With QOMAC loads.
5. See Figure 4-V-1.

Figure 4-V-1 shows the ITOS load profile, constructed from the data in Table 4-V-1. The upper curve represents the total load; the lower curve represents the load on the unregulated bus. The load on the regulated bus, not shown separately in Figure 4-V-1, is the difference between the two curves shown. The load profile is being continuously updated to reflect the latest load requirements. In certain cases, the precise power-time relationship is difficult to define. However, any future revision of the load requirements is expected to be of a minor nature and is not expected to affect the capability of the power subsystem to support the mission even under worst-case conditions.

ECLIPSE	
SUN ANGLE (DEGREES)	DURATION (MIN)
30	0
45	22
60	31

NOTE
TOP CURVE = TOTAL LOAD
BOTTOM CURVE = UNREGULATE BUS LOAD

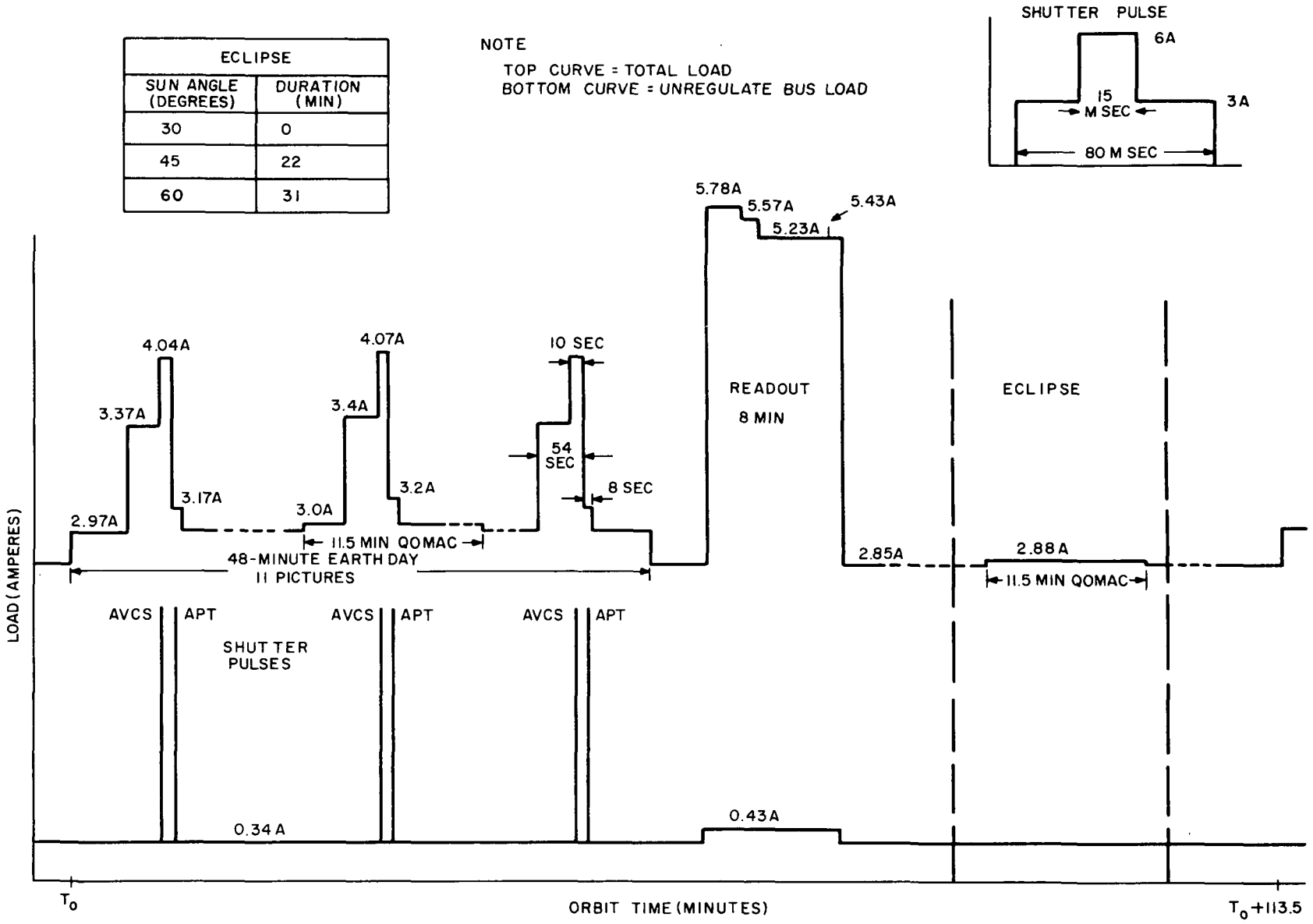

Figure 4-V-1. Power Supply Subsystem, Load Profile

The subsystem power drain is not included in the operational load since it is a function of solar array output and satellite eclipse conditions. The subsystem losses that are relatively independent of orbital conditions are listed in Table 4-V-2. The figures presented are typical values since the losses vary with spacecraft load.

TABLE 4-V-2. POWER SUPPLY SUBSYSTEM LOSSES

Description	During Satellite Eclipse (ma)	During Satellite Day (ma)
Series Voltage Regulator	0.140	0.160
Charge Controllers	0.003	0.072
Shunt Limiter Control Amplifiers	0.0	0.40
Telemetry	0.096	0.096

Analog telemetry will be interrogated as required, and the average load will be considered zero. The digital telemetry will be assumed to have a duty cycle of 1/6, resulting in an average current of 0.016 ampere, and the shunt loss totals will be 0.159 ampere (night) and 0.288 ampere (day).

The subsystem loads during the preoperational mode (launch through solar array deployment, which occurs at the end of the initial orientation maneuver) are listed in Table 4-V-3. This phase of the mission is expected to last less than 24 hours. Until the panels are deployed, the batteries (and the solar array at reduced power levels) support the preoperational loads.

Since the power supply subsystem is designed on a worst-case basis, it will normally be able to support a greater load than anticipated.

TABLE 4-V-3. POWER SUPPLY SUBSYSTEM LOADS DURING PREOPERATIONAL MODE

Equipment	Load (ma)
MBS*	170
QOMAC*	30
Momentum Coil*	75
Momentum Wheel Assembly**	196
Pitch Control Electronics	131
Roll or Pitch Sensors	12
Dual Subcarrier Oscillator	24
Digital Solar Aspect Indicator or Acquisition Sensor	24
Beacon Transmitter	85
Dual Time Base Unit	75
Dual Decoder (including command receiver) **	140
Scanning Radiometer**	20
Scanning Radiometer	280
TOTAL	1187

*Only two of the three coils will be operating during the acquisition phase; the maximum current for the operating coils is 200 milliamperes.

**Power is supplied by the unregulated bus (-26 to -36 volts).

B. FUNCTIONAL DESCRIPTION

1. General

A block diagram of the ITOS power supply subsystem is shown in Figure 4-V-2. The power supply subsystem consists of a solar array, a shunt limiter, batteries, charge controllers, and series voltage regulators. The solar array converts incident energy from the sun to electrical energy. The shunt limiter prevents the array bus voltage from exceeding prescribed limits by shunting array current which is not needed to recharge the batteries and supply the spacecraft load. The shunt limiter consists of three shunt dissipators, mounted on the solar panels, and two control amplifiers, located in the power supply electronics. The batteries supply power to the spacecraft during eclipse periods and also supply peak loads during satellite day. The charge controllers provide protection for the batteries by limiting charge currents to proper levels during charge and overcharge periods. The redundant series voltage regulators maintain the regulated bus within limits during variations in load current and input voltage. Only one regulator at a time can be connected into the system; the regulators are selected by ground command.

Certain loads are powered from the unregulated bus, as noted in Table 4-V-1. The shutter buses and the two squib load buses (one from each battery) are powered directly from the batteries with special buses. An enable plug is provided to enable external battery charging through the external power input with all loads disconnected. When the plug is removed, all load power is interrupted.

A ground plate next to the power supply electronics unit is the main spacecraft grounding point. Subsidiary ground plates are provided on the APT and the AVCS equipment panels, connected to the main ground plate by cables. The main ground plate is the only point on the spacecraft which is electrically connected to the spacecraft frame.

The operation of the ITOS power supply subsystem is similar to the TOS subsystem, except that the ITOS solar panels are deployed and the voltage in the battery charge controllers is limited. Table 4-V-4 presents a summary of the design features of this subsystem.

TABLE 4-V-4. SUMMARY OF ITOS POWER SUPPLY SUBSYSTEM PARAMETERS

Parameter	Value
POWER SUPPLY ELECTRONICS	
Units per spacecraft	1
Minimum input voltage to battery	-26.5 volts
Maximum array current capability (with external shunt dissipators connected, 1-ampere regulated load, and two batteries connected)	12 amperes
Regulated bus output with maximum steady-state 6-ampere load	-24.5 volts ±1 percent
Unregulated output voltage	-26 to -36 volts
Regulated bus output with a 10-ampere transient load, less than 1 millisecond in duration, and rise and fall time no less than 200 microseconds, in addition to steady-state load	-24.5 volts ±1 percent
Charge current limit to each battery	0.95 ± 0.08 ampere
Maximum battery voltage limit at battery temperature:	
10°C	32.94 volts
25°C	31.79 volts
Battery trickle charge by ground command	0.15 ±0.05 ampere per battery
Weight	11.2 pounds (max)
SOLAR ARRAY	
Panels per spacecraft	3
Dimensions, each of three identical panels	63.8 by 36.38 inches

TABLE 4-V-4. SUMMARY OF ITOS POWER SUPPLY SUBSYSTEM PARAMETERS (Continued)

Parameter	Value
SOLAR ARRAY (Continued)	
Panel shape	Curved
Solar cell area	2 by 2 cm each
Base resistivity	1 to 2 ohm-cm
Cover glass thickness (microsheet)	0.006 inch
Air-mass-zero efficiency (with cover glass)	9.8 to 10.1 percent
Short-circuit current (I_{sc})	124.42 ma at 27°C (9.8 percent)
Open-circuit voltage (V_{oc})	0.58 volt at 27°C
Maximum-power-point current (I_{mp})	113.02 ma at 27°C (9.8 percent)
Maximum-power-point voltage (V_{mp})	0.46 volt at 27°C
Circuits per panel	5
Strings per circuit	9 (equal to 9 parallel cells)
Strings per panel	45
Strings per array	135
Series cells per string	76
Array diode type	JAN IN1206
Radiation degradation factors (6 months):	
Voltage	0.920
Current	0.821
Panel weight (with shunt dissipator)	19.4 pounds (max)
Array weight	58.2 pounds (max)
BATTERY (NICKEL-CADMIUM)	
Batteries per spacecraft	2
Cells per battery	22 in series

TABLE 4-V-4. SUMMARY OF ITOS POWER SUPPLY SUBSYSTEM PARAMETERS (Continued)

Parameter	Value
BATTERY (NICKEL-CADMIUM) (Continued)	
Storage capacity	4 ampere-hours per cell
Weight	15.0 pounds each (max)
Charge control method	Taper charging with voltage and temperature control
Operating temperature	10 to 35°C
Charge rate	0.95 ±0.08 ampere per battery (normal maximum), taper charge rate determined by battery voltage and temperature
Maximum depth of discharge	18.8 percent (readout during day at 60-degree sun angle)

2. Solar Array

The solar array is mounted on three curved panels, each hinged to a side of the spacecraft at the edge near the thermal fence. Prior to deployment, the panels are held against the sides of the spacecraft. After the initial orientation, the panels are deployed so that they are perpendicular to the spacecraft sides. Each panel is approximately 37 inches wide, measured along the hinge line, and 64 inches long. The solar array for ITOS is unlike the arrays on the TOS and TIROS spacecraft, which used a cylindrical hat structure with solar cells mounted on the top and sides. On ITOS, 2- by 2-cm cells are used instead of the 1- by 2-cm cells used on the TOS and TIROS spacecraft, and the ITOS cells are bonded directly to an aluminum honeycomb structure rather than to printed circuit module boards mounted on aluminum structural members as on the TOS and TIROS spacecraft.

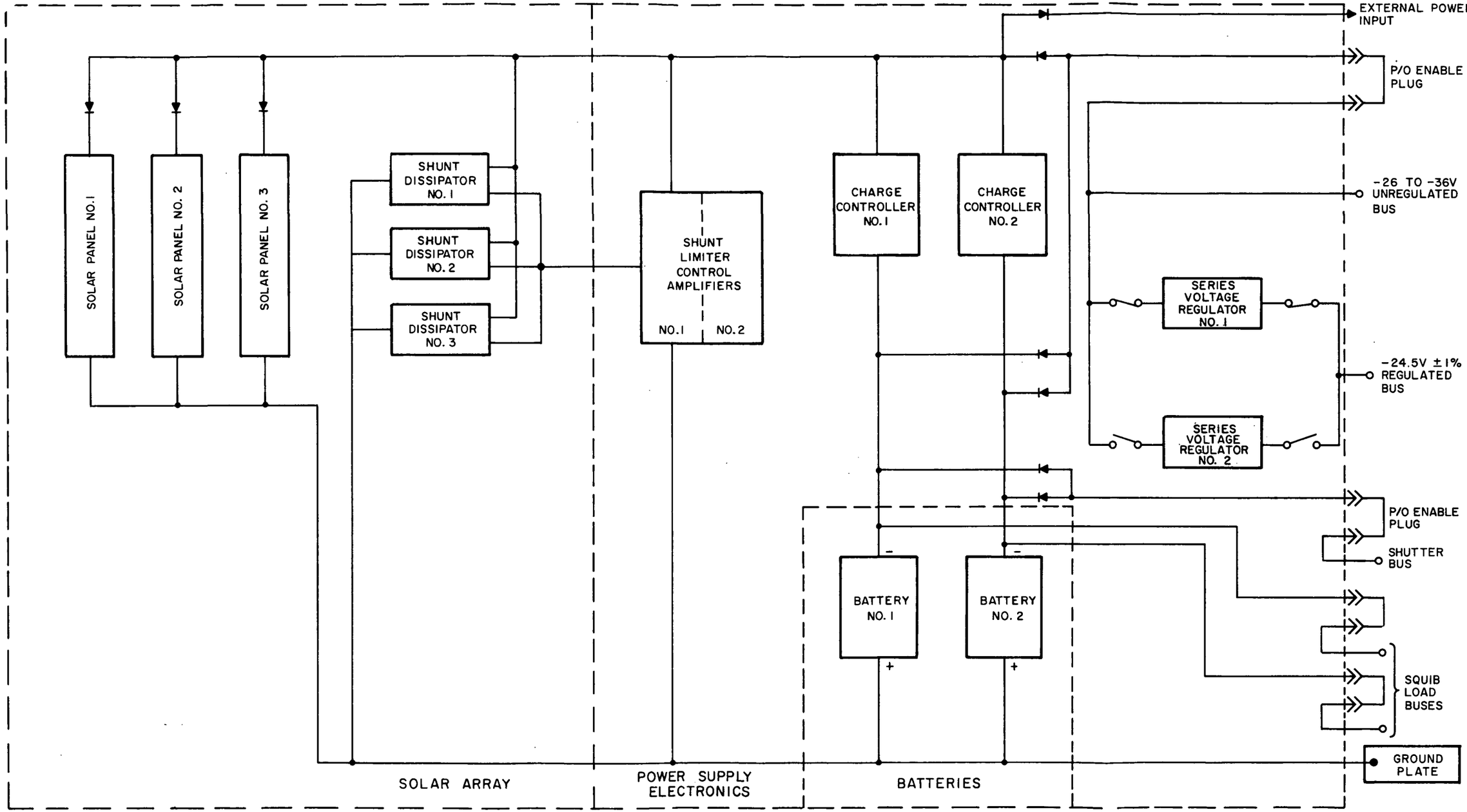

Figure 4-V-2. Power Supply Subsystem, Block Diagram

3. Batteries

The ITOS batteries employ rectangular 4-ampere-hour capacity cells, the same type of cell used on TOS. The cells are arranged in two groups of 22 cells each. The cells of each battery are wired in series, and the two batteries discharge in parallel into the system. (The TOS batteries have 21 cells in series.) The batteries are mounted on the baseplate of the spacecraft.

4. Series Voltage Regulators

The series voltage regulators, mounted on the baseplate, are part of the power supply electronics. The voltage regulators for ITOS are electrically similar to the TOS regulators, but they handle a higher load current. As in TOS, the regulators are redundant units and are selected by the ground command.

5. Charge Controllers

Battery charging is controlled by two taper charge circuits, one for each battery. Both of these circuits are in the power supply electronics. The charge current to the battery is limited to a maximum value when the battery voltage is below the limit prescribed by the battery temperature. When the battery voltage reaches the voltage limit, the charge controller reduces charge current into the battery to hold the battery voltage at the prescribed limit. The voltage limit corresponds closely to the point where the battery has been returned to a fully charged state. The battery will continue to charge at reduced rates after the voltage limit is reached.

The voltage limit thus ensures that the charge current will be reduced to a safe overcharge rate for the battery. Some overcharging of the battery is required in order to sustain satisfactory charge-discharge cycling performance during the entire mission. Use of a voltage limit allows initial charge rates as high as C/4, as compared to C/10 for TOS for a similar battery temperature range.* The TOS current-limiting technique would have doubled the battery size and weight of ITOS.

---

*C represents the nominal battery capacity in ampere-hours.

The overcharge characteristic is a result of several iterative design cycles. A higher overcharge voltage limit results in greater overcharge rates and higher thermal dissipation. The final voltage-temperature characteristics have been modified at high temperatures to reduce thermal dissipation as well as to allow adequate overcharge to meet the cycling demands of the mission.

The charge current can be reduced to the trickle charge rate (150 ± 50 milliamperes per battery) upon command from a ground station. Although the voltage limit ensures that a fully charged battery will be charged at a reduced rate, the trickle charge feature further reduces the heat dissipation in the battery, during 100-percent suntime operation, by further reducing the charge current. This mode of operation should be used when telemetry indicates that the battery temperature may exceed 35°C.

6. Shunt Limiter

The ITOS shunt limiter is similar in concept to the TOS shunt limiter, but due to the higher power-handling requirement, the unit has six rather than four dissipating sections.

The transistor and the resistor parts of the dissipator are mounted on the back of the solar array panels. The two redundant control amplifiers for the dissipators are contained in the power supply electronics.

The control amplifier compares the solar array bus voltage to a reference, and if the array voltage exceeds the reference voltage, it provides drive current to the dissipators. The dissipators then load the solar array to maintain the array voltage at the desired maximum value.

Shunt limiting is essential to ITOS because of the wide variation of solar energy input to the array, a consequence of operating over the 30- to 60-degree sun angle range. Since an increase in solar energy input increases the voltage level of the array output, the array voltage is limited to prevent the overstressing of components.

The array output at the beginning-of-life is designed to exceed the load requirements because effectiveness of the solar array is reduced during the mission life.

7. System Protection

All system loads are fused with Littelfuse High Reliability Subminiature Picofuses. This fuse requires no encapsulation and is available in ratings from 0.125 to 5.0 amperes. As discussed in Paragraph D.7, a 2-to-1 safety margin is used to select fuse ratings. The largest fuse rating that is used on the regulated bus is 2 amperes.

An evaluation of the load resistance at the regulator output caused by a short-circuit load shows that 0.5 ohm is the lowest possible resistance. The effect of a 0.5-ohm fault is a maximum current increase of 49 amperes. Since the normal load is 3 amperes, the total current through the regulator is 52 amperes. Each load is separately fused; the maximum rating is 2 amperes. If it is assumed that the short circuit on the regulated bus has a resistive load of 0.5 ohm and an inductive value of 5 microhenries, then the current, I, is given by:

$$I = \frac{V}{R} \left(1 - \epsilon^{-\frac{Rt}{L}}\right)$$

where:

V is the regulated bus voltage (24.5 volts),

R is the resistance,

t is the time after the short circuit, and

L is the inductance.

The exponential current rise will be near full value (49 amperes) after five time constants, or when $\frac{Rt}{L} = 5$. This occurs after 50 microseconds. A 2-ampere fuse will conduct 49 amperes for less than 300 microseconds before it ruptures. The regulator is protected from the fault condition since it is capable of handling 50-ampere transients with a 12-volt series drop (making 600 watts of dissipation) for 300 microseconds.

C. EQUIPMENT DESCRIPTION

1. Solar Array

The solar array for ITOS consists of three solar panels. A block diagram for one solar panel is shown in Figure 4-V-3. Each panel has redundant panel outputs and two temperature sensor outputs. An input from the shunt limiter control amplifier in the PSE is required for operation of the shunt dissipator on the panel. The output power from each panel is connected in the PSE to the outputs from the other panels for a total solar array output. The temperature sensors are connected to telemetry conditioning circuits in the PSE. Each panel comprises five circuits (A, B, C, D, and E) with nine "strings" of solar cells in each circuit, or 45 strings per panel. Each string consists of 76 series-connected solar cells.

The panel output with the shunt dissipator in the biased-off condition is shown in Figure 4-V-4. The lower curve is the minimum output required from the panel after routine flight acceptance testing. Maximum values are also shown, in the upper curve, since panel outputs above these values may exceed the subsystem power dissipation capabilities. The panel output characteristics shown in Figure 4-V-4 were obtained from the characteristics of a basic solar cell listed in Table 4-V-5.

The effects of shadowing on the solar panels by the thermal fence have been minimized by mounting the solar cells away from the hinge line. The solar cells will be wired to minimize magnetic dipoles created by current loops on the panel.

The solar panels are curved to provide extra clearance between the panels and the spacecraft adapter during the launch phase, when the panels are in the stowed or folded position. Analysis of the performance of this array is based on the mathematical model where each panel is divided into four flat sections. (An error analysis was performed showing that the worst error between the performance of the curved panel and the model would be 0.25 percent.) The curved panel is shown in Figure 4-V-5.

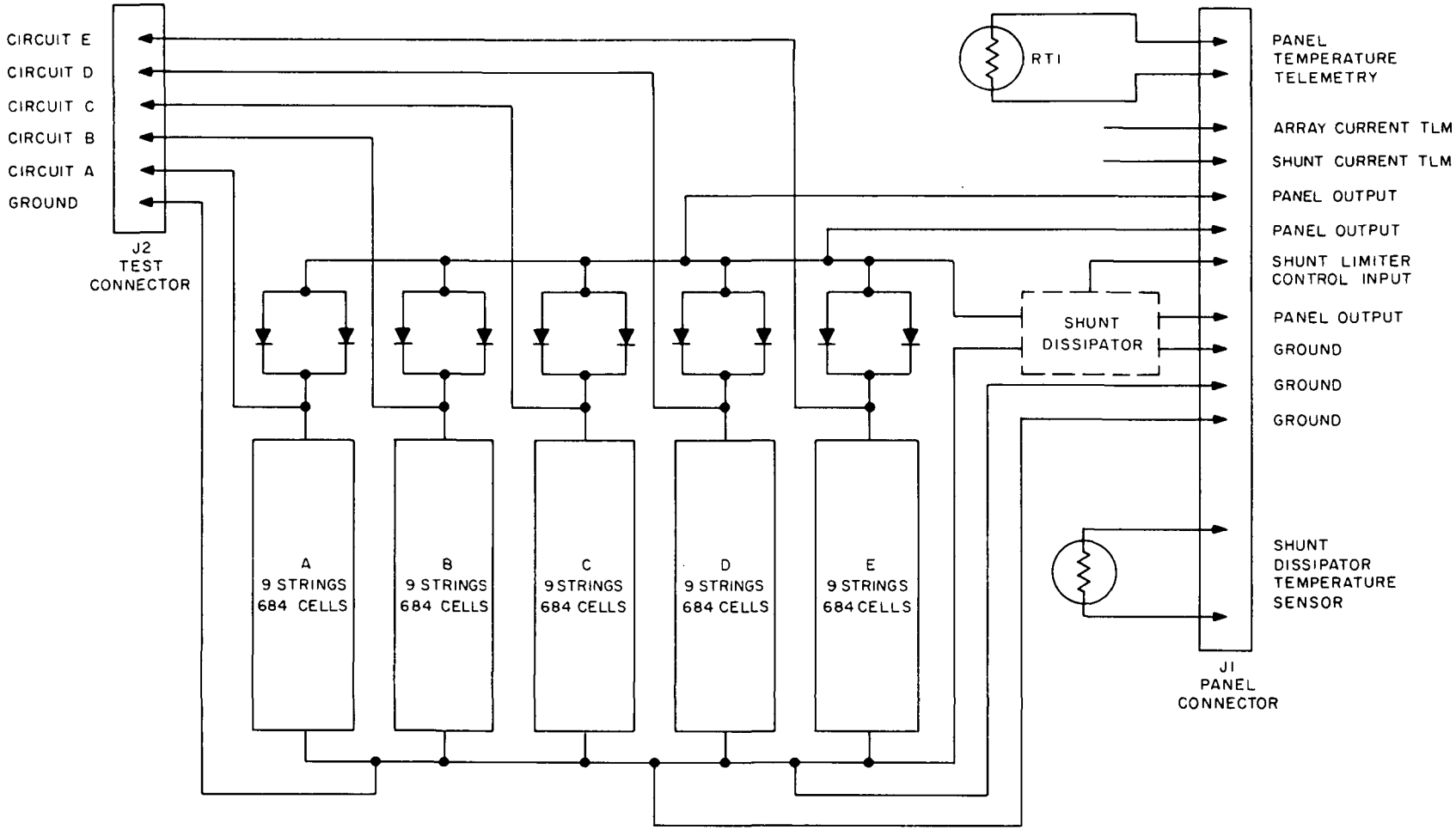

Figure 4-V-3. Solar Panel, Block Diagram

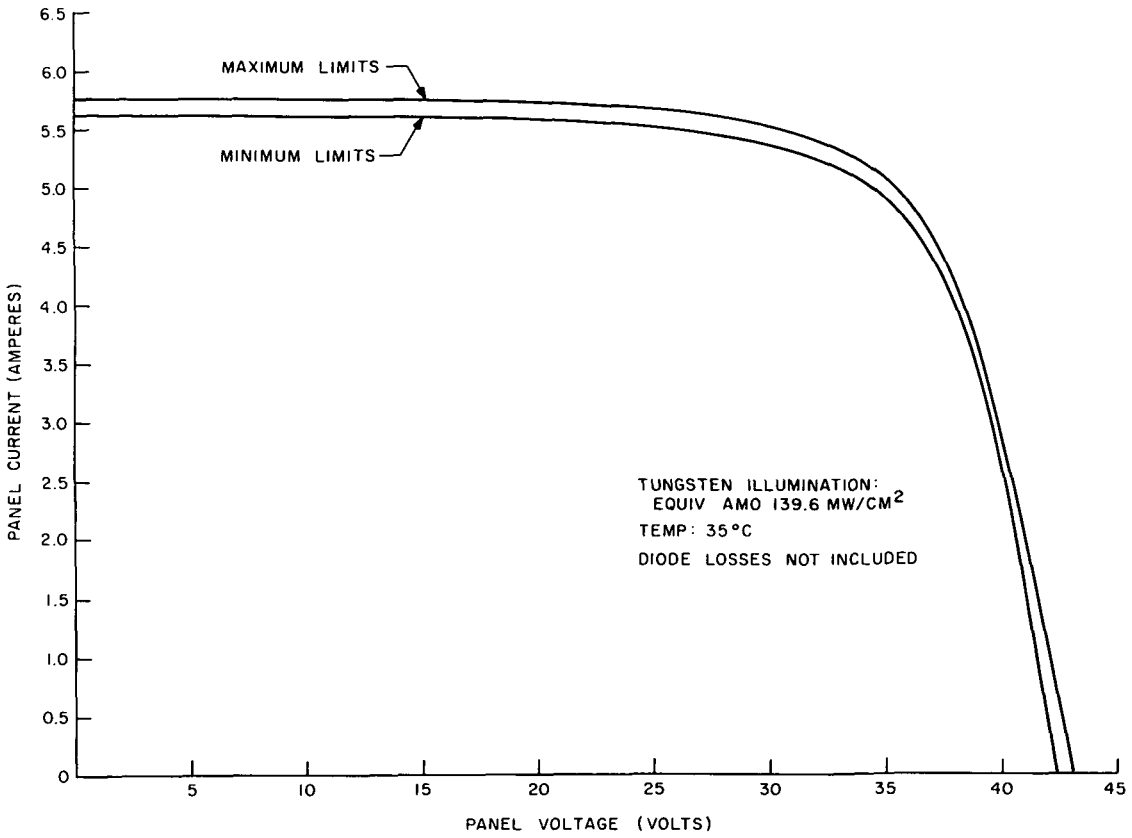

Figure 4-V-4. Solar Panel Output Characteristics at Beginning of Life

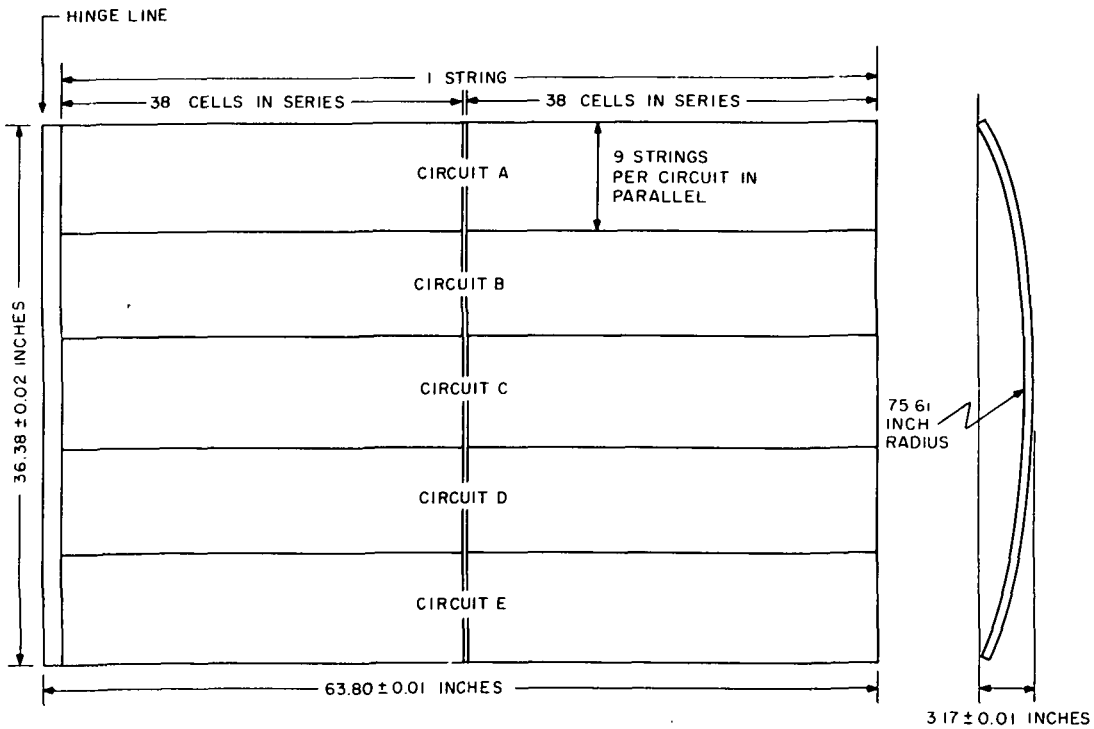

Figure 4-V-5. Solar Panel, Outline Drawing

TABLE 4-V-5. SOLAR CELL CHARACTERISTICS

Characteristic	Value
Air-Mass-Zero Efficienty (cell with cover glass)	9.8 to 10.1 percent at +27 °C
Area	2 by 2 cm
Base Resistivity	1 to 2 ohm-cm
Cover Glass Thickness (microsheet)	0.006 inch
Short Circuit Current (I_{sc})	124.42 ma at 27 °C (9.8 percent)
Maximum-Power-Point Current	113.02 ma at 27 °C (9.8 percent)
Maximum-Power-Point Voltage	0.46 volt at 27°C
Open Circuit Voltage (V_{oc})	0.58 volt at 27°C
Initial Temperature Coefficients:	
I_{sc}	+64 μa per °C
V_{oc}	-2.2 mv per °C

The solar cells are generally assembled in 10-by-9-cell modules. The mechanical packing factor of module area to panel area is 92 percent. (The unused panel area is not included in this estimate.) The active silicon to module area factor is 95 percent. The procedure and materials used in the bonding of the solar cell assemblies and cover glass to the aluminum honeycomb substrate are similar to those used in the Nimbus and Lunar Orbiter programs. It is expected that preinsulated honeycomb will be used.

To maximize the output of each panel, the modules are connected in series along the length of the panel rather than across the width of the curved surface. In this manner, each module in a series string will be at the same incidence angle to the sun and will produce the same amount of current, the net amount of current in the string being that produced by the module with the least current. Maximum output is attained when all modules generate the same current. If the modules were connected across the curved surface, the string output would be controlled by the module with the least illumination intensity, and, therefore, the

least current. Each string would be producing much less power than the average illumination intensity would bring from a flat panel. Analysis shows that 47 percent more power is produced with the series strings oriented along the panel than with the strings across it.

The panel is designed to operate in a thermal environment of -100 to +50°C. The panel weight breakdown is given in Table 4-V-6.

TABLE 4-V-6. SOLAR PANEL WEIGHT BREAKDOWN

Component	Weight (pounds per panel)
Substrate and Structure	10.30
Solar Cell Modules (cells, cover glass, cell interconnections, solder, cover glass adhesive)	3.68
Adhesives	0.38
Insulation	0.50
Miscellaneous (connections, diodes, wire, etc.)	1.54
Shunt Dissipator	3.0
TOTAL	19.4

2. Batteries

a. Mechanical

The batteries on the ITOS spacecraft consist of two sets of nickel-cadmium storage cells. Each battery contains 22 four-ampere-hour cells, connected in series. The cells are rectangular and encased in stainless steel, with the positive terminal insulated by means of a ceramic-to-metal seal. The negative terminal is electrically common with the cell case. In the battery assembly, the cells are insulated from one another and from the supporting aluminum chassis. The cells are mounted in two parallel rows of 11 cells each,

compressed, and held in place by holddown clips. The maximum total weight of each battery is 15.0 pounds. The batteries are wired so that the individual cells and temperature sensing units can be monitored through the electrical connector. The temperature sensing units are used for temperature telemetry and charge control. This battery design is virtually identical to that used on a previous RCA classified space program.

b. Electrical

A schematic diagram of the battery is shown in Figure 4-V-6. The sealed nickel-cadmium battery is capable of repeated charge-discharge cycling, and it has been employed in all RCA orbiting spacecraft power supply subsystems. Typical charge-discharge curves, at 20°C, are shown in Figure 4-V-7.

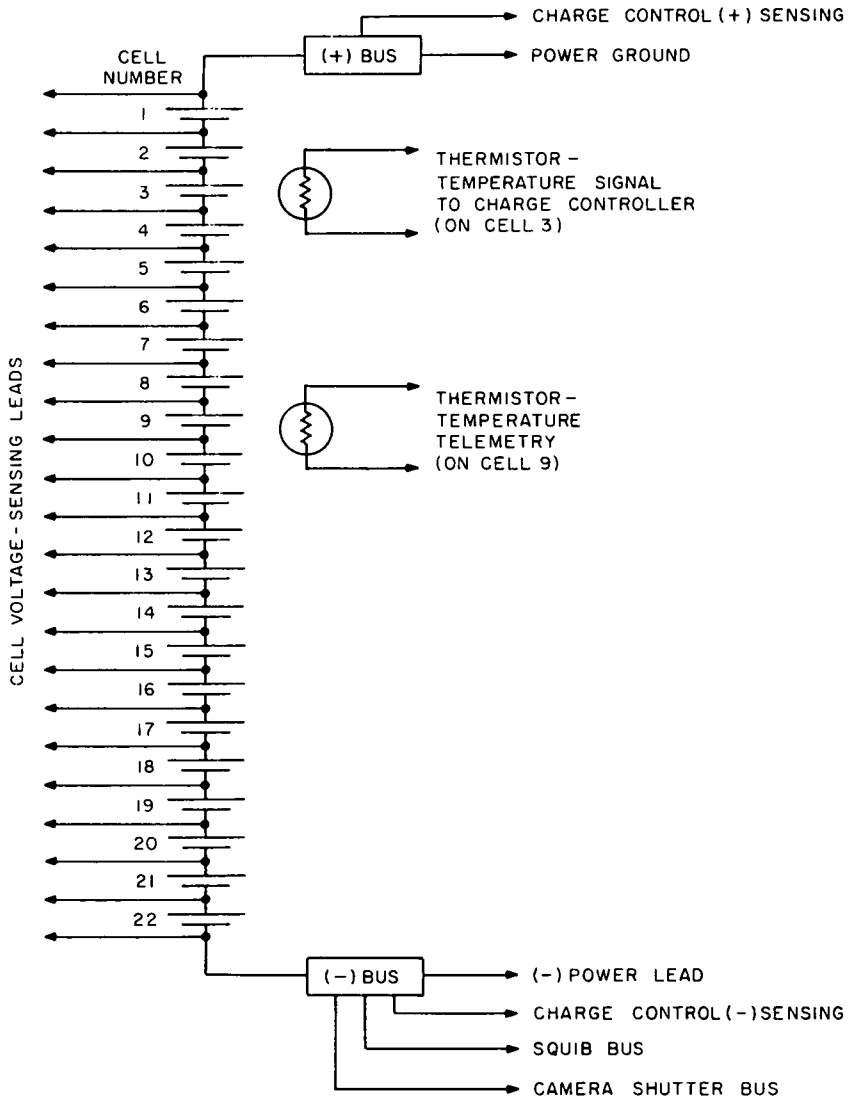

Figure 4-V-6. Battery, Schematic Diagram

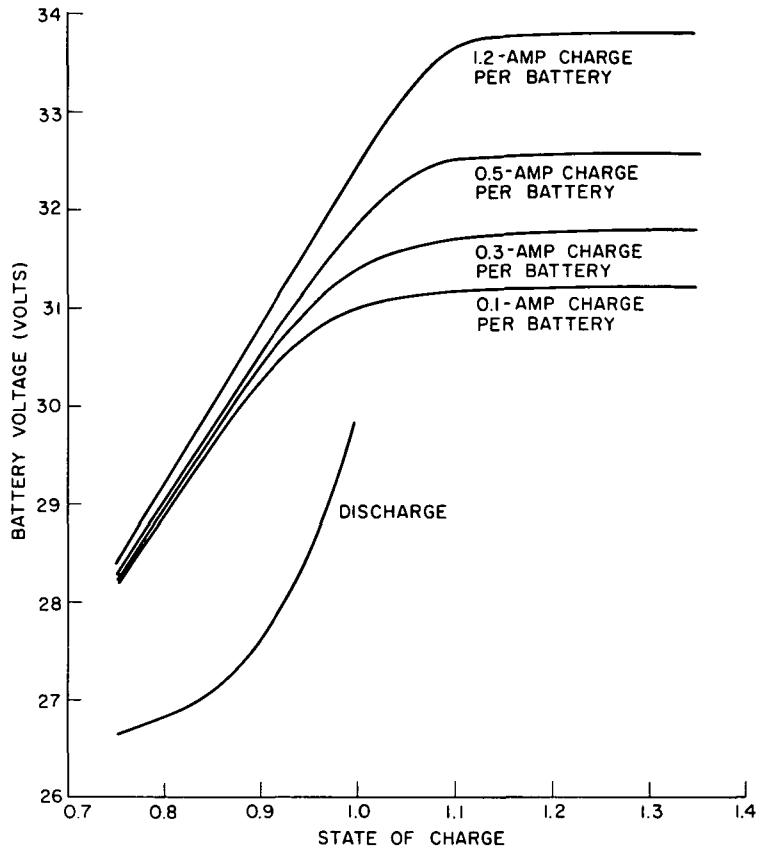

Figure 4-V-7. Battery Voltage Versus State of Charge at 20°C

c. System Considerations

The major change from TOS to ITOS battery performance is that ITOS will be required to operate at greater depths of discharge during eclipse periods. In TOS the average depth of discharge was less than 5 percent. Using the load profile defined in Figure 4-V-1, and assuming a 31-minute eclipse period (corresponding to 60-degree sun angle), the depth of discharge of the ITOS batteries will be 18.8 percent.

In order to replace energy lost during eclipse periods, the battery must be recharged from the solar array during each sunlight period. The recharge capability of the battery is usually limited by the current, which can be sustained during continuous overcharge. In simple (constant current) charge control systems, the current limit is set to one value during charge and overcharge. The ITOS charge control system employs a taper charge controller which permits relatively high currents in the charge mode and causes reduction of the current to a

safe level in the overcharge mode. (Overcharge current must be limited to prevent excessive gas pressure.) The charge controller senses battery voltage, temperature, and charge current.

Figure 4-V-8 shows the range of battery charge-discharge profiles. When the sun angle is 30 degrees, the satellite is in sunlight for 100 percent of the time. Under such conditions, the batteries are subjected to continuous overcharge; however, the charge controller, which senses the battery voltage, reduces the current to a safe level.

At sun angles greater than 36 degrees, the batteries are subjected to repetitive charge-discharge cycling. Figure 4-V-8 shows a single charge-discharge cycle with a sun angle of 60 degrees, where eclipse time is maximum.

3. Power Supply Electronics

a. General

The block diagram of the power supply electronics (PSE) is shown in Figure 4-V-9. This unit contains the two series voltage regulators, the two charge controllers, and the shunt dissipator control amplifiers. The PSE unit on ITOS performs all of the functions previously performed by the voltage regulator, shunt limiter, charge controller, and power distribution unit assemblies in the TOS APT and AVCS satellites. The ITOS charge controller is more sophisticated in its design and operation than the TOS unit, since a closed-loop current regulator is provided which allows more accurate control of the current limit setting and also establishes current limiting as a function of battery voltage and temperature. The voltage regulator and power distribution unit are combined in ITOS, providing a substantial improvement in load regulation and output impedance. All the circuits in the PSE are mounted on plug-in printed circuit boards, except for the power transistors. The PSE assembly is 9 by 5.75 by 7.25 inches; the maximum weight of the unit is 11.2 pounds.

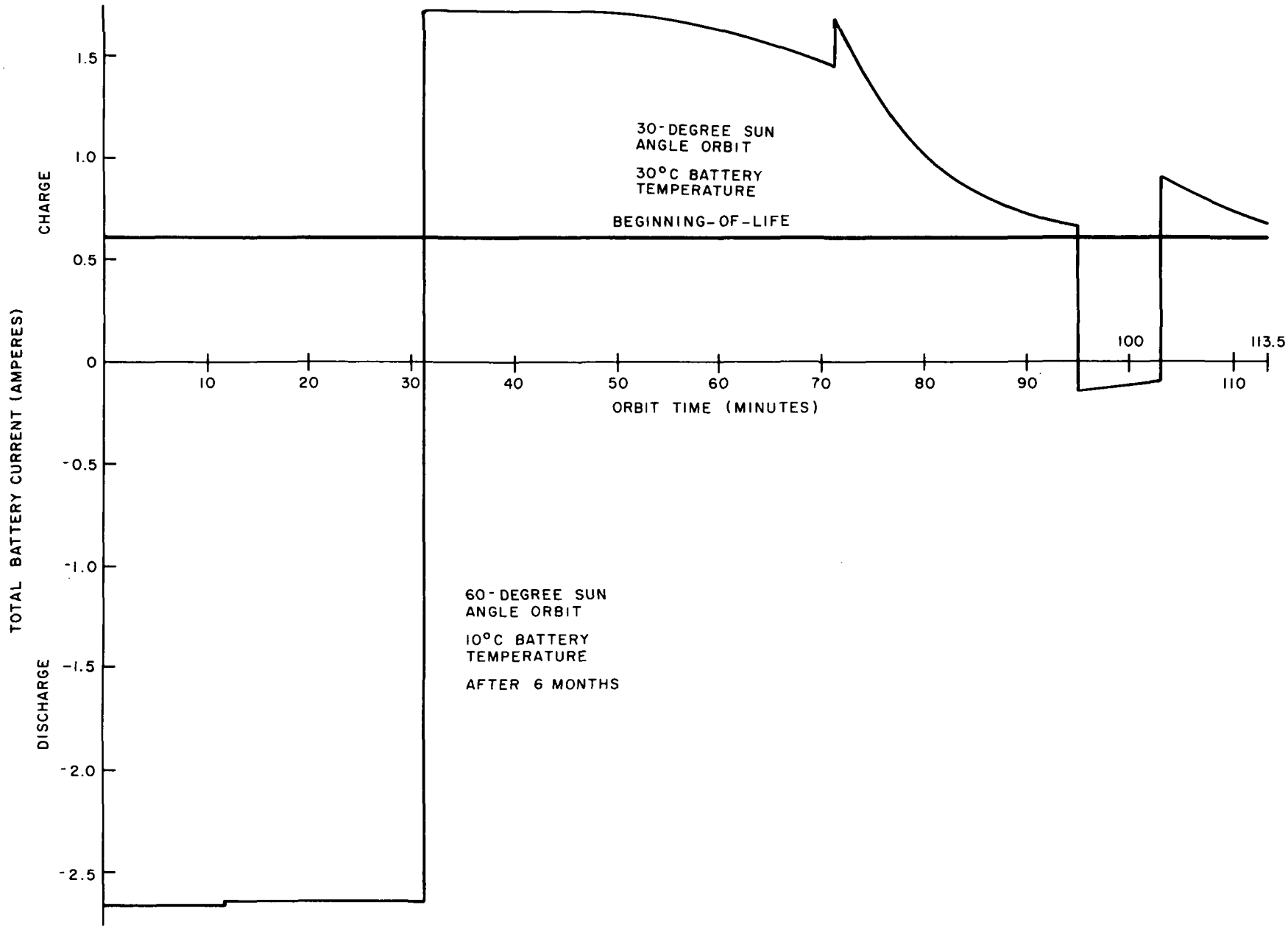

Figure 4-V-8. Battery Charge Discharge Profiles

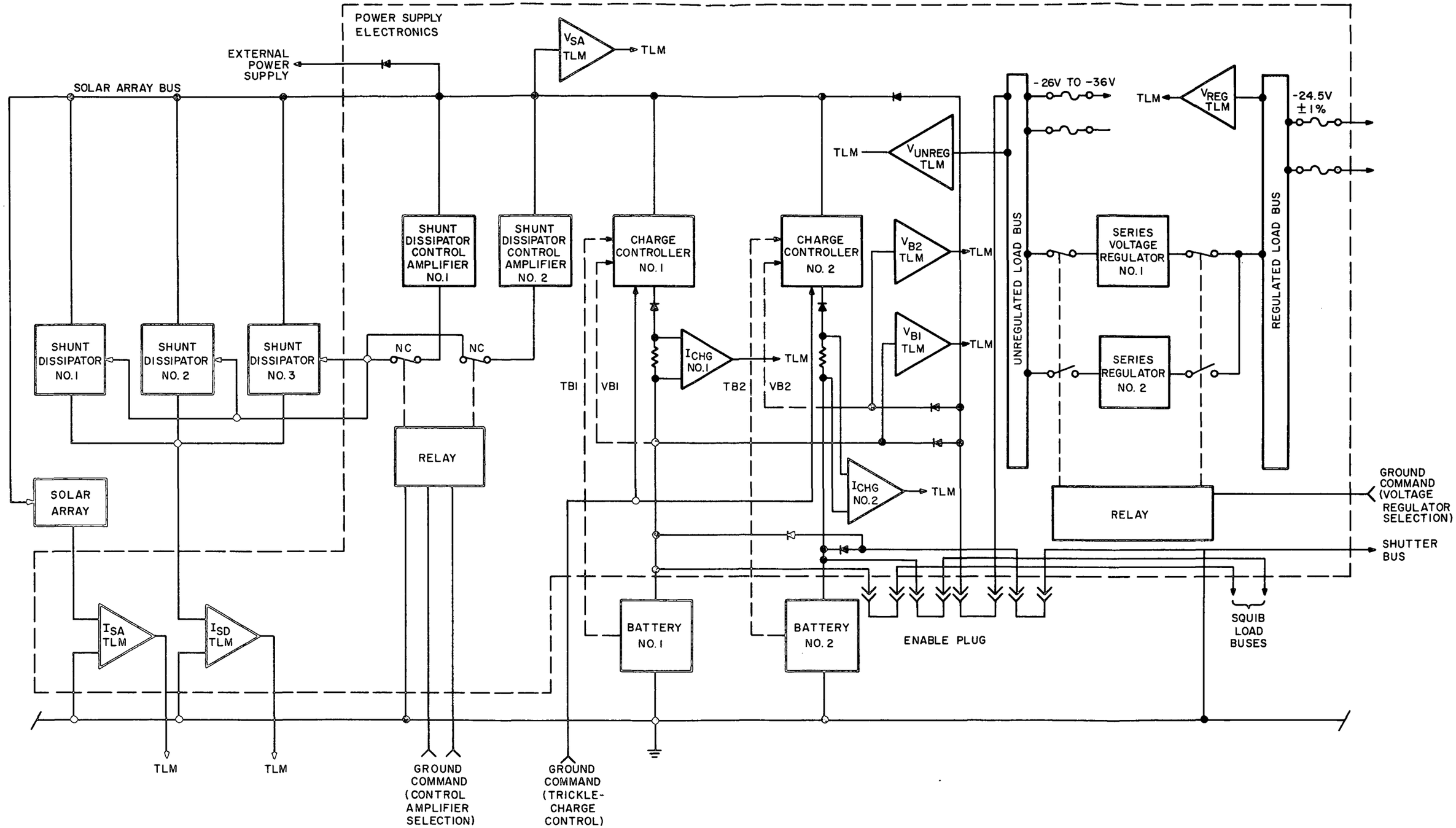

Figure 4-V-9. Power Supply Electronics, Block Diagram

b. Charge Controllers

1) Function

Each charge controller controls the battery charge during the satellite day while protecting it from current, voltage, and temperature excesses. The charge controller performs this function by (1) monitoring battery charge current, battery temperature, and battery terminal voltage and (2) controlling battery charge current. The charge controller accepts input signals corresponding to each of the parameters and compares these inputs with built-in references. Deviations or error signals are amplified, and battery charging current is adjusted to decrease the error. The two normal operating regions for the charge controller are shown in Figure 4-V-10.

2) Region I Operation

In Region I, maintaining charging current close to the safe maximum for battery recharge is desirable. Therefore, the tolerance requirements on the charge current dictate a closed-loop or feedback type of current regulating circuit. The current limit is 0.95 ampere ±8 percent per battery.

Figure 4-V-11 is a circuit diagram of the current regulating function of the charge controller in Region I operation. The function may also be represented mathematically as:

$$i_B = f\left[V_{R1}\left(\frac{G_i}{1 + hG_i}\right)\right]$$

where:

i_B is the battery charge current,

V_{R1} is the reference voltage, derived from a temperature-compensated Zener diode and a voltage divider,

G_i is the forward gain or transconductance of the transistor circuitry, and

h is the feedback element that senses the battery charge current and transforms the current level.

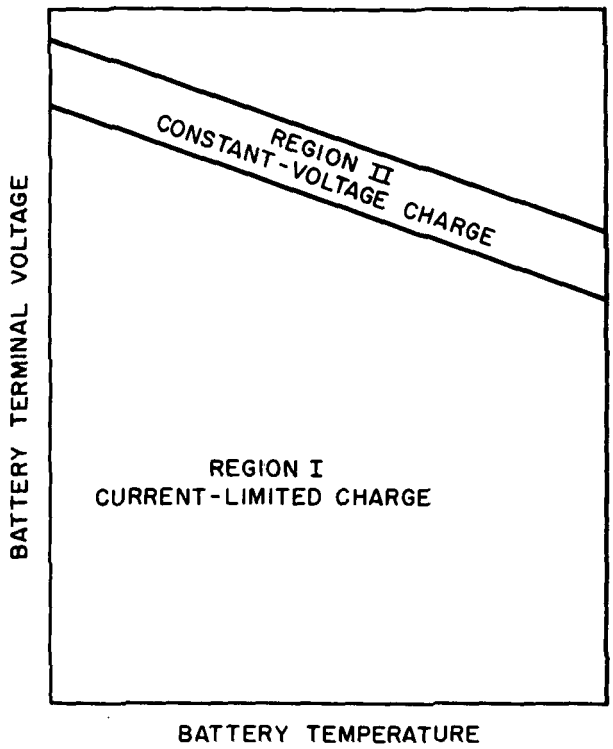

Figure 4-V-10. Regions of Normal Charge Controller Operation

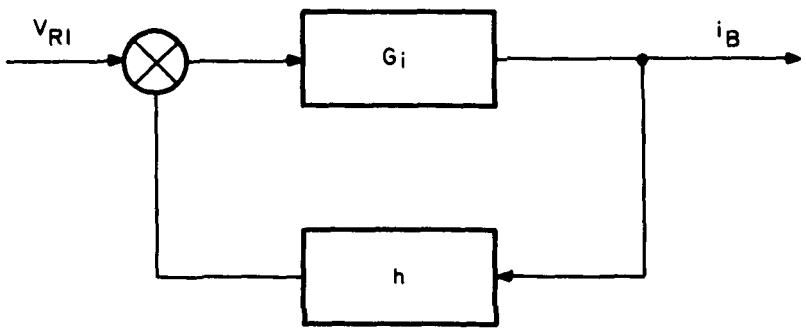

Figure 4-V-11. Charge Controller Functional Diagram, Region I

After transformation by the feedback element, the current level is compared to the reference voltage, V_{R1}. The difference between the two is the error, E, which controls the charge current.

3) Region II Operation

In Region II, the charge current is voltage limited. The limiting voltage is a function of battery temperature, as shown in Figure 4-V-10. Normally, at the beginning of the charge cycle, the battery causes the charge controller to operate in Region I, the constant current mode. As the battery is charged, its terminal voltage increases. Should the voltage/temperature combination enter Region II, the charge controller senses this condition and limits the current to maintain the battery voltage within this region.

Within Region II, the charge controller becomes essentially a voltage regulator with an output voltage related to temperature. Figure 4-V-12 illustrates this mode of operation.

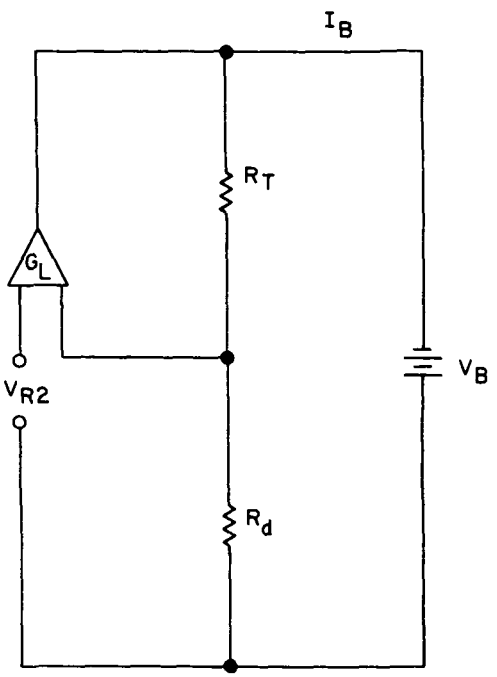

Figure 4-V-12. Charge Controller Functional Diagram, Region II

If the gain of the amplifier is high, it can be shown that

$$V_B = V_{R2}\left(1 + \frac{R_T}{R_d}\right)$$

where:

V_B is the battery voltage,

V_{R2} is the reference voltage for the voltage/temperature circuit,

R_T is the resistance of a temperature sensitive resistor mounted on the battery and having a negative temperature coefficient,

R_d is the constant resistance, and

G_L is the effective transconductance of the transistor circuit in Region II.

As the battery temperature increases, resistance R_T decreases, thereby reducing the value of voltage V_B at which the circuit will regulate. The curve in Figure 4-V-13 shows battery performance. Figure 4-V-14 illustrates the effects of the specific voltage limit value (Figure 4-V-13) on battery temperature and thermal dissipation. As shown, peak dissipation does not exceed 15 watts per battery. The 30-watt maximum is dictated by the thermal control flap arrangement.

c. Series Voltage Regulator

The voltage regulator compares the regulated bus voltage at the input to the load fuses to a fixed reference voltage; it causes the voltage drop across the series control element to vary, holding the output voltage within -24.5 ± 0.25 volts. The circuit maintains this regulation for variations in input voltage, load current, and temperature.

d. Shunt Limiter

The shunt limiter limits the upper value of the unregulated bus voltage to a maximum of 36.0 volts.* To perform this function, the impedance characteristic of the shunt limiter is changed from high resistance to low resistance (from solar bus to ground) as the threshold or cut-in voltage of the circuit is reached. Since the solar array is almost a constant current source in the region of operation, the circuit dissipates the excess array power not required by the subsystem loads or the battery. The high circuit transconductance requires only a small change in solar array voltage (above the shunt limiter threshold) to produce a large change in shunt current. The net result is a circuit current voltage characteristic with a very steep slope (low dynamic resistance). The complete limiting action is confined to a solar bus voltage differential of only a few tenths of a volt. The maximum shunt limiter rating is 375 watts. The shunt dissipators are mounted on the backs of the solar panels and provided with adequate radiation shielding and heat sinks.

* The TOS limit was 34 volts. The increase for ITOS is the result of the higher voltage produced by the 22-cell battery (as compared to that produced by the 21-cell TOS battery).

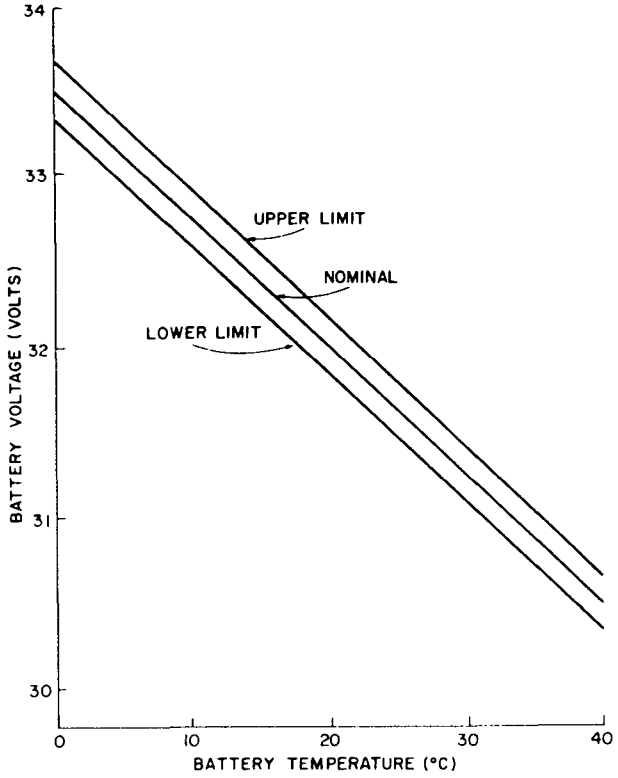

Figure 4-V-13. Battery Charging Voltage Limits Versus Temperature

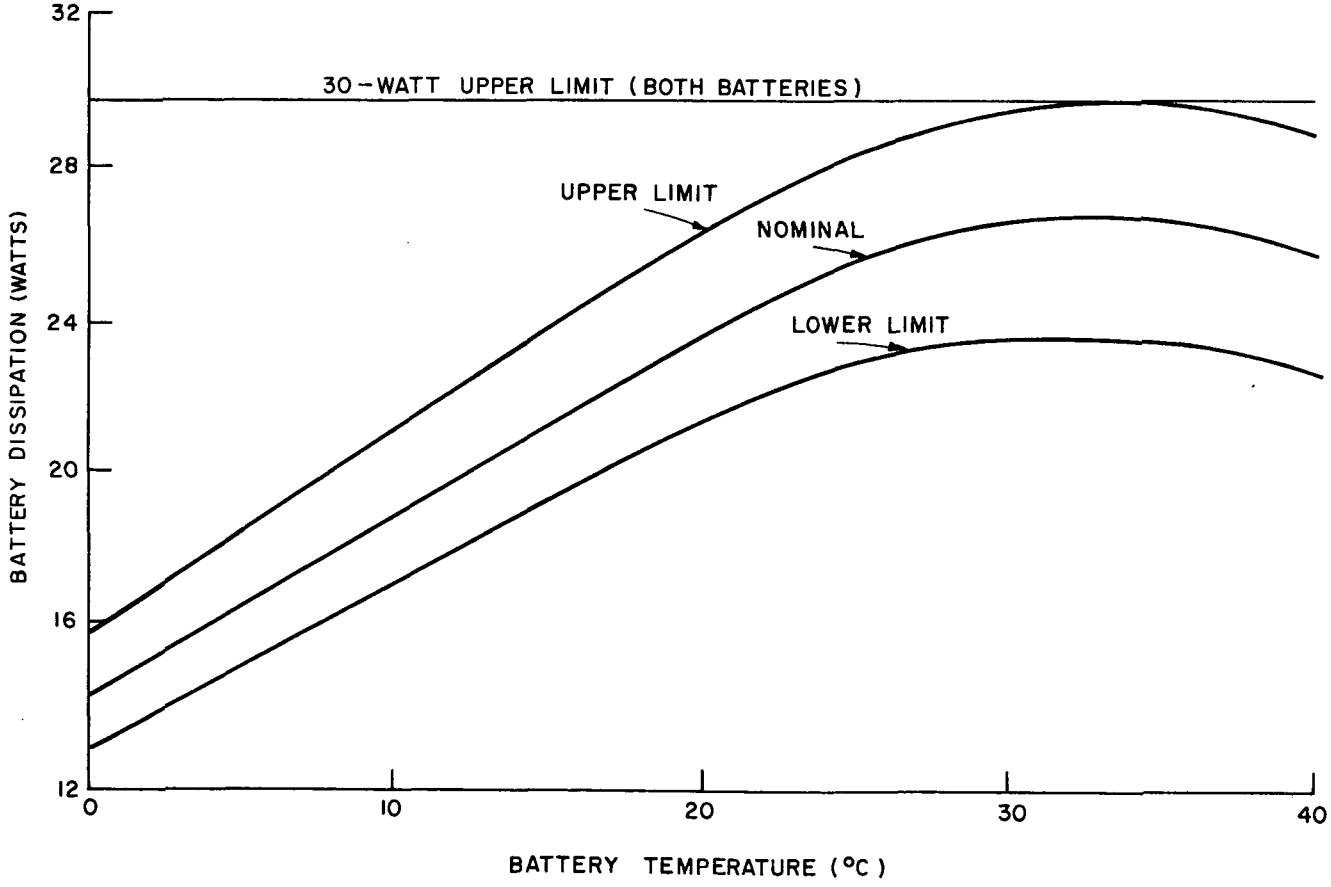

Figure 4-V-14. Battery Dissipation (Continuous Overcharge) Versus Temperature

D. SYSTEM ANALYSIS

1. Tradeoff Studies

NOTE

A considerable part of this analysis is based on component data and mission requirements available or assumed at the time the analysis was performed. Since that time, some revisions have been made in both the data and the requirements, but the general conclusions remain valid.

a. Solar Array

The primary goal of the tradeoff study of the solar array was to determine the geometric configuration of the array that would result in the smallest solar array area possible without the use of sun orienting mechanisms. Figure 4-V-15 shows the three configurations considered and the area in square feet required by each configuration to produce an array power output of 131 watts at a gamma angle of 60 degrees, the worst-case gamma angle. The cylindrical case represents the TIROS solar array configuration. The other two cases consider flat solar panels mounted (a) normal to the spin axis and (b) at 30 degrees to the spin axis.

For the ITOS sun angle range of 30 to 60 degrees, a configuration of flat panels in the orbit plane is the most efficient geometry not using solar orientation in terms of power conversion capability per unit area of the array.

b. Power Conditioning Circuits

The power conditioning circuits include the basic electronics circuits required in a solar cell and battery system to maintain a regulated bus voltage, control the charge and discharge of the battery, and dissipate the excess power produced by the array. The TOS and TIROS power conditioning circuits may be termed a dissipative series regulator system; the ITOS spacecraft will use an expanded version of the TOS system. An alternative type of power-conditioning system, a direct energy transfer (DET) system, was also considered for ITOS. A block diagram of a DET system is shown in Figure 4-V-16.

CONFIGURATION	TOTAL CELL AREA REQUIRED TO PRODUCE POWER OUTPUT OF 131 WATTS (AT A GAMMA ANGLE OF 60 DEGREES)
CYLINDER (56 IN. DIAMETER) 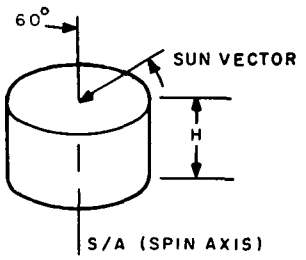	55.0 SQ FT (H = 2.6 FT)
FLAT PANELS FIXED 30° TO THE SPIN AXIS 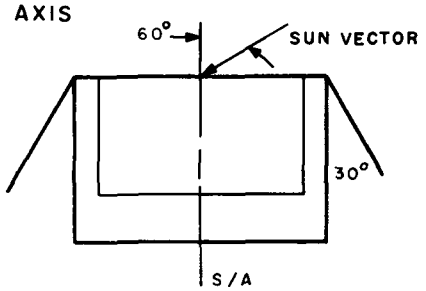	50.9 SQ FT
FLAT PANELS FIXED NORMAL TO THE SPIN AXIS 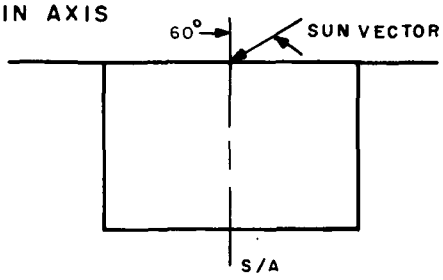	38.2 SQ FT

Figure 4-V-15. Solar Array Configuration Comparison

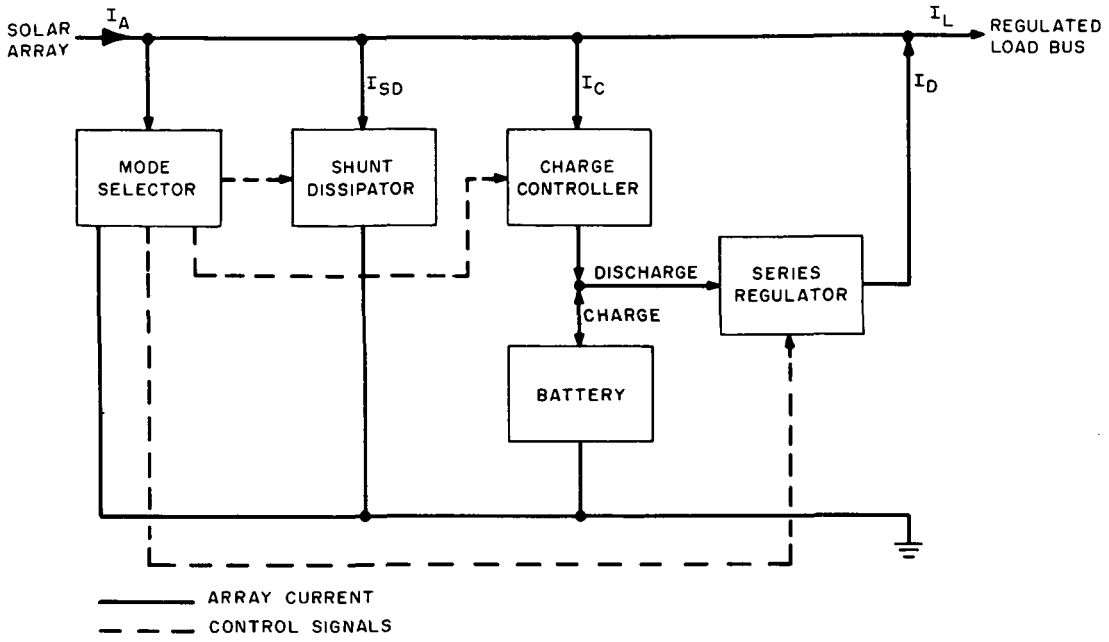

Figure 4-V-16. Direct Energy Transfer System, Block Diagram

In general, the DET system is more efficient than the dissipative series regulator system and would permit as much as a 20-percent reduction in the array size requirement and a consequent, similar percentage reduction in array cost and weight. The increased efficiency of the DET system results from the direct connection between the array and the load and the consequent avoidance of series losses.

The basic TOS system has a series voltage regulator, a battery charge controller, and a shunt dissipator. Both the series regulator and the shunt dissipator have voltage reference circuits, and the charge controller contains its own current reference circuit. Similar reference functions are required in the DET system; however, in the DET system, it is essential that these units operate in a prescribed sequence. To accomplish this, the series regulator and shunt dissipator voltage reference circuits are combined into one voltage reference circuit termed a "mode selector". In addition, the current reference of the battery charge controllers is controlled by the mode selector. By controlling current flow in the shunt dissipators, the battery chargers, and the series regulator, the mode selector becomes the regulating element for the regulated output bus.

The block diagram of Figure 4-V-16 shows a DET system with a single battery string. In the TOS system, the voltage regulator is in series with the solar array and the spacecraft load. In the DET system, the series regulator regulates only the voltage at the battery. The charge controllers are, in effect, boost chargers, since the battery must be charged from a bus voltage that is lower than the battery voltage. The shunt limiter regulates the output of the array. The desired sequence of power supply operation is dictated by the array current and load current demands. When the array current, I_A, exceeds the load current, I_L, the following conditions exist:

$$I_A > I_L,$$

$$I_D = 0, \text{ and}$$

$$I_A = I_{SD} + I_C + I_L.$$

Battery discharge current, I_D, must be prevented from flowing through the regulator. The shunt dissipator current, I_{SD}, must be zero until the battery charge current, I_C, has reached its allowable maximum.

When the load current exceeds the array current, the following conditions must exist:

$$I_L > I_A,$$

$$I_{SD} = 0,$$

$$I_C = 0, \text{ and}$$

$$I_A + I_D = I_L.$$

The control in both cases can be provided by comparing the regulated bus voltage with the mode selector reference voltage and providing drive signals for the other units in the power system. The amplified deviations must first be fed through threshold circuits; the threshold outputs then control the current flow in each unit of the power subsystem.

The situation is depicted in Figure 4-V-17, where V_R is the desired regulated bus voltage. ΔV is the total voltage deviation of the regulated bus, corresponding to the maximum battery discharge current at one extreme and to the maximum shunt dissipator current at the other extreme.

The boost chargers can have the additional provision of a voltage limit or taper charge. The voltage limit is used to permit higher initial charge rates than possible with a constant current. Based on battery voltage (as a function of battery temperature), the power conditioning electronics will taper or reduce the initial battery current to a safe level when a prescribed voltage limit is reached.

A preliminary design analysis of both the DET system and an expanded TOS system (XTS) was made, taking into consideration the requirements of the ITOS mission and load profile. A comparison of the two systems indicated several differences.

The XTS would weigh 135 pounds, as compared to 120 pounds for the DET system; this is a clear weight advantage for the latter.

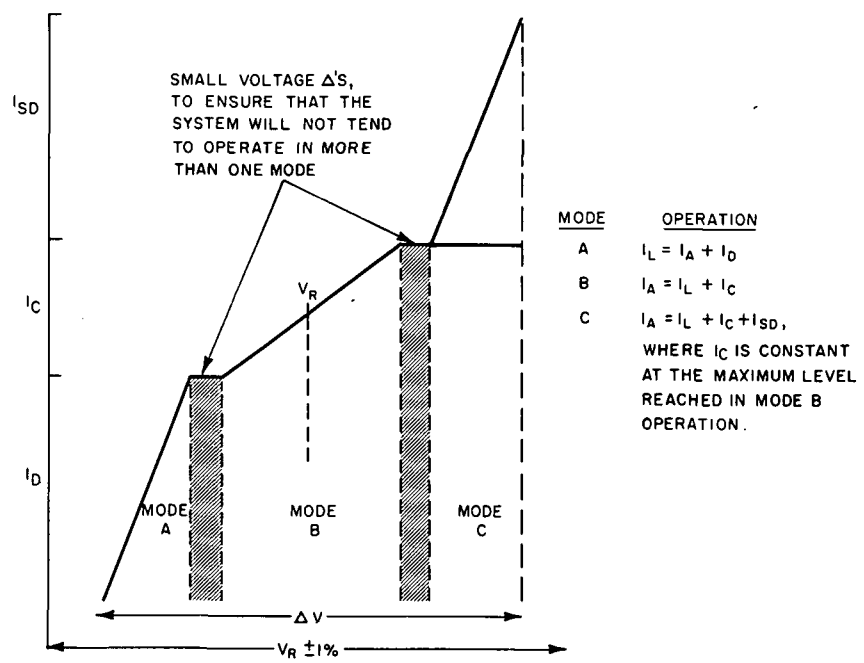

Figure 4-V-17. Power Supply Current Versus Regulated Load Voltage Deviations

The additional cost required during the design phase would be greater for the DET system, but the additional production cost per spacecraft would be greater for the XTS. The difference in recurring costs would be due primarily to the difference in the solar array size required for the two systems. The required area, based on the TIROS M load and a 25-percent growth potential, would be 42 square feet for the DET system and 52 square feet for the XTS.

The two systems are estimated to be equal in reliability.

The XTS was found to be somewhat superior to the DET system in regulation (no load to full load), transient response, and RFI generation. The most significant difference between the two systems is in output impedance. A comparison of the output impedances is shown in Figure 4-V-18. In the boost charger mode (batteries charging), the output impedance of the DET system significantly exceeded that of the XTS.

It was concluded from this study that the weight and cost savings indicated for the DET system were not sufficient to offset the smaller output impedance of the XTS. Consequently, the dissipative type of regulator system (XTS) was selected for ITOS; the DET system will be considered for future use. Indications are that further development of the DET system could produce significant improvements in performance.

c. Power Dissipation

A study was performed to evaluate several subsystem configurations and component locations with regard to their ranges of minimum-to-maximum power dissipation within the insulated body of the spacecraft. With the operational spacecraft orbit loads assumed to be constant, the significant variations in spacecraft power dissipation were found to be in the batteries and in the subsystem electronics.

Table 4-V-7 presents the results of this study. For the study, the shunt dissipator transistors were assumed to be located within the insulated body; in addition, a 25-percent growth factor was included in the value for the operational load.

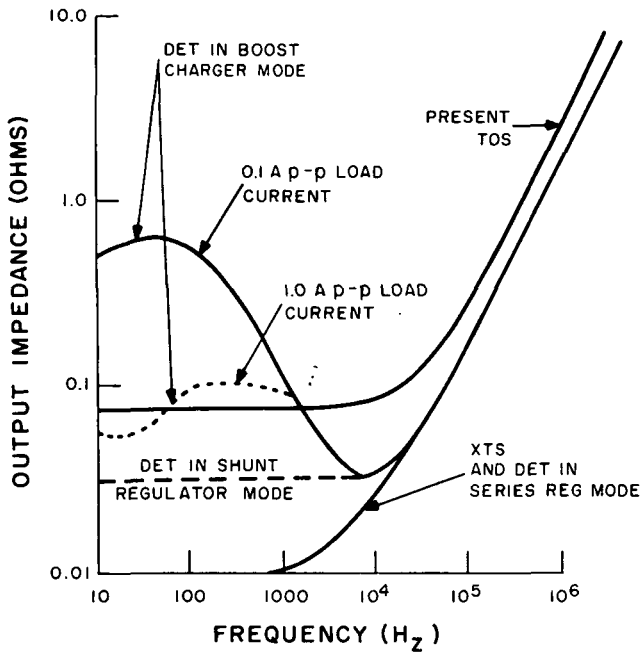

Figure 4-V-18. Comparison of Output Impedances of Power Conditioning Systems

TABLE 4-V-7. ESTIMATED POWER DISSIPATION IN THE ITOS SPACECRAFT

Contributing Factor	Power Dissipation (watts)	
	Minimum	Maximum
Operational Load (including 25-percent growth factor)	87.0	87.0
Battery Dissipation (orbital average)	4.0	76.0
PSE Dissipation		
Charge Controller	3.0	4.8
Series Regulator	7.1	39.0
Shunt Transistor	1.0	58.2
PSE Losses	2.6	8.3
TOTALS	104.7	273.3

A thermal analysis was performed using the estimated power dissipation values. This analysis indicated that a substantial difference in temperature could exist between the maximum and minimum cases. Various methods were considered to reduce the differences between the cases; these methods are listed in Table 4-V-8. Each method was evaluated to determine the ratio of maximum-to-minimum power dissipation, the feasibility for ITOS, and its development status.

TABLE 4-V-8. ALTERNATIVE METHODS OF REDUCING POWER DISSIPATION

Method	Spacecraft Dissipation (watts)		Dissipation Ratio	Feasibility Considerations	Complete Development Required
	Min	Max			
1. Locate shunt dissipator transistors outboard	105	185	1.76	Low temperature	Yes
2. Use multiple series transistors in shunt dissipator:					
a) 2 stages	105	240	2.28		Yes
b) 3 stages	105	221	2.10		Yes
3. Reduce charge controller drop (auxiliary array)	104	225	2.16		No*
4. Array switching	105	210	2.00	Greatly dependent on operational procedures**	Yes
5. Combination of 2b and 3	104	209	2.01		Yes

*Basically a modification of the method used on the Lunar Orbiter satellite.

**Shunt dissipator power monitored as a function of sun angle, array degradation, and load switching.

The method selected was that of placing the shunt dissipator power transistors outside the spacecraft body, on the back of the array panels along with the shunt power resistors. This method was selected primarily because it produced the lowest dissipation ratio.

d. Battery Charging

One important consideration throughout the study phase was weight reduction; the need to reduce weight led to a tradeoff study of the methods of battery charging. The use of a current limit and of a voltage limit to control charge current into the battery would result in a reduction of the capacity requirement for the battery. This, of course, would reduce the weight of the battery. In general, there can be almost a 2-to-1 reduction in battery capacity when a voltage limit is used. The required capacity then becomes a function of depth of discharge rather than of charge rate.

A disadvantage of using a battery voltage limit, aside from the requirement for additional circuits in the charge controller, is that an increase in solar array area is required to compensate for the peak battery charge current, which is higher than the peak current when a constant-current charge system is used. It is estimated that a reduction of 28 pounds in the weight of the batteries would be accompanied by an increase of 5 percent in the total array area.

e. Current Telemetry Circuit Tradeoff Study

The performance characteristics of a magnetic amplifier circuit and a DC amplifier circuit were compared with regard to accuracy, linearity, shunt loss, insertion loss, weight, volume, parts count, reliability, and response time. The results of this comparison are shown in Table 4-V-9.

Neither circuit offers any significant advantage over the other in accuracy or linearity. The major advantage of the magnetic amplifier circuit is that it introduces no insertion loss; it also requires less shunt dissipation and fewer parts than the DC amplifier circuit, if more than one current sensor circuit is needed. The reason for this is that only one inverter circuit is necessary to drive a number of magnetic current sensors. The DC amplifier type

TABLE 4-V-9. COMPARISON OF MAGNETIC AMPLIFIER AND DC AMPLIFIER CURRENT TELEMETRY

Tradeoff	Magnetic Amplifier Circuit	DC Amplifier Circuit	Better Circuit
Accuracy	2 percent	2 percent*	No preference
Linearity	2 percent (zero based)	1 percent (terminal based)	No preference
Shunt Loss			
1 Circuit	19 ma	17 ma	
4 Circuits	40 ma	68 ma	Magamp
Insertion Loss	None	0.25 v (design goal) (0-10 a) 2.5 w per circuit (0-1 a) 0.25 w per circuit	Magamp
Parts Weight			
1 Circuit	0.36 lb	0.06 lb	DC amplifier
4 Circuits	0.96 lb	0.25 lb	DC amplifier
Parts Volume			
1 Circuit	10.08 cu in	2.1 cu in	DC amplifier
4 Circuits	18.25 cu in	8.4 cu in	DC amplifier
Parts Count			
1 Circuit	22	23	Magamp
4 Circuits	55	92	Magamp
Reliability (P_S)			
1 Circuit	0.9643	0.9955	DC amplifier
4 Circuits	0.9072	0.9822	DC amplifier
Response Time (Max)	5 sec	0.02 sec	DC amplifier

*This accuracy is based on the use of three calibration curves for three different temperatures.

of current telemetry has the advantage of much less weight and volume as well as higher reliability and quicker response time. However, the DC amplifier circuit introduces a 0.25-volt insertion loss (the drop across the current sensing resistors). A further disadvantage of this circuit is its greater shunt loss, if more than one circuit is used. The DC amplifier circuit maintains the same full-scale accuracy as the magnetic amplifier circuit if calibration curves at three different temperatures are used. However, the DC amplifier circuit is better suited for switched telemetry, because of its much faster response time.

Based on these comparisons, the DC amplifier circuit has been selected as the current telemetry circuit for ITOS.

2. End-of-Life Analysis

The detailed solutions given in the following sections have been obtained using a digital computer. The computer program for this analysis was originally developed for the TIROS IX satellite. It has since been augmented and perfected through its use in a number of RCA satellite projects. The computer program accepts as one input the current voltage characteristics of the power supply subsystem devices, including solar cell I-V characteristics at various temperatures. Battery characteristics are entered as functions of the battery state-of-charge and temperature. The load profile and predicted orbit temperature profile for the solar array and batteries are other inputs. The computer solves for the various voltages and currents at each minute during the orbit, using the current and voltage equations for the ITOS power supply subsystem. During the orbital run, the battery current is integrated, and the existence of an energy balance can then be readily computed.

The computer program inputs for the end-of-life analysis are summarized or referenced in Table 4-V-10. Figure 4-V-19 shows the solar cell characteristic curves.

Figure 4-V-20 is a plot of the temperature variation of a solar panel versus time in orbit, at a particular location (node 13, +X panel) on that solar panel. Because of its curvature, a solar panel is not uniformly illuminated in the general case. For this reason, different points, or nodes, on a particular solar panel are at different temperatures.

TABLE 4-V-10. COMPUTER PROGRAM INPUT DATA FOR WORST-CASE END-OF-LIFE ANALYSIS

Item	Value or Reference
Battery Characteristics	See Figure 4-V-7.
Solar Cell Characteristics	See Figure 4-V-19.
Load Profile	See Figure 4-V-1.
Orbit Daytime Array Temperatures	See Figure 4-V-20.
Battery Temperatures vs. Sun Angle	33°C at 30-degree sun angle 26°C at 45-degree sun angle, 18°C at 60-degree sun angle
Satellite Eclipse Period	
Sun Angle 30 Degrees	None
Sun Angle 45 Degrees	22 minutes
Sun Angle 60 Degrees	31 minutes
Orbit Period	113.5 minutes
Charge Current Limit (both batteries)	1.75 a
Battery Voltage Limit	See Figure 4-V-13.
Minimum Voltage Across Charge Controller at Current Limit	2 volts
Diode Drop in PSE During Battery Discharging	0.5 volt
PSE Losses	
Daytime	288 ma
Nighttime	159 ma
Total Battery Capacity	480 amp-min

TABLE 4-V-10. COMPUTER PROGRAM INPUT DATA FOR WORST-CASE END-OF-LIFE ANALYSIS (Continued)

Item	Value or Reference
Solar Cell Temp. Coefficients of I_{sc}	+140 μa/°C
Solar Cell Temp. Coefficients of V_{oc}	-2.35 mv/°C
Array Degradations (percent of original value)	
Solar Constant	96.7 percent
Power Prediction	97.0 percent
Wiring Loss	98.0 percent
Thermal Cycling	99.0 percent
Array Diode Drop (including telemetry voltage drop)	0.9 volt
Solar Cells per String	76
Strings per Array	135
Assumed Parallel String Loss (due to to random cell failures)	3

For computation purposes, the solar panels were divided into four flat segments. Eight families of temperature time plots were stored in the computer, four for the two solar panels located normal to the local vertical when in orbit, and four for the solar panel along the local vertical. The eight plots completely define the instantaneous variation of the cell temperature for a given sun angle and time of life.

The specific design of the power supply subsystem is determined from the end-of-life analysis. The solar array size is determined by a parametric study of the series and parallel arrangements of the solar cells and the minimum charge current limit rates for

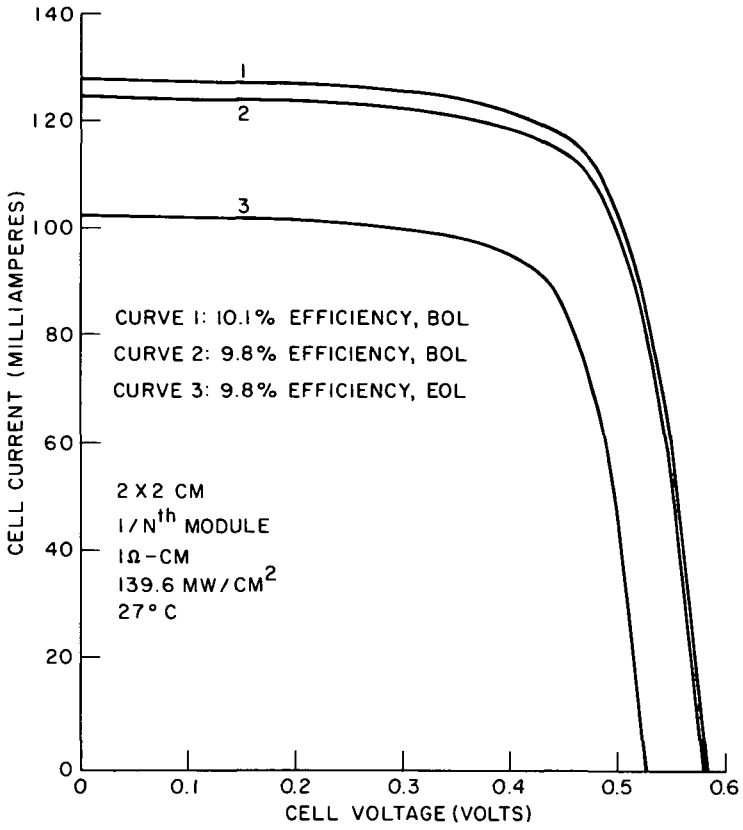

Figure 4-V-19. ITOS Solar Cell Output Curve at End of Life

the battery are established. A worst-case approach is used throughout the analysis. Therefore, the comparison of the results of the analysis with typical performance in orbit, even at the 6-months-in-orbit point, should show a much longer array lifetime using typical array degradation values.

From the computer results, the average array current at sun angles of 30, 45, and 60 degrees was determined. The curves for these current values are shown in Figure 4-V-21, along with the required array currents needed for energy balance at these sun angles. The required array current at any sun angle is equal to the sum of the load current, the power-supply subsystem losses, and the battery recharge current. The required current increases with sun angle because eclipse period increases with sun angle.

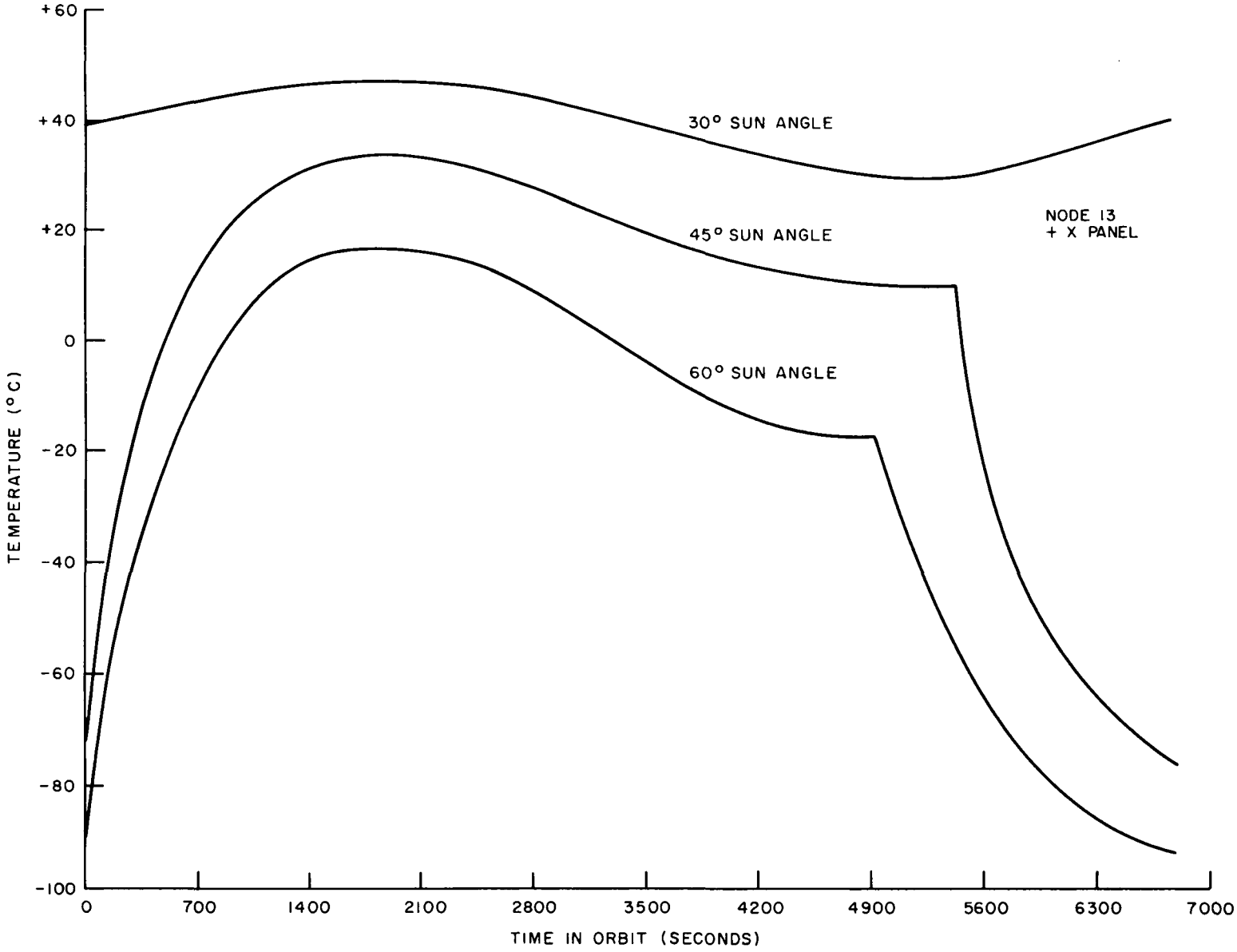

Figure 4-V-20. Solar Panel Temperature Versus Time in Sunlight at End of Life

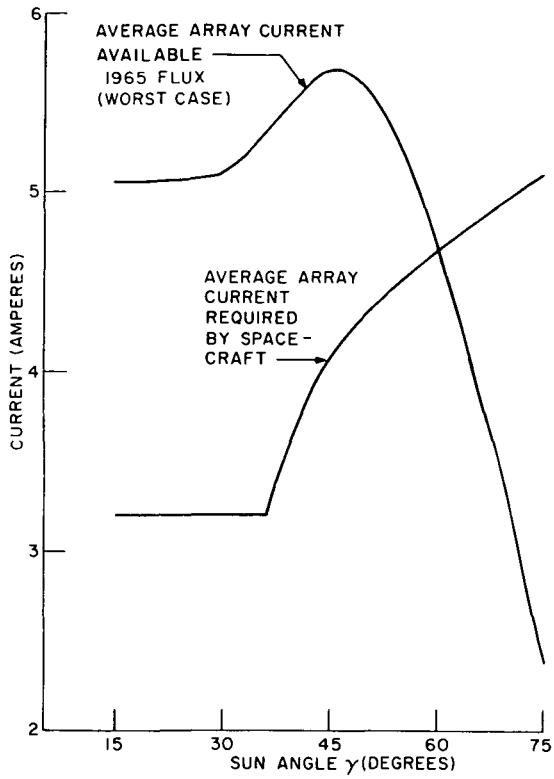

Figure 4-V-21. Daytime Average Array Current Available and Average Required Versus Sun Angle at End of Life

Conditions at the end of 6 months, as yielded by the computer program, are plotted in Figure 4-V-22 for the case of a 45-degree sun angle, for one orbital period. The voltage-limited battery voltage and the tapered charge current are illustrated in this figure. The end-of-life battery performance is based on meeting the worst-case loading over the 6-month lifetime with the ability to maintain sufficient voltage at the end of discharge to keep the regulated bus output within the ±1 percent tolerance. The worst-case voltage requirement at the battery is 26.5 volts, which comprises the following:

Regulated voltage	24.50 volts
Upper 1-percent tolerance	0.25 volt
Diode and wiring drop	0.50 volt
Regulator series drop	1.25 volts
TOTAL	26.50 volts

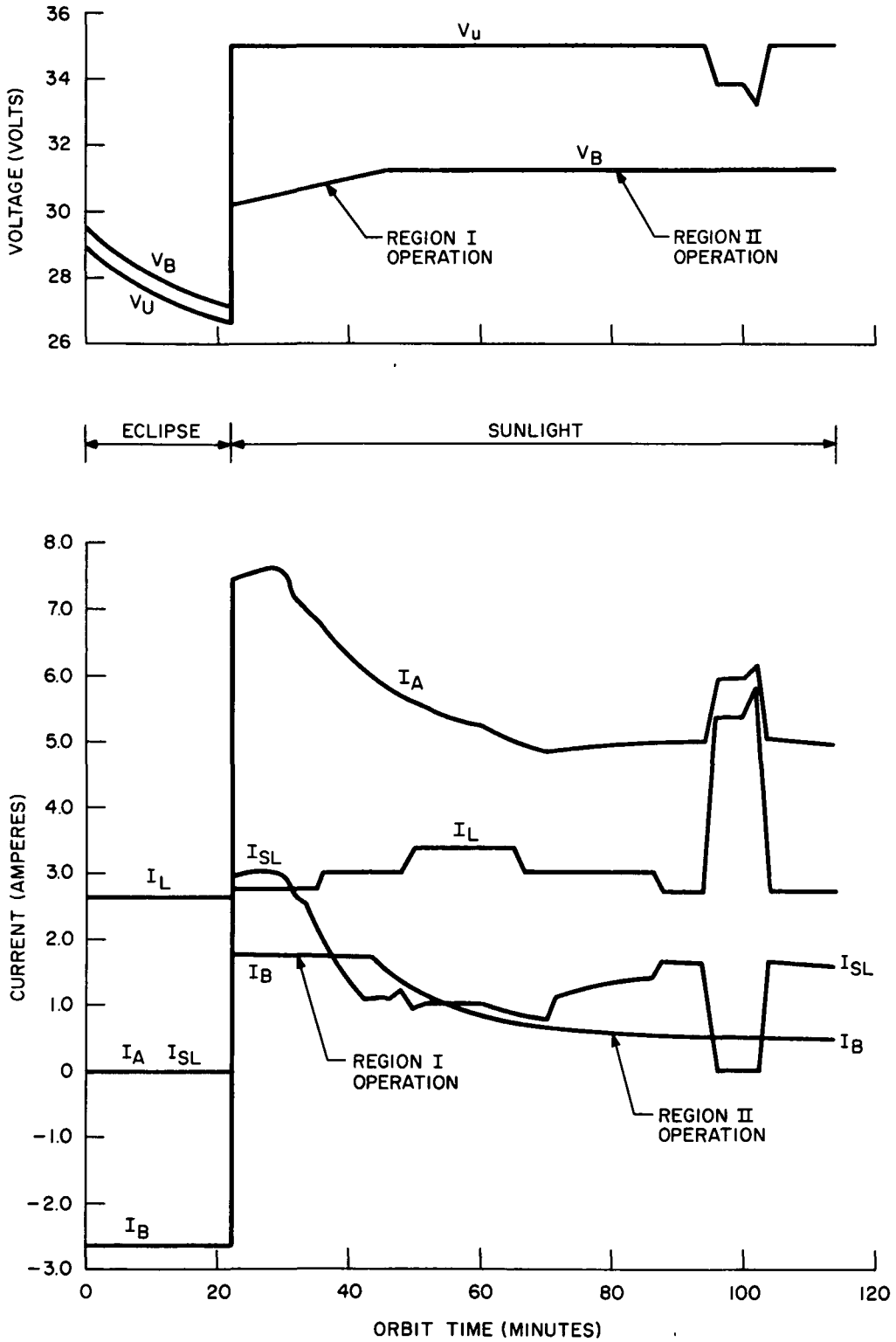

Figure 4-V-22. Power Supply Subsystem Voltages and Currents at a 45-Degree Sun Angle at End of Life

The worst-case mission for the battery is that which produces the maximum depth of discharge at the end of 6 months of charge-discharge cycling. This would occur with a launch in January at a 45-degree sun angle; by June the spacecraft would have a 60-degree sun angle. The battery would cycle every orbit for 6 months (2,300 cycles) and would endure maximum depth of discharge (31 minutes of eclipse) at the end of 6 months. Minimum depth of discharge would occur at the beginning of the mission.

When a satellite readout takes place during eclipse, the battery experiences a greater discharge. The additional battery discharge has the following characteristics:

Current Drain	2.50 amperes
Duration	8 minutes
Discharge	20 ampere-minutes

TABLE 4-V-11. REQUIRED MISSION FOR ITOS BATTERIES

Mission Month	Average Monthly Sun Angle (degrees)	Eclipse Period (minutes)	Readouts in Eclipse		Average Discharge Per Orbit (amp-min)	Average Depth of Discharge (percent)	Battery Mounting Temp. (°C)
			Full	Half			
Jan	45	22.0	70	60	72.1	15.0	30.0
Feb	46.5	23.5	10	60	73.3	15.3	29
Mar	48	24.5	0	30	74.8	15.6	28
Apr	50	26.2	0	0	79.2	16.5	27
May	55	29.0	0	0	87.7	18.3	23
Jun	60	31.0	0	0	90.3	18.8	20

However, by specifying a 45-degree sun angle launch in January with a sun angle drop to 60 degrees by June, the spacecraft orbit is defined. Since the ground stations are also known, the number of readout periods per month can be calculated. The effect of these readouts has been taken into account in Table 4-V-11. This table shows the average monthly discharge and depth of discharge for worst-case battery operation.

The battery mounting temperature is a function of sun angle and life in orbit. The battery cell temperature is assumed to be 5°C warmer than the mounting temperature. The battery voltage is inversely proportional to the temperature, i.e., a warmer battery will have a lower end-of-discharge voltage.

From battery test data, a prediction was made of end-of-discharge voltage over a cycling lifetime for the 15-percent depth-of-discharge and an initial launch condition temperature of 35°C. This prediction is shown graphically in Figure 4-V-23. Also shown in Figure 4-V-23 is a prediction of end-of-discharge voltage versus battery charge-discharge cycles for 18.8-percent depth-of-discharge and 25°C end-of-life condition. The dashed line shows an interpolation between the beginning-of-life and 6-month (end-of-life) conditions, indicating the anticipated battery performance when subject to the worst-case conditions defined in Table 4-V-11. This interpolation indicates that the battery will meet the required lifetime performance requirements under worst-case conditions.

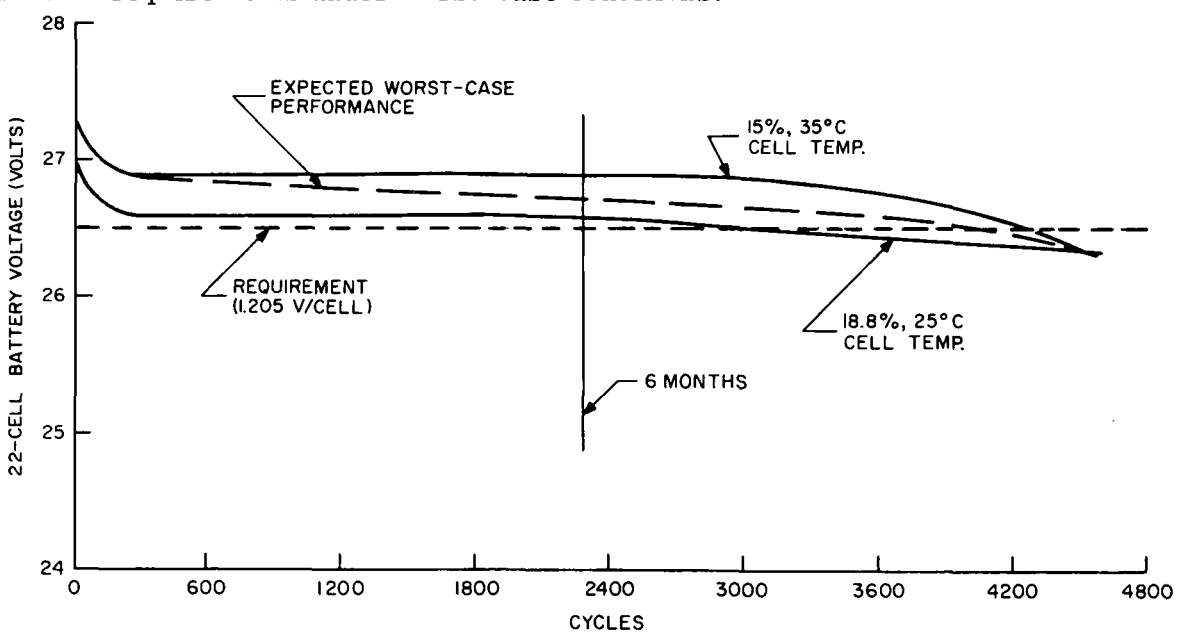

Figure 4-V-23. ITOS Nickel Cadmium Battery, End-of-Discharge Voltage Versus Battery Charge-Discharge Cycles

3. Beginning-of-Life Analysis

The device parameters determined from the end-of-life analysis were taken as a basis for determining the worst-case condition of heat generation at the beginning-of-life, which is the time of maximum solar array output. From this analysis the maximum voltage, current, and power rating requirements of the power supply subsystem electronics were developed. The assumptions used in this section are more typical of actual subsystem performance at beginning-of-life than those made for the end-of-life performance.

For the purposes of the beginning-of-life analysis, some changes were made in the computer program input data used for the end-of-life analysis. The items changed and the associated values or references are listed in Table 4-V-12.

TABLE 4-V-12. CHANGES IN COMPUTER PROGRAM DATA FOR BEGINNING-OF-LIFE ANALYSIS

Item	Value or Reference
Solar-Array Output	See Figure 4-V-4 (maximum curve)
Battery Temperatures:	
Sun Angle 30 Degrees	+33°C
Sun Angle 45 Degrees	+31°C
Sun Angle 60 Degrees	+23°C
Charge Current Limit	1.9 a
Solar Cell Temp Coefficients:	
of I_{sc}	+64 μa/°C
of V_{oc}	-2.2 mv/°C
Array Degradations	
Solar Constant	103.3 percent
Power Prediction	103.0 percent
Albedo	104.0 percent
Ultraviolet	100.0 percent
Thermal Cycling	100.0 percent
Assumed Parallel String Loss	None

Figure 4-V-24 shows both the day-averaged array current available at sun angles of 30, 45, and 60 degrees and the average shunt limiter current. This figure shows the worst-case condition at the 30-degree sun angle, based on the assumption that the initial orientation load (1.096 amperes), power supply loss (0.288 ampere), and battery charge current at 33°C (0.63 ampere) will still exist after the solar panels have been deployed. The shunt limiter current is 10 amperes (12 amperes array output minus 2.0 amperes total effective load); this is very nearly the maximum current and establishes the rating of the unit. At the shunt voltage of 36 volts, the dissipation is 360 watts. The shunt limiter is rated to dissipate the maximum array current less the fixed loads in the satellite and the minimum battery charging.

Figure 4-V-25 shows the power supply subsystem voltages and currents for a 45-degree sun angle, versus orbit time.

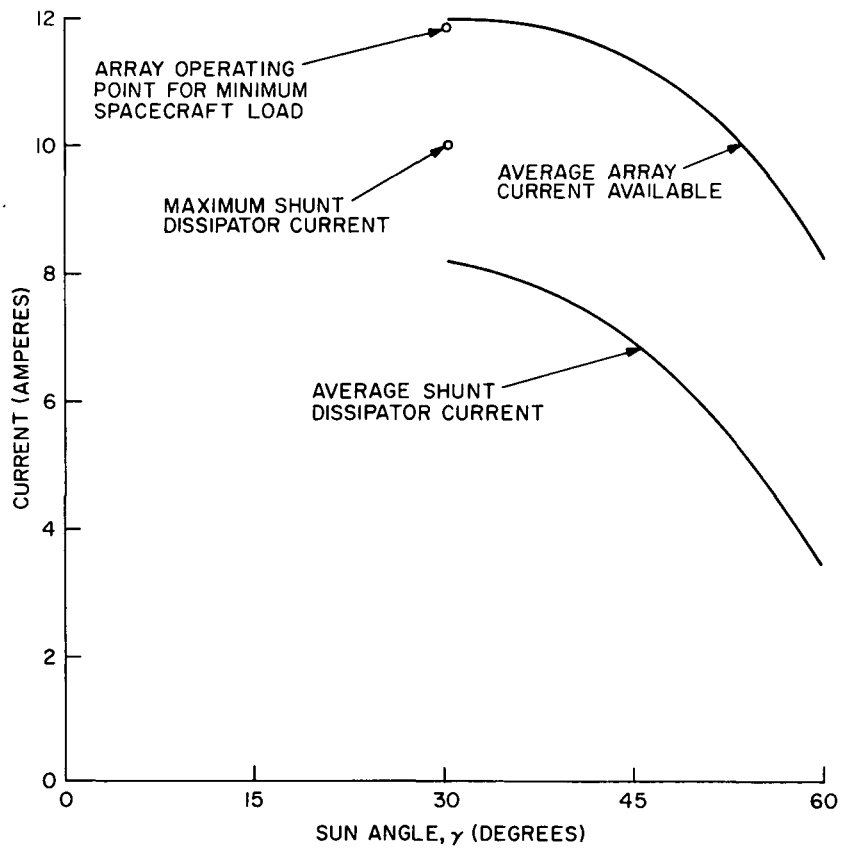

Figure 4-V-24. Average Available Array Current and Average Shunt Limiter Current Versus Sun Angle for Beginning-of-Life Conditions

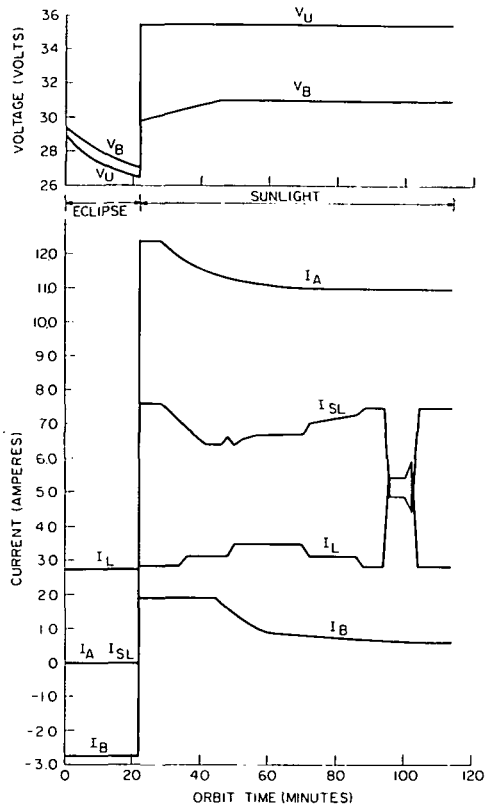

Figure 4-V-25. Power Supply Subsystem Voltages and Currents for 45-Degree Sun Angle at Beginning-of-Life

4. Preoperational Mode Analysis

The power supply subsystem design developed from the end-of-life and beginning-of-life analyses was analyzed to determine its performance and capability during the preoperational mode; i.e., the period from liftoff through proper orbit orientation and solar array deployment. This period is assumed to last for less than 24 hours.

The solar array output in the preoperational mode with the solar panels folded against the spacecraft sides is shown in Figure 4-V-26. The daytime averaged solar array output current and the required current are plotted against sun angle (measured between the spacecraft spin axis and the sun vector). Two cases are shown, representing 88- and 73-percent suntime. The array output is very nearly the same for both cases. In the 88-percent suntime case, the array current is below the required current curve for sun angles below 18 and above 162 degrees. Capability to support the preoperational load is then limited by the capacity of the batteries for sun angles less than 18 and greater than 162 degrees. The

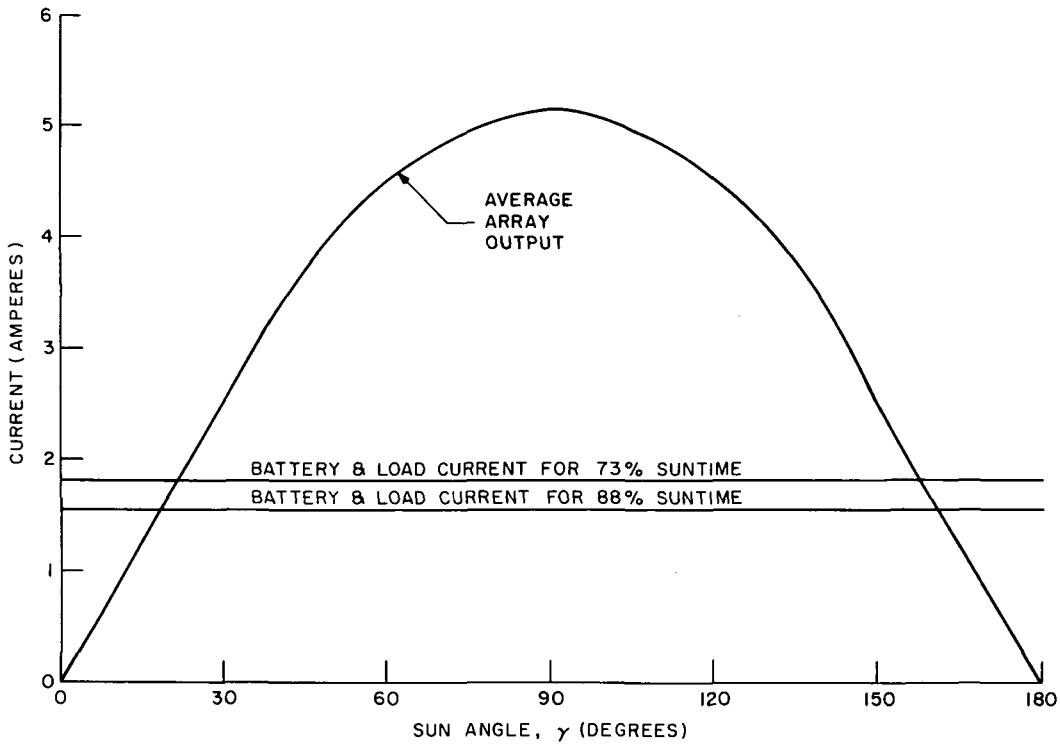

Figure 4-V-26. Solar Array Output and Load Demands Versus Sun Angle During Initial Orientation Maneuver

less than 18 and greater than 162 degrees. The situation is similar for the 73-percent suntime case, except that the limitations are more pronounced. As shown on Figure 4-V-26, the array current is below the required current for sun angles below 22 and above 158 degrees. The solar panel steady-state temperature used for both cases are given in Table 4-V-13.

TABLE 4-V-13. STEADY-STATE ARRAY TEMPERATURES DURING INITIAL ORIENTATION MANEUVER

Sun Angle (degrees)	Solar Array Temperature (°C)	
	73-Percent Suntime	88-Percent Suntime
30	-5.5	-7.0
60	+17	+20
90	+23	+25
120	+21	+23
150	+3	+2

Figure 4-V-27 shows the solar array output current for one revolution of the spacecraft during the orbit, based on a spin rate of 2 rpm. The zero output current point indicates that there is not a solar panel on the fourth side of the spacecraft. The 88-percent suntime case is illustrated in this figure.

5. Analysis of Typical Performance

a. Evaluation of ESSA 2 Data

In analyzing the typical expected performance of ITOS, a limited evaluation of telemetry data from the ESSA 2 power supply subsystem was performed. Because of differences in orbital conditions of ESSA 2 and ITOS, ESSA 2 degradation factors could not be applied directly to the ITOS array. The ITOS spacecraft has three large surfaces containing 1-ohm-cm solar cells; ESSA 2 has 19 smaller surfaces containing 10-ohm-cm solar cells. Differences in tamperature, operating point on the solar array I-V curve, amount of back shielding and radiation environment (1966 for ESSA 2 and 1968 for ITOS) invalidate direct comparisons, even though the two spacecraft have nearly the same orbit.

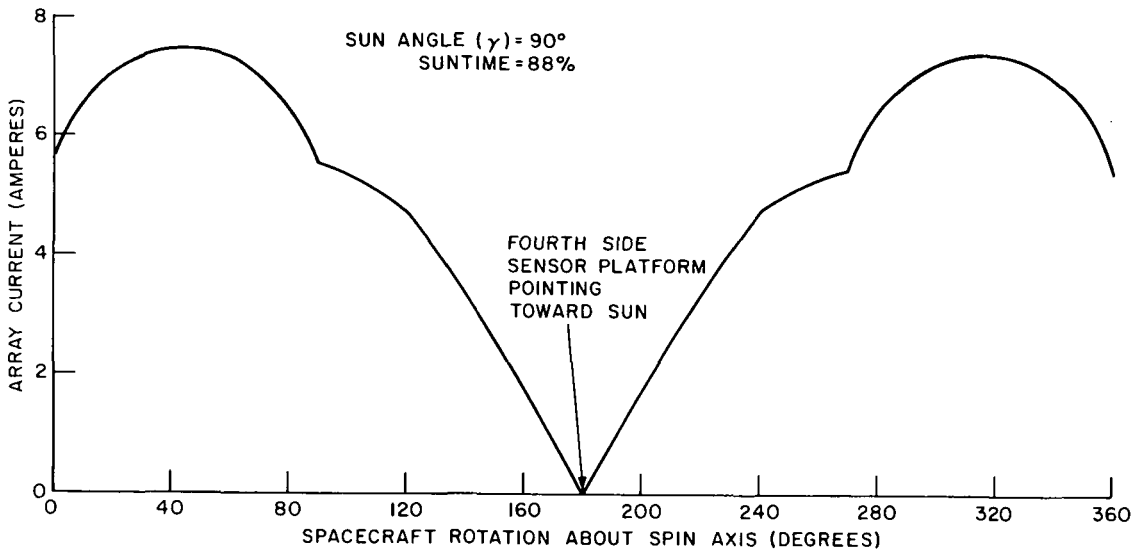

Figure 4-V-27. Solar Array Output During Initial Maneuver (Solar Panels Folded)

However, the evaluation of ESSA 2 data is significant because it permits a valid comparison to be made between array performance prediction and actual performance in orbit.

The prelaunch estimation of ESSA 2 typical performance in orbit was not based on worst-case factors. ESSA 2 actual orbital performance was later compared with this estimate in order to judge the accuracy and validity of the estimate. Analysis of the ESSA 2 telemetry data proved to be arduous because of the scatter of the values and because of variations in sun angle and array temperature. Results for array voltage higher than 31 volts were computed separately from results for array voltage lower than 31 volts so that results associated with degradation of array current alone could be evaluated apart from those associated with degradation of both current and voltage.

After 8 months of operation in orbit, current had degraded to 0.9 and the power to 0.85 of original values. Thus the actual power loss at close to the maximum power point was 15 percent after 8 months in orbit; the prelaunch estimate was 14-percent power loss after 6 months in orbit and 20-percent loss after 9 months.

Because a typical performance estimate is closer to actual performance than is a worst-case performance estimate, a typical performance estimate was made for ITOS. For this estimate, the expected 1968 radiation environment was used with nominal ITOS performance factors for sun angles ranging from 15 to 75 degrees.

b. Typical ITOS Array Degradation

Array degradations after 6 months, 12 months, and 2 years were calculated for ITOS based on the predicted 1968 radiation environment. The calculated degradations were used in the computer energy balance program to establish the nominal capability of the array as a function of sun angle. Average daytime array current and load current are shown in Figure 4-V-28. The efficiencies of the battery and of the system were used in making the load current calculation; these values are also shown in Figure 4-V-28. The worst-case curve for the array, after 6 months of operation in a 1965 radiation environment, is also represented in the figure.

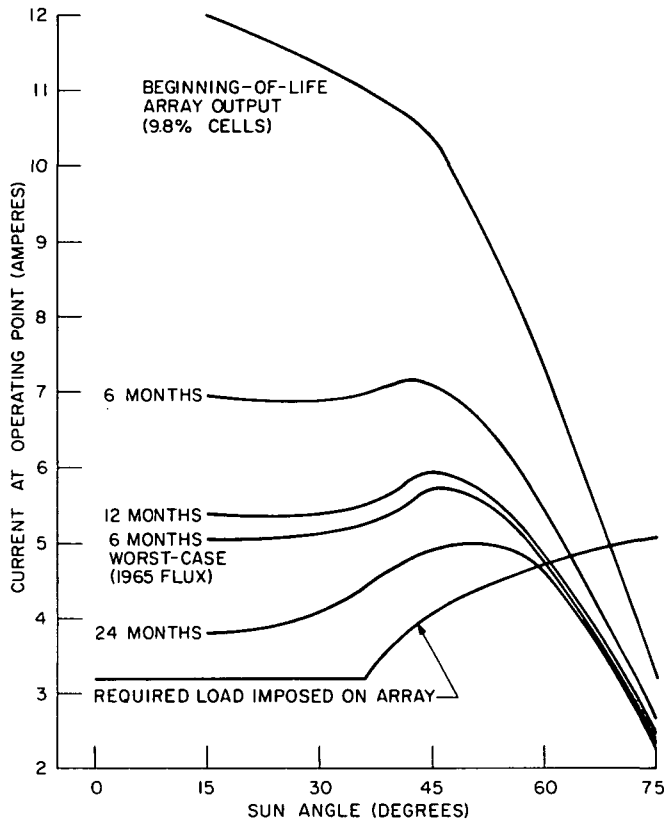

Figure 4-V-28. Typical ITOS Daytime Average Solar Array Output and Load Current Requirements

It is evident that energy balance is achieved at all sun angles of less than 60 degrees, even after 2 years of typical performance. The 6-month worst-case array was designed to supply the load and to achieve energy balance at the 60-degree sun angle. After 2 years, the typical array suffers greater degradation from the radiation environment than does the 6-month worst-case array; however, none of the worst-case factors have been applied except 0.25 percent for model inaccuracy and 2 percent for voltage losses due to resistance in the wiring. All other factors, including the solar constant, have been assumed to be 1.0.

The curves, other than those for beginning-of-life, are shown to have relatively low array capability at sun angles of 30 degrees and less. This is because the curves are based on computations of array output that involve the load operation point, which is also shown. At

the higher temperatures at which the array will operate in 100-percent suntime, this load operation point is to the right of the array maximum power point. If the load were increased, the array voltage would decrease and the output current would increase. This increase would be limited after the maximum power point had been attained, and with further load increases the array would be unable to supply the load demand. For example, the array capability after 24 months at a 30-degree sun angle is shown to be 4.1 amperes. If the load were increased to make the array operate at a maximum power point, the array voltage would be 28.2 volts. This voltage is too low to charge the batteries or even to keep the batteries in a charging state. However, it is above the regulator input specification value of 26.5 volts, so the load requirements would be satisfied.

6. Performance After Battery Failure

a. Open Battery

ITOS will contain two 4-ampere-hour batteries interconnected by diodes to the common loads. A study was made of the possible modes of operation of the power supply subsystem in the event of a battery failure. The first failure mode studied was one in which one of the two batteries failed, becoming an open circuit. The recharge rate for the other battery was assumed to be the nominal 0.95-ampere rate, with nominal current limiting.

No energy balance problem would exist at sun angles below 36 degrees, which corresponds to 100-percent suntime and negligible battery discharge. As the sun angle increases, the eclipse period increases, having a twofold effect on the battery:

- As the eclipse period increases, the depth of discharge increases.
- As the sun illumination period (percent of suntime) decreases, battery recharge time decreases.

This relationship between sun angle and eclipse period is shown in Figure 4-V-29.

It has been found that the critical energy balance point at the beginning-of-life is a 27.5-minute eclipse, with one open battery. As shown in Figure 4-V-28, this corresponds to a 52-degree sun angle. Thus, energy balance would be maintained at sun angles below 52-degrees.

At the end of 6 months, there is a greater drain on the battery due to data readout than at the beginning-of-life, which causes the battery to discharge even during daylight. Because of this 8-minute daylight discharge, the daylight time for recharge is decreased by 8 minutes. Energy balance can only be maintained with an eclipse period of 24 minutes or less, which corresponds to a 47.5-degree sun angle.

If readout should occur during eclipse at the end of 6 months, the increased battery load would be more severe and a longer illumination period would be required for recharge. Energy balance could only be achieved with a 21-minute eclipse period or a 44-degree sun angle.

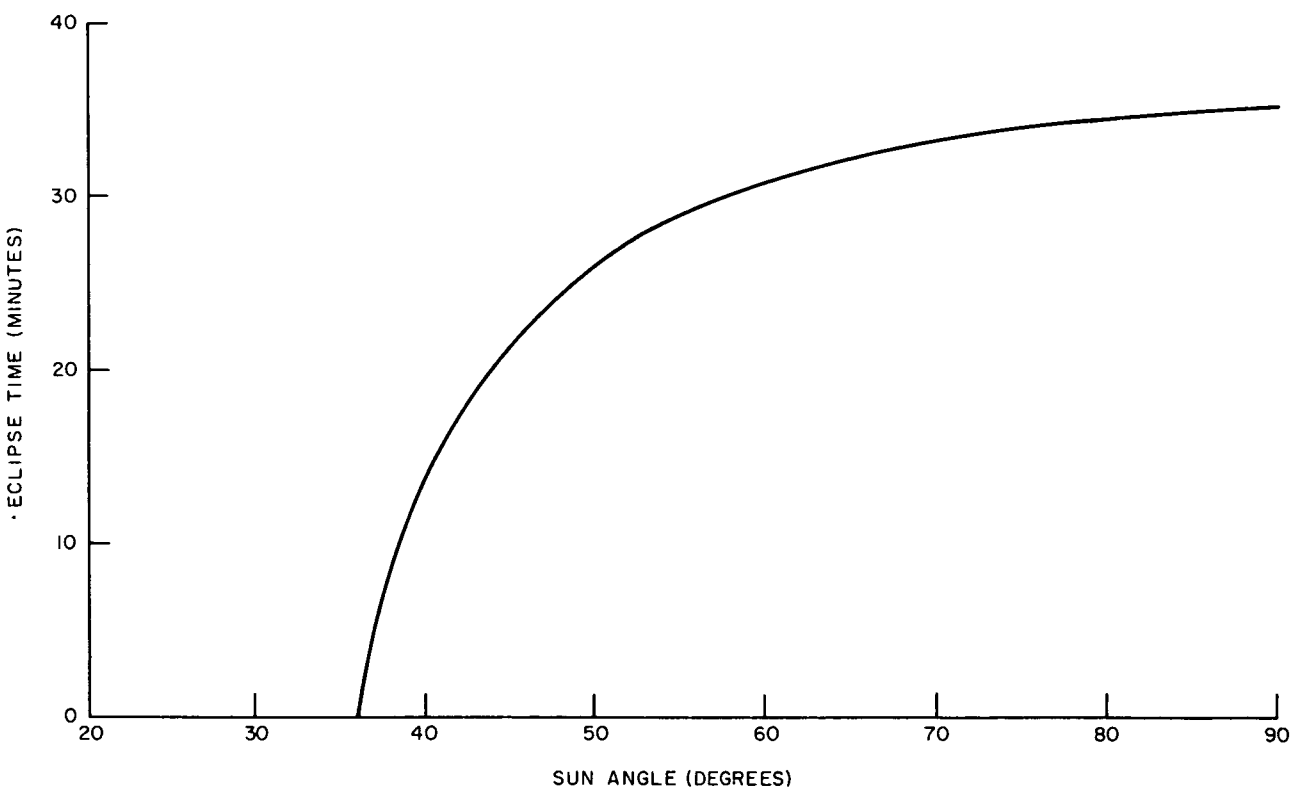

Figure 4-V-29. ITOS Eclipse Time Versus Sun Angle

In order to operate at a 60-degree sun angle at the end of 6 months, the average nighttime load would have to be reduced. Energy balance could be maintained with a 1.9-ampere load compared with the present 2.8-ampere load; a load reduction of 0.9 ampere during eclipse will allow the spacecraft to operate satisfactorily.

b. Shorted Battery Cells

Partial or complete cell short circuiting may occur, the partial short circuit failure mode being the more probable. In this mode, the battery would still accept charge current, but during discharge it would behave more like a 21-cell battery and would deliver little current. Exact effects are dependent on the degree of shorting, which is difficult to predict.

An extreme case of shorting is a dead short circuit across a cell. In this case, battery charging would exist, and the battery voltage would not reach the voltage limit unless each cell were to reach a voltage 22/21 times the planned voltage limit. Continuous overcharging at the nominal 0.95-ampere rate would produce high pressure in the cells, which might cause the seals to fail and release electrolyte into the spacecraft.

In view of the established reliability of batteries, the likelihood of a cell failure is small and a cell failure resulting in a short circuit is remote. It is possible to guard against shorted batteries by including a command-operated isolating switch in the battery line, but, with this safeguard, the possibility of switching both batteries off accidentally exists.

c. Reliability Analysis

NOTE

The following reliability analysis is based on 6 months of operation (2,300 charge-discharge cycles) at 17.5-percent depth-of-discharge. It is included here because it is compatible with the worst-case battery life of 6-month operation (2,300 charge-discharge cycles) varying from 15.0 to 18.0-percent depth-of-discharge.

A considerable amount of battery cycle testing has been conducted by Crane Laboratories on storage cells of the type selected for ITOS. The results given here were obtained from the crane data. For ITOS, the data reported is based on cell "wearout", which is defined as cell voltage diminishing to 1.205 volts (the average cell voltage required to produce 26.5 volts minimum from the battery). Six months in the ITOS orbit is equivalent to a maximum of 2300 charge-discharge cycles (assuming that nighttime occurs every orbit) and battery performance is characterized by a gradual deterioration with time in orbit. The 2300-cycle case represents continuous operation at a 60-degree sun angle. While this is an unrealistic situation, the assumption serves to establish a boundary on battery reliability. As discussed above, the possibility of open or short circuits is extremely remote so that, as indicated by the data in Table 4-V-14, battery reliability is not affected by the use of one or two batteries, but is highly influenced by depth-of-discharge and battery temperature.

Table 4-V-13 summarizes the probability of battery survival for the case of 6 months of operation (2300 cycles) at 17.5-percent depth of discharge. Extremely high reliability is indicated for temperatures between 10 and 20°C. Above 20°C, reliability diminishes; at 30°C, it is slightly under 90 percent.

Table 4-V-13 also summarizes probability of battery survival for 1 year of operation (4600 cycles). Only at 10°C (and slightly higher temperatures) is battery reliability above 90 percent for 17.5 percent depth-of-discharge. At 20°C, the probability of supplying 1.205 volts per cell diminishes to a low value (0.6554).

The numbers given in Table 4-V-14 are somewhat pessimistic since they refer only to the greatest depth-of-discharge corresponding to a 60-degree sun angle. If the sun angle were less than 60 degrees, reliability would improve. For sun angles of 36 degrees or less, the battery would have 0-percent depth-of-discharge and increased lifetime, since there would be no wearout due to charge-discharge cycling.

The 17.5 percent depth-of-discharge case represents normal battery operation at a 60-degree sun angle, whereas 35-percent depth-of-discharge would only occur if one battery were to fail, leaving the second one to bear the full load.

TABLE 4-V-14. PROBABILITY OF BATTERY SURVIVAL
(FOR 6 MONTHS AND 1 YEAR)

Temperature (°C)	+30 to -30 V Battery Terminal Voltage Range (mv)	Average Cell Voltage (volts)	Probability for 1.205 Volts at End-of-Life
Battery, 6-Month Lifetime (2300 cycles) at 17.5-Percent Depth-of-Discharge			
10	30	1.235	0.9999
20	30	1.225	0.9938
30	100	1.210	0.8849
Battery, 1-Year Lifetime (4600 cycles) at 17.5-Percent Depth-of-Discharge			
10	30	1.225	0.9938
20	50	1.215	0.6554
30	130	1.192	Negligible

The probability of survival for 6 months (2300 cycles) with 35-percent depth of discharge is small under all circumstances, but, as discussed previously, the system would be incapable of recharging the battery from this state anyway. In the event of one battery failure at large sun angles, the eclipse load would have to be reduced to within the capability of one battery.

In summary, for the battery design case (i.e., 6 months at 17.5-percent depth-of-discharge), reliability is 88 to greater than 99 percent between 10 and 30°C. These results are pessimistic because of the assumption of continuous spacecraft operation at a 60-degree sun angle. For 1-year operation, the reliability would diminish considerably at temperatures exceeding 10°C.

7. Fusing

The study of electrical fusing was made with the intention of increasing power supply reliability. Factors under consideration were:

- Protection of the power supply itself by removal of a faulty load, so that normal operation is resumed without overstress,
- Availability of suitable fuses,
- Choice of fuse size to achieve a balance between circuit protection and reliability,
- Availability of current from the regulator to remove the fault by fuse destruction, and
- Current limitation due to connectors, circuits, and components to a value too small to blow a fuse when a fault condition occurs.

These factors dictate that fuse ratings be large enough to withstand normal currents and expected operational transients but small enough to provide protection. A margin of safety is required between maximum normal stress and fuse operation. To apply this margin, information is required about time-current characteristics of available fuses, circuit transients and their effects on fuses, environmental conditions and their effects on fuse characteristics, and fuse thermal inertia, which determines speed of response.

For other programs, samples of suitable buses were tested on a statistical basis to establish verification of manufacturer-published time-current curves and to secure data for determining:

- Tolerance bands about these curves,
- Relative effects of transient and steady current for fuse blowing, and
- Effects of temperature, vacuum, and vibration conditions on fuses and ratings.

Two suitable fuse types are available for use on ITOS. They are (1) the Littelfuse High-Reliability Subminiature Picofuse and (2) Pyrofuze exothermic fuse wire. Compared to the Picofuse, the Pyrofuze wire has the following two disadvantages:

- Larger size. The Pyrofuze wire must be at least 1 inch long for repeatable results. Moreover, each change in length gives a different time versus current curve.
- Encapsulation. When fused, the wire vaporizes and is deposited around the container. Encapsulation changes the response time, and larger tolerance bands are required.

The Littelfuse Picofuse has been used in other space programs, and it is suitable for ITOS applications, which require fast response for currents of 5.0 amperes and lower. These fuses are hermetically sealed and have excellent shock and vibration characteristics.

On the basis of these considerations, it is recommended that Littelfuse Picofuses be used for ITOS, and that Pyrofuze fuses be used only if an application calling for a slower response is encountered.

Picofuses are available in 11 sizes, ranging from 0.125 to 5.0 amperes. A time-current plot for this type of fuse is shown in Figure 4-V-30. The plot shows the relationship between the amount of current above which the fuse is certain to blow and the time that current is applied. The curves are labeled according to the manufacturer's published ratings.

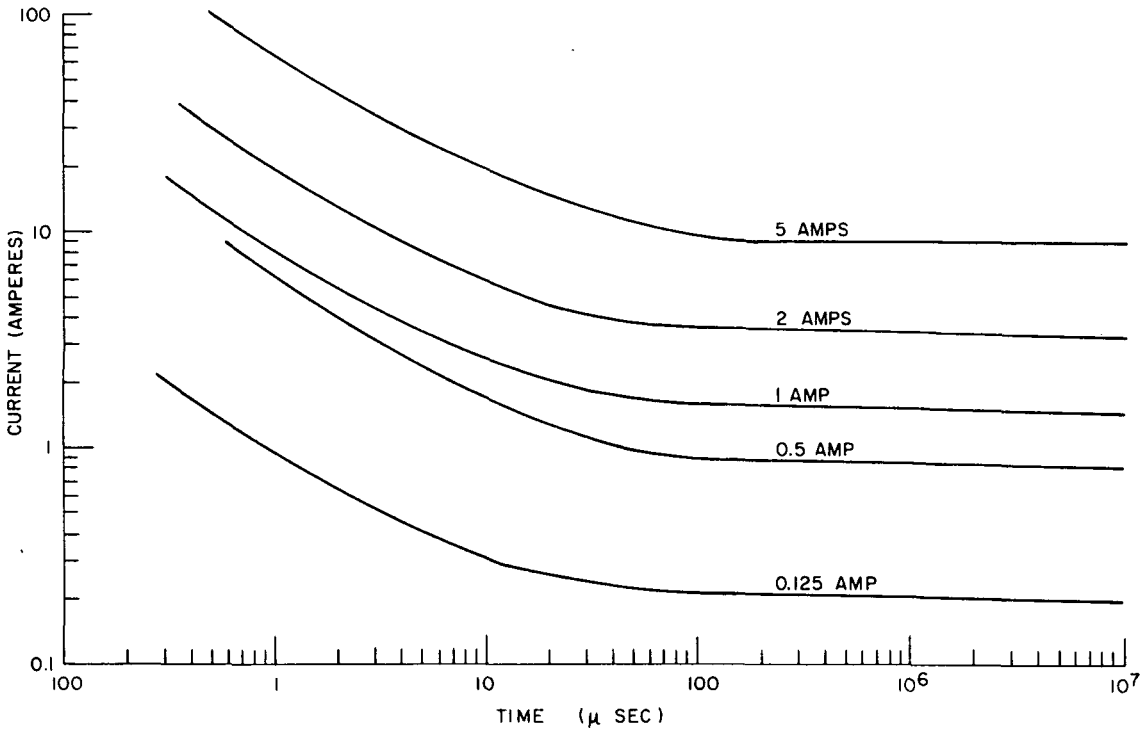

Figure 4-V-30. Picofuse Time-Current Curves at 25°C

A safety margin of 2-to-1 has been applied to the manufacturer's rating to guard against unwanted open fuses. Thus, a 0.5-ampere load would be protected with a fuse rated at 1 ampere. As shown in Figure 4-V-30, a current of approximately double the rating is certain to blow the fuse. Therefore, a safety margin of up to 4-to-1 exists, using a 2-to-1 derating factor as a criterion for selecting fuse size. Fuse sizes shown in Table 4-V-14 are based on that criterion.

E. POWER DISSIPATION

1. General

The power dissipation in the main body of the spacecraft was evaluated for each mode of the ITOS mission. For purposes of the power dissipation study, the spacecraft body was divided into an AVCS equipment panel, an APT equipment panel, and the baseplate. An iterative procedure was used to relate predicted temperatures to the estimates of power dissipation of the equipment on these surfaces.

2. Initial Orientation Maneuver

In predicting the power dissipation during the initial orientation maneuver, the following assumptions were made:

Solar panel position:	Stowed
Spacecraft spin rate:	2 rpm
Sun angle range:	30 to 150 degrees
Suntime:	88 and 73 percent

Figure 4-V-31 shows the baseplate temperatures (derived by thermal analysis) used to determine the battery temperatures. Figure 4-V-32 shows the corresponding total power dissipation of all the components located on the baseplate.

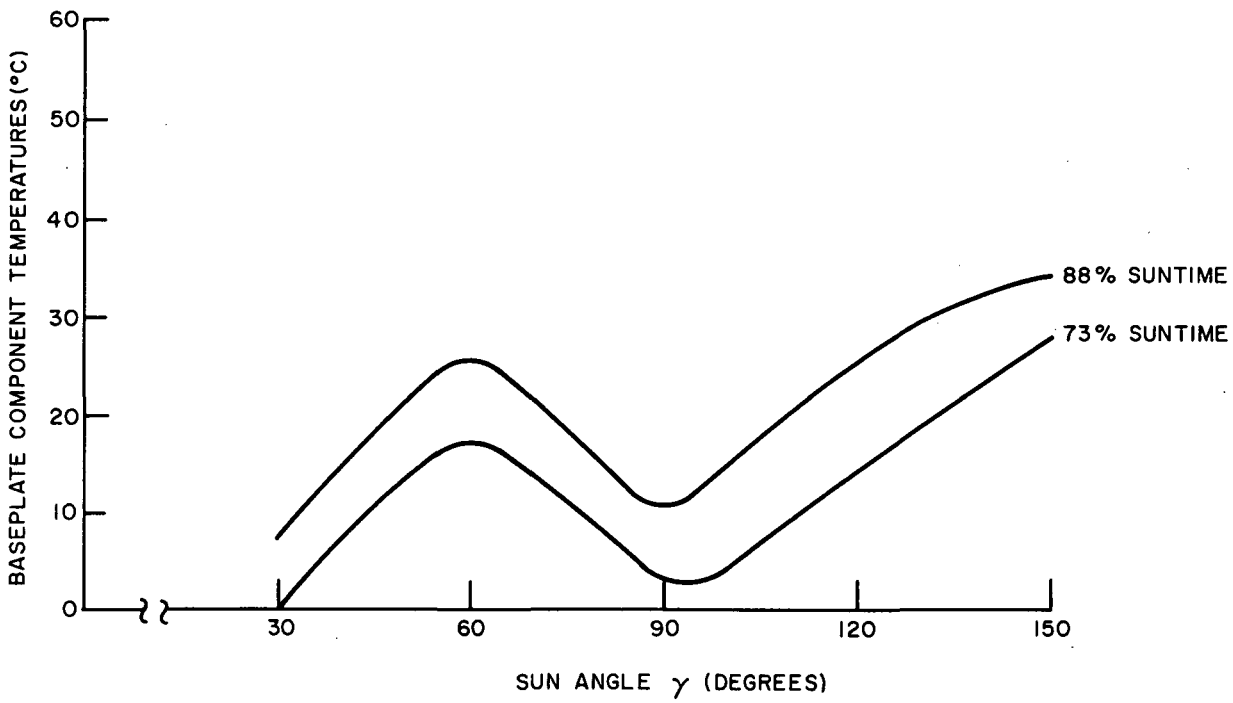

Figure 4-V-31. Baseplate Component Temperatures Versus Sun Angle During Initial Orientation Maneuver

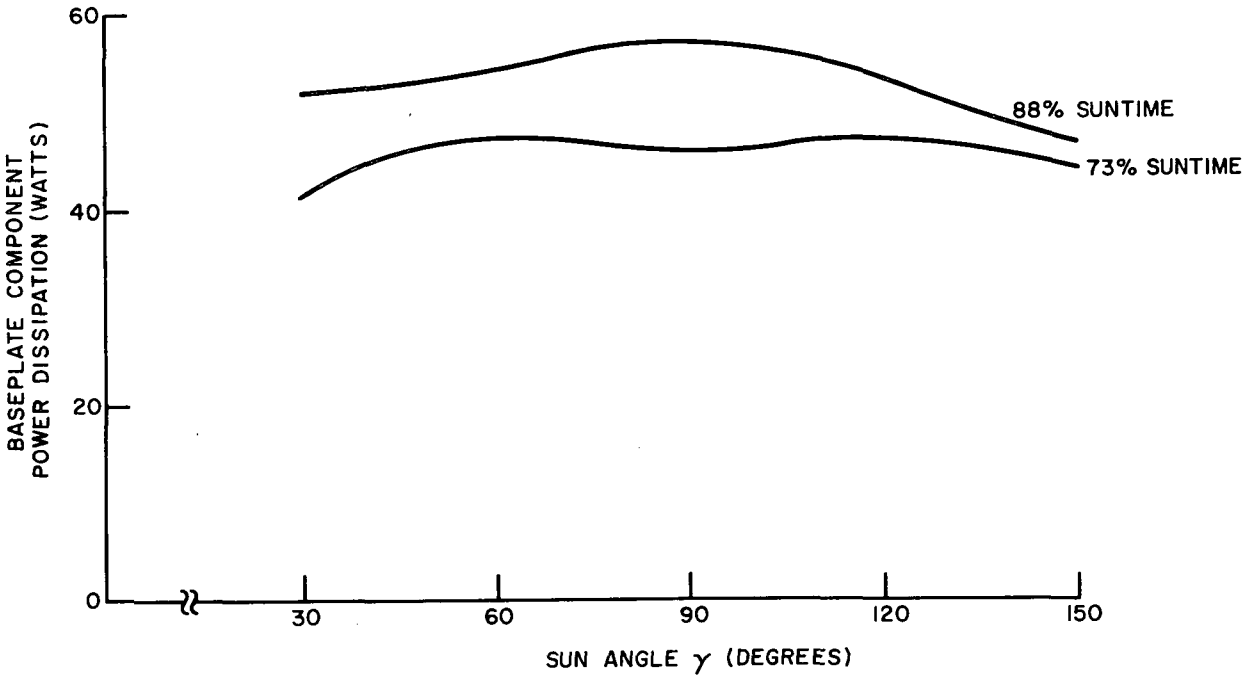

Figure 4-V-32. Baseplate Power Dissipation Versus Sun Angle During Initial Orientation Maneuver

3. Operational Mode

In predicting the power dissipation during the operational mode, the following assumptions were made:

Solar panel position: Deployed

Sun angle range: 30 to 60 degrees

Average dissipation per orbit was calculated from the ITOS load profile shown in Figure 4-V-1 for the AVCS equipment panel, the APT equipment panel, and the baseplate. This study showed that the power in the AVCS and APT equipment panels remains constant at 4.8 and 18.4 watts, respectively, for all conditions studied. The baseplate power, however, varies with sun angle and length of life. Figure 4-V-33 presents the beginning-of-life and 6-month baseplate power dissipation for the range of sun angles. Thermal analysis showed that with this dissipation the temperatures assumed initially were still valid.

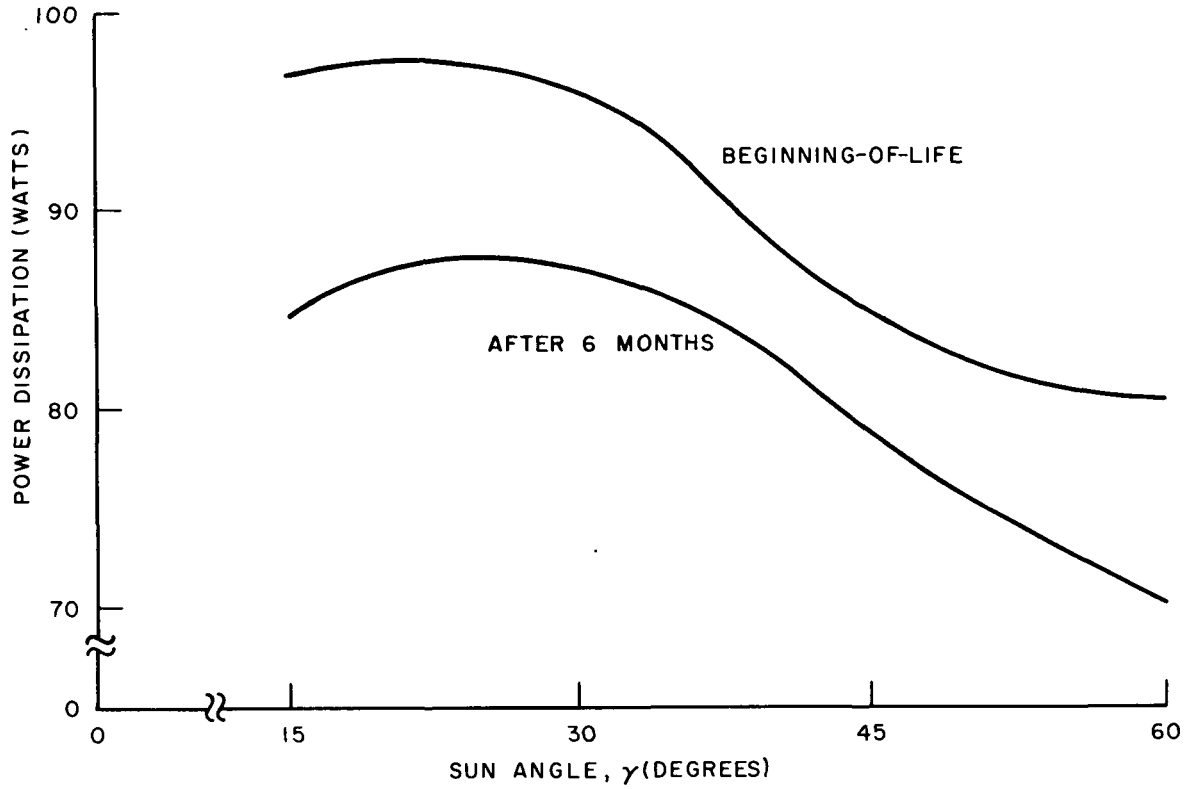

Figure 4-V-33. Baseplate Power Dissipation Versus Sun Angle During Operational Mode

F. TELEMETRY POINTS

1. General

A list of the required telemetry measurements for the ITOS power supply subsystem is shown in Table 4-V-15. These measurements are basically the same as those used on the TOS satellites. The following measurements were added for ITOS:

- The shunt limiter control amplifier ON/OFF indication,
- The shunt dissipator temperature on each solar panel, and
- The high-temperature cutout override verification indication.

The array voltage, the battery voltages, and the regulated and unregulated bus voltages use suppressed-zero measuring circuits for increased accuracy. There channels are sufficient to enable fault analyses to be performed if necessary, and successfully completed command may be confirmed.

TABLE 4-V-15. POWER SUPPLY SUBSYSTEM TELEMETRY LIST

Designation	Description	Location of Sampling Point	Telemetry*
I_{1A}, I_{1B}, and I_{1C}	Solar array current	PSE	AD
I_2	Shunt limiter current	PSE	A
I_3	Battery No. 1 charge current	PSE	AD
I_4	Battery No. 2 charge current	PSE	AD
V_1	Solar array voltage	PSE	AD
V_2	Battery No. 1 voltage	PSE	AD
V_3	Battery No. 2 voltage	PSE	AD
V_4	Unregulated bus voltage	PSE	AD
V_5	Regulated bus voltage	PSE	A
V_6	Shunt limiter control amplifier ON/OFF	PSE	A
V_7 **	Regulator selection	PSE	A
V_8 **	Charge current cutoff verification	PSE	A
T_1	Battery No. 1 temperature	PSE	A
T_2	Battery No. 2 temperature	PSE	A
T_3	Shunt dissipator temperature	Solar panel 1	AD
T_4	Shunt dissipator temperature	Solar panel 2	AD
T_5	Shunt dissipator temperature	Solar panel 3	AD
T_6	PSE temperature	PSE	D

*A = Analog.
D = Digital.
AD = Analog and digital.
**Combined in PSE.

TABLE 4-V-15. POWER SUPPLY SUBSYSTEM TELEMETRY LIST (Continued)

Designation	Description	Location of Sampling Point	Telemetry*
T_7	Solar panel 1 temperature	Panel 1	AD
T_8	Solar panel 2 temperature	Panel 2	AD
T_9	Solar panel 3 temperature	Panel 3	AD

*A = Analog.
D = Digital.
AD = Analog and digital.

In general, only voltages, currents, and temperatures are required to determine the equipment status. The telemetry circuits are all located in the power supply electronics.

2. Battery Charge and Solar Array Current Telemetry

The telemetry circuit shown in Figure 4-V-34 provides a means for sensing current and converting it to an analog telemetry signal.

Two common base amplifiers (transistors Q4 and Q5 in Figure 4-V-34) produce a voltage gain by virtue of the input-to-output impedance transformation. Fixed bias is applied to the base of Q4 by the voltage divider connected across zener diode CR1. The temperature-dependent characteristics of the base-emitter junctions of transistors Q1 and Q4 are virtually identical; therefore, the bias voltage divider tends to track variations in base-to-emitter voltage, V_{BE}, of Q4 due to changes in ambient temperature. The bias circuit of transistors Q3 and Q5 is similar to that of Q1 and Q4 with diode CR2 acting as a fixed-base voltage source. Zener diode CR2 also maintains a maximum voltage limit on the telemetry output, thus preventing excessive voltages from being applied to the telemetry encoder. Transistor Q2 serves as a constant current source for the bias network. Resistors R1 and R2 form a voltage divider which determines bias voltage at the base of Q2. The resistance of R7 determines the collector current flowing in Q2. Variable resistor R5 sets the bias for the first stage and thus controls the offset level of the telemetry characteristic. This adjustment does not, however, affect the circuit gain or slope of the telemetry characteristic.

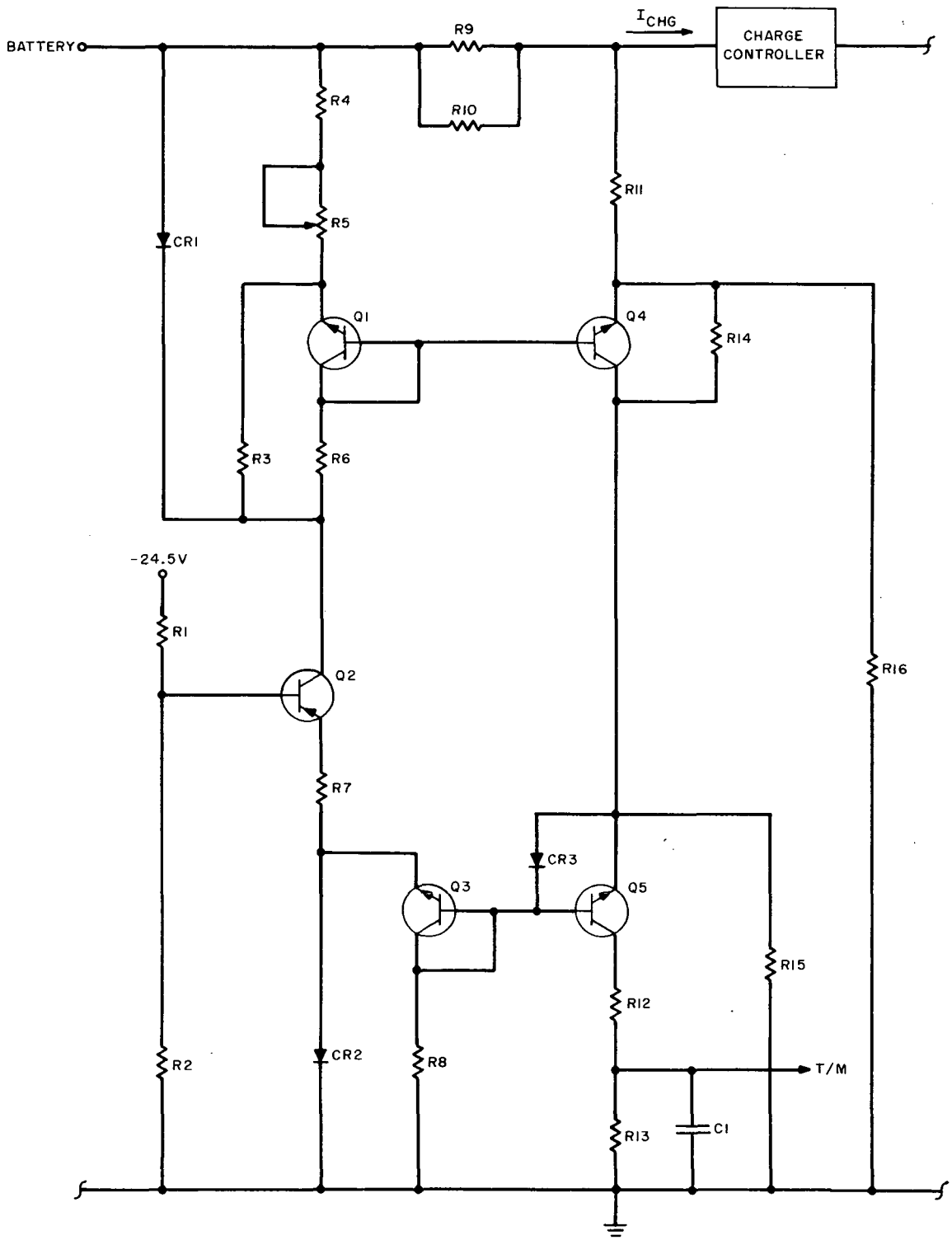

Figure 4-V-34. Battery Charge and Solar Array Current Telemetry Circuit, Schematic Diagram

Current-sensing parallel resistors R9 and R10 are connected in series with the current to be measured. Two resistors in parallel reduce the risk of losing the function in the event that one resistor should fail by opening. As the current varies through its range, a voltage is developed across the sensing resistors. Transistors Q4 and Q5 amplify this voltage drop to produce the telemetry signal. Resistor R11 aids in stabilizing the voltage gain through degeneration. In order to achieve linear amplification, the transistors are operated in the central portion of the collector load lines. A voltage offset prevents transistor Q5 from operating with its collector current in the cutoff region, while the initial current through resistor R15 accomplishes the same result in the circuit of transistor Q4. Therefore, when the signal current is zero, collector currents are minimum and the telemetry signal is a nominal 0.5 volt. Resistors R14 and R16 are used to reduce the error in telemetry output voltage caused by supply voltage variations. The collector current flowing in a transistor is not entirely independent of collector voltage and tends to increase slightly with an increase in applied voltage. Compensation for this effect is achieved by modifying the bias on the transistor with R16 in a manner that reduces base current as voltage increases. Resistor R14 is used to "swamp" variations of collector resistance with temperature. Capacitor C1 prevents high-frequency noise from appearing in the telemetry output.

3. Voltage Telemetry

A typical voltage telemetry circuit is shown in Figure 4-V-35; this circuit provides zero suppression for greater telemetry accuracy and better resolution and is used to measure battery, regulated bus, and unregulated bus voltages.

The output across resistor R2 is present when the voltage to be telemetered exceeds the reference voltage established at the base of transistor Q1 by the zener diode CR3. The resulting voltage across the base-emitter junction of Q1 and R1 provides a collector current in Q1 virtually independent of the collector voltage. The voltage gain of the circuit is a direct function of the R2/R1 ratio. Therefore, the offset and slope of the telemetry curve are provided respectively by CR3 and R2/R1. The capacitor C1 across R2 prevents high-frequency noise from appearing in the output.

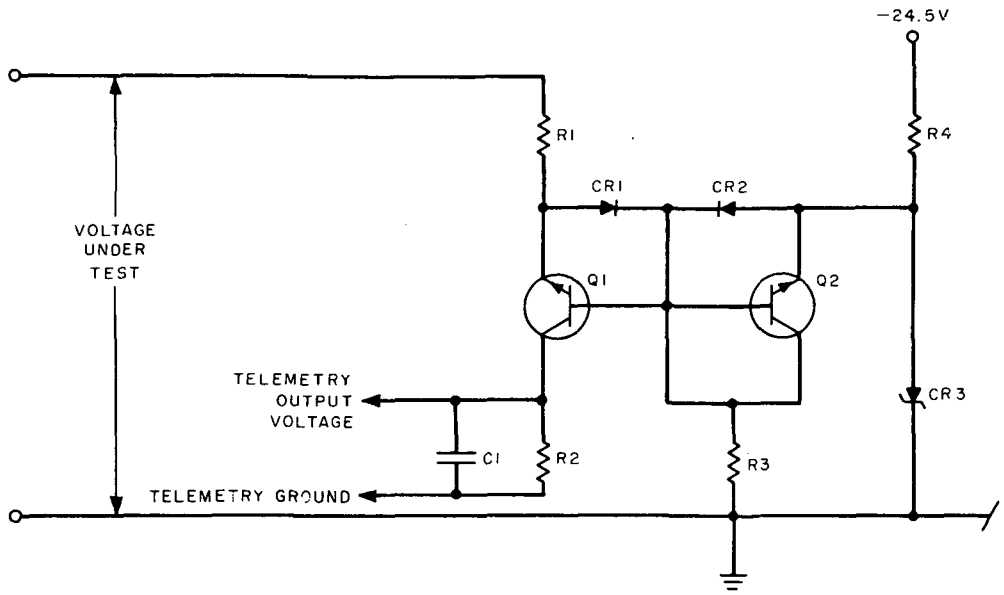

Figure 4-V-35. Typical Voltage Telemetry Circuit, Schematic Diagram

The regulated bus voltage telemetry circuit differs slightly from the typical circuit. Components CR3 and R4 are replaced by two resistors and two Zener diodes, since the reference voltage is supplied from the unregulated bus, as shown in Figure 4-V-36.

4. Temperature Telemetry

A typical temperature telemetry circuit is shown in Figure 4-V-37. Thermistor R_T is mounted in the area to be measured. Any change in temperature causes a change in the thermistor resistance, and, in turn, a change in the current flowing through the output resistor R2. A temperature-compensated Zener diode provides a well regulated voltage source for the resistor-thermistor network. Capacitor C1 prevents high frequency noise from appearing in the output.

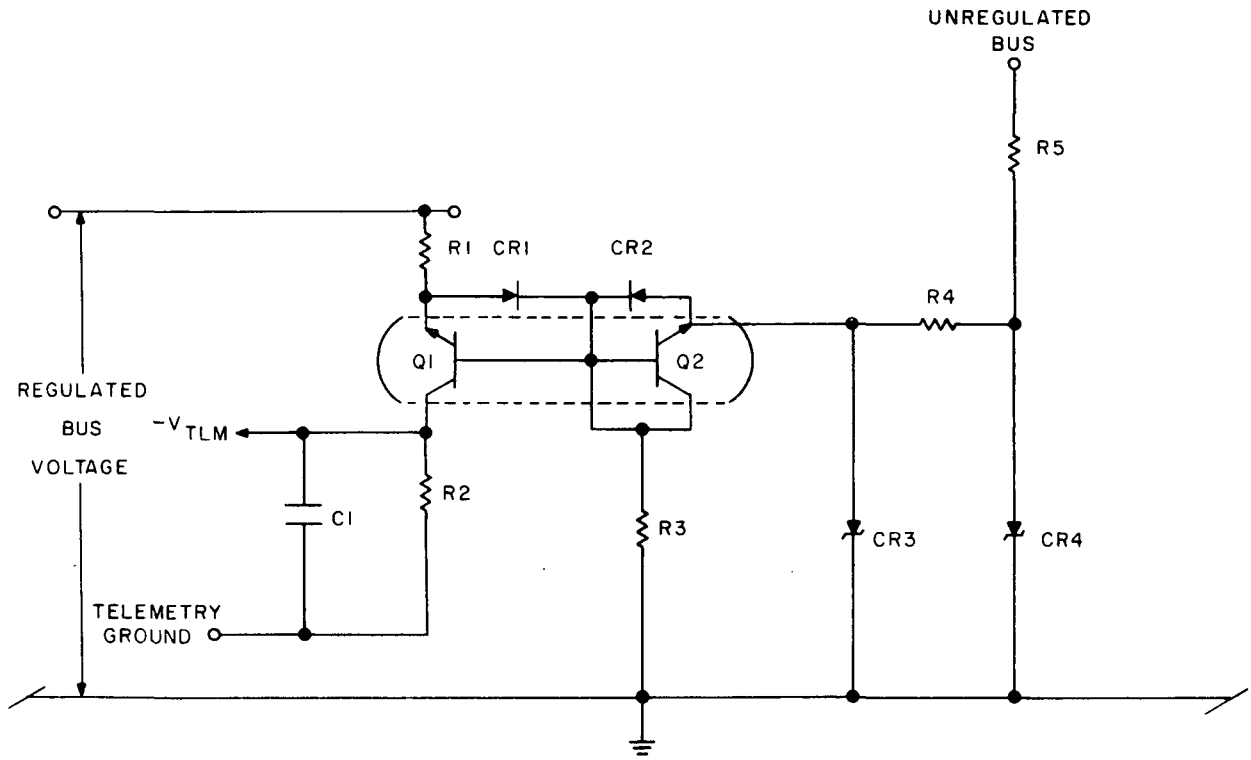

Figure 4-V-36. Regulated Bus Voltage Telemetry Circuit, Schematic Diagram

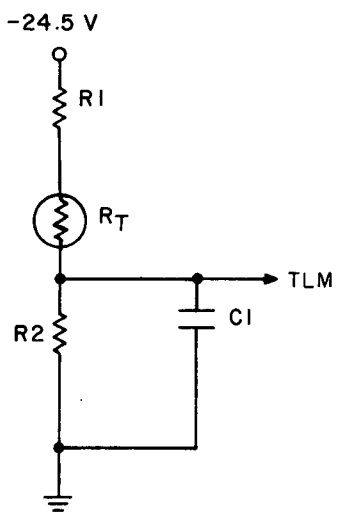

Figure 4-V-37. Temperature Telemetry Circuit, Schematic Diagram

SECTION VI

PRIMARY ENVIRONMENTAL SENSOR SUBSYSTEMS*

A. INTRODUCTION

This section presents the functional descriptions and principal characteristics of the three redundant, primary environmental sensor subsystems aboard the ITOS spacecraft. The subsystems and the equipment in each subsystem are as follows:

- Two Advanced Vidicon Camera Subsystems (AVCS), each composed of a camera sensor assembly, a camera electronics unit, and a three-channel magnetic tape recorder. The tape recorder comprises a tape transport assembly and recorder electronics for recording and playing back the data generated by the camera sensor.

- Two Automatic Picture Transmission (APT) subsystems, each composed of a camera sensor assembly and a camera electronics unit.

- Two Scanning Radiometer (SR) subsystems, each composed of a scanning radiometer and electronics, a processor, and a three-channel tape recorder and electronics. The two SR processors are packaged as a single unit.

Power and signal switching circuits, which are controlled by ground command, provide a means for selecting an AVCS camera** and tape recorder for operation. The switching arrangement is such that it is possible to select either of the two cameras for operation with either of the two tape recorders. A similar switching arrangement provides comparable flexibility in the selection of a radiometer and tape recorder for operation.

*Refer to Summary of Current Design Revisions Not Covered in this Report, following the Preface, for a brief description of revisions made since the cut-off date for this report.

**In this particular context and for simplicity of expression, the term "camera" signifies the camera sensor assembly and camera electronics unit of one AVCS subsystem, excluding the tape recorder.

To meet the mission requirements, one AVCS camera and one AVCS tape recorder will obtain and store cloud cover pictures from the daylight portion of the orbit. Concurrently, in the primary mission mode, one of the two APT subsystems will provide daytime cloud cover pictures for real-time transmission to local users. One scanning radiometer and one recorder will be in operation during the nighttime portion of the orbit and will measure and record data in both the visible and infrared regions for subsequent playback. The SR subsystem will also transmit infrared data in real time to provide nighttime cloud cover pictures to APT stations. Secondary modes of operation will permit either visible or infrared SR data transmission to be substituted for APT subsystem operations and also will provide for continuous (day and night) recording of the SR signals for subsequent playback.

SR data and AVCS pictures stored on the spacecraft tape recorders are played back and transmitted to the ground upon command by a CDA station, from which they are relayed over telephone-type lines to ESSA facilities for meteorological analysis.

B. AVCS SUBSYSTEM

1. General

The AVCS subsystem (Figure 4-VI-1) is used to take a series of wide angle, high resolution television pictures of the earth and its cloud cover, to store these pictures on one of two satellite-borne tape recorders, and, on command, to play them back for transmission to a CDA station. Picture-taking operations of the AVCS subsystem are controlled by a program of instructions that is prepared by TOC and transmitted to the satellite by a CDA station. This program is stored and processed by the active programmer in the satellite's command subsystem, described in Part 4, Section VIII. Before each picture-taking operation, commands transmitted to the satellite select the AVCS camera and the tape recorder to be used.

In the record mode, the active programmer controls the AVCS camera for a sequence of pictures starting just after the satellite crosses the earth's terminator into the daylight portion of the orbit. A complete picture sequence lasts approximately 48 minutes, during which 11 pictures, or frames, are taken at intervals of 260 seconds and stored on the

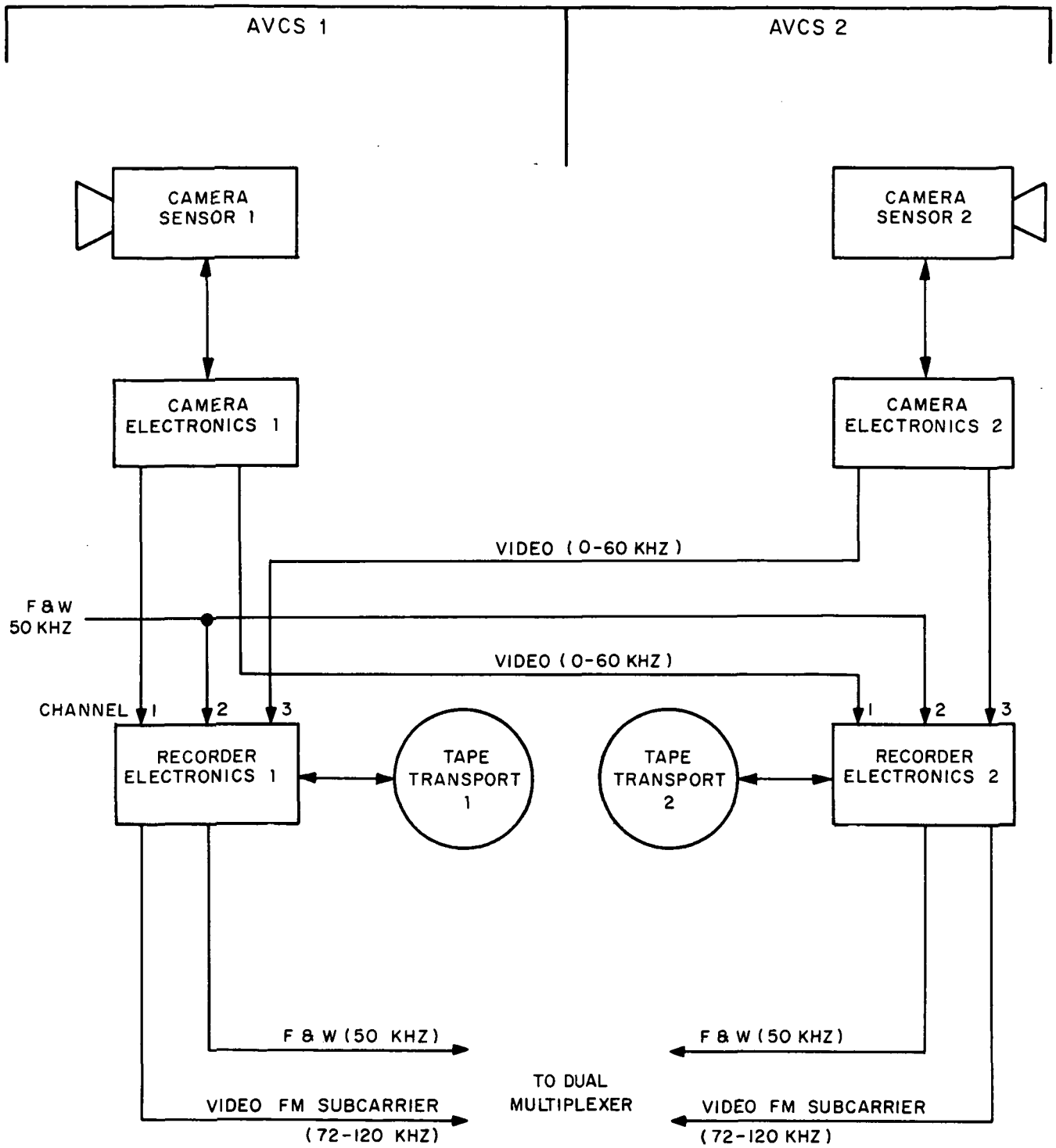

Figure 4-VI-1. AVCS Subsystem, Block Diagram

selected tape recorder. When the last picture in the sequence is taken and recorded, the command subsystem provides a "power off" signal for the AVCS subsystem. A "power on" command and the picture-taking sequence are repeated during succeeding orbits until the active programmer is either reloaded or turned off. The repeat time is determined by the data loaded into the programmer and normally is the time of one orbital revolution. Consequently, successive picture sequences start at approximately the same latitude as the first, but are displaced in longitude by approximately 28.5 degrees at the equator. This displacement produces a slight lateral overlap at the equator in coverage. The amount of lateral overlap increases with increasing latitude. The overlap of successive pictures along the orbital track is a function of the fixed picture-taking rate and is about 50 percent.

In the playback mode, which is initiated by CDA station command, the pictures stored by the satellite's AVCS tape recorder are played back and transmitted to the CDA station.

In the direct AVCS readout mode, picture data is transmitted as it is read out of the AVCS camera to the tape recorder. This operation is terminated when the S-band transmitter is turned off (although the programmed picture sequence is not interrupted) before the satellite travels out of station communication range. The real-time picture data may be used for evaluation of camera performance and later compared with the played back picture data for assessment of tape recorder and AVCS subsystem performance.

2. Functional Description

This portion of the discussion offers a more detailed, time-oriented functional description of AVCS subsystem operation in the two principal modes: record and playback. During this discussion, refer to the timing diagram of the AVCS subsystem operation, shown in Figure 4-VI-2.

a. Record Mode

The first picture in a sequence is taken 45.5 seconds after the programmer alarms (overflows) at time T_0, where T_0 is the subpoint night-to-day transition time reference in the programmer counter. For the 6.5-second interval before T_0 and for 45.5 seconds after T_0, the AVCS camera is prepared for picture-taking. At T_0 minus 6.5 seconds (refer to

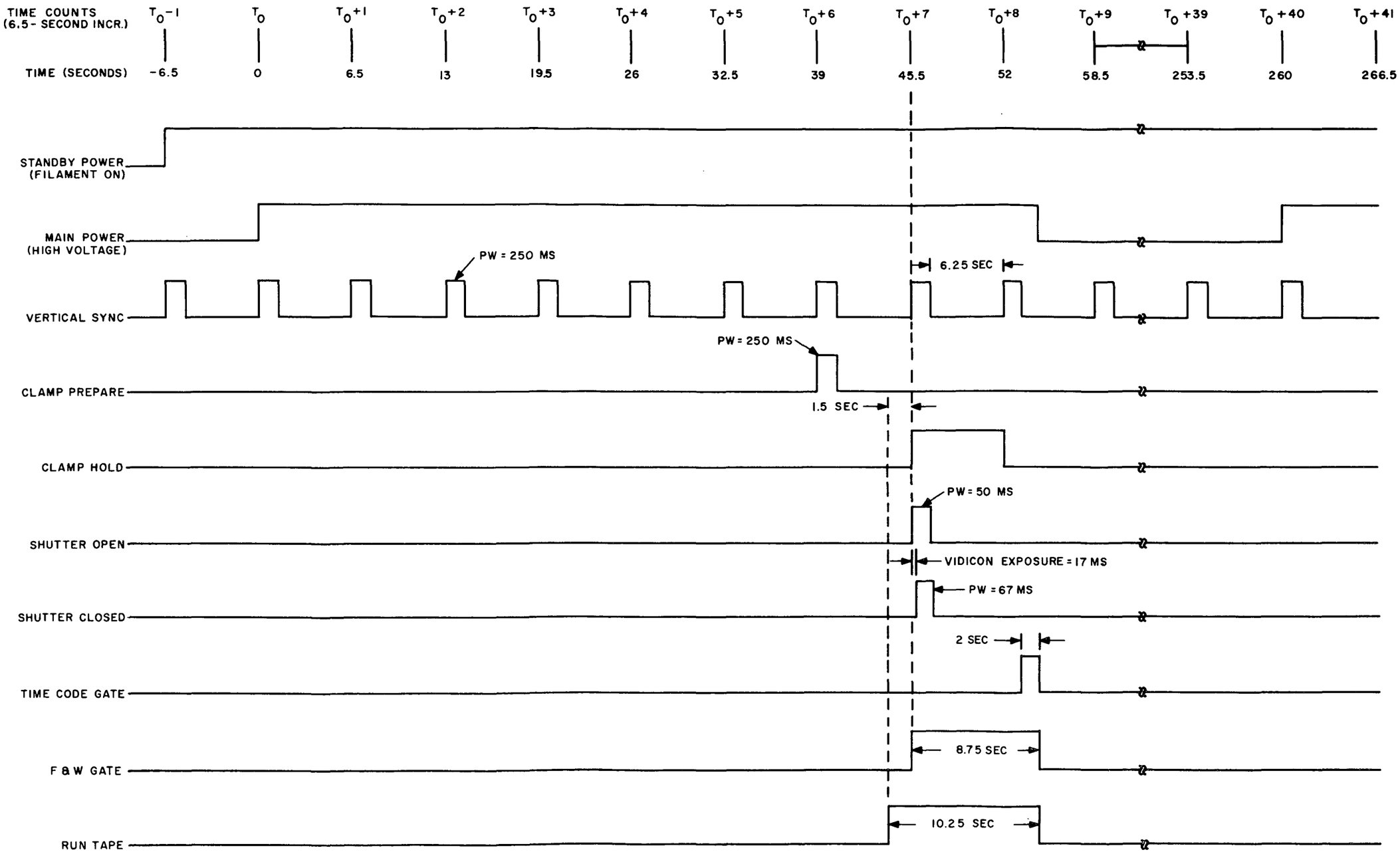

Figure 4-VI-2. AVCS Subsystem, Timing Diagram

Figure 4-VI-2), the command subsystem delivers a "standby power" signal to the camera electronics unit. This signal activates a solid-state switch that applies -24.5 volts DC to a low-voltage power supply that supplies +6.3 volts DC to the vidicon filament. At T_o the command subsystem applies the following to the camera electronics:

- A train of 250-millisecond vertical sync pulses with a pulse spacing of 6.5 seconds.
- Two trains of pulses, the video blanking and horizontal sync pulses (not shown in Figure 4-VI-2). The pulses in both trains recur at intervals of 7.5 milliseconds, or at a repetition rate of 133-1/3 pps.
- A "main power" signal that activates a solid-state switch to energize the high voltage power supply and other camera circuits.

The horizontal sync pulses and the 250-millisecond vertical sync pulses are used to initiate the horizontal and vertical sweep generators and the vidicon blanking circuits. The utility of the video blanking is explained later.

With the application of high voltage, the vidicon beam is turned on and scanned completely across the image area seven consecutive times (T_o to T_o +45.5 seconds) before exposure. This scanning operation deposits a uniform charge (black level) on the vidicon photoconductor preparatory to exposure. At the beginning of the sixth 6.5-second interval, or one frame before exposure, a "clamp prepare" pulse coincident with the vertical sync pulse conditions a video clamp circuit for operation. During the 6.25 seconds following the clamp prepare pulse, samples of the vidicon dark current are applied to the video clamp which subtracts the vidicon dark current signal and establishes a DC reference for the video signal.

Optical exposure occurs at T_o +45.5 seconds with the sequential application of "shutter open start" and "shutter close stop" pulses. The delay between the leading edges of these pulses determines the exposure time, about 20 milliseconds. The shutter pulses operate a solenoid-actuated, double-bladed focal plane shutter. The shutter blades move sequentially from one side of the lens to the other as shown in Figure 4-VI-3. Exposure alters the

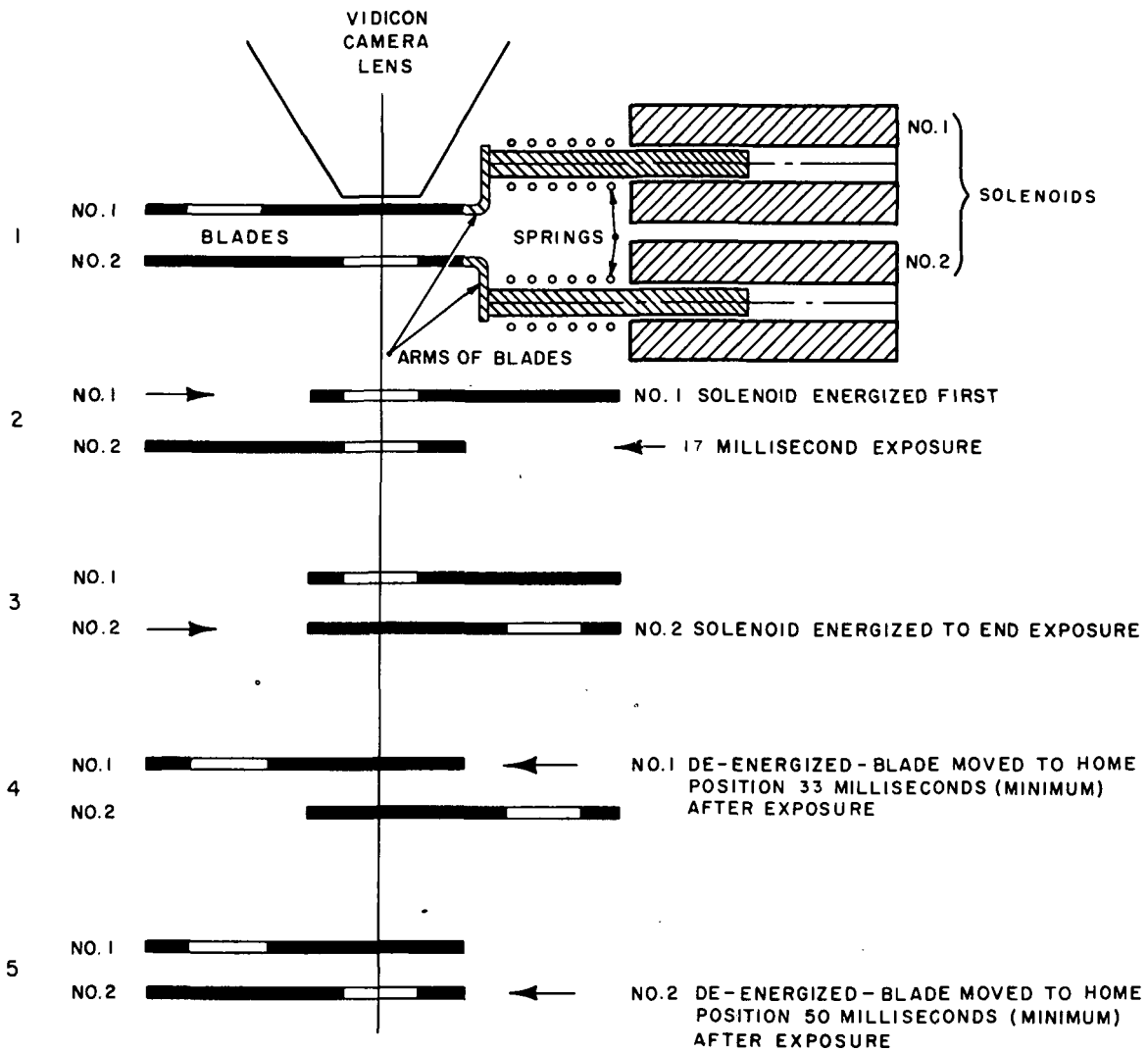

Figure 4-VI-3. Operation of the Double-Bladed Focal Plane Shutter

uniform charge pattern of the photoconductor by causing each resolution element to discharge in proportion to the amount of incident light.

Coincident with optical exposure, an incandescent lamp is energized and its light output is directed through a 15-step gray-scale transparency (by means of a lens and prism arrangement) onto the vidicon photoconductor alongside the TV image area to serve as a reference when the TV pictures are processed at the ground facility.

Shutter actuation occurs during vertical retrace time, at the conclusion of which the horizontal and vertical scan pattern is resumed to read out the data imaged on the vidicon. As

the electron beam traverses the photoconductor, it deposits a charge on the resolution elements that have been discharged by exposure to varying intensities of light. The charging currents developed during the deposition process constitute the video signal which, after preamplification in the camera sensor assembly, is delivered to the camera electronics unit. There the video signal is further amplified, the video blanking pulse is inserted at the beginning of each scan line as a back porch to the horizontal sync pulse, and the picture time code data is added after the 250-millisecond vertical sync period following the end of video readout. (See Figure 4-VI-4.) Video readout lasts 6.25 seconds, and the inclusion of the time code takes an additional 2 seconds. During the interval of vertical sync the video output is at black level. No horizontal pulses appear during this interval. This signal has been changed to simplify the data processing at DAPAF.

The composite video signal and time code are applied to an FM modulator in the tape recorder electronics. The frequency deviation of the FM modulator is a linear function of the video amplitude and ranges from 72 to 120 kHz. This subcarrier is applied to the record head* through an amplifier. The tape recorder drive motor is turned on 1.5 seconds before vidicon exposure to permit the motor to attain synchronous speed before data readout begins. Accordingly, at T_o +44 seconds, a programmer-generated "run tape" signal is applied to a power switch that applies -24.5 volts to the record electronics and to a power amplifier whose output drives the tape recorder motor. The power amplifier is driven by a 400-Hz signal that is applied continuously from the active time base generator.

When the tape recorder attains synchronous speed, a 50-kHz signal from the time base generator is gated by the programmer to channel 2 of the tape recorder. This signal is applied to the tape recorder from T_o +45.5 to T_o +54.25 seconds and is used by the ground data processor to correct for flutter and wow products of tape recorder speed variations.

The first picture-taking and recording cycle is terminated at T_o +54.25 seconds by terminating the "main power" signal, but is repeated at 260-second intervals until all 11 pictures in the sequence are taken. At the end of the sequence, "standby power" is removed.

*Video signals from camera 1 are applied to channel 1 of both tape recorders, and those from camera 2 are applied to channel 3 of both recorders, but only one recorder and one camera are active at any given time.

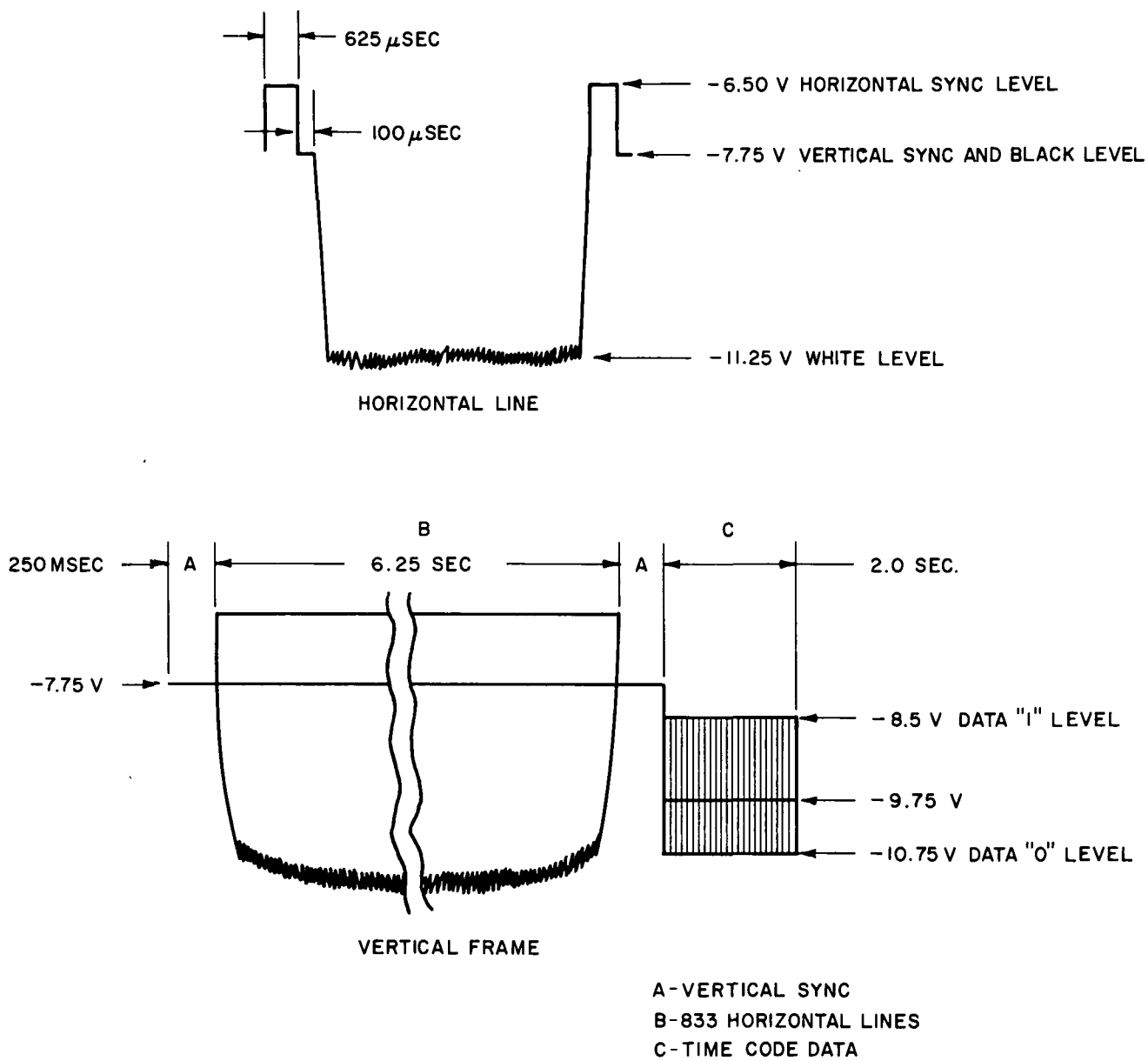

Figure 4-VI-4. Composite Video Signal

The entire sequence is repeated once during each orbital revolution of the satellite, until the programmer is reloaded or turned off by ground command.

b. Playback Mode

When the satellite comes within communications range of a CDA station, playback is initiated by the transmission of a "recorder playback" command to the satellite.* In response to this command, the command subsystem delivers a signal (see Table 4-VIII-1) which causes the recorder that was operative during the picture-taking and recording sequence(s) to be actuated in the following way: (1) connects operating power to the appropriate video and flutter-and-wow playback electronics of the recorder and (2) connects a drive voltage that causes the tape recorder motor to run in the playback direction. During playback, the 72- to 120 kHz video signal (from channel 1 or channel 3) is preamplified and limited and applied through an output amplifier to the multiplexer. The amplified and limited 50-kHz flutter-and-wow signal (from channel 2) is also fed to the multiplexer through a separate output amplifier.

When the playback end-of-tape sensor is reached, a momentary -24.5-volt "end-of-playback" signal is generated, recorder playback power is removed and the AVCS subsystem is returned to the record mode, ready for another picture-taking and recording sequence.

To play back the 11 pictures taken during a single orbit takes slightly less than 2 minutes. Up to 4 complete picture sequences (4 orbits) can be stored on the tape recorder before commanding playback.

c. Direct Mode

The direct mode is activated whenever a "transmitter ON" command is sent to the satellite while a picture-taking sequence is in progress. Besides turning on a transmitter in the playback video link, this command introduces a "direct command" to the active tape recorder. This signal connects power to the appropriate playback electronics (but not to

*A "transmitter ON" command to turn on an S-band transmitter in the playback video link is also required.

the playback motor drive circuits) at the same time that power is being applied to the record electronics. Because of a permanent connection between the output of the record amplifier and input to the playback limiter in each channel of the tape recorder, the TV pictures and flutter-and-wow data are transmitted to the CDA station, in real time, as they are being recorded on tape.

3. AVCS Camera Sensor and Camera Electronics Assembly

a. General Description

The major elements of the AVCS subsystem are shown in the block diagram in Figure 4-VI-5. The camera sensor contains a lens, shutter, gray-scale calibrator, hybrid vidicon, deflection yoke, and preamplifier. The camera electronics assembly contains the video processing, vidicon shading correction, deflection, shutter drive, and power supply circuitry.

The video preamplifier within the sensor housing preamplifies and buffers the vidicon signal to ensure an adequate signal-to-noise ratio at the input to the following video amplifier stages.

Several stages of equalization are used in the video amplifier, including high frequency peaking and aperture correction, to linearly advance the phase of the video signal with increasing frequency. Low frequency video equalization and gain control are also included in the video amplifier, as well as a low pass filter that attenuates frequencies beyond the required passband.

The output of the video amplifier is applied to a video clamp that restores the DC video component and removes the video dark current signal.

A complementary emitter-follower is used to buffer the video clamp and drive the vidicon shading correction circuits. The shading correction circuit is essentially a high-level balanced modulator that can vary the video gain over a 3-to-1 range without imposing the modulating signal on the video. By varying the video gain inversely as a function of the shaded video signal, vidicon and/or lens shading components are reduced.

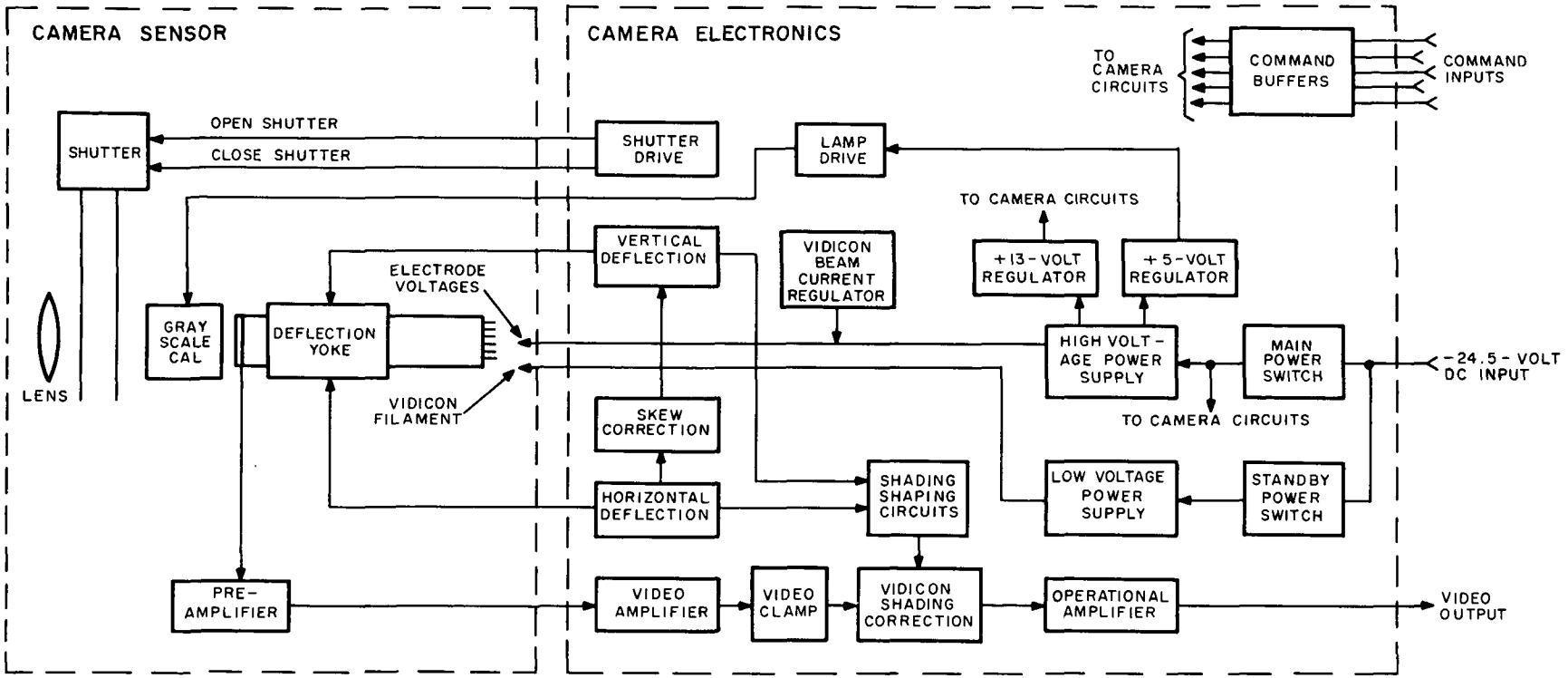

Figure 4-VI-5. AVCS Camera Sensor and Electronics, Modified Block Diagram

Following the shading correction modulator an operational amplifier combines and processes the camera output video signal. Inputs to this amplifier include vertical and horizontal base line correction (part of the shading correction signals), porch and synchronization timing signals, and time code data. This amplifier also performs both black and white level clipping. The composite video signal is then applied to an FM modulator in the tape recorder electronics.

Vertical and horizontal deflection generators supply the sawtooth signals for the vidicon deflection yoke. These signals are also applied to the shading correction circuit signal generators and to a skew correction circuit.

The shutter drive circuit provides the required drive for the mechanical double-bladed focal plane shutter. The exposure time is controlled by the application of two timing signals that are digitally derived from the spacecraft clock and delivered by the programmer. The configuration of the shutter drive circuit permits simultaneous or random sequential application of the regulated and unregulated bus voltages without any degradation to components or performance.

A vidicon beam current regulator maintains a constant vidicon cathode current, regardless of variations in vidicon parameters such as temperature, filament voltage, and filament aging.

The gray-scale calibrator assembly, utilizing an incandescent lamp as a light source, provides 15 linear density steps (0.13 Neutral Density). The light output from the lamp source is directed through the gray-scale transparency by means of a lens and prism arrangement and impressed on the vidicon photoconductor. The gray scale serves as a reference when the TV pictures are processed at the ground facility.

Minus 24.5-volt DC power is applied to a high voltage DC-to-DC converter that supplies all the vidicon electrode voltages as well as an output to a +13-volt regulator and a +5-volt regulator used by the camera electronics circuits. A low voltage DC-to-DC converter provides +6.3 volts for the vidicon filament.

The principal characteristics of the AVCS camera sensor and electronics are given in Table 4-VI-1. All subsystem interface signals, with the exception of telemetry output voltages are listed and described in Table 4-VI-2. For a complete list of the telemetry points, refer to Table 4-IX-13 in Section IX.

The discussion continues with a more detailed description of the lens assembly, hybrid vidicon, video clamp, and shading correction circuits.

b. Lens Assembly

The AVCS camera is equipped with a Kinoptik lens that provides a 108-degree field of view, a focal length of 5.7 millimeters, and a lens aperture of f/1.8. The lens aperture, as controlled by the iris, is adjustable through a range of f/1.8 to f/16. The lens is equipped with a low-reflectance coated Corning Glass fused-silica window for protection against radiation bombardment. In addition, the lens is equipped with a Bausch and Lomb Y-10 solid glass haze filter to limit the spectrum response and to enhance the cloud cover. The haze filter wavelength versus percent transmission characteristics are listed below:

Wavelength (millimicrons)	Percent Transmission
460	0.25
500	63.5
590	89.8
600	90.1
690	91.4

c. AVCS Hybrid Vidicon

The vidicon converts the optical image, formed by the lens and timed by the shutter, into an electrical signal. The vidicon is a 1-inch "hybrid vidicon" which is electrostatically focused and magnetically deflected as compared to the more common "all magnetic vidicon" which utilizes magnetic fields for focus and deflection. Because focusing in the hybrid vidicon is achieved by electrostatic fields, a focus coil is not required, resulting in a considerable saving of weight and power. The vidicon photoconductor (ASOS) is capable of storing an image for 9 seconds with little degradation.

TABLE 4-VI-1. AVCS CAMERA AND ELECTRONICS CHARACTERISTICS

Characteristic	Value
Pictures per Orbit	11
Time for an 11-Picture Sequence	Approximately 48 minutes
Time between Pictures	260 seconds
Vidicon	1-inch hybrid (electrostatically focused)
Lens	f/1.8, 5.7 mm focal length
Field of View	Approximately 108 degrees across the picture diagonals; effectively 89 ±1 degree across the picture flats.
Ground Resolution	Approximately 2 miles per scan line at picture center
Line Resolution (vertical and horizontal)	Approximately 800 TV lines
Aspect Ratio	1:1
Shutter	Double-bladed, focal plane
Preparation, Picture-Taking, and Recording Cycle Duration	54.25 seconds
Vidicon Exposure Time	17 milliseconds
Vidicon Readout Time	6.25 seconds
Vertical Sweep Period	6.5 seconds
Vertical Blanking and Retrace	250 milliseconds
Horizontal Sweep Period	7.5 milliseconds per line
Horizontal Lines per Frame	833 (non-interlaced)
Video Signal	See Figure 4-VI-4.
Time Code	
Number of Bits in Complete Burst	24 return to bias
Bit Rate	120 bits per second
Amplitude	See Figure 4-VI-4.

TABLE 4-VI-2. AVCS CAMERA ELECTRONICS AND SPACECRAFT INTERFACE SIGNALS

Interface Signal	Description
	SPACECRAFT POWER
-28 Volts DC	Unregulated. Powers the solenoids in the shutter drive circuit when the shutter drive signals described in this tabulation are present.
-24.5 Volts DC	Regulated within ±2 percent. This is the main power source for the AVCS. It is switched on and off by the Standby Power and Main Power signals described later in this tabulation.
	TIMING
Standby Power	Applied one 6.5-second period before T_0. It activates a solid-state switch that applies -24.5 volts to the low voltage DC-DC converter whose + 6.3 volt output provides the vidicon filament power. It is on for the entire 11-picture sequence.
Main Power	Applied at T_0 for 54.25 seconds and cycled on/off every 260 seconds. It activates a solid-state switch which applies -24.5 volts to the high voltage DC-DC converter and to the remaining camera circuits.
Vertical Sync	There are eight vertical frames during the Main Power interval, the last frame being the video readout. The vertical sync is utilized to initiate vertical deflection sweep and retrace. This signal is also used to inhibit vidicon dark current sampling during vertical deflection retrace and provides the blanking signal for the beam current regulator.
Clamp Prepare	One vertical frame prior to the video readout, the clamp prepare pulse initiates discharge of the dark current storage capacitor. This allows the clamp circuit to resample the vidicon dark current just before the picture-taking frame.
Clamp Hold	This signal lasts for the entire vertical frame during video readout and is used to inhibit the vidicon dark current sampling circuit. The dark current storage capacitor will then maintain its reference voltage during this entire interval.

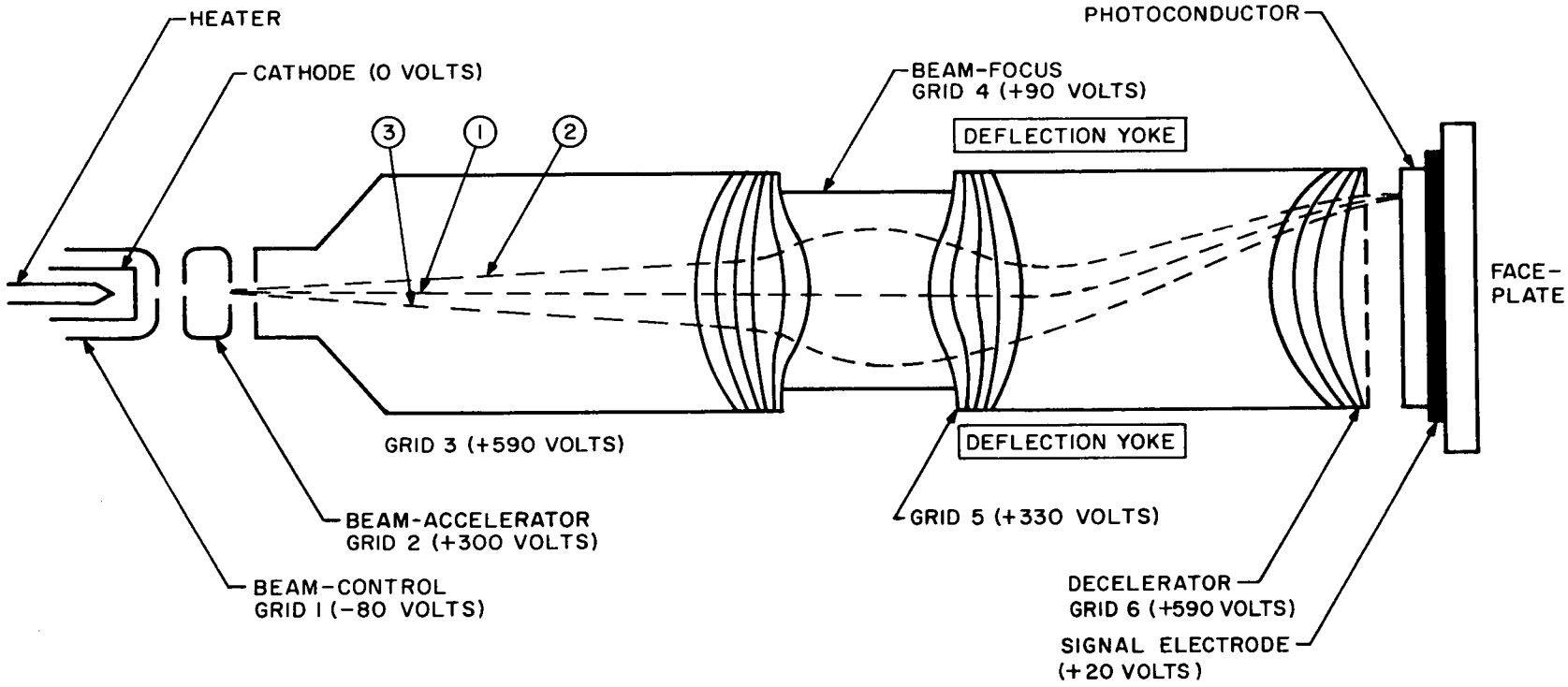

Figure 4-VI-6. Hybrid Vidicon Tube

TABLE 4-VI-2. AVCS CAMERA ELECTRONICS AND SPACECRAFT INTERFACE SIGNALS (Continued)

Interface Signal	Description
TIMING (Continued)	
Video Blanking	This signal gates off the video operational amplifier during horizontal retrace and establishes the rear porch on a horizontal line of the composite video signal.
Horizontal Sync	Applied to the horizontal deflection circuit to initiate horizontal sweep and retrace. It is also used as follows: (1) Provides the blanking signal for the beam current regulator. (2) Gates the switches in the clamp sampling circuitry. (3) Gates the camera video information on/off to provide the video sync tip.
Shutter Open, Shutter Close	Shutter operation is controlled by these two pulses; the delay between their leading edges determines the shutter exposure time.
Time Code Gate	This signal is used to gate the time code data into the video output amplifier.

Figure 4-VI-6 shows the position of the vidicon electrodes, their potentials with respect to the cathode, the equipotential lines of the fields created by them, and the approximate path of the deflected electron beam. The radial distances, however, are greatly exaggerated. Grids 3, 4, and 5 form a low voltage Einzel-type electrostatic lens.

The paths of three electrons are shown. The first electron's direction is straight down the tube. Since its path is normal to the equipotential lines between grids 3, 4, and 5, it is undeflected by these fields. The magnetic field produced by the deflection yoke causes the electron to be deflected upward. When the electron enters the accelerating field between grids 5 and 6, a velocity component is added in a direction normal to the equipotential lines and the path of the electron is changed to one that is parallel to the axis of the vidicon.

This collimating field produced by grids 5 and 6 causes the electron beam to land nearly normal to the target. The result is less shading due to beam landing error than with conventional "all magnetic" vidicons.

The second electron is a divergent electron which enters the field between grids 3 and 4 at an angle. Since this is a decelerating field, the component of the electron velocity which is normal to the equipotential lines is reduced. This causes the electron's path to curve outward and decrease speed. When the electron enters the accelerating field between grids 4 and 5, it is accelerated towards the axis of the vidicon. As before, the collimating field of grids 5 and 6 "straightens out" the electron path after it has been deflected by the magnetic field of the yoke. The third electron's path is similar to that of the second, except that it is divergent in the opposite direction.

The conversion of light energy to electrical modulation takes place at the target. The target consists of a transparent conducting film (signal electrode) deposited on the inner surface of the optically-flat glass faceplate and a thin layer of photoconductive material deposited on the signal electrode. The photoconductor is a continuous semiconductive layer, which is so thin that it has a high lateral resistance and can therefore be considered as many separate elements. The transverse resistance of each element depends upon the amount of light falling on the element. Each of the elements acts as a capacitor shunted by a variable resistor as shown in Figure 4-VI-7.

The video output circuit consists of a load resistor connected from the target ring to the target voltage source and a coupling capacitor connected from the target ring to the video preamplifier.

The cycle of operation for the hybrid vidicon as used in this camera consists of the following cycle of events:

1. Photoconductor preparation.
2. Exposure.
3. Readout.

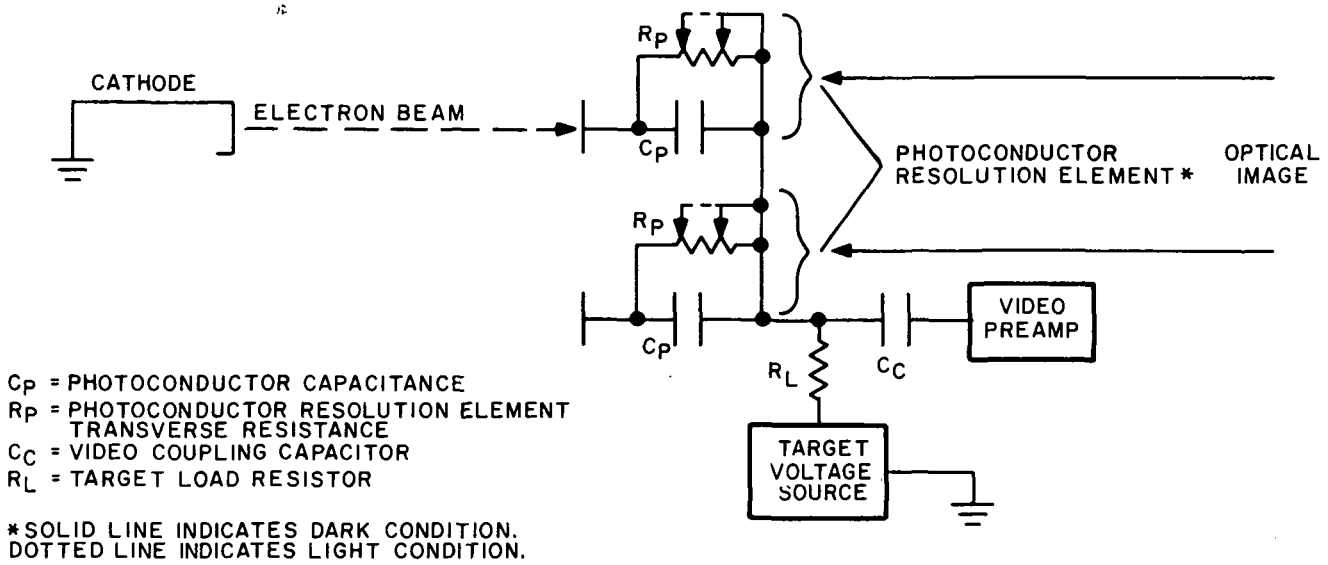

Figure 4-VI-7. Equivalent Circuit of Vidicon Target, Schematic

The preparation period is actually a combination erase and prepare period. During the six scans prior to exposure, the residual charge pattern from the previous cycle is neutralized and the beam side of the photoconductor is brought to cathode potential. When the beam side of the photoconductor is at cathode potential, the electrons in the beam will not land on the photoconductor but will be collected by the electrodes in the gun. Since the shutter is closed during this period, the transverse resistance of each resolution element is high and, therefore, very few electrons can move through the photoconductor. At the end of the vidicon preparation period, the photoconductor is fully charged. The beam side is at cathode potential (V_K is approximately 0 volt) and the signal electrode side is at the target potential (V_T is approximately 20 volts positive). The preparation sequence is illustrated in Figure 4-VI-8 A/B.

When the shutter opens, the lens focuses the optical image on the photoconductor through the glass faceplate and transparent signal electrode. The presence of light increases the conductance of the photoconductor, and conduction from the beam side to the signal electrode

side takes place, effectively discharging the capacitive component. In other words, the electrons stored on the beam side are allowed to pass through the resolution element to the more positive signal electrode. Since the electron beam is not scanning the photoconductor, electrons passing through the resolution element are not replaced. Thus, the beam side of each resolution element assumes a potential somewhere between V_K and V_T (Figure 4-VI-8 C). When the shutter closes and removes the light, each resolution element returns to the low conductivity (high transverse resistance) condition. The beam side of the photoconductor now has a charge pattern that corresponds to the image pattern that was focused on it, as indicated in Figure 4-VI-8D.

However, even in the absence of light, the photoconductor is not a perfect insulator. This inherent characteristic allows some electron movement through the photoconductor (from the beam side to the signal electrode side). Refer to Figure 4-VI-8E. Since this electron movement occurs in the unexposed (dark) areas as well as picture areas, it is referred to as dark current. Dark current is very sensitive to temperature changes, increasing as temperature increases. If compensation for dark current changes were not made, the output

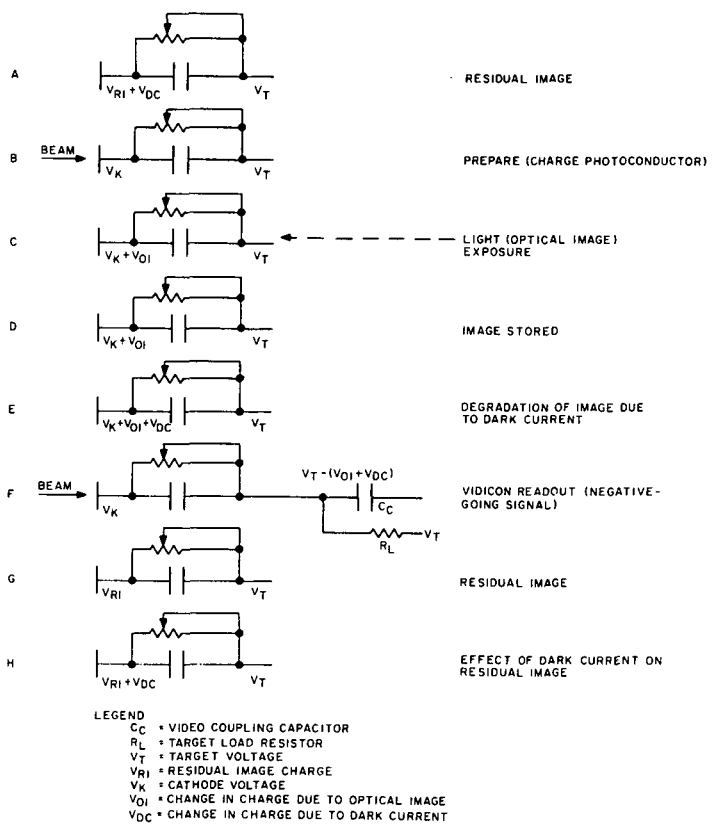

Figure 4-VI-8. Vidicon Signal Sequence Diagram

voltage for scene black would change with changes in temperature. It is the function of the video clamp, described later, to adjust for the variation in dark current due to temperature.

During vidicon readout, the shutter is closed. The beam scans the photoconductor once, depositing a sufficient number of electrons to lower the beam side of each resolution element almost to cathode voltage (V_K). Electrons that approach resolution elements that are already near V_K (black or dark areas) do not land but are collected by the high electrodes, mostly grid 2. Electrons deposited on the beam side of the resolution element replace charges that were lost from the capacitive component during optical exposure and during dark current degradation. Thus, the potential on the beam side of the resolution element is quickly dropped toward V_K. The charging current (electrons deposited) flows through the photoconductor capacitor Cp, load resistor R_L, target voltage supply, vidicon cathode, and back to the photoconductor by way of the beam. The circuit is shown in Figure 4-VI-7. The voltage drop caused by this current (in the order of a few nanoamperes) through R_L is coupled by capacitor C_c to the preamplifier. The amount of current and hence the peak video signal is proportional to the light intensity falling on the resolution element, and the change in charge due to dark current (see Figure 4-VI-8 F, G, H).

d. Video Clamp

The video clamp (Figure 4-VI-9) serves two functions: (1) it restores the DC video level and (2) it compensates for the vidicon dark current pedestal.

To understand the operation of the clamp, first consider the video signal shown in Figure 4-VI-10. This is the case wherein there is no light input to the vidicon. Notice, however, that there is a signal output even through there was no incident light. This residual dark current signal is always present to some degree in the vidicon output and would pose no problem if the level was fixed. Unfortunately, this is not the case, since dark current is temperature sensitive. The higher the vidicon photoconductor temperature, the greater the dark current signal. Dark current then, makes the output from a vidicon appear to sit on a dark current pedestal as shown in Figure 4-VI-11. In this illustration, the dark current is shown to be about one-half of the total useful video swing. Under some conditions, this dark current signal may become two to three times as great as the useful video level.

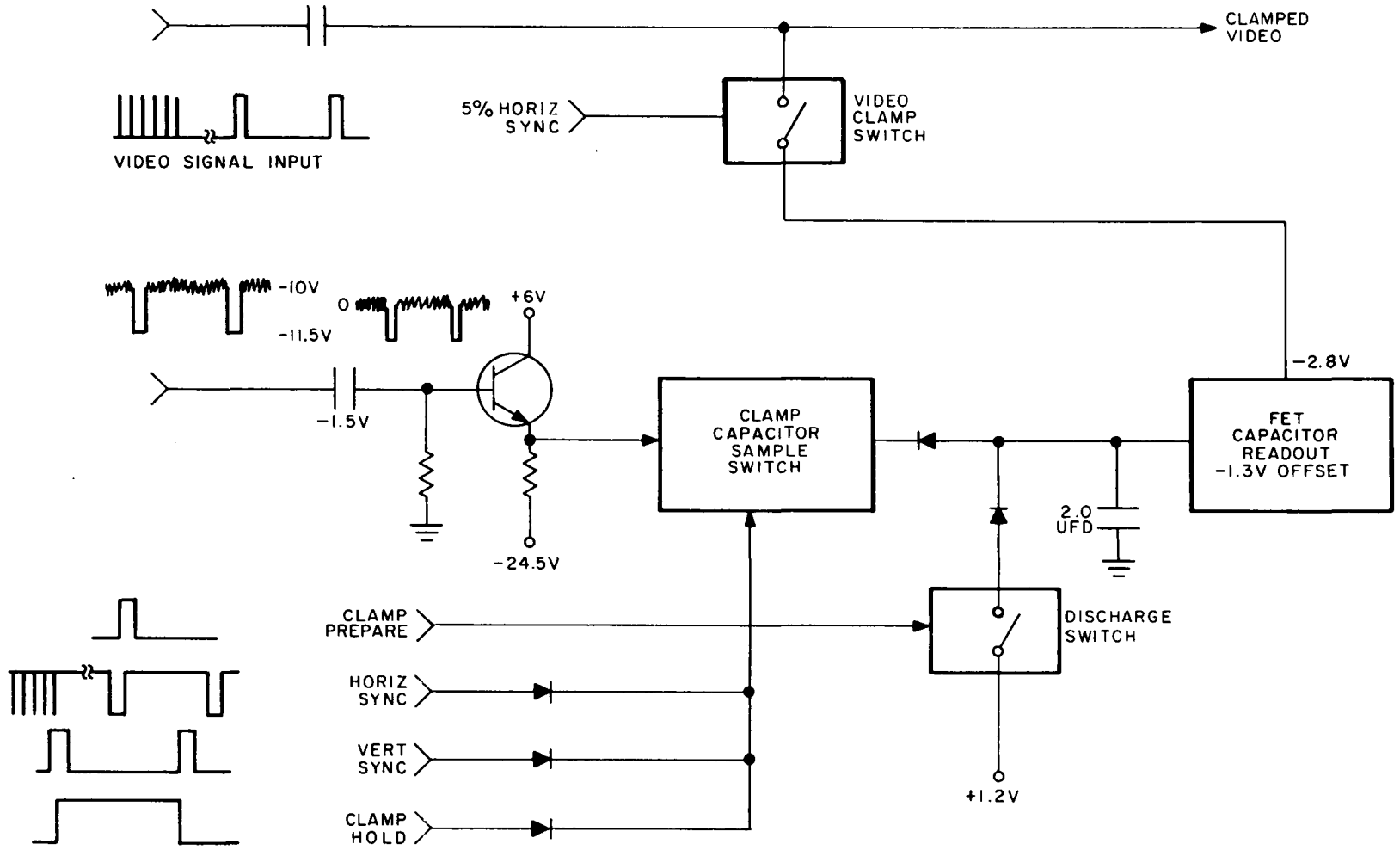

Figure 4-VI-9. Video Clamp, Block Diagram

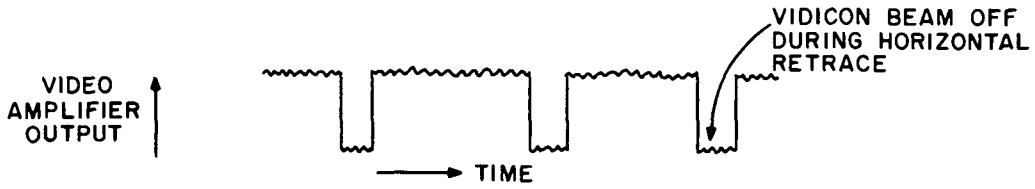

Figure 4-VI-10. Video Signal With No Incident Light

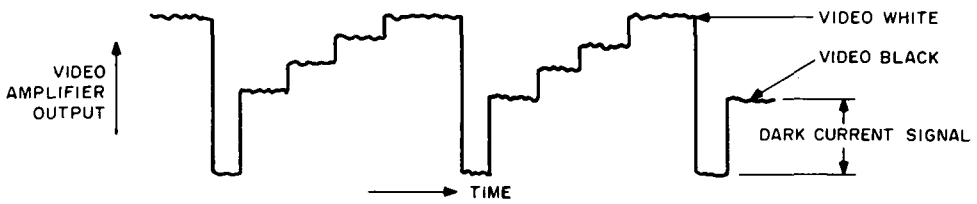

Figure 4-VI-11. Dark Current Pedestal

Besides restoring a DC level to the video, the clamp must also provide a means for removing the dark current signal without losing useful video. These two tasks are accomplished simultaneously by sampling the dark current signal for one complete vertical scan prior to an optical exposure. Thus, an average of the dark current for the entire vertical scan is obtained at the same temperature as the following scan during which optical exposure takes place.

Refer to the simplified schematic diagram in Figure 4-VI-12 and assume that the 2.0 μF storage capacitor at the gate of Q22 is discharged to approximately 0.6 volt. Also assume that the dark current in the composite video signal is 1.5 volts peak-to-peak at the video amplifier output. This signal is applied through a 1 μF coupling capacitor to the base of emitter follower Q18. The output from the emitter follower is fed to a series switch, Q20, that is gated by the 5-percent horizontal sync pulses only during the time that the dark current pulses are present.

Sampling of the first portion of each pulse is delayed by the 200K and 1000 pF time-constant in the collector of the dark current sample gate, Q19. Delay at the end of the dark current signal results directly from the video amplifier. Because the video is delayed approximately 5 μsec, the trailing edge of the video sample will be automatically removed when the sample

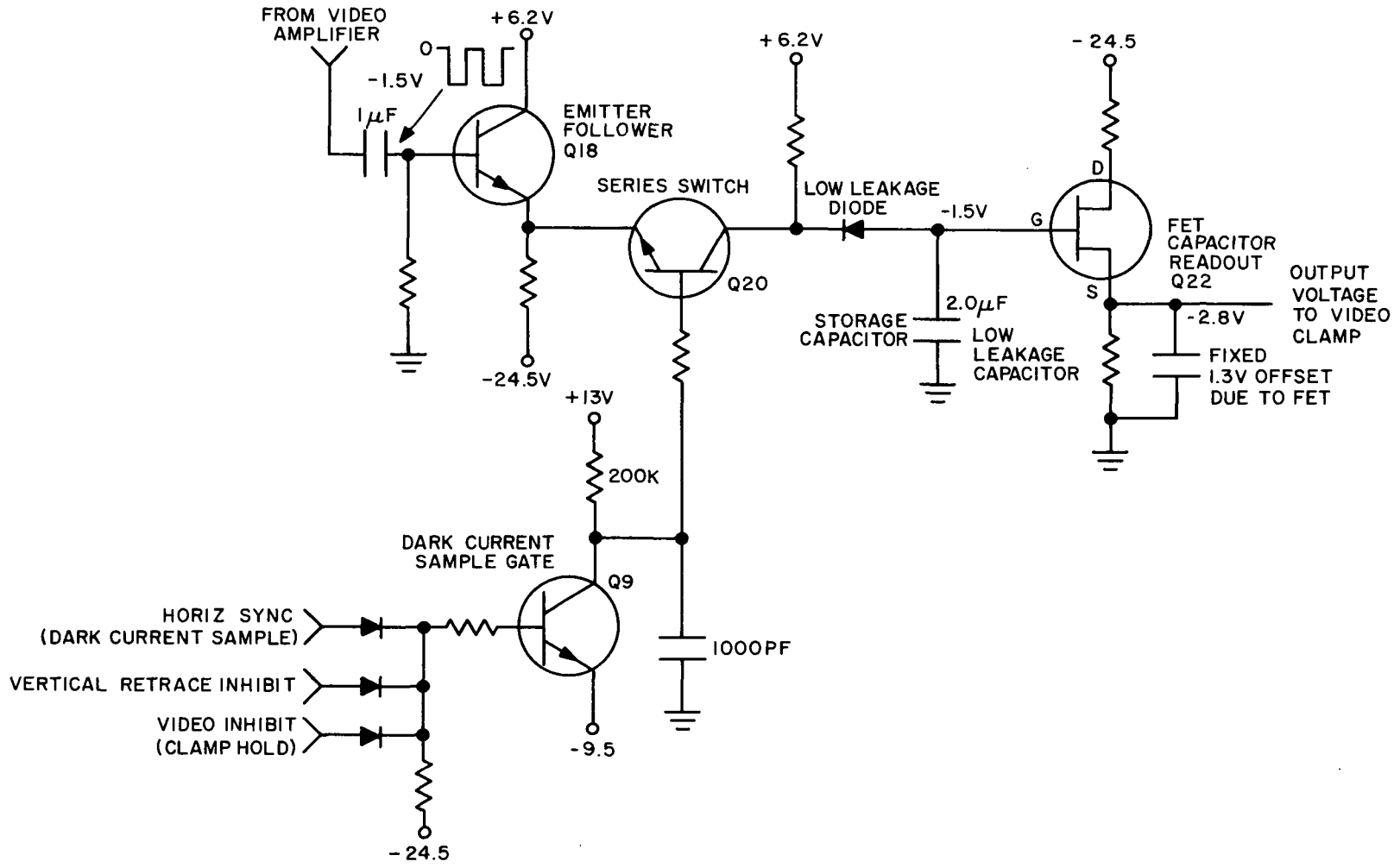

Figure 4-VI-12. Vidicon Dark Current Sampling, Simplified Schematic

gate is turned off. Thus only the center portion of each pulse is sampled and applied through a diode to the low leakage 2.0 μF storage capacitor.

The remaining portion of the clamping circuit is shown in the partial schematic diagram in Figure 4-VI-13. A typical 1.5-volt peak-to-peak video dark signal is sampled and stored on a 2.0 μF capacitor as -1.5 volts DC. This voltage is read out with a field-effect transistor giving a -1.3 volts DC offset to the -1.5-volt DC signal, resulting in a net -2.8 volts for the video clamp. In clamping the video to -2.8 volts, the video black always appears at -1.3 volts. Figure 4-VI-14 shows the timing diagram for sequencing the dark current sampling.

The only remaining consideration is the switch used to discharge the dark current storage capacitor after video readout. Since the vidicon target temperature can vary from one exposure to the next, a corresponding change in the dark current signal may also be expected. Consequently, one scan prior to optical exposure, a 250-millisecond "clamp prepare" pulse is applied to a transistorized discharge switch (see Figure 4-VI-9) to remove the dark current charge accumulated on the 2.0 μF storage capacitor.

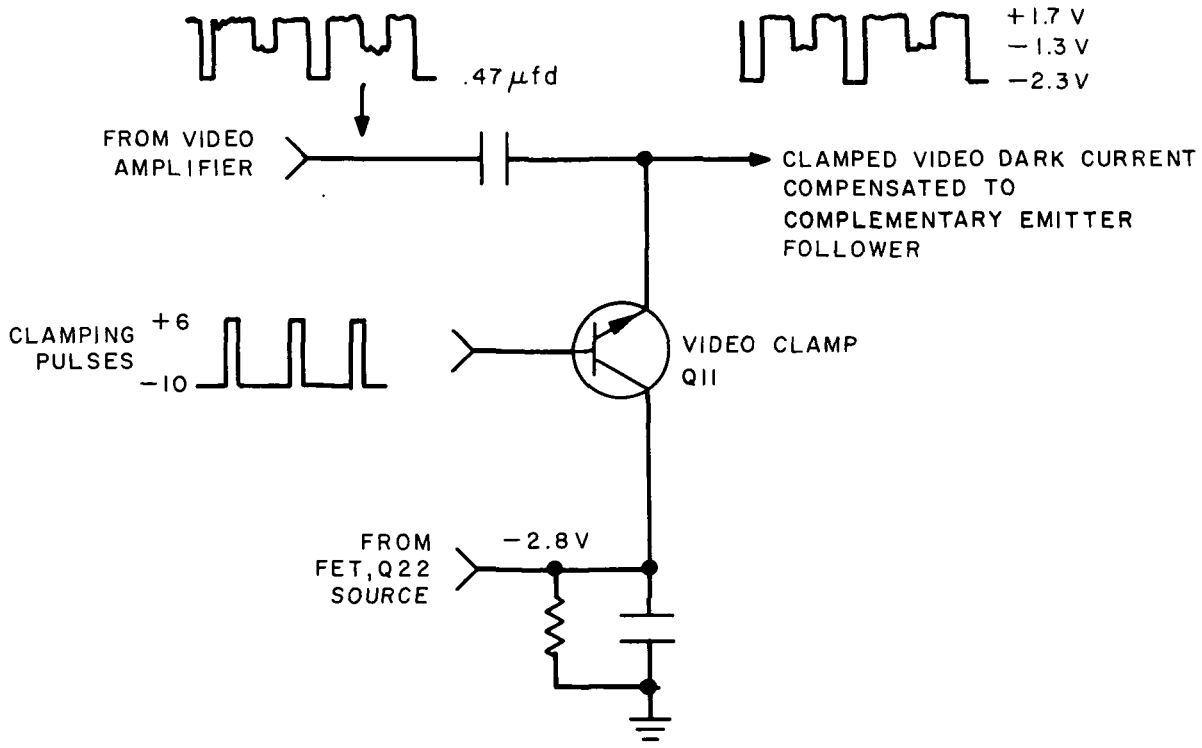

Figure 4-VI-13. Clamp Circuit, Partial Schematic

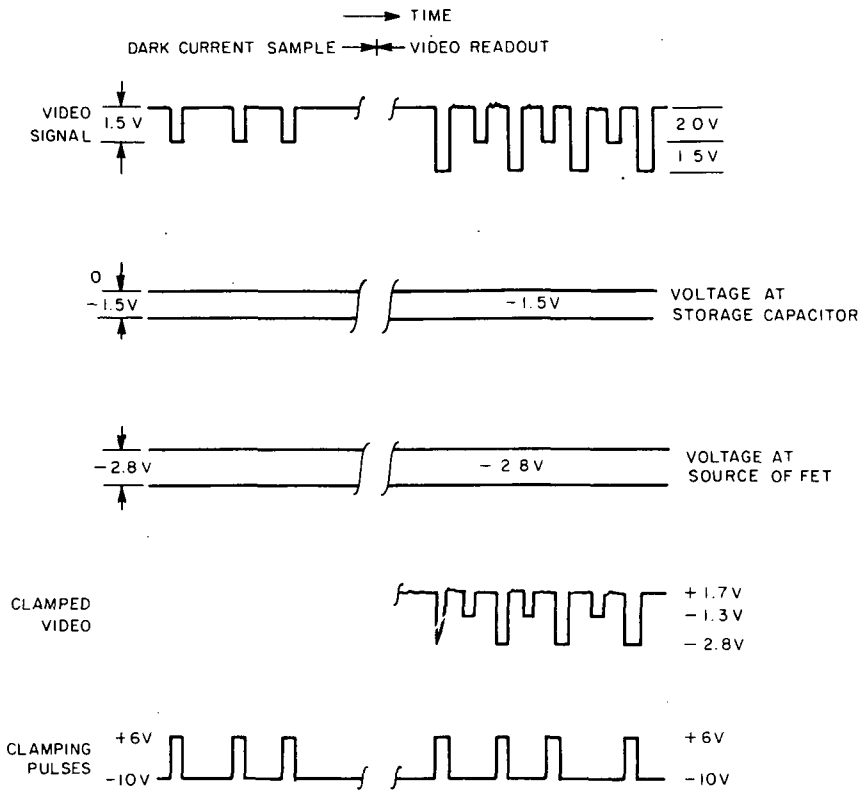

Figure 4-VI-14. Dark Current Sampling, Timing and Sequencing Diagram

e. Shading Correction

The shading correction circuit (Figure 4-VI-15) reduces the effect of non-uniformities in the vidicon and changes in the relative illumination of the lens to an acceptable level. Shading due to the lens alone or the vidicon alone is generally less than the maximum permissible. However, the two together may produce an unacceptable level of shading, and hence the need for correction.

Lens shading is caused by decreased lens efficiency, and reduced illumination on the image plane toward the edge of the image. It is generally symmetrical about the optical axis of the lens. The shape approximates a parabola in both the horizontal and vertical directions.

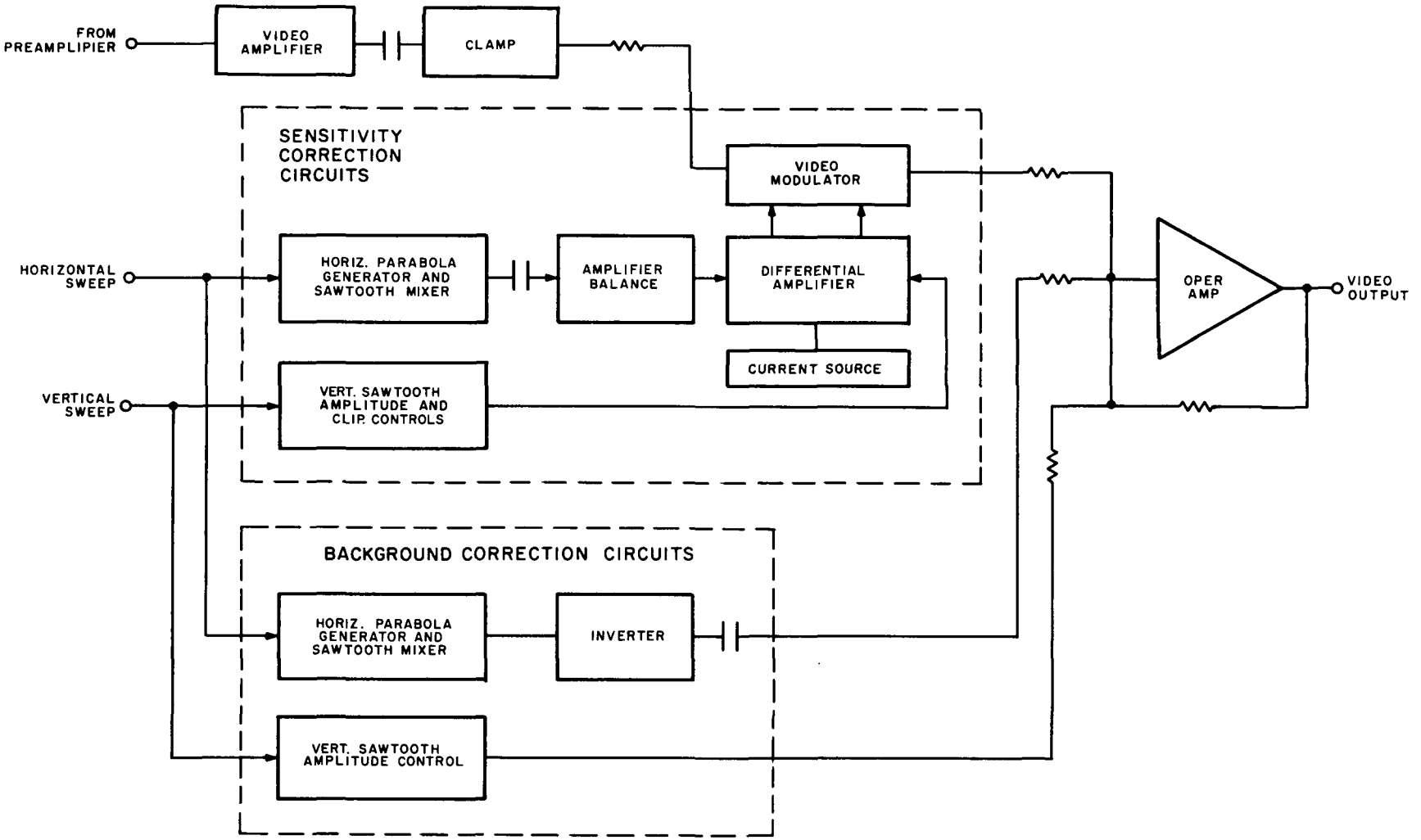

Figure 4-VI-15. Shading Correction Circuit, Block Diagram

The shape of the vidicon shading is similar to the lens shading except that there is often some horizontal tilt, either to the right or to the left. In the vertical direction, there is often a loss of storage within the photoconductor. This means the signal output at the end of the read frame is of a lower amplitude than the signal output at the beginning of the frame, for equal values of illumination. Therefore, vertical shading usually has a tilt component in only one direction, as well as a parabolic component.

It would be desirable to correct the vertical parabolic shading component and the loss of storage component independently. The loss of storage component can be corrected with a sawtooth signal which is already available from the vertical deflection generator. The generator of a vertical parabola with a 6.5-second period would require either a very large integrating capacitor, a medium size capacitor with an operational amplifier, or a diode network to construct a linear parabola from positive and negative sawtooth signals. In short, the vertical parabola is much more difficult to generate than a horizontal parabola and, for the reason to be given later, it was felt that the usefulness of a vertical parabola did not warrant the additional circuitry that would be required. Further consideration of vertical shading reveals that the parabolic shading and the loss of storage shading tend to cancel each other in the first half of the vertical scan and to add in the second half of the vertical scan as shown in Figure 4-VI-16.

The resultant vertical shading can be corrected by sawtooth signals with positive slope that starts in the middle of the vertical scan. Thus if the parabolic and sawtooth components of vertical shading are present in the proper proportion there is no need for vertical parabolic shading correction.

In addition to the sensitivity variations described above, there is also background shading (or black level shading) which is due to vidicon dark current variations. Although the background and sensitivity shadings have similar shapes, the tilt and parabolic components of each may not have the same relative magnitudes. It is, therefore, desirable to control the sensitivity shading correction and the background shading correction independently.

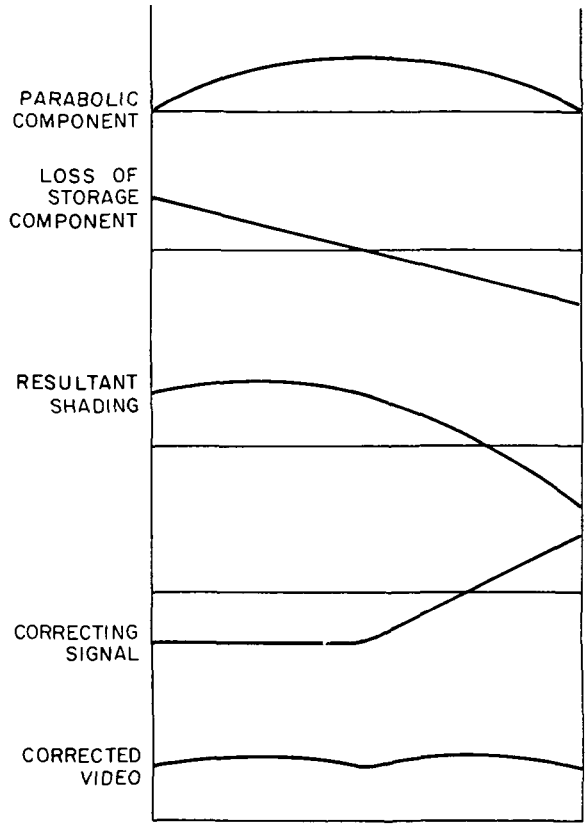

Figure 4-VI-16. Vertical Shading Components

The shading correction circuit is capable of correcting or minimizing the following shading components:

Sensitivity Correction

- Horizontal parabola,
- Horizontal sawtooth, both positive and negative slopes, and
- Vertical sawtooth, positive slope only, which can be started at any part of the vertical scan.

Background Correction

- Horizontal parabola,
- Horizontal sawtooth, both positive and negative slopes, and
- Vertical sawtooth, positive slope only.

The sensitivity shading correction circuitry can correct for 60 percent of shading, provided the shape of the shading closely approximates a combination of sawtooth and parabola. The background shading correction circuitry can correct for 50 percent of background shading, provided it also approximates a combination of sawtooth and parabola.

The shading due to dark current in the vidicon is very dependent on temperature, whereas lens shading is not. It would be difficult and costly in terms of weight and power to have the shading correction circuitry track the change in vidicon shading over temperature. When the shading correction circuitry is set up for a particular lens-vidicon combination, a compromise is made to get the best overall performance over the temperature range.

The heart of the sensitivity correction circuitry is the video modulator (Figure 4-VI-15). This is a network of six diodes and eight resistors, shown in Figure 4-VI-17, that serve as a variable attenuator. The correcting signals are applied to the network at points A and B. These signals are of equal amplitude but opposite polarity. Since the network is balanced, the signal at A and the signal at B cancel at point C. Consequently, the correction signal itself does not appear in the video.

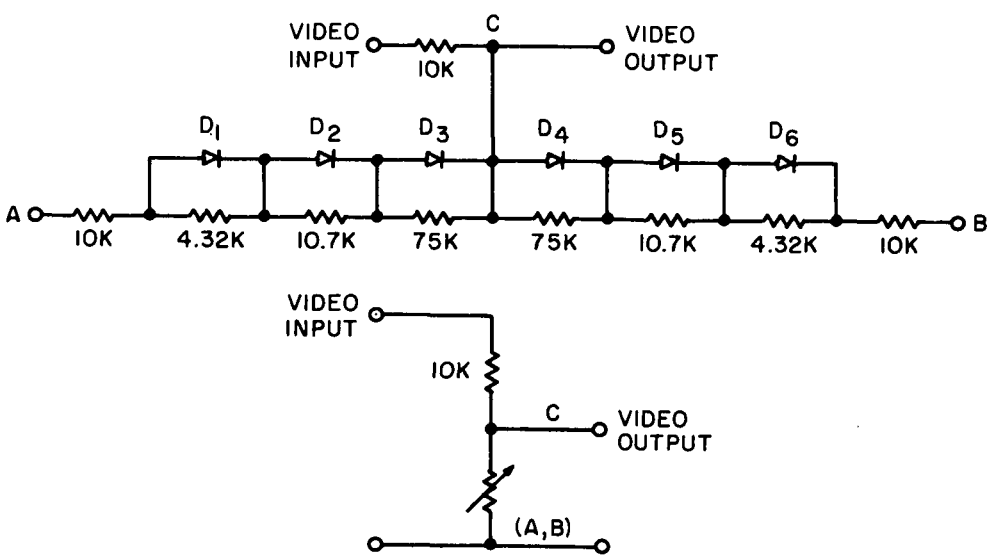

Figure 4-VI-17. Video Modulator Operation, Simplified Schematic

As point A goes positive and point B goes negative, diodes D3 and D4 will start conducting when the potential across the 75-kilohm resistors is approximately 0.6 volt. When D3 and D4 are conducting, the 75-kilohm resistors are effectively shorted, and the impedance of each half of the network has decreased by 75 kilohms. As the amplitude of the signals at A and B increase further, more resistors are shorted out until finally only the two 10-kilohm resistors remain. Because points A and B are driven by emitter followers with very low impedances, they are effectively at AC ground. Thus, the impedance from point C to AC ground can change from 50k when no diodes are conducting to 5-kilohms when all diodes are conducting. Since the characteristic curves of the diodes have "rounded knees", there is a continuous impedance change with no discontinuities. The transfer ratio of the modulator can vary between 0.33 and 0.83, giving a gain change ratio of 2.5 to 1.

The two signals applied to points A and B are supplied from the differential amplifier shown in Figure 4-VI-15. This circuit and the associated current source perform the following functions:

- Mix the horizontal and vertical correction signals,
- Provide a gain of two for the correction signals,
- Control the DC level of the video modulator so that the modulator will not shift the video black level,
- Control voltage offset points A and B so that the diodes in the video modulator will begin conducting at the proper part of the correction signal, and
- Provide two outputs of equal amplitude but opposite polarity.

The vertical sensitivity correction signal is direct-coupled to one side of the differential amplifier. Direct coupling is necessary because the period of the vertical signal is 6.5 seconds. The horizontal correction signal as well as a DC balance voltage is connected to the other side of the differential amplifier. The amplifier balance controls the "difference" voltage between points A and B, and is set up so that maximum sensitivity correction can be obtained with a minimum of video signal attenuation. Minimum attenuation occurs when all

diodes are not conducting; the amplifier balance should be set so that all diodes are "off" during the readout of vidicon areas which have minimum sensitivity. When areas of higher sensitivity are read out, the correction signals will have switched "on" one or more pairs of diodes, thus attenuating the video signal from these areas and making it equal in amplitude to the video signal from the low sensitivity areas.

The current source is adjusted so that the voltage level of point C, in Figure 4-VI-17, is exactly equal to the voltage of picture black. When this is done, there will be no DC current flow between the video modulator and the rest of the video circuits.

The horizontal parabola generator and sawtooth mixer integrates the horizontal sawtooth, thus generating a parabola which is mixed with the horizontal sawtooth.

The background correction signals are added to the video by an operational amplifier as shown in Figure 4-VI-15. The horizontal parabola generator and sawtooth mixer for background correction is identical to the one for sensitivity correction. The signal from the parabola generator is inverted before it is added to the video in the operational amplifier so that the parabola will be of proper polarity.

The vertical sawtooth amplitude control is simply a potentiometer which adds a vertical sawtooth with variable amplitude.

4. AVCS Tape Recorder

a. General

Each of the redundant AVCS tape recorders consists of (1) a tape transport assembly that includes a playback preamplifier and (2) a recorder electronics assembly that contains the motor drive circuits and record/playback signal electronics. The principal elements of the AVCS tape recorder are shown in the block diagrams in Figure 4-VI-18 and 4-VI-19.

Of the three data recording channels in each tape recorder, channels 1 and 3 are used for recording and playing back camera video (from cameras 1 and 2, respectively) and picture time code. Channel 2 records a constant 50-kHz tone which is used by CDA station

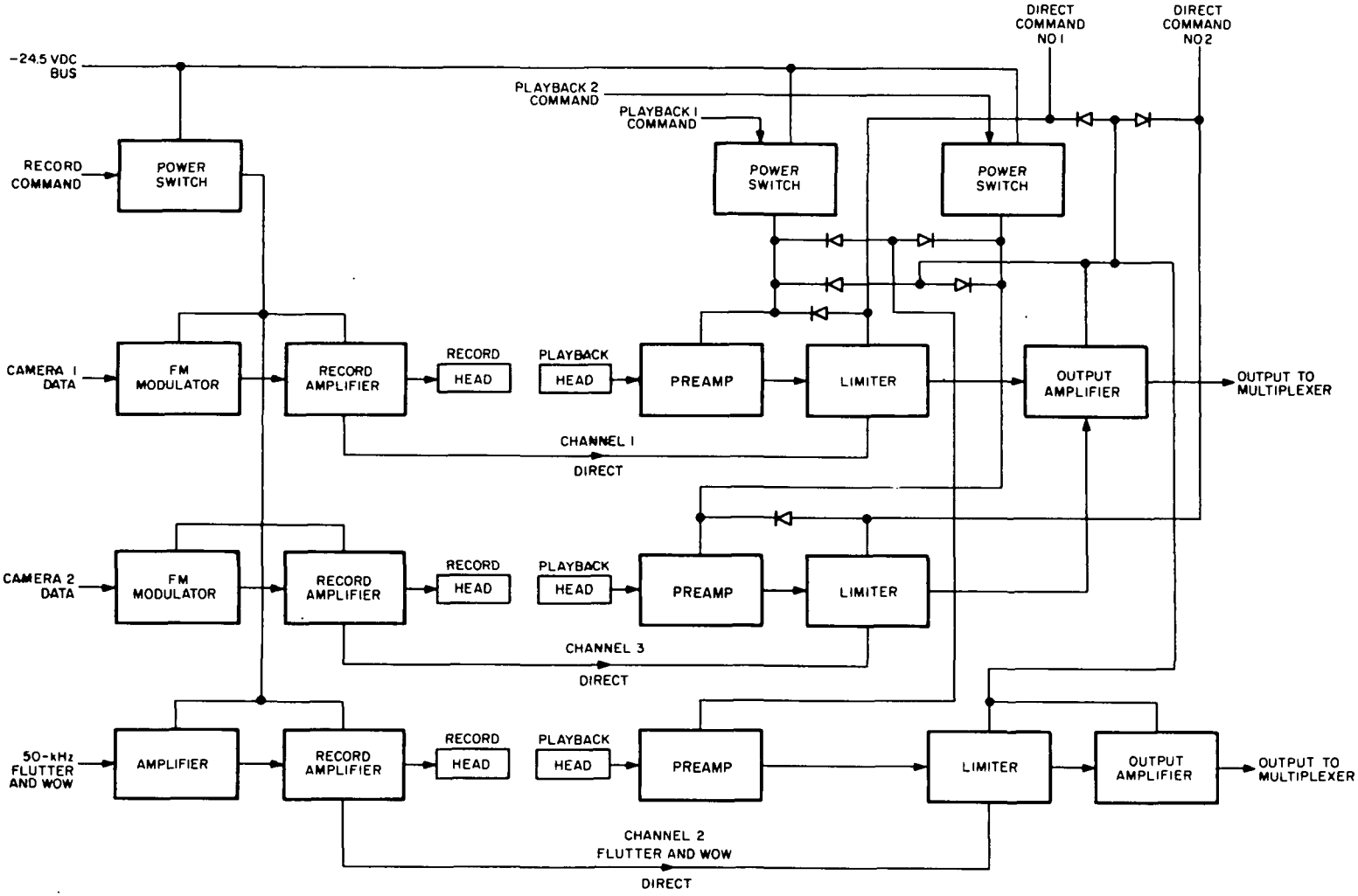

Figure 4-VI-18. AVCS Tape Recorder Record/Playback Electronics, Block Diagram

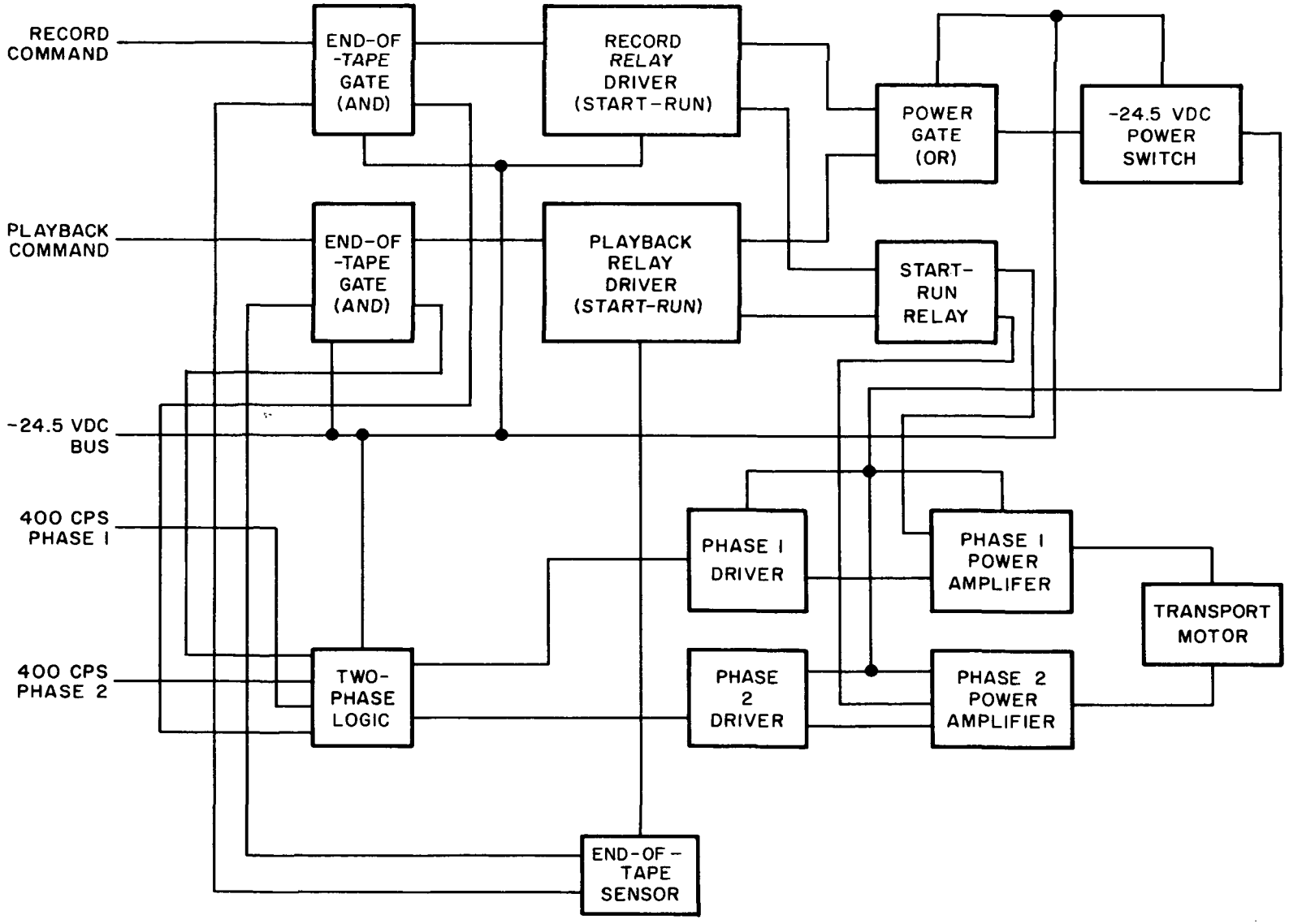

Figure 4-VI-19. AVCS Tape Recorder Drive and Control, Block Diagram

processing equipment to detect tape recorder speed variations and to compensate for these variations in the received video.

The record and playback electronics are powered by the spacecraft's -24.5-volt DC regulated bus. Power is applied to the appropriate record and/or playback electronics through power switches that are actuated by spacecraft commands. The motor drive circuit is also powered from the regulated -24.5-volt source, but from a separate bus, and is synchronized by a stable 400-Hz frequency from the command subsystem.

AVCS tape recorder characteristics are summarized in Table 4-VI-3, and the spacecraft interface signals and their effect on recorder operation are listed in Table 4-VI-4.

The succeeding paragraphs describe in more detail the tape transport, motor-drive circuit, video record and playback circuits, and the flutter-and-wow record and playback circuits, in that order.

TABLE 4-VI-3. AVCS TAPE RECORDER CHARACTERISTICS

Item	Characteristics
Tape speed, record or playback	30 inches per second
Record time or playback time	9.1 minutes maximum (end-to-end)
Heads	One 3-channel record head; one 3-channel playback head; one permanent magnet erase head, full tape width
Tape	1360 feet of 0.25-inch wide, 0.0011-inch thick, Mylar base, instrumentation magnetic tape
Pressurization	16.5 psia with 90 percent nitrogen and 10 percent helium
Seal	O-ring, sealed flange, and pressure fitting
Weight	
Transport	11.75 pounds
Electronics	5.5 pounds

TABLE 4-VI-3. AVCS TAPE RECORDER CHARACTERISTICS (Continued)

Item	Characteristics
Dimensions	
Transport	15.4 inches maximum diameter by 7 inches in height
Electronics	8-1/2 by 4-3/8 by 4-1/8 inches
Motor	2-phase, reversible
Speed	12,000 rpm
Operating voltage	48 volts p-p, 400 Hz square wave
Supply voltage	-24.5 VDC
Power Consumption (tape transport and electronics)	
Record	670 mA
Playback	565 mA
Input Signals	
Video Channel	Camera video ranging in amplitude from -6.5 ± 0.2 volts DC (horiz. sync tip) to -11.5 ± 0.2 volts DC (white level) at a baseband of 0 to 60 kHz; and time code with a pulse amplitude from -8.5 to -10.75 volts
Flutter-and-Wow Channel	50-kHz square wave, 4.4 ± 0.6 volts in amplitude.
Output Signals	
Video Channel	Amplitude limited FM subcarrier ranging in frequency from 72 to 120 kHz at an amplitude of 2 volts ± 1 db p-p
Flutter-and-Wow Channel	50-kHz square wave, 2 volts ± 1 db p-p

TABLE 4-VI-4. AVCS TAPE RECORDER AND SPACECRAFT INTERFACE SIGNALS

Signal	Description
Power Bus 1 (-24.5 VDC regulated)	This voltage shall be present whenever the tape recorder is in the record, the playback, or the standby mode. Power for the signal processing circuits shall be drawn from this line.
Power Bus 2 (-24.5 VDC regulated)	This voltage shall be present whenever the tape recorder is in the record, the playback, or the standby modes. Power for the motor drive circuits shall be drawn from this line.
Record Command	On receipt of a record command, the tape recorder shall operate in the record mode unless one of the playback commands is present. In this case the record command shall be ignored. In the record mode, the two FM modulators and the three record amplifiers shall be activated to process and store the incoming AVCS data and the flutter-and-wow information. The motor drive circuits shall be activated to drive the transport mechanism in the record direction. The record command shall arrive 1.5 seconds prior to the arrival of the incoming AVCS data.
Playback Command 1	On receipt of playback command 1, the tape recorder shall operate in the playback 1 mode. The playback amplifiers for channel No. 1 (that stores AVCS data from sensor No. 1) and channel No. 2 (that stores flutter-and-wow information) shall be activated. The motor drive circuits shall be activated to drive the transport mechanism in the playback direction. The record mode of operation shall be inhibited.
Playback Command 2	On receipt of playback command 2, the tape recorder shall operate in the playback 2 mode. The playback amplifiers for channel No. 3 (that stores AVCS data from sensor No. 2) and channel No. 2 (that stores flutter-and-wow information) shall be activated. The motor drive circuits shall be activated to drive the transport mechanism in the playback direction. The record mode of operation shall be inhibited.

TABLE 4-VI-4. AVCS TAPE RECORDER AND SPACECRAFT INTERFACE SIGNALS (Continued)

Signal	Description
Direct Command 1	On receipt of direct command 1, the tape recorder shall operate in direct mode 1 when the record command is received. Channel No. 1 and channel No. 2 of the record and playback electronics shall be activated in direct mode 1.
Direct Command 2	On receipt of direct command 2, the tape recorder shall operate in direct mode 2 when the record command is received. Channel No. 2 and channel No. 3 of the record and playback electronics shall be activated in direct mode 2.
Motor Phase 1	This control signal shall be supplied continuously to the subsystem for use in the motor drive circuits. It shall be a square wave at 400 Hz.
Motor Phase 2	This control signal shall be supplied continuously to the subsystem for use in the motor drive circuits. It shall be a square wave at 400 Hz delayed by 90 degrees with respect to that of phase 1.
Flutter Clock Signal	The flutter clock signal shall be present for 8.75 seconds during readout of the AVCS camera, for use in the flutter-and-wow channel during record mode. It shall be a square wave at 50 kHz.
Playback End-of-Tape	The tape recorder shall provide a signal indicating that the end-of-tape has been reached during playback. This signal shall consist of two levels: -24 volts DC when not at end-of-tape and an open circuit when at end-of-tape during playback or when the recorder is in the OFF mode.
Telemetry Power	Upon command, -24.5 volts DC regulated voltage shall be supplied for monitoring telemetry points such as pressure and temperature.

b. Tape Transport Assembly

The tape transport assembly consists of a base casting on which the following are mounted: two coaxial reels, a capstan, record head, playback head, erase head, three tape-rollers, flywheel, and negator-spring assembly. A constant torque is applied to each of the two tape reels counter to the direction of rotation by negator springs to provide constant tape tension. As the tape unwinds from one reel, it makes a 180-degree wrap around the capstan, passes over three rollers, and then loops around the capstan again for 180 degrees, but in the opposite direction, before it is taken up by the second reel. The closed loop formed with respect to the capstan reduces flutter, since any transient changes in tape tension produce essentially equal and opposing torques at the capstan. The slight twist required to move the tape from the plane of one reel to the plane of the other is imparted by the rollers. With this arrangement, head tracking is not affected by the twist.

The tape is 1/4-inch wide and 1360 feet long, and has a Mylar base coated on one side with an iron oxide magnetic medium. The tape is wound and threaded so that the oxide-coated side does not contact any part of the transport except the magnetic heads. The record and playback heads contain three tracks each. The erase head is a single permanent magnet, spanning the full width of the tape, which removes the previous recorded information after the tape passes the playback head and again before information is recorded on the tape. Therefore, the tape is erased twice before each recording operation.

The capstan is driven by a reversible, 2-phase, synchronous motor through a Mylar belt. The mean angular momentum of the transport is reduced to less than 0.02 pound-inch per second by means of the flywheel mounted on the shaft of the capstan. For both record and playback, the speed of the 12,000-rpm motor is reduced by the pulley and belt coupling between the motor and capstan shafts, to provide a tape speed of 30 inches per second.

The recorder incorporates redundant end-of-tape sensing devices. One end-of-tape indicator consists of a 6-foot length of silver-coated conductive tape fastened near each end of the magnetic tape, and is sensed by a two-contact pickup located near the reels. The sensor near the bottom reel is also used to deflect the tape and provide the proper wrap angle around the heads. Should the normal end-of-tape stops fail to function, two microswitches, one at

each end, actuated by tape reel diameter build-up, will interrupt the drive motor power source, stopping the recorder. A fail-safe tape mounting is also used to anchor the ends of the tape to both reels.

(1) Life Limiting Parts

(a) Motor

The design life requirements for the synchronous two-phase motor are for 13 equally spaced, 4-minute operational periods per day for 18 months following a storage period of 2 years.

(b) Drive Belt

The drive belt is fabricated from Kapton polyimide film, type H, with a yield strength of 12,000 psi and a modulus of elasticity of 3.1×10^5 after forming. The Kapton belt is designed for 1-year minimum life.

(c) Negator Springs

The negator springs are 0.004-inch thick Haver with a minimum design life of 13,000 cycles. A cycle is defined as unwinding and rewinding any one segment of the spring on the storage drum through the required number of cycles. Operational requirements for the system impose 26 cycles of the springs per day. The 13,000-cycle design life of the springs provides a minimum operational life of 16 months.

(d) Magnetic Tape

A test program is being performed on magnetic tapes to select the tape which provides the best characteristics for the thermal environment. The tape selected for the best thermal characteristics will then be subjected to a life test. The test is included as a part of the program approved for the ITOS tape transports. (Test results will be available after completion of the program.)

(2) Lubrication

Lubrication of the AVCS tape transport assembly is restricted to the bearings. Barden close-tolerance, precision bearings are used throughout the system. Bearing loads are minimal so that the life limiting item for a bearing assembly is the lubricant. Lubrication for the bearings is provided by ESSO "ANDOK" C grease. This grease was selected for its long life characteristic and its channeling characteristic to minimize torque. The lubrication life for "ANDOK" C grease in a similar environment was predicted by Humble Oil and Refining Company to be in excess of 4 years. Selection of this lubricant was based on tests performed by AED for the HDRSS program.

c. Motor Drive Circuit

A solid-state power amplifier, excited by a 400-Hz squarewave synchronizing signal from the command subsystem and powered by -24.5 volts DC supplied through the power switching circuits is used to drive the tape recorder motor. For the record mode, separate "start" and "run" taps, switched by a latching relay, are provided on the circuit's output transformer. The "start" tap allows the motor to accelerate rapidly to synchronous operating speed. The acceleration period is internally controlled and lasts approximately 2.5 seconds. After the motor has reached synchronous speed, the motor windings are switched to the "run" taps. Motor reversal is accomplished by reversing the phase of the 400-Hz signal at one of the two motor windings.

d. Video Signal Record and Playback Circuits

Channel 1 and channel 3 of the recorder are used, respectively, for recording video data from camera 1 and camera 2. Since only one camera will be activated at a time, only one of the two channels will be recording video data on a given pass.

The video signal from the active camera is applied to an FM modulator wherein the signal is amplified and fed to a voltage-controlled oscillator to produce an FM subcarrier with a deviation ranging from 72 to 120 kHz. This subcarrier is then applied to a record amplifier to the appropriate channel of the record head.

During playback, the recorded FM subcarrier is amplified by the playback preamplifier circuit, limited, amplified again by the playback amplifier circuit, and routed to the multiplexer. During playback mode and direct mode operation, the active record and playback channels are selected by command. See Table 4-VI-4.

3. Flutter-and-Wow Record and Playback Circuit

During TV-picture recording, a stable 50-kHz signal generated in the command subsystem is gated into a limited-bandwidth record amplifier and then to channel 2 of the record head. During readout, this signal is amplified, limited, and filtered to provide a constant amplitude FM signal having a center frequency of 50 kHz and frequency deviations proportional to the flutter-and-wow characteristics of the recorder.

C. AUTOMATIC PICTURE TRANSMISSION SUBSYSTEM

1. General

The Automatic Picture Transmission (APT) subsystem is used to take wide angle TV pictures of the earth and its cloud cover during subpoint daylight. These pictures are transmitted in real time to APT field stations for reproduction on facsimile equipment. The APT subsystem is controlled by ground-initiated commands that are transmitted to the satellite from the CDA stations and are processed and stored by the satellite's command subsystem. The program of commands directs the APT subsystem to start taking a sequence of 11 pictures at a predetermined point in the orbit. Once the sequence is initiated, the camera will take a picture, under satellite command, once every 260 seconds until the prescribed 11 pictures have been taken. These pictures are transmitted to all APT field stations within communications range of the satellite by a transmitter in the real-time data link. The sequence is repeated automatically during each orbit of the satellite until the command subsystem is turned off or programmed otherwise by a CDA station.

The APT camera employs a high-persistency vidicon that permits very slow (200-second) readout of the exposed image and thus permits narrow-band transmission of the video signal which, in turn, allows the use of relatively simple equipment at the APT field stations.

There are two APT subsystems aboard the spacecraft, only one of which is selected by ground command for operation during any picture-taking sequence. The output of either subsystem may be connected by ground command to either of two transmitters in the real-time data link.

2. Functional Description

The major elements of the redundant APT subsystems are shown in Figure 4-VI-20. Each subsystem comprises a camera sensor assembly that converts optical images into electrical signals and a camera electronics module that incorporates the timing, control, video processing, and power circuits for the associated camera sensor. All APT subsystem operations are controlled by a sequence timer in the camera electronics module; the

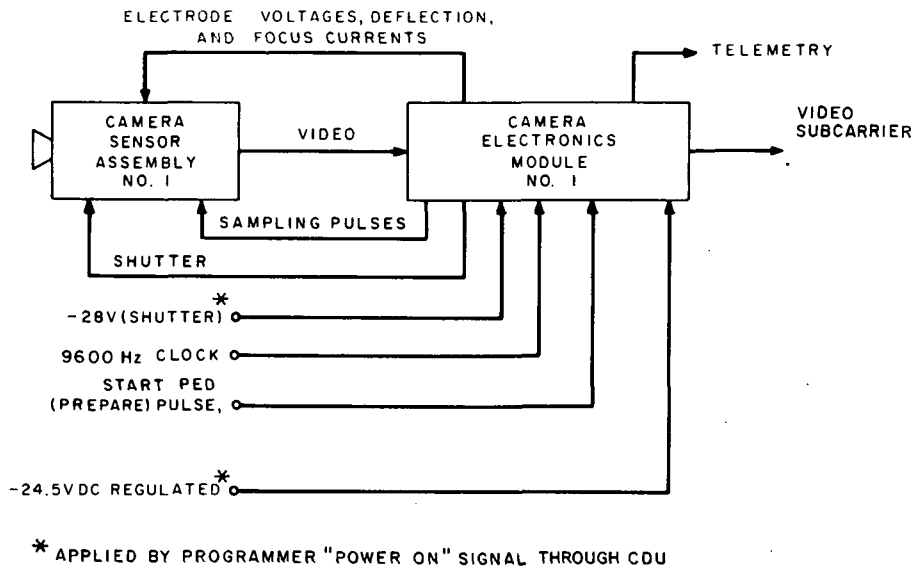

Figure 4-VI-20. APT Subsystem, Block Diagram (One of Two Redundant Cameras)

sequence timer, in turn, is controlled by the selected programmer in the command subsystem. The digital functions in the sequence timer are performed by integrated circuits.

For the following discussion, refer to Figure 4-VI-21, a timing diagram of APT camera operation. The first picture of a sequence is exposed 57.5 seconds after the programmer overflows at time T_0, where T_0 is the subpoint night-to-day transition-time reference in the programmer counter logic. Approximately 182 seconds before T_0 a "power on" signal from the programmer connects -24.5 volts DC from the regulated bus of the spacecraft to the APT subsystem. A -28-volt DC potential from the unregulated bus is also applied at this time to the shutter drive control circuit in the camera electronics module. With the application of primary power, the APT subsystem enters a warmup and stabilization period during which the circuits in the camera electronics module attain a stable operating status and the vidicon filament is energized. At T_0 + 52 seconds,* a "prepare" signal from the active programmer

*During the 52-second period after T_0, the AVCS camera is executing its prepare-expose-and-readout cycle. The APT camera shutter is actuated about 3-1/4 seconds after power is removed from the tape motor drive in the AVCS subsystem.

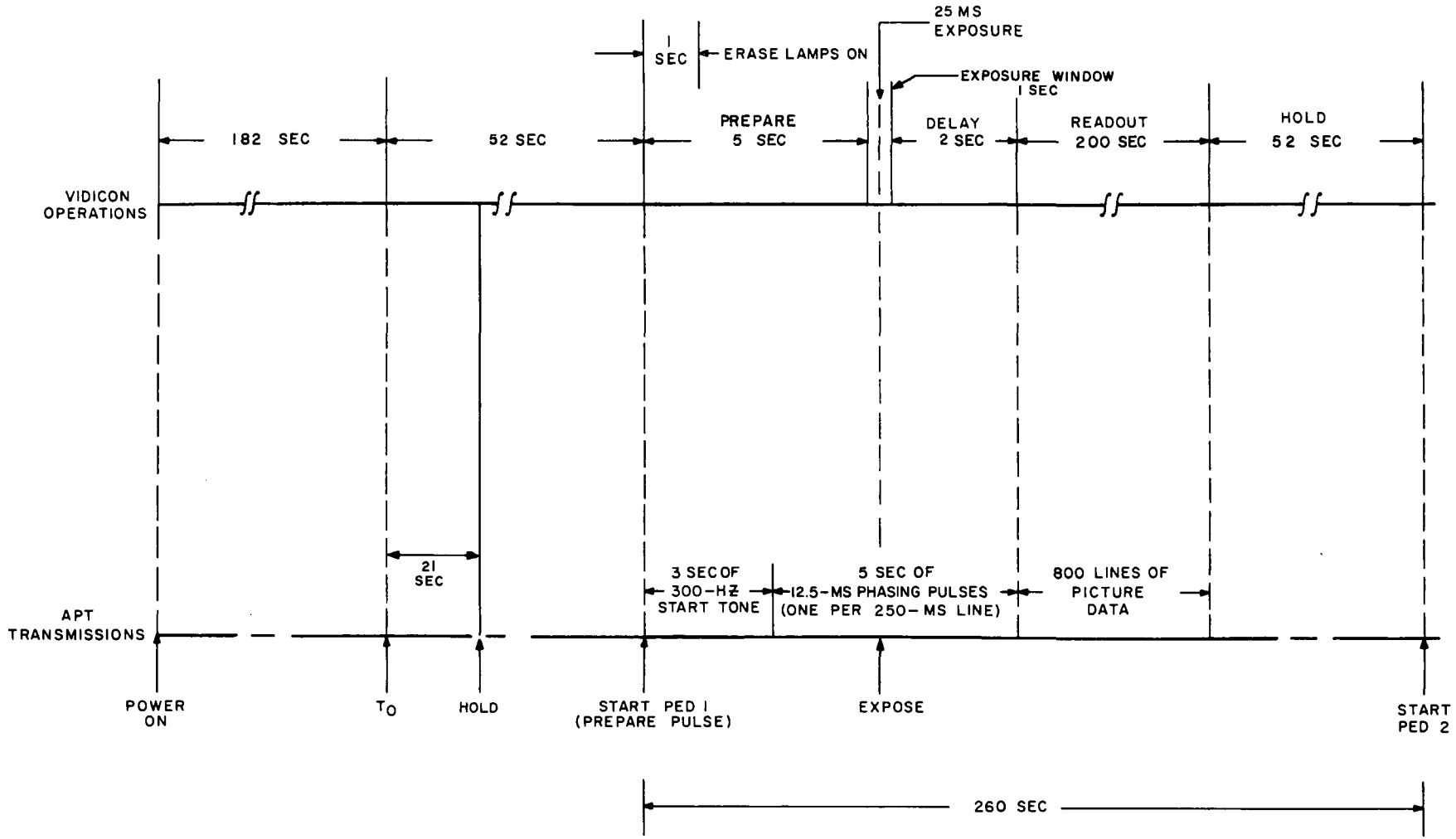

Figure 4-VI-21. APT Subsystem, Timing and Sequencing Diagram

is applied to the sequence timer to initiate the picture-taking and readout period. (The first 8 seconds of this period are known as the prepare-expose-delay, or PED, cycle.) Coincident with the leading edge of the prepare pulse, the horizontal and vertical sweep circuits are enabled, and the erase lamps, mounted around the periphery of the vidicon and in proximity to the photoconductive layer, are turned on. The lamps are energized for 1 second, during which the vidicon is flooded with light to completely discharge the photoconductor to a uniform white level, thereby removing any residual image from the previous exposure. At the same time as the lamps are energized, the vidicon beam is gated on and scanned rapidly across the image area by a 4-kHz vertical deflection voltage and a 4-Hz horizontal deflection voltage. This rapid scanning process lasts 5 seconds and deposits a uniform black-level charge on the photoconductor. Vidicon scanning is terminated and the beam is gated off 1/2 second before exposure.

During the 1-second exposure window, the sequence timer delivers an "expose" pulse to the shutter drive circuit in the camera electronics module. This circuit controls the operation of two solenoids that actuate the double-bladed, focal plane shutter in the camera sensor assembly. The shutter blades are actuated sequentially and, in moving from one side of the lens to the other, expose the vidicon for 25 milliseconds. Exposure alters the uniform charge pattern of the photoconductor by inducing each resolution element to discharge in proportion to the amount of incident light.

After a 2-second delay period, the video readout cycle is begun by gating on the vidicon beam and the horizontal and vertical sweep voltages. During the 200-second readout period, 800 discrete lines of video are produced. As the electron beam scans the photoconductor line by line, it deposits a charge on the resolution elements that have been discharged by exposure to varying intensities of light. The charging currents flowing through a load connected externally to the vidicon target electrode produce the video signal. To improve the signal-to-noise ratio, a sampling technique is used to extract the video in the stored image. During the active portion of each scan line, which lasts 237.5 milliseconds, the vidicon beam is turned on for 22 microseconds out of every 208-1/3 microseconds for a total of 1140 times per line. Consequently, the output of the vidicon is a train of 22-microsecond pulses having

a repetition rate of 4800 pps. The amplitude of each pulse is proportional to the light incident at the sampling point. This video pulse train is amplified and detected by video processing circuits to produce an analog signal that is used to amplitude-modulate a 2400-Hz subcarrier. The maximum video modulation frequency is 1680 Hz, corresponding to an 800 TV line response; the video processor attenuates all frequencies above this value at a rate of 24 decibels per octave. The amplitude-modulated subcarrier is applied through a buffer amplifier to the selected transmitter in the real-time data link.

In addition to the video information, the 2400-Hz subcarrier is modulated with a 300-Hz start tone and a series of 12.5-millisecond phasing pulses, both generated in the camera electronics module. The 300-Hz start tone is generated during the first 3 seconds of the PED cycle and is used at the APT field stations to automatically transfer the receiving and processing equipment from a standby to an operational status. For the 5 seconds of the PED cycle immediately following the start tone, a group of 12.5-millisecond phasing pulses, occurring at the rate of 1 pulse every 250 milliseconds, is provided to synchronize the horizontal scan circuits in the APT processing equipment to the vidicon scanning frequency. During the 200-second period that follows, the facsimile equipment in the APT field stations reproduces, line by line, the picture data readout of the vidicon.

At the conclusion of the 200-second readout period, the sequence timer places the APT subsystem in a "hold" status for 52 seconds. During the hold period, the 2400-Hz subcarrier is modulated with a DC level corresponding to peak white. The arrival of the next programmer "prepare" pulse, displaced from the previous one by 260 seconds, initiates another PED and readout cycle. When a complete sequence of 11 pictures is taken, the programmer removes -24.5- and -28-volt DC power from the APT subsystem. Subsystem power is reapplied 182 seconds before T_0 on the next orbit. Thus the picture-taking sequence is repeated, as described in the preceding discussion, once during each orbital revolution, until the active programmer is reloaded or turned off.

3. APT Subsystem and Spacecraft Interface Signals

All subsystem interface signals, with the exception of telemetry output voltages, are listed and described in Table 4-VI-5. For a complete list of the telemetry points in the APT subsystem, refer to Table 4-IX-13.

TABLE 4-VI-5. APT SUBSYSTEM AND SPACECRAFT INTERFACE SIGNALS

Interface Signal	Description
	SPACECRAFT POWER
-24.5 VDC	Regulated within ±2 percent. This is the main power source for the APT subsystem and is switched on and off in accordance with the "power on" signal described below.
-28 VDC	Unregulated. Powers the solenoids that operate the shutter when the shutter drive circuit is triggered by the sequence timer. This power source is also switched on and off by the "power on" signal.
	TIMING
9600 Hz	A synchronizing signal supplied by the time-base generator to the sequence timer. The clock signal is from 0 to +4.4 volts peak-to-peak.
Power On	A -24.5-volt DC level that is switched on 234 seconds before the first "prepare" signal is delivered to the APT subsystem. The "power on" signal is maintained at -24.5 volts DC throughout the entire 11-picture sequence.
Prepare	A 0 to +4.4 VDC pulse, 1.25 seconds in duration. It is delivered to the sequence timer 5.5 seconds prior to vidicon exposure.
	OUTPUT
Video	An amplitude-modulated 2400-Hz subcarrier, 2.8 volts peak-to-peak amplitude (10,000-foot-lambert scene), 95 percent modulation, 1680 Hz modulation-signal bandwidth.
Telemetry	See Table 4-IX-13 in Section IX for a complete list of the telemetry points in the APT subsystem.

4. APT Subsystem Characteristics

The salient characteristics of the APT subsystem are summarized in Table 4-VI-6.

TABLE 4-VI-6. APT SUBSYSTEM CHARACTERISTICS

Characteristics	Description or Value
Picture Coverage	
Picture projection*	1700 miles square
Pictures per orbit	11
Time for a 11-picture sequence	Approximately 52 minutes
Time between pictures	260 seconds
Picture overlay (along orbital track)	50 percent
Camera and Associated Electronics	
Lens	f/1.8, 5.7 mm focal length
Field of view	Approximately 108 degrees across the picture diagonals; effectively 89 ±1 degrees across the picture flats
Ground resolution	Approximately 2 miles per scan line
Image area (scanned)	0.48 inch square
Resolution (horizontal)	25-percent response at 600 TV lines
Aspect ratio	1:1
Prepare-expose-delay (PED) cycle duration	8 seconds
Vidicon exposure time	25 milliseconds
Vidicon readout time (frame period)	200 seconds
Horizontal sweep period	250 milliseconds per line
Horizontal sweep time	237.5 milliseconds
Horizontal blanking and retrace	12.5 milliseconds
Horizontal lines per frame	800 (noninterlaced)
Video sampling pulse width	22 microseconds
Video sampling pulse rate	4800 pps
Number of video sampling pulses per line	1140
Start tone frequency	300 Hz
Start tone duration	First 3 seconds of PED cycle
Phasing-pulse repetition rate	4 pps
Phasing-pulse width	12.5 milliseconds
Phasing-pulse gating time	Last 5 seconds of PED cycle
Video subcarrier	2400 Hz
Modulation frequency	1680 Hz maximum
Type of modulation	Amplitude, double-sideband with carrier
Percentage of modulation	95 percent
Video subcarrier amplitude for start tone, phasing pulses, and video	2.8 volts p-p (white), 0.07 volts p-p (black)
Signal-to-noise ratio	32 db minimum

*Based on an altitude of 775 nautical miles.

5. APT Subsystem Assemblies

The camera sensor assembly and the camera electronics module that comprise an APT subsystem are similar to those used successfully on Nimbus, TIROS, and TOS satellites. In addition, ITOS will employ a double-bladed, solenoid-actuated shutter. The solenoids will be controlled by a shutter drive circuit of the improved design with the following exception. For the APT subsystem, the two timing signals that control shutter operation will be supplied by logic internal to the camera electronics module. However, the two timing signals can originate from a source in the spacecraft other than the electronics module, should future requirements so dictate.

D. SCANNING RADIOMETER SUBSYSTEM

1. Introduction

The scanning radiometer (SR) subsystem measures emitted radiation from the earth during day and night and measures reflected radiation from the earth during daytime. The data obtained is transmitted in real time to local user stations, and is also recorded for later playback to the CDA stations.

The scanning radiometer is a new meteorological instrument built by Santa Barbara Research Center especially for the ITOS spacecraft. The radiometer is unique in its use of two spectral regions and high spatial resolution. The radiometer measures reflected radiation from the earth in the 0.52- to 0.73-micron region (visible) during daytime, and measures emitted radiation from the earth in the 10.5- to 12.5-micron region (infrared) during day and night.

The subsystem permits determination of the surface temperature of the ground, sea, or cloud tops that are viewed by the radiometer. The 10.5- to 12.5-micron spectral region permits the surface temperature to be determined in the daylight as well as at night since the reflected solar radiation in this wavelength region is a small percentage of the emitted radiance. The visible region measurement of reflected solar radiation has a higher calibration accuracy than the camera systems presently used and is not subject to shading which occurs in the vidicon camera systems. Table 4-VI-7 shows some of the characteristics of the scanning radiometer.

TABLE 4-VI-7. SCANNING RADIOMETER SUBSYSTEM PARAMETERS

Parameter	Visible Channel	IR Channel
Resolution Angular Ground at 775 n mi	 5.3 milliradians 4 n mi	 5.3 milliradians 4 n mi
Spectral Region	0.52 to 0.73 microns	10.5 to 12.5 microns
Sensitivity, Noise Equivalent Irradiance	7.5×10^{-10} w cm^{-2}	4.2×10^{-10} w cm^{-2}
Dynamic Range	20 to 8.5k foot-lamberts (Scene Brightness)	185 to 330°K (Scene temperature)
Detector	Silicon Photovoltaic	Thermistor bolometer
Electrical Bandwidth	455 Hz	455 Hz
Diameter of Optics	5 inches	
Scan Rate	48 rpm	
Power Requirement	7 watts	
Weight	19.2 pounds	

The SR subsystem comprises: (1) two scanning radiometers, (2) a dual SR processor, and (3) two scanning radiometer recorders (SR recorders). A block diagram of the subsystem is shown in Figure 4-VI-22. Each radiometer and tape recorder can be turned on or off by command from a CDA station. Each half of the SR processor is associated with one radiometer and is powered when that radiometer is powered.

The units of the subsystem are mounted on the spacecraft as shown in Figure 2-I-3. The radiometer mounting is required to permit them to scan approximately 150 degrees without obstructions. The radiometers are mounted such that the spacecraft structure provides the maximum sun shielding.

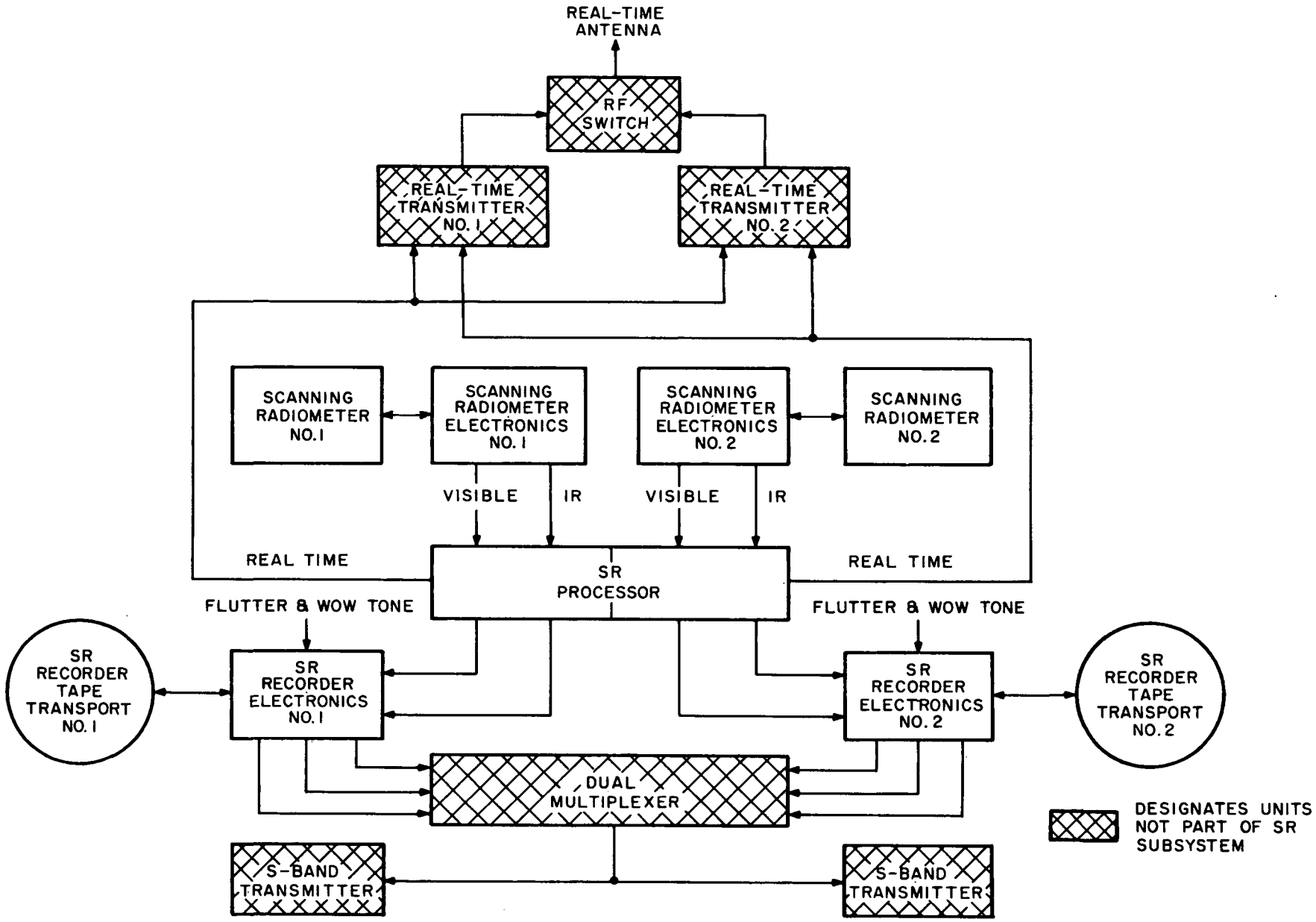

Figure 4-VI-22. Scanning Radiometer Subsystem, Block Diagram

As the spacecraft proceeds along its orbit, the radiometer scans the earth's surface from horizon to horizon, perpendicular to the orbital plane. The radiometer scans the earth by means of a continuously rotating mirror which is inclined 45 degrees to its axis of rotation (parallel to the satellite's velocity vector). Thus, the optical axis scans in a plane perpendicular to the satellite's velocity vector as shown in Figure 4-VI-23.

The manner in which the mirror rotates causes a scan across the earth (shown as scan n). As the scan is completed, and the mirror returns to the starting point, a certain time has elapsed (equivalent to one scan period), and the satellite has progressed along its scan track by approximately 5 miles. Another area is then scanned, shown as scan n + 1, and this is repeated throughout the orbit.

The scanning radiometer output is processed in the SR processor, where time code data and scanning radiometer telemetry data are combined with the IR and visible radiation signals, for recording on tape. (Time code and telemetry data are not included in the real-time transmitted data.)

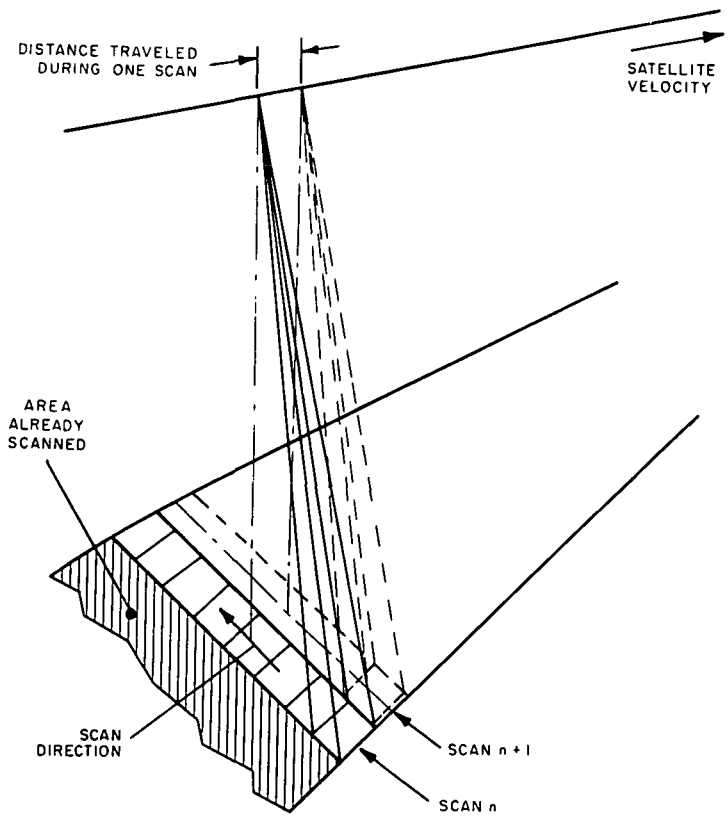

Figure 4-VI-23. SR Scan Projection

The SR processor outputs are frequency modulated in the SR recorder. The subcarrier frequency range is from 2.4 to 3.3 kHz. The two frequency-modulated radiometer signals and a 3.125-kHz flutter-and-wow signal are recorded simultaneously on the three recorder channels.

The recorder tape speed is 1.875 inches per second; it has a total recording capability of 145 minutes.

When the playback command is received, power is removed from the record circuits; power is applied to the playback circuits; the direction of tape travel is reversed; and all three tape tracks are played back simultaneously at a tape speed of 30 inches per second (16 times the record speed). When played back the subcarrier frequency range becomes 38.4 to 52.8 kHz.

In normal operation the SR signals are only recorded during the nighttime portion of each orbit. However, during at least one orbit per day, no CDA ground station contact is available, but the recorders will store at least two orbits of data. The command structure of the spacecraft will permit one orbit to be stored on each recorder or both orbits to be stored on one recorder. On occasion two orbits in succession do not have satisfactory CDA station contact. In this case recording can take place on both recorders.

Playback of the recorders can be commanded to occur either simultaneously or separately. Where simultaneous playback is commanded, only the IR channel of each recorder will be transmitted, together with the associated flutter-and-wow signals. When only one recorder is being played back both the IR and the visible channels together with the one flutter-and-wow signal will be transmitted.

An alternative operating mode permits recording to take place continually (during both day and night). In this case switching from one recorder to another takes place automatically as the spacecraft crosses the night/day terminator. On receipt of the playback command the recorder that is not recording will be played back. If the night/day switching is to take place while playback is in progress, the switchover is delayed until playback is complete.

2. Scanning Radiometer and Electronics

a. General

The ITOS scanning radiometer and the scanning radiometer electronics are shown in Figure 4-VI-24. The scanning radiometer performs the optical scanning, and the electronics package contains most of the radiometer control and detection electronics.

The radiometer outputs for a typical scan are shown in Figure 4-VI-25. There is a small portion before the earth scan wherein the amplifier DC level is restored by viewing outer space. (In the infrared and visible radiation regions, outer space has effectively no radiation output.) From this point on, the tilt of the signal depends on the low frequency response of the amplifier. Following the DC clamp there is a small portion where outer space is seen. This assures that the DC restore will be entirely in space even though the spacecraft may be as low as 600 nautical miles. The earth is then scanned, producing the variable output shown. After the earth scan, there is a brief repeat scan of outer space. The amount of tilt can be determined by comparison of the pre-earth view of space with the postearth view.

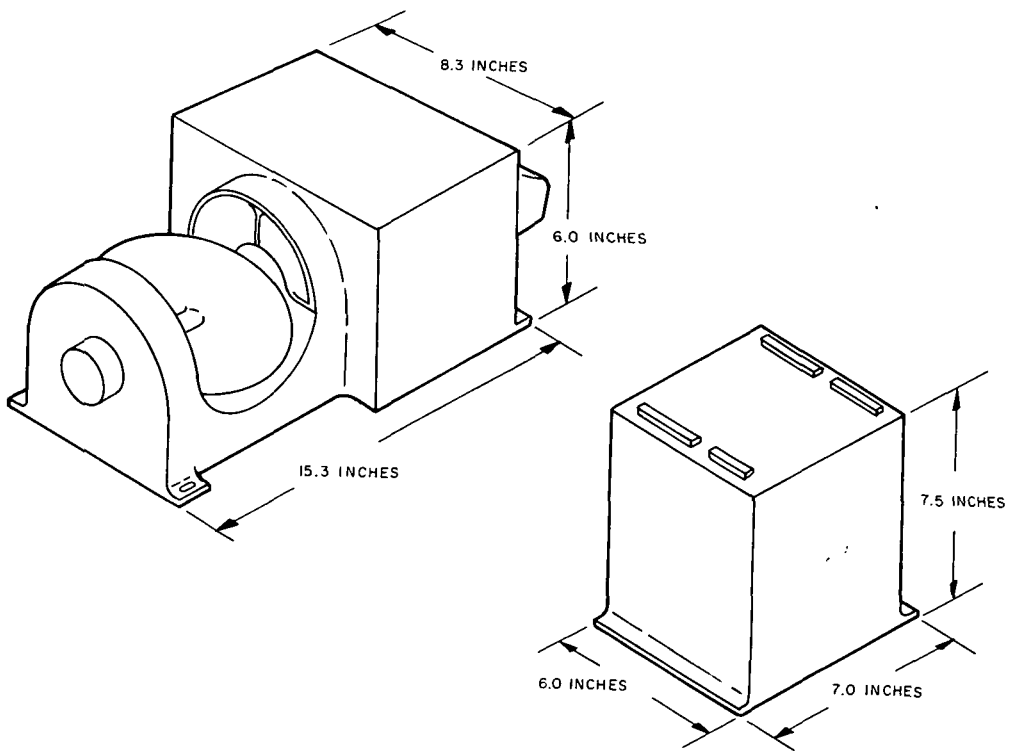

Figure 4-VI-24. Scanning Radiometer and Electronics

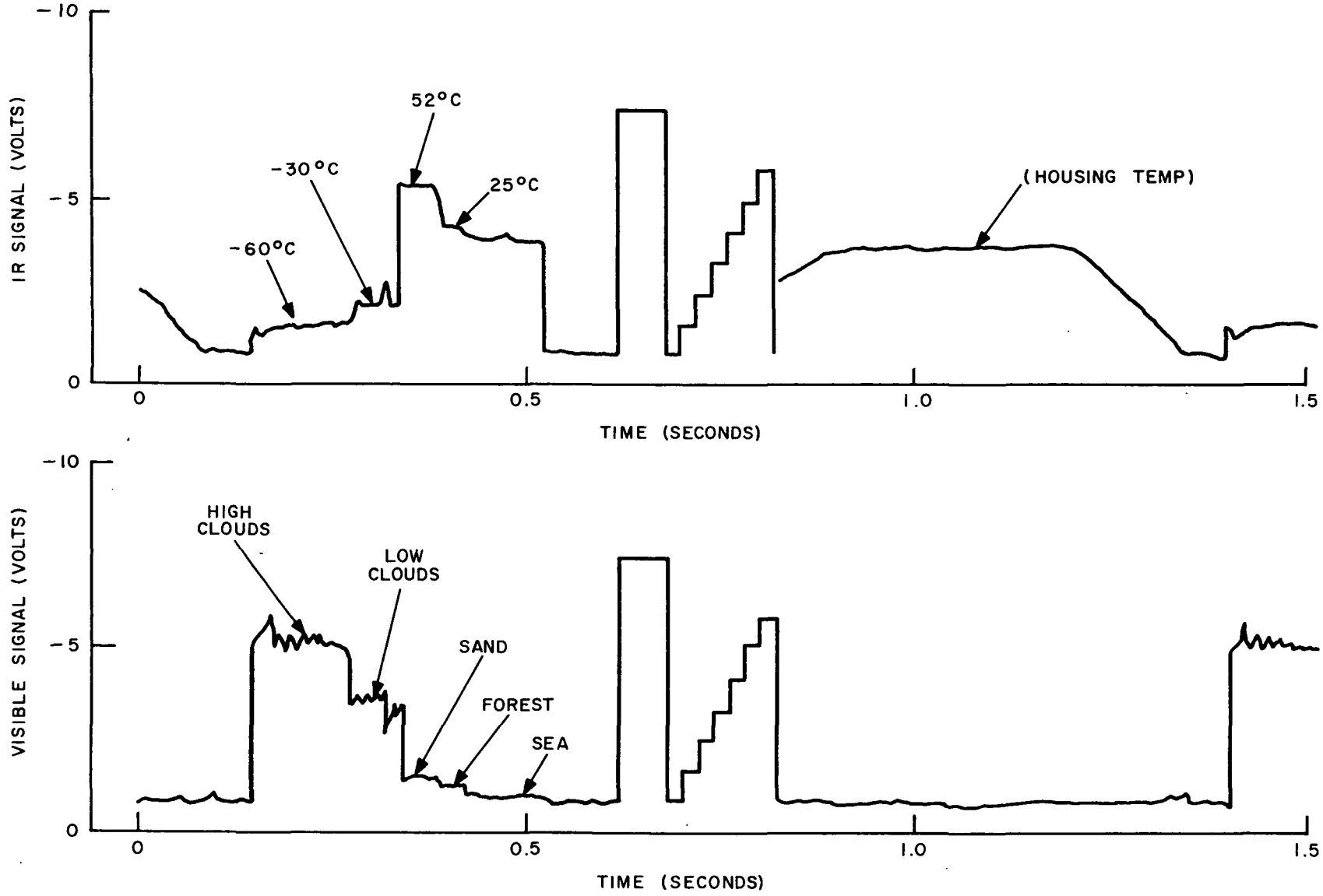

Figure 4-VI-25. IR and Visible Channel Signals

The synchronization pulse is then added. The synchronization pulse is preceded and followed by periods of "front and back porch", where the video signal is replaced by an internally generated zero signal. This assures that the edges of the synchronization pulses are always measured from zero to the point of maximum excursion. Following this, there are voltage calibration steps, starting with the zero clamp level. The steps consist of approximately 1-volt increments at the output of the radiometer. The radiometer then scans the internal housing of the unit and starts the amplifier restore period again, prior to another earth scan.

The output format of the visible radiation channel is identical to the IR output format. However, it can be seen in Figure 4-VI-25 that the brightest (or whitest) objects are not necessarily the warmest. This also explains why the radiometer housing exhibits evidence of IR radiation but almost no visible radiation (it is black).

On-board calibration is provided for both channels. The IR channel is calibrated at the cold extreme of the range by measuring the response to outer space. This area has essentially zero output radiance in the IR range. On the warm side, the radiometer measures the IR radiation from the inside of the radiometer housing, during the back scan period. The housing temperature can be determined from the telemetry outputs of the four temperature sensors located in the housing. The radiance level from the housing will be approximately 60 percent of the radiance from a 330°K scene.

The visible channel calibration occurs once each scan, when the visible calibration is commanded ON. Outer space provides a "black level" calibration point and an incandescent lamp located close to the detector provides a "white level". This lamp is operated below its rated voltage in order to assure long life and constancy of the radiation output. This technique of calibration does not evaluate the performance of the optical system, since the power required to operate a lamp which would also check the optics would be beyond the capability of the spacecraft power supply.

The path followed by the satellite subpoint is shown for two successive orbits in Figure 4-VI-26. The useful scanned area appears wider towards the north and south because of the Mercator projection used in the map. The useful area is actually constant in width, the only possible variation being that due to changes in satellite altitude. At the equator, there is an overlap of nearly 1 degree great circle arc.

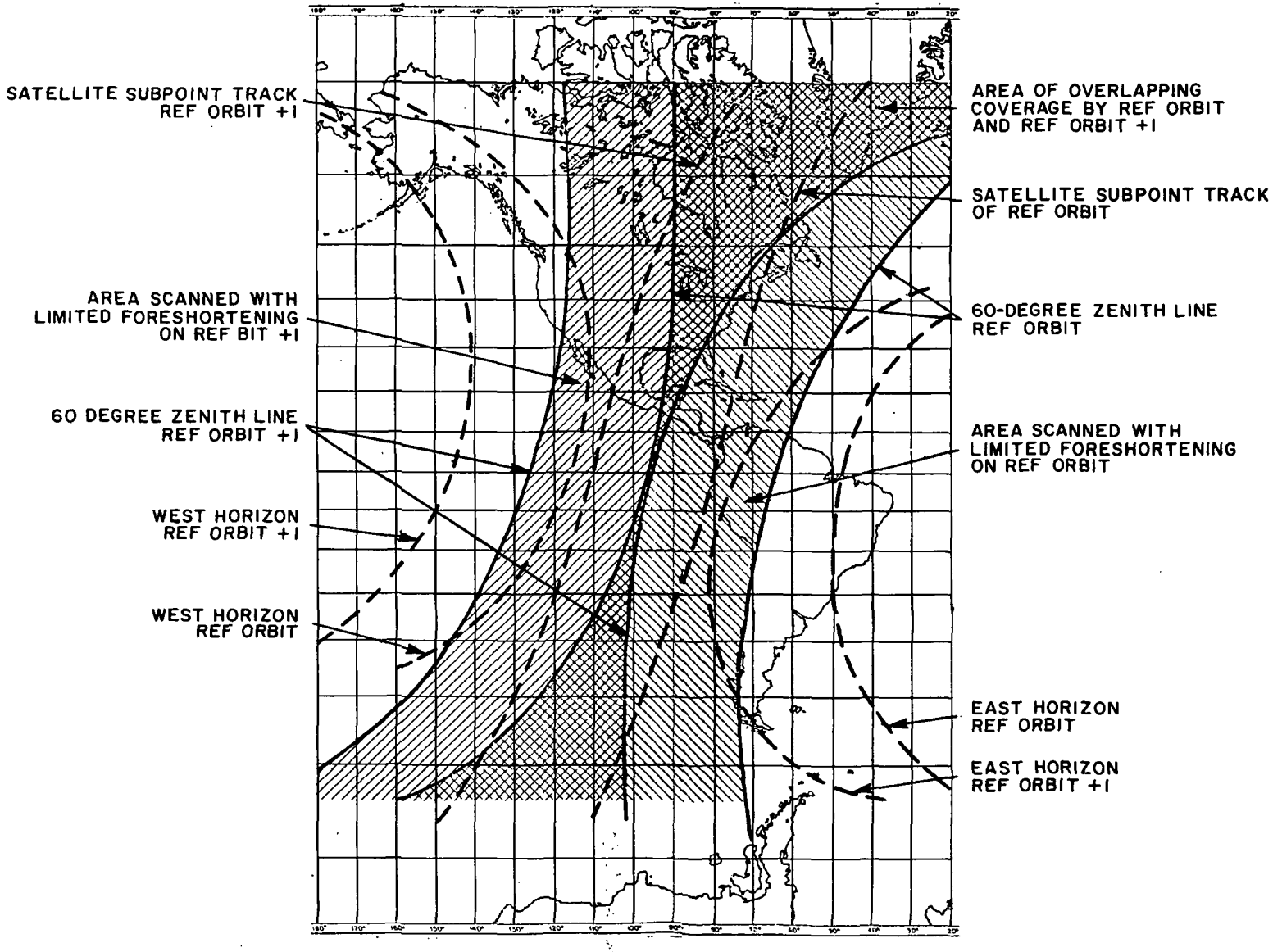

Figure 4-VI-26. Scanning Radiometer Coverage (Altitude: 775 Nautical Miles)

As shown in Figure 4-VI-27, the earth scan can include all land in the ±55-degree nadir angle range. However, due to foreshortening at the angular extremes, the useful nadir angle is limited to ±45 degrees. This corresponds to a 60-degree zenith angle, as shown. It has been determined that the data remains usable (without excessive foreshortening) if the zenith angle does not exceed 60 to 65 degrees. With an altitude of 775 nautical miles, there is sufficient overlap so that all regions of the earth below the satellite can be viewed with a zenith angle of 60 degrees.

Due to the large scan angle of the radiometer there will be periods when it will scan across the sun. Figure 4-VI-28 shows this geometric relationship between the spacecraft and the sun. Though the radiometer may be in the sun at other times, the only periods in the orbit where the sun comes into the field of view will be when the satellite is in the plane of the page.

The spacecraft is expected to operate at sun angles (γ) between 30 and 60 degrees. It can be seen that for sun angles greater than 35 degrees, either the earth or the spacecraft will mask the radiometer from the sun. At sun angles between 30 and 35 degrees, the earth does not provide masking at an altitude of 775 nautical miles, and the radiometer will scan the sun for about 1 minute. If the sun angle decreases below 30 degrees, the scanning time across the sun increases, until at 0 degrees the radiometer scans the sun continuously.

The radiometer is designed to withstand direct solar exposure. The IR channel will be measuring radiation when sun sensing occurs. All data taken during scans in which direct sun exposure occurs will be completely lost, but the radiometer recovers rapidly when the solar input stops.

Direct solar exposure of the visible channel occurs during the night (satellite subpoint) when useful data is not expected, but the detector will be exposed to a much higher solar energy level. However, the radiometer design provides adequate protection to assure that the detector will survive the direct solar exposure.

The estimated weight of the scanning radiometer is 12.2 pounds, and the estimated weight of the electronics package is 7.0 pounds.

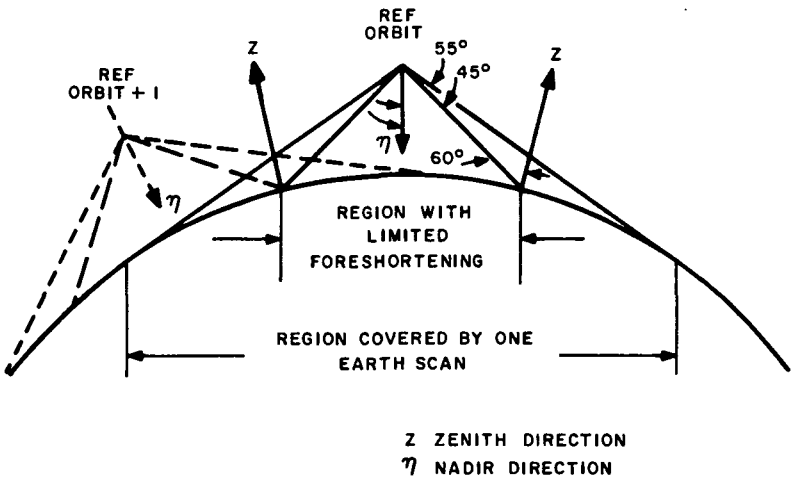

Figure 4-VI-27. Radiometer Scan Geometry

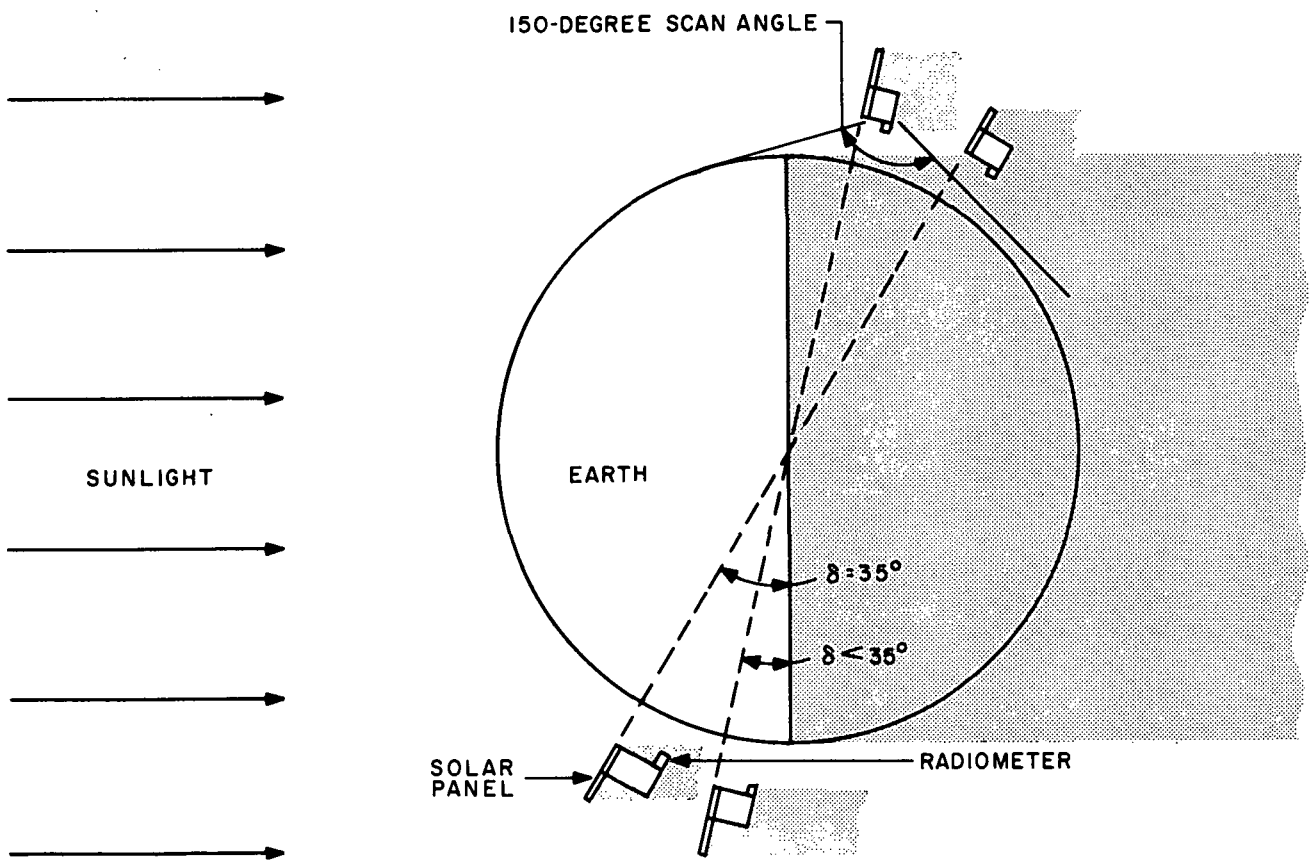

Figure 4-VI-28. Orbital Conditions for Direct Radiometer Sun Scanning

b. Scanning Radiometer

The major components in the scanning radiometer are: a motor-driven scanning mirror, collecting optics, a beamsplitter, a radiation filter, a photovoltaic silicon detector, and a thermistor bolometer detector; see Figure 4-VI-29.

The scan mirror is driven through a gear train by a 2000-rpm hysteresis synchronous motor; the scan mirror rotates at 48 rpm. The motor is operated from a power amplifier which requires a two-phase 100-Hz square wave input. The scanning radiometer contains backup circuits which assure that the mirror will continue to rotate, even if there is a loss of the -24.5-volt power line or the 400-Hz clock signal. The backup circuits include a 400-Hz oscillator and switch-over provisions to operate the mirror drive from the unregulated -28- to -36-volt line. The backup 400-Hz oscillator circuit also includes a method of synchronizing the mirror position with the 0.4-pulse-per-second count from the time base generator. The scan drive motor is turned on immediately prior to launch and operates continuously even when the radiometer is not being used. The motor may be commanded off if the radiometer subsystem becomes nonoperational.

In operation, earth or space radiation reflects from the rotating mirror to the collecting optics. The collecting optics is a 5-inch diameter Cassegrainian system. The radiation is then focussed and directed to the beamsplitter, which divides it into two portions. Long-wavelength radiation (IR) passes through the beamsplitter (which is a dichroic mirror), and short-wavelength radiation (visible) is deflected to the visible detector section. The IR radiation level is measured by a solid-state radiant energy detector (thermistor bolometer).

The visible radiation after being reflected from the beamsplitter passes through a filter which transmits energy in the wavelength range of 0.52 to 0.73 microns. The visible radiation level is measured by a photovoltaic silicon detector.

The 10.5- to 12.5-micron region was selected for IR detection in order to avoid spurious radiation indications. As indicated in Figure 4-VI-30, the earth atmosphere has absorption bands at the 2.7-micron region (water and carbon dioxide), 4.2-micron region (carbon monoxide and carbon dioxide), 5- to 8-micron region (water vapor), a very sharp, highly

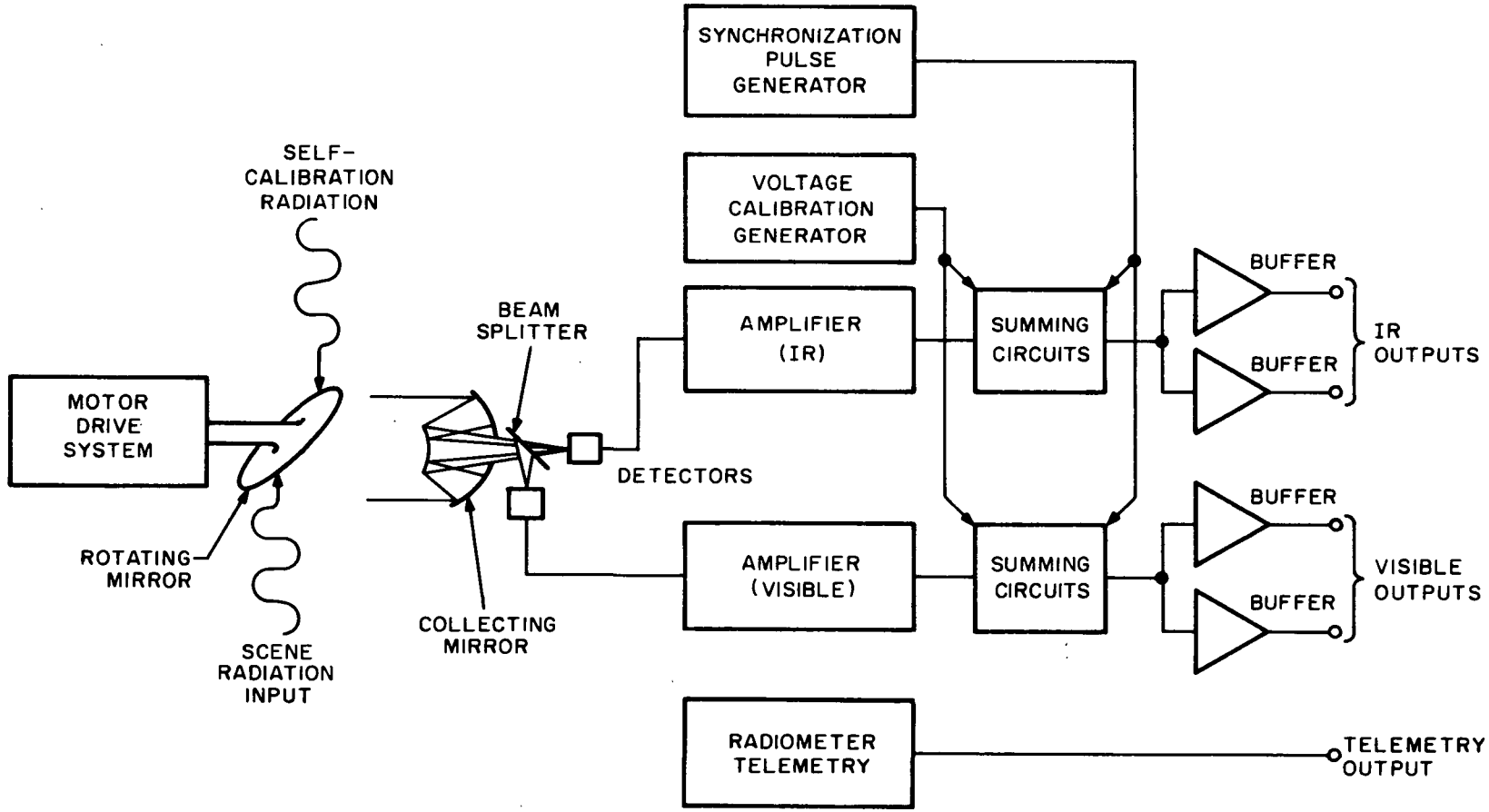

Figure 4-VI-29. Scanning Radiometer Block Diagram

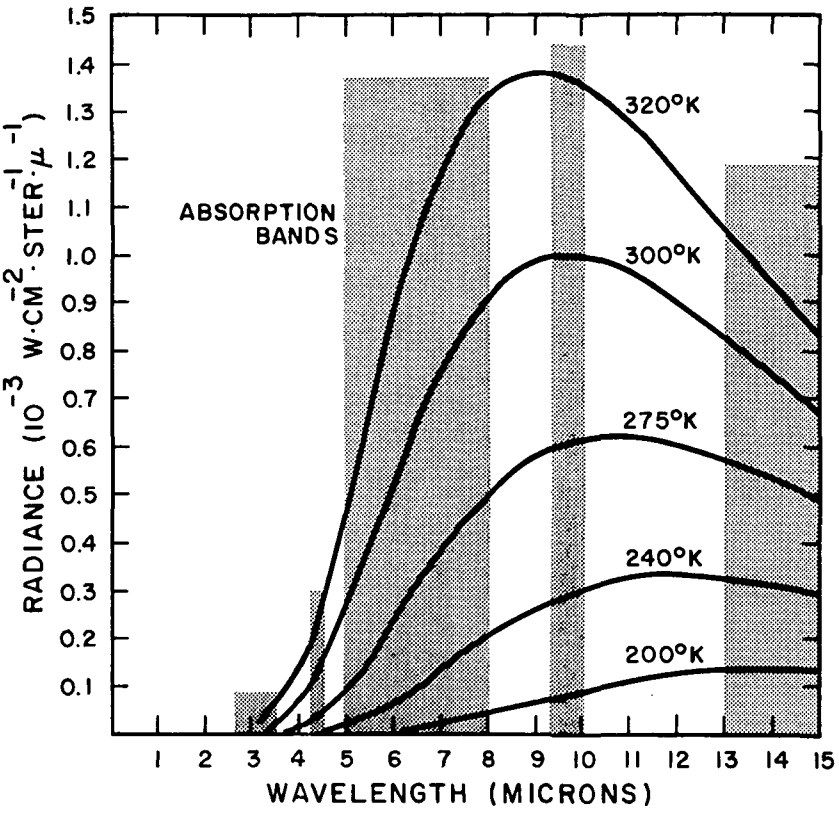

Figure 4-VI-30. Earth Atmosphere Radiation Absorption Bands

absorbing line in the 9.6-micron region due to ozone absorption, and the carbon dioxide absorption band in the 13- to greater than 15-micron region. Since the available filters are not "ideal", it is necessary to specify half-power points (50-percent transmission) of 10.5 and 12.5 microns, in order to define the required filter.

In addition to showing the atmospheric absorption bands, Figure 4-VI-30 also shows the function of radiance versus wavelength with temperature as the parameter.

Figure 4-VI-31 indicates the typical radiation transfer characteristic of the IR channel as a function of scene temperature. The maximum signal is adjusted to have an amplitude of approximately 6 volts at 330°K. A 0.2-volt signal would be expected from a scene temperature of approximately 180°K. The noise limit is approximately 60 millivolts. (With reference to meteorological scene temperatures, 185°K is equivalent to the temperature of a very high cloud, 320°K corresponds to desert surface temperature, and outer space would be approximately 4°K.) In order to differentiate between high clouds and outer space, it is necessary to

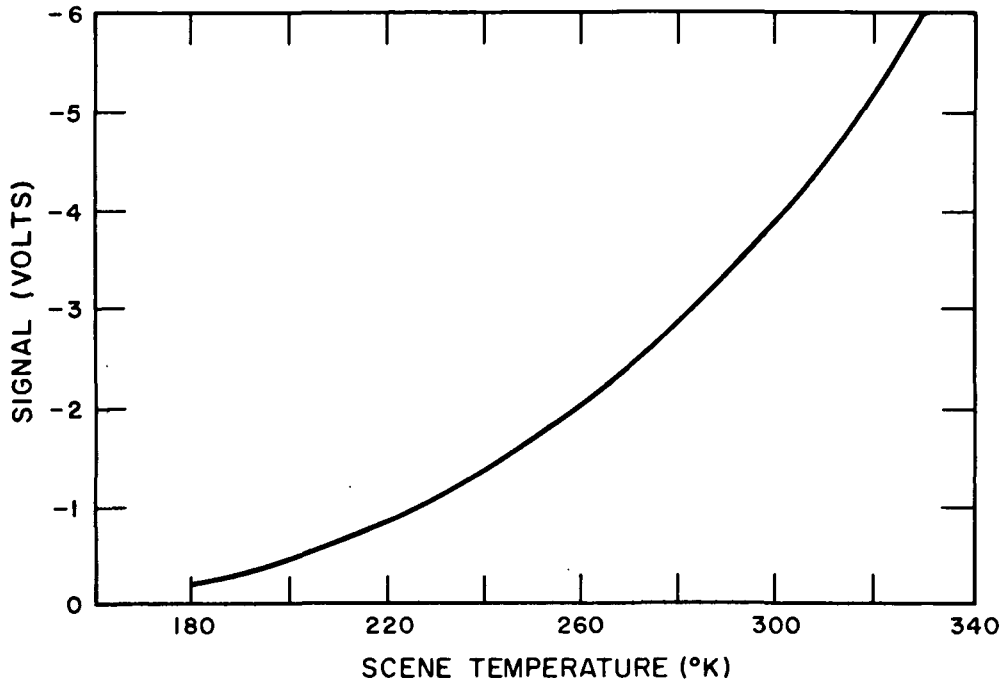

Figure 4-VI-31. Typical IR Radiance Transfer Curve

distinguish between 185 and 4°K. The difference between -0.2 volt and the 60-millivolt noise level make this transition readily discernible.

The short wavelength response of the radiometer is in the 0.52- to 0.73-micron region. One of the reasons for selecting the visible part of the spectrum for the second channel was the ease of relating the gray shades of the picture to normal visual experiences. An additional advantage is in the different appearance of terrestrial features in the two spectral regions. This helps resolve some of the questions of interpolation which might arise if only a one-wavelength region were sensed.

The long wavelength limit was chosen to be 0.73 micron as a result of ESSA analyses on photos taken during the MA-8 and MA-9 Mercury missions. Limiting the wavelength at this point also results in pictures of greater contrast, particularly between clouds and earth.

The transfer characteristics of the visible channel are shown in Figure 4-VI-32. Photometric units are used to permit ready comparison with TV cameras. (The maximum scene

brightness given on the graph is equivalent to a scene radiance of about 25 milliwatts per square centimeter per steradian in the spectral interval from 0.52 to 0.73 micron.) The detector is expected to be nearly linear throughout its entire range. Since the signal-to-noise ratio will be about 400-to-1 at 8000 foot-lamberts, the noise level will be approximately equal to 20 foot-lamberts. It is doubtful that as great a range as this will be achieved at the ground because of limitation in the communication link.

S/N

As a part of the design effort, a study involving the scanning radiometer life and lubrication characteristics is presently in progress. The radiometer bearings will operate in an oil vapor atmosphere of Bendix Pioneer P-10 with a reservoir in a sintered nylon block. The Santa Barbara Research Center is conducting this study and will prepare a report covering the lubrication techniques and life tests performed.

c. Scanning Radiometer Electronics

The scanning radiometer electronics contains the following circuits:

- Video amplifiers (2),
- Buffer amplifiers (4),
- Time multiplexer circuits (2),
- Synchronization pulse generator,
- DC-to-DC converter,
- Power line filters,
- Day/night mode selector relay,
- Electronics on/off relay,
- Scanning radiometer electronics temperature sensor, and
- Telemetry circuits.

The radiometer electronics are designed to establish a desired gain characteristic as a function of the input radiance level. The radiometer electronics also includes the circuits necessary to provide system calibration. The signal and telemetry outputs of the radiometer are connected to the SR processor.

The AC signal from the preamplifier in the scanning radiometer is further amplified by the video amplifier in the radiometer electronics. The scanning radiometer is designed to provide an output signal which is 0 volt offset for no scene radiance, and -6 volts offset for a scene radiance equivalent to 330°K. (The radiance level is usually equated to the temperature of an ideal black body for ease of meteorological interpretation.)

Two pickups on the mirror shaft provide pulses which are used in the electronics package to generate the line scan synchronizing signal and to initiate the amplifier restoring period.

The synchronization pulse occurs after the radiometer field of view is swept off the earth and is approximately 80 degrees from the nadir. The same pulse which generates the synchronization signal also initiates the delay which starts the voltage calibration signal. The voltage calibration signal consists of seven voltage levels ranging from -6 to 0 volts. The synchronization signal and the voltage calibration signal are time-multiplexed into the radiometer output signal. A summing circuit adds the synchronization and voltage calibration signal into the video lines; the composite outputs are buffered to provide signals for the real time transmission and for the tape recorders.

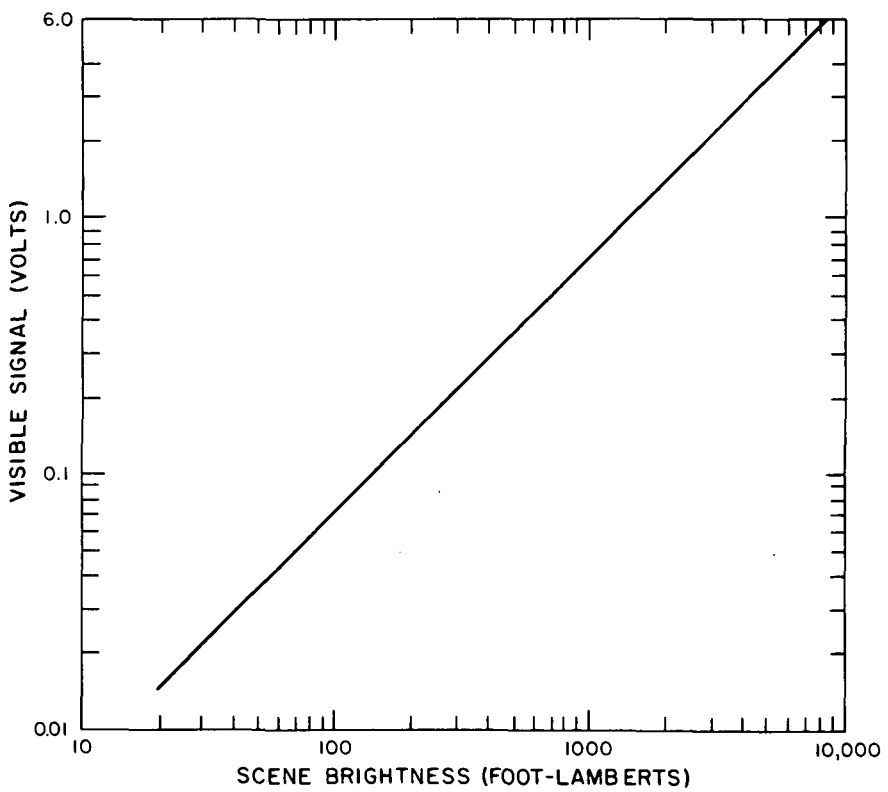

Figure 4-VI-32. Visible Channel Transfer Characteristics

The synchronization signal consists of a single -8-volt pulse of 60-millisecond duration. The voltage calibration signal is included to permit amplitude calibration, and since there are several discrete levels, the signal also permits analysis of circuit gain and linearity. Telemetry functions are provided to help establish the calibration of the radiometer and to determine its operational characteristics.

3. SR Processor

The SR processor is used to time-multiplex the radiometer telemetry signal into the radiometer data signal when the sensor is viewing the radiometer housing during each mirror revolution. The resultant signal is supplied to the SR recorders only; it is not applied to the real-time transmitters. Table 4-VI-8 lists all of the input and output functions for one side of the SR processor.

TABLE 4-VI-8. SR PROCESSOR INPUT AND OUTPUT FUNCTIONS

Input Functions	Output Functions
Commutator On/Off	IR composite signal (2)
IR	Visible composite signal (2)
IR Real Time	Modulated real-time signal (2)
Time Code	Test point (3)
Horizon Sensor	Telemetry (3)
IR Telemetry (12)	
Full-Scale Calibration (2)	
Zero-Scale Calibration (2)	
Visible Telemetry (12)	
-24.5 Volts	
Ground (3)	
Night/Day Signal	
Visible/IR Select	
-24.5-Volt Modulator Power	
4.8 kHz	

During each scan (1.25 seconds per scan), one channel of data is multiplexed into the radiometer video output. The 0.6-second commutation period occurs during the time that the radiometer mirror rotates from the 270- to the 90-degree position (angles are referenced to the radiometer mirror-drive system). During the commutation period, the radiometer mirror is "looking" at the radiometer housing. Initiation and termination of the commutation period are controlled by two pulses generated by the mirror-drive system. These pulses are referred to as the "telemetry ON" and the "telemetry OFF" pulses.

The radiometer output to the processor is a DC signal with the synchronization pulse and the voltage-calibration staircase inserted. The voltage-calibration staircase is initiated at the time when the mirror reaches the 270-degree rotational position. Sixteen subcommutation gates are used in the processor; hence, one complete telemetry readout occurs every 16 scan lines of radiometer operation (20 seconds). There are sixteen distinct informational items which are multiplexed into the radiometer output signal. Among the most important are:

- Constant frequency tone to indicate whether visible or IR radiation is being transmitted (this also marks the telemetry frame).
- Temperature telemetry for housing (four points).
- Radiometer telemetry points (diagnostic items such as mirror rotation rate).
- Satellite pitch and roll sensor output.
- 0.0- and 5.0-volt reference signals.
- Time code (satellite reference). This signal is generated in the redundant time base generators. It is a 24-bit binary code which is updated and read out every half second.

The following telemetry points are also directed to the spacecraft telemetry system:

- Motor rotation indicator,
- Electronics power on/off, and
- Temperature sensor for radiometer cavity.

Figure 4-VI-33 is a block diagram of one side of the SR processor. The sequencing of the commutation gates is controlled by a simple counter and steering logic. When a telemetry on pulse is received, the counter advances one count while the logic disables the video output of the radiometer and enables the output of the selected commutation gate. The video output may be visible or IR signals, depending upon selection. When the telemetry off pulse is received, the video output is reenabled and the telemetry gate output is disabled. The outputs of the video output gate and the 16 telemetry gates are summed and distributed to either SR recorder.

Since the SR processor contains a complete subcommutation system for each radiometer, the outputs are combined in OR gates in the recorders to provide the redundant coupling of either radiometer output to either recorder. Each commutation circuit is associated with one radiometer. The commutation circuits are implemented with integrated circuitry, and each of the commutation systems contains its own power converter.

4. SR Recorders

a. General

A simplified block diagram of the SR recorder is shown in Figure 4-VI-34. Two video inputs (one IR and one visible) from the SR processor are applied to channels 1 and 3 of the recording circuits of either of two tape recorders, along with a 3.125-kHz signal. This 3.125-kHz signal provides a pilot tone from which tape recorder flutter-and-wow can be detected (and compensated for) in the ground equipment.

The output of the SR processor frequency-modulates the subcarriers of channels 1 and 3. The two modulated signals and the 3.125-kHz flutter-and-wow signal are recorded separately on three tape tracks at a tape speed of 1.875 inches per second; each track has a total recording capability of 145 minutes. The record circuits are powered during the record cycle only. The flutter-and-wow channel playback preamplifier is enabled during the record cycle for telemetry monitoring of the tape motion.

When the playback command is received, power is removed from the record circuits; power is applied to the playback circuits; the direction of tape travel reverses; and all three tape

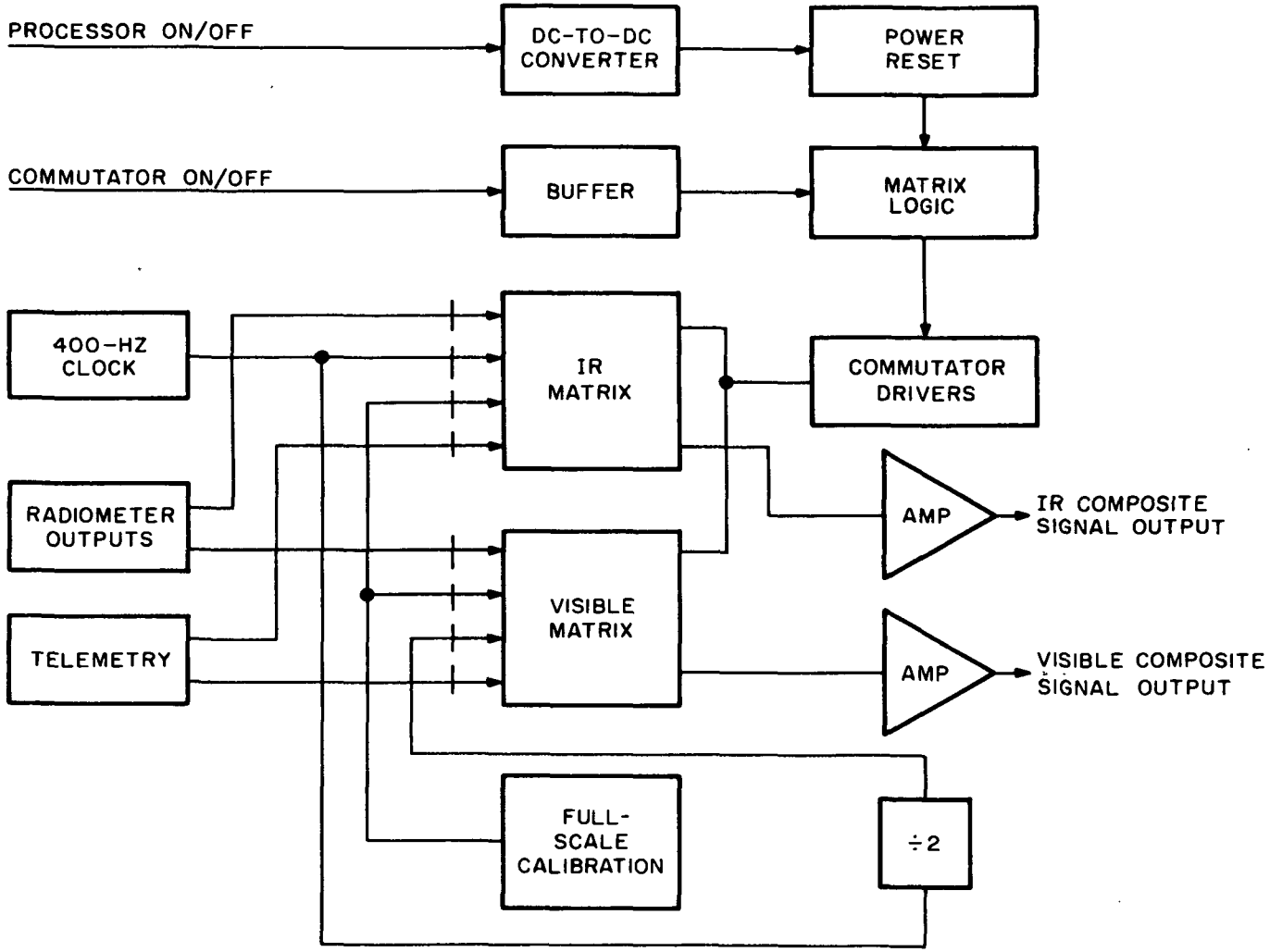

Figure 4-VI-33. SR Processor Block Diagram

tracks are played back simultaneously at a speed of 30 inches per second (16 times the record speed).

The tape recorder enclosure consists of a spun-aluminum dome and base pan. The enclosure is 14 inches in diameter and approximately 7.5 inches deep; it is hermetically sealed and pressurized to 16.5 psia with a mixture of 90-percent nitrogen and 10-percent helium. The tape recorder is bolted to the equipment panel at three points. The maximum weight of the tape recorder is approximately 20 pounds.

Table 4-VI-9 summarizes the SR recorder's characteristics.

TABLE 4-VI-9. SR RECORDER CHARACTERISTICS

Description	Characteristic
Recording Speed	1.875 inches per second
Playback Speed	30 inches per second
Total Record Time	145 minutes
Playback Time	9.1 minutes maximum (end-to-end)
Heads	One three-channel record head, One three-channel playback head, and One permanent magnet erase head (full tape width)
Pressurization	16.5 psia (90-percent nitrogren and 10-percent helium)
Tape	1360 feet of 0.25-inch wide, 0.0011-inch thick, Mylar base, instrumentation magnetic tape
Seal	O-ring, flange, and pressure fitting
Weight	20 pounds
Size	14-inch diameter by 7.5-inch height

TABLE 4-VI-9. SR RECORDER CHARACTERISTICS (Continued)

Description	Characteristic
Motor (Hysteresis Synchronous, Two-Speed)	
Record Speed	750 rpm by use of a set of eight-pole field and quadrature windings and excitation frequency of 50 Hz
Playback Speed	12,000 rpm by use of a set of four-pole field and quadrature windings and excitation frequency of 400 Hz
Starting Voltage	49 volts, p-p
Running Voltage	24.5 volts, p-p
Power Input	-24.5 ± 0.5 volts DC
Ground Command Input Pulses	Playback: -23 volts, p-p Record: TBU
Dual Time-Base Unit Inputs	
50 Hz	TBU: square wave
400 Hz	TBU: square wave
3.125 kHz	TBU: square wave
SR radiometer infrared and visual inputs	Single ended; between 0 and -8 volts; information spectrum of 0 to 450 Hz

b. Functional Description

(1) Record Mode

(a) Power Distribution

During the record cycle, the logic circuits apply -24.5-volt DC power to (1) the two combination FM modulators and video record amplifiers, (2) the flutter-and-wow

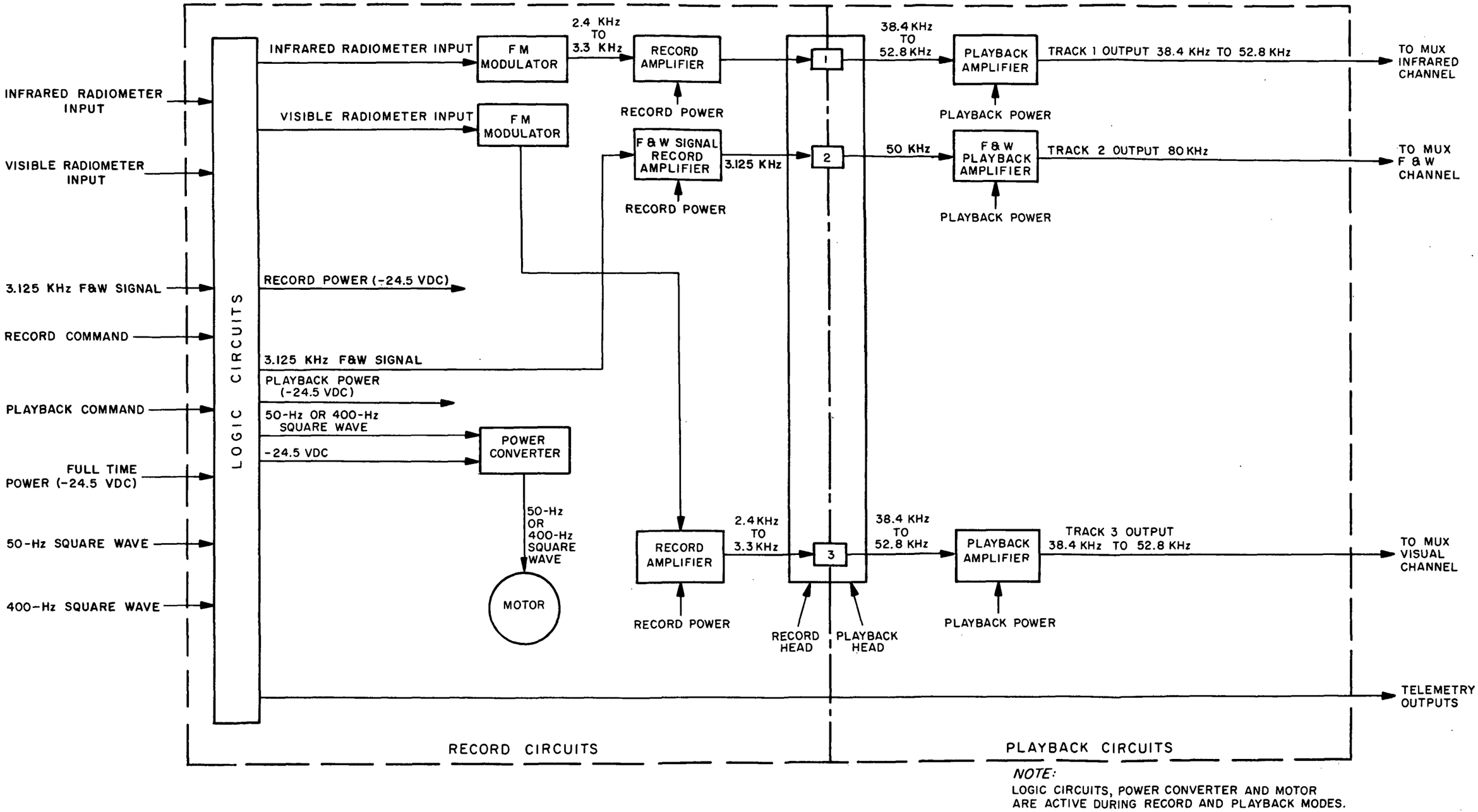

Figure 4-VI-34. SR Recorder Block Diagram

record amplifier, and (3) the motor drive circuits, thereby activating these circuits. In addition, the 50-Hz TBU signal is applied to the motor drivers.

The motor drive circuits amplify the 50-Hz signal and apply it to the drive motor. Switches in the control logic select the motor speed, direction of rotation, and torque during starting and running.

(b) Signal Distribution

IR and visible radiometer outputs are applied to the respective modulators where they each frequency-modulate a subcarrier with a maximum frequency deviation between 2.4 and 3.3 kHz. The IR frequencies correspond to (1) 2.4 kHz, sync tip; (2) 2.635 kHz, hot; and (3) 3.3 kHz, cold. The modulated signals are applied to their respective record amplifiers. At the same time, the 3.125-kHz signal is applied to the flutter and wow record amplifier. The record amplifiers apply drive to the tracks of the record head. A permanent magnet erase head provides a saturated-erase condition at the tape immediately before the tape passes the record head. If recording continues until the end of the tape is reached, the recorder stops, and awaits a playback command.

(2) Playback Mode

(a) Power Distribution

When the playback command is received from the ground station, power is removed from the record circuits and the -24.5-volt DC power is applied to (1) the two playback amplifiers, (2) the flutter-and-wow playback amplifiers, and (3) the motor drive circuits. The logic circuits remove the 50-Hz signal from the motor driver circuits and apply the 400-Hz signal; the motor drive circuits amplify this 400-Hz signal and apply it to the motor to control the motor speed. Playback tape speed is 16 times the record tape speed.

(b) Signal Distribution

The tracks are recorded in one direction and played back in the reverse direction. When the tape recorder reaches the end-of-tape position during the playback mode, the tape recorder will stop; all the tape recorder circuits will be automatically returned to the standby mode condition. The tape recorder will begin to record again when the subsystem is commanded into the record mode.

Since playback tape speed is 16 times the recording tape speed, the instantaneous frequencies are multiplied by 16 during playback. The 3.125-kHz flutter-and-wow frequency is translated to 50-kHz, plus or minus the small deviation caused by the flutter-and-wow of the tape recorder. The modulated radiometer signal frequencies (2.4 to 3.3 kHz) are translated to a maximum deviation of 38.4 to 52.8 kHz.

The two signal playback channels contain identical linear amplifiers followed by limiters and output circuits. The playback amplifiers can be selectively powered to facilitate data handling in the spacecraft if two recorders are played back simultaneously. The 50-kHz playback amplifier is a linear amplifier circuit comprised of two feedback amplifier sections.

(3) Erase Head

A permanent magnet erase head, effective for all tracks, is mounted adjacent to the record head so that the recorded signal is erased immediately after playback, and immediately before recording, thus ensuring a "clean" tape and optimum signal-to-noise ratios. This head is not in contact with the tape and therefore does not cause tape degradation.

(4) Tape Transport

Each tape transport consists of a base casting on which are mounted two coaxial tape reels, a tape-drive motor, a capstan, two magnetic tape heads, a permanent magnet erase head, three tape rollers, and a negator spring assembly. The two tape reels are torqued against each other by the negator spring assembly to provide constant tape tension. The tape passes around the capstan in one direction as it leaves one reel, around the three tape rollers, and then around the capstan in the opposite direction

before being taken up by the other reel, thus forming a closed loop with respect to the capstan. Transient changes in tape tension tend to oppose and to cancel the torque at the capstan, thereby reducing tape flutter.

The slight twist required to move the tape from the plane of one reel to the plane of the other reel is accomplished by the tape rollers. With this arrangement, head tracking is not affected by the twist, even for significant differences in the effective diameters of the two reels. (The effective diameter of a reel is the nominal diameter plus an amount equal to twice the thickness of the tape wound on the reel.)

The record head and the playback head are similar three-channel heads. Recording or playing back occurs on all three tape tracks simultaneously.

The tape is 1/4-inch mylar-base tape, 1360 feet long, with an oxide coating on one side to provide the magnetic medium. The tape is wound on the tape transport in such a fashion that the oxide-coated side of the tape does not contact the tape rollers or the capstan.

A synchronous motor drives the capstan by means of a Mylar belt. The motor has two field windings (eight-pole and four-pole) and two quadrature windings (eight-pole and four-pole), as shown in Figure 4-VI-35. During recording, a set of eight-pole field and quadrature windings and an excitation frequency of 50 Hz produce a synchronous motor speed of 750 rpm. During playback, a set of four-pole field and quadrature windings and an excitation frequency of 400 Hz produce a synchronous motor speed of 12,000 rpm. The belt-and-pulley coupling between the motor and the capstan provides a tape speed of 1.875 inches per second for record and 30 inches per second for playback. The motor receives the excitation signals from the motor drive circuits. Starting and running torque of the motor, and the direction of rotation, are controlled by the logic circuits and the motor drive circuits.

The torque of the motor is controlled by using a lower inductance portion of the motor winding during the first 2 seconds of record and playback operation, so that the motor reaches its synchronous speed quickly. The torque is then reduced by switching in the full motor inductance.

Primary end-of-tape sensing is performed during each cycle of the recorder and is activated at a specific position on the tape. The clockwise redundant end-of-tape switch is located on the metal bracket opposite the upper tape reel; the counterclockwise redundant end-of-tape switch is located opposite the lower tape reel. The two switches are micro switches which are actuated when the build-up of tape on their respective reels presses against the flexible leaf-spring of the switch. As the tape unwinds from the reel, the pressure against the leaf-spring decreases, tending to release the switch; however, the flexibility of the leaf-spring permits the switch to remain actuated for a short period, thus providing a time delay of approximately 1 minute. A fail-safe tape mounting is also used, which physically anchors the end of the tape to the reels.

(a) Motor Design Life

The design life of the motor is 13 months continuous operation under orbital environmental conditions. The scanning radiometer recorder motor brushes are capable of wearing a minimum of 0.041 inch without degradation of motor performance or commutator damage. The motor is a direct drive to the capstan. The results of an accelerated life test, performed on another program using a similar motor, indicated that the life of the motor was approximately 2 years continuous operation. The scanning radiometer recorder motor will be subjected to life tests in conjunction with the life tests performed on the magnetic tape. Test results will be available after completion of the program.

(b) Negator Springs Design Life

The negator springs are procured to the same requirements as those for the AVCS transport (see Section VI, Paragraph B.4.b.(1)(c)). Negator spring cycling is approximately 14 cycles per day. This rate of cycling provides a minimum design life of approximately 3 years.

(c) Magnetic Tape

A test program is being performed on magnetic tapes to select the tape which provides the best characteristics for the thermal environment. The tape selected for

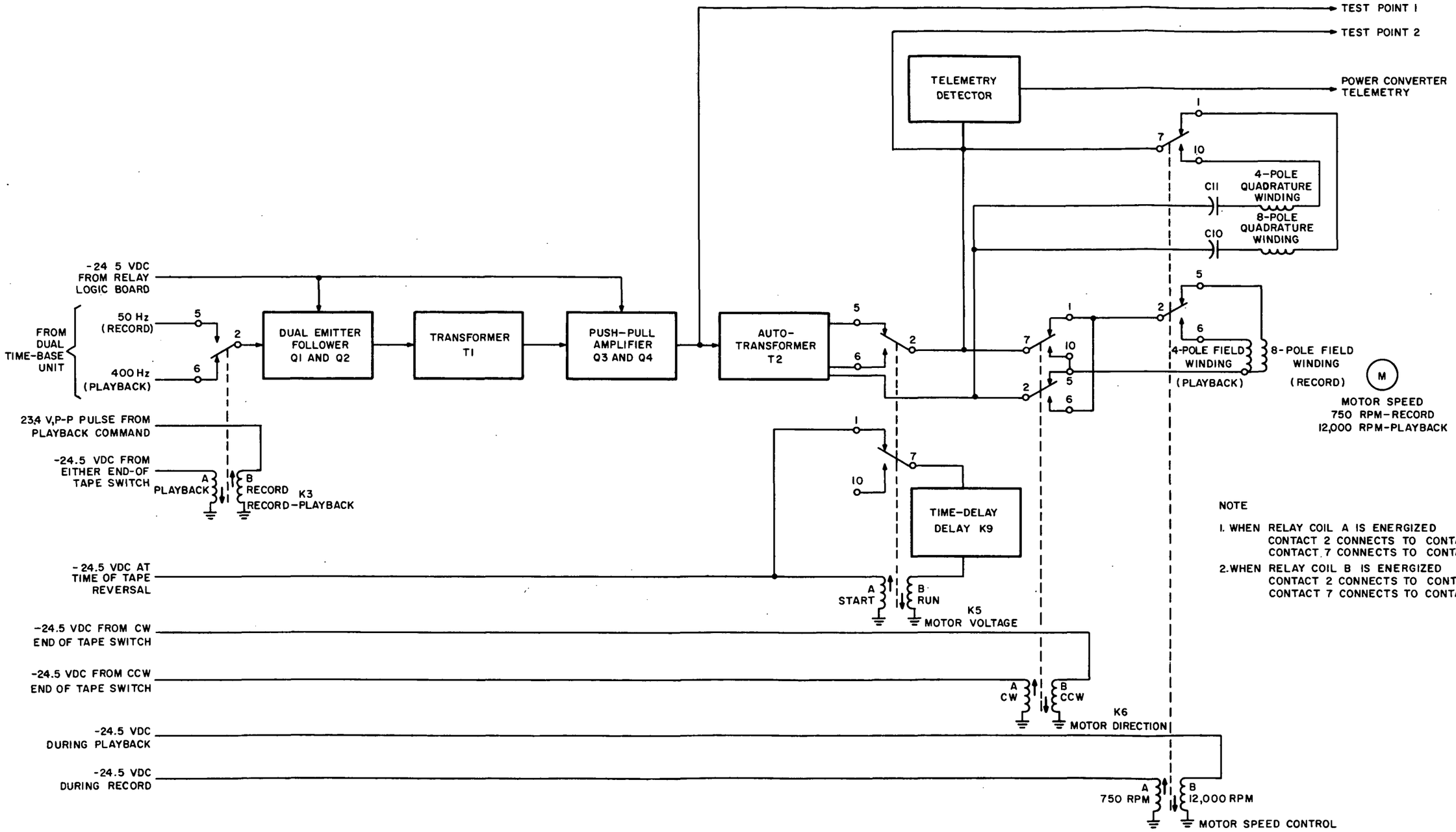

Figure 4-VI-35. Power Converter Block Diagram

the best thermal characteristics will then be subjected to a life test. The test is included as a part of the program approved for the TIROS tape transports. Test results will be available after completion of the program.

(d) Bearing Lubrication

The bearing lubrication used on the scanning radiometer recorder is the same as that used for the AVCS tape transport assembly (see Section VI, Paragraph B.4.b.(2)).

(5) Temperature and Pressure Transducers

One temperature transducer and one pressure transducer are located inside the tape recorder transport enclosure to provide telemetering of the immediate environment of the tape transport. The temperature transducer is a thermistor with a negative temperature coefficient. This transducer provides the temperature telemetry for the hottest point in the tape recorder. The pressure transducer is located on the transducer assembly board. This transducer provides a negative DC voltage which is proportional in absolute value to the pressure inside the tape recorder enclosure. The pressure transducer is a variable potentiometer in which the wiper arm is mechanically connected to a pressure-sensitive bellows.

SECTION VII

SECONDARY SENSOR SUBSYSTEM

A. INTRODUCTION

The secondary sensor subsystem is designed to gather earth heat-balance data and to identify proton flux levels at the spacecraft altitude. It comprises a solar proton monitor (SPM), a flatplate radiometer (FPR), a data format converter (DFC), and an incremental tape recorder (ITR). The data collected by the solar proton monitor and the flat plate radiometer during orbit is stored in the incremental tape recorder. The data format converter controls the monitor, the radiometer, and the recorder; it provides the desired data format and the interfaces of the sensor units with each other and with the spacecraft. Data from the sensors, time code, in-orbit telemetry, and a clock signal are recorded on three channels in the recorder. On playback, the three channels modulate three subcarrier oscillators in the data format converter. These signals are combined and transmitted to the ground station on the S-band link. The interrelation of the units within the secondary sensor subsystem is shown in Figure 4-VII-1. The secondary sensors are supplied to the spacecraft as GFE.

When the beacon transmitter is on and is not commanded to transmit other data, the solar proton monitor output frequency-modulates the IRIG channel 9 subcarrier oscillator, to give a direct readout capability.

B. SECONDARY SENSORS

1. Solar Proton Monitor

The solar proton monitor (SPM), will give continuous data coverage of solar proton activity in the vicinity of earth. It will provide information about the effects of solar activity on the environments encountered during manned spaceflight missions and supersonic transport flights and the effects of these environments on high frequency communications at high latitudes. The performance of SPM on the ITOS spacecraft also will determine whether it can be used in an early-warning network for protection from increased solar activity during manned space-flight missions.

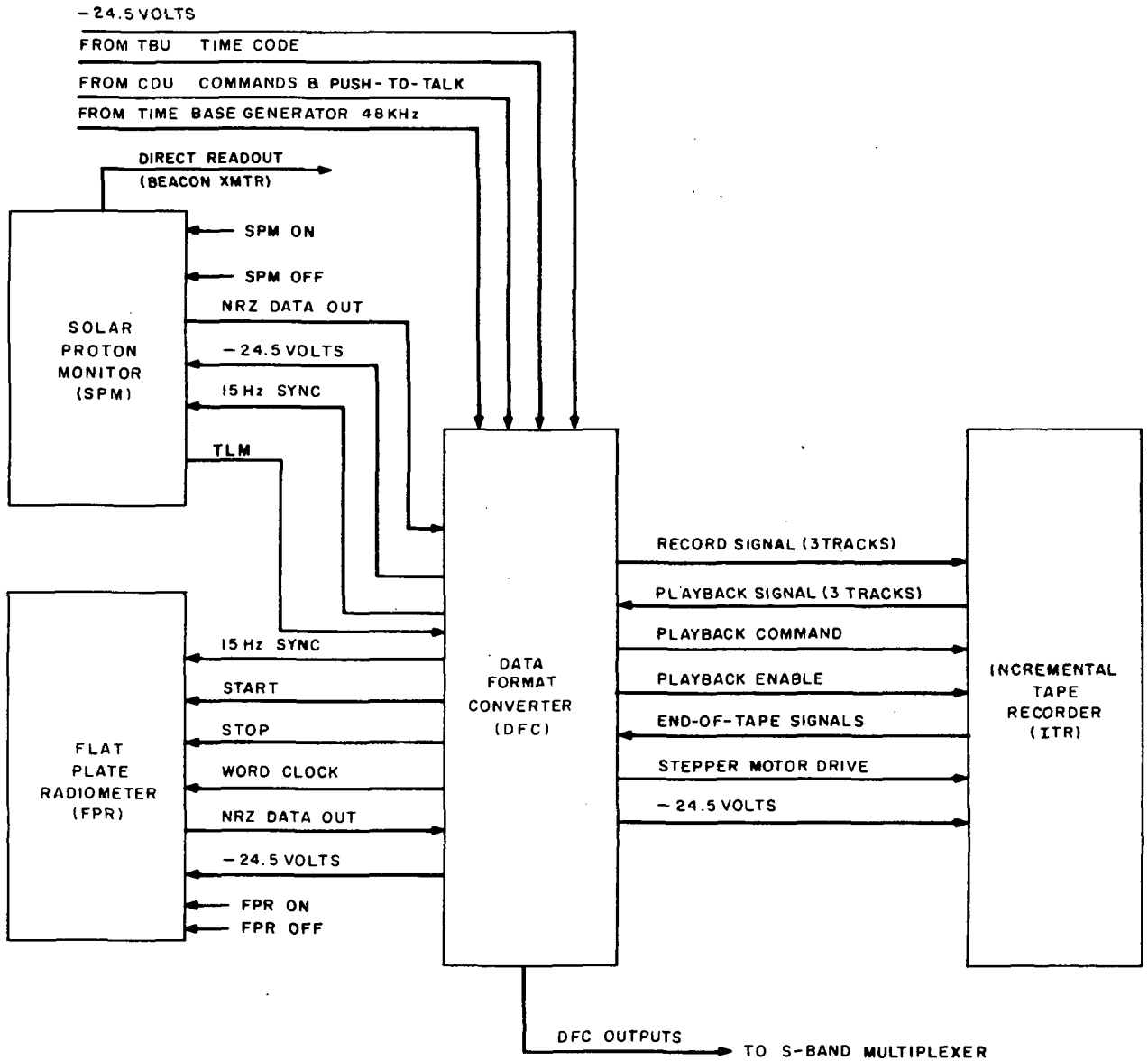

Figure 4-VII-1. Secondary Sensor Subsystem, Block Diagram

The SPM consists of six solid-state detectors. The sensitivity to proton intensities and the required field of view of each detector are given in Table 4-VII-1. Detectors 4 and 5 are identical; their outputs are fed to thresholding discriminators which are commutated to provide sequential readout of six energy levels. Detector 6 is an energetic electron detector with E_e greater than 250 keV. It is designed to detect and monitor electron fluxes in the outer radiation belt, thus clearly indicating the polar-cap boundary. The energetic electrons that are detected define the region in which solar proton flux measurements are not contaminated by the energetic electrons.

The locations of the detectors on the spacecraft are shown in Figure 4-VII-2. Detectors 1 through 4 are mounted on the surface that faces away from the earth, so that the axes of their fields of view are parallel to the earth's magnetic field in the vicinity of the poles. Detectors

TABLE 4-VII-1. SOLAR PROTON MONITOR, DETECTOR CHARACTERISTICS

Detector	Energy Response	Field of View	Remarks
1	$E_p \geq 60$ MeV	2π steradians	180-degree field of view
2	$E_p \geq 30$ MeV	2π steradians	180-degree field of view
3	$E_p \geq 10$ MeV	2π steradians	180-degree field of view
4 & 5	a. $E_p = 0.1$ to 0.3 MeV	40 degrees full angle	No. 4 oriented parallel to earth's magnetic field;
	b. $E_p = 0.3$ to 1.0 MeV		No. 5 oriented perpendicular to earth's magnetic field
	c. $E_p = 1.0$ to 3.3 MeV		
	d. $E_p > 3.3$ MeV		
	e. $\Delta E_p > 3.6$ MeV		
	f. $\Delta E_p > 100$ keV		
6	a. $E_e \geq 250$ keV	15 degrees full angle	Energetic electron detector; oriented perpendicular to earth's magnetic field
	b. E_e: Upper level		

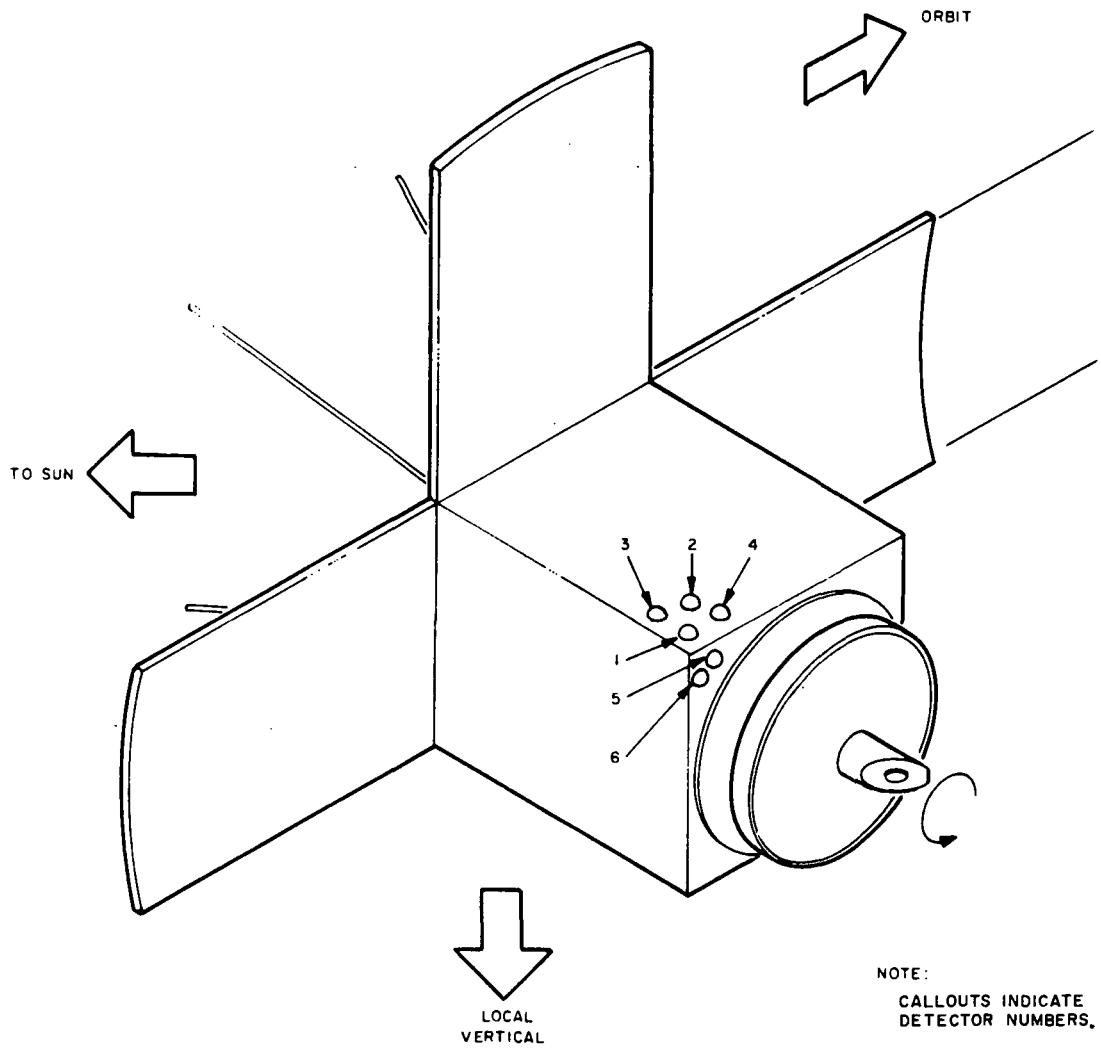

Figure 4-VII-2. Solar Proton Monitor, Detector Location Diagram

5 and 6 are mounted on the surface that is perpendicular to the spin axis and faces away from the sun, so that the axes of their fields of view are perpendicular to the earth's magnetic field at every position in the orbit. The output of the detectors are processed by the solar proton electronics unit. To limit signal losses from the detectors, the electronics unit is mounted within 1.5 feet of the detectors.

The output from the SPM electronics is a nonreturn-to-zero pulse train. Its data frame comprises 20 nine-bit words, and the frame time is 12 seconds, which corresponds to 15 bits per second. One of the 20 words is a Barker frame marker, which is a fixed pseudorandom binary sequence with properties giving it a very high probability of detection. Words are extracted by counting bits from the frame marker. A -24.5-volt power input, supplied to the SPM by the data format converter, is controlled by a ground command to the converter. The converter provides a 15-bit-per-second signal input to synchronize the SPM data readout with the incremental tape recorder; however, the internal data format of the SPM is asynchronous with the time code recording and the flat plate radiometer data frame.

The output of the SPM also modulates the channel 9 subcarrier of the beacon link when this channel is not commanded to transmit other data. This direct readout capability has the same data format as the recorded signal.

2. Flat Plate Radiometer

The flat plate radiometer (FPR) comprises four detectors that provide data for evaluating terrestrial heat balances. Two of the detectors are thermistor bolometers; the other two are thermopiles. The FPR is mounted between the two scanning radiometers on the earth-facing side of the spacecraft. The detectors have a field of view of 2π steradians and face the earth. One thermistor bolometer and one thermopile are painted white, and their sensitivity falls within the infrared spectrum. The other two detectors are painted black, so that their spectral sensitivity is broader.

The FPR electronics commutates the outputs from the four detectors and 11 telemetry points and converts the commutated data into 8-bit words (7 data bits plus 1 marker bit). Since the precision required for the data from the four sensors is greater than that provided by 7 bits,

the data for each of the four sensors is contained in two words. Fifteen words constitute one FPR frame of data, made up as follows: four sensors at two words each and seven telemetry sensors at one word each. Every 32 seconds, the data format converter provides a start-to-read pulse which initiates the data sampling cycle. The 15-word sequence is read out serially at 15 bits per second, the data readout taking 8 seconds. The data format converter provides a 15-bit-per-second signal to synchronize the FPR data readout with the incremental tape recorder. A -24.5-volt power input, supplied to the FPR by the converter, is controlled by ground command.

C. DATA FORMAT CONVERTER

1. General Description

The data format converter (DFC) comprises the power switching and tape recorder controller, input data processor, and output data processor. The DFC controls the state of the SPM, the FPR, and the ITR; processes SPM and FPR signals, analog telemetry, and time clock data; and multiplexes three subcarrier oscillators that are frequency-modulated by the tape recorder readout.

2. Power Switching and Tape Recorder Controller

The operation of each secondary sensor is controlled by the application and removal of its power. FPR ON and SPM ON commands connect power to the respective sensors. A DFC ON command connects power to the DFC and the ITR. A DFC OFF command removes power from all units. Power is also controlled by end-of-tape switches in the ITR. The switch signals are used by the DFC to turn off the recorder at the end of the record mode and to switch to record mode at the end of the playback mode.

In record mode, the DFC applies a 15-pps signal to actuate the ITR stepper motor, which drives the tape. Recording continues until a PLAYBACK or DFC OFF command is received or until the end-of-tape is reached. When a playback command is given, the DFC generates a playback-enable command and initiates a 9-second delay sequence. After the 9-second delay, the DFC generates a playback command. The two commands remove 6 volts DC and apply ground potential to the appropriate inputs of the ITR.

During the playback mode, the DFC also supplies -24.5-volt power to the playback motor. The playback command is affected by the controller only when the S-band transmitter is on. When the transmitter is off, playback mode is inhibited and the tape recorder remains in the record mode so that no data will be lost.

3. Input Data Processor

a. Data Format

All data processed by the DFC is recorded on three tracks of the ITR. There are three types of input: (1) SPM and FPR data, (2) clock data, and (3) analog telemetry and time code. The SPM data is resynchronized by the DFC and recorded on track 1. The clock data is a continuous sequence of 0's which in NRZ code is a 7.5-Hz square wave, and are recorded on track 2. The DFC also combines FPR data with time code and telemetry, and this is recorded on track 3. The data, DFC output characteristics, and respective tape recorder channel assignments are given in Table 4-VII-2.

The information on track 3 is organized into frames of 60 words each. A data word consists of 8 bits; the first bit serves as a word marker and is fixed at a logical 0. A frame marker word consists of 8 bits fixed at a logical 1. The words constituting a data frame are shown in Table 4-VII-3.

TABLE 4-VII-2. DFC OUTPUT CHARACTERISTICS

Data	Characteristics	Tape Recorder Track
SPM	15 pps, NRZ; frame sync added and word and frame length determined by SPM	1
Clock	7.5-Hz square wave	2
FPR, Telemetry, and Time Code	15 pps, NRZ; 8-bit word, 60-word frame	3

TABLE 4-VII-3. DATA FRAME FORMAT

Word	Type
1	Frame marker
2	Frame marker
3	Time code, bits 1 through 7, least significant
4	Time code, bits 8 through 14
5	Time code, bits 15 through 21
6	Time code, bits 22 through 24 and spare, most significant
7 through 21	FPR
22 through 24	Calibration
25 through 60	Telemetry and spare data words

The analog telemetry points include the solar panel temperatures, unregulated bus voltage, battery charge current, unregulated bus current, array current, array voltage, command receiver AGC, and tone detector outputs.

b. SPM Data Processing

The SPM output consists of 15-pps, NRZ, time-division-multiplex data. Each data frame comprises 20 words, the first word of each frame being a synchronization word with a 111001001 pattern. A data word consists of 9 bits, of which the first 4 bits are the exponent and the next 5 are the characteristic. This data is passed serially through a 1-bit register which stores each bit until the write pulse records it on tape.

c. Clock Data Processing

The clock signal is derived from the time base unit which provides the DFC with 9.6-kHz input. In the DFC, the 9.6-kHz signal is first converted to a 15-Hz pulse train and then applied to a divide-by-2 circuit to produce a 7.5-Hz square-wave clock. This

7.5-Hz square-wave signal corresponds to a continuous sequence of 0's in the NRZ code and is recorded on track 2. The clock recording indicates the time at which a given bit of data was recorded on tracks 1 and 3.

d. FPR Data Processing

The output of the FPR consists of 15-pps, NRZ, time-division-multiplex data during an interval determined by the input processor. Each frame comprises 15 words of 8 bits each. A word consists of 1 marker bit and 7 data bits. This data is passed serially through a 1-bit register which stores each bit until the write pulse records it on tape. The marker bit, generated by the FPR, is fixed at a logical 0 by the input processor when the bit counter is in "count 0".

e. Time Code Processing

Time code information supplied by the time base unit (TBU) consists of a 120-pps pulse train of 24 bits. Time code data is updated every 0.25 second. Since time code burst cycle is asychronous with respect to the frame word, an acquisition interval is required. During the acquisition interval, the input processor records two frame marker words while a buffer register awaits the time code data. This data is shifted into the buffer register, which is free during the frame marker word recording interval. The signals required for these operations are (1) time code data, (2) 24 shift pulses during the time code burst, and (3) the "rest" pulse when no data or shift pulses are present.

The 24 bits of time data, once stored in the 24 bit register, are split into three words which contain 7 bits of data each and one word with 3 bits of data and 4 unused bits. In addition, each word carries a word marker bit. Word marker bits are inserted into the bit stream by the counter when it is in the "count 0" state.

f. Digital Telemetry Processing

Spacecraft telemetry in the form of analog voltages ranging from 0 to 5 volts is commutated and then converted into 8-bit words which each contain 7 data bits and 1 bit for word synchronization. Each analog input is connected to an input switch. The switch has the same

input characteristics as the analog telemetry commutator on board the spacecraft: input impedance, 2 megohms minimum, back current from any one channel, less than ±1 microampere. The outputs of these switches are summed by an amplifier which drives a sample-and-hold circuit. The sample-and-hold circuit stores the signal during the digitizing operation. The logic required to operate the commutating gates is derived from a 60-state word counter, which selects the data to be recorded on track 3 of the ITR. During word counter states 1 to 21, no analog signals are processed, and therefore no input switches are required.

Listed in Table 4-VII-4 are a number of digital telemetry points provided for monitoring various significant circuit and environmental conditions.

TABLE 4-VII-4. DIGITAL TELEMETRY POINTS

Telemetry Point	Number of Points
Solar Panel Temperatures	3
Solar Cell Patch	3
Array Current	1
Battery Voltage and Current	4
Unregulated Voltage and Current	2
Receiver AGC	2
Decoder Tones	4
Pitch Loop Gain Switch and Motor Voltage	4
Thermal Controller Position	4
Sidewall Temperature	2
Thermal Fence Temperature	3
Telemetry Commutator Output	1

4. Output Data Processor

The output data processor combines the outputs of three oscillators which are frequency modulated by the output of the ITR in the playback mode. The output data processor consists of:

- A power switch which supplies power to the voltage controlled oscillators and summing amplifier,
- Three voltage controlled oscillators, and
- A summing amplifier which combines the outputs of the three oscillators.

The characteristics of the oscillators are outlined in Table 4-VII-5.

D. INCREMENTAL TAPE RECORDER

1. General Description

The incremental tape recorder (ITR) is a miniaturized, digital, three-track tape recorder of proved design. It is packaged to provide reliable data storage and readout facilities on board an earth-orbiting satellite. To ensure long and reliable operation, the tape transport is sealed in an environment of dry helium at a pressure of approximately 1 atmosphere.

The tape recorder electronics comprises entirely solid-state circuitry mounted and encapsulated on four printed circuit boards. The boards are housed in a machined magnesium enclosure which also serves as a mounting base for the tape transport. The high gain recording amplifiers are electrically insulated from the remainder of the circuits. Input and output connectors are mounted at opposite ends of the electronics assembly to minimizing cross coupling.

Data is recorded at a rate of up to 15 pulses per second and stored at a density of 300 bits per inch. The tape reels hold 90 feet of tape which can store in excess of 320,000 bits per track, or a total of 960,000 bits for the three tracks. The playback rate is 2000 bits per second, and playback of the entire tape (which is capable of storing the data of three orbital

TABLE 4-VII-5. CHARACTERISTICS OF VOLTAGE CONTROLLED OSCILLATORS

Oscillator Characteristic	IRIG Channel		
	17B	19B	21B
Center Frequency (F_C)	144 kHz	160 kHz	176 kHz
Deviation	±4 kHz	±4 kHz	±4 kHz
Baseband Frequency	DC to 2 kHz	DC to 2 kHz	DC to 2 kHz
Input Data	FPR, time code, telemetry	clock	SPM
Format	NRZ	NRZ	NRZ
Data Rate	DC to 2 kbps	DC to 2 kbps	DC to 2 kbps
Input Sensitivity	0 to -5.0 volts DC, -2.5 volts DC produces F_C, less negative input decreases frequency	0 to -5.0 volts DC, -2.5 volts DC produces F_C, less negative input decreases frequency	0 to -5.0 volts DC, -2.5 volts DC produces F_C, less negative input decreases frequency
Input Impedance	300 kohm, min	300 kohm, min	300 kohm, min
Linearity from Best Straight Line (percent of p-p deviation)	±1.0 percent	±1.0 percent	±1.0 percent
Maximum Amplitude Modulation Output	±10 percent	±10 percent	±10 percent
Subcarrier Harmonic Distortion	<1 percent	<1 percent	<1 percent
Supply Voltage	-24.5 ±1.0 volts DC	-24.5 ±1.0 volts DC	-24.5 ±1.0 volts DC
Current per SCO	15 ma	15 ma	15 ma
Temperature Stability	Less than ±60 Hz between -20 and 85 °C	Less than ±60 Hz between -20 and 85 °C	Less than ±60 Hz between -20 and 85 °C
Outputs per SCO	1	1	1
Size	2.25 in^3	2.25 in^3	2.25 in^3
Weight	2.6 oz	2.6 oz	2.6 oz

passes) requires 2.7 minutes. A permanent magnet automatically erases the tape after playback. End-of-tape sensors and mechanical locks prevent the tape from coming off the reels.

2. Tape Transport Assembly

The tape transport assembly comprises two motors, a precision gear train with electromagnetic clutch, a capstan, a record/playback and erase head subassembly, and a tape reel subassembly. The tape transport assembly is mounted between two plates that are doweled and bolted together to form a chassis. The tape reel subassembly is held in place by shoulder-type ball bearings set in the two plates. All the other components of the tape transport are attached to the larger of the two plates.

The gear train comprises precision aluminum gears and stainless steel pinions which minimize noise and ensure long life. The ball bearings are prelubricated, and the gears are greased during assembly with a military-specification lubricant. A simplified diagram of the transport mechanism is shown in Figure 4-VII-3.

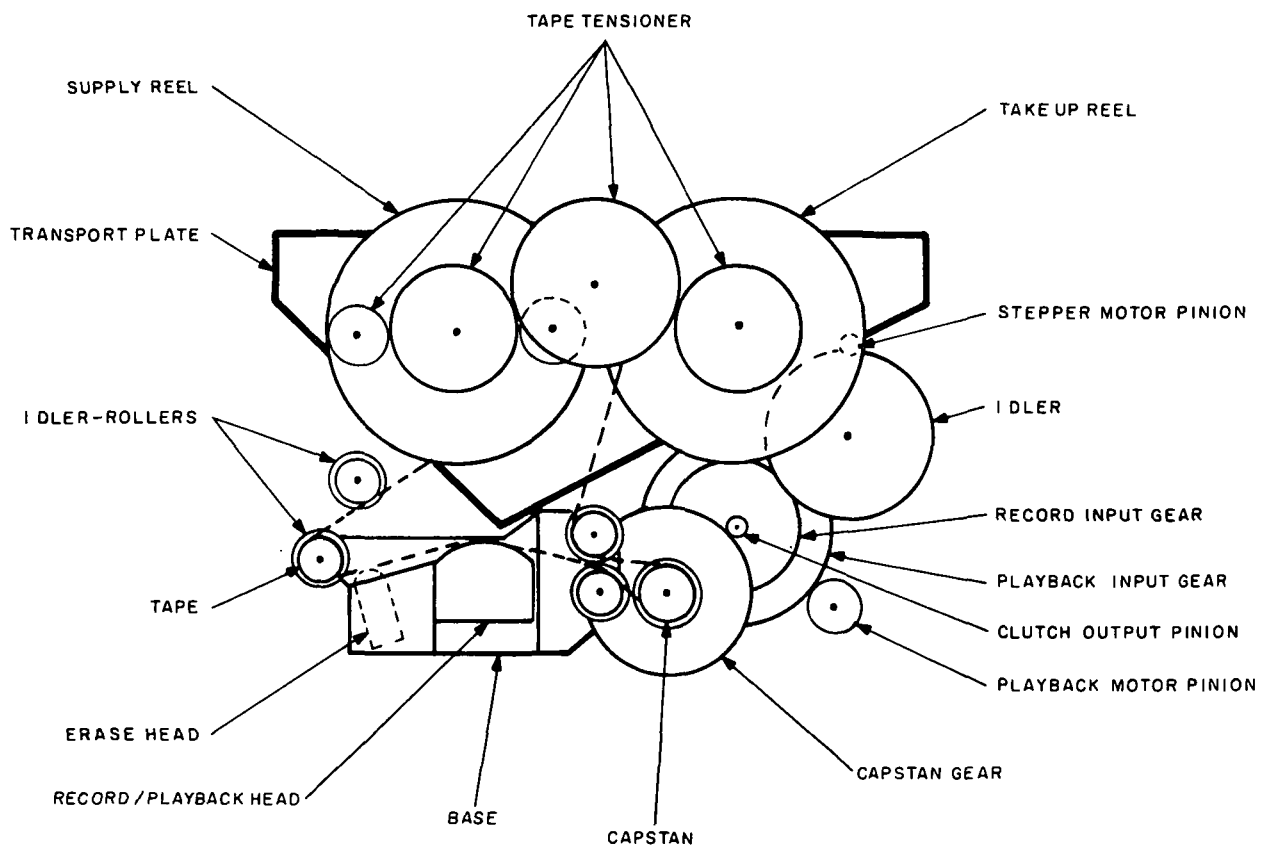

Figure 4-VII-3. Tape Transport Mechanism, Simplified Diagram

a. Tape Drive

The tape is driven during both record and playback by the capstan which, in turn, is powered through the gear train and the clutch. The clutch serves as a mechanical switch between the recording and playback motors. During the recording mode, a two-phase stepper motor drives the record input gear, which is frictionally coupled to the clutch output pinion that drives the capstan. While the clutch is deenergized in the record mode, the clutch output pinion remains engaged with the capstan gear. The stepper motor is powered by a pulse train from the record/playback control circuit in the recorder electronics. This pulse train causes the rotor of the stepper motor to rotate in 45-degree steps. The precision gear train reduces this to a 1-degree rotation of the capstan, which is translated into a 1/300-inch motion of the tape.

During playback, the clutch is energized, which frees the record input gear and engages the playback motor pinion. A DC motor drives the playback motor gear. A Zener diode across the motor input gives it a nominal speed of 8000 rpm. The gear ratio between the playback motor pinion and playback input gear produces a playback rate of 2000 pulses per second. The speed variation from one end of the tape to the other is ±15 percent. Bit jitter, defined as random movement of a bit about its nominal position, is ±100 microseconds. The motor is totally enclosed and its input filtered to minimize noise pickup by the record/playback heads during the playback mode.

b. Tape Reel Subassembly

The tape reel subassembly consists of the tape, tape reels, tape tensioning devices, and end-of-tape sensors. The tape, using a mylar base 1 mil thick and 1/4 inch wide, is 92 feet long. During loading, each tape end is threaded into a slotted keeper mounted on the reel hub, and the keeper is rotated so that the tape end wraps around it. When the tape is adequately anchored, a locking screw is inserted to prevent the keeper from loosening. The end-of-tape sensors are static precious metal contacts. To provide end-of-tape signals, 12-inch metallized strips are bonded to the ends of the tape. As the tape approaches four or five turns from either end, the metallized strip touches the sensor, causing the input of a switching circuit to be grounded and thereby stopping the drive. In the unlikely event that both the

external stop and the end-of-tape signals fail, the capstan slips against the tape until a ground signal is received to reverse the recorder operation. The correct tape tension is provided by a negator constant-rate spring system mounted on the supply reel.

c. Record/Playback and Erase Head Subassembly

A simple head performs both record and playback functions. It is a four-track head of conventional design; however, only three of its tracks are used in this application. The head is rigidly attached to a precision-machined base which also supports three idler rollers and the erase head. The idler rollers guide the tape to and from the capstan. The base and head are preassembled, and the head is aligned with the idler rollers to establish a tape track of the required accuracy. The erase head is a simple bar magnet, mounted so that the tape passes within 0.002 inch of its face without touching it.

d. Tape Recorder Electronics

The tape recorder electronics comprises three record amplifiers, three playback amplifiers, stepper drive circuitry, and control circuitry. A block diagram of the tape recorder electronics is shown in Figure 4-VII-4.

(1) Stepper Drive Circuitry

The stepper drive input is a 15-pps signal from the DFC. This signal is sequenced by the stepper drive logic to produce four pulse trains, as depicted in Figure 4-VII-5. Two of the pulse trains drive one transistor bridge, while the other two drive a second bridge. The output from each bridge is a series of voltages having an "on" period of 32.9 milliseconds and an "off" period of 33.8 milliseconds. The "off" period occurs after one half of the bridge is shut off and before the other half is turned on. This "off" period conserves power and ensures that both halves are not on simultaneously, which would cause a failure. The output of each bridge drives one phase of the stepper motor. A damping network across each stepper motor winding presents a resistive load across each bridge output.

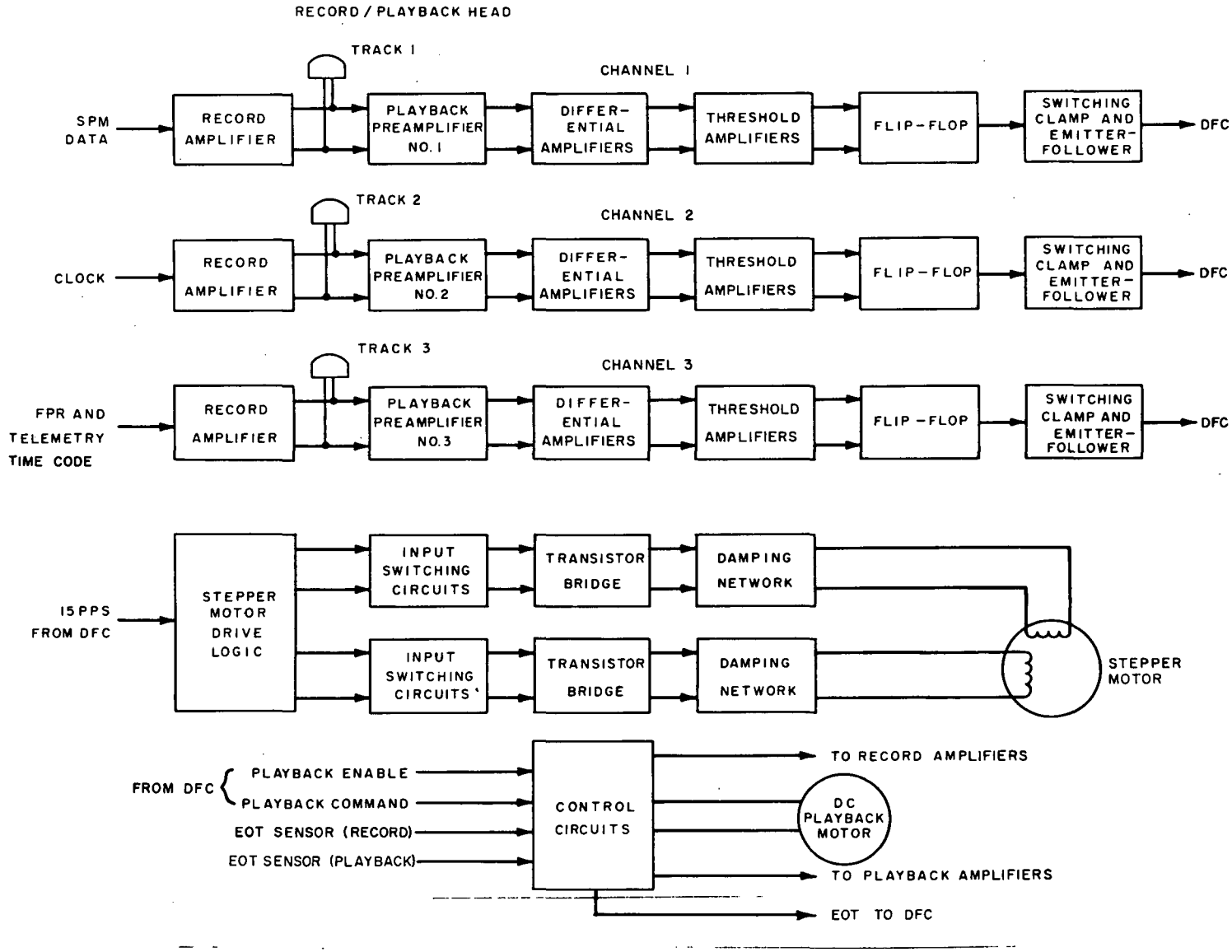

Figure 4-VII-4. Incremental Tape Recorder Electronics, Block Diagram

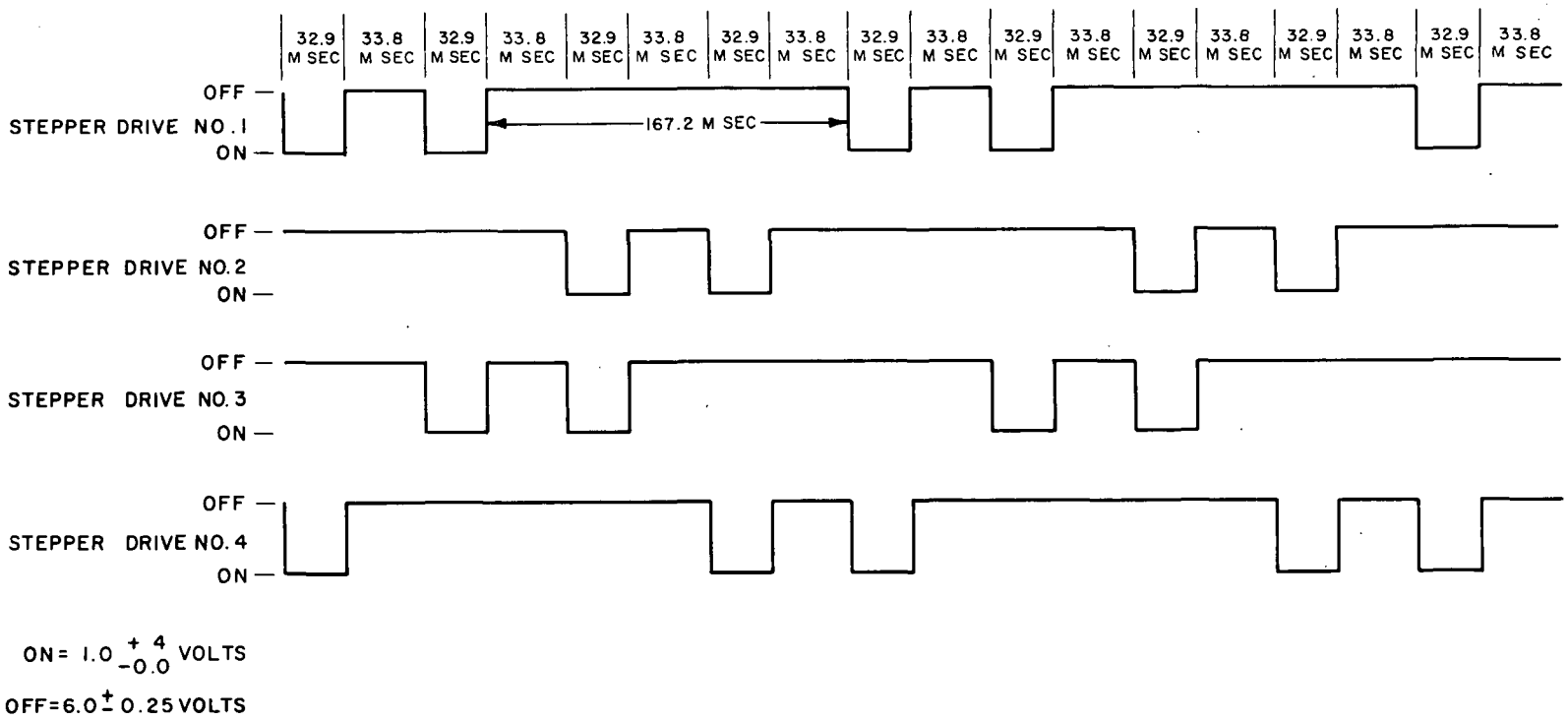

Figure 4-VII-5. Stepper Drive Signal Phasing

(2) Record Amplifiers

Each of the three record amplifiers comprises three switching transistors that amplify the NRZ data from the DFC. The switching transistors alternately drive the center-tapped record/playback head coil, with a 2.7-milliampere output current, sufficient to saturate the tape in either direction. Recording is accomplished by reversing the direction of the current in the head coil. A reversal occurs after the tape has completed its advance and is at rest. In the clock track, the head current reverses every 66.7 milliseconds, 3 milliseconds before the start of a stepping pulse. The current reversal in the other two data tracks is dependent upon the input data.

(3) Playback Amplifiers

Each of the three playback amplifiers processes data from one of the three record/playback heads. The signals coming from the head are of the order of several millivolts. The preamplifier is linear and has a closed-loop gain of 1300. The input is capacitively coupled to a differential stage with a high, common mode rejection for noise occurring in both windings of the head coils. This stage is directly coupled to another differential amplifier which drives two single-ended threshold amplifiers (one from each output of the differential amplifier). Each threshold amplifier drives one side of a flip-flop that is biased to a given threshold level. The output of the flip-flop drives a switching clamp that feeds an emitter-follower to produce a low impedance square-wave output.

(4) Control Circuits

The control circuits comprise transistor switching circuits that accept command signals from, and provide end-of-tape signals to, the programmer in the DFC. When the playback enable input to the control circuit is grounded, -24.5 volts are applied to the three playback amplifiers and the DC playback motor, while the record amplifiers are inhibited. When the playback command input is grounded, there is a 9-second delay, after which a transistor turns on and applies power to the clutch. The 9-second delay allows the DC playback motor to attain running speed.

When the conductive strip at the end of the tape shorts the contacts of a sensor during the record mode, a transistor turns on. This inhibits the transistor bridge operation and stops the stepper motor. The transistor also grounds an output to the DFC programmer, which puts the DFC into standby mode. Similarly, during the playback mode, shorting of the sensor contacts inhibits the clutch and playback motor until the power to the recorder is shut off by the programmer.

e. Packaging

The four printed circuit boards and the necessary connectors are housed in a magnesium enclosure, machined to provide maximum electrostatic shielding for the electronics. The enclosure mates with and provides a base for the tape transport. A removable dust cover closes off the bottom section, and the transport housing covers the top section. The enclosure provides tight joints and good ground paths to the baseplate.

Input and output connectors are mounted at opposite ends of the enclosure to minimize coupling between signal and power leads. Feedthrough filters are provided for the internal connection of critical electronic circuits requiring shielding. Fourteen test points permit the following parameters to be monitored during a test: (1) record amplifier outputs, (2) playback amplifier outputs, (3) NRZ data inputs, (4) stepper drive outputs, (5) end-of-tape outputs, and (6) clutch power outputs. During tape recorder operation, three telemetry points allow (1) tape transport pressure, (2) record power, and (3) playback power to be monitored.

The layout of the printed circuits minimizes the effects of crosstalk and noise on the differential amplifiers. Minimum lead lengths and shield planes provide additional protection. Components are located so as to minimize stress due to board flexing, and the boards are stiffened by sandwiched polyurethane spacers bonded to the two board combinations.

f. Life Limiting Parts and Lubrication

(1) Motor Stepper

The design operational life for the motor stepper is for a minimum period of 2 years of continuous operation at a rate of 15 steps per second.

(2) Motor Playback

The design operational life is for a minimum period of 400 hours. Since orbital requirements are for 32 minutes operation per day, life of the motor is approximately 2 years.

(3) Magnetic Clutch

The design life for the magnetic clutch is for a minimum period of 2 years at a rate of 15 steps per second.

(4) Negator Springs

The minimum life of the negator springs on the incremental tape transport assembly is 2500 cycles. Worst-case orbital conditions (record and playback every orbit) result in negator spring cycling of 4600 cycles per year. The present spring design has a minimum life of 6.5 months and an average life of 9.7 months under worst-case conditions.

(5) Magnetic Tape

The 3M 590 magnetic tape used in the incremental tape recorder is the same as that used in the tape transport for a classified program. An operational life of 12 months or more is indicated from the results obtained on the classified program.

(6) Bearing Lubrication

Bearings used in the incremental tape recorder are Barden precision bearings, lubricated with Esso "ANDOK" C grease (the same as that used for the AVCS and scanning radiometer recorders).

SECTION VIII

COMMAND SUBSYSTEM*

A. FUNCTION

The satellite command subsystem receives commands transmitted from the CDA ground stations, recognizes and rejects spurious commands, accepts and decodes valid commands, and distributes the appropriate control signals and voltages, with the proper timing, throughout the satellite to effect the command operations. The command functions include those that respond immediately to ground station command and those that take place in a programmed sequence of variable duration and begin at a programmed orbit time. Remote camera functions, scanning radiometers functions, and attitude control functions are in the latter category. The command subsystem also performs ancillary timing and telemetry functions.

The command subsystem performs the following specific functions:

- Provides for selective commanding of an individual satellite in a multiple-satellite system and for the selection of one of the satellite's two redundant command channels for receiving the commands.
- Provides immunity from spurious commands, including commands intended for other satellites in the same system.
- Decodes received commands and, depending on the commanded function, either processes and distributes them for real-time response or stores the command program for remote operations.
- Regenerates the commands, as detected in the satellite, for retransmission to the ground station for use in command verification.
- Routes commands and internally sequenced signals to the various subsystems of the satellite where they are required for initiation or control of operations.

*Refer to Summary of Current Design Revisions Not Covered in this Report, following the Preface, for a brief description of revisions made since the cut-off date for this report.

- *Generates timing signals from which all required satellite timing and synchronizing* signals are derived and from which a coded time identification signal is generated to accompany picture, radiometer, and secondary sensor data.
- Provides for satellite response to telemetry requests by certain specially equipped stations other than CDA stations.
- Provides storage and delayed initiation for remote picture-taking, radiometry, and attitude correction commands.

The command functions are implemented by components that comprise two redundant command channels. These are (1) a dual decoder unit, comprising two identical command decoders, each of which receives an input from one of two identical command receivers, (2) a dual programmer unit, comprising two identical programmers, (3) two command distribution units, and (4) a dual time base generator unit, comprising two identical time base generators and two time code generators. Cross-coupling within the subsystem provides for selecting individual components to make up the command receiving channel in order to prevent a single component failure from disabling the subsystem or degrading its performance. A block diagram showing the primary functional relationships among these units is presented in Figure 4-VIII-1.

A command transmitted to the satellite by a ground station comprises, in sequence, two audio-frequency tones modulated on the radio frequency carrier, and binary coding of one of the tones by frequency-shift-keying (FSK). Power is always applied to both receivers and to the "enable" tone detectors in the decoders. The first tone transmitted to the satellite is the enable tone, which, if correct in frequency and duration, causes power to be applied to an FSK tone detector in one of the command decoders. The frequency and duration of the ensuing FSK tone are then checked. If the frequency and duration of the FSK tone are correct, power is applied to the command decoding circuits. The first portion of the binary FSK coded command message contains a satellite address. The address is decoded, and, if the address and the format of the address (two data "1's" in each 12 bits) are both correct, decoder power is latched on, thus opening the circuits for command execution. Each command that follows must be preceded by a correct address and must be in correct (2-out-of-12) format in order to maintain the decoder power latch. If these conditions are met, the ensuing commands are decoded and routed either to the command distribution units (CDU's) for real-time operations or to

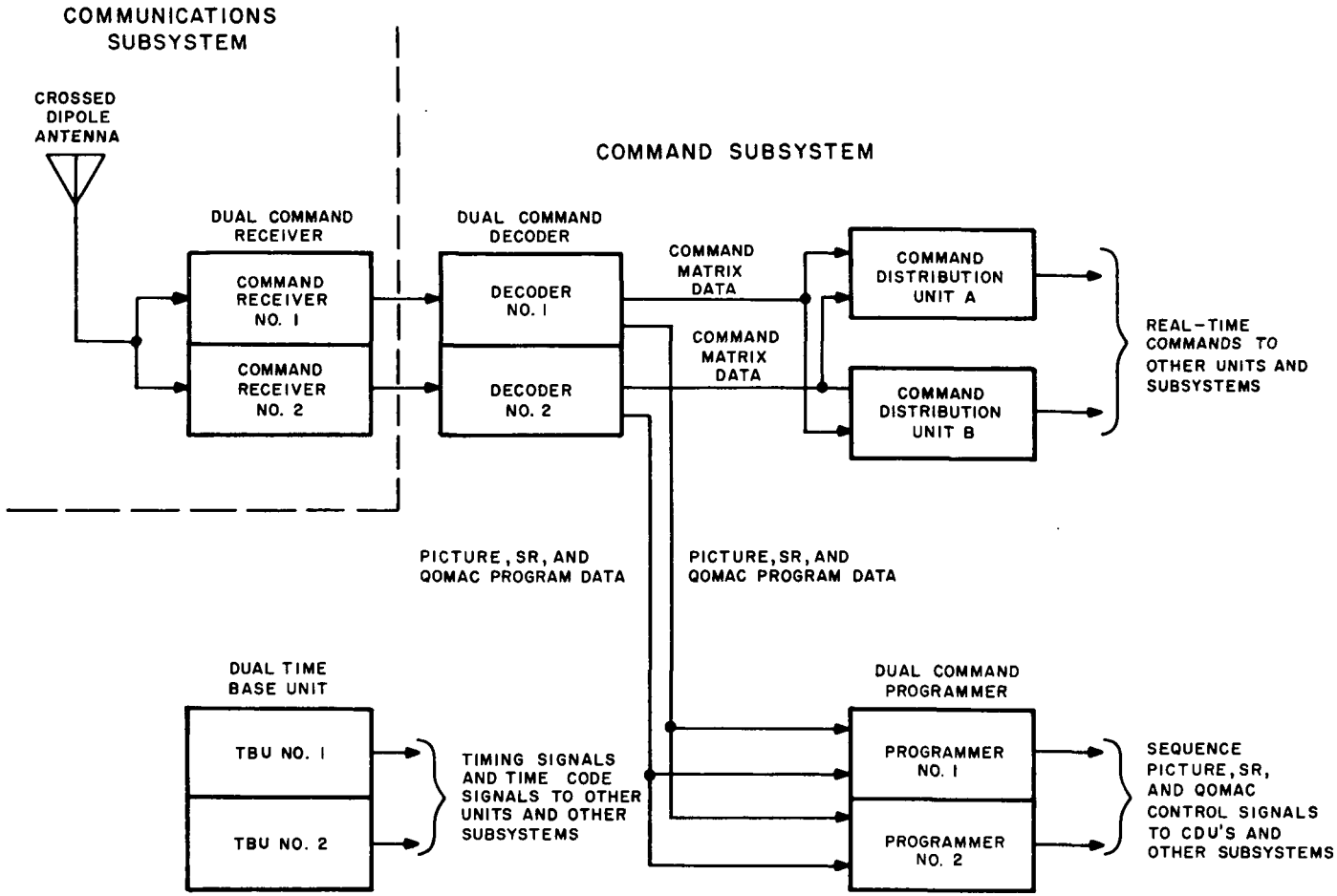

Figure 4-VIII-1. Command Subsystem, Block Diagram

the programmers for storage and control of remote operations. If remote operations are programmed, the programmer produces sequenced signals for control of attitude correction or camera and radiometer operations at programmed intervals. These signals are distributed to the appropriate camera or attitude control circuits. A list of the commands used in the ITOS system is given in Table 4-VIII-1.

TABLE 4-VIII-1. ITOS COMMANDS

1.	Command Group I ON, II OFF
2.	Command Group II ON, I OFF
3.	Select AVCS Camera No. 1, Not No. 2
4.	Select AVCS Camera No. 2, Not No. 1
5.	Select Neither AVCS Camera
6.	Select AVCS Recorder No. 1, Not No. 2
7.	Select AVCS Recorder No. 2, Not No. 1
8.	Select Neither AVCS Recorder
9.	Playback AVCS Recorder
10.	Select Multiplexer No. 1, Not No. 2
11.	Select Multiplexer No. 2, Not No. 1
12.	Select S-Band Xmtr No. 1, Not No. 2
13.	Select S-Band Xmtr No. 2, Not No. 1
14.	S-Band Xmtr ON
15.	S-Band Xmtr OFF
16.	Select APT Camera No. 1, Not No. 2
17.	Select APT Camera No. 2, Not No. 1
18.	Select Neither APT Camera
19.	Select SR No. 1, Not No. 2
20.	Select SR No. 2, Not No. 1
21.	Select Neither SR
22.	Both SR Motors ON
23.	SR Motor No. 1 OFF
24.	SR Motor No. 2 OFF

TABLE 4-VIII-1. ITOS COMMANDS (Continued)

25. Disable SR Real-Time Day Mode
26. Visible SR Real-Time Day Mode
27. IR SR Real-Time Day Mode
28. Visible SR Calibrate ON
29. Visible SR Calibrate OFF
30. Select SR Recorder No. 1
31. Select SR Recorder No. 2
32. Select Neither SR Recorder
33. Playback Single SR Recorder
34. Playback Both SR Recorders
35. Select Real-Time Xmtr No. 1, Not No. 2
36. Select Real-Time Xmtr No. 2, Not No. 1
37. Select Neither Real-Time Xmtr
38. Select Real-Time Xmtr, Day Only
39. Select Real-Time Xmtr, Day and Night
40. Flat Plate Radiometer ON
41. Flat Plate Radiometer OFF
42. Solar Proton Monitor ON
43. Solar Proton Monitor OFF
44. Data Format Converter ON
45. Data Format Converter OFF
46. Playback ITR
47. Programmer No. 1 ON, No. 2 OFF
48. Programmer No. 2 ON, No. 1 OFF
49. Both Programmers OFF
50. Load Picture Mode Program
51. Load QOMAC Mode Program
52. Time Base Unit No. 1 ON, No. 2 OFF
53. Time Base Unit No. 2 OFF, No. 1 ON

TABLE 4-VIII-1. ITOS COMMANDS (Continued)

54. Enable QOMAC Power
55. Disable QOMAC Power
56. Magnetic Bias Positive
57. Magnetic Bias Negative
58. Step Magnetic Bias Switch
59. Magnetic Bias Power OFF
60. Momentum Coil No. 1 ON
61. Momentum Coil No. 2 ON
62. Both Momentum Coils OFF
63. Momentum Positive
64. Momentum Negative
65. Select Pitch Loop No. 1
66. Select Pitch Loop No. 2
67. Pitch Loop in Open Loop Mode
68. Pitch Loop in Closed Loop Mode
69. Pitch Loop Motors in Parallel Drive
70. Select Pitch Sensor Electronics No. 1
71. Select Pitch Sensor Electronics No. 2
72. Select Roll Sensor No. 1
73. Select Roll Sensor No. 2
74. Damper Caging Release
75. Despin Release
76. Unfold Solar Panels
77. Beacon No. 1 ON, No. 2 OFF
78. Beacon No. 2 ON, No. 1 OFF
79. Both Beacons OFF
80. Telemetry Commutator No. 1 ON
81. Telemetry Commutator No. 2 ON
82. Telemetry Commutator Manual Advance
83. Telemetry Commutator Auto Advance

TABLE 4-VIII-1. ITOS COMMANDS (Continued)

84.	Acquisition Mode Telemetry ON
85.	Acquisition Mode Telemetry OFF (Operational Mode ON)
86.	Telemeter Pitch Sensor, Not Roll Sensor
87.	Telemeter Roll Sensor, Not Pitch Sensor
88.	Regulator No. 1 ON, No. 2 OFF
89.	Regulator No. 2 ON, No. 1 OFF
90.	Shunt Reg. Control Ampl. No. 1 ON
91.	Shunt Reg. Control Ampl. No. 1 OFF, No. 2 ON
92.	Shunt Reg. Control Ampl. No. 2 ON
93.	Shunt Reg. Control Ampl. No. 2 OFF, No. 1 ON

B. DESIGN

The ITOS command subsystem is functionally similar to its counterpart on the TOS spacecraft. However, the TOS decoder-programmer unit, which contains two decoders, two programmers, and one time base generator, has undergone mechanical redesign to separate these components into three units in the ITOS design. The three units are a dual decoder, a dual programmer, and a dual time base unit. This repackaging reduces the complexity of the individual units and facilitates handling during the debugging and electrical testing of ITOS. Because ITOS is more complex than the TOS spacecraft, more commands are required to control its operation. To handle the increased number of commands, the size of the command distribution units (CDU) has been increased, and the CDU circuits are housed in two boxes.

The ITOS command format has a capacity of 128 commands, compared with 66 commands for TOS. The 66-command limitation of the TOS command subsystem is imposed by the 2-out-of-12 command code format. Although the ITOS command format also uses a 2-out-of-12 code, the total number of available ITOS command functions has been approximately doubled. Each command is preceded by a "group select" command (a 2-out-of-12 code) which causes the decoding circuits in one group to be enabled, while those in the other group are disabled. Because two codes must be used to identify the group select

commands, the number of available codes for spacecraft functions is reduced to 64, which is, in effect, doubled to 128 by the group select feature. The command capacity thus allows for the growth of the ITOS command subsystem.

This method of extending command capacity was selected for the following reasons:

- Minimal modification of basic logic is required in the TOS decoder.
- No change in command format is required.

C. SUBSYSTEM DESCRIPTION

1. Command Decoder

a. General

Each of the two channels of the decoder consists of a tone detector and digital decoder. Both channels are normally "off", that is, power is applied only to the command receivers and to the tone detectors in the decoders. Only one channel normally receives commands when the spacecraft is in contact with a ground station. This channel is turned on by the ground station command and is used to command all spacecraft functions; the second receiver-decoder channel offers a backup capability in case of degradation or malfunction of the first.

The two groups of decoding circuits are designated Group I and Group II. In the absence of a group select command, Group I is automatically selected when switched power is applied by the decoder. Once a group is selected, all succeeding commands are decoded by that group until a new group select command is given.

b. Inputs and Outputs

Power for each decoder is derived from the spacecraft unregulated bus. Each decoder contains a power supply which consists of a regulator and a DC-to-DC converter. The regulator provides a -23-volt (±1 percent) output, which is supplied to all of the decoder

circuitry except the digital integrated circuits. The regulated voltage is converted to provide a +5 volt (±1 percent) supply for the digital integrated circuits and a +5.35 volt (±1 percent) supply for the output interface circuits.

The signal input of each decoder channel is connected directly to the signal output of a command receiver. The audio input signal to each channel of the decoder from its associated receiver consists of two tones: an "enable" tone and an FSK tone. The receipt of an enable tone of the correct frequency for the specified period of time and of the specified amplitude causes power to be applied to the FSK detector in the decoder. When the frequency, duration, and amplitude of the FSK tone have been identified as correct, power is applied to the digital decoding circuits. The digital command message, including a spacecraft command address as well as other digital command data, is modulated on the FSK tone in the ground station. The FSK tone is characterized by a center frequency tone, f_c, which is shifted to f_c + 7.5 percent to represent a data "1", and to f_c -7.5 percent to represent a data "0".

Four separate tones, two enable tones and two FSK tones, are available in the ground station equipment for commanding the ITOS spacecraft. One pair is assigned to each receiver-decoder combination in the spacecraft. If a failure occurs in one spacecraft channel, the second pair of decoder tones is used to address the second channel. The use of four separate tones increases the security of the system. This arrangement also provides maximum isolation between channels and guarantees that the opposite channel will not be enabled during commanding, which would be the case if a common enable tone were used. Commercial broadcast programming makes it advisable to select tone frequencies from as high in the audio spectrum as possible, while the receiver bandwidth limits the upper end of the spectrum to about 12 kHz.

The command transmission to the satellite consists of three sequences: the power latching sequence, the group select sequence, and the command sequence. The first two sequences are required to gain access to the satellite decoding circuits and to select one of the two groups of decoding gates in the command distribution units for processing the commands.

The third sequence is the command itself. The sequences comprise the following individual command message elements.

Latching sequence:

- Enable tone (frequency, amplitude, duration),
- FSK center frequency tone (frequency, duration, amplitude), and
- FSK spacecraft address (2-out-of-12 code) and dummy command (all 0's).

Group select sequence:

- Sync 1 (4 continuous data "1" bits),
- Spacecraft address (2-out-of-12 code),
- Sync 1 (4 continuous data "1" bits),
- Group select command (2-out-of-12 code), and
- Command termination bit.

Command sequence:

- Sync 1 (4 continuous data "1" bits),
- Spacecraft address (2-out-of-12 code),
- Sync 1 (4 continuous data "1" bits),
- Real-time, or direct, command (2-out-of-12 code),
- Command termination bit (1 data bit, data "1" or data "0"), and
- Programmer data. If a QOMAC, or picture-taking program is to be commanded, a series of 28 binary-coded data bits follows a real-time load programmer command ("Load Picture Program" or "Load QOMAC Program").

Sync is denoted by a shift to the data "1" frequency followed by a return to center frequency. Each data bit is denoted by a shift to the data "1" frequency or to the data "0" frequency followed by a return to center frequency. The outputs from each decoder are as follows:

1. 24 command-bit lines to each CDU. Each received command causes 2 of these output lines to become activated, depending on group selection and command coding.
2. Digital data outputs to programmers. A data "1" output line and a data "0" output line from each decoder are used to distribute digital data to both programmers. In addition, a data "0" output line distributes pulses to the telemetry commutator to provide "manual stepping" of the commutator.

3. Data verification. All data bits are retransmitted to the ground station in real-time over the data verification telemetry channel in the format shown in Figure 4-VIII-2. This output is a three-level signal in which the levels represent a data "1", a data "0", or center frequency. Data verification begins following receipt of the sync pulse of the spacecraft address and continues until after completion of a command termination bit. All verification data bits are transmitted back to the ground station in the same format and polarity as the command message to the spacecraft except for the command termination bits. These bits are data "0's" if the address and command formats are correct; if the address or the command format is incorrect, the CTB is the same polarity as in the input data. In addition to the data itself, a level is generated when any data is present; this level keeps a relay energized in the CDU which causes the verification data to be switched into the telemetry channel.

4. Power outputs. Each decoder supplies -23.0-volt (±1 percent) power continuously to its associated command receiver. In addition, when a decoder has been "enabled" and is in the operational mode, -23.0-volt (±1 percent) power is supplied to the CDU's.

5. Tone telemetry request. If the enable tone is sent for the appropriate length of time, this output is generated and sent to the CDU where it initiates the readout of one frame of telemetry from the commutator associated with the beacon that is operating at the time.

6. "Power on" telemetry signal. When the decoder enters the operational mode, it supplies a telemetry output to inform the ground station that decoder and CDU power is on.

7. Switched ground output. Whenever a decoder is in the standby condition (before -23-volt power is switched on), a ground signal is supplied as an output to the dual programmer to inhibit data inputs from that decoder to the programmer. When a decoder enters the operational mode, the ground signal is removed so that data inputs can be received by the programmer from that decoder.

c. Functional Operation (see Figure 4-VIII-3)

A decoder channel is made up of an analog tone detection and demodulation section and a digital data-handling section. The enable tone detection circuit is continuously supplied with power, but power is applied to the other command circuits only in response to the reception of the proper command tones in the correct sequence and for the correct time durations.

After the enable tone has been received for a minimum of 6 seconds, the FSK tone detector is enabled. At the same time a 3- to 6-second timing interval begins during which a valid spacecraft address must be received in order for the FSK tone detector to remain enabled. At the completion of the enable tone, the FSK tone is initiated by the ground station. When the FSK tone has been received by the spacecraft for a minimum of 1 second, power is temporarily supplied to the rest of the decoder circuits (and to the CDU's), and FSK data may then be processed. The FSK modulation is detected and shaped into digital data bits, and this data is checked by the digital section for the presence of a valid spacecraft address. If the correct address is received before the 6-second timing interval is completed, power is latched on to the decoder and further data may be processed. If the correct spacecraft address is not received within the 6-second interval, the switched decoder and CDU power turns off and the sequence of sending the enable tone for 6 seconds and the FSK tone for 1 second must be repeated before power is again applied to the data-handling section of the decoder. A correct address consists of a sync duration followed by 12 bits of command data, two of which must be data "1's" located in the correct positions in the word.

Following receipt of a correct address, the next sequence of data must correspond to a valid command word. A valid command word consists of a sync duration followed by 12 bits, 2 of which must be data "1's". An additional bit is sent to terminate the command. The command word is checked for correct format and, if acceptable (2-out-of-12 data "1's"), at the end of the last command bit, 2 of the decoder's 24 command bit outputs, corresponding to the 2 data "1's" in the word, are activated and presented to the CDU, where the actual decoding and command processing takes place. The command bit outputs are activated for one bit period and are terminated after receipt of the command termination bit. All of the data, except for the sync bit of the spacecraft address, is retransmitted on the data verification channel. In addition, during the command execution, a marker bit in the form of a long data "0", lasting

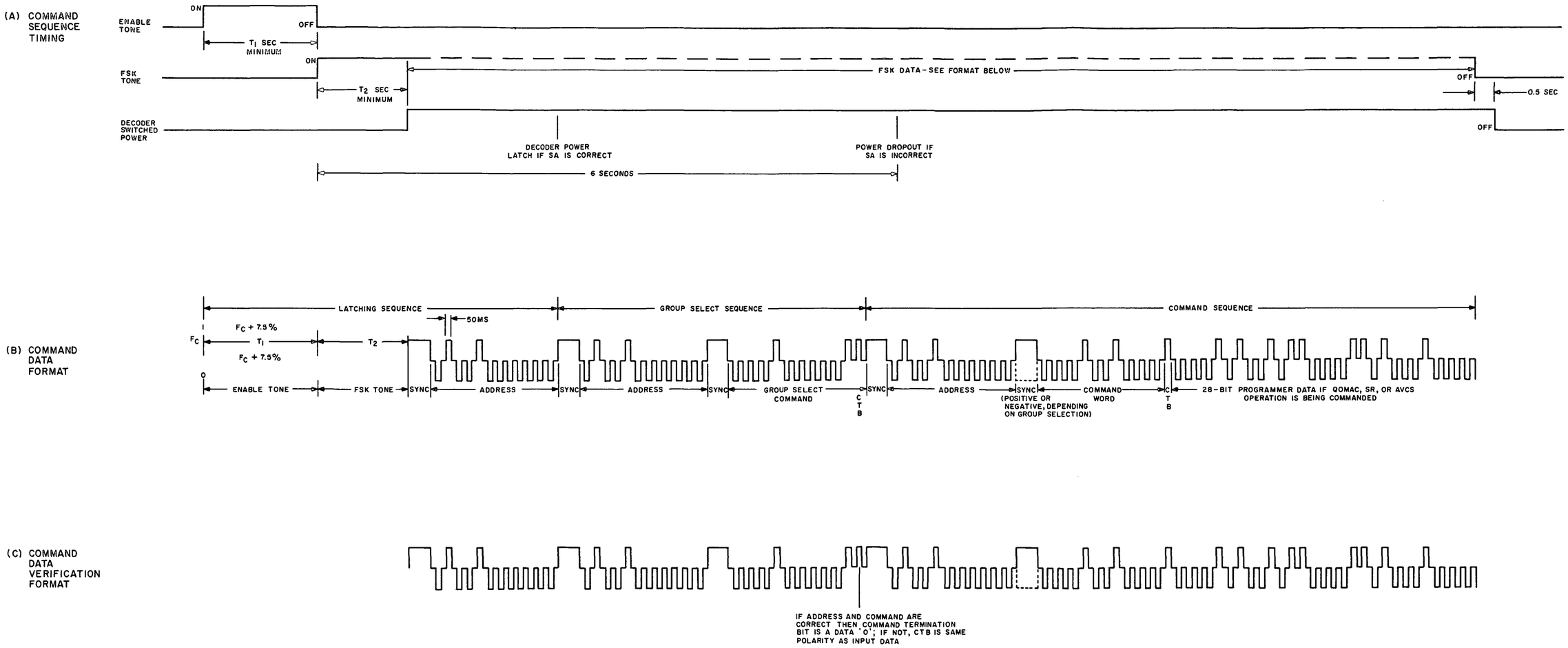

Figure 4-VIII-2. Command Sequence Timing and Data Format

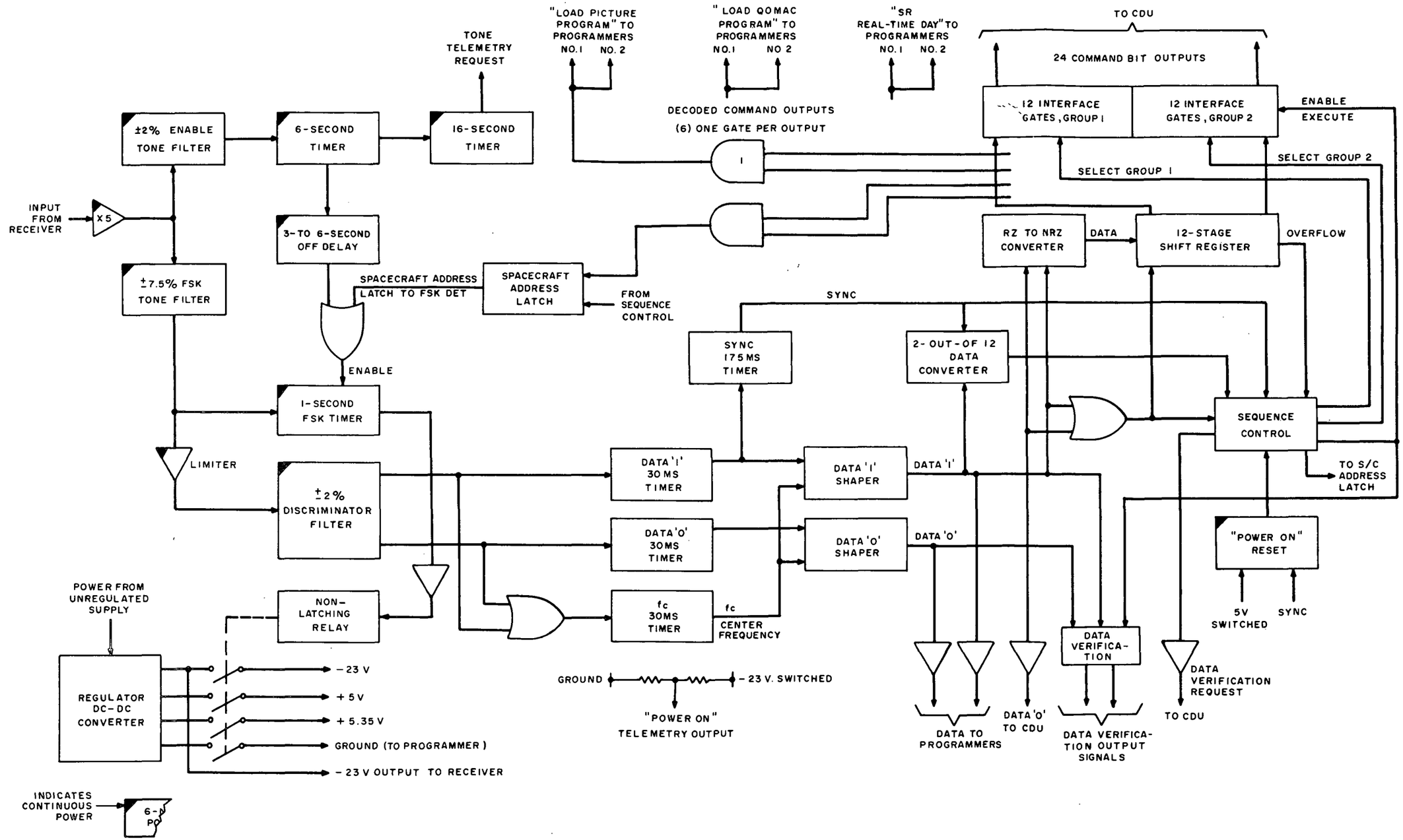

Figure 4-VIII-3. Command Decoder, Block Diagram

from the trailing edge of the 12th command bit until the command is terminated, is transmitted on the data verification channel if the address and command word are valid. If either is not valid this marker is a data "1".

If the command word received is one of the load programmer commands ("Load Picture Program" or "Load QOMAC Program"), 28 bits of digital programmer data then follow the command and are distributed to one of the registers in one of the programmers by the decoder. These data bits are also transmitted on the verification channel but the "hold-on" signal needed by the CDU relay is provided by the programmer instead of by the decoder.

After decoder power has been latched on, each new command sent must be preceded by the correct spacecraft address before it can be executed. If the address is incorrect, the logic circuits reset and await a correct address. However, decoder power remains latched on and there is no requirement to receive the address within a 6-second period. Once latched on, decoder power remains latched on until 1/2 second after the FSK tone has terminated. At that time, the decoder enters the standby mode and the entire sequence of enable tone, FSK tone, and address must be repeated to regain access to the decoding circuits. This operation is analogous to a "push-to-talk" system and has the advantage that, when the spacecraft is beyond communications range of a CDA station, the command decoding system is turned off and is thus inaccessible to spurious command.

Telemetry may be requested by sending an enable tone for a minimum of 22 seconds. In addition to enabling the FSK tone detector, an enable tone of this duration causes a tone telemetry request output to be generated and initiates, via the CDU, a readout of one frame of commutator telemetry. This same telemetry information may, of course, be obtained by the normal method of addressing the satellite and sending the appropriate digital command.

d. Operation of Circuits

(1) Analog Circuits

The input buffer amplifier of the decoder provides a gain of 5 to increase the voltage level of the tones from the receiver to a working level for the detection and demodulator circuits and to provide drive to the tone filters.

The enable tone is coupled through a ±2 percent bandpass filter to a detector circuit where it is converted to a DC level. This level is then integrated by an RC network to provide the 6-second timing. When the integrated signal exceeds a threshold voltage, a level is generated which enables the FSK tone detection circuit. If the enable tone is present for 22 seconds, a second RC integrator causes the "tone telemetry request" signal to be generated.

When the enable tone terminates, a 3- to 6-second "off delay" monostable multivibrator is triggered. The multivibrator keeps the FSK tone detection circuitry enabled for 3 to 6 seconds, during which the spacecraft address must be received. If the correct address is not detected within this period, the enable signal is removed from the FSK tone detector. If the address is detected within the period, a level is generated which maintains the enabled condition of the FSK tone detection circuitry for as long as the FSK tone is received.

The FSK tone is coupled through a ±7.5 percent bandpass filter to a detector circuit and converted to a DC level. This level is passed through an RC integrator to obtain the 1-second timing. When the integrator threshold is exceeded, a relay becomes energized causing -23-volt power to be applied to the rest of the analog circuitry, the output buffers, and the CDU, and causes +5-volt power to be applied to the digital integrated circuits. The FSK tone output of the ±7.5 percent bandpass filter is also coupled to a limiter amplifier which drives a discriminator filter. The signal at the "1" output of the discriminator filter peaks with a shift from the FSK tone center frequency, f_c, to f_c +7.5 percent. The signal at the "0" output of the discriminator filter peaks at a frequency of f_c -7.5 percent. The signal levels at the "1" and "0" outputs are 10 decibels down from the peaks when the FSK tone is at center frequency. Each detected "1" or "0" data level is timed for 30 milliseconds by an RC integrator before a valid data pulse is generated. The detected data "1" and data "0" pulses are combined in an OR gate before integration to obtain an indication of a return to center frequency. The center frequency level obtained is integrated for 30 milliseconds before a center frequency (CF) pulse is generated. The data "1" pulse output is coupled to a sync pulse integrator which times this signal for an additional 175 milliseconds (in addition to the previously timed 30 milliseconds) before producing a sync pulse output. In this way, the 30-millisecond data "1's" are distinguished from the 205-millisecond sync pulses even though both are at the same data "1" level.

The four signals (data "1," data "0," CF, and sync) are converted through buffer circuits to pulse levels compatible for use with the digital integrated circuits. Output signals generated by the integrated circuits are converted through output buffer circuits to voltage levels appropriate for spacecraft distribution.

(2) Digital Integrated Circuits

The digital integrated circuit section of the decoder contains the following circuits:

- Data shaping circuits,
- 12-stage shift register,
- Control logic,
- Spacecraft address check circuit,
- 2-out-of-12 check circuit,
- Data verification circuit, and
- Command decoding circuits.

The data, CF, and sync pulses received from the analog section are pulses whose durations have been shortened by the timing integrators. Thus, a data "1" pulse having an original duration of 50 milliseconds has been reduced to a 20-millisecond pulse because of the 30-millisecond integration time. Following the trailing edge of this pulse, a 30-millisecond interval (the CF integration time) elapses before a 20-millisecond CF pulse is generated. This form of the data is reshaped to its original format by two direct-coupled bistable multivibrators which are "set" by the data pulses and "reset" by the CF pulses. The reshaped data pulses are supplied to the programmers and to the data verification network. The data "1" and data "0" pulses are OR'ed to obtain decoder shift pulses. The return-to-zero (RZ) format data is converted to nonreturn-to-zero (NRZ) format at the input to the first stage in the decoder shift register. This conversion provides for shifting data into the register at a time when the first-stage inputs are not changing.

When power is initially applied to the digital logic, an RC network causes the "reset" multivibrator to assume the state which locks the control logic in the reset state. The control logic consists of a four-state sequencer and bistable multivibrator. When a valid address is received, this circuit maintains the enabled condition of the FSK detector in the analog section. When a sync pulse is detected, the shift register and the data format checker are reset and the reset clamp to the control logic is released. After the trailing edge of the sync pulse, a data "1" (the sync pulse is actually a long data "1" pulse) is shifted into the first stage of the register and serves as a marker bit to detect register overflow. At the same time the control logic enters state 2. While in this state, the decoder is prepared to accept 12 bits of data which contain 2 data "1's" occupying those bit positions that correspond to the spacecraft address wired into that particular unit.

The 2-out-of-12 format check is accomplished by a four-state counter which advances state with each incoming data "1" pulse. A sync pulse always resets this counter and is not itself counted as a valid data "1" pulse. The counter is not advanced by the same shift pulse as the register, and this allows checking of a command before it is fully shifted into the register. The states of the counter are as follows:

State	A	B	Action
1	0	0	Reset.
2	1	0	1 data "1" pulse received.
3	1	1	2 data "1" pulses received.
4	0	1	3 or more data "1" pulses received.

Thus, only when the counter is in state 3 does data successfully pass the 2-out-of-12 check.

When the 11th data bit of the spacecraft address has been stored in the shift register, the marker bit has reached the 12th register stage, and a gate is enabled which permits the 2-out-of-12 command word check and the check for a correct spacecraft address. The address is actually examined during the leading part of the 12th data bit. Thus the inputs to the AND gate that decodes the address bits have to be taken from the register one bit early. If the 12th data bit of the address is to be a data "1", the AND gate input must come from the input to the

first stage of the register (which serves as an RZ-to-NRZ converter). If the decoded address is correct and the 2-out-of-12 checker is in state 3, the shift pulse which stores the 12th data bit in the register also causes the control logic to enter state 3, and the spacecraft address multivibrator sets, thus providing the FSK tone detector latch. If the wrong address is received, the control logic reverts to state 1, the reset state. While in state 3, the decoder is ready to accept the sync pulse which precedes the command bits. When this pulse is detected, the register is reset, the 2-out-of-12 counter is reset and, following the trailing edge, a marker bit is again shifted into the register's first stage. At that time, the sequencing logic enters state 4. If the logic were in state 3, and if a shift pulse were detected without a sync pulse, the logic would reset to state 1. While the control logic is in state 4, the decoder is prepared to accept a command word consisting of 12 bits of data of which 2 are data "1's". Normally, the command that follows the spacecraft address will be a "group select" command designating which group of interface circuits will be enabled. As the bits are shifted into the register, the data "1's" are tallied, at their leading edges, in the 2-out-of-12 counter. When the 12 bits are stored in the shift register, as indicated by the overflow of the marker bit, and if the 2-out-of-12 counter is in state 3, indicating that exactly two data "1's" were received, an "execute" bistable multivibrator is set. The group select command is decoded in the sequence control and a signal from the sequence control enables the 12 command bit output gates associated with the selected command group. Commands that follow are processed in the same way except that when the execute multivibrator becomes set, the two interface gates associated with the register stages containing data "1's" in the selected group produce outputs. Each output gate is connected to an output buffer which converts a +5-volt pulse from the gate to a +5.35 volt pulse for use in the CDU where the decoding of most of the commands actually takes place. At the same time that a command is executed, the control logic is reset to state 1. When the command termination bit is received, the "execute" multivibrator is reset and the command bit outputs are deenergized. If a sync pulse is detected while the control logic is in state 4, prior to register overflow, the control logic reverts to state 2 until a correct spacecraft address is again received.

In addition to the address and group select commands, three other commands are decoded in the decoder. The remainder are decoded in the CDU's and other units.

The data which is distributed to the programmers is taken from the outputs of the digital shaping circuits after passing through output buffers. Data from the same source is used to generate the data verification signals. The data "1" and data "0" pulses are summed together to form a three-level signal which is sent to the CDU for further processing before being transmitted back to the ground as data verification.

In addition, during the execution of a command (when the "execute" multivibrator is set) the output is forced to the data "0" level for the duration of the command. This then provides a 100-millisecond command execution "marker", the signal necessary to activate the CDU relay, which, in turn, permits the verification bits to be transmitted over the telemetry channel, is generated by the following logical condition of the control logic: ($\overline{\text{State 1}}$) and Execute Command.

2. Programmer

a. General

The differences between the ITOS programmer and the TOS programmer are predicated on the following extensions of spacecraft functions:

- The presence of both AVCS and APT cameras on the same spacecraft, necessitating changes in timing and picture sequencing.
- The additon of the scanning radiometer (SR) sensory system, necessitating nighttime operation.
- A spin rate of one rotation per orbit, obviating the need for spin synchronization of the sensory subsystems.

The required programmer changes have been implemented by extending proven techniques used in the TOS equipment.

Two identical programmer circuits, each with its own DC-to-DC converter, are housed in a single dual programmer unit to provide full redundancy of the programmer function. The term "programmer" is used to describe either of these redundant circuits; "dual programmer" refers to the unit containing the two programmer circuits.

Either programmer can control remote operations (i.e., remote from CDA station contact) of the APT camera subsystem, the AVCS camera subsystem, the SR subsystem, and the QOMAC coil. During a CDA station contact, command data programs transmitted from the ground are routed to the programmer from one of the satellite decoders and are loaded into and stored in the selected programmer registers. The programmer then generates, at properly timed intervals, the signals required to control remote operation of the sensory subsystems and of the QOMAC coil, in accordance with the command program. The programmer receives timing input signals from the TBU which establish the counting rates for interval timing.

b. Functional Operation (See Figure 4-VIII-4.)

(1) Program Data Loading

When a "Programmer (No. 1 or 2) ON, (No. 2 or 1) OFF" command is received by the spacecraft, a latching relay becomes energized and power is applied to the DC-to-DC converter in the designated programmer, which, in turn, supplies voltages to the integrated circuits and to the interface circuits. At power turn-on, the programmer becomes completely reset and then enters a standby mode. The programmer remains in the standby mode until a load command is received. This command may be a "Load Picture Program" or a "Load QOMAC Program" command. If the command is a "Load Picture Program" command, the 28 bits of digital data which follow contain instructions pertaining to remote operation of the AVCS or APT camera subsystems and of the SR subsystem.

The 28 bits of data which follow a "Load Picture Program" command constitute either a "T_o word" or a "rephasing word". Word identification is given by the first 2 of the 28 bits. These two bits are decoded and an enabling signal is sent to either the T_o word control logic or to the rephasing word control logic, to enable the loading of the remaining bits of the program data into the appropriate register. The T_o word data (Table 4-VIII-2) includes the T_o delay time (i.e., time from loading of the programmer until T_o, the night-to-day transition of the orbit) and the orbit correction factor, which establishes the exact duration of the orbit in the orbit counter. The rephasing word data (Table 4-VIII-3) includes the number of phasing correction counts, the polarity of the phasing correction, the mode of SR operation (day and night or night only), and the APT picture sequence selection.

TABLE 4-VIII-2. FORMAT OF T_o WORD*

Bit No.	Function
1, 2	Bit 1 is a data "1", bit 2 is a data "0" in the T_o word.
3	Not used.
4 through 14	2's complement of the number of 6.5-second intervals from the end of loading the programmer until the first transition of the spacecraft from orbit night to orbit day (T_o). Called "T_o delay time".

TABLE 4-VIII-2. FORMAT OF T_o WORD* (Continued)

Bit No.	Function
15, 16	Not used.
17 through 26	2's complement of the number of 6.5-second intervals in the true orbit time minus 640 counts. Called the orbit correction factor.
27, 28	Not accepted by programmer.
*T_o word must be preceded by "Load Picture Program" command.	

TABLE 4-VIII-3. FORMAT OF REPHASING WORD*

Bit No.	Function
1, 2	Bit 1 is a data "0", bit 2 is a data "1" in the rephasing word.
3 through 6	2's complement of the selected number of phasing correction counts; from 1 to 15 counts can be programmed.
7	Polarity of the phasing correction. A data "1" causes the selected number of phasing counts to be subtracted from the orbit count; a data "0" causes the selected number of phasing counts to be added to the orbit count.
8 through 14	Not accepted by programmer.
15	A data "1" causes the SR to operate during both day and night portions of the orbit. A data "0" causes the SR to operate during orbit night only (normal mode of operation).
16 through 26	These 11 bits represent the 11 pictures in the full APT camera sequence. Any combination of the 11 APT pictures may be omitted or included in the sequence by programming a data "0" for each picture to be included and a data "1" for each picture to be omitted.
27, 28	Not accepted by programmer.
*Rephasing word must be preceded by "Load Picture Program" command.	

At the trailing edge of a 100-millisecond "Load Picture Program" command pulse, the data verification level is generated and the 2-stage picture program word identification counter and decoder are enabled. The first two bits of the word are decoded to determine if the remaining 26 bits contain a T_0 word or a rephasing word. If the data is a T_0 word, the T_0 control logic enables the 12-stage orbit-correction shift register and 12 bits of data are shifted into the register. The first bit to enter the register is not used. The other 11 bits form the 2's complement of the T_0 delay time. After loading, these bits are parallel-transferred to the 11-stage counter and the remaining bits of the program are then shifted into the register. Of these, only bits 17 through 26 are used; these bits represent the true orbit time minus 640 counts and are called the orbit correction factor. After loading has been completed, the 11-stage counter commences counting the T_0 delay time with counts occurring at 6.5-second intervals. The orbit correction factor continues to be stored in the register until after the T_0 delay has been counted out. At count T_0 +640, the factor is parallel-transferred, without destruction in the register, to the counter and is counted out to T_0 to establish the corrected orbit duration. The orbit correction factor remains stored in the register and controls the corrected orbit duration of succeeding orbits until the programmer is turned off or the register is reloaded.

If the data following a "Load Picture Program" command is a rephasing word, the 5 data bits following the two word identification bits are shifted into the rephasing shift register and transferred to the rephasing counter. Bits 8 through 14 are not accepted by the programmer. Bits 15 through 26 are shifted into the register and stored to control remote APT and SR operation. Bit 15 is stored in the SR mode stage of the register and its condition controls the outputs of the orbit counter decoding logic to the SR subsystem. If a data "1" is stored in this stage, the output signals during orbit counting cause the SR to operate during both the day and night portions of the orbit. If a data "0" is stored, the SR operates only during the night portion of the orbit. The 11 bits stored in the remaining stages of the shift register control the APT sequence by controlling the generation of the APT prepare pulse for each individual APT picture during the sequence. Bit 16 controls the prepare pulse immediately following programmer loading. During the APT sequence, each time the bit in stage 11 is shifted out of the register it causes an APT prepare pulse to be generated or inhibited. During the first night portion of the orbit following loading of a rephasing word, the counter in

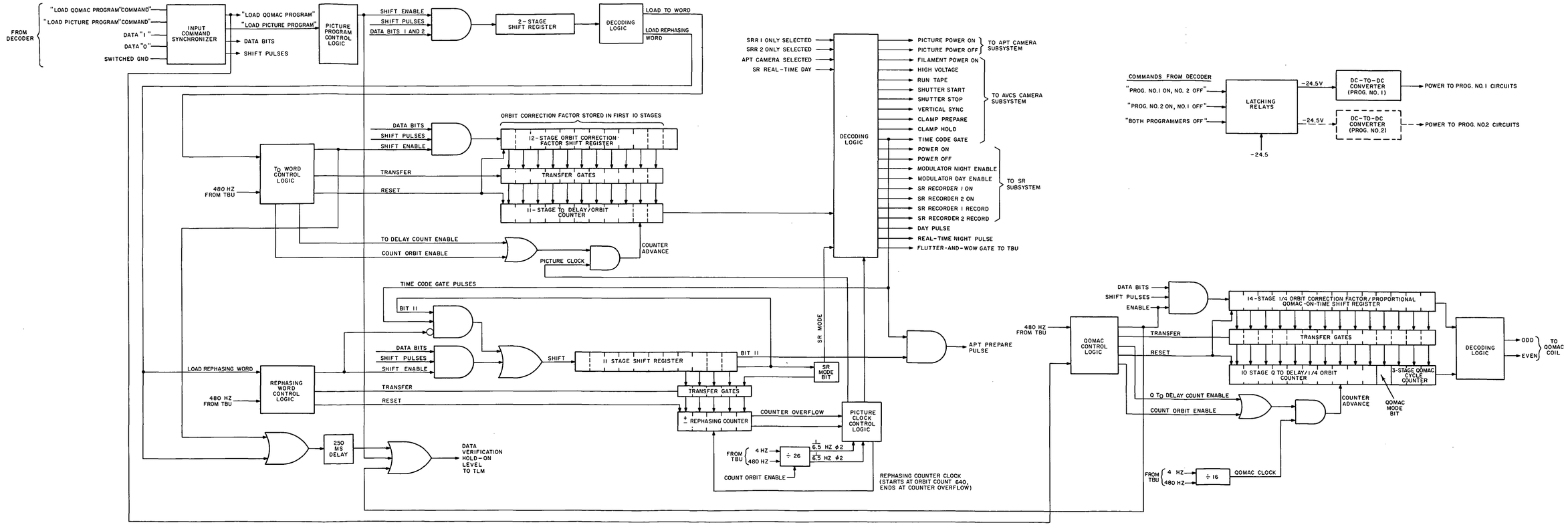

Figure 4-VIII-4. Programmer, Block Diagram

which rephasing word bits 3 through 6 are stored commences counting (at T_0 + 640) and causes the programmed number of counts to be added to or subtracted from the number of picture clock pulses generated in the picture clock control logic and supplied to the orbit counter. Thus time T_0 may be shifted in either direction with respect to the night-to-day transition point in the orbit.

If the command is a "Load QOMAC Program" command, the following 28 bits of data contain instructions for remote operation of the QOMAC coil (Table 4-VIII-4). The trailing edge of the 100-millisecond command pulse enables the 14-stage shift register, and the 28-bit digital data word begins to shift into the register. At the same time, the data verification hold-on level is generated. When the first 14 bits of data have been shifted into the register, an overflow signal causes the parallel transfer of these bits into the "count" registers. The first three bits, representing the number of QOMAC cycles to be performed, are transferred into a three-stage counter. If the program is a proportional QOMAC program, these bits are not used. The fourth bit is the QOMAC mode bit, denoting whether normal QOMAC or proportional QOMAC operation is to be performed. The remaining 10 bits are transferred into the 10 stages of the register which count the delay until QT_0, the time of beginning remote QOMAC operation. When these bits have been transferred, the shift register resets and the remaining 14 bits of the program enter the shift register. These bits are transferred into the counting registers later, after QT_0, to control the actual QOMAC operations. When this second group of 14 bits is stored, as indicated by an overflow signal, no further data bits can be accepted (without a new "Load QOMAC Program" command) and the programmer enters a "count" mode. The data verification level is then terminated.

(2) AVCS, APT, and SR Sequencing (See Figures 4-VIII-5 and 4-VIII-6.)

During the day portion of the orbit, the AVCS and APT camera subsystems will normally perform 11 picture-taking cycles each, the APT picture data being transmitted in real time to local stations and the AVCS data being recorded for later playback to a CDA station.

TABLE 4-VIII-4. FORMAT OF THE QOMAC PROGRAM WORD*

Bit No.	QOMAC (Bit 4 must be a data "0")	Proportional QOMAC (Bit 4 must be a data "1")
**1 through 3	2's complement of the number of QOMAC cycles to be performed from 1 to 8.	Not used.
**4	Data "0"	Data "1"
5 through 14	2's complement of the delay time until the first quarter orbit timing begins. Delays of from 1 to 1024 counts in 4-second increments may be programmed.	Same as for QOMAC.
15 through 21	Not used.	2's complement of the actual portion of each quarter orbit, in 16-second increments, during which the QOMAC coil will be energized when proportional QOMAC operation is being used.
22 through 28	2's complement of the true quarter-orbit time minus 256 counts, in 4-second increments; corrects the quarter-orbit counter to the exact quarter-orbit time.	Same as for QOMAC.

*QOMAC program word must be preceded by a "Load QOMAC Program" command.
** If bits 1 through 4 are all data "1's", QOMAC operation stops and the QOMAC logic returns to the standby condition.

SR sequencing will be normally performed during the nighttime portion of each orbit. When the normal mode of SR operation; i.e., nighttime operation, has been selected, by coding bit 15 of the rephasing word as a data "0", the detailed camera-sequencing program, after data reception and storage, proceeds as described below.

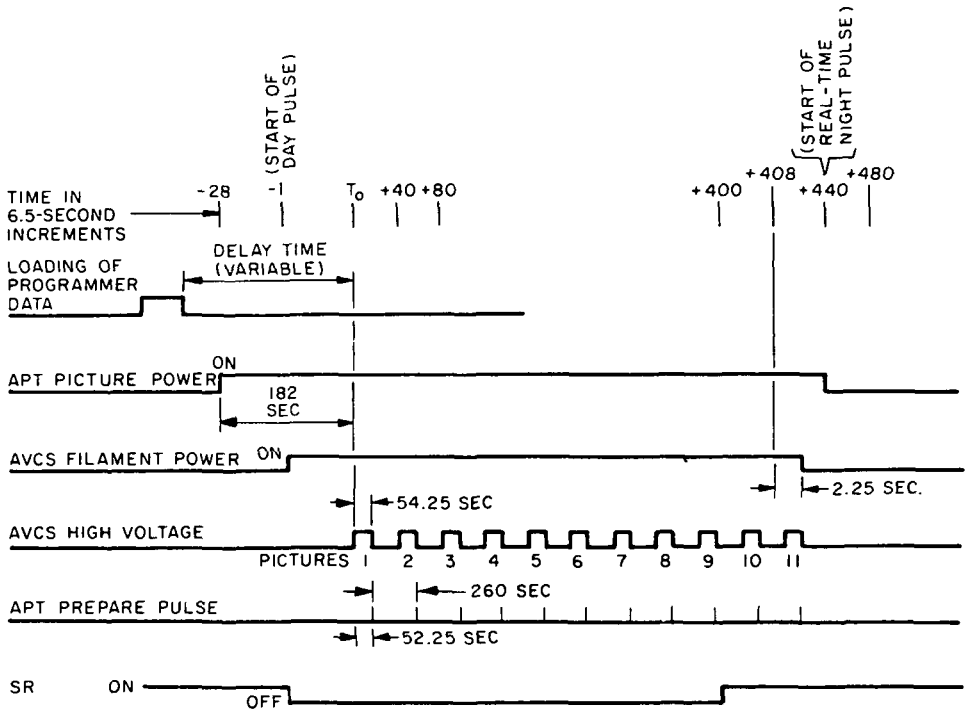

Figure 4-VIII-5. Camera and Scanning Radiometer, Timing Diagram

The picture program counter is advanced in 6.5-second increments; the times referred to in this discussion are in terms of counts of this 6.5-second period.

1. T_o is defined as the time of transition from nighttime to daytime operation. This is the time at which the programmer orbit counter overflows (or resets). The loading of data may occur during the daylight portion of the orbit. In such cases, after the reception of data, if count 440 (beginning of real-time night) has not been reached, AVCS filament power and APT picture power are turned on and normal camera sequencing (as defined below) proceeds until count 440. If count 440 has already been reached at the time of programmer loading, then camera operation will not take place until the following orbit.

2. At T_o -28 counts (i.e., 182 seconds before T_o), APT power is turned on.

3. At time T_o -1 count (i.e., 6.5 seconds before the night-to-day transition) the "day" pulse is generated.

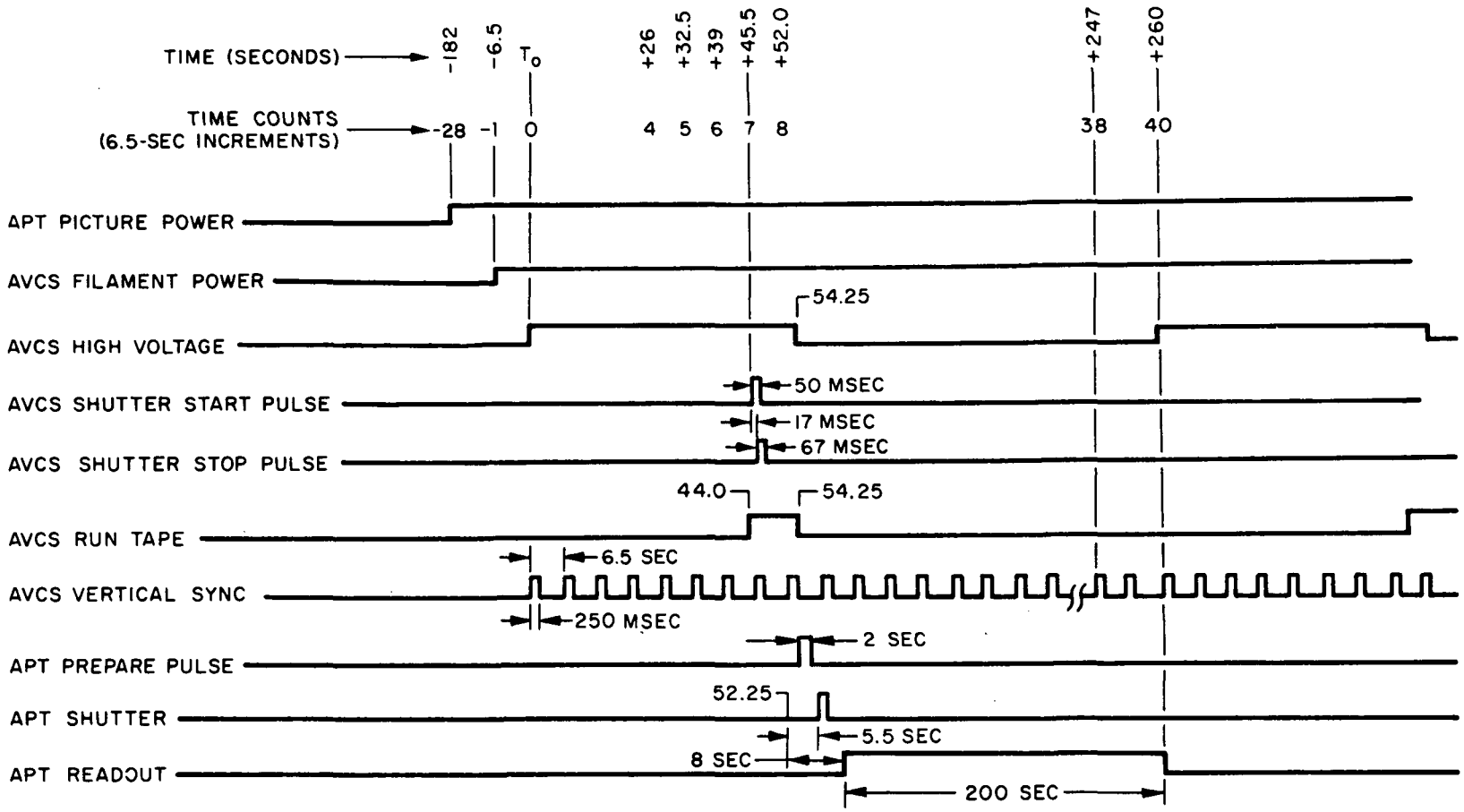

Figure 4-VIII-6. AVCS and APT Camera Control, Timing Diagram

4. At T_0 -1 count, the AVCS filament power on pulse is generated.

5. At T_0, AVCS high voltage is turned on and the vertical sync pulse, having a period of 6.5 seconds and a pulse width of 250 milliseconds, is supplied to the AVCS camera.

6. At T_0 +6 counts, the AVCS clamp prepare pulse is generated.

7. At T_0 +6 counts +5.0 seconds, the AVCS run tape signal is generated, causing power to be applied to the AVCS tape recorder.

8. At T_0 +7 counts, the AVCS clamp hold pulse and the AVCS shutter start pulse are generated. 17 milliseconds after the AVCS shutter start pulse is generated the AVCS shutter stop pulse is generated. Also at T_0 +7 counts, the TBU flutter and wow gate is generated.

9. At T_0 +8 counts +0.25 second, the APT prepare pulse is generated. The time of the prepare pulse is chosen so that any transients due to the APT shutter (which is activated by the camera 5.5 seconds after the prepare pulse) will not affect the quality of the AVCS picture. Likewise, during APT camera readout, which lasts until approximately T_0 +40 counts, no AVCS camera transients occur that might affect APT picture quality. Also at T_0 +8 counts +0.25 second, the AVCS time code gate pulse is generated.

10. At T_0 +8 counts +2.25 seconds, the AVCS high voltage, run tape, and time code gate signals are terminated.

11. At T_0 +40 counts, the AVCS high voltage is again turned on and the operations described in steps (4) through (9) are repeated; this process continues to be repeated at 40-count intervals.

12. At T_0 +400 counts, the SR power on pulse is generated, applying power to the scanning radiometer. If the "Select SRR 1" or "Select SRR 2" command has been received, the selected SR recorder is turned on at this time also.

13. When T_0 +408 counts (plus an additional 2.25 seconds) is reached, 11 AVCS pictures have been taken and stored on tape and AVCS filament power is turned off to terminate AVCS picture-taking for the remainder of the orbit.

14. When T_0 +440 counts is reached, the readout of the 11th APT picture has been completed, and the APT picture power off pulse is generated to terminate APT picture-taking for the remainder of the orbit. This pulse also signals the transition from the daytime to the nighttime portion of the orbit and is designated the "real-time night pulse". At this time the SR modulator night enable pulse is also generated.

15. At T_0 +640 counts, the 11th stage of the orbit counter is set and the contents of the first 10 stages of the orbit correction shift register (programmer data bits 17 through 26) are transferred into the first 10 stages of the orbit counter. The counter then counts in usual binary fashion until the next T_0 or overflow of the counter. An overflow from the first 11 stages of the counter indicates a one-orbit displacement from time T_0. Twenty-eight counts before T_0, APT power is again turned on. One count before T_0, SR power is turned off and AVCS picture power is again turned on. Succeeding events recur as described above.

16. The programmer continues to repeat the same picture-taking and scanning radiometer operations until either a "Both Programmers OFF" command or a new "Load Picture Program" command is received from a CDA station.

The normal orbit sequencing of the camera subsystems and of the scanning radiometer subsystem may be altered to achieve two additional operational modes. The difference between the normal mode described above and the other modes involves the periods of operation of the APT camera subsystem and of the scanning radiometer (SR) subsystem. These two subsystems do not operate concurrently in any of the three modes, except for brief overlap periods. As described above, in the normal mode, the APT subsystem operates during orbit day and the SR subsystem operates during orbit night. In the first alternative to the normal mode, the SR subsystem is commanded (by inserting a data "1" in bit position 15 of the rephasing word) to operate during both the day and the night portions of the orbit and to record

the SR data. The "SR Power OFF" pulse is not generated at count T_0 -1, and SR operation continues both day and night throughout the orbit. The SR data is recorded by the selected SR recorder, or by both recorders if both have been selected, alternating between SRR 1 and SRR 2 on successive orbits. The switchover between SR recorders occurs at the time of the day enable pulse (count T_0 -1).

The second alternative mode of operation causes the SR subsystem to provide real-time day coverage to properly equipped (passive) local stations as the satellite transmits within contact range of the stations. This mode of operation is obtained by sending the "SR Real-Time Day Mode" command and by inserting a data "1" in bit position 15 of the rephasing word. If APT operation is not present before or commanded after the receipt of an "SR Real-Time Day Mode" command, the programmer generates an "SR modulator day enable" level beginning at the time of the day pulse and terminating with the start of real-time night operation. This enables transmission of SR data over the real-time communications link.

(3) QOMAC Sequence

After a "Load QOMAC Program" command has been received and the associated 28 bits of program data have been stored, the QOMAC sequence logic enters a count mode. Clock pulses from the TBU, having a period of 4 seconds, drive the QOMAC quarter-orbit counter which, initially, contains data bits 5 through 14 of the program. The first clock pulse to be counted occurs from 4 to 4.3 seconds after the trailing edge of the 28th data bit. When a number of clock pulses equal to the 2's complement of bits 5 through 14 has been counted, the counter overflows. The time of overflow is referred to as QT_0. The delay time until QT_0 can be from 1 to 1024 counts (in 4-second increments). At QT_0 the counter resets and begins to count the quarter-orbit time in 4-second increments.

If data bit 4 in the program is a data "0", the program is a normal QOMAC program. At QT_0 the QOMAC "odd" output is initiated. Counting then continues until count QT_0 +256; at that time, data bits 22 through 28 are transferred from the storage register into the first seven stages of the counter. These bits represent a correction factor and cause the first nine stages of the counter to overflow after the programmed time interval of the corrected quarter orbit. Quarter-orbit times from 385 to 512 counts (in 4-second increments) may be

programmed. When overflow occurs, the QOMAC "odd" signal is terminated and the QOMAC "even" signal is initiated. Counting continues until count 256 is again reached, at which time the correction factor is again transferred to the counter. When the next overflow of the first nine counter stages occurs, signifying completion of the second quarter orbit, stage 10 of the counter overflows again. At this time the QOMAC "even" signal is terminated, completing one QOMAC cycle. A three-stage counter, initially containing the programmed number of QOMAC cycles in 2's complement form, is advanced each time one cycle is completed. The QOMAC cycle is repeated, as described above, until the cycle counter overflows indicating the completion of the programmed number of cycles. At that time, the QOMAC sequencer enters a standby mode and no further QOMAC output signals are generated until another QOMAC program is received.

(4) Proportional QOMAC

If data bit 4 in the load QOMAC program is a data "1", the program is a proportional QOMAC program. Counting operations proceed as for a normal QOMAC program, except that no output signal is initiated until a programmed time after T_0 +256. Immediately after the QT_0 +256 transfer of data bits 22 through 28 into the first 7 stages of the quarter-orbit counter, the contents of stages 3 through 9 of the counter are compared with bits 15 through 21, which are stored in a separate register. When these numbers are equal, the QOMAC "odd" output is initiated. Counting and quarter-orbit correction continues as in a normal program until a quarter orbit is completed. At that time, the QOMAC "odd" output is terminated and the QOMAC "even" output is initiated. The logical equivalent of the 2's complement of the contents of stages 3 through 9 of the counter are then compared with stored bits 15 through 21. When the two are equal, the QOMAC "even" output is terminated. Counting continues until a quarter orbit is completed but no further QOMAC output is generated during the completion of the quarter orbit interval. The proportional QOMAC ODD-EVEN cycle, like the normal QOMAC cycle, is complete at the end of the second quarter orbit, even though proportional QOMAC operation ceases before the end of the second quarter orbit. The same sequence of events, as described above, is reinitiated at each quarter-orbit overflow of the counter.

The QOMAC cycle counter is inhibited in the proportional QOMAC mode of operation, functioning only as a storage register for bits 1, 2, and 3. If bits 1, 2, and 3 are all data "1's", the QOMAC sequencer assumes a standby mode and does not generate QOMAC output signals. In the proportional QOMAC mode, the "on" times for the "odd" and "even" QOMAC outputs are equal and programmable in 16-second increments, but are limited to a maximum time which is equal to the true quarter orbit time minus 1024 seconds. The proportional QOMAC cycle is illustrated in Figure 4-VIII-7.

c. Programmer Interfaces

(1) Programmer Inputs and Outputs

The ITOS programmer receives the following inputs:

1. Power (-24 volts regulated and ground).
2. A "Programmer No. 1 ON, No. 2 OFF" command from the CDU which causes a latching relay to apply power within programmer No. 1.

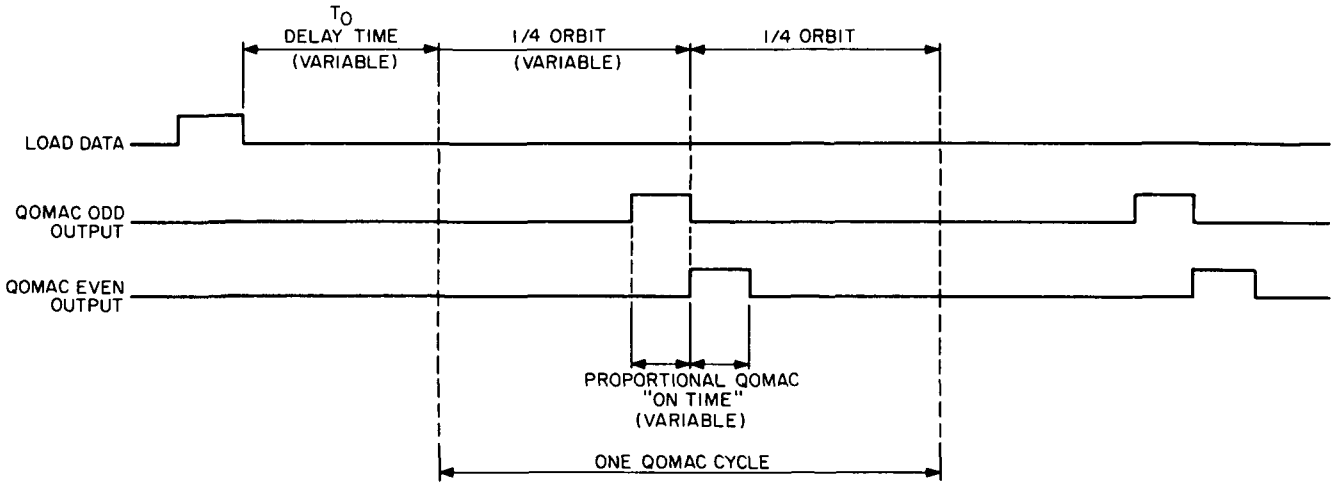

OPERATIONAL LIMITS

VARIABLE	TIME DURATION	COUNTS	TIME INCREMENT (SEC)
T_O DELAY	4 SEC TO 68 MIN 16 SEC	1 TO 1024	4
1/4 ORBIT TIME	25 MIN 40 SEC TO 34 MIN 8 SEC	385 TO 512	4
QOMAC "ON TIME"	16 SEC TO (1/4 ORBIT TIME -1024 SEC)	1 TO ~41	16

Figure 4-VIII-7. Proportional QOMAC Cycle

3. A "Programmer No. 2 ON, No. 1 OFF" command from the CDU which causes a latching relay to apply power within programmer No. 2.

4. A "Both Programmer OFF" command from the CDU, which causes a latching relay to remove power within both programmers.

5. A "Load Picture Program" command from either decoder, which resets the programmer and enables it to be loaded with 28 bits of picture and SR digital data.

6. Binary picture-mode data in a 28-bit digital format from either decoder. This data forms a T_0 word, containing delay time until T_0, an orbit correction factor, or a rephasing word, containing orbit phasing correction magnitude and polarity, SR recording selection, and APT picture sequence selection.

7. A "Load QOMAC Program" command from the CDU which enables the programmer to accept 28 bits of QOMAC program digital data.

8. Binary QOMAC data in a 28-bit format from either decoder. This data forms either a normal QOMAC program word or a proportional QOMAC program word, each of which contains a delay time until QOMAC operation begins (at QT_0), a quarter-orbit correction factor, and, in the case of proportional QOMAC, the duration of the operating time in each quarter orbit. The normal QOMAC word also contains the number of QOMAC cycles to be performed.

9. A switched ground from either decoder, indicating that the associated decoder has its power turned off and inhibiting receipt of spurious data from that decoder.

10. An "SR recorder 1 only selected" signal and an "SR recorder 2 only selected" signal from the CDU which causes the timed control signals for SR recorder operation to be directed to the designated recorder. These signals are produced by the CDU in response to the "Select SR Recorder No. 1" and the "Select SR Recorder No. 2" commands.

11. An "Enable SR Real-Time Day Mode" command from either decoder, which causes the programmer to generate "SR modulator day enable" signals during the day portion of each orbit and to omit the "SR power off" signals at T_o -1, provided that APT operation has not been selected. Real-time operation of the SR 1 subsystem then takes place during the day portion of the orbit.

12. An "APT camera selected" signal from the CDU, which terminates daytime SR operation if it is in progress and prevents that mode of operation from being enabled.

13. A 480-pulse-per-second clock pulse from the time base unit, which is used throughout the programmer as a strobing pulse for many shifting functions.

14. A 4-pulse-per-second clock pulse from the time base generator, from which are derived a clock pulse with a 6.5-second period for timing all camera and SR remote operations, and a clock pulse with a 4-second period for timing QOMAC remote operations.

The programmer outputs are as follows:

1. A "picture power on" pulse to the APT camera subsystem.

2. A "picture power off" pulse to the APT camera subsystem.

3. A "prepare" pulse to the APT camera subsystem.

4. A "filament power on" level to the AVCS camera subsystem (from T_o until T_o +408).

5. High voltage to the AVCS camera subsystem.

6. A "run tape" signal to the AVCS camera subsystem.

7. "Shutter start" pulses to the AVCS camera subsystem.

8. "Shutter stop" pulses to the AVCS camera subsystem.

9. A "vertical sync" pulse to the AVCS camera subsystem.

10. A "clamp prepare" pulse to the AVCS camera subsystem.

11. A "clamp hold" pulse to the AVCS camera subsystem.

12. A "time code gate" to the AVCS camera subsystem.

13. A "power ON" pulse to the SR subsystem.

14. A "power OFF" pulse to the SR subsystem.

15. A "modulator night enable" level to the SR modulator.

16. A "modulator day enable" level to the SR modulator.

17. An "SR recorder 1 record" level to the SR subsystem.

18. An "SR recorder 2 record" level to the SR subsystem.

19. A "Select SR recorder 1" level to the CDU.

20. A "Select SR recorder 2" level to the CDU.

21. A "day" pulse (T_o -1).

22. A "real-time night" pulse.

23. A "QOMAC odd" signal to the vehicle dynamics subsystem.

24. A "QOMAC even" signal to the vehicle dynamics subsystem.

25. A "data verification hold-on" signal to the telemetry subsystem.

26. A "programmer status telemetry" signal to the telemetry subsystem.

27. A "QOMAC status" telemetry signal to the telemetry subsystem.

28. A "flutter-and-wow gate" to the TBU.

3. Command Distribution Unit

a. General

The ITOS command distribution units (CDU's) perform the same functions performed by the TOS AVCS and APT CDU's. Most of the differences between these units and the TOS CDU's are the result of the increased spacecraft functions in the ITOS design. Two CDU's are used in ITOS and designated CDU A and CDU B.

As on TOS, the ITOS CDU's contain the circuitry to perform the following functions:

- Transform the command bits received from either decoder into command functions.
- Distribute the command functions to the appropriate subsystems.
- Process telemetry data and command verification data.
- Generate a "push-to-talk" signal, as an automatic turn-off signal, when CDA ground station contact is lost.

b. Command Decoding

Each CDU has as inputs 24 command lines from each decoder (12 in command group I; 12 in command group II). Each decoder also supplies its -23-volt switched power to that part of the command decoding matrix associated with its 24 command lines. The 2-out-of-12 coding results in a signal being present on two of the command lines in the group selected. Since command group selection is accomplished in the decoder, only those command lines corresponding to the group selected will be activated. Each command line provides one of the two inputs to appropriate decoding AND gates in the matrix. An AND gate is capable of driving the coil of at least one relay. Diode OR gates couple the outputs of the corresponding AND gates of each decoder.

Using the basic 2-out-of-12 code format, the number of commands required for ITOS exceeds the number of codes available. Therefore, to satisfy the ITOS requirements with minimum impact on the decoder, CDU, and on the ground station, the group selection

scheme is used. This arrangement permits the use of each 2-out-of-12 command code twice without ambiguity, and increases the number of command functions.

Each CDU contains decoding gates for both command groups. To switch from one group to the other, a group selection command must be sent corresponding to the desired group, and all the following commands are interpreted as part of that group.

c. Specific Decoding

(1) AVCS Camera Selection

Selection of either AVCS camera, or neither camera, is accomplished by controlling the power input. Figure 4-VIII-8 shows the circuitry which performs this function. In addition, the latching relays also provide some control signals for the AVCS tape recorders by controlling the direct picture power.

(2) AVCS Tape Recorder Selection

The AVCS tape recorders are controlled, or both turned off, by power switching relays. In addition, the CDU distributes playback commands. Figure 4-VIII-9 shows the circuitry used to select a tape recorder. Nonlatching relays control the playback by controlling data enable signals applied to the tape recorders. These relays, in turn, are controlled by "push-to-talk" signals. The S-band push-to-talk signal insures that a recorder ends its playback mode if the decoder drops out. The recorder end-of-tape signal inhibits playback if a tape recorder is at the end of tape.

(3) S-Band Transmitter and Multiplexer Selection

The S-band transmitters, summing amplifiers, and multiplexers are selected by the circuits shown in Figure 4-VIII-10. The transmitter selection circuits and multiplexer selection circuits are interlocked such that the multiplexer unit receives power when the selected S-band transmitter is turned on. The S-band push-to-talk signal insures that the S-band transmitter in use is turned off at the end of each CDA ground station contact.

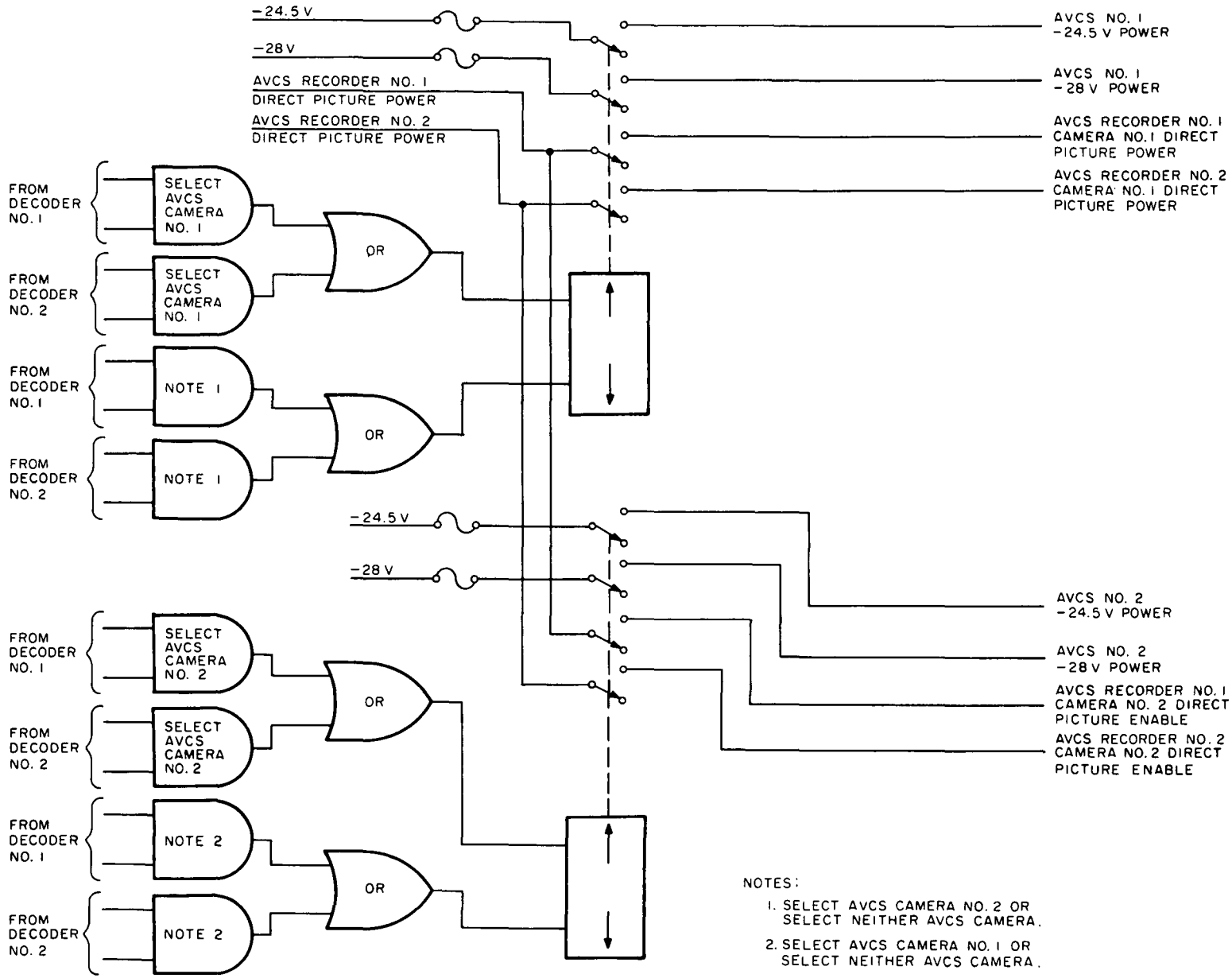

Figure 4-VIII-8. AVCS Camera Selection Circuits

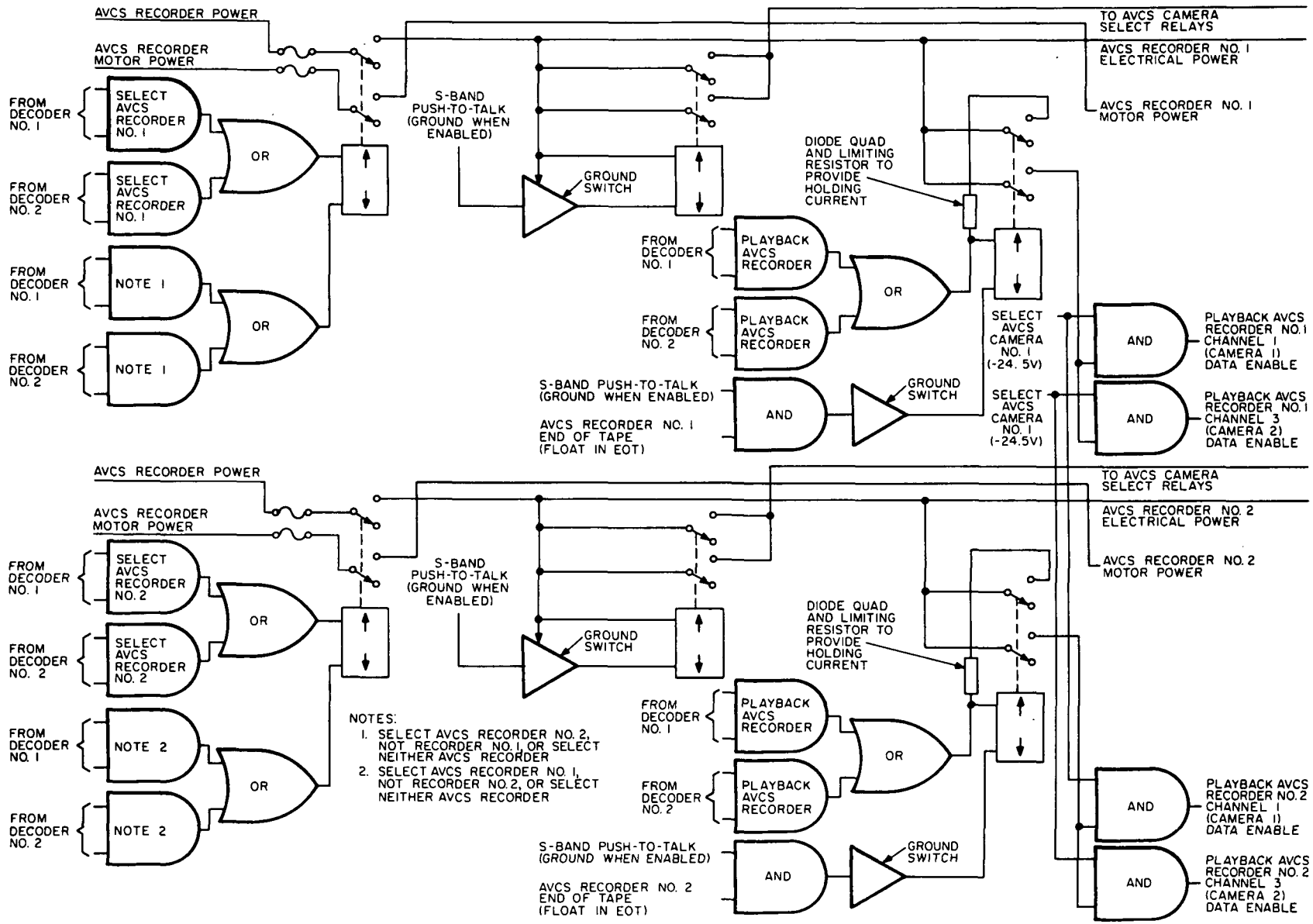

Figure 4-VIII-9. AVCS Tape Recorder Selection Circuits

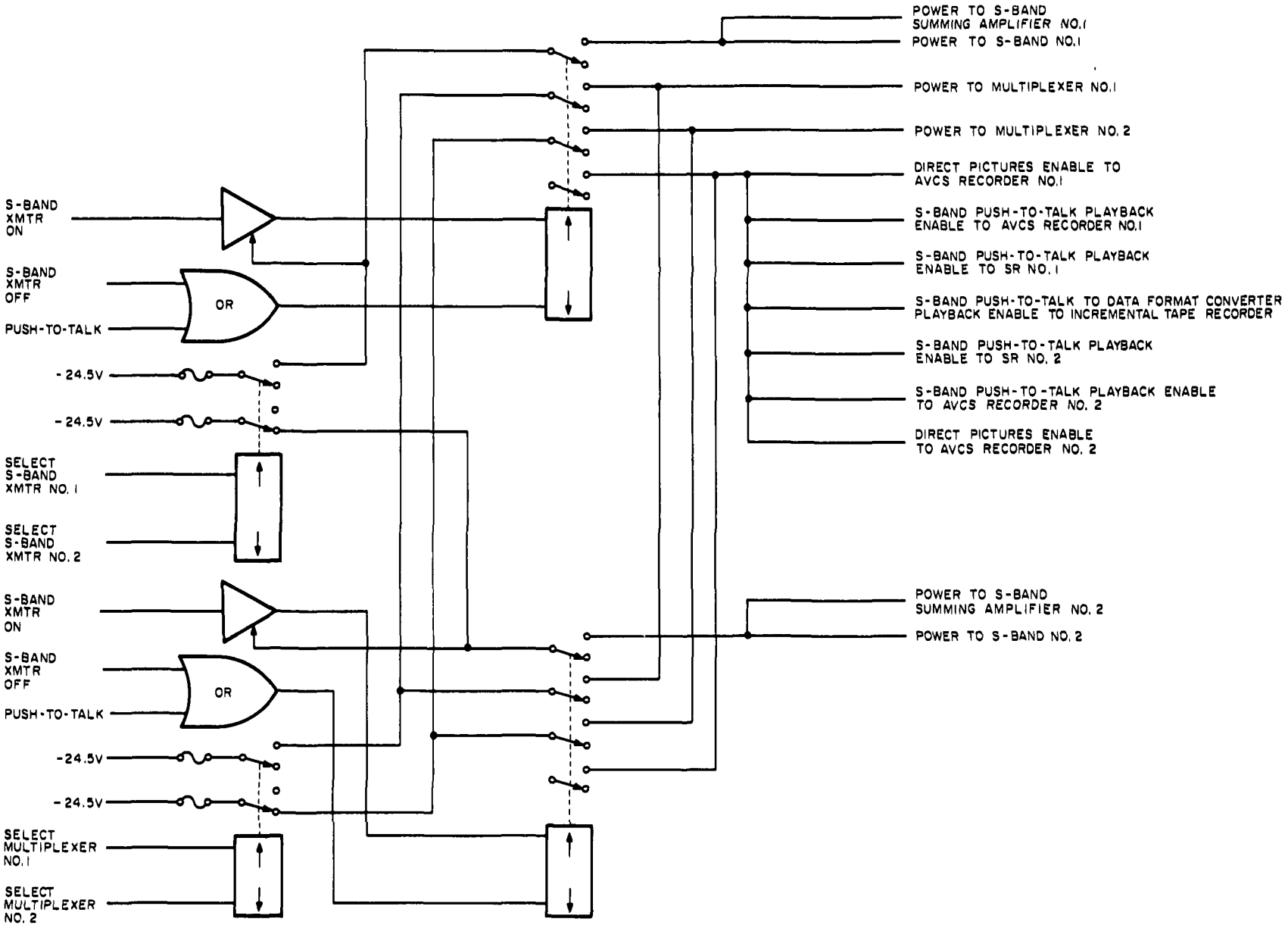

Figure 4-VIII-10. S-Band Transmitter and Multiplexer Selection Circuits

(4) APT Camera Selection

Selection of one APT camera for operation, or neither camera, is accomplished by controlling the power inputs to each camera. The commands select the relays which control the power relays which are also controlled by the programmer; they connect power to the selected camera. Figure 4-VIII-11 shows the circuitry for APT camera selection.

(5) SR Selection

One of the two scanning radiometers is selected, or neither is selected, by discrete commands, as shown in Figure 4-VIII-12. In addition, the SR's are controlled by the programmer. Relays which control the input power and relays in the radiometers are controlled by the commands and the programmer signals.

The SR motors can both be turned on, or each motor can be turned off, independently of the electronics. The commands are decoded by the circuits shown in Figure 4-VIII-13.

(6) SR Visible and IR Channel Selection

The visible channel of each radiometer is arranged to operate in two modes, the data mode and the calibrate mode. Figure 4-VIII-14 shows how either the visible or the IR channel is selected for real-time transmission in the daytime through the SR processor.

In the calibrate mode, as shown in Figure 4-VIII-15, the visible channel calibration signal is turned on or off; however, the push-to-talk signal ensures that the calibration signal is turned off when CDA ground station contact is lost.

(7) SR Recorder Selection

The SR recorders are controlled with power switching relays by discrete commands which select either, both, or neither recorder and playback either or both recorders. Figure 4-III-16 shows the circuitry used to select a recorder. Nonlatching relays control the playback; they are controlled by push-to-talk signals which ensure proper operation. Logic levels and set and reset signals interlock the operation of the tape recorders and the programmers.

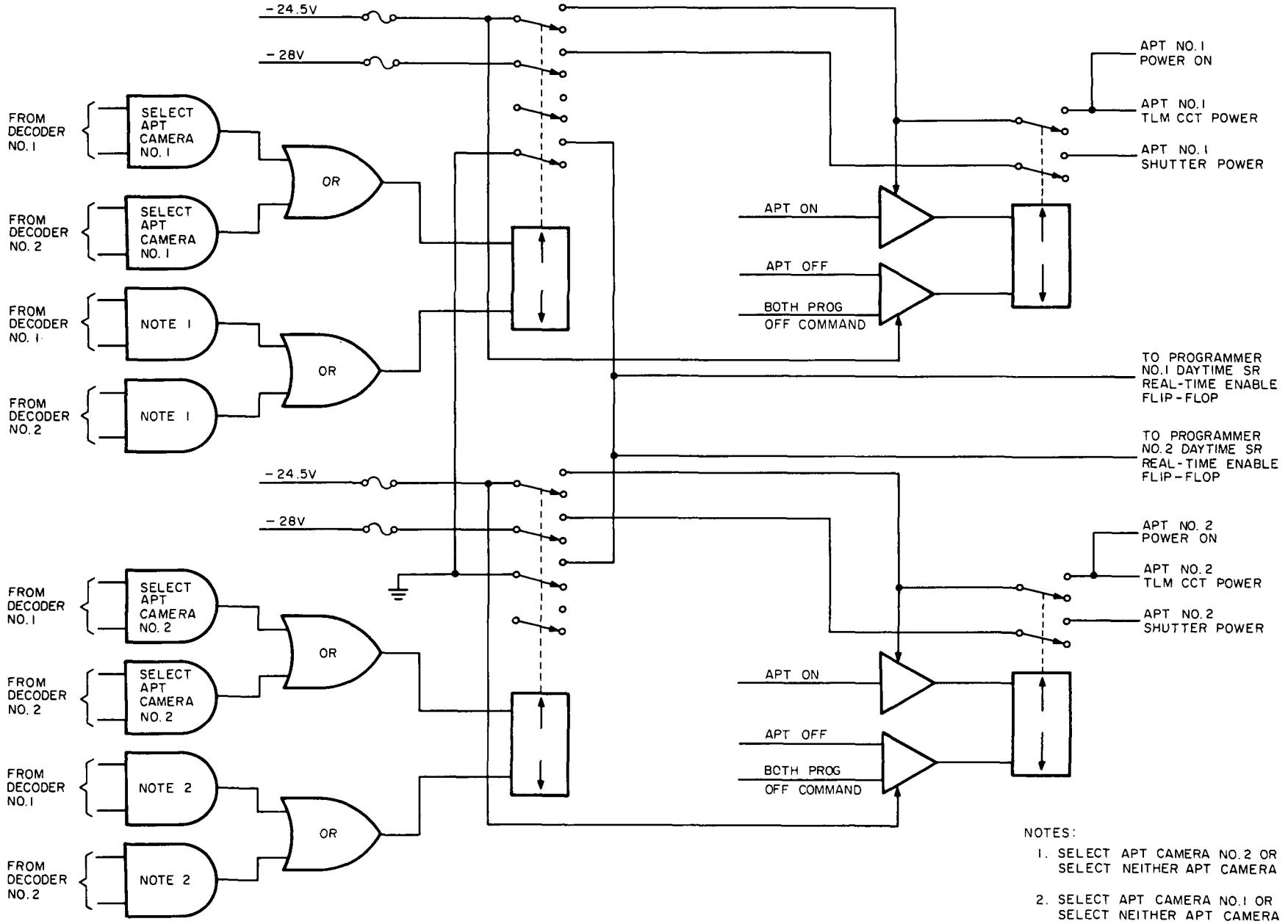

Figure 4-VIII-11. APT Camera Selection Circuits

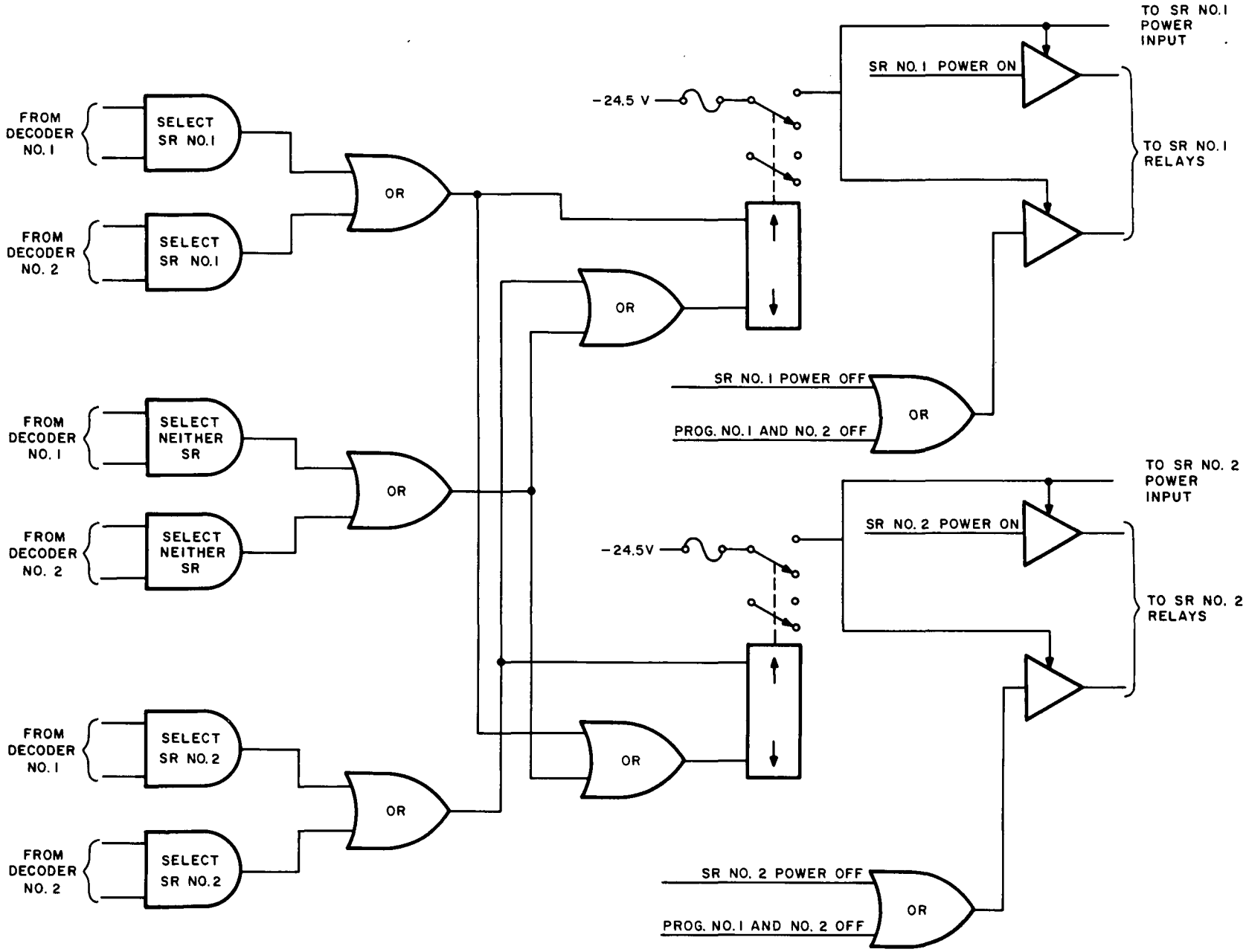

Figure 4-VIII-12. SR Selection Circuits

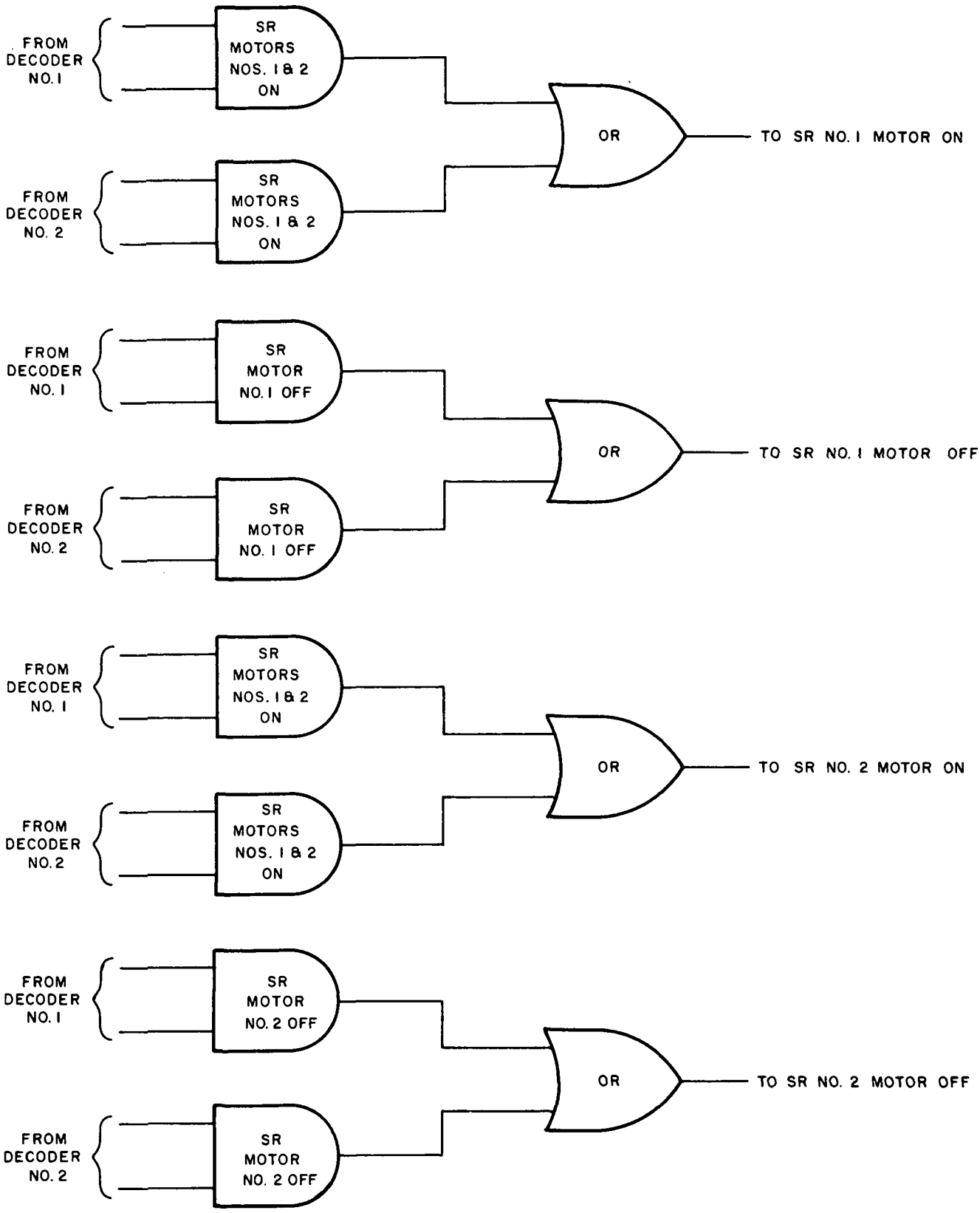

Figure 4-VIII-13. SR Motor Selection Circuits

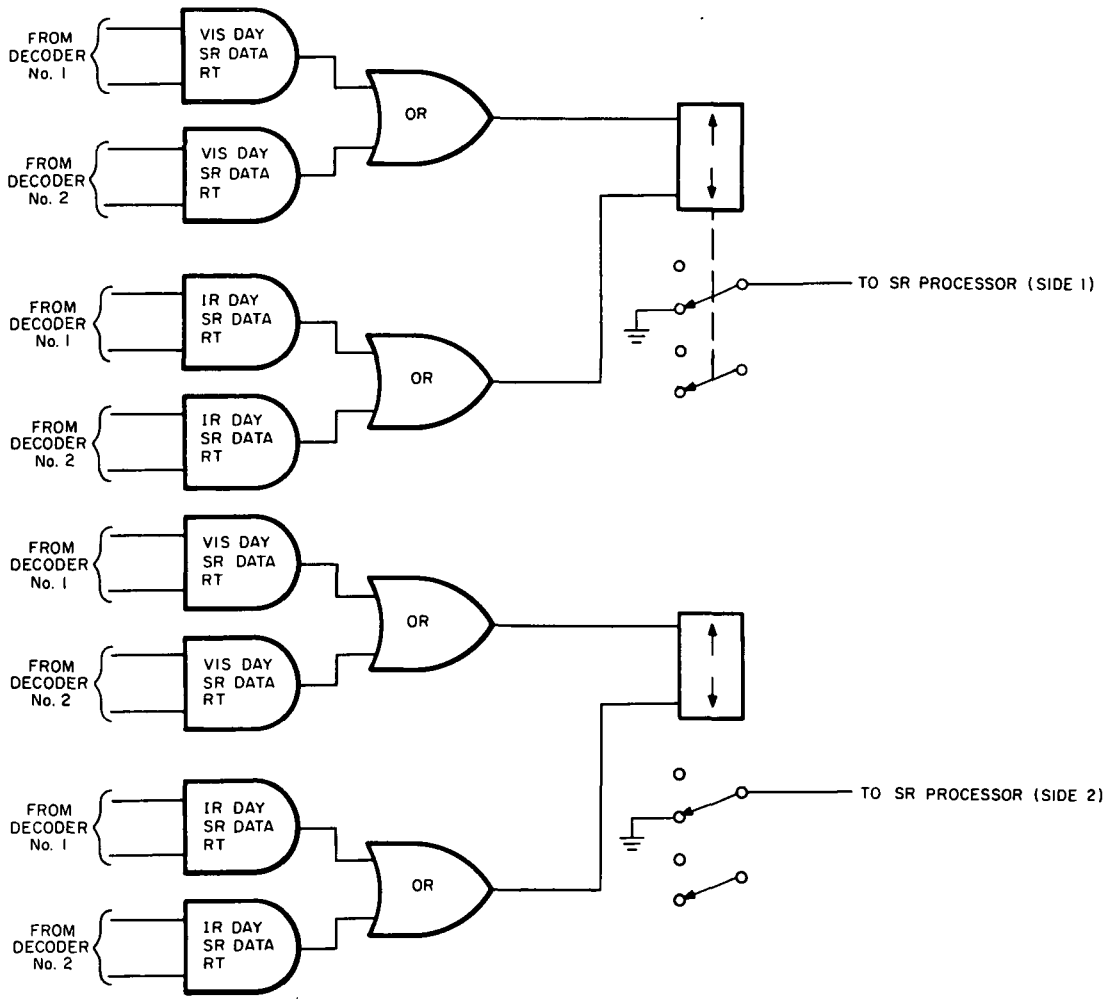

Figure 4-VIII-14. SR Visible and IR Channel Selection Circuits

(8) Real-Time Transmitter Selection

Selection of one real-time (RT) transmitter, or neither transmitter, is controlled by relays, as shown in Figure 4-VIII-17. Day only or day and night operation is also selected by discrete commands. One of the transmitters is normally turned on during both the day and the night portions of each orbit, but they may be operated during the day only to conserve power. When a transmitter is selected, the coaxial relay is also activated, connecting the selected transmitter to the real-time antenna.

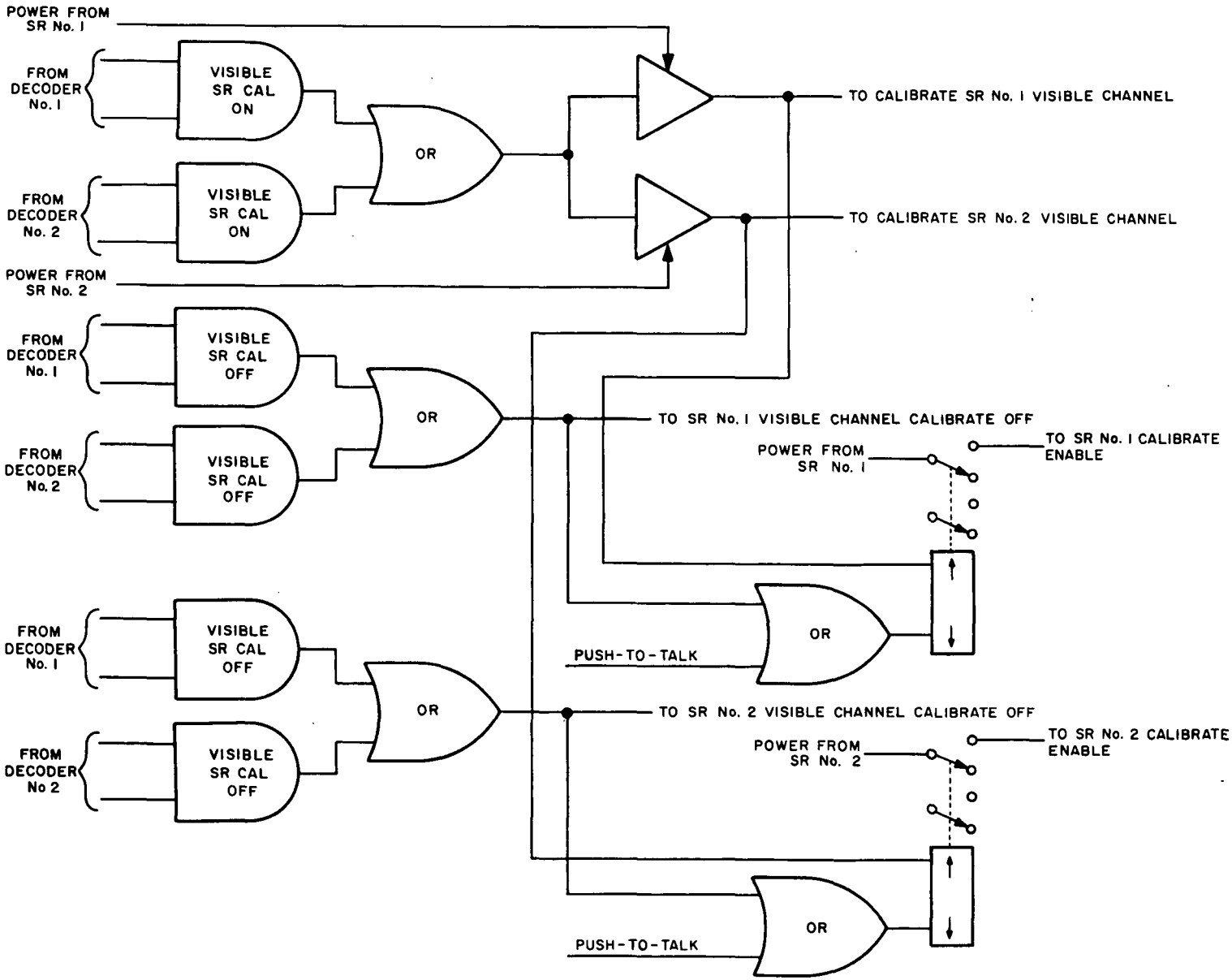

Figure 4-VIII-15. SR Visible and IR Channel Calibration Selection Circuits

(9) Programmer Selection

Either programmer, or neither, can be selected; the decode circuits are located in the CDU, and the control relays are in the programmer. Figure 4-VIII-18 shows the circuitry used to select a programmer.

(10) TBU Selection

Time base unit (TBU) No. 1 or No. 2 is normally turned on, and, when a TBU is selected, the time base and time code generators are reset. The decode circuits are located in the CDU; the control relays are in the TBU; see Figure 4-VIII-19.

(11) Beacon Selection

Either beacon transmitter and associated SCO's, or neither, are selected by real-time commands indicated in Figure 4-VIII-20. One beacon is powered at a time.

(12) Telemetry Commutator Selection

Control of the telemetry commutators is accomplished by switching the frequency of the driving (clock) signal to each commutator. The circuits that perform these functions are shown in Figure 4-VIII-21. Each commutator samples 120 channels at a fixed rate of 15 channels per second during automatic advance or at a rate determined by the positions of the data "0" bits in the 28-bit word during manual advance. Telemetry power is also controlled by relays activated by direct commands.

(13) Acquisition Mode Telemetry Selection

During the initial orientation maneuver (acquisition), the various sensors shown in Figure 4-VIII-22 supply data to the CDA ground station. When the "Acquisition Mode Telemetry ON" command is decoded, power is applied to the acquisition sensor and to the DSAI; then data from these units is applied to the 2300-Hz SCO and to the commutator. The data applied to the commutators is switched whenever data verification is required.

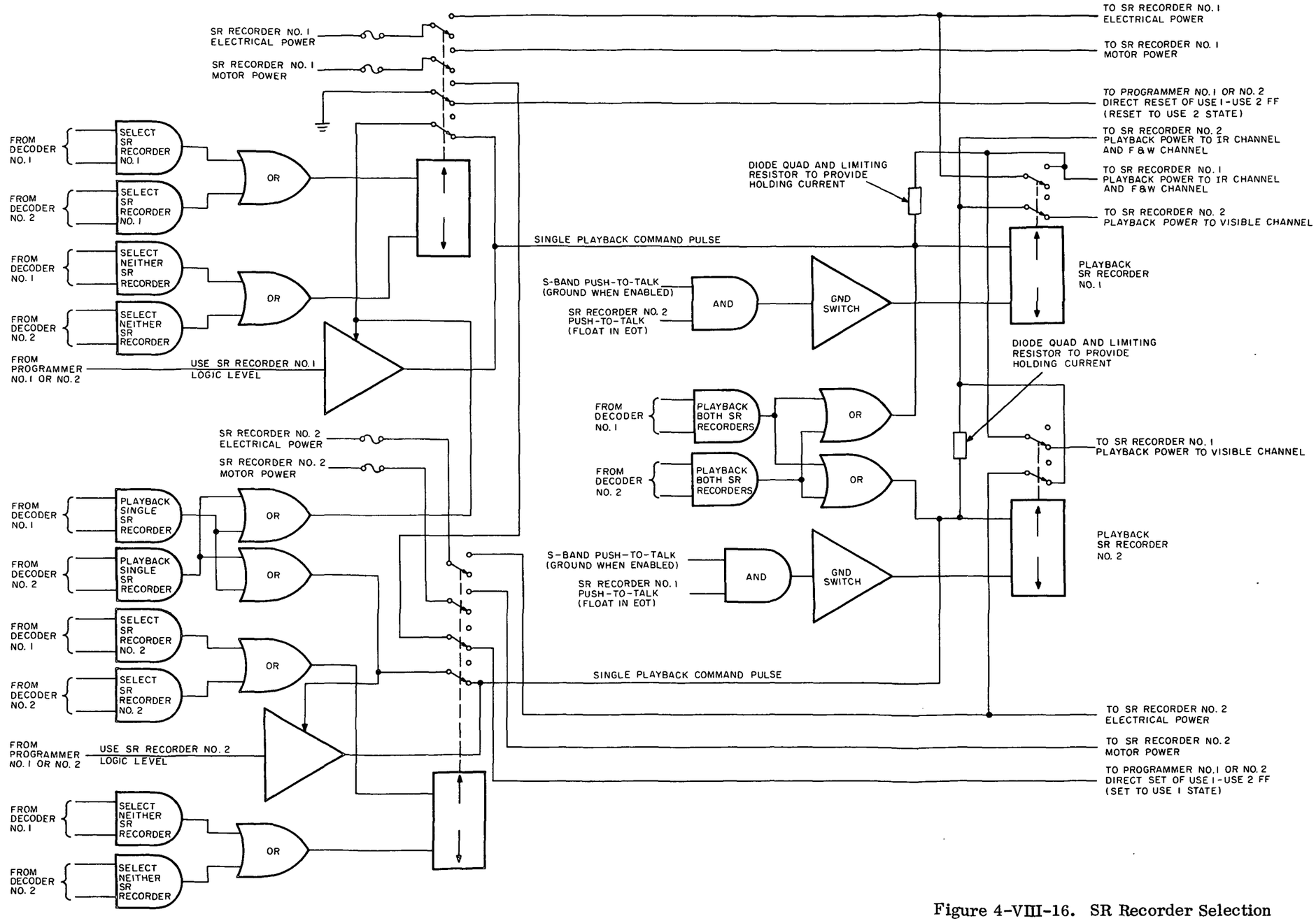

Figure 4-VIII-16. SR Recorder Selection Circuits

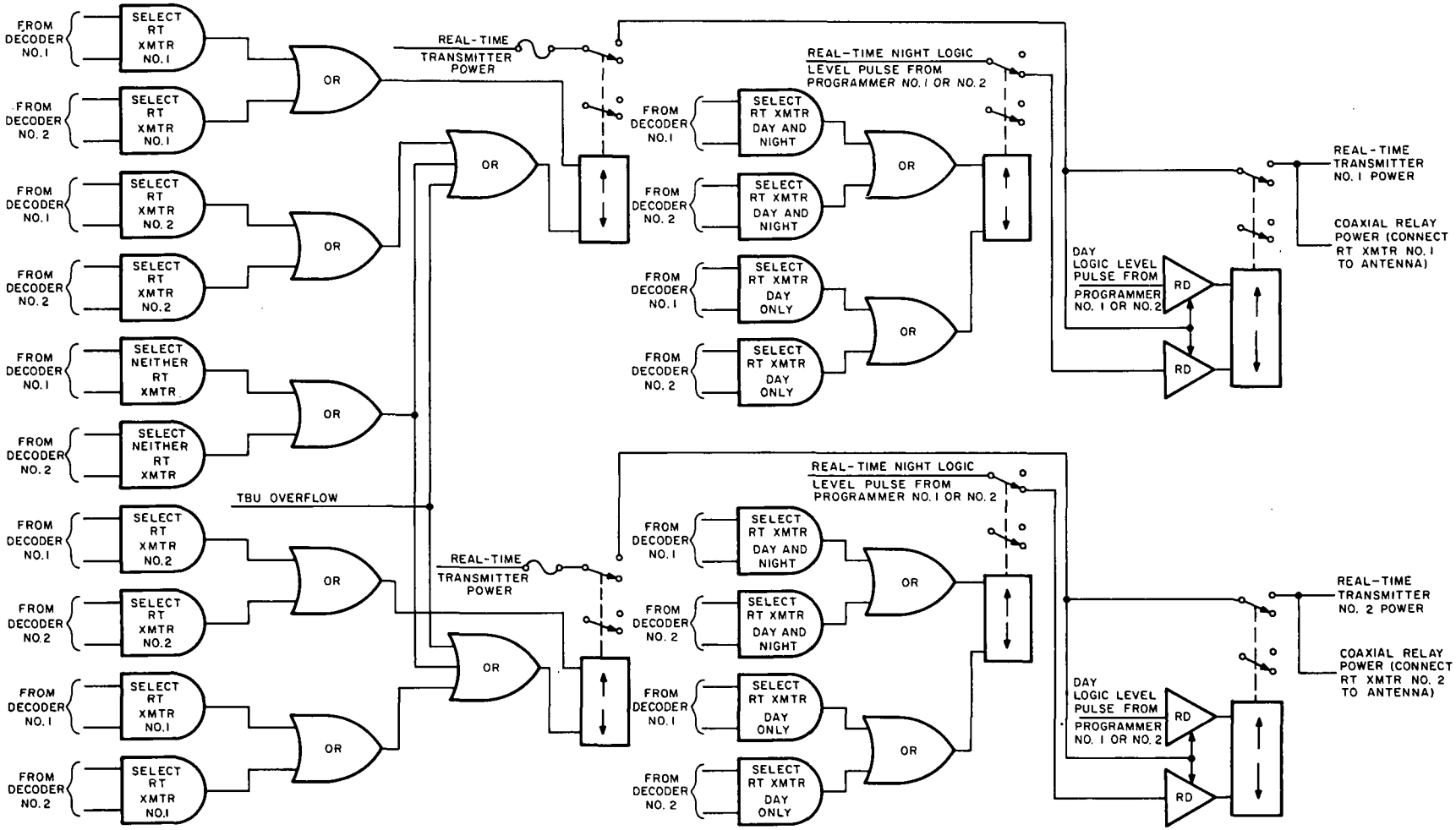

Figure 4-VIII-17. RT Transmitter Selection Circuits

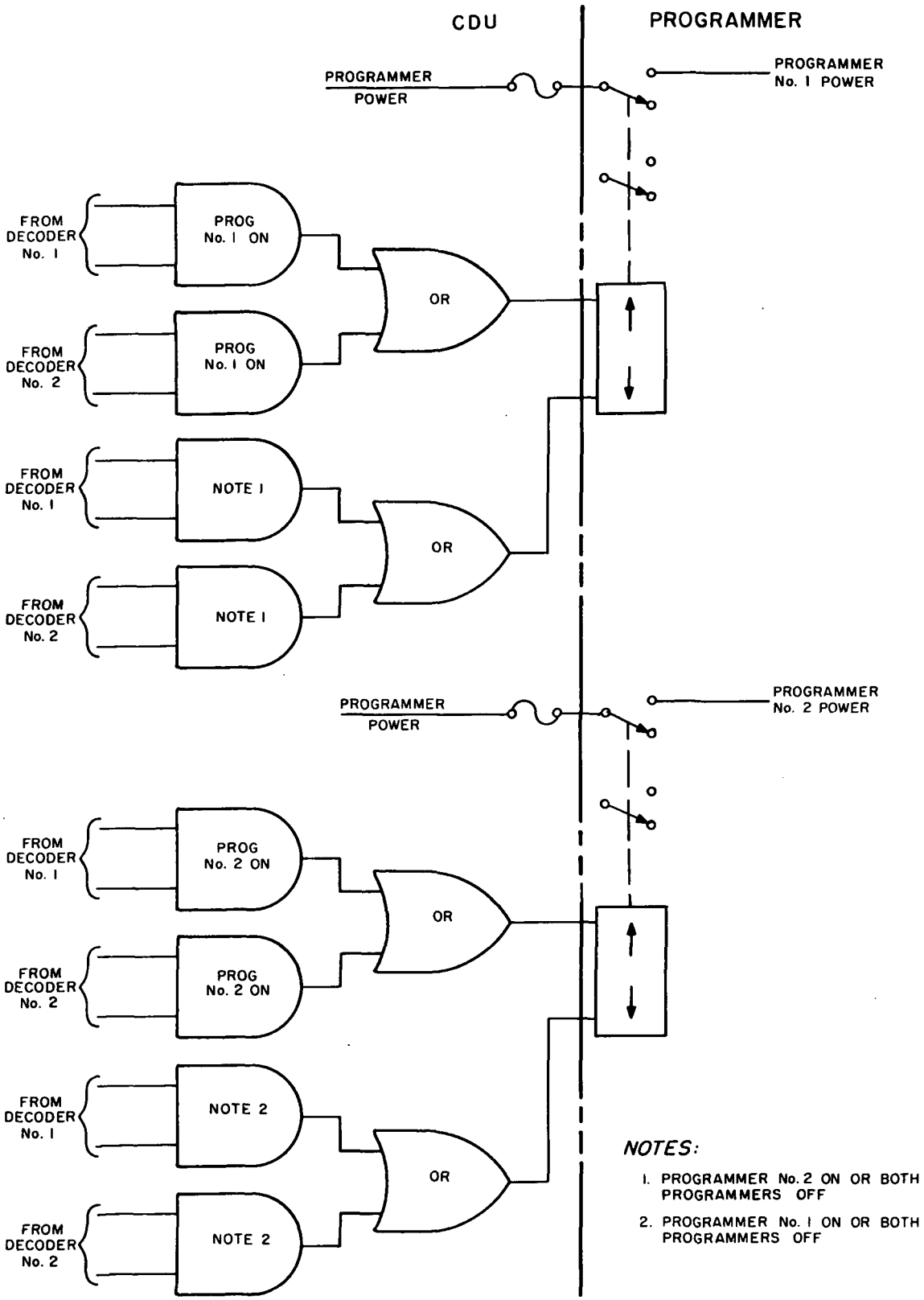

Figure 4-VIII-18. Programmer Selection Circuits

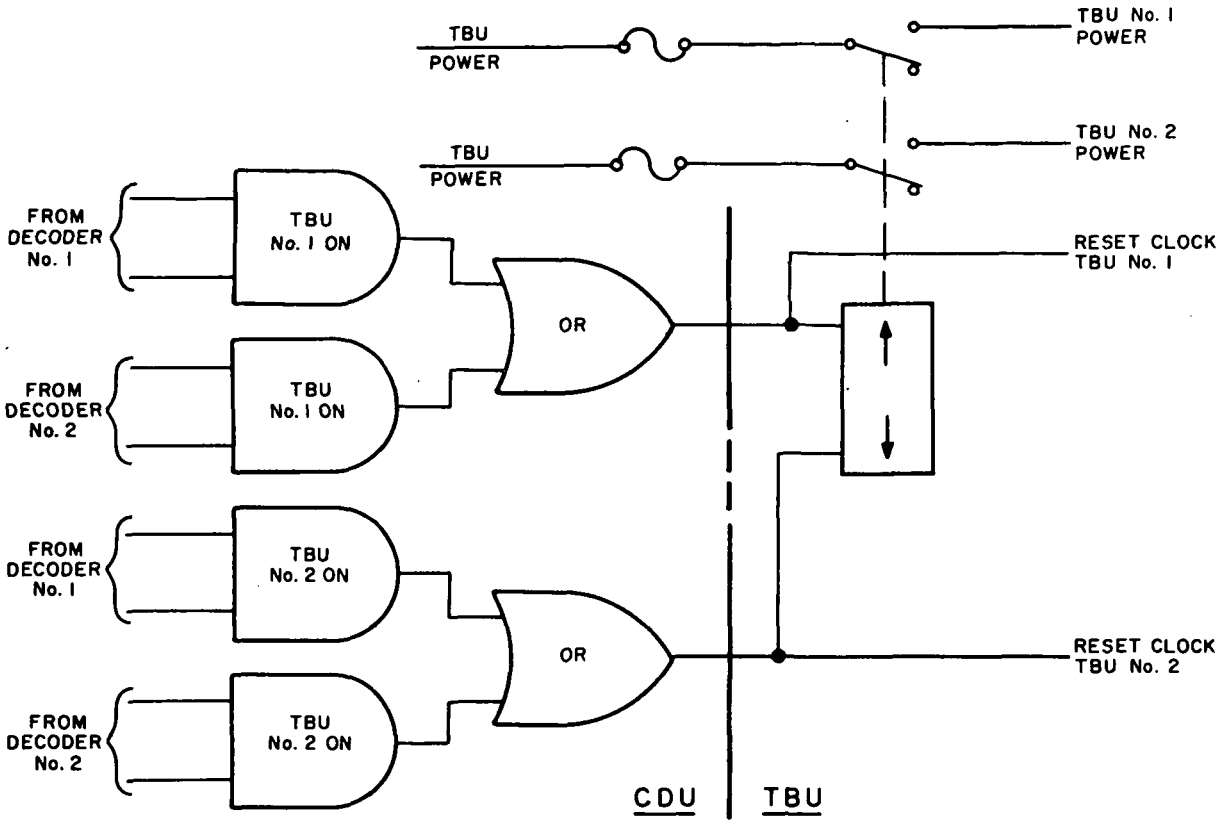

Figure 4-VIII-19. TBU Selection Circuits

4. Dual Time Base Unit

a. General

The dual time base unit (TBU) generates basic timing signals required by the various parts of the spacecraft for synchronization and timekeeping. Two identical time base generators and two identical time code generators are contained in the dual TBU, one time base generator and one time code generator forming TBU No. 1 and the other pair forming TBU No. 2. Two ground commands are provided which turn on one TBU while turning off the other.

The time base generator section of each TBU generates the timing signals for synchronizing and coordinating all timing functions aboard the spacecraft. All of the timing signals required by the various sensors, programmers, secondary equipment, and telemetry circuits originate within the time base generator section of the TBU. The general configuration is similar to

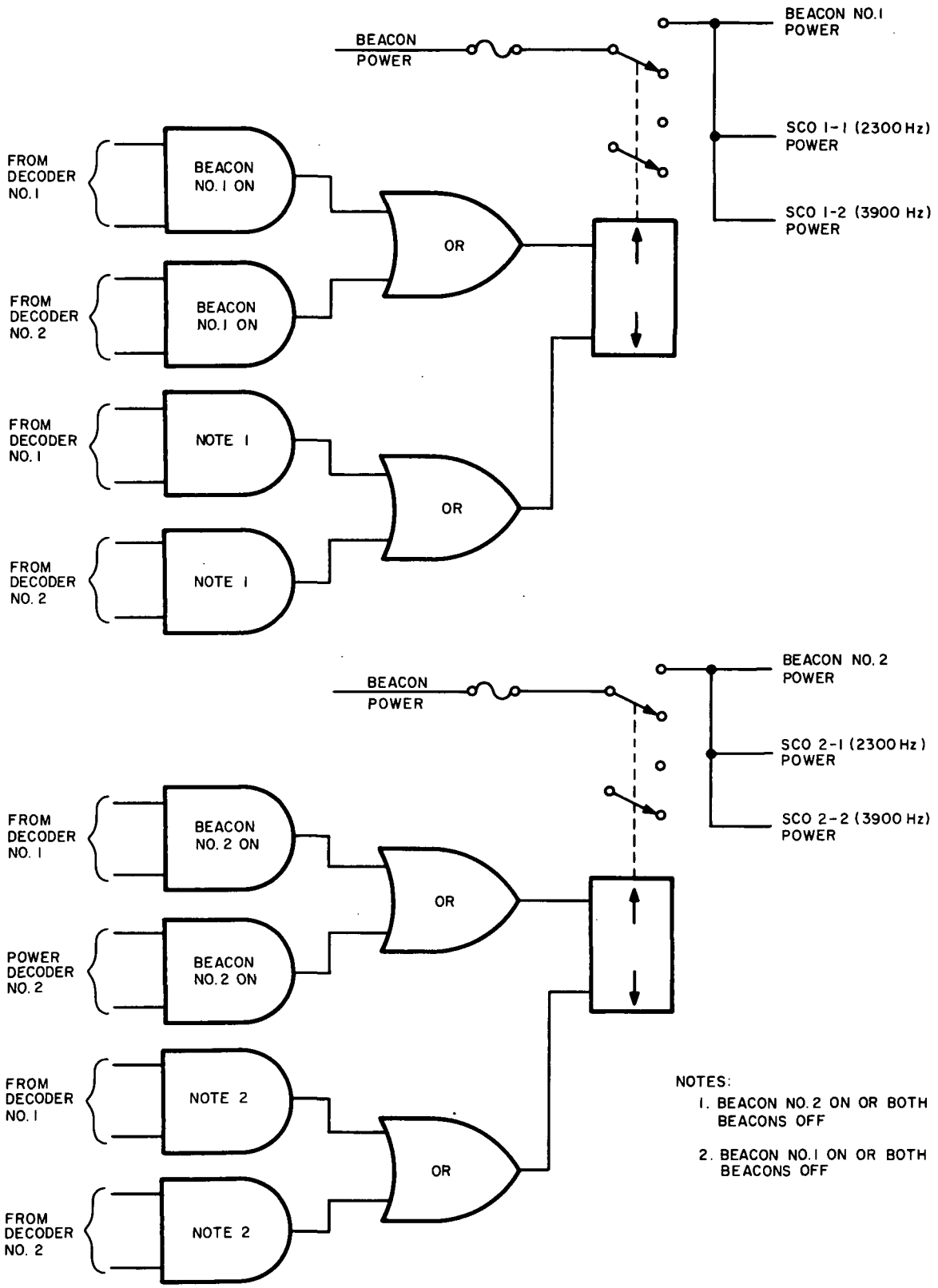

Figure 4-VIII-20. Beacon Selection Circuits

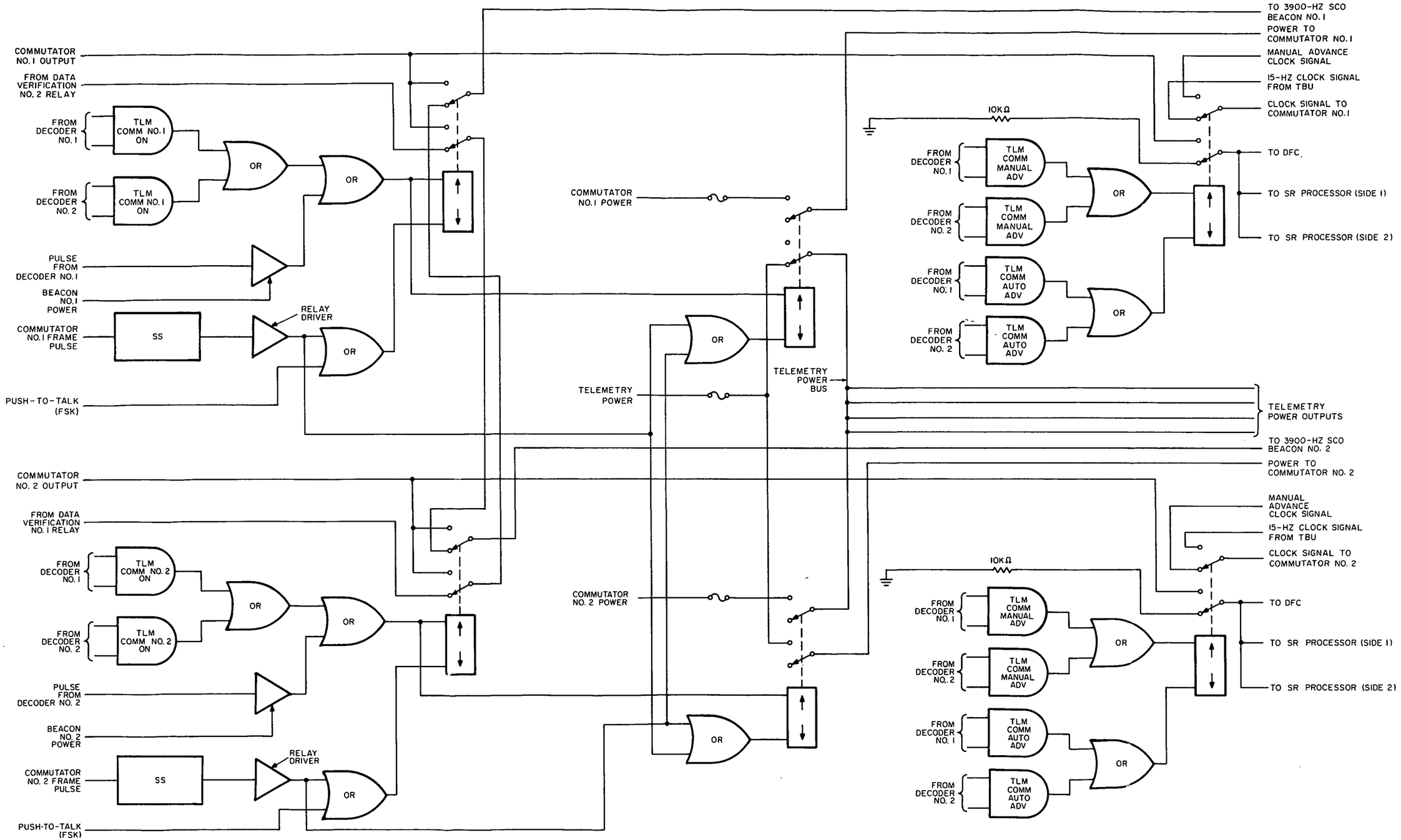

Figure 4-VIII-21. Telemetry Commutator Selection Circuits

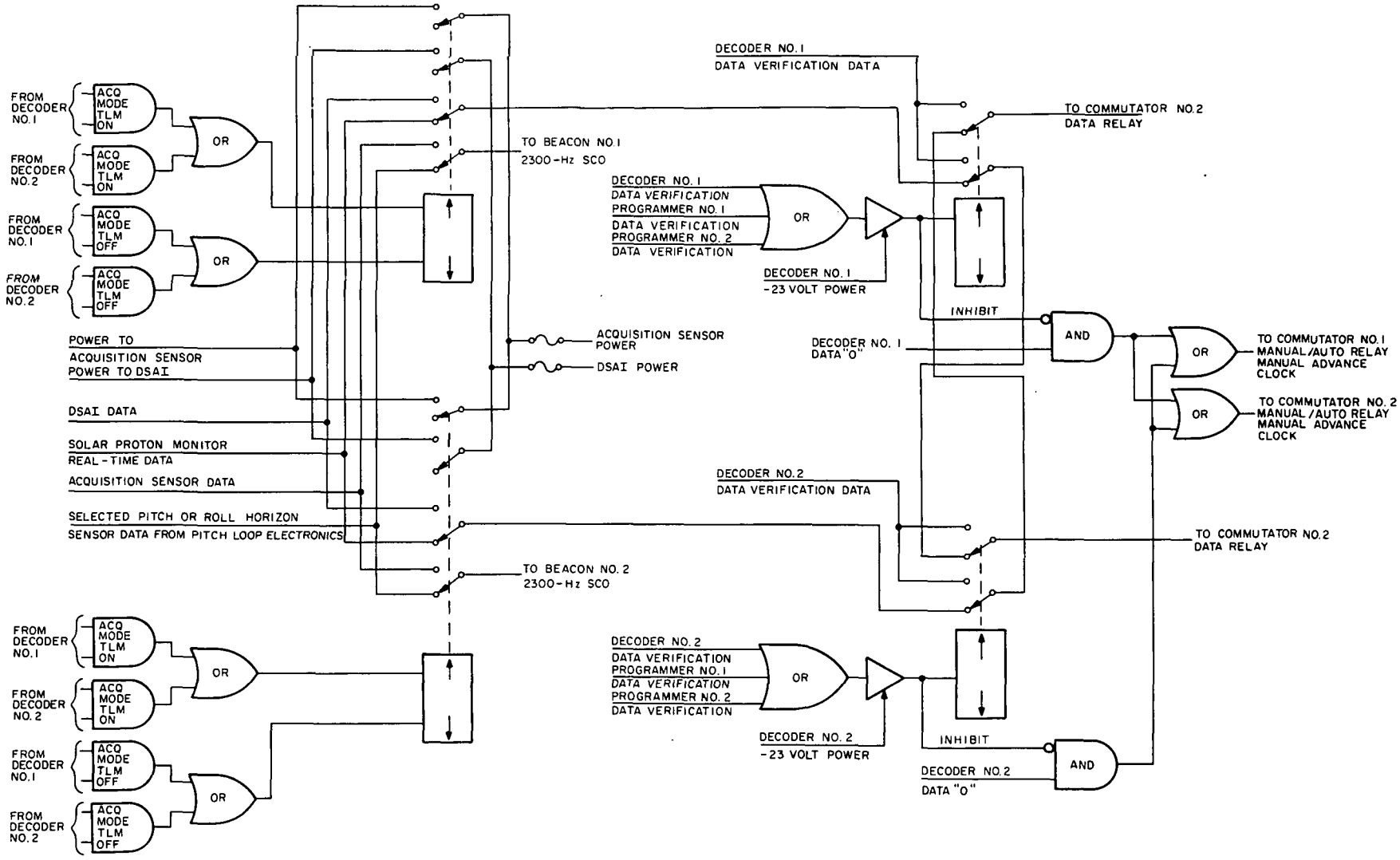

Figure 4-VIII-22. Acquisition Mode Telemetry Selection Circuits

that of the TOS time base generator. Each time base generator includes a high stability crystal oscillator and a digital dividing chain followed by interface circuits. The time code generator section of each TBU generates a time identification code that is supplied to the primary and secondary sensor subsystems for simultaneous recording with remote data in order to identify the times at which the various sensory data are acquired. The time code is also supplied to the beacon and telemetry elements of the communications subsystem.

Power is supplied to each TBU independently by separate DC-to-DC converters which are turned on and off by the aforementioned ground commands.

The expanded functional requirements of the ITOS spacecraft demand a greater number of timing signals than were used on the TOS spacecraft. Other design differences which have affected the time base units are as follows:

1. Spin synchronization is not used on ITOS.
2. The scanning radiometer subsystem has been added to the ITOS spacecraft.
3. A single time base is used for both APT and AVCS subsystems on ITOS.
4. A secondary sensors subsystem (flat plate radiometer and solar proton monitor) has been added to the ITOS spacecraft.

The presence of the scanning radiometer subsystem on the spacecraft requires continuous operation of the time base generator. Continuous operation would not be possible with the existing TOS configuration for the following reasons: (1) the TOS time base generator shares a DC-to-DC converter with the associated programmer; (2) several outputs of the TOS time base generator are inhibited when the programmer is in the QOMAC mode; and (3) the TOS time code generator, being part of the programmer, does not allow for extended, uninterrupted, and continuous timekeeping, unless switching between programmers is curtailed.

Therefore, the ITOS time base and code generators are arranged to operate independently of the programmers and each has its own DC-to-DC converter.

b. Response to Commands

Each TBU contains two time base generators and two time code generators. Selection of one set is accomplished by two real-time commands, which control the power input to the selected unit. The commands are as follows:

1. TBU No. 1 ON, TBU No. 2 OFF
2. TBU No. 2 ON, TBU No. 1 OFF

Inputs to the time base and code generators are as follows:

1. -24.5 volts, regulated, which drives the DC-to-DC converter.
2. Three control pulses, two from the active programmer, and one from the CDU. These pulses control the power inputs to the converters, the 50-kHz flutter and wow signal to the AVCS recorders, and the time code outputs of the time code generators.

c. Time Base Generator Description (See Figure 4-VIII-23.)

The time base generator section of the TBU consists of a 2.4-MHz crystal oscillator and a digital countdown chain. The output of the oscillator is divided to provide the necessary frequencies to fulfill the various timing and synchronizing requirements of ITOS. Integrated circuits are used for the dividing chain and discrete elements for the output interfaces. A typical interface circuit used in the time base generator unit is illustrated in Figure 4-VIII-24. The outputs of the redundant time base generator circuits are combined in an OR gate to provide a single output of the circuit in operation to each user, whenever this configuration is feasible.

d. Time Code Generator Description

The time code generator generates a 24-bit serial digital readout to be used by the AVCS, SR, secondary sensor and telemetry subsystems for time identification. The output consists of a binary count of the number of 1/2-second increments elapsed from the time

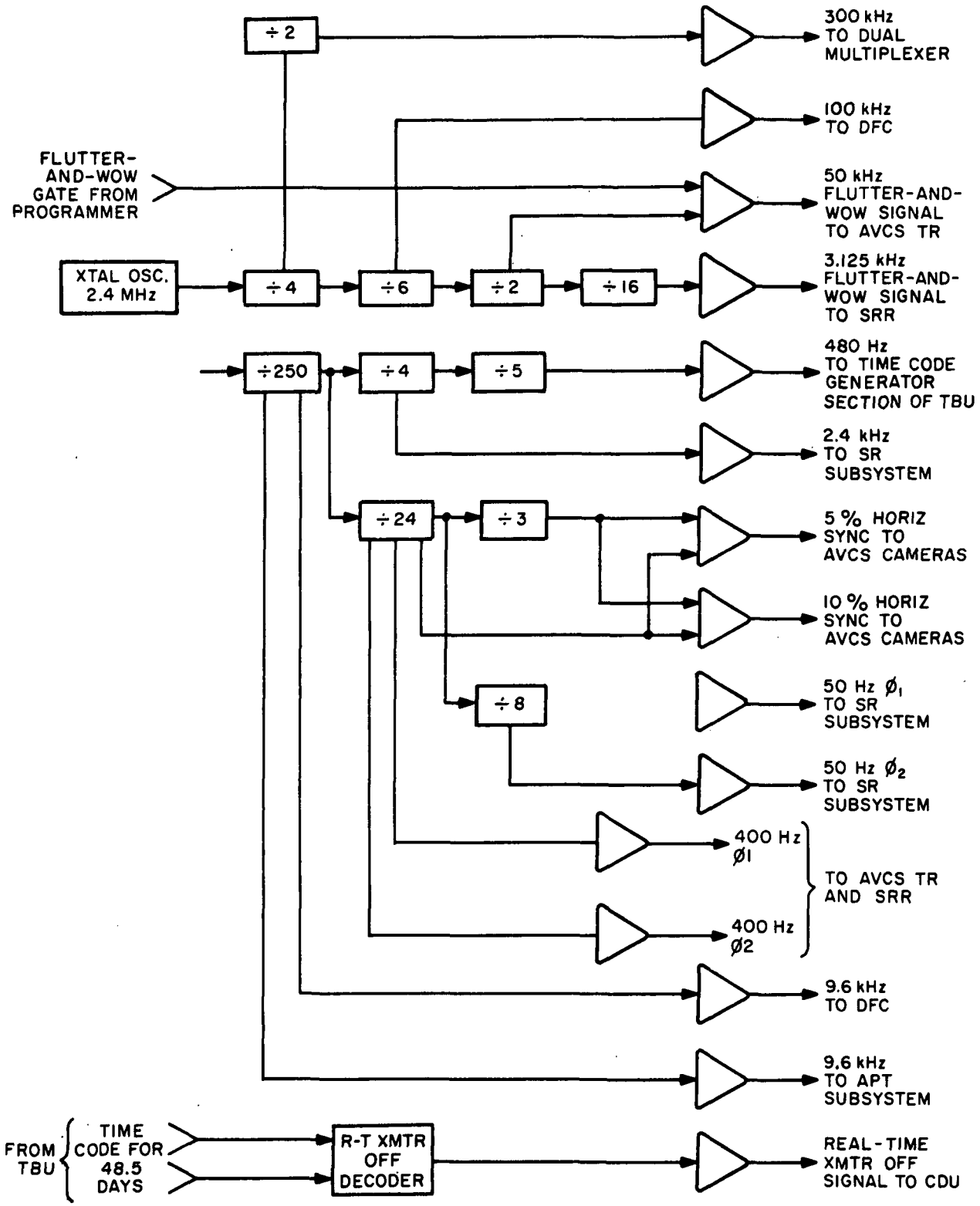

Figure 4-VIII-23. Time Base Generator, Block Diagram

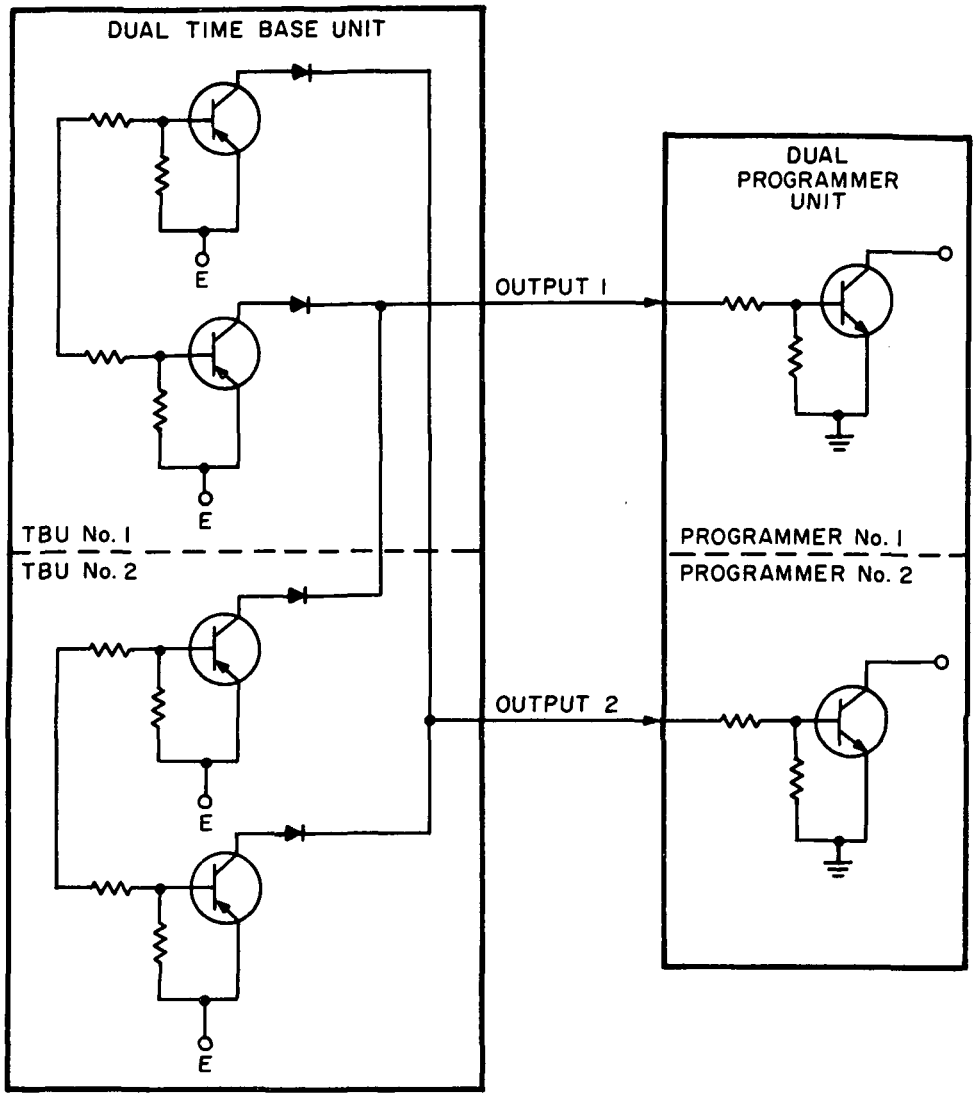

Figure 4-VIII-24. Time Base Generator, Typical Interface Circuits

unit power is turned on. The maximum cumulative capacity of the elapsed time function is 2^{24} half-second intervals, or 97 days, 2 hours, 10 minutes, and 8 seconds.

The main differences between the ITOS and TOS time code generator designs are as follows:

- The word length is extended from 20 to 24 bits;
- The data rate is increased from 50 to 60 Hz;
- Redundant operation is provided on ITOS;

- A dividing chain is added which subdivides 2.4 kHz to provide the programmer with a 4-Hz input signal rather than the 400-Hz input used on TOS;
- Each generator can be reset with a TBU (1 or 2) ON command pulse; thus, resetting can be accomplished without switching time base generators.
- Each generator provides a signal to terminate APT camera operation when the time count reaches 48.5 (± 0.2) days.

A block diagram of the time code generator is shown in Figure 4-VIII-25. Upon application of power, or on command, the shift register resets to a zero count. After approximately 150 milliseconds, the register is released to count 60-Hz pulses. Binary counting is accomplished by applying a burst of 24 pulses to the register every half second. The register output is fed back, through an "add 1" circuit, to its input. At the completion of each counting cycle, the time code is updated by 1/2-second count.

This technique is similar to the one used on TOS AVCS but with an increased number of bits and a higher burst rate. The output of the register is available in NRZ (non return-to-zero) form, for use by the secondary sensors subsystem, and in an RZ (return-to-zero) form, to supply a three-level time code signal to the AVCS and SR subsystems. An NRZ-to-RZ converter provides the latter output. The data format of the RZ output is shown in Figure 4-VIII-26.

The input signals to the time code generator are as follows:

- -24.5-volt power (common with the time base generator),
- +5.25 and +6 volts from a DC-to-DC converter, shared with the TBG,
- 480 Hz from TBG (same side),
- A TBU (No. 1 or No. 2) ON command pulse, which applies power to one TBU, removes power from the other TBU, and also resets the time code register, and
- A "time code lock" signal which inhibits operation of the 24-bit register.

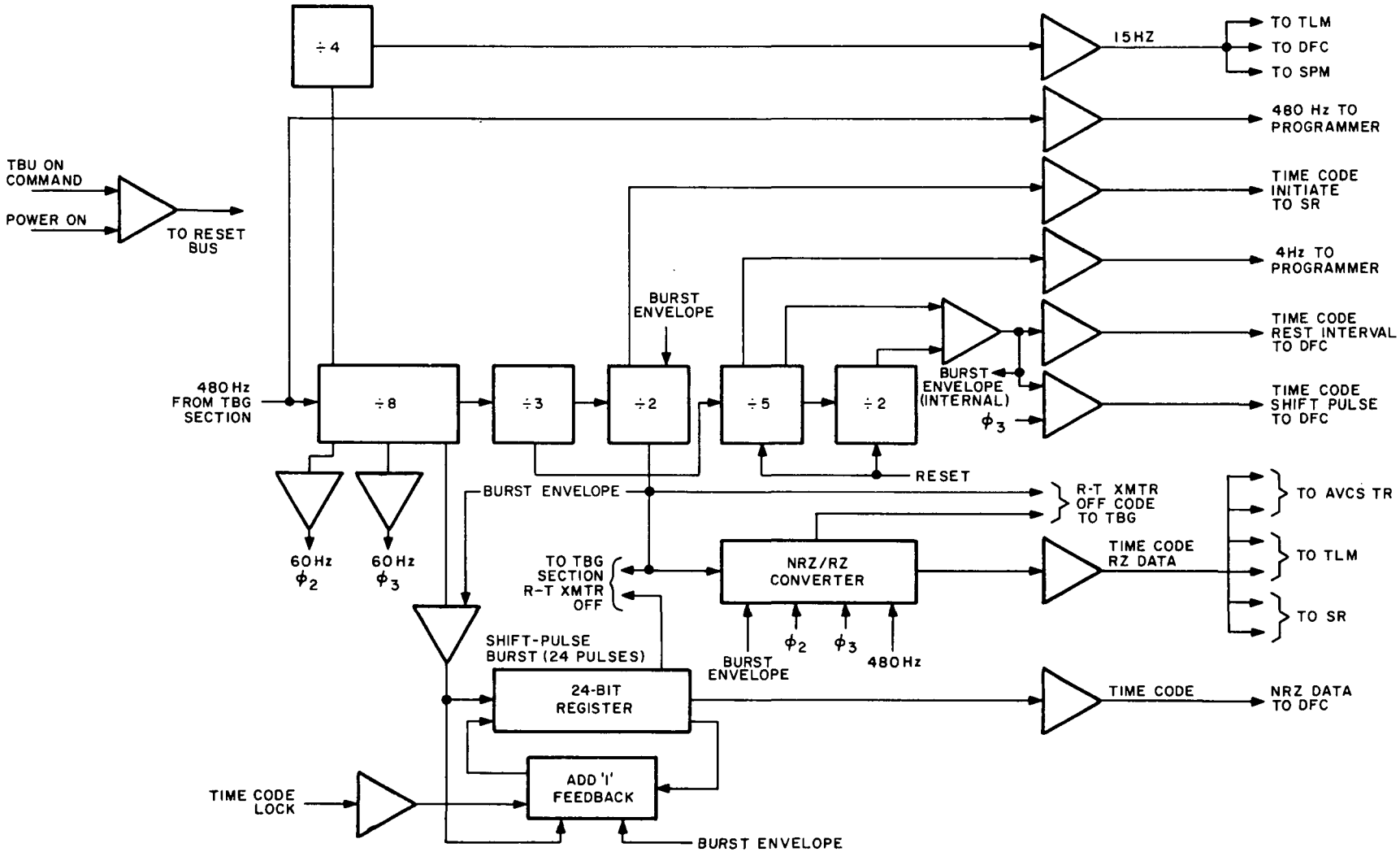

Figure 4-VIII-25. Time Code Generator, Block Diagram

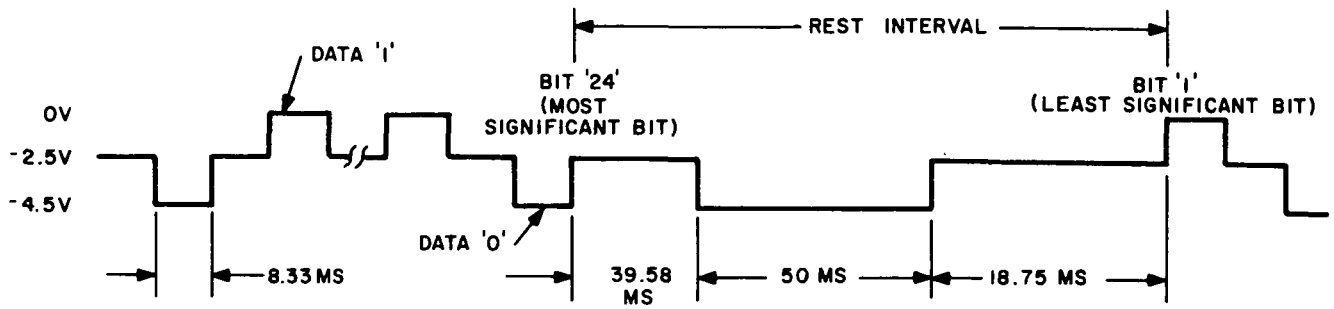

Figure 4-VIII-26. Data Format of the RZ (Three-Level) Output of the Time Code Generator

The output signals from the time code generator are as follows:

- A 24-bit RZ three-level code (least significant bit first),
- A 24-bit NRZ code (least significant bit first),
- A 15-Hz signal to the DFC, the SPM, and the telemetry circuits,
- A 480-Hz signal to the programmers,
- A "time-code initiate" signal to the scanning radiometer subsystem,
- A 4-Hz signal to the programmers,
- A "time-code rest interval" signal to the DFC,
- A time code shift pulse to the DFC,
- The time code signal in RZ format to the AVCS and SR subsystems and to the telemetry circuits,
- The time code signal in NRZ format to the DFC, and
- A "real-time transmitter OFF" code, representing a time count of 48.5 ± 0.2 days, to the CDU via the time base generator section of the TBU.

SECTION IX

COMMUNICATIONS SUBSYSTEM*

A. INTRODUCTION

The communications subsystem provides four separate RF links for handling the communications traffic between the ITOS spacecraft and the ground stations. These four links are:

- Command link for transmitting command messages from the CDA stations to the spacecraft.
- Beacon telemetry link for transmitting tracking signals, telemetry data, attitude data, solar proton monitor data, and command verification from the spacecraft to the CDA stations.
- Real-time video link for transmitting APT camera and scanning radiometer data from the spacecraft to the APT stations.
- Playback video link for transmitting the recorded AVCS picture, radiometer and secondary sensor data to the CDA stations.

The total requirements and the essential characteristics of the four communications links are summarized in Table 4-IX-1. The communications subsystem is designed to permit operation of all four links concurrently and to be compatible with the CDA and APT ground stations.

In this section, the four communications links are treated separately. For each link there is a discussion of bandwidth and modulation requirements and an analysis of link performance. A summary of CDA ground station equipment is shown in Figure 4-IX-1.

*Refer to Summary of Current Design Revisions Not Covered in this Report, following the Preface, for a brief description of revisions made since the cut-off date for this report.

TABLE 4-IX-1. SUMMARY OF ITOS COMMUNICATIONS LINKS

Link Carrier Frequency		Information Signal	Baseband Bandwidth	SCS Input Signal	Subcarrier Frequency	Modulation Subcarrier RF Carrier	Signal Bandwidth in RF Spectrum
1.	Command 148 MHz	Enable tones and digital commands; bipolar RZ train	10 bits/sec	RV carrier (AM)		FSK/AM	22.6 kHz
2.	Beacon and Telemetry, 136.77 MHz	Housekeeping telemetry and command verification:	59 Hz	Pulse amplitude	3.9 kHz	FM/PM	8.5 kHz (total)
		attitude data:	160 Hz	Modulated analog	2.3 kHz	FM/PM	
3.	Real Time 137.5 MHz	Analog APT video and SR data	1600 Hz	AM subcarrier	2.4 kHz	AM/FM	28.4 kHz
4.	Playback 1697.5 MHz	Recorded analog video (AVCS)	60 kHz	FM subcarrier	White: 120 kHz Black: 84 kHz Sync: 72 kHz	FM/FM	2.1 MHz (total)
		Flutter correction	1.0 kHz	FM subcarrier		FM/FM	
		Radiometer data	7.2 kHz	FM subcarrier	45.6 kHz	FM/FM	
		Secondary sensors data	2.0 kHz	FSK subcarriers	17B, 19B, 21B*	FSK/FM	
		Pilot tone					

*IRIG standard subcarrier frequencies 144, 160, and 176 kHz, respectively.

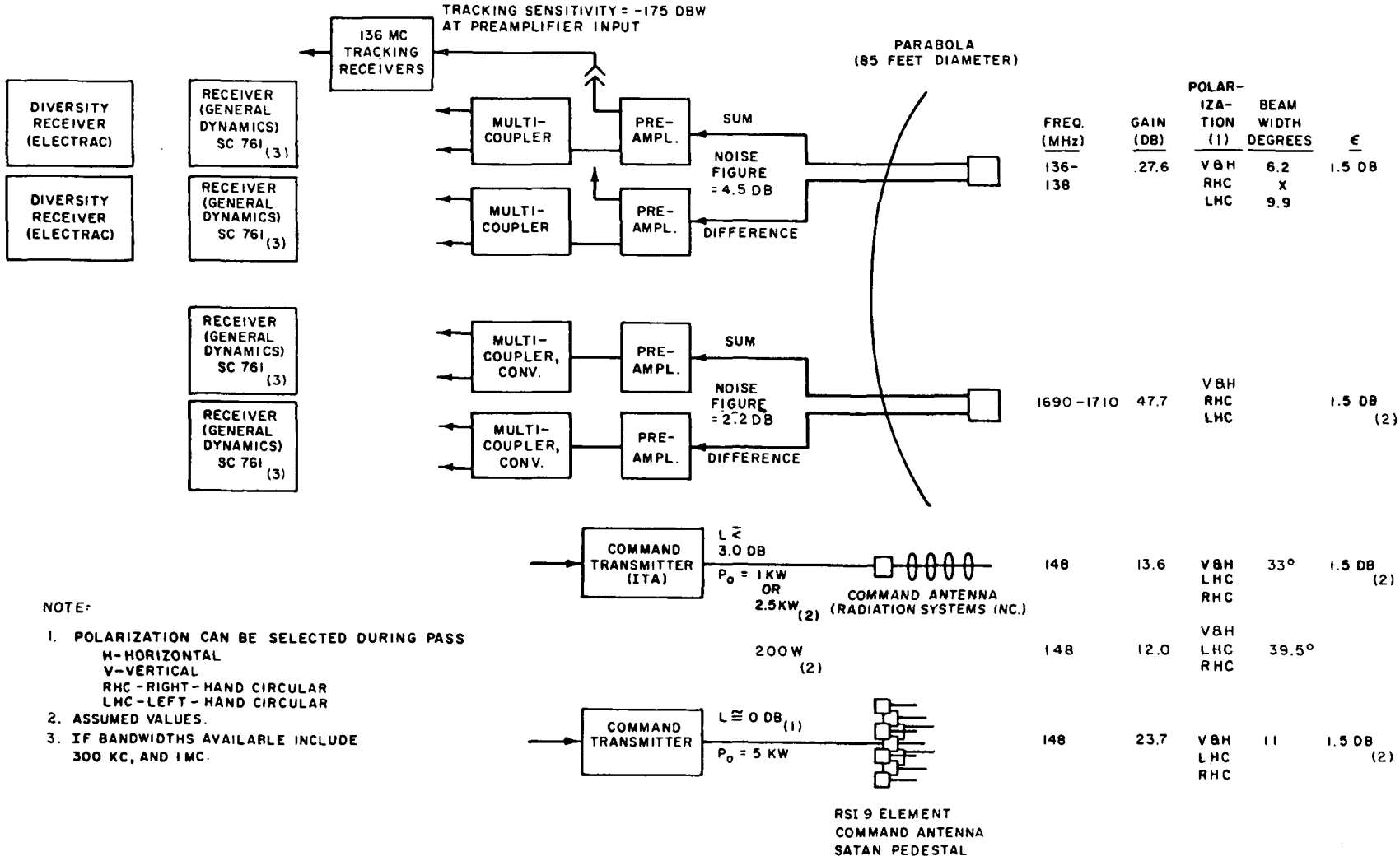

NOTE:

1. POLARIZATION CAN BE SELECTED DURING PASS
   - H-HORIZONTAL
   - V-VERTICAL
   - RHC-RIGHT-HAND CIRCULAR
   - LHC-LEFT-HAND CIRCULAR
2. ASSUMED VALUES.
3. IF BANDWIDTHS AVAILABLE INCLUDE 300 KC, AND 1 MC.

Figure 4-IX-1. ITOS Ground Station Configuration

B. COMMAND RECEIVER LINK

1. General

The block diagram of the command and beacon telemetry link is shown in Figure 4-IX-2. A common four-element antenna is used for command reception and beacon transmission. The command signal transmitted from the CDA stations is a circularly polarized electromagnetic wave. The spacecraft command and beacon antenna is similar to the TOS APT antenna and is linearly polarized for command reception at 148 MHz. For beacon transmission, the antenna produces a circularly polarized wave. Commands are transmitted only from the CDA stations, and are in the form of two tone pairs, each of which consists of an enable tone and a frequency-shift-keyed (FSK) subcarrier and amplitude-modulates the 148-MHz RF carrier. Each pair of tones is associated with one of the two sections of the dual spacecraft decoder. The tone pair is transmitted sequentially (only one tone present at any given time). The received RF command signal is routed through the beacon antenna coupler and the command receiver coupler to the two channels of the dual command receiver. The fact that the antenna is linearly polarized while the transmitted electromagnetic wave is circularly polarized causes a 3-db polarization loss. Another loss of 3 db is incurred due to the splitting of the RF power, which is then applied to the two command receiver channels, which are identical.

Command receiver channel No. 1 is connected to decoder channel No. 1, while channel No. 2 is connected to decoder channel No. 2 The outputs of the receiver channels are identical and consist of either an enable tone or an FSK subcarrier.

2. Signal Characteristics

The requirements of the RF command system are identical to those of the present TOS system. The first signal of the command tone pair is an unmodulated sinusoidal enable tone. The second tone is FSK modulated with the 10-bits-per-second, return-to-zero, bipolar command data. Each tone amplitude-modulates the 148-MHz RF carrier with a modulation index of 90 percent. Only one tone is transmitted at a time. Two unique pairs of tones are used, one pair to address each of the redundant decoder channels. The enable tone bandwidths

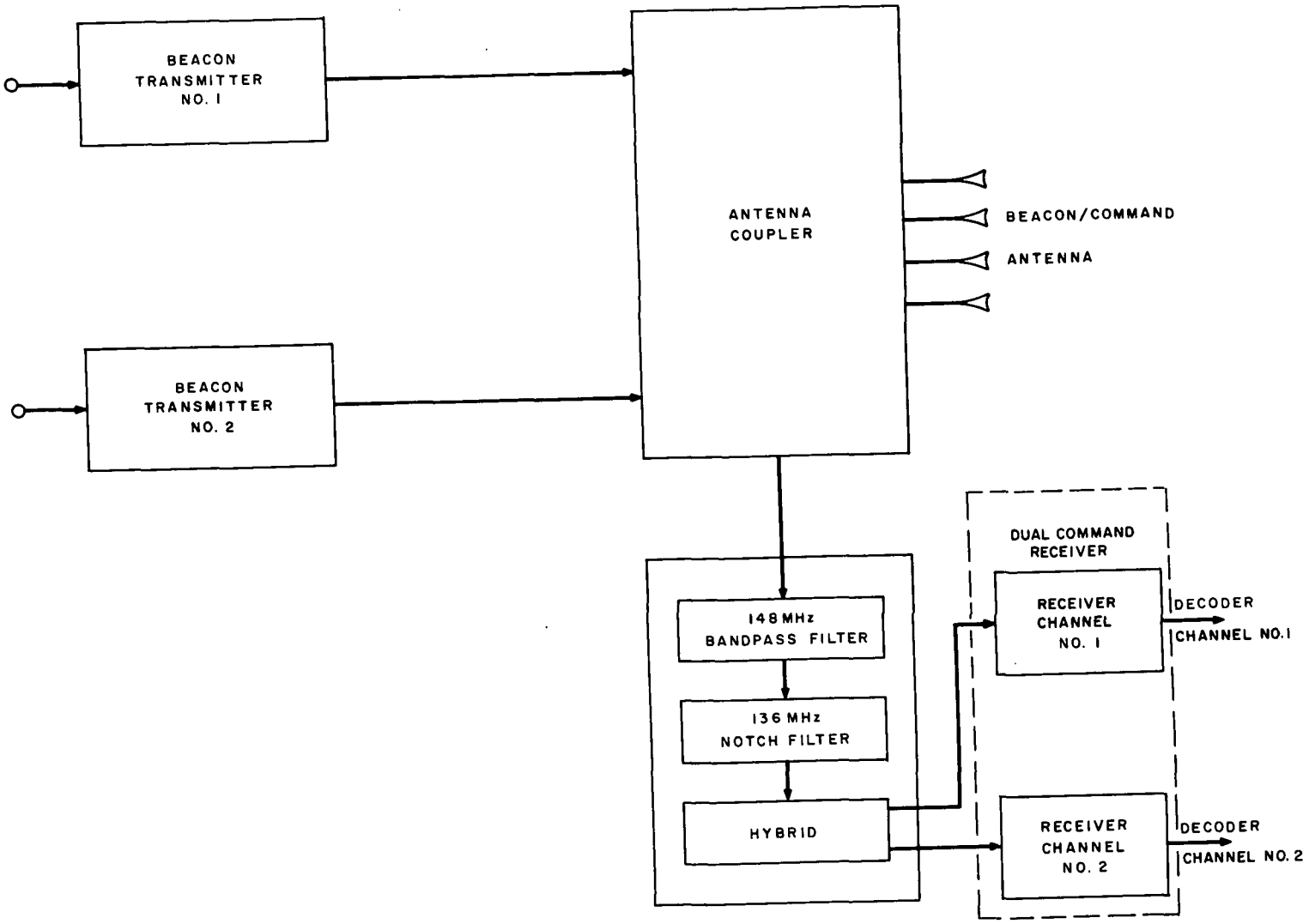

Figure 4-IX-2. Command and Beacon Telemetry Link, Block Diagram

are: decoder channel No. 1, ±78 Hz; decoder channel No. 2, ±108 Hz. The FSK subcarrier bandwidths are: decoder channel No. 1, ±550 Hz; decoder channel No. 2, ±785 Hz.

Each command decoder is tuned to a given enable tone and a given FSK subcarrier. The 3-db bandwidths are ±2 percent of the center frequency for the enable tones, and ±6.75 to ±8.75 percent of the center frequency for the FSK subcarriers. The FSK subcarriers are modulated by a bipolar, return-to-zero waveform at a rate of 10 bits per second. A bit "1" produces a maximum frequency shift of the FSK subcarrier in a given direction; a bit "0" produces a maximum frequency shift in the other direction. A rest period, when the center frequency is transmitted, always follows a "1" or a "0". The bit information is extracted by filtering the FSK subcarrier by bandpass filters centered at the maximum and the minimum subcarrier frequencies, respectively. The outputs of these filters are then envelope-detected.

3. Command and Beacon Telemetry Antenna Subsystem

a. Antenna

The various components of the command and beacon telemetry antenna subsystem are from the flight-proven TOS APT spacecraft. The antenna proper is common to both the command subsystem and the beacon subsystem. The baseline antenna is composed of four dipoles. For beacon transmission at 136.77 MHz, the dipoles are fed in phase quadrature and produce a circularly polarized wave. For command reception, the dipoles are connected in phase, yielding a linearly polarized receiving antenna. The antenna coupler provides the proper phasing.

The received amplitude-modulated RF carrier is applied to a 148-MHz bandpass filter, a 136-MHz notch filter that provides rejection of the beacon signal (136.77 MHz) and the real-time signal (137.5 MHz), and to a hybrid power splitter which feeds RF power to the dual command receiver. Both command receiver channels are operating continuously.

Although the baseline antenna is the same basic unit used on TOS APT, the antenna pattern is expected to be somewhat different because the dimensions of ITOS are different, and because the three solar panels introduce an element of asymmetry in the spacecraft geometry.

At the command frequency, the spacecraft dimensions are of the same order of magnitude as the wavelength of the RF carrier. Therefore, the spacecraft geometry has an important effect on the pattern and the gain. Preliminary antenna measurements have been performed with the antenna mounted on a model of the spacecraft. The antenna directivity can be derived from Figure IX-3. The value of antenna directivity used in the link calculations was -14 db, and does not include the coupler loss of -1.0 db. The results of the command link calculation are compared in Part 4, Section IV, Paragraph B.5 with those obtained for the TOS APT link.

The antenna contour plots of Figures 4-IX-3 and 4-IX-4 are made on a Mercator-like projection, where the antenna directivity over the total sphere about the spacecraft is shown. Unlike the mercator projection, equal latitude and equal longitude differences are plotted as equal linear dimensions. The value of this type of presentation is that it allows an evaluation of the antenna on a single plot. The equivalent information in the more familiar polar plots would have required 90 curves. The coordinate system (relative to spacecraft configuration) used in these measurements is shown in Figure 4-IX-5. An important consideration in the evaluation of these plots is that equal areas in the rectangular presentation do not map as equal surface area on the sphere about the antenna.

The normalized area (unit radius) subtended on the sphere is

$$\int_{\phi_1}^{\phi_2}\int_{\Theta_1}^{\Theta_2} \sin\Theta \, d\Theta \, d\phi \left[\int_{\phi_1}^{\phi_2}\int_{\Theta_1}^{\Theta_2} \sin\Theta \, d\Theta \, d\phi \right]$$

For the total sphere,

$$\phi_1 = 0 \qquad \phi_2 = 2\pi$$

$$\Theta_1 = 0 \qquad \Theta_2 = \pi$$

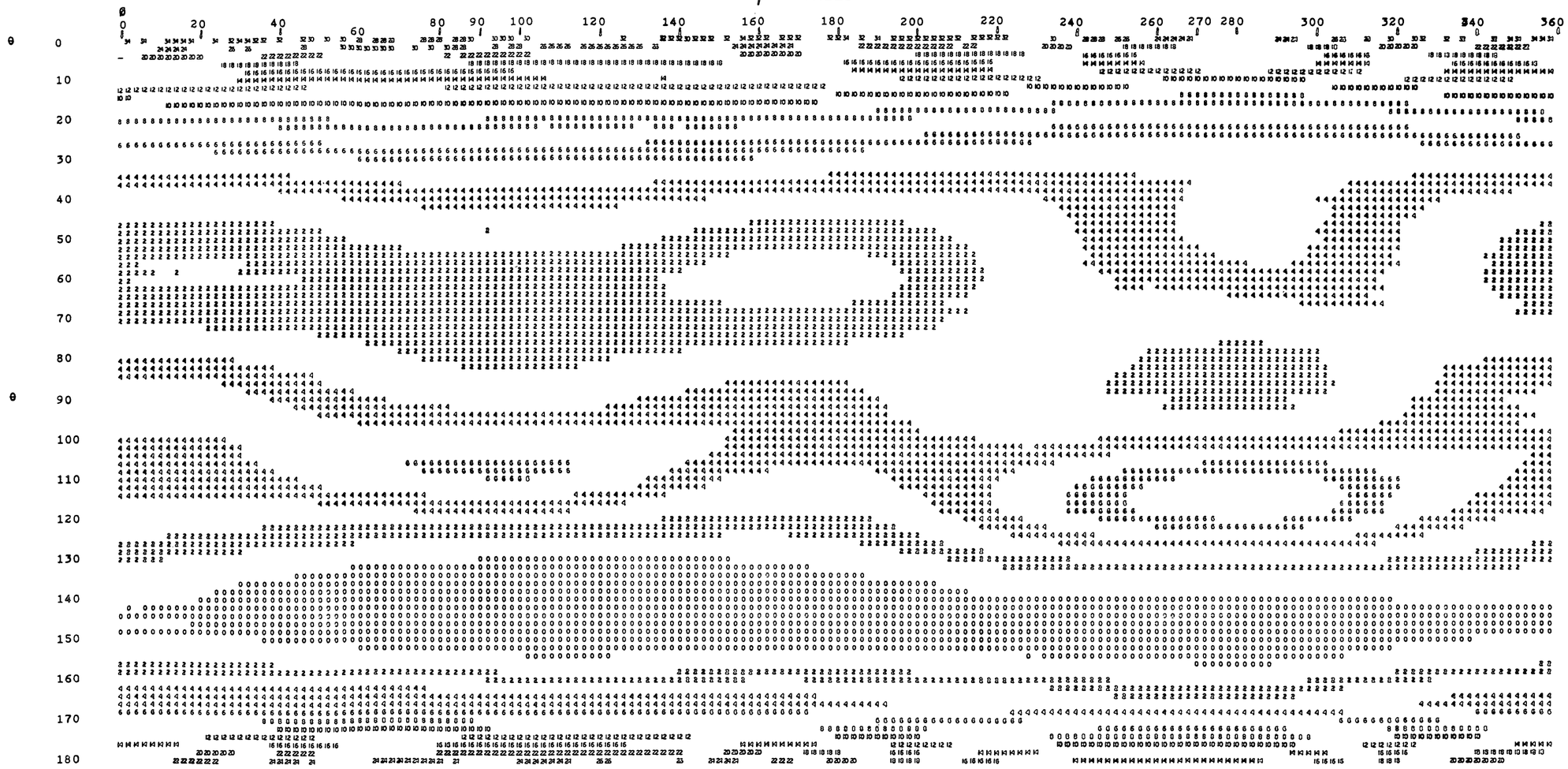

Figure 4-IX-3. Quadripole Command Antenna Contour Pattern, Solar Panels Folded (Linear Horizontal Transmission, Scale Factor 2.5:1, 371 MHz, 3-db Isotropic Level)

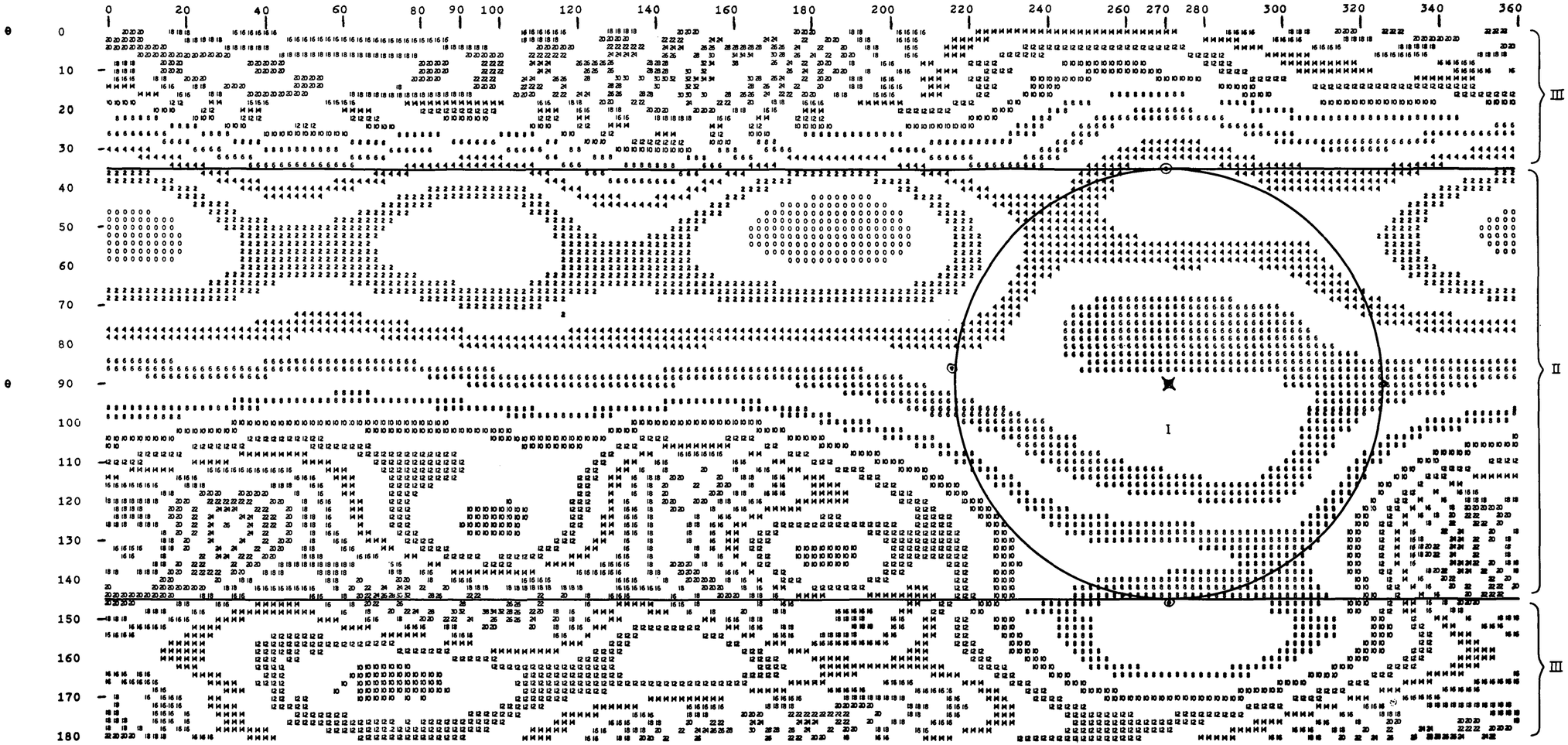

Figure 4-IX-4. Quadripole Command Antenna Contour Pattern Solar Panels Deployed (Horizontal Transmission; Scale Factor 2.5:1, 371 MHz, 6-db Isotropic Level, Preliminary Data)

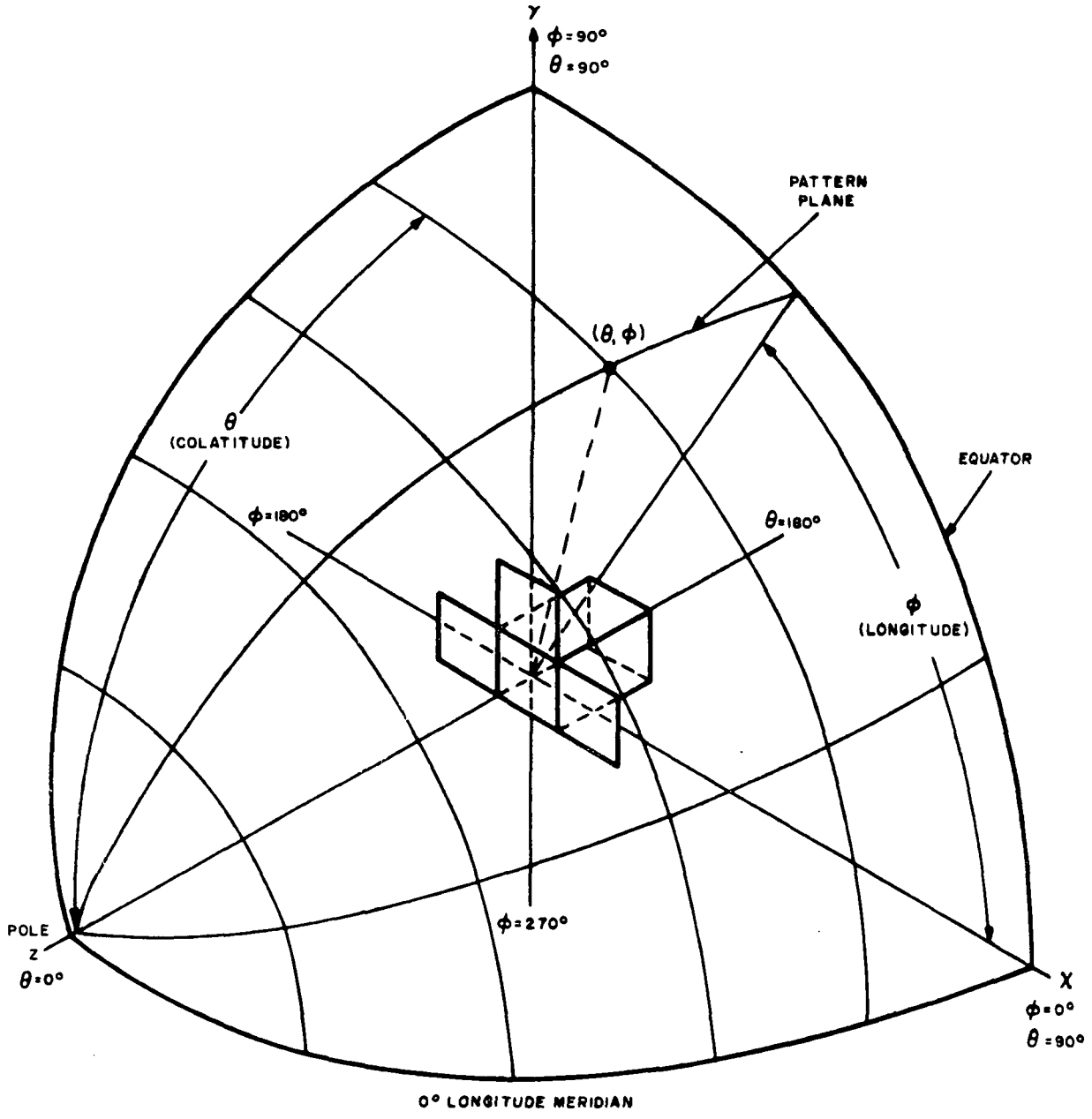

Figure 4-IX-5. Relation of the ITOS Spacecraft to the Spherical Coordinate System as Used in Antenna Pattern Measurements

and

$$\iint \text{Sin}\,\Theta\, d\,\Theta\, d\,\phi = 4\,\pi,$$

which is the solid angle in steradians.

Using the above relationship, the antenna pattern of Figure 4-IX-3 will be evaluated. This figure is the command antenna pattern with the solar panels folded.

The numerical values on the figure represent the field intensity, in decibels, below the peak value measured. The entire sphere has been integrated and an isotropic level of 3 db was calculated; this means the average value of field intensity is 3 db below the peak value. In the presentation, odd numbers have been omitted from the plot to emphasize contours; however, it is easy to identify a region around Θ = 120 degrees where the pattern is close to isotropic level. The requirements for system operation with margin (Table 4-IX-3) is for a directivity of -14 db relative to isotropic or better. Therefore, regions where the numerical printout is 17 or higher correspond to a command null. In Figure 4-IX-3, there are two regions where the directivity is poorer than -14 db, one along Θ = 0 degree, and the other about Θ = 180 degrees (the expected null points of a dipole pattern). An approximate evaluation shows the area affected by these nulls is less than 0.5 percent of the total area, or in other terms, the pattern is below -14 db for a solid angle less than 0.5 percent of the total spherical angle.

The antenna contour plot of Figure 4-IX-4 is the command pattern with the solar panels deployed. This pattern is divided into three regions: Region I is that portion of the pattern visible from earth in the operational mode (spacecraft stabilized); Region II is the portion of the pattern that would be visible if the spacecraft were to lose pitch lock and rotate about the pitch axis; and Region III is the portion of the pattern that would be visible in the event the pitch axis were to be rotated relative to the orbital plane.

The requirement for Region I is a directivity better than -7 db to allow a 200-watt transmitter to command the spacecraft. The requirement for Region II is a directivity of -14 db

for operation with a 1-kilowatt transmitter. There are no requirements for Region III, since operation out of the orbital plane is not anticipated.

Evaluation of Figure 4-IX-4 shows that requirements for Region I are exceeded. The isotropic level is -6 db and, combined with -7 db directivity, translates into a 13-db value on the figure. All values are better than 9 db, providing 4-db performance beyond the requirements.

For Region II, it is desired that a value of 20 (6 + 14) be met. For values from 35 to 120 degrees, this value is exceeded. From 120 to 140 degrees, there are regions where the antenna directivity falls below -14 db, particularly around $\phi = 30$ degrees and $\phi = 350$ degrees. This loss of directivity is caused by shadowing from the solar panels. This means that if there should be a failure in the pitch lock mechanism and the spacecraft begins to rotate, there will be certain orbits where difficulty may be encountered in commanding the spacecraft. Whether or not the command will get through will depend on the rotational position of the spacecraft and the difference between the worst-case link calculation and the actual link operation. The worst value measured for any significant area is -25, which occurs at $\Theta = 125$ degrees and $\phi = 30$ degrees. There is a 3-db margin in the link calculation (Table 4-IX-3). The slant range is less than maximum, and more than likely, the system will exceed specifications somewhat. These considerations make it likely that the commands will get through. However, if the command cannot be effected, the subsequent orbit will be such that the view angle from earth that the pattern sees is well above system threshold.

Thus, in summation, there can be a combination of circumstances in conjunction with failure of the pitch lock mechanism where, on a particular orbit, commands will not be received. However, this condition will not exist on the subsequent orbit.

b. Bandpass Filter, Notch Filter, and Hybrid

The bandpass filter and notch filter used on ITOS are those used on TOS APT. The hybrid power splitter is a new unit. The overall insertion loss of these units, including cabling, is 8 db.

4. Dual Command Receiver

The dual command receiver is the same as used on the TIROS and TOS spacecraft with the exception of some changes in the electrical specifications. Two identical command receiver channels are used for redundancy. The receiver is a solid-state unit which is fixed-tuned to the command frequency. The command receiver specifications are listed in Table 4-IX-2.

TABLE 4-IX-2. COMMAND RECEIVER SPECIFICATIONS

Characteristics	Values
Noise Figure	10 db max
IF Bandpass Characteristics	
Center Frequency	20.000 ± 0.003 MHz
-6-db Bandwidth	50 kHz (min)
-60-db Bandwidth	100 kHz (min)
Midband Response Variation	Less than ±1 db over a 35-kHz band (nominal) centered at 20.00 ±0.003 MHz
Sensitivity	0.77-volt rms audio for 1 microvolt input modulated 90 percent with 1-kHz signal
AGC Control Range	
Input	2 microvolts to 10 millivolts
Output	0.9 to 1.6 volts rms
Noise Output at 1 microvolt input	<350 millivolts
RF Input Source Impedance	50 ohms
Audio Output Load Impedance	5.6 kilohms ±10 percent
Spurious Responses and Image Rejection	At least 50 db down from 148 MHz
Audio Frequency Response (+1.5, -1.0 db)	1.0 to 12.0 kHz
Operating Temperature	-15 to +60°C
Power Supply	
Voltage	-23 volts DC ±3 percent
Power Consumption	0.4 watt (max, each receiver)
Weight	2.5 pounds
Size (both receivers in one integral unit)	6.5 by 5.9 by 2.9 inches

5. Subsystem Analysis and Link Calculation

a. Link Geometry and Path Loss

The ITOS satellite will orbit the earth at an altitude of 775 nautical miles. Given orbit altitude, the slant range, R, may be calculated from the following formula:

$$R = -r \sin \psi + \left[(r^2 \sin^2 \psi - 1) + (r + H)^2 \right]^{1/2} \text{ nautical miles}$$

where

r is radius of earth = 3440 nautical miles,

ψ is ground antenna elevation angle, and

H is altitude of the satellite = 775 nautical miles

The corresponding path loss, L, at a given frequency of transmission, is

$$L = \frac{\lambda^2}{[4\pi R]^2}$$

where

λ is wavelength = 2.03 meters (for f = 148 MHz)

R is slant range in kilometers - range in nautical miles x 1.852.

Approximate path losses as a function of ground antenna elevation angle for a satellite orbit of 775 nautical miles are given in Table 4-IX-3.

b. RF Power Margin Calculation

The minimum required output voltage of the dual command receiver is 0.77 volt rms (sinusoidal signal). The dual decoder is designed to respond to input levels equal to or greater than the threshold value of 0.70 volt rms. The receiver output is 0.77 volt rms when the input level is -107 dbm, which is the receiver threshold. Sufficient margin should be maintained above this threshold to ensure reliable operation. The summary of link

TABLE 4-IX-3. PATH LOSSES AS A FUNCTION OF ELEVATION ANGLE FOR THE 148-MHz COMMAND LINK

Elevation Angle, ψ (degrees)	Path Loss, L (db)
0	148.6
5	148.0
10	146.8
15	145.6
20	144.6
25	143.7
30	143.0

calculations is given in Table 4-IX-4. For comparison, the summary of TOS APT link calculations is given in the same table.

The calculations were performed for a 1 kw (60 dbm) transmitter with a 12-db-gain antenna. The spacecraft antenna gain is without the coupler loss. The link calculations for ITOS show that the input RF level to the receiver is 3.0 db above the -107 dbm threshold. The margin for TOS APT is 6.2 db. The difference in margin is accounted for in the spacecraft antenna directivity. The estimate for the worst-case ITOS antenna directivity is -14 db. For TOS APT, the directivity of -.38 db is obtained at the worst-case look angle. For the ITOS operational mode, the directivity is better than -3 db, adding 11 db to the 3 db for a total of 14 db margin.

TABLE 4-IX-4. WORST-CASE LINK CALCULATION

	ITOS	TOS APT	Remarks
Transmitter Power (1 kw)	60.0 dbm	53.0 dbm	
Ground Antenna Gain	12.0 db	12.0 db	Avien antenna
Line Losses Transmitter-to-Antenna	-3.0 db	-3.0 db	
Space-Loss	-148.0 db	-148.0 db	5 degree elevation at 148 MHz
Polarization Loss	-3.0 db	-3.0 db	Circular-to-linear
Spacecraft Antenna Directivity	-14.0 db	-3.8 db	
Coupler Loss	-1.0 db	-1.0 db	
Band Pass Filter Loss (148 MHz)	-2.5 db	-2.5 db	
Notch Filter Loss	-0.5 db	-0.5 db	
Spacecraft Cable Loss	-0.5 db	-0.5 db	
Hybrid Insertion Loss	-0.5 db	-0.5 db	
Hybrid Power Splitter	-3.0 db	-3.0 db	Power split between two receivers
Received RF Power (each receiver)	-104.0 dbm	-100.8 dbm	0.70 volt at decoder
Command Receiver Threshold	-107.0 dbm	-107.0 dbm	
Margin Above Threshold	+3.0 db	+6.2 db	

If during the mission the performance should degrade to that shown in the worst-case analysis, the performance may be improved by using the RSI-9 antenna. The link calculation has been done under the assumption that the Avien, Inc. ground antenna is used, mounted on the 85-foot dish. The antenna has a gain of 12 db and a 3-db line loss. If the

RSI-9 antenna on the SATAN pedestal is used, the antenna gain is 23.7 db and the line loss is 1.7 db. The net improvement over the Avien antenna is +13.0 db. For a 1-kw transmitter, this yields a ITOS margin of 16.0 db. For the RSI antenna on the 85-foot dish, the margin is +4.6 db. The margins are shown in Table 4-IX-5.

TABLE 4-IX-5. COMMAND LINK RF MARGIN COMPUTATION FOR THREE DIFFERENT ANTENNAS

Link Parameter	Avien Inc. Antenna	RSI-9 on SATAN Antenna	RSI on 85-foot Dish Antenna
Transmitter Power (1 kw)	60.0 dbm	60.0 dbm	60.0 dbm
Ground Antenna Gain	12.0 db	23.7 db	13.0 db
Ground Line Losses	-3.0 db	-1.7 db	-3.4 db
	69.0 db	82.0 db	70.6 db
Other Link Losses	-173.0 db	-173.0 db	-173.0 db
Received Power	-104.0 dbm	- 91.0 dbm	-102.4 dbm
Command Receiver Threshold	-107.0 dbm	-107.0 dbm	-107.0 dbm
RF Margin	3.0 db	16.0 db	4.6 db

c. Receiver Bandwidth Requirements

The minimum IF bandwidth of the receiver should be able to handle the modulation bandwidth, the maximum doppler shift, the maximum frequency offset due to frequency instability in the transmitter, and the receiver local oscillator.

(1) Doppler Shift

The doppler shift is indicated by the following expression and is a maximum at the minimum elevation angle:

$$\Delta F = \frac{FV}{C} \cos B,$$

where V is the spacecraft velocity, C is the velocity of light, and B is the angle between the ground station and the direction of the spacecraft velocity vector. At the command link frequency of 148 MHz, the maximum doppler shift is ±2.9 kHz, or a total of 5.8 kHz.

(2) Frequency Stability

The receiver local oscillator stability is specified at ±0.005 percent maximum, yielding a maximum frequency instability of ±6.4 kHz or a total of 12.8 kHz over a temperature range from -15 to +60°C. The IF filter, center frequency stability is specified at ±4 kHz or a total of 8 kHz.

(3) Modulation Bandwidth

The modulation bandwidth is a maximum of ±11.3 kHz or a total of 22.6 kHz. This is the bandwidth required when the highest frequency FSK tone is being transmitted.

(4) Worst-Case IF Bandwidth

The frequency instability is obtained by adding all the individual frequency instabilities and uncertainties. This yields the worst-case IF bandwidth.

Transmitter Instability*	0.400 kHz
Receiver Local Oscillator Instability	12.8 kHz
Receiver IF Filter Instability	8.0 kHz
Total Receiver Frequency Uncertainty	21.2 kHz
Doppler Shift	5.8 kHz
Maximum Modulation Bandwidth	22.6 kHz
Worst-Case IF Bandwidth	49.6 kHz

* Telegram 13/2238Z Oct. GMOR

The IF bandwidth specifications for the ITOS receiver given in paragraph B-4 of Part 4, Section IX, are repeated below:

IF Passband (±1 db)	40 kHz (min)
-3 db Bandwidth	48 kHz (min)
-6 db Bandwidth	50 kHz (min)
-20 db Bandwidth	60 kHz (max)
-70 db Bandwidth	110 kHz (max)
-60 db (min)	beyond 110 kHz

The above IF filter characteristics will meet the expected bandwidth requirements during operation. The bandwidth has been opened from 40 kHz (-6 db) in TOS to 50 kHz (-6 db). The worst-case bandwidth of 49.6 kHz over -15 to +60°C would result in a 6-db signal loss in the highest FSK sideband of the IF signal. This loss corresponds to an effective index loss from m to 3/4 m, or 2.5 db. The 110-kHz rejection has been tightened from -60 to -70 db to increase immunity from interfering signals. A bound of -60 db minimum has been set on the IF response above 110 kHz.

(5) Minimum Bandwidth Requirement Over Spacecraft Temperature Range

This discussion describes the IF bandwidth requirement based on predicted component temperature variation in orbit (not specification worst-case component temperature variation) and data obtained from environmental test of eight TOS dual command receivers. The result shows that even though the worst-case calculation indicates a 6-db signal loss in the highest FSK sideband of the IF signal, the actual operating environment will not produce this worst-case condition.

The expected temperature variation of the ITOS baseplate is from 10 to 30°C (compared to the component specification of -51 to +60°C). The worst local oscillator drift rate is -0.13 kHz/°C and the worst IF crystal filter center frequency drift is -0.15 kHz/°C as determined in environmental tests on eight TOS dual command receivers.

The IF center frequency deviation from nominal is produced by (1) variations in local-oscillator frequency and IF crystal filter characteristics due to temperature; (2) accuracy tolerance in initial calibration; (3) doppler shift; and (4) transmitter instability. The frequency deviation is as follows:

Local Oscillator Drift	=	0.13 kHz/°C x 20°C	= 2.6 kHz
IF Crystal Filter Drift	=	0.15 kHz/°C x 20°C	= 3.0 kHz
IF Center Frequency Calibration Accuracy			= 1.0 kHz
Doppler Shift			= 2.9 kHz
Transmitter Instability			= 0.2 kHz
Total IF Center Frequency Deviation			= 9.7 kHz

The modulation bandwidth as determined in Paragraph B.5.c of Part 4, Section IX, is ±11.3 kHz. Therefore, the IF bandwidth must be able to pass a signal which has components 9.7 kHz + 11.3 kHz = 21.0 kHz from nominal center frequency. To reiterate, this is for predicted system performance and not the worst-case specification performance. The signal loss due to IF filter characteristics is approximately 1 db compared to a 6-db signal loss for the worst-case conditions.

(6) Interference Signals

Interference signals are expected due to the physical proximity of the beacon, real-time, and S-band transmitters. Interfering signals might produce a desensitization of the receiver, reducing the effective threshold margin. Intensive tests on the TIROS and TOS receivers have shown that for the interfering signals at frequencies around 136 MHz (12 MHz away from command frequency) negligible desensitization occurs if the interfering level is maintained below -30 dbm. Interfering signals lying in the receiver pass band have to be maintained below -113 dbm. The interference levels from the transmitters and the required isolation between the transmitters and the command receiver port are given in Table 4-IX-6.

TABLE 4-IX-6. INTERFERENCE LEVELS AT THE COMMAND RECEIVER PORT

Source of Interference	Transmitter Level	Allowable Interference Level at Command Receiver Port	Minimum Isolation Required
Beacon at Command Freq, 148 MHz	-100 dbm	-125 dbm	25 db
Beacon at Image Freq, 108 MHz	-50 dbm	-125 dbm**	25 db*
APT at Command Freq, 148 MHz	-80 dbm	-125 dbm	45 db
APT at Image Freq, 108 MHz	-50 dbm	-125 dbm**	25 db*
S-Band at Command Frequency	-90 dbm	-125 dbm	35 db
S-Band at Image Freq	-70 dbm	-125 dbm**	5 db*
Beacon Power at 136.7 MHz (250 m watts)	+24 dbm	-40 dbm	64 db
APT Power at 137.5 MHz (5 watts)	+37 dbm	-30 dbm	67 db

* 50-db image rejection is provided by the receiver internal circuitry.

** Effective interference level at IF.

The required isolation will maintain receiver desensitization below a negligible value. The total interference level in the receiver IF passband is the sum of the interference powers of the first six entries in Table 4-IX-6. The interference level is -117.2 dbm.

(7) Random Noise Temperature

The overall link noise temperature is made up of the receiver noise temperature, the noise temperature due to prereceiver circuit losses, the cosmic noise temperature, and the earth noise temperature. The receiver noise temperature is the most important contributor to the overall link noise temperature.

(a) Receiver Noise Temperature

The noise figure, F, of the receiver is specified at 10 db max. This corresponds to a receiver temperature of

$$T_R = 290° (F-1) = 2610° K.$$

(b) Prereceiver Circuit Noise Temperature

The prereceiver circuit includes all cables and filters between the antenna and the receiver input. The losses in the prereceiver circuit contribute noise power proportional to the actual circuit noise temperature, T_L, and given by

$$T = \left(1 - \frac{1}{L}\right) T_L$$

where L is the circuit loss expressed as a power ratio.

Taking T_L to be approximately equal to 320° K with a -5-db circuit loss, then:

$$T = \left(1 - \frac{1}{3.16}\right) 320°K = 218°K.$$

The noise power is split equally between the two receiver channels which yields the effective circuit noise temperature of

$$T_c = \frac{218°}{2} = 109°K.$$

(c) Cosmic Noise Temperature

The cosmic noise temperature as a function of frequency is given in Figure 4-IX-6. The figure shows the maximum value at the galactic center, the coolest 95 and 99 percent of the radio sky, and the minimum value of cosmic noise temperature; the sky temperature, T_s, for 95 percent of the sky is 700°K from the "95 percent" curve. However, since the earth covers an important portion of the sky (110-degree angle), a correction, ΔT, proportional to the fraction of solid angle intercepted by the earth should be applied. The correction, $\Delta T°K$, is given by

$$\Delta T°K = (T_s \text{ for 95 percent sky})\,(4\pi \text{ steradians}) \times \frac{\text{solid angle subtended by earth}}{4\pi \text{ steradians}}$$

$$= 700°K \times \frac{2\pi(1-\cos 55°)}{4\pi} = 149°.$$

The effective sky temperature is:

$$T_{se} = T_s - \Delta T = 700-149 = 551°K$$

The effective temperature at the receiver port, T_{se}, is obtained by taking the 8-db loss from antenna to receiver into account,

$$T_{se} = \frac{551°K}{6.3} = 87.5°K.$$

(d) Earth Noise Temperature

The earth noise temperature at the command antenna is given by

$$T_E = \frac{2\pi\,(1-\cos 55°)}{4\pi} \times 300°K = 63.9°K.$$

There is an 8-db loss between receiving antenna and receiver port which yields the effective earth noise temperature at the receiver port of

$$T_{Ee} = \frac{63.9°}{6.3} = 10.1°K$$

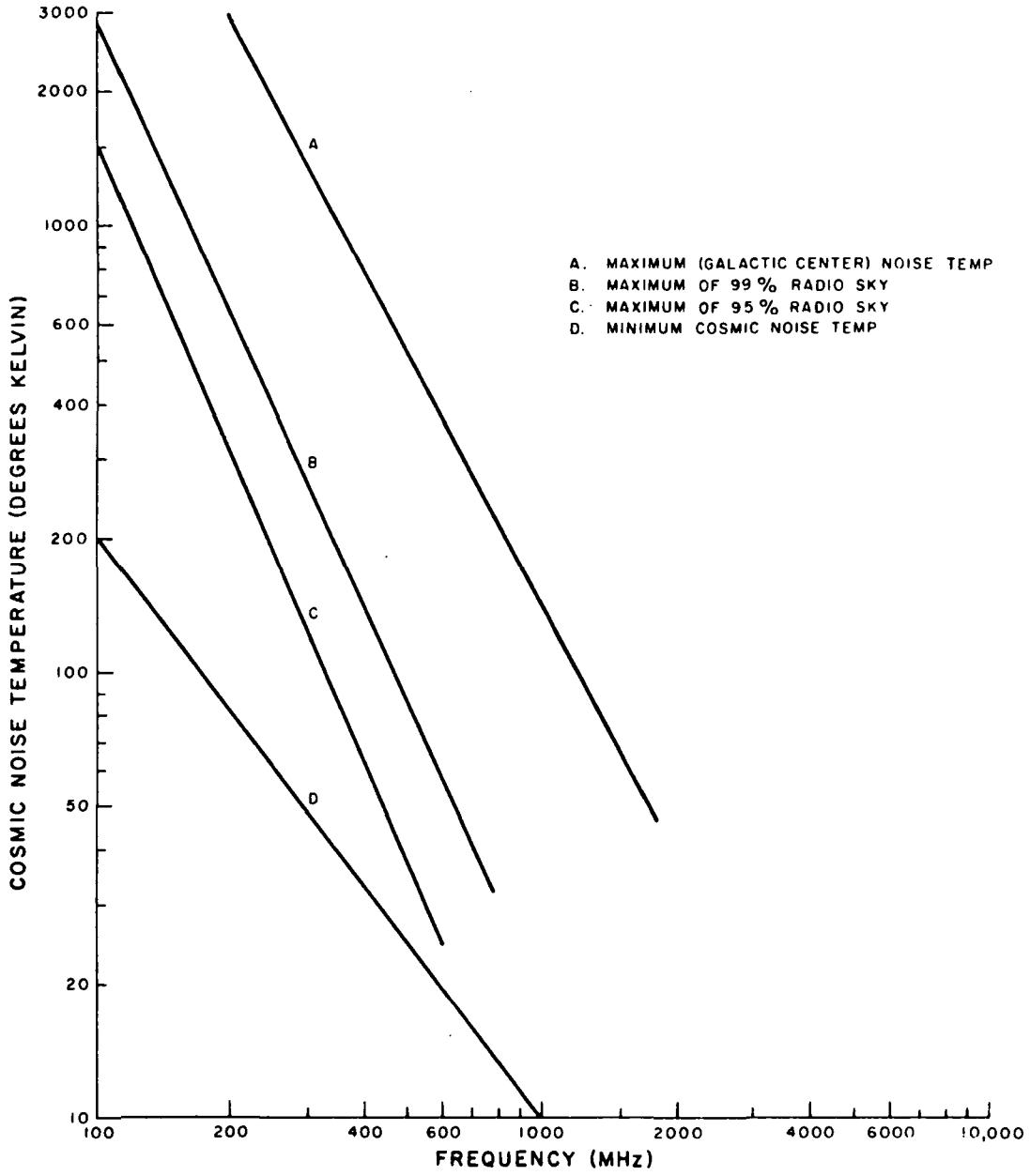

Figure 4-IX-6. Cosmic Noise Temperature Versus Frequency

(e) Total IF Noise Power

The overall system noise temperature is then given by the summation below:

Receiver	2610.0°K
Prereceiver Circuit	109.0°K
Cosmic	87.5°K
Earth	10.1°K
System	2816.6°K

The system noise temperature is then T_{sys} = 2816.6°K

The noise power in the IF is N, and $N = kT_{sys}B_{IF}$

where

k = Boltzman's constant = 1.38×10^{-23} Joules/°K and

B_{IF} = Receiver IF noise bandwidth = 48 kHz

The total IF noise power is

$N = 1.38 \times 10^{-23} \times 2.816 \times 10^{3} \times 48 \times 10^{3} = 1.87 \times 10^{-15}$ watts or

N = -117.3 dbm for an IF bandwidth of 48 kHz.

(8) Carrier-to-Noise Ratio

For an IF bandwidth of 48 kHz and a receiver RF power input of -107 dbm, the IF carrier-to-random-noise ratio is

C_{IF}/N_{IF} = -107 dbm + 117.3 dbm = 10.3 db.

The IF carrier-to-interference ratio at RF power threshold is

-107 dbm + 117.6 dbm = 10.6 db.

The total average power of combined random noise and interference is

$$P_n \text{ total} = -114.4 \text{ dbm.}$$

The overall carrier-to-noise ratio (including interference power) is

$$\frac{C}{N_t} = +7.4 \text{ db for an IF bandwidth of 48 kHz.}$$

(9) Subcarrier Signal-to-Noise Ratio

The command system performance is not limited by the 7.4-db carrier-to-noise ratio in the IF. The parameter of importance is the subcarrier-to-noise ratio in the subcarrier bandwidth, B_{sc}.

The subcarrier-to-noise ratios for random noise only and for total noise and interference are given in Table 4-IX-7.

TABLE 4-IX-7. SUBCARRIER-TO-NOISE RATIOS AT RF POWER THRESHOLD

Subcarrier	Bandwidth (Hz)	Random Noise Only S_c/N_c (rms/rms)	Random Noise and Interference (rms/rms)
FSK 2	1570	21.3 db	18.4 db
FSK 1	1100	22.8 db	19.9 db
TONE 2	216	29.9 db	27.0 db
TONE 1	156	31.3 db	28.4 db

The frequencies $f_c + \Delta f$ and $f_c - \Delta f$ are extracted by the two bandpass filters having a ± 2 percent bandwidth. These tones are subsequently envelope-detected and trigger a threshold device. Next, they are integrated and digitally processed. The detected-pulse signal-to-noise ratio is improved by 5.7 db above the subcarrier signal-to-noise ratio by the tone

filters. This yields a demodulated signal-to-noise ratio in excess of 24.1 db rms/rms (27.1 db peak/rms). This corresponds to a bit-error probability of less than 1 part in 10^6.

C. BEACON AND TELEMETRY LINK

1. General

The beacon and telemetry link of the ITOS spacecraft will provide for the telemetering and transmission of spacecraft operating parameters to the CDA stations. These operating parameters are housekeeping telemetry, attitude (roll and pitch), digital solar aspect indicator (DSAI), and acquisition sensor data and command data verification. In addition, solar proton monitor data are transmitted. The beacon and telemetry link, shown in Figure 4-IX-7, uses a dual signal conditioner with redundant commutators, a dual subcarrier oscillator assembly, and redundant transmitters. The beacon antenna coupler and the beacon antenna are nonredundant. The beacon antenna is the same unit used for command reception; however, for beacon transmission, the crossed dipoles are fed in phase quadrature, producing circular polarization.

The two subcarrier oscillators associated with beacon transmitter No. 1 (SCO 1-1 and SCO 1-2) have the same respective frequencies as the subcarrier oscillators associated with beacon transmitter No. 2 (SCO 2-1 and SCO 2-2). The highest frequency SCO (3.9 kHz, IRIG channel No. 9) carries the housekeeping telemetry or command verification data. The lowest frequency SCO (2.3 kHz, non-IRIG standard deviation channel) carries one of the following signals: acquisition sensor, telemetry, digital solar aspect sensor, roll sensor No. 1, roll sensor No. 2, pitch sensor, or solar proton monitor data. Each subcarrier set is turned on simultaneously with the associated beacon transmitter. The CDU relay chain, described in Section 4-VIII, performs the function of cross-strapping the various signals to the selected SCO unit. In addition, the CDU relay chain selects the various signals under the following priority list:

3.9-kHz Subcarrier

Set No. 1	Set No. 2
1. TLM Commutator No. 1	1. TLM Commutator No. 2
2. TLM Commutator No. 2	2. TLM Commutator No. 1
3. Decoder Channel No. 1 (command data verification)	3. Decoder Channel No. 2
4. Decoder Channel No. 2 (command data verification)	4. Decoder Channel No. 1

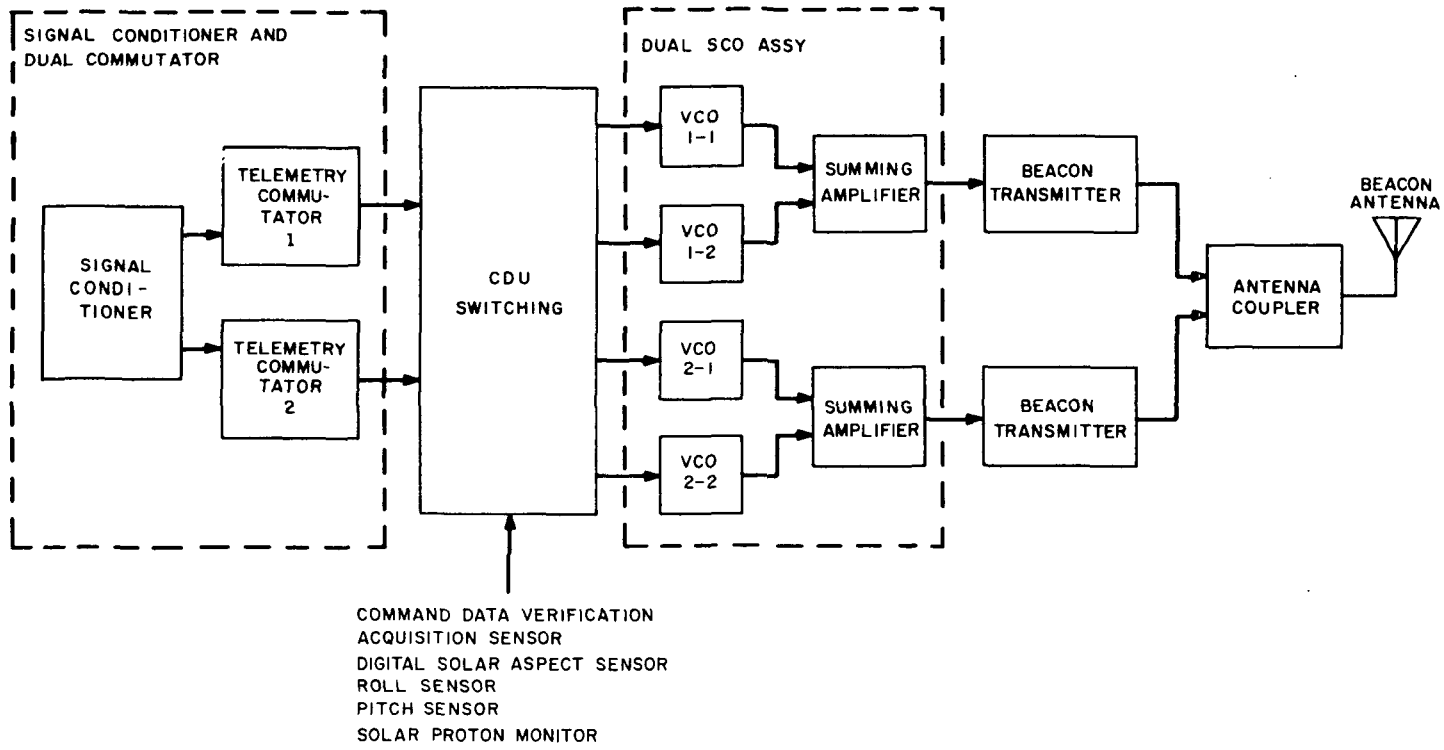

Figure 4-IX-7. Block Diagram of the Beacon/Telemetry Link

2.3-kHz subcarrier

Set No. 1	Set No. 2
Acquisition Mode:	Acquisition Mode:
1. DSAI Data	1. DSAI Data
2. Acquisition Sensor Data	2. Acquisition Sensor Data
Operational Mode:	Operational Mode:
1. Roll Sensor Data	1. Roll Sensor Data
2. Pitch Sensor Data	2. Pitch Sensor Data
3. Solar Proton Monitor Data	3. Solar Proton Monitor Data

2. Signal Characteristics

a. Housekeeping Telemetry

The telemetry commutator samples 120 channels at a rate of either 15 channels per second or at a rate controlled by the programmer driving signal. The commutator can be stopped at any desired point for continuous examination of data. When power is first applied to the commutator, a 1.2-second delay ensues before commutation begins. During this time, a 24-bit time code is transmitted. Telemetry may be requested by the standard digital command or by the transmission of a longer-than-normal enable tone. This added command capability is provided to permit the commanding of telemetry from a facility that does not possess the equipment required to generate the normal digital commands. However, if the beacons have been turned off, the emergency telemetry analog command has no facility to turn a beacon back on.

b. Command Data Verification

If housekeeping telemetry is not being requested, command data verification from the two decoder channels have priority. In this case, the decoded data bits will be transmitted back to the ground station.

Each CDU has a data verification relay. On beacon system No. 1, only housekeeping telemetry has priority over decoder channel No. 1 data verification, which in turn has priority over decoder channel No. 2 data verification. On beacon system No. 2, the relative priorities of decoder channel No. 1 and decoder channel No. 2 data verification are reversed. The reason for interchanging priorities is to provide for data verification from the programmed decoder channels even if the other decoder generates an erroneous signal and energizes its data verification relay.

The data verification relays are nonlatching devices that are energized by the associated decoder channel when sync is detected and stay energized until the last bit of the 12-bit word is received. In addition, at the command "load programmer", the associated relay now controlled by the programmer remains energized until the programmer indicates that it has received a full complement of bits. Hence, should there be any spurious bits generated in the equipment between their detection and retransmission to the programmer, the register loads too quickly and the data verification relay is deenergized prematurely. Conversely, if a bit is lost between its generation and the programmer acceptance, the programmer fails to deenergize the data verification relay, thereby indicating that erroneous data are stored in the programmer register.

c. Acquisition Sensor

The acquisition sensor is used to determine the attitude of the satellite during the injection and attitude acquisition operation sequences. This sensor is described in Section 4-IV of this report.

d. Digital Solar Aspect Indicator

The digital solar aspect sensor (DSAI) is a separate telemetry device that can modulate either one of the two 2.3-kHz subcarriers. The purpose of this device is to measure the angle between the pitch axis and the sun vector during the injection and attitude acquisition operation. The DSAI provides a digital readout.

e. Roll Sensors

The signals from these sensors are described in Section 4-IV of this report. The selection of either sensor No. 1 or No. 2 is performed in the vehicle dynamics subsystem. The beacon and telemetry subsystem receives either signal on the same input line. The required 3-db bandwidth is 160 Hz. This is the largest bandwidth required by any of the attitude data signals.

f. Pitch Sensor

This signal is described in more detail in Section 4-IV of this report. The required 3-db bandwidth is 160 Hz.

g. Solar Proton Monitor

The real-time transmission of solar proton monitor data over the beacon and telemetry link is a backup for the primary mode of transmission over the S-band playback link. In the real-time mode, the modulating signal is derived directly from the solar proton monitor electronics and not from the data format converter, as in the playback mode.

The SPM output consists of 15-pps, NRZ, time division multiplex data. Each data frame comprises 20 words, the first word of each frame being a synchronization word with a 111001001 pattern. A data word consists of 9 bits, of which the first 4 bits are the exponent and the next 5 are the characteristic. These data modulate the 2.3-kHz VCO subcarrier of the dual SCO assembly and are transmitted to earth over the beacon and telemetry transmitter.

3. Link Components

a. Beacon Antenna

The beacon antenna is composed of a beacon antenna coupler (common with the command receiver link) and a crossed dipole antenna (common with the command receiver link). The beacon antenna coupler provides the 136-MHz beacon signal from either beacon transmitter with the proper phase quadrature to the crossed-dipole antenna.

The estimated worst antenna gain is -11.5 db, corresponding to some dips in the pattern. Directivity accounts for -10 db of the gain; the loss in coupler and cabling accounts for the remaining -1.5 db.

The preliminary patterns for the beacon antenna are shown in Figures 4-IX-8 through 4-IX-11. The design requirement for the beacon antenna is -10 db directivity. The mode of operation is to utilize vertical and horizontal diversity at the receiving site; therefore, both horizontal and vertical patterns are presented. The combined output of the vertical and horizontal patterns, then, must be above 10 db, which translates into a requirement that the directivity of the two patterns should at no point be less than -13 db. Figures 4-IX-8 and 4-IX-9 show the antenna patterns with the solar panels stowed. The isotropic level is approximately -3 db; therefore, for the antenna to meet the requirements, at no point simultaneously must the value on the plots be greater than 16. The patterns meet this requirement.

Figures 4-IX-10 and 4-IX-11 show the vertical and horizontal antenna patterns with the solar panels deployed. The peak value of field intensity is 10 on these figures, due to a malfunction in the digital encoder. Therefore, applying the criteria used in Figures 4-IX-8 and 4-IX-9 to meet the -10-db goal at any point on both plots, the values should be 26, or less. The directivity requirements exist only for Regions I and II as explained in the command antenna section. In Region I, the operational portion of the pattern, the -10-db requirement is exceeded by at least 6 db, providing substantial improvement over the subcarrier links, as calculated in Tables 4-IX-13 and 4-IX-14. The carrier tracking link already has such a large margin (Table 4-IX-15), that an additional 6 db is of small consequence. In Region II, there are small areas between Θ = 120 degrees and Θ =140 degrees where the combined directivity approaches -10 db; however, the substantial margins in the link should ensure satisfactory operation.

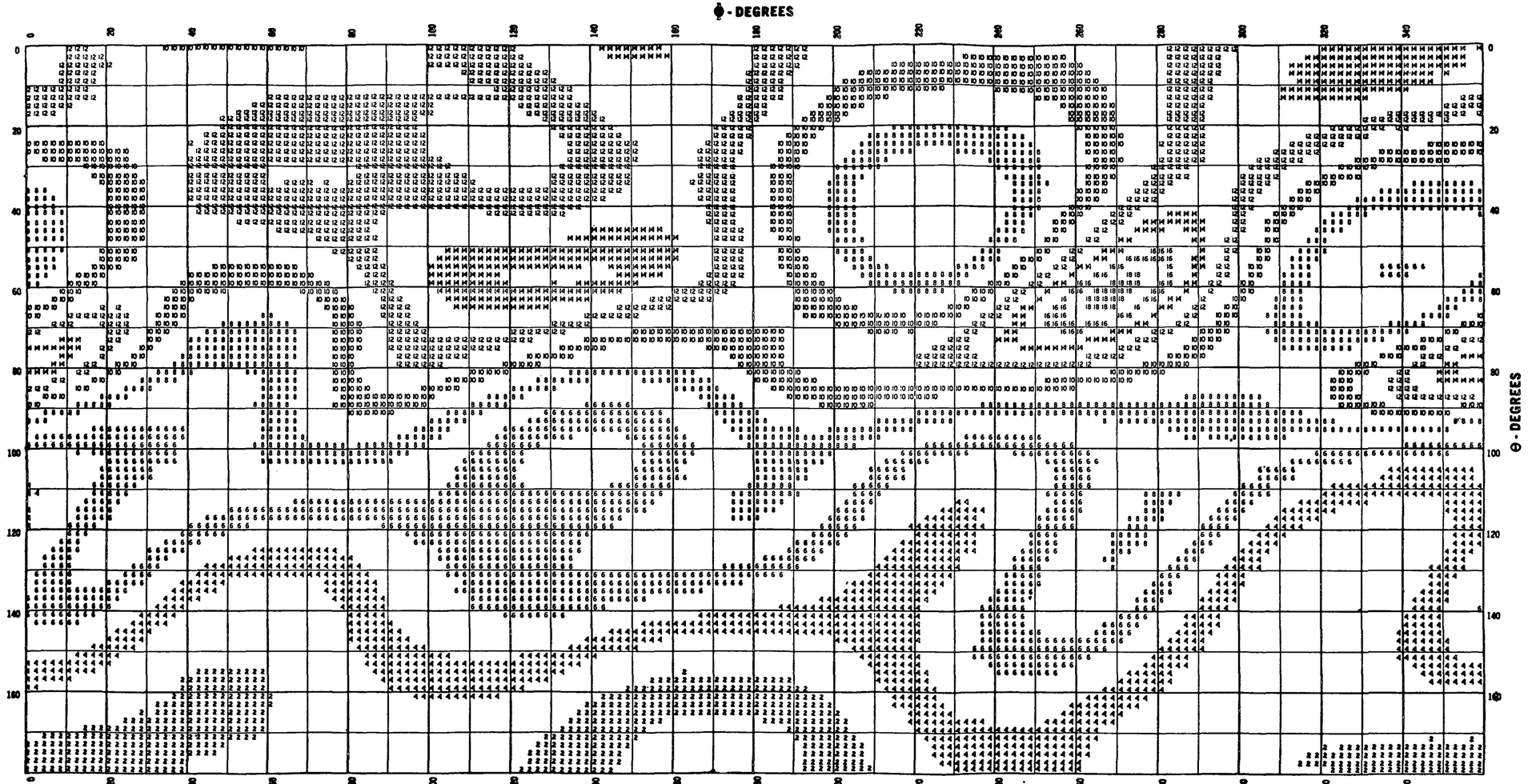

Figure 4-IX-8. Beacon Antenna Pattern, Solar Panels Stowed, (Vertical Polarization, Scale Factor 2.5:1, 342 MHz, 2.7-db Reference Level)

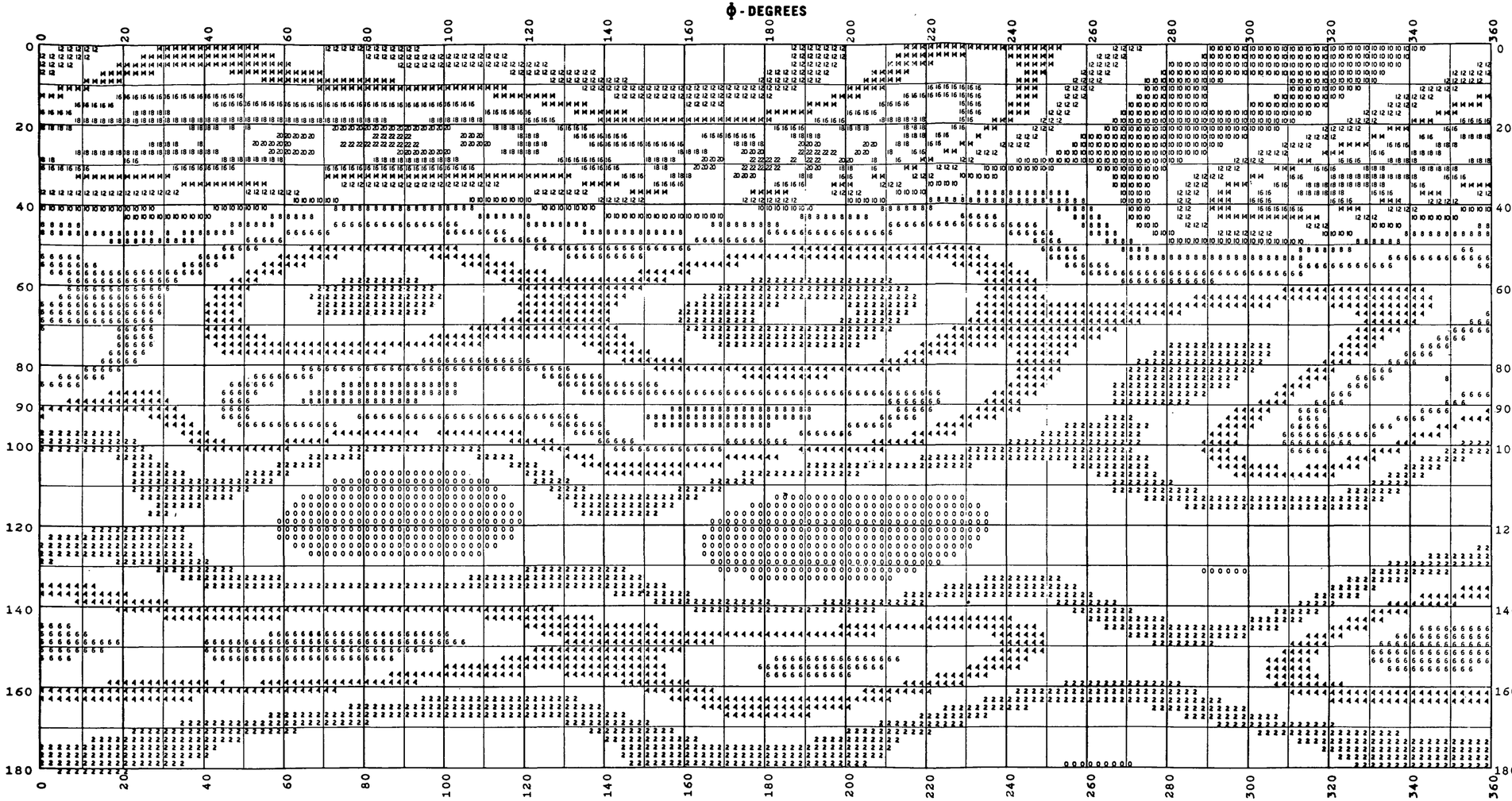

Figure 4-IX-9. Beacon Antenna Pattern, Solar Panels Deployed, (Vertical Polarization, Scale Factor 2.5:1, 342 MHz, 2.7-db Reference Level)

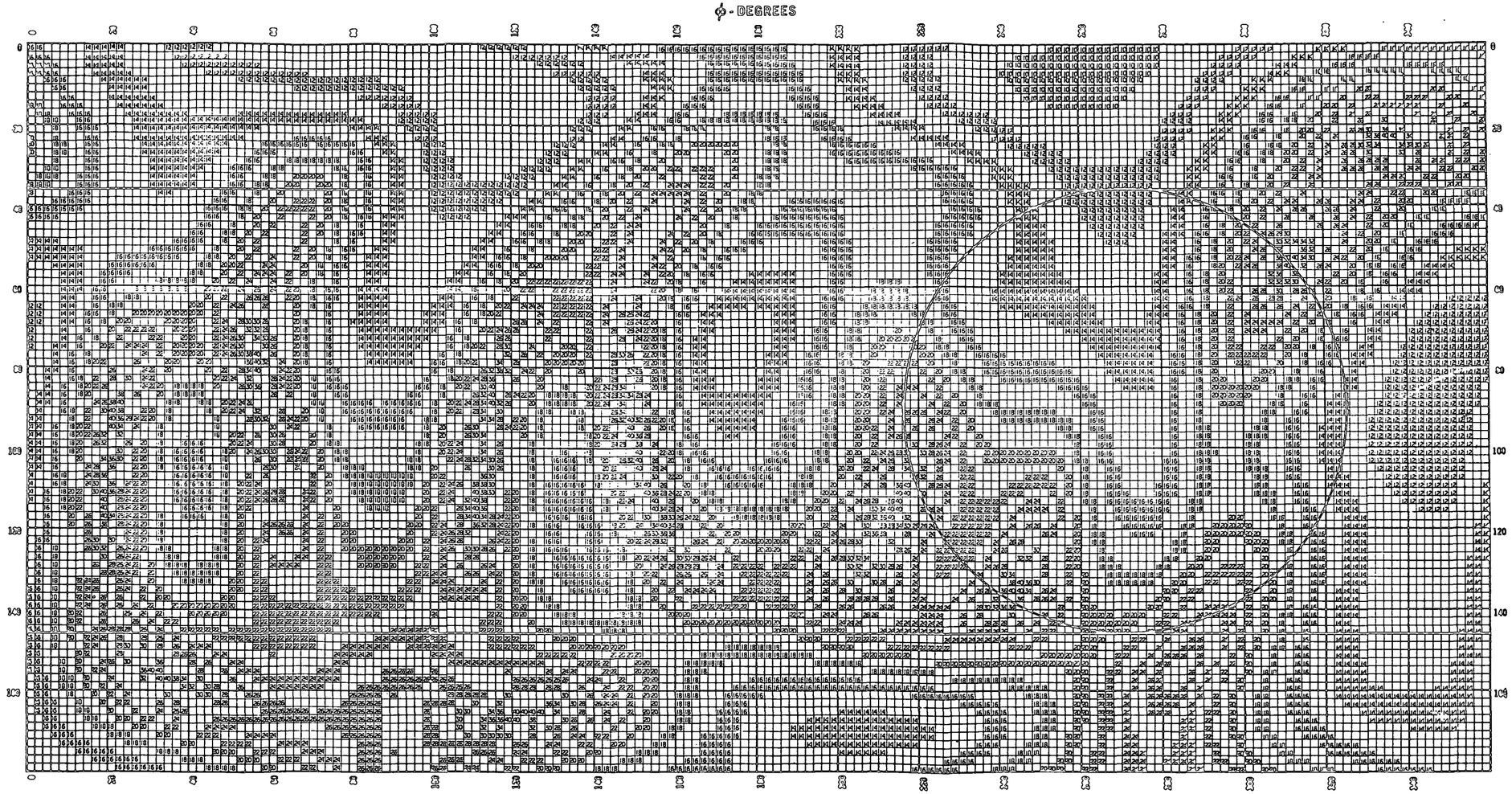

Figure 4-IX-10. Beacon Antenna Pattern, Solar Panels Deployed (Vertical Polarization, Scale Factor 2.5:1, 342 MHz, 3-db Reference Level)

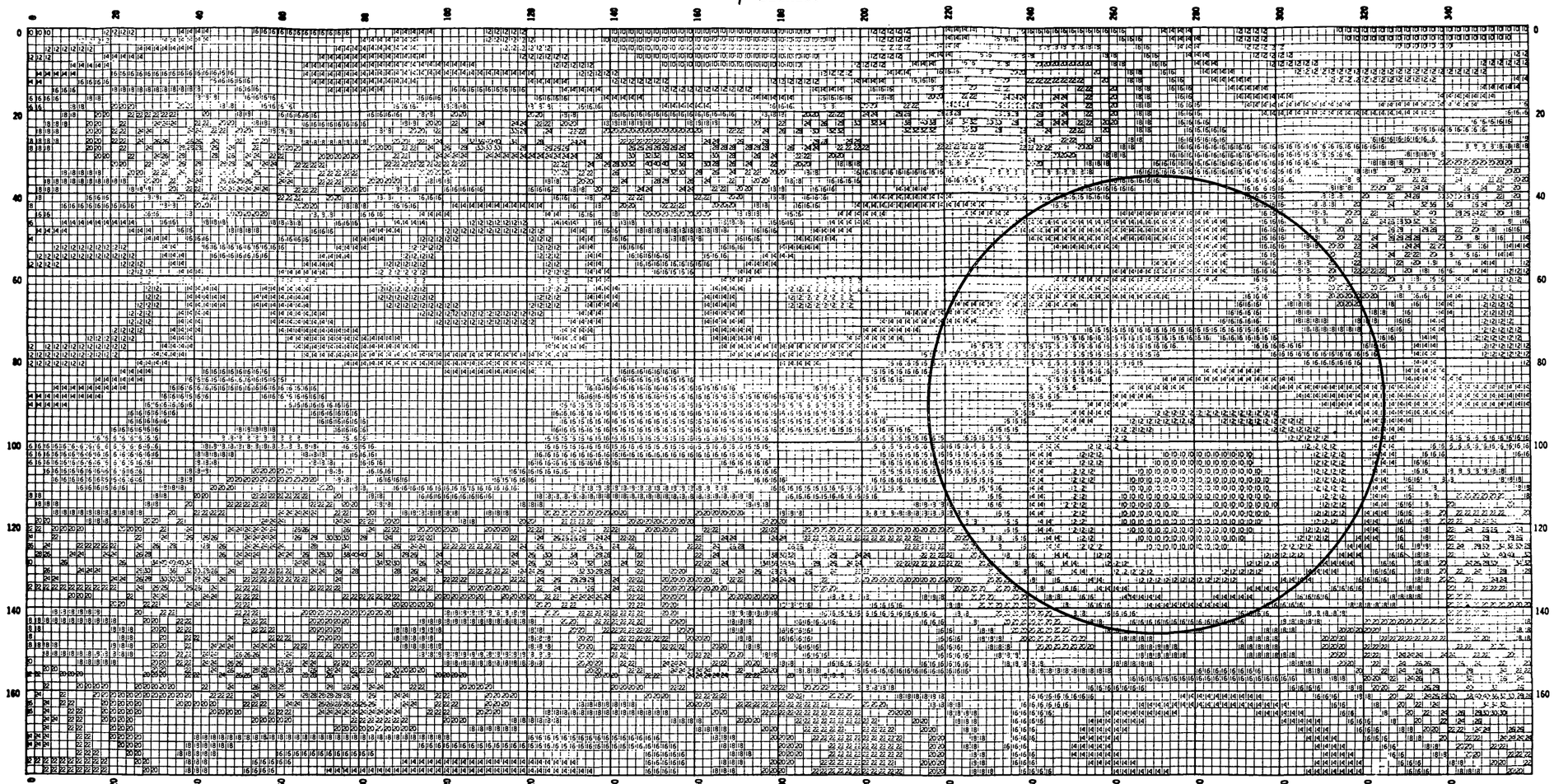

Figure 4-IX-11. Beacon Antenna Pattern, Solar Panels Deployed (Horizontal Polarization, Scale Factor 2.5:1, 342 MHz, 3-db Reference Level)

b. Beacon Transmitter Characteristics

The beacon transmitter is essentially the same as the present TOS beacon transmitter. However, the RF output is phase-modulated (PM) by two FM subcarriers instead of three, as in TOS beacon transmitter. The characteristics of the transmitter are given in Table 4-IX-8.

TABLE 4-IX-8. BEACON TRANSMITTER CHARACTERISTICS

Characteristic	Value
Modulation	Phase-modulated
Frequency	136.77 MHz
Frequency Stability	±0.005 percent
RMS Phase Deviation	0.86 radian
Subcarrier Inputs	
2.3-kHz Subcarrier	
Bandwidth	1240 Hz
Carrier Phase Deviation	0.70 radian +15 percent -10 percent
3.9-kHz Subcarrier	
Bandwidth	702 Hz
Carrier Phase Deviation	0.50 radian +15 percent -10 percent
RF Power Output	250 milliwatts
RF Information Bandwidth	8.5 kHz

The modulation linearity of the beacon transmitter shall be such that with the two subcarriers present and with the 2.3- and 3.9-kHz subcarriers modulating the carrier with a phase index of 0.70 and 0.50 radian, respectively, all intermodulation products from 700 Hz to 10.1 kHz shall be at least 30 db down from the 3.9-kHz tone. Intermodulation terms shall be measured at the output of a true FM detector.

The transmitter design shall minimize the spurious output (both radiated and conducted) in the 146- to 151-MHz range and in the subharmonics of this frequency band. When operating in a 1.5:1 VSWR or less, the level of any discrete frequency or broadband noise in a 40-kHz

noise bandwidth shall be as follows: (1) less than -100 dbm for bands centered from 148.25 to 148.75 MHz, (2) less than -70 dbm for all other bands centered from 146 to 151 MHz, and (3) less than -50 dbm in the band from 108 to 109 MHz. These frequency bands cover the command receiver RF bands and their image frequencies assuming that the center frequency is the same as TOS.

c. Dual Subcarrier Oscillator

A dual subcarrier oscillator assembly is used on ITOS. It consists of four voltage-controlled oscillators; two operate on a 2.3-kHz center frequency and two on a 3.9-kHz center frequency (IRIG channel No. 9). The VCO's form redundant pairs. Their characteristics are given in Table 4-IX-9.

TABLE 4-IX-9. DUAL SCO ASSEMBLY CHARACTERISTICS

Parameter	Attitude and Solar Proton Monitor Data	Housekeeping Telemetry
Center Frequency (f_c)	2.3 kHz	3.9 kHz (IRIG standard)
Deviation (percent f_c)	±20 percent	±7.5 percent
Deviation Bandwidth	40 percent	15 percent (IRIG standard)
Input Baseband	DC to 160 Hz	DC to 59 Hz
Subcarrier Information Bandwidth	1240 Hz	702 Hz
Input Sensitivity	0 to -5.0 volts DC with -2.5 volts DC producing f_c. Less negative input decreases frequency.	0 to -5.0 volts DC with -2.5 volts DC producing f_c. Less negative input decreases frequency.
Input Impedance	350 kohms min	350 kohms min
Load Impedance	33 kohms, +100 percent, -10 percent	33 kohms, +100 percent, -10 percent
Linearity (from best straight line: percent of p-p deviation)	±1 percent	±0.25 percent

TABLE 4-IX-9. DUAL SCO ASSEMBLY CHARACTERISTICS (Continued)

Parameter	Attitude and Solar Proton Monitor Data	Housekeeping Telemetry
Maximum Amplitude-Modulation on Output	±10 percent	±10 percent
Subcarrier Harmonic Distortion	less than 3 percent	less than 1 percent
Output Voltage	adjustable: 0 to 1.0 volt p-p into 8000 ohms load	adjustable: 0.10 to 1.0 volt p-p into 8000 ohms load
Output Impedance	39 kohms ±10 percent (AC coupled)	39 kohms ±10 percent (AC coupled)
Supply Voltage	-24.5 ±1.0 volts DC	-24.5 ±1.0 volts DC
Current per SCO	12 ma	12 ma
Center Frequency Drift (long term)	less than ±1 percent of deviation BW at 22°C	less than ±1 percent of deviation BW at 22°C
Temperature Stability	less than ±1.5 percent of deviation BW from -15 to +60°C	less than ±1.5 percent of deviation BW from -15 to +60°C
Number of Outputs per SCO	1	1
Size	1.91 by 1.58 by 1.031 inches	1.91 by 1.58 by 1.031 inches

d. Signal Conditioner and Telemetry Commutators

When driven by a 15-Hz signal from the programmer, the telemetry commutator normally samples 120 channels at a rate of 15 channels per second. The commutator can also be stopped in any position by controlling the number of pulses from the programmer. The output voltage from the telemetry commutator ranges between 0 and -5 volts DC.

Two commutators are used for redundancy. All telemetry points are applied through the signal conditioner to both commutators. A number of points are conditioned and analog points are combined in the signal conditioner. The commutators are solid-state devices and meet the specifications shown in Table 4-IX-10.

TABLE 4-IX-10. TELEMETRY COMMUTATOR CHARACTERISTICS

Characteristics	Values
Number of Channels	120
Sampling Rate	15 channels per sec or slower
Driving Programmer Signal	15 pps or variable
Input Signal Level	0 to -5 volts
Output Signal Level	0 to -5 volts into 10 kilohms minimum
PAM Ungated Output	99 percent duty cycle
Frame Pulse	18 ±2 volts, one data channel
Time Code Gate	Input date enables 1.2-second delay
Power Supply	-23 to -25 volts DC
Current	160 ma
DC Output (from +10-volt DC supply)	10 ma

4. Subsystem Analysis and Link Calculation

a. Receiver IF Bandwidth

(1) Receiver IF Information Bandwidth

A signal-to-noise ratio of 38.4 db rms/rms is obtained at the demodulator threshold of 12 db. A margin of 7.8 db above the 12-db FM threshold of the subcarrier demodulator is obtained with the phase index of the highest subcarrier frequency (3.9 kHz) set at 0.50 radian. With this phase index, a negligible amount of power lies outside the first pair of 3.9-kHz sidebands of the carrier frequency. The RF information bandwidth is then

$$\text{Information Bandwidth} = 2\ (3,900 + 351) = 8,500 \text{ Hz.}$$

(2) Doppler Shift

At a ground antenna elevation of 5 degrees, the maximum doppler shift at 136.77 MHz is ±2.65 kHz or a total of 5.3 kHz.

(3) Transmitter Frequency Uncertainty

The transmitter frequency instability is ±0.005 percent or ±6.8 kHz, which yields a total of 13.6 kHz.

The total RF bandwidth is:

Information	8.5 kHz
Doppler Shift	5.3 kHz
Instability	13.6 kHz
Total RF bandwidth	27.4 kHz

The ground station phase lock loop receiver tracks the frequency shifts due to doppler and transmitter frequency uncertainty. Therefore, the IF bandwidth of the receiver need only be wide enough to pass the 8.5-kHz information bandwidth. It has an IF bandwidth of 30 kHz which is adequate to handle the total RF bandwidth.

b. Subcarrier Phase Deviations

The RF input into the phase lock loop receiver can be expressed as $g(t) \approx A_c \cos(w_c t + \phi(t))$, where $\phi(t)$ is the phase modulation due to the two subcarriers of frequencies (f_A) and (f_B). The $\phi(t)$ is given by

$$\phi(t) = b_A \sin w_A t + b_B \sin w_B t.$$

The output of the phase lock detector is proportional to sin $\phi(t)$. It can be shown* that the demodulated subcarriers are

$$2J_1(b_A)\, J_o(b_B)\, A_c \sin w_A t \text{ (subcarrier } f_A) \text{ and}$$

$$2J_1(b_B)\, J_o(b_A)\, A_c \sin w_B t \text{ (subcarrier } f_B).$$

The individual subcarrier signal-to-noise power ratio is given by:

$$S_c/N_c = 2J_1^2(b_A)\, J_o^2(b_B) \left(\frac{Pc}{\eta B_{scA}}\right) \qquad \text{(for subcarrier A)}$$

where

$Pc = A_c^2/2$ is average carrier power,

η is IF noise density (watts in 1 Hz), and

B_{sc} is subcarrier bandwidth.

The distortion signals from the phase detector can be shown to be as follows:

Frequency	Power Level
$f_A \pm 2f_B$	$2J_1^2(b_A)\, J_2^2(b_B)\, P_c$
$f_B \pm 2f_A$	$aJ_1^2(b_B)\, J_2^2(b_A)\, P_c$
$3f_A$	$2J_o^2(b_B)\, J_3^2(b_A)$
$3f_B$	$2J_o^2(b_A)\, J_3^2(b_B)$

For small phase indices, the subcarrier signal-to-noise power ratio expression becomes approximately equal to $\frac{b^2}{2\eta B_{sc}}$.

* B. D. Martin, The Pioneer IV Lunar Probe: A Minimum Power FM/PM System Design, JPL TR-32-215, 1962.

It is desirable to design the system such that both subcarriers have approximately equal margin above the FM threshold. The phase deviation b_B of the 2.3-kHz subcarrier was selected to satisfy the following equation:

$$\frac{b_A}{\sqrt{B_{scA}}} \approx \frac{b_B}{\sqrt{B_{scB}}}$$

The subcarrier bandwidths are given below:

Channel A (3.9-kHz subcarrier IRIG channel No. 9)

Center Frequency	3.9 kHz
Deviation (Δf)	± 7.5 percent of center frequency
Baseband (f_m)	59 Hz
Subcarrier Bandwidth	702 Hz
RF Carrier Phase Index	0.50 radian

Channel B (2.3 kHz)

Center Frequency	2.3 kHz
Deviation	±20 percent
Baseband	160 Hz
Subcarrier Bandwidth	1240 Hz
RF Carrier Phase Index	0.70 radian

The 3-db attitude data bandwidth is 160 Hz in ITOS as compared to 25 Hz in TOS. In order to obtain a reasonable demodulated baseband signal-to-noise, a nonstandard deviation has to be selected. With this deviation, the composite subcarrier spectrum extends from 1.68 to 4.25 kHz. A voice channel of the TOS long lines can handle a spectrum extending from 1.60 to 4.4 kHz. An increase of subcarrier deviation beyond ±20 percent would extend the composite subcarrier spectrum beyond the capacity of a voice channel of the long lines. The composite spectrum is shown in Figure 4-IX-12.

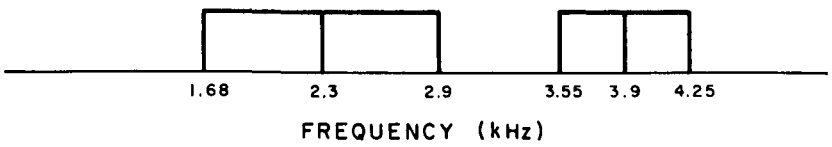

Figure 4-IX-12. Composite Subcarrier Spectrum of Demodulated Beacon and Telemetry Baseband

c. Distortion Products

The calculated distortion products occur at 0.7, 5.5, 6.9, 8.5, 10.1, and 11.7 kHz, and they fall outside the subcarrier spectrum. In addition, the subcarrier filters will provide at least 20-db attenuation of the intermodulation products. As an example, the unfiltered 0.7-kHz product is 30 db below the 2.3-kHz subcarrier tone.

d. Link Calculation

The circularly polarized beacon signal is intercepted by the 85-foot parabolic dish antenna system using polarization diversity reception. The ground station parameters are summarized in Table 4-IX-11.

TABLE 4-IX-11. CDA GROUND STATION PARAMETERS (BEACON RECEPTION)

Antenna Gain	27.6 db at 136.77 MHz
Polarization	Polarization diversity reception (-1.0 db)
Receiver Noise Figure	4.5 db
IF Bandwidth	30 kHz
Phase Lock Loop Threshold	-145 dbm

(1) System Noise Temperature

The receiver noise temperature, T_R, corresponding to a noise figure, F, of 4.5 db is

$$T_R = 290\ (F-1) = 530°K.$$

The sky noise temperature at 136 MHz for 95 percent of the sky is obtained from the set of curves given in Figure 4-IX-6 and is $T_s \approx 800°K$.

The total effective system temperature is

$$T_{sys} = 530 + 800 = 1330°K.$$

The noise power density at IF is then

$$\eta = K\,T_{sys} = -167.4 \text{ dbm in 1 Hz.}$$

Using the above value for η, the noise power for each subcarrier has been derived as shown in Table 4-IX-12.

TABLE 4-IX-12. SUBCARRIER NOISE POWER COMPUTATIONS

Subcarrier Channel	3.9 kHz	2.3 kHz	PLL
Subcarrier Bandwidth	702 Hz	1240 Hz	100 Hz
Subcarrier Bandwidth in db Hz	28.5 db Hz	30.9 db Hz	20 db Hz
Noise Power Density in 1 Hz	-167.4 dbm	-167.4 dbm	-167.4 dbm
Subcarrier Noise Power	-138.9 dbm	-136.5 dbm	-147.4 dbm

(2) Link Losses

The space loss at 2.5 degrees elevation, 775 nautical miles altitude, at 136 MHz is -147.6 db.

(3) Subcarrier Modulation Losses

The demodulated subcarrier power is given by $2J_1^2 (b_A)\ J_o^2 (b_B)\ P_c$

where P_c is the total carrier power, b_A is the peak phase deviation produced by the subcarrier of interest, and b_B is the peak phase deviation of the second subcarrier. The factor $2J_1^2 (b_A)\ J_o^2 (b_B)$ is the fraction of the carrier power recovered in the subcarrier. It is the modulation loss. The loss in the carrier frequency term is $J_O^2 (b_A)\ J_o^2 (b_B)$.

The modulation losses are given below:

	Modulation Loss
3.9-kHz subcarrier (housekeeping telemetry)	-11.1 db
2.3-kHz subcarrier (attitude and solar proton monitor data)	-7.9 db
Extracted carrier loss	-2.2 db

(4) Summary of Link Loss Calculations

The tabulation of the worst-case link calculations are given in Tables 4-IX-14, 4-IX-15, and 4-IX-16. The results are summarized below in Table 4-IX-13.

TABLE 4-IX-13. SUMMARY OF LINK CALCULATIONS

3.9-kHz Subcarrier S/N	19.8 db rms/rms in 702-Hz bandwidth 5 degree elevation
Margin above 12-db FM Threshold	7.8 db
Baseband S/N at Subcarrier Threshold	38.4 db rms/rms in 59-Hz bandwidth and ±7.5 percent deviation
Worst-Case Baseband S/N	46.2 db rms/rms or 49.2 db peak/rms
2.3-kHz Subcarrier S/N	20.6 db rms/rms in 1240-Hz bandwidth 5 degree elevation
Margin above 12-db Threshold	8.6 db

TABLE 4-IX-13. SUMMARY OF LINK CALCULATIONS (Continued)

Baseband S/N at Subcarrier Threshold	31.9 db rms/rms in 160-Hz bandwidth and ±20 percent deviation
Worst-Case Baseband S/N	40.5 db rms/rms or 43.5 peak/rms
PLL Carrier Tracking	
Receiver Carrier Power	-110.2 dbm @ 5 degree elevation
CDA Receiver Threshold	-145.0 dbm
Margin	34.8 db

TABLE 4-IX-14. WORST-CASE LINK CALCULATION FOR 3.9-kHz CHANNEL

Beacon Transmitter Power	24 dbm
Modulation Loss	-11.1 db
Spacecraft Antenna Gain (includes losses)	-11.5 db
Space Loss at 5 Degree Elevation	-147.1 db
Diversity Reception Loss*	-1.0
Receiving Antenna Gain (85 feet)	27.6 db
Received Subcarrier Power	-119.1 dbm
Subcarrier Noise Power	-138.9 dbm
Subcarrier-to-Noise Ratio	19.8 db rms/rms
FM Detector Threshold (assumed)	12.0 db
Margin above Threshold at 5° Elevation	7.8 db
Baseband S/N at Threshold	38.4 db rms/rms in 59-Hz baseband

*If one of the diversity channels falls below threshold, a 3-db loss is incurred.

e. Estimated S/N Degradation in Long Lines

The signal-to-noise ratios given previously cover only the link and receiving equipment noise. The multiplexed subcarriers at the CDA receiver output are transmitted via long lines to Suitland. These lines introduce additional noise.

TABLE 4-IX-15. WORST-CASE LINK CALCULATION FOR 2.3-kHz CHANNEL

Transmitter Power (0.250 W)	24 dbm
Modulation Loss	-7.9 db
Spacecraft Antenna Gain (includes losses)	-11.5 db
Space loss at 5-Degree Elevation	-147.1 db
Diversity Reception Loss*	-1.0 db
Receiving Antenna Gain (85 feet)	27.6 db
Received Subcarrier Power	-115.9 dbm
Subcarrier Noise Power	-136.5 dbm
Subcarrier-to-Noise Ratio	20.6 db rms/rms
FM Detector Threshold (assumed)	12.0 db
Margin above Threshold at 5-Degree Elevation	8.6 db
FM Improvement above Subcarrier S/N	19.9 db (±20 percent deviation)
Baseband S/N at Threshold	31.9 db rms/rms in 160-Hz bandwidth

*If one of the diversity channels falls below threshold, a 3-db loss is incurred.

Published measurements on TOS long lines* have shown the subcarrier-to-noise ratio to be 33.0 db rms/rms for the beacon and telemetry channel over a bandwidth of approximately 3000 Hz from Gilmore to Suitland. The long lines from Wallops to Suitland have a better ratio. The design goal for both lines is 23 db rms/rms.

*TOS Communications Test Results, Report TER-111, Telcom, Inc., prepared for ESSA-NESC, March 30, 1966.

TABLE 4-IX-16. LINK CALCULATION FOR CARRIER TRACKING

Transmitter Power (0.250 W)	24 dbm
Modulation Loss	-2.2 db
Spacecraft Antenna Gain (includes losses)	-11.5 db
Space Loss at 5 Degree Elevation	-147.1 db
Diversity Reception Loss	-1.0 db
Receiving Antenna Gain (85 feet)	27.6 db
Receiving Carrier Power	-110.2 dbm
Phase Lock Loop Tracking Threshold	-145.0 dbm
Margin above Threshold at 5 Degree Elevation	34.8 db
Noise Power	-147.4 dbm
S/N in Loop Bandwidth	37.2 db rms/rms

With this value of subcarrier-to-noise ratio, the demodulated baseband S_o/N_{LL} contributed by the lines alone (i.e., assuming a noiseless subcarrier into the line) is given in Table 4-IX-17. The signal-to-noise ratio due to the link S_o/N_o is combined with the long line S/N to yield the overall S/N at Suitland. The ratios are combined according to the following equation:

$$\frac{N_T}{S_o} = \frac{N_{LL}}{S_o} + \frac{N_o}{S_o} .$$

TABLE 4-IX-17. S/N CONTRIBUTION BY THE LONG LINES

Subcarrier	Baseband Link S/N at Threshold	Baseband Long Lines S/N	Net S/N	Bandwidth
2.3 kHz (±20 percent dev.)	31.9 db rms/rms	46.7 db rms/rms	31.8 db rms/rms	160 Hz
3.9 kHz (±7.5 percent dev.)	38.4 db rms/rms	55.7 db rms/rms	38.4 db rms/rms	59 Hz

The long lines are not expected to produce any appreciable degradation of the demodulated baseband signal-to-noise ratio.

5. Telemetry List

The list of housekeeping telemetry points is shown in Table 4-IX-18. The analog telemetry signals from redundant commutators are combined in OR-type circuits. The digital signals are combined into multilevel signals. The combining of the analog signals could take place in the signal conditioner or in the boxes concerned, depending on the degree of complexity involved. The combining of digital signals will be done in the boxes concerned.

TABLE 4-IX-18. ASSIGNMENT OF TELEMETRY POINTS FOR ITOS

Telemetry Commutator Channel	Assignment	Type
1	-0.5-v DC calibration	Analog
2	-1.5-v DC calibration (commutator 1)	Analog
	-3.5-v DC calibration (commutator 2)	Analog
3	-3.5-v DC calibration (commutator 1)	Analog
	-1.5-v DC calibration (commutator 2)	Analog
4	-4.5-v DC calibration	Analog

TABLE 4-IX-18. ASSIGNMENT OF TELEMETRY POINTS FOR ITOS (Continued)

Telemetry Commutator Channel	Assignment	Type
5	Satellite identification	Single level digital
6	DFC A/D converter output	Multilevel digital
7	Command receiver No. 1 AGC	Analog
8	Command receiver No. 2 AGC	Analog
9	Decoder selection	Multilevel digital
10	-5.0-v DC marker	Single level digital
11	Solar array current - panel A	Analog
12	Solar array current - panel B	Analog
13	Solar array current - panel C	Analog
14	Solar array voltage	Analog
15	Unregulated bus voltage	Analog
16	Regulated bus voltage	Analog
17	Shunt dissipator current	Analog
18	Shunt limiter control ampl. selection	Multilevel digital
19	Regulator selection and high temp. cut-out override verification	Multilevel digital
20	-5.0-v DC marker	Single level digital
21	Shunt dissipator temperature No. 1	Analog
22	Shunt dissipator temperature No. 2	Analog
23	Shunt dissipator temperature No. 3	Analog

TABLE 4-IX-18. ASSIGNMENT OF TELEMETRY POINTS FOR ITOS (Continued)

Telemetry Commutator Channel	Assignment	Type
24	Battery No. 1 voltage	Analog
25	Battery No. 1 current	Analog
26	Battery No. 1 temperature	Analog
27	Battery No. 2 voltage	Analog
28	Battery No. 2 current	Analog
29	Battery No. 2 temperature	Analog
30	-5.0-v DC marker	Single level digital
31	Solar panel A temperature	Analog
32	Solar panel B temperature	Analog
33	Solar panel C temperature	Analog
34	Picture programmer No. 1 status	Multilevel digital
35	Picture programmer No. 2 status	Multilevel digital
36	QOMAC programmers Nos. 1 and 2 status	Multilevel digital
37	Programmers Nos. 1 and 2 IR operation control status	Multilevel digital
38	Real-time transmitter daytime radiometer modulation selection	Multilevel digital
39	Real-time transmitter operation mode selection	Multilevel digital
40	-5.0-v DC marker	Single level digital
41	Time base unit selection and beacon transmitter selection	Multilevel digital

TABLE 4-IX-18. ASSIGNMENT OF TELEMETRY POINTS FOR ITOS (Continued)

Telemetry Commutator Channel	Assignment	Type
42	Data format converter status	Multilevel digital
43	Solar proton monitor output power	Analog
44	Solar proton monitor bracket temperature	Analog
45	Flat plate radiometer status	Multilevel digital
46	Incremental recorder power status	Multilevel digital
47	Incremental recorder enclosure pressure	Analog
48	SR processor No. 1 or 2, negative power	Multilevel digital
49	SR processor No. 1 or 2, positive power	Multilevel digital
50	-5.0-v DC marker	Single level digital
51	Momentum coil status	Multilevel digital
52	Magnetic bias switch position	Multilevel digital
53	Magnetic bias power status and polarity	Multilevel digital
54	QOMAC power and mode status	Multilevel digital
55	Scanning radiometer selection	Multilevel digital
56	Scanning radiometer No. 1 or 2, phase No. 1 power	Multilevel digital
57	Scanning radiometer No. 1 or 2, motor monitor	Multilevel digital
58	Scanning radiometer No. 1 housing cavity temperature	Analog

TABLE 4-IX-18. ASSIGNMENT OF TELEMETRY POINTS FOR ITOS (Continued)

Telemetry Commutator Channel	Assignment	Type
59	Scanning radiometer No. 2 housing cavity temperature	Analog
60	-5.0-v DC marker	Single level digital
61	Scanning radiometer (SR) recorder selection	Multilevel digital
62	SR recorder No. 1 status	Multilevel digital
63	SR recorder No. 1 motor drive current phase 1	Analog
64	SR recorder No. 1 enclosure pressure	Analog
65	SR recorder No. 1 transport temperature	Analog
66	SR recorder No. 2 status	Multilevel digital
67	SR recorder No. 2 motor drive current - phase 1	Analog
68	SR recorder No. 2 enclosure pressure	Analog
69	SR recorder No. 2 transport temperature	Analog
70	-5.0-v DC marker	Single level digital
71	AVCS recorder selection	Multilevel digital
72	AVCS recorder No. 1 status	Multilevel digital
73	AVCS recorder No. 2 status	Multilevel digital
74	AVCS recorder No. 1 enclosure pressure	Analog
75	AVCS recorder No. 1 transport temperature	Analog
76	AVCS recorder No. 2 enclosure pressure	Analog

TABLE 4-IX-18. ASSIGNMENT OF TELEMETRY POINTS FOR ITOS (Continued)

Telemetry Commutator Channel	Assignment	Type
77	AVCS recorder No. 2 transport temperature	Analog
78	AVCS recorder No. 1 or 2 motor drive current - phase one	Analog
79	Multiplexer selection	Multilevel digital
80	-5.0-v DC marker	Single level digital
81	S-band transmitter selection	Multilevel digital
82	S-band transmitter No. 1 or 2 RF power output	Analog
83	S-band transmitter No. 1 temperature	Analog
84	S-band transmitter No. 2 temperature	Analog
85	Real-time transmitter selection	Analog
86	Real-time transmitter No. 1 temperature	Analog
87	Real-time transmitter No. 2 temperature	Analog
88	Real-time transmitter No. 1 or 2 RF power output	Analog
89	Real-time transmitter No. 1 or 2 RF driver stage output	Analog
90	5.0-v DC marker	Single level digital
91	APT camera selection	Multilevel digital
92	APT camera No. 1 vidicon target temperature	Analog
93	APT camera No. 2 vidicon target temperature	Analog

TABLE 4-IX-18. ASSIGNMENT OF TELEMETRY POINTS FOR ITOS (Continued)

Telemetry Commutator Channel	Assignment	Type
94	APT camera No. 1 or 2 G-1 regulator voltage output	Analog
95	APT camera No. 1 or 2 vidicon filament current	Analog
96	APT camera No. 1 or 2 horizontal and vertical deflection	Analog
97	APT camera No. 1 or 2 -6.3-volt regulator output	Analog
98	APT camera No. 1 or 2 hold and ped. internal	Multilevel digital
99	Active thermal control flap position No. 1	Analog
100	-5.0-v DC marker	Single level digital
101	AVCS camera selection	Multilevel digital
102	AVCS camera No. 1 head temperature	Analog
103	AVCS camera No. 2 head temperature	Analog
104	AVCS camera No. 1 or 2 filament current	Analog
105	AVCS camera No. 1 or 2 standby power	Analog
106	AVCS camera No. 1 or 2 power and regulator	Analog
107	Pitch loop selection and index selection	Multilevel digital
108	Pitch loop mode	Multilevel digital
109	Pitch sensor and roll sensor selection	Multilevel digital
110	-5.0-v DC marker	Single level digital

TABLE 4-IX-18. ASSIGNMENT OF TELEMETRY POINTS FOR ITOS (Continued)

Telemetry Commutator Channel	Assignment	Type
111	Drive motor No. 1 or 2 voltage	Analog
112	Pitch loop No. 1 or 2 converter, plus 15 volts	Analog
113	Pitch loop No. 1 or 2 converter, minus 15 volts	Analog
114	Flywheel bearing temperature	Analog
115	Baseplate temperature	Analog
116	APT side wall temperature	Analog
117	AVCS side wall temperature	Analog
118	Thermal fence temperature	Analog
119	Thermal control reservoir - APT side temperature	Analog
120	Spare	—

D. REAL-TIME VIDEO LINK

1. General

The sensor input for the real-time video link is obtained from either one of the two redundant APT cameras or from one of the two redundant scanning radiometers. Under normal operating conditions, the input is obtained from one APT camera during the daylight and from one of the scanning radiometers during the nighttime portion of the orbit. A back-up mode permits an input to be obtained from a radiometer during the daytime portion of the orbit.

The signal output of the selected sensor amplitude modulates a 2.4-kHz subcarrier; this modulated subcarrier in turn frequency modulates one of the 137.5-MHz real-time transmitters. The output of the selected transmitter is coupled through a coaxial switch and notch filter to a pair of half-wavelength dipoles mounted on the extremity of one of the solar panels. Figure 4-IX-13 shows a simplified block diagram of the real-time data video link.

2. Video Signal Characteristics

a. APT Signals

The APT data are divided into frames, normally 11 frames being transmitted during each orbit. The total coverage of each frame at the nominal orbit altitude is 1700 by 1700 nautical miles, and the resolution at the center of each picture is 2 nautical miles. Each frame contains 800 lines, and is preceded by a 300-Hz "start" tone which is transmitted for 3 seconds, followed by a phasing signal consisting of 12.5-millisecond phasing pulses transmitted every 250 milliseconds for a period of 5 seconds. The duration of each video line is also 250 milliseconds. Each line commences with a 12.5-millisecond blanking period.

The video signal has a baseband of 1600 Hz, frequencies above 1600 Hz being attenuated at a rate of 24 db per octave. The modulator stage combines the video signal with a 2400-Hz sinewave to produce the 2400-Hz amplitude-modulated video subcarrier used for modulating the TV transmitter. A white level corresponds to 100-percent subcarrier amplitude, and a black level corresponds to 2.5-percent subcarrier amplitude. During the phasing cycle, the subcarrier is held at the white level except during the phasing pulses which are at black level. During the 800 video lines, the blanking pulse is held at the white level. The modulated subcarrier is applied as an FM modulating signal to the 137.5-MHz TV transmitter.

b. SR Signals

The scanning radiometer scans at a rate of 48 lines per minute and has a field of view of 5.3 milliradians. The earth scan occupies 110 degrees of the 360-degree rotation, and the sensor resolution is 4.0 nautical miles at the center of the scan. The dynamic

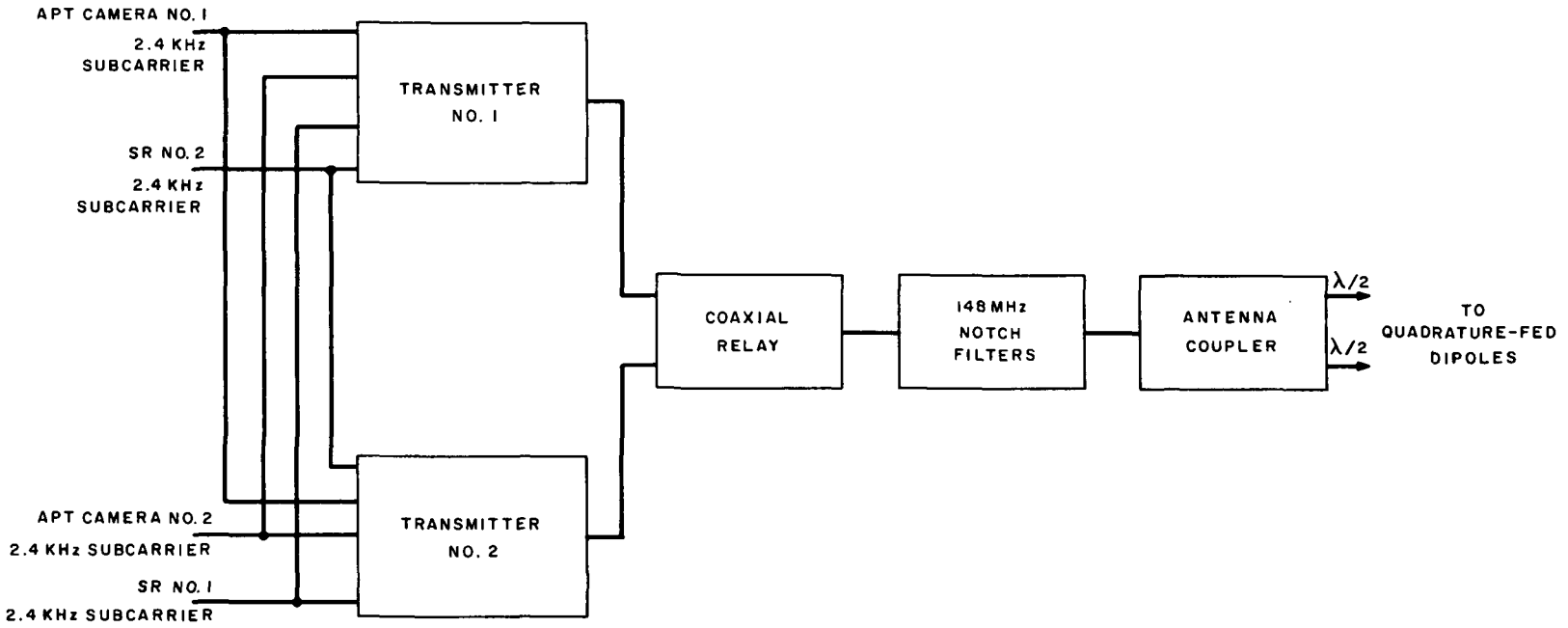

Figure 4-IX-13. Real-Time Transmission Link, Block Diagram

range of the IR detector is such that the sensor responds to radiation in the temperature range from 185 to 330°K in the spectral region from 10.5 to 12.5 microns, and has a temperature resolution of 4.0°K at 185°K and 1.0°K at 300°K. The visible channel detector responds to a scene brightness of 20 to 8500 foot-lamberts in the spectral region from 0.52 to 0.73 microns.

A marker pulse sequence is generated commencing at a point 75 degrees following the nadir. It consists of one pulse of 60-milliseconds duration with a back and front porch of 20 milliseconds. The sync pulse is 25 percent greater than the "hot" level, while the porches are at approximately the cold level. The spectrum of the SR video signal is from DC to 450 Hz. The spectrum of the SR sync signal is from DC to 1250 Hz.

A modulator in the SR processor combines the radiometer output signals with a 2.4-kHz sine wave to produce the 2400-Hz amplitude-modulated subcarrier used for modulating the real-time transmitter. The output signals from the SR processor are shown in Figure 4-IX-14. For the IR channel, "cold" corresponds to 100-percent subcarrier amplitude, and "hot" corresponds to 5-percent subcarrier amplitude. This results in compatibility of the ground display between APT and SR since clouds will always appear white on the facsimile display. The modulated subcarrier is in turn applied as an FM modulating signal to the 137.5-MHz real-time transmitter.

3. Real-Time Transmitter

a. Video Coupler

The video coupler, which is an integral part of the transmitter, couples the output of either APT camera system or either SR processor to the operating TV transmitter. The video coupler has four inputs.

b. Transmitter

The real-time transmitter operates at a center frequency of 137.5 MHz and produces a minimum of 5 watts of RF output power. Solid-state circuitry is employed throughout the transmitter.

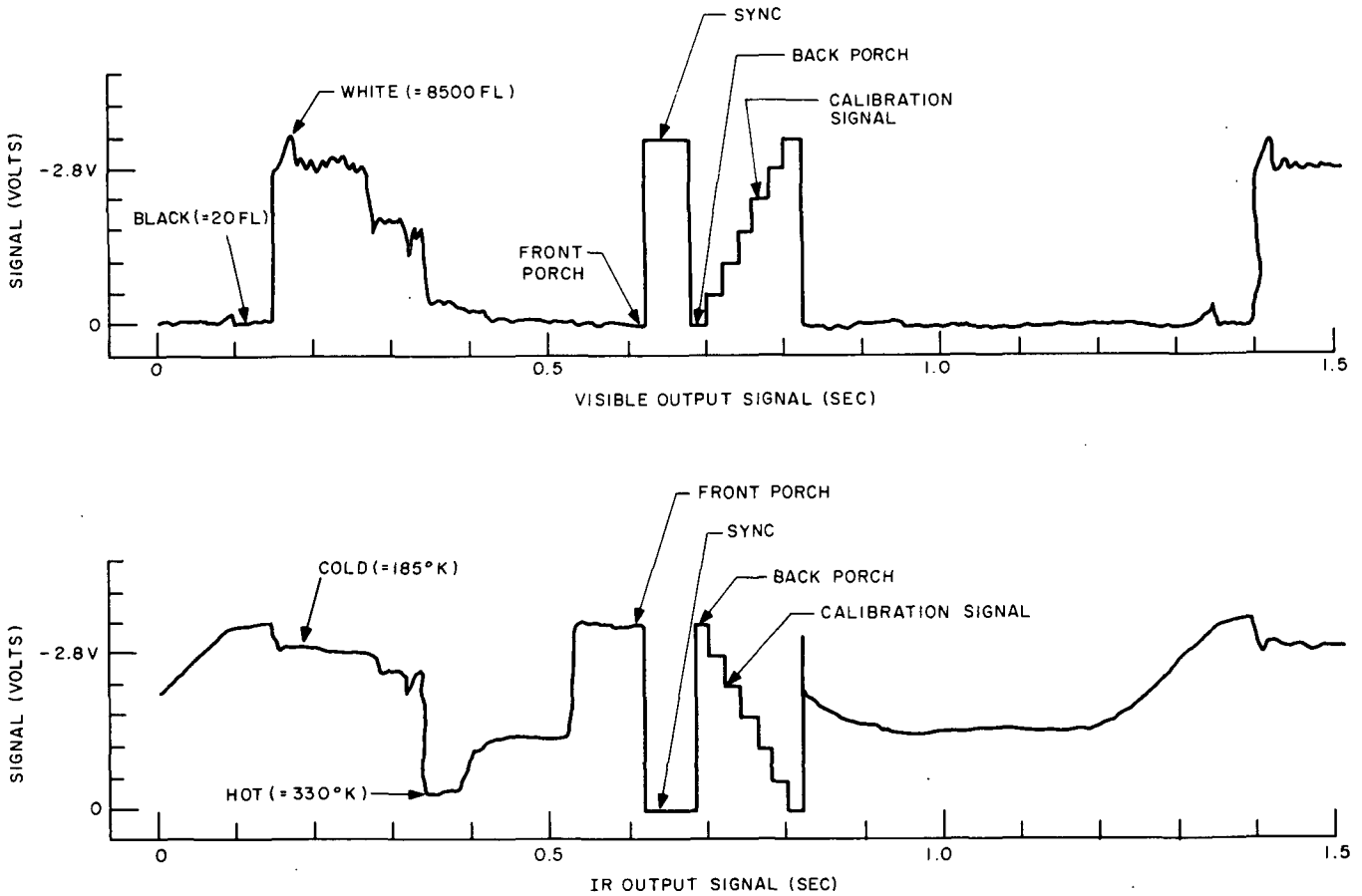

Figure 4-IX-14. Real-Time IR and Visible Channel Output Signals from SR Processor

Figure 4-IX-15 shows a simplified block diagram of the transmitter. The amplitude-modulated 2.4-kHz subcarrier is applied to a voltage-controlled oscillator. The output of the VCO is amplified and applied to the power amplifier. The modulation sensitivity of the transmitter is such that a 1-volt rms signal at 2.4 kHz will produce a 9 ±1 kHz deviation of the center frequency.

The following parameters are monitored as telemetry inputs:

- Power amplifier heat sink temperature
- RF drive, and
- RF output.

An additional telemetry signal indicates the transmitter selection. The real-time transmitter meets the following specifications:

Modulation	FM
Frequency	137.5 MHz
Frequency Stability	±0.005 percent

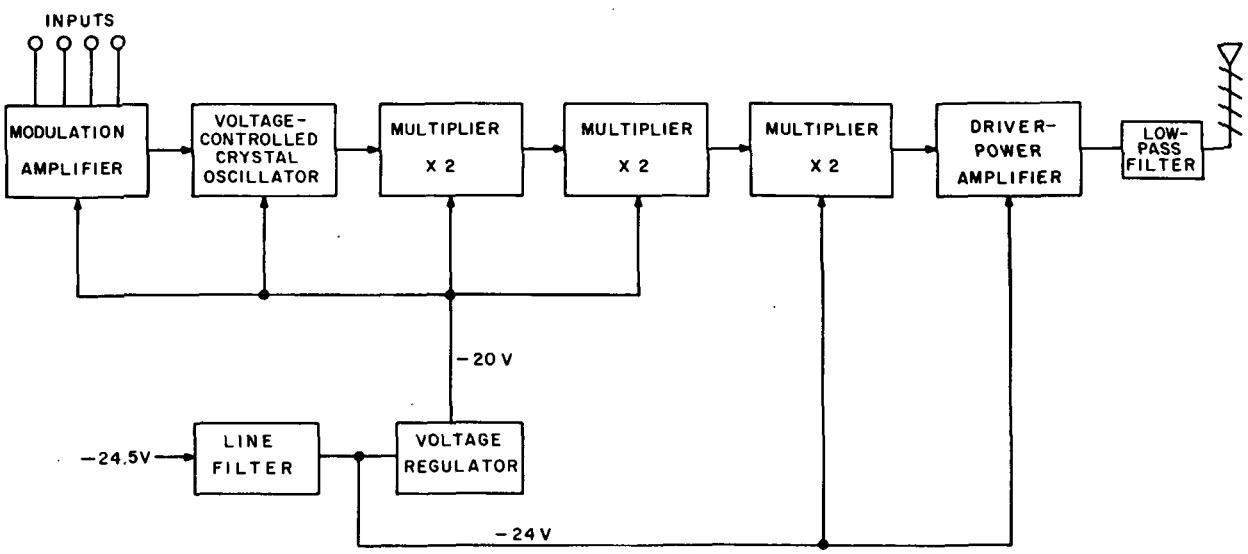

Figure 4-IX-15. Real-Time Transmitter, Block Diagram

Peak Deviation	9 ± 1 kHz
Modulation Bandwidth	5 kHz
Power Output (min)	5 watts
Power Input (max)	18 watts
Efficiency (min)	30 percent

4. Real-Time Antenna

The real-time antenna is composed of APT half-wave quadrature-fed dipoles, the antenna coupler, a 148-MHz notch filter, and the RF coaxial switch. Except for the antenna and the antenna coupler, all other components are existing flight-proven equipment.

The antenna is composed of two half-wave dipoles installed at the extremity of solar panel A, as shown in Figure 4-IX-16 (a). The two dipoles are fed in phase quadrature. This produces an antenna pattern which concentrates the RF power in the region ±55 degrees about the local vertical in the direction of the earth and minimizes the power wasted in back and side lobes. The baseline antenna coupler is also shown in Figure 4-IX-16 (b). The electrical feed to one dipole has an electrical length L. The other feed has a length L +90 degrees.

The minimum antenna gain imposed by systems requirements is -5.3 db (including all losses from transmitter port to free space). The spacecraft losses are contributed by the coaxial switch, the notch filters, and the antenna coupler. The measured antenna directivity on the spacecraft, with solar panels deployed, (no losses included) is plotted in Figure 4-IX-17. The pattern is shown in the same format as the beacon and command antenna patterns. In this case, only Region I is of concern since the real-time system is operational only when the spacecraft is stabilized. The pattern of Figure 4-IX-17 shows the measured pattern exceeds the requirement.

The preliminary characteristics of the baseline antenna are given in Table 4-IX-19.

TABLE 4-IX-19. BASELINE ANTENNA CHARACTERISTICS

Characteristic	Value
Frequency	137.5 MHz
Polarization	linear

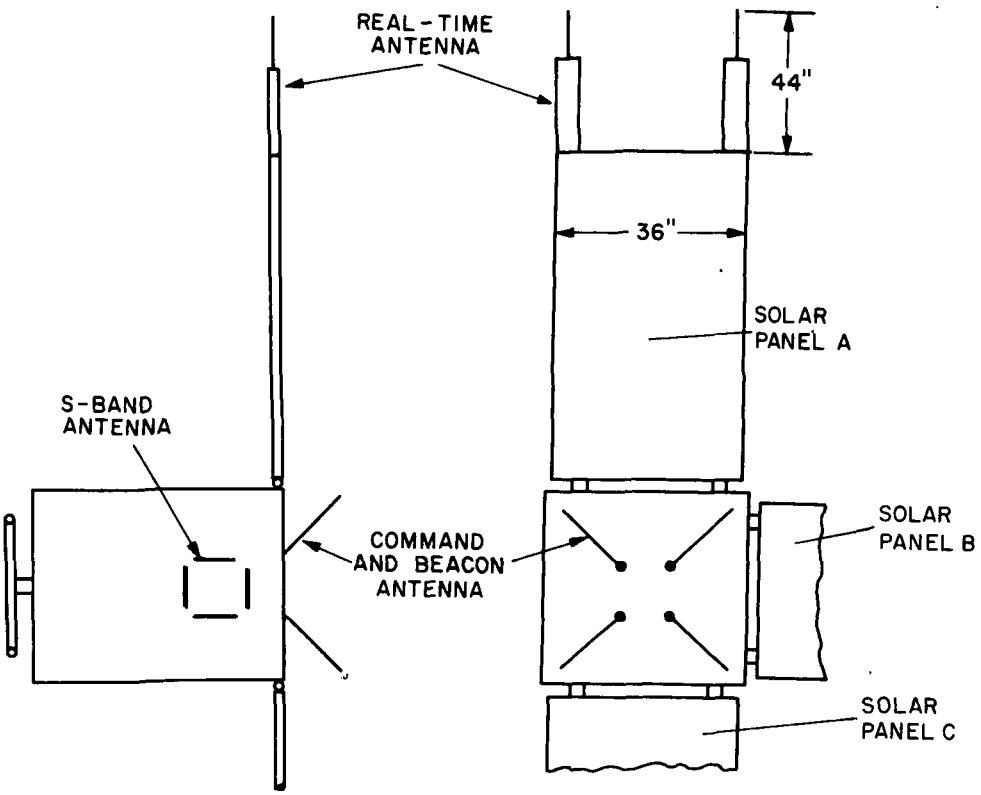

(a) REAL-TIME ANTENNA

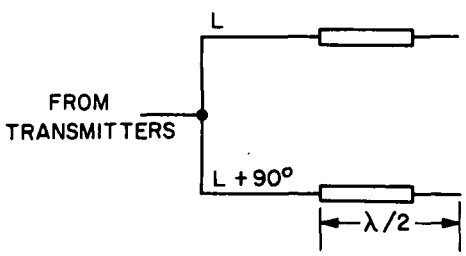

(b) REAL-TIME ANTENNA COUPLER

Figure 4-IX-16. Baseline Real-Time Video Link Antenna

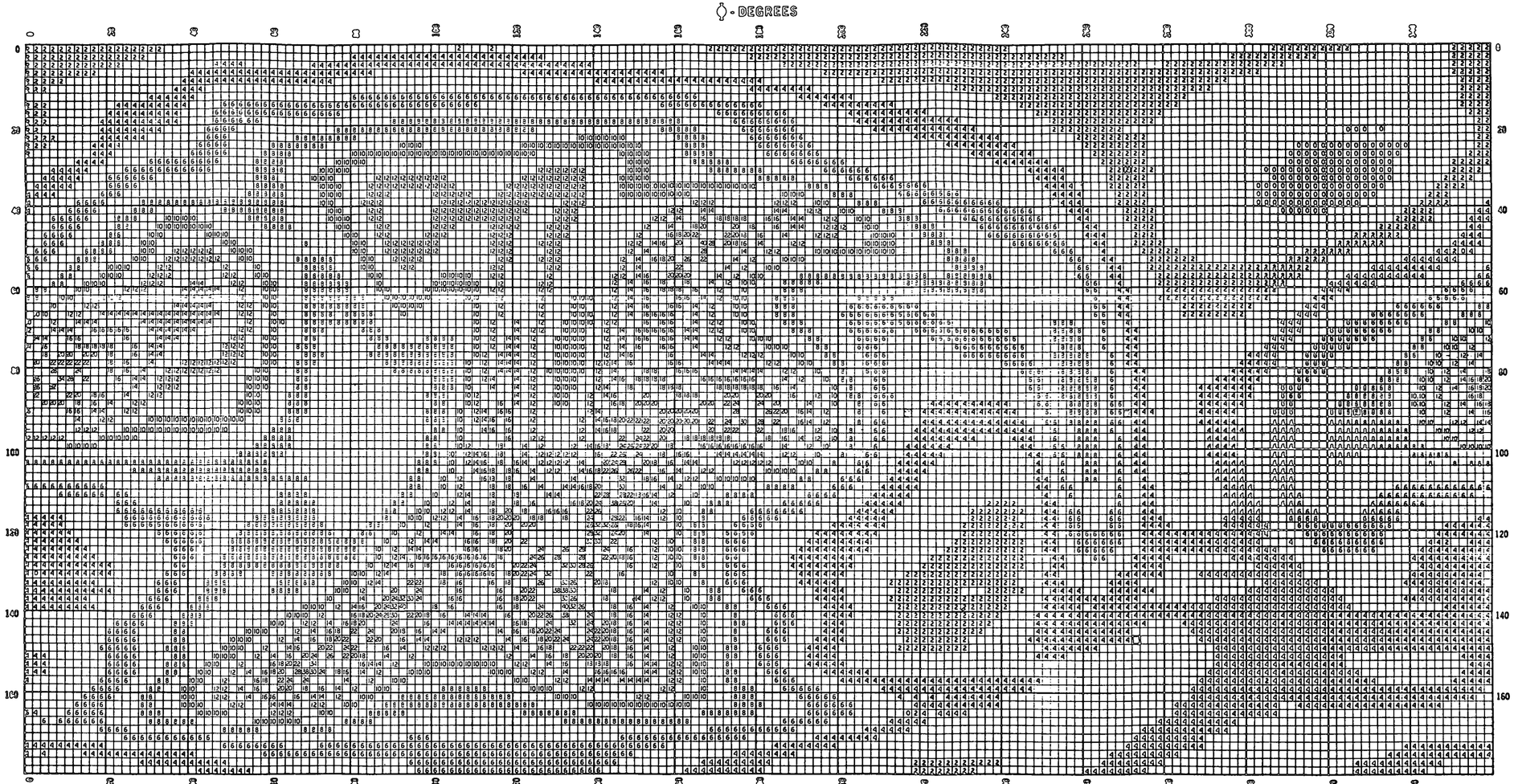

Figure 4-IX-17. Real-Time Antenna Gain (Right-Circular Polarization, Scale Factor 2.5:1, 344 MHz, Preliminary Data)

TABLE 4-IX-19. BASELINE ANTENNA CHARACTERISTICS (Continued)

Characteristic	Value
Minimum Gain (including all losses from antenna port to free space)	-5.3 db (over 120-degree cone centered on stabilized local vertical)
VSWR	1.5 (maximum)
Power Capability	10 watts
Weight	2 pounds maximum (antenna alone) 1 pound maximum (coupler)

The antenna polarization is linear. This is the simplest way of achieving compatability with the APT field stations which are equipped with an 8-turn helical antenna right-hand circular (RHC) polarized; however, there is a 3-db polarization loss.

The coaxial switch and the 148-MHz notch filter are the same equipment used on TOS APT. The notch filter is necessary to provide the proper isolation between the real-time transmitter and the command receiver at command frequency. The following minimum isolations are required between the real-time transmitter port to the command receiver port:

Real-time transmitter port to command receiver port at APT frequency: 67 db

Real-time transmitter port to command receiver port at command frequency: 45 db

Real-time transmitter port to command receiver port at command image frequency (108 MHz): 25 db

5. Subsystem Analysis and Link Calculation

a. RF Link Calculation

The results of the link analysis are summarized in Table 4-IX-20. There is a 3-db loss between the linearly polarized spacecraft antenna and the circularly polarized

ground antenna. The remaining losses and gains are due to antenna coupling and antenna directivity.

Since the receiver is assumed to have a noise figure of 4.5 db maximum, the receiver noise temperature is 530°K. A sky noise temperature of 800°K is taken for 95 percent of the radio sky. The system noise temperature is then 530 +800 = 1330°K. Therefore, in a 50-kHz IF bandwidth, the noise power is -120.3 dbm.

The highest C/N at FM threshold occurs for the highest modulation index, corresponding to the maximum 2.4-kHz subcarrier level from the APT camera subsystem. The highest modulation index occurs for a white scene and results in a full 10-kHz peak deviation of the FM carrier (applying worst-case transmitter deviation tolerance). This worst-case signal results in a threshold at C/N of 10:0 db.

b. Verification of RF Bandwidth Requirements

The total information bandwidth is: bw = 2 (f_d + f_H) where f_d is peak deviation and f_H is maximum modulating frequency. For the real-time link, f_H = 2.4 + 1.6 = 4.0 kHz; f_d = 10 kHz; thus, an information bandwidth of 28 kHz is required to include 99 percent of the power.

The doppler shift of the signal is 5.3 kHz, while the allowance for transmitter instability is 13.8 kHz (20.005 percent of 137.5 MHz). The total bandwidth required in 47.1 kHz. The 50-kHz IF bandwidth of the field station receiver is therefore adequate.

TABLE 4-IX-20. REAL-TIME LINK PARAMETERS (FIELD STATIONS)

Parameter	Worst-Case Value
Transmitter Power (5 watts min)	+37.0 dbm
Transmitter Antenna Gain (including 1-db loss; over ±60 degrees about local vertical)	-5.3 db
Polarization Loss	-3.0 db
Path Loss (5 degree elevation angle)	-147.2 db

TABLE 4-IX-20. REAL-TIME LINK PARAMETERS (FIELD STATIONS) (Continued)

Parameter	Worst-Case Value
Receiver Antenna Gain	+12.5 db
Line Losses	-1.0 db
Received Power	-107 dbm
Effective Noise Temperature	1330°K
Predetector Noise Bandwidth	50 kHz
Equivalent Noise Input	-120.3 dbm
$(C/N)_{IF}$	+13.3 db
Threshold	+10.0 db
RF Margin	3.3 db
AM Subcarrier S/N (at threshold)	+28.8 db
Video Black-to-White Level/rms (5-degree elev. - worst-case C/N)	34.6 db

c. Real-Time Baseband Signal-to-Noise Ratio

The signal-to-noise ratio at the output of the receiver can be determined by considering both the signal-to-noise ratio at the discriminator output (subcarrier) and the signal-to-noise ratio after the AM detector (demodulated). This ratio is determined for the case where the received signal carrier-to-noise ratio is at the threshold level, and where the signal is varying from black to white at the baseband frequency. The subcarrier signal-to-noise ratio is:

$$(S/N)_{FM} = (C/N)\ 3\frac{\Delta f^2}{f_H^2} \times \left(\frac{B_{IF}}{2f_H}\right),$$

$$= 28.9 \text{ db rms/rms},$$

where $(C/N)_{IF}$ = 10.0 db at threshold,

Δf = 8 kHz (worst-case),

f_H = 4.0 kHz, and

B_{IF} = 50 kHz.

The demodulated S/N can be calculated from the subcarrier-to-noise ratio. The peak FM deviation Δf corresponds to the peak subcarrier level A_p (white). The peak voltage into the transmitter is A_p = 2.8 volts p-p. The minimum voltage is A_m (black) = 0.070 volt p-p. This yields the AM modulation index, m, with respect to the average subcarrier:

$$m = \frac{A_p - A_m}{A_p + A_m} = 95 \text{ percent.}$$

However, since the peak deviation of 9 ±1 is assigned to the white level and not to the average subcarrier level, the fraction of unmodulated subcarrier power which goes into a demodulated black-to-white sinusoidal signal is $\frac{(1 - \alpha)^2}{4}$

where $\alpha = \frac{A_m}{A_p}$, and the demodulated ratio is:

$$S_o/N_o \text{ (rms/rms)}^2 = \frac{(1 - \alpha)^2}{4} \; S_c/N_c \text{ (assuming } B_{sc} = 2f_m),$$

where B_{sc} is the subcarrier bandwidth and f_m is the highest baseband frequency (bandwidth DC to FM).

S_o/N_o can also be obtained directly by the following equation:*

$$S_o/N_o \text{ (rms/rms)}^2 = (C/N)_{IF} \frac{(1 - \alpha)^2}{16} \times \frac{\Delta f \times B_{IF}}{3 \left[\frac{f_m}{3} + f_{sc}^2 f_m \right]}$$

With $\alpha = \frac{0.07}{2.8} = 0.025$, Δf = 8 kHz,

* Final Report for HRIR Real-Time Transmission Study (AED R-2534), Contract NAS 5-3776, October 15, 1964.

B_{IF} = 50 kHz, f_{sc} = 2.4 kHz, f_m = 1.6 kHz, and

$(C/N)_{IF}$ = 10.0 db at threshold,

S_o/N_o = 10.0 + 12.6 = 22.6 db rms/rms at threshold.

At 5 degrees elevation:

S_o/N_o = 22.6 + 3.3 = 26 db rms/rms (worst-case).

To obtain the black-to-white level/rms signal-to-noise ratio, add +9 db to the rms/rms S/N, yielding: S_o/N_o at carrier threshold = 31.6 db p-p rms, and worst-case S_o/N_o at 5 degrees elevation = 35 db p-p/rms.

d. Scanning Radiometer Baseband Signal-to-Noise Ratio

The calculations previously given for APT data also apply to scanning radiometer data up to and including the signal-to-noise ratio at the output of the FM receiver and are therefore not repeated.

The SR subcarrier swings between 2.8 volts p-p ("cold") to 0.14 volt p-p ("hot"). The minimum value differs from that of the APT signal, which is 0.070 volt. The demodulated signal-to-noise ratio at the output of the AM detector is modified by the reduced baseband of the video signal (450 Hz). Substituting this value in the expression given in the previous section yields the following baseband S/N at carrier threshold:

S/N at threshold = 10.0 + 18.6 + 9.0 = 37.6 db p-p/rms.

The +9 db was added in the above expression to yield the hot-to-cold/rms signal-to-noise ratio. The AM-FM improvement is 18.6 db above carrier-to-noise ratio. The worst case S/N for 5 degree elevation is 3.3 db above the threshold value, or:

S/N = 40.9 db hot-to-cold/rms.

e. CDA Station Margins

APT and SR margins available at CDA stations which monitor APT transmissions are higher than those computed for the APT field station data link. Minimum CDA ground-antenna gain is 27.0 db versus a field station gain of 12.5 db; therefore, the link margins increase by a minimum value of 14.5 db.

f. Net Signal-to-Noise Ratio Including the Effect of Sensor Noise

The signal-to-noise ratios given here are the link contributions only. The sensors S/N are approximately:

APT = 30 db p-p/rms (sensor)

SR = 44 db p-p/rms (sensor).

The overall system S/N is then (worst-case):

APT system = 29 db p-p/rms, at the field stations.

SR = 39 db p-p/rms, at the field stations.

E. PLAYBACK VIDEO LINK

1. General

The S-band link is the major means of data communication from the spacecraft to the CDA stations. Information that has been recorded throughout the satellite orbit is replayed on command and transmitted as one multiplexed signal on a 1.7-GHz carrier. At the CDA stations this signal is demultiplexed, recorded, and subsequently retransmitted down long lines to the NESC at Suitland, Maryland. A detailed description of the methods used to transmit the data from the CDA stations to NESC is given in Subsection 5.II.E.

There are three major sources of data for the playback video link: (1) advanced vidicon camera system (AVCS), (2) scanning radiometer (SR), and (3) secondary sensors. The AVCS produces a high resolution, television-type signal that provides cloud-cover data during the daytime portion of the orbit; SR produces a high resolution infrared and visible signal that provides cloud cover data during the nighttime portion of the orbit, emitted earth radiance measurements during day and night, and reflected earth radiance during the day. The two secondary sensors, the solar proton monitor and the flat-plate radiometer, provide digital signals representing their respective inputs.

The AVCS and SR sensors are fully redundant, and each of the sensors provides inputs to the corresponding tape recorder. The secondary sensors are not redundant, and their outputs are recorded on a single incremental tape recorder. (Telemetry data are also recorded on the incremental tape recorder on a time-shared basis.) The AVCS and SR signals modulate subcarrier oscillators whose output is recorded; the secondary-sensor outputs have a digital format which is recorded directly. During playback, each secondary-sensor data channel frequency-modulates a subcarrier oscillator. The various subcarriers are combined in one of the redundant multiplexer sections to produce a composite signal having a frequency range from 11 to 480 kHz (see Figure 4-IX-18).

The above spectrum frequency-modulates one of the two S-band transmitters. The two transmitters are permanently connected to the antenna coupler which supplies the crossed-dipole S-band array with quadrature-phased signals. The radiated wave is either right-hand

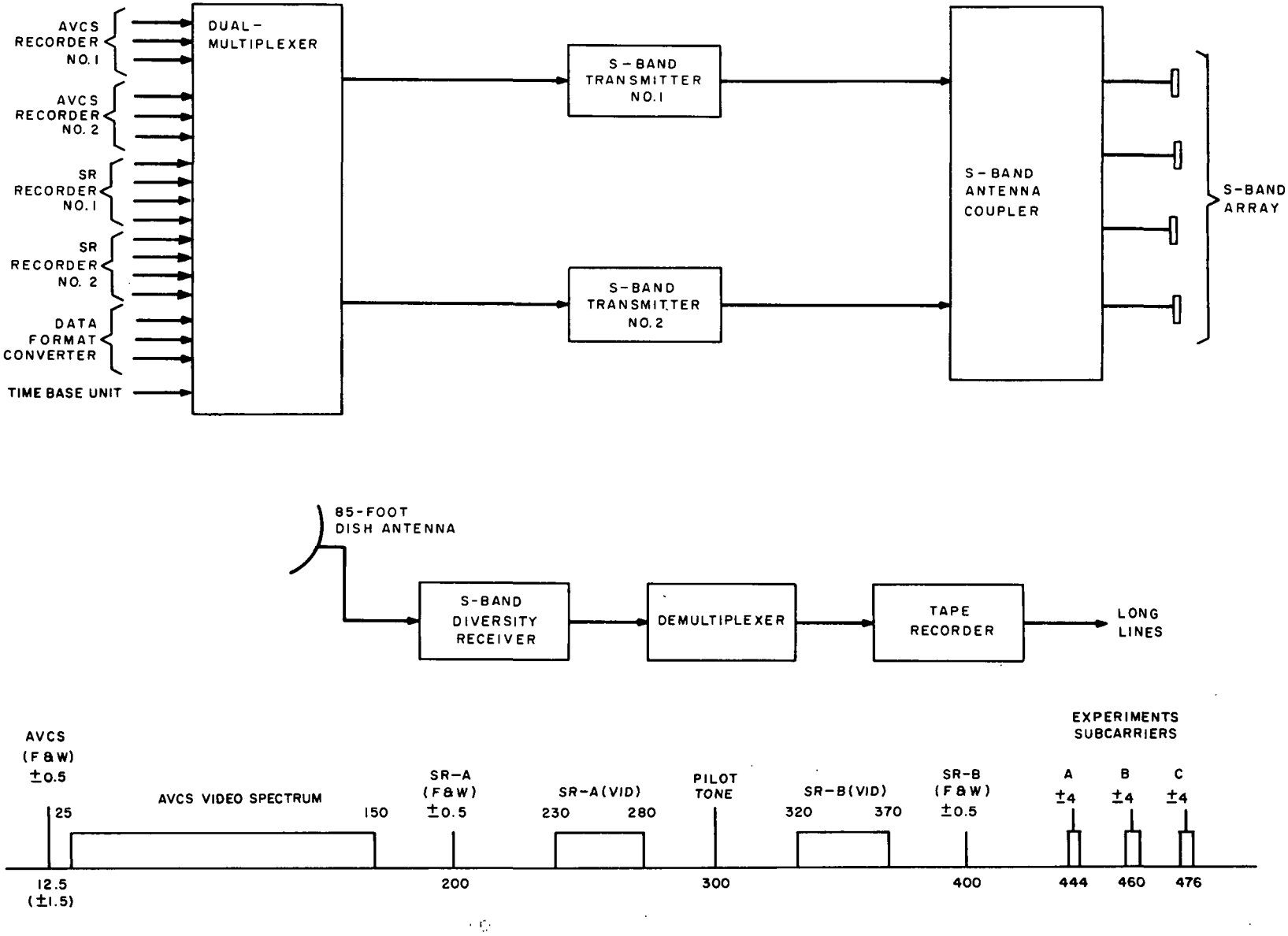

Figure 4-IX-18. Playback Video Link, Block Diagram

circular (RHC) or left-hand circular (LHC) polarized depending on which transmitter has been selected. The selection of a transmitter is made by application of DC power from the CDU.

At the CDA station, the S-band signal is received by the 85-foot antenna and demodulated by an FM receiver. The subcarriers are then demultiplexed, shifted to their original frequency bands (i.e., those occupied before multiplexing), and recorded on a tape recorder. The tape recorder playback is fed into the long lines for transmission to Suitland, Maryland. There, each of the subcarriers is individually demodulated by a second FM discriminator into a baseband.

2. Signal Characteristics

a. AVCS Signals

The AVCS video signal has a baseband of 60 kHz, and its data is made up of discrete frames. Normally, 11 frames are recorded during each orbit. Each frame contains 900 lines, of which the first 33.3 and the last 33.3 lines are held at the black level; the remaining 833.3 lines contain video data. Each of the 833.3 lines is preceded by a blacker-than-black sync pulse of 625-microsecond duration; a line and a sync pulse occupy a period of 7.5 milliseconds.

Each frame is followed by a time code signal which contains 24 RZ bits. The first bit of the code is the least significant digit, and the time code resolution is 0.5 second. The code bit rate is 60 bits per second; the duration of each bit is 8.3 milliseconds. The time code is not synchronous with the picture timing; however, one complete time code follows each frame.

The composite video signal modulates a voltage-controlled oscillator to produce a 72-kHz sync tip, an 84-kHz black level output, and a 120-kHz white level output. These signals are recorded on a selected AVCS tape recorder; a second track of this recorder is fed simultaneously an accurate 50-kHz unmodulated signal. When a command "replay AVCS tape recorder" is received, the direction of tape motion is reversed and playback takes place. The instantaneous output frequency of the video channel is doubled to provide a 144-kHz sync tip, a 168-kHz black level output, and a 240-kHz white level output.

b. Scanning Radiometer Signals

The scanning radiometer has a field of view of 5.3 milliradians and scans at a rate of 48 lines per minute. The earth portion of the scan occupies 110 degrees of the 360 degree rotation; its resolution is 4 nautical miles at the center of its scan. The infrared channel is sensitive to the radiation in the spectral region between 10.5 and 12.5 microns; it detects the radiation from sources between 185 and 330°K and has a resolution of 4.0°K at 185°K, and 1.0°K at 300°K. The visible channel detector responds to a scene brightness of 20 to 8500 foot-lamberts in the spectral region from 0.52 to 0.73 micron.

The baseband spectrum of the SR video signal and sync is from DC to 450 Hz. A marker (sync) pulse is generated 75 degrees following the nadir. It consists of a 60-millisecond pulse with front and back porches of 20 milliseconds duration. The sync pulse is 25 percent greater than the "hot" level while the porches are at approximately the cold level. The spectrum of the sync signal is from DC to 1250 Hz, but is subsequently limited in the SR tape recorder to approximately the 450-Hz level. The period from 90 degrees following one nadir to 90 degrees in advance of the next nadir is time-shared between telemetry, time code, and calibration signals.

The composite outputs from the IR processor frequency-modulate a voltage-controlled oscillator in the tape recorder electronics. The oscillator output frequency of 2.4 kHz corresponds to the white level, and that of 3.3 kHz to the black level. The SR tape recorder has three record tracks. The composite IR and visible outputs from the SR processor are recorded on tracks D1 and D3, respectively, while, simultaneously, an accurate 3.125-kHz signal is being recorded on track D2. This channel, called the flutter-and-wow channel, will be frequency-modulated by tape speed variations, and thus provide data for later ground correction of time base error on the primary data channels.

During the record mode, the composite infrared and visible channel signals from the SR processor are applied to the respective FM modulators in the SR tape recorder electronics where they frequency-modulate a 2.85-kHz subcarrier with a maximum frequency deviation from 2.4 to 3.3 kHz. These modulated radiometer signals are then applied to their respective record amplifiers which apply drive power to tracks of the record head, resulting

in the recording of data on tape tracks D1 and D3. If recording continues until the end-of-tape is reached, the recorder stops and the second SR recorder is commanded to start recording.

When the playback command is received from the ground station, -24.5-volt DC playback power is applied to the two playback amplifiers, to the flutter-and-wow playback amplifiers, and to the motor driver circuits of the tape recorder, and tape playback commences. Playback tape speed (30 inches per second) is sixteen times record tape speed (1.875 inches per second). Therefore, the instantaneous frequencies are multiplied by 16 during the playback mode. The 3.125-kHz flutter-and-wow carrier is translated to 50 kHz plus or minus the small deviation caused by tape speed variations of the tape recorder. The maximum swing of the modulated radiometer signal frequencies is translated from 2.4 to 3.3 kHz to 38.4 to 52.8 kHz. These signals are applied to the dual multiplexer and used to frequency-modulate the S-band transmitter.

c. Secondary Sensors

The secondary sensor data are recorded on three channels of the incremental tape recorder; one channel contains a clock signal, another the solar proton monitor data, and a third contains the flat plate radiometer data, telemetry, and time code. The data input is an NRZ pulse train having a bit rate of 15 bits per second.

The solar proton monitor data are divided into 20 words of 9 bits each. The first word of each frame contains a Barker Code, thereby identifying the start of a frame.

The third-track data are divided into 60 words of 8 bits each. The first bit is designated as a "word marker" and is fixed at a logical "0". A special word designated as a "frame marker" consists of 8 bits at logical "1". Each data frame consists of the following words: word 1, frame marker; word 2, frame marker; words 3 through 6, time code; words 7 through 21, flat plate radiometer; and words 22 through 60, telemetry and spare data words.

On a command "playback incremental recorder", the direction of tape motion is reversed and the recorder is replayed continuously at a nominal rate of 2 kilobits per second NRZ (1 kHz). The outputs of the three tracks frequency-shift-key three oscillators centered at 144.0, 160.0, and 176 kHz, respectively. The oscillators accept signals up to 2 kHz.

3. Dual Multiplexer

The dual multiplexer unit provides redundant multiplexing functions for the AVCS and SR tape recorder playback signals and the experiment (flat plate radiometer, solar proton monitor, and telemetry) subcarriers. Mutual cross strapping of signal lines between the AVCS tape recorders and the redundant sections of the dual multiplexer and between the SR tape recorders and the redundant sections of the dual multiplexer is provided, thus resulting in independent redundancy among these units, including multiplexer redundancy for the special operating mode of simultaneous playback from both SR recorders. Selection of the desired multiplexer section is effected by logic power switching in the command distribution unit (CDU). A block diagram of the dual multiplexer, showing the basic signal interfaces is presented in Figure 4-IX-19.

Input signals to the dual multiplexer are of the following types:

- A constant amplitude, frequency-modulated video subcarrier from either of two video tracks of each of two redundant AVCS tape recorders, only one of which is active at a given time; this video signal is accompanied by a separate flutter and wow signal resulting from playback of a recorded reference subcarrier on a third track of the tape.

- A pair of constant amplitude, frequency-modulated video subcarriers and one or two frequency-modulated flutter-and-wow subcarriers from two redundant scanning radiometer tape recorders; each tape recorder provides three tracks of playback signals two video (IR and visual) and one flutter-and-wow; playback at any given time may be from the three tracks of either recorder, or from one video track and one flutter-and-wow track of both recorders simultaneously.

- A single, composite signal of three constant amplitude, frequency-shift-keyed subcarriers originating in the Data Format Converter (DFC), the first carrying solar proton monitor data, the second carrying clock sync, and the third carrying time-multiplexed data including spacecraft telemetry, flat plate radiometer data, and time code data.

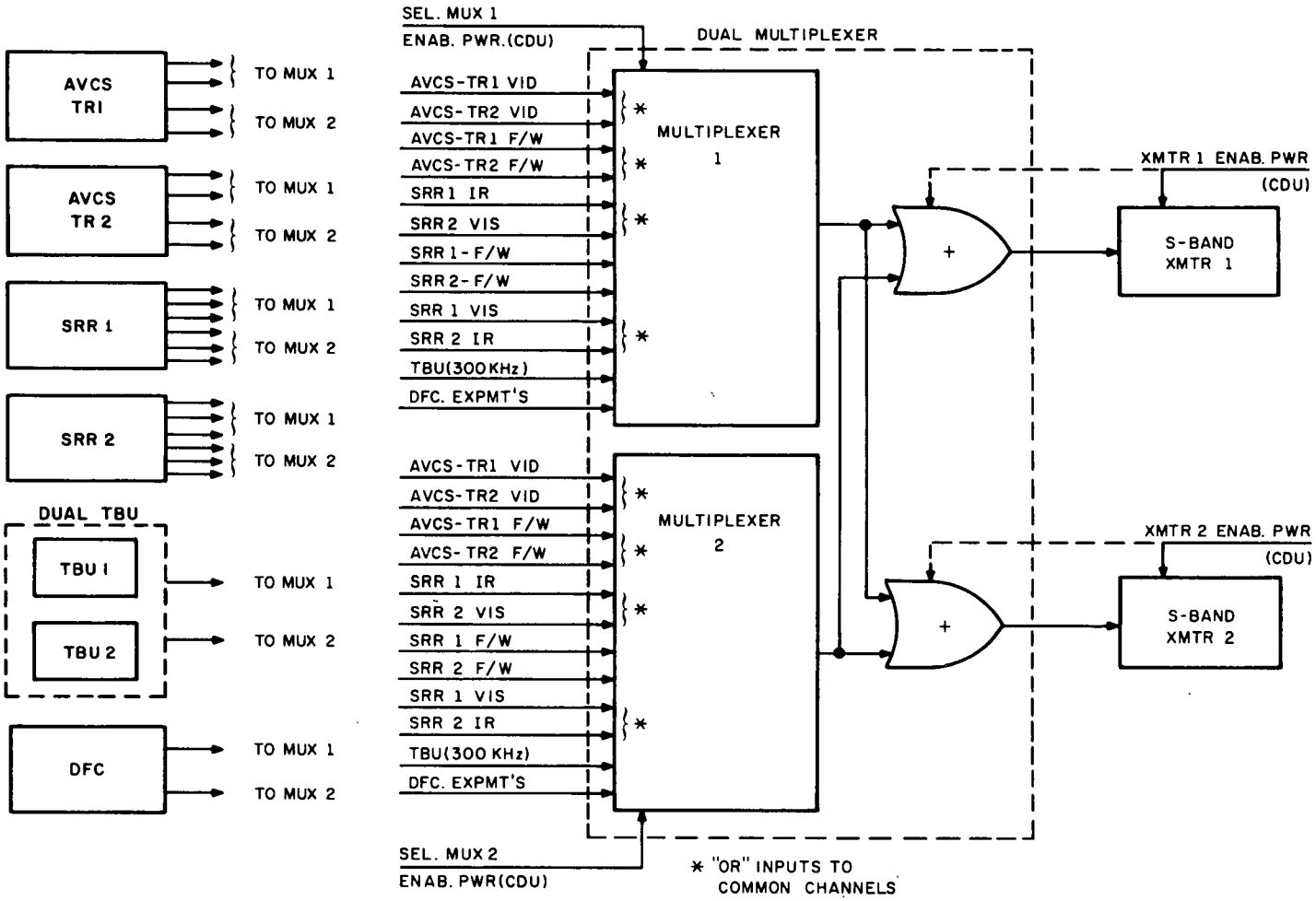

Figure 4-IX-19. Dual Multiplexer, Basic Signal Interfaces

- A single, unmodulated clock reference signal from either of the redundant time base units.

The primary operations performed by the dual multiplexer are the basic multiplexing functions plus the OR-gating operation to provide either of the composite output signals to either of the two S-band transmitters. Each of the basic multiplexing functions includes OR-gating of redundant inputs, signal conditioning, filtering, frequency translation, division, multiplication, and level setting. All individual subcarriers are then summed into a composite signal which is applied to both of the multiplexer output summing amplifiers and used to frequency-modulate one of the redundant S-band transmitters. Only one of the two basic multiplexer sections will be powered at a given time by the CDU.

With identical baseband signals continuously present at the input to both dual multiplexer output summing amplifiers, selection of the desired S-band transmitter (and its associated multiplexer output summing amplifier) is effected by power switching in the CDU, and the composite of modulated subcarriers then frequency-modulates the powered transmitter.

Output signals from the two transmitters are diplexed in the hybrid coupling network of the S-band antenna such that one transmitter produces a right-hand circularly polarized radiation field from the S-band antenna array, whereas the other transmitter produces a left-hand circularly polarized field. The directive antenna array produces a shaped conical beam about the spacecraft nadir and maintains the circular polarization over the beamwidth. The remote playback (S-band) link is operational only when the spacecraft is stabilized and earth-oriented. The transmitters operate on the same frequency and only one is active any given time.

4. S-Band Transmitter

Space-qualified transmitters operating at 1.7 GHz are limited in number. In considering ITOS requirements, a survey was made of the S-band transmitters that were either proposed for or are presently used on Nimbus-A, -B and -C satellites. This survey resulted in the development of a set of specifications for the ITOS S-band transmitter having the requirements listed in Table 4-IX-21.

The linearity requirement of ±1 percent is the same as for the TOS AVCS transmitter. The power efficiency, the weight, and the dimensions are estimates based on characteristics of existing S-band transmitters. An evaluation is currently in progress of various S-band transmitters.

5. S-Band Antenna and Coupling Network

a. Requirements

At a satellite altitude of 775 nautical miles, the earth subtends an angle of 110 degrees, and the S-band antenna must have a radiation pattern that covers nadir angles from 0^{o} to $\pm 55^{o}$. For a given orbit and a given frequency of operation, there exists an ideal radiation pattern that provides a uniform power density at all ground stations regardless of the satellite elevation. This characteristic is shown as curve A in Figure 4-IX-20. For optimum reception of the radiated signal, the satellite antenna polarization is circular, and polarization diversity reception is employed on the ground.

b. Description of the Baseline S-Band Antenna and Coupling Network

The baseline antenna for ITOS is a four-dipole array shown in Figure 4-IX-17. Its radiation pattern peaks in the vicinity of the maximum nadir angles used for data readout, thereby compensating for the increased range.

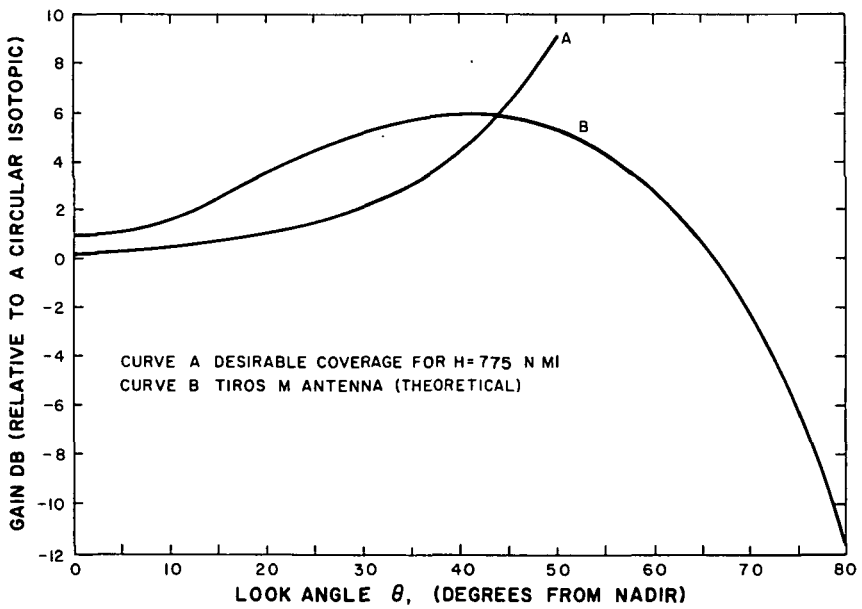

Figure 4-IX-20. S-Band Antenna Radiation Pattern

TABLE 4-IX-21. S-BAND TRANSMITTER SPECIFICATIONS

Parameter	Value
Center Frequency	1697.5 MHz
Modulation	FM
Frequency Accuracy	
Settability	±0.002 percent
Stability (-15 to 60°C)	±0.005 percent
RF Bandwidth	3.3 MHz, min frequency response ±1 db
Peak Deviation	±1.5 MHz ±1 percent linearity
Deviation Sensitivity	1 MHz peak/2.12 volts peak (1 MHz peak/1.5 volts rms sinusoidal)
Modulation Bandwidth	10 to 750 kHz
Spurious Output	
148.25 to 148.75 MHz	less than -90 dbm/48 kHz
108.25 to 108.75 MHz	less than -70 dbm/48 kHz
146 to 151 MHz	less than -17 dbm/48 kHz
Baseband Input Impedance	600 ±60 ohms
Output Impedance (into a VSWR of 2:1, any phase angle)	50 ohms, nominal
RF Power Output	2 watts min
Minimum Efficiency	5 percent
Power Input	-24.5 volts ±1 percent; 50 watts max
Duty Cycle (normal operation)	10 minutes "on" and approximately 100 minutes "off"
Weight	6 lb, max

- The transmitter operating into a short or open circuit shall not cause a catastrophic failure.
- The transmitter shall survive input voltage excursions from -23 volts to a maximum of -36 volts.

As shown in Figure 4-IX-21, the antenna consists of two orthogonal pairs of dipoles placed over a ground plane. The dipole pairs are fed in quadrature to produce circular polarization. The four dipoles are arranged in the form of a square at a height, h, above the ground plane and a spacing, d, between each pair of parallel elements. The spacing between the parallel elements has been selected to achieve equal E- and H-plane patterns for a given dipole pair. The height, h, has been selected to produce a dimple in the antenna pattern as shown by curve A in Figure 4-IX-16. Each dipole is energized from a split-tube balun located at the end of a coaxial line.

The baseline coupling network is shown in Figure 4-IX-22. It consists of three hybrids in a stripline configuration whose interconnecting lengths are such that the North-South and East-West pairs are in phase but there is a 90-degree differential between the two in-phase pairs. Eight connectors are mounted on the stripline board. The approximate stripline board dimensions are 7 by 5 inches, and it is 1/8-inch thick. Two of the connectors serve as transmitter inputs, two connectors have 10-watt coaxial terminations, and four connectors feed the antenna elements.

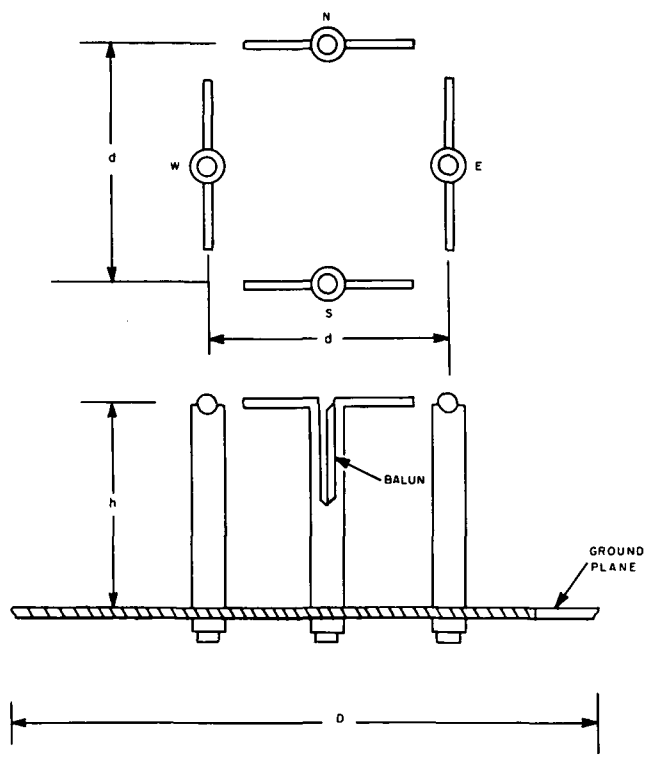

Figure 4-IX-21. Baseline S-Band Antenna for ITOS

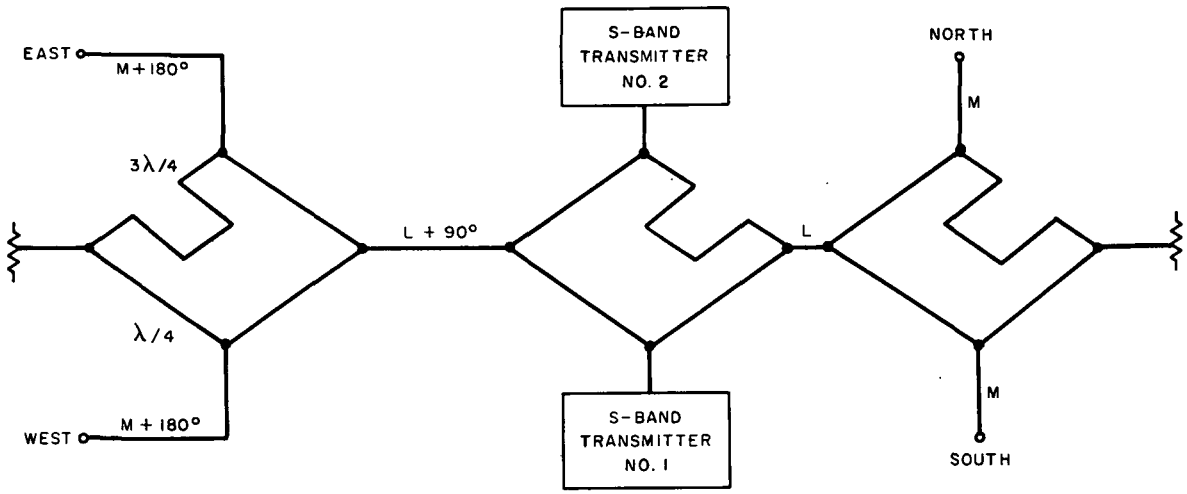

Figure 4-IX-22. Baseline Coupling Network for S-Band Antenna Printed on a Stripline Board

c. Design Considerations

(1) Ellipticity

The calculated axial ratio over the 110-degree beamwidth is 0.5 db for the four-dipole array. Polarization loss for the S-band link will not degrade rapidly with the ellipticity of the satellite antenna. If polarization loss is constrained to 0.5 db and if the receiving ground antenna is perfect, the satellite may be as poor as 6.4 db*. With a ground antenna having a 3-db ellipticity, the satellite may have an ellipticity as high as 3 db and still produce a loss of only 0.5 db. The specifications which follow consider this point, so that the ellipticity is specified realistically.

---

*Microwave Engineer's Handbook, 1966, p. 169.

(2) Backlobes

A backlobe level, which is 20 db below the peak of the pattern, is considered good design practice. This is the maximum level for nadir angles between 90 and 180 degrees. Specifying backlobe levels lower than 20 db below the peak would provide insignificant gain increase in the desired beamwidth. For example, a backlobe level of -25 db would increase gain by only 0.1 db.

(3) Ground Plane

The minimum ground plane diameter, consistent with the desired pattern, must be determined experimentally. At this juncture, minimum diameter is estimated to be 14 inches.

d. S-Band Antenna and Coupling Network Specifications

The specifications for the S-band antenna and coupling network are given in Tables 4-IX-22 and 4-IX-23. Since further design effort on the antenna and coupling network is necessary, the tabulated characteristics are of a preliminary nature.

6. Subsystem Analysis and Link Calculation

a. RF Link Calculation

The path losses and receiving margin for the S-band link (spacecraft transmitter-to-ground station receiver) were computed using the satellite communication equipment characteristics specified earlier in this section and the following CDA ground station parameters:

Parameter	Value
85-foot Antenna Gain (measured)	47.7 db at 1700 MHz
Polarization Diversity	Right-hand circular or Left-hand circular
Receiver Noise Figure	2.2 db
Predetection Bandwidth	3 MHz

TABLE 4-IX-22. S-BAND ANTENNA SPECIFICATIONS

Electrical Characteristics	
Frequency band	1690 to 1710 MHz
Type	Four dipole array over ground plane
Phasing	quadrature
Polarization	RH circular or LH circular
Gain	$\pm$1 db of curve B, Figure 4-IX-16, for $0^o < \theta < 20^o$ $\pm$2 db of curve B, Figure 4-IX-16, for $20^o < \theta < 55^o$
Backlobes, $90° < \theta < 180°$	20 db below peak
Ellipticity	6 db max over beamwidth
Power Capability	10 watts
VSWR	1.5 max over band into coupling network
Mechanical Characteristics	
Dipole Spacing	2.88 inches
Dipole Height	3.07 inches
Ground plane, min	14-inch diameter
Weight (design goal)	1.5 lb (max)

The worst-case link calculation up to the predetection IF bandwidth is given in Table 4-IX-24. A margin of 7.6 db above FM threshold was obtained under worst-case conditions with the 2-watt transmitter. This margin is sufficient to take care of other system uncertainties. The variation in RF margin with changing ground antenna elevation and spacecraft antenna nadir angle is given in Table 4-IX-25.

TABLE 4-IX-23. COUPLING NETWORK SPECIFICATIONS

Characteristics	
Frequency Band	1690 to 1710 MHz
Type	printed stripline
Ports	2 inputs
Input Impedance	50 ohms
Insertion Loss	1.0 db max
VSWR (when connected to the antenna)	1.5 max
Isolation Between Transmitters Including Connectors and Terminals (design goal)	20 db min
Mounting	adjacent to the ground plane
Size	7 by 5 by 1/8 inches (less connectors)
Weight (design goal)	1.4 lb (max, less cabling)

TABLE 4-IX-24. WORST-CASE S-BAND LINK CALCULATION

S-Band Transmitter Power Output (2 watts)	3 dbw
Net Spacecraft Antenna Gain (corresponding to 5-degree elevation of ground antenna)	0.4 db
Polarization Loss	-0.5 db
Free Space Loss (5-degree elevation, 775 nautical miles altitude at 1700 MHz)	-169.5 db
Gain of the 85-foot Antenna (measured)	47.7 db
Received RF Power	-118.9 dbw
Receiver Noise Density (total temperature 361°K)	-203.1 dbw in 1 Hz
Noise Power in 3-MHz IF	-138.3 dbw
IF Carrier-to-Noise Power	19.4 db
Margin above FM Threshold (12 db)	7.6 db

TABLE 4-IX-25. VARIATION OF RF MARGIN WITH ELEVATION AND NADIR ANGLES

Elevation (degrees)	Nadir (degrees)	Look Angle (degrees)	Antenna Gain		Propagation Loss (db)	Combined Antenna Gain & Propagation Loss (db)	C/N Margin over FM Threshold (db)
			Nominal (db)	Minimum (db)			
0	55.2	34.8	4.3 ±2.0	2.3	170.5	-168.2	6.9
5	54.9	35.1	4.4 ±2.0	2.4	169.5	-167.1	8.0
10	54.0	36.0	4.6 ±2.0	2.6	168.0	-165.4	9.7
15	52.5	37.5	4.8 ±2.0	2.8	167.0	-164.2	10.9
20	50.5	39.5	5.2 ±2.0	3.2	166.4	-163.2	11.9
30	45.5	44.5	5.8 ±2.0	3.8	164.5	-160.7	14.4
40	39.0	51.0	6.0 ±2.0	4.0	163.7	-159.7	15.4
50	31.9	58.1	5.4 ±2.0	3.4	162.5	-159.1	16.0
60	24.2	65.8	4.2 ±2.0	2.2	161.5	-159.3	15.8
90	0.0	90	1.0 ±1.0	0	160.6	-160.6	14.5

b. System Noise Temperature

The system noise temperature, T_{sys}, is equal to the receiver noise temperature plus the antenna noise temperature. The receiver noise temperature is given by:

$$T_R = (\text{Noise Figure} - 1)\ 290°K$$

Noise Figure = 2.2 db = power ratio of 1.51 to 1;

hence,

$$T_R = (1.66-1)\ 290°K = 191°K$$

The measured antenna noise temperature is

$$T_{ANT} = 170°K.$$

$$T_{sys} = T_R + T_{ANT} = 191 + 170°K = 361°K.$$

The receiver noise density in a 1-kHz band is given by

$$P = K\ T_{sys} = 203 \text{ dbw in 1 Hz}$$

where K is Boltzman's constant = -198 dbm/°K/1 Hz.

c. Verification of RF Bandwidth Requirement

As a first-order approximation, the information bandwidth is determined by the AVCS channel 2, which has a ±580 kHz deviation and an upper channel frequency of 480 kHz. The doppler shift at a nominal frequency of 1700 MHz and 775 nautical miles is ±32.3 kHz. The long-term transmitter frequency instability is ±0.005 percent or ±85.0 kHz at 1700 MHz. The minimum RF bandwidth of the ground receiver is a total of 24 MHz, as tabulated below:

Information	(2 x 580) + (2 x 480)	=	2,120.0 kHz
Total Doppler shift at 1700 MHz	(2 x 32.0)	=	64.0 kHz
Total transmitter instability	±0.005 percent at 1700 MHz	=	170.0 kHz
RF Bandwidth		=	2,354.0 kHz

Hence, a 3-MHz receiver IF bandwidth is satisfactory.

d. RF Deviation Allotments (Subcarrier Signal-to-Noise)

The subcarrier signal-to-noise ratio, S_c/N_c, for a specified channel bandwidth, $(f_H - f_L)$, is given by the following expression:

$$S_c/N_c = \frac{3\ \Delta f^2\ B_{IF}}{2(f_H^3 - f_L^3)} \left(\frac{C}{N}\right)_{IF}$$

Frequencies f_H and f_L are the edges of the channel under consideration, Δf is the peak carrier deviation, B_{IF} is the IF bandwidth (B_{IF} = 3 MHz), and $(C/N)_{IF}$ is the carrier-to-noise ratio.

In most practical cases, where the channel bandwidth $(f_H - f_L)$ is much smaller than the average subcarrier frequency ($f_{s/c} = (f_H + f_L)/2$), the above expression may be simplified to the following:

$$S_c/N_c \approx \frac{1}{2} \frac{\Delta f^2\ B_{IF}}{(f_H - f_L)\ f^2_{s/c}} \left(\frac{C}{N}\right)_{IF}$$

Table 4-IX-26 shows the results of the calculation of RF deviation allotment; it can be seen from the table that sufficient margin is maintained above the subcarrier demodulator FM threshold. The peak deviation of the secondary sensors channel had been selected such that the performance of the system is controlled by the RF receiver threshold. The tabulated signal-to-noise ratios do not include sensor or spacecraft tape recorder noise contribution. The total RF deviation, when summed on a peak basis, is 0.58 MHz. The transmitter is capable of deviating $\pm$1.0 MHz with 1-percent linearity.

TABLE 4-IX-26. RF DEVIATION ALLOTMENT; SUBCARRIER SIGNAL-TO-NOISE DUE TO LINK ALONE

CHANNEL	PEAK CARRIER DEVIATION (kHz)	MULTIPLEXER FREQUENCY BAND (kHz)	WORST CASE SUBCARRIER S/N (rms/rms)
AVCS	100	25 - 150	30.7
AVCS-F/W	20	12.5 ± 1.5	44.4
SR-A-F/W	35	200 ± 1.5	31.2
SR-A-(VIS)	100	230 - 280	26.5
(I-R)		230 - 280	
PILOT	25	300 ± 0.1	39.6
SR-B-(VIS)	100	320 - 370	23.5
(I-R)		320 - 370	
SR-B-F/W	50	400 ± 1.5	28.4
SECONDARY SENSORS A	50	444 ± 4	23.2
-B	50	460 ± 4	22.9
-C	50	476 ± 4	22.6

e. Baseband Signal-to-Noise Ratios

The overall baseband signal-to-noise ratio is determined by the sensor, the spacecraft tape recorder, the link, the ground tape recorder, and the long lines signal-to-noise ratios. The individual noise sources are independent. Consequently, the total noise power at the display equipment is the sum of individual noise powers properly referenced to the same signal level and measured in the same baseband bandwidth.

The composite subcarriers at the output of the ground receiver are demultiplexed and shifted to their original frequencies; the AVCS subcarrier is doubled. They are recorded

on tape recorders and played back at 1/8 the record speed for the AVCS video, AVCS flutter and wow, secondary sensor channels and at 2:1 speed ratio for the scanning radiometer channels. The 8:1 slowdown reduces the baseband, deviation, and subcarrier bandwidth by a factor of 8. The before-playback center frequencies of the secondary sensors subcarriers are 144.0, 160.0, and 176.0 kHz. At playback, the center frequencies are 18.0, 20.0, and 22.0 kHz, respectively.

(1) AVCS Baseband Link Signal-to-Noise Ratio

The frequency deviations of the doubled AVCS subcarrier corresponding to grey levels are (1) sync tip, 144 kHz; (2) black level, 168 kHz; and (3) white level, 240 kHz. Assuming that the baseband S/N is measured for a scene which is composed of alternating black and white bars several resolution elements wide, the subcarrier frequency will vary from 168 to 240 kHz, yielding a peak-to-peak swing of 72 kHz and an average subcarrier frequency, $f_{s/c}$, of 204 kHz. The rms/rms signal-to-noise ratio can be calculated for a sinusoidal pattern; the peak-to-peak/rms signal-to-noise ratio will be 9 db above the rms/rms signal-to-noise ratio.

The baseband signal-to-noise ratio, S_o/N , is given by

$$S_o/N_1 = (S_c/N_c) = \frac{3}{2} \frac{\Delta f_{s/c}^2 \, B_{s/c}}{f_m^3}$$

where S_c/N_c is the subcarrier-to-noise ratio in bandwidth $B_{s/c}$, f_m is the maximum baseband frequency, and $f_{s/c}$ is the peak subcarrier deviation. The 8:1 slowdown at tape playback reduces the deviation, the subcarrier bandwidth, and the baseband by a factor of 8, resulting in no change in S_o/N_1. In baseband $f_m/8$, the calculation can be carried out with the parameters at their preplayback values. The improvement obtained above the subcarrier-to-noise ratio in 150-kHz channel bandwidth is -1.8 db. This yields the following worst-case baseband S/N:

- AVCS Video 1 (link) S_o/N_1 = 28.9 db rms/rms or 37.9 (black-to-white level/rms noise)

The baseband S_o/N_1 at the end of the long lines is calculated to be 29 db p-p/rms within a 7.5-kHz baseband. This includes contribution from individual S/N terms tabulated below:

AVCS Camera	32 db (p-p/rms)
AVCS Tape Recorder	35 db (p-p/rms)
Multiplexer	49 db (p-p/rms)
Link	37.9 db (p-p/rms)
Demultiplexer	49.0 db (p-p/rms)
Long Lines	38.9 db (p-p/rms)

(2) SR Baseband Link Signal-to-Noise Ratio

The SR video signal produces a peak subcarrier deviation of 7.2 kHz with a baseband of 7.2 kHz. The link baseband signal-to-noise ratios are given below.

- SR Video A (link) S_o/N_1 = 46.8 db rms/rms
- SR Video B (link) S_o/N_1 = 43.8 db rms/rms

The overall signal-to-noise ratio at the end of the long lines was calculated to be approximately 36.6 db (p-p/rms) in a bandwidth of 7.2 kHz.

The SR video signals are recorded and then played back with a 2:1 slowdown. The individual signal-to-noise ratios are tabulated below:

Radiometer	45 db (p-p/rms)
SR Tape Recorder	40 db (p-p/rms)
Multiplexer	49 db (p-p/rms)
Link	43.8 db (p-p/rms)
Demultiplexer	49 db (p-p/rms)
Long Lines	46.5 db (p-p/rms)

(3) Secondary Sensors

The secondary sensor subcarriers are constant bandwidth IRIG channels: 17B (144 kHz), 19B (160 kHz), and 21B (176 kHz). They have a peak deviation, Δf, of ±4 kHz and accept a maximum baseband frequency, f_m, of 2 kHz. Based on a modulation index, m, of 2, ($m = \Delta f/fm$), the FM improvement is $3\ m^2\ (m+1)$ or 15.6 db. Table 4-IX127 shows the worst-case subcarrier-to-noise ratio for each subcarrier, the FM improvement, and the baseband signal-to-noise ratio for each. (Baseband S/N = Subcarrier S/N + FM Improvement; p-p/rms = rms/rms +9 db).

TABLE 4-IX-27. SECONDARY SENSORS CHANNEL CHARACTERISTICS

IRIG Channel	Sub-carrier (kHz)	Worst-Case Subcarrier S/N (db rms/rms) (8-kHz bandwidth)	FM Improvement Above Subcarrier (db)	Baseband S/N (2-kHz bandwidth)	
				(db rms/rms)	(db p-p/rms)
21B	176	23.2	15.6	38.8	47.8
19B	160	22.9	15.6	38.5	47.5
17B	144	22.6	15.6	38.2	47.2

SECTION X

SPACECRAFT TESTING

A. ITOS TEST PHILOSOPHY

ITOS, as a multisensor spacecraft, lends itself to parallel qualification testing of its subsystems, which ensures that each unit of each subsystem demonstrates satisfactory operation prior to integration in the spacecraft. This approach reduces the test time on the assembled spacecraft, where testing is a serial function, by increasing the parallel test paths prior to integration. It permits greater flexibility in time and cost scheduling and minimizes the time required for integration, environmental verification, and calibration of the spacecraft.

The concept of parallel qualification testing in which not only individual units but also essentially complete subsystems are tested prior to spacecraft integration is not new to the TIROS/TOS program. However, it will be applied more extensively on ITOS than on other TIROS/TOS spacecraft since ITOS is more complex.

The qualification test program for the ITOS spacecraft is presented in the test flow diagram in Figure 4-X-1. The four levels of testing in the program, in order of their performance, are:

- Unit tests,
- Unit combination tests,
- Subsystem interface tests, and
- Spacecraft tests.

In addition to the qualification test program, a spacecraft design validity test program will be performed to demonstrate the ability of the ITOS spacecraft to satisfy the thermal, mechanical, electrical, and RF requirements. A thermal test model and a mechanical test model will be constructed for the design validity test program.

After the thermal test program, the thermal test model will be reconfigured as an RF test model to demonstrate antenna radiation patterns, isolation network performance, and immunity of the command receiver to desensitization by the spacecraft transmitter. The mechanical test model will serve to verify the integrity of the mechanical design. Following mechanical testing, this model will be reconfigured with prototype components as an electrical test model and be used to prove the integrity of the ITOS electrical design prior to integration of the flight spacecraft.

B. UNIT AND SUBSYSTEM QUALIFICATION TESTING

1. Test Philosophy

During the manufacturing cycle, each unit of the spacecraft is tested under simulated flight conditions to demonstrate its flight worthiness. These tests are designed to obtain the maximum required data in minimum operation time without endangering the required life of the units through overtesting. These operational verification tests demonstrate that the units will operate within design performance limits after exposure to specified temperature, vibration, and thermal vacuum levels.

2. Test Conditions

a. Types of Tests

The units, unit combinations, and subsystems to be tested at each level and the types of tests to be performed are shown in Figure 4-X-1.

b. Vibration Tests

The unit or subsystem shall be mounted on a fixture which has no major resonances below 2000 Hz. The mounting of the unit or subsystem shall duplicate the final equipment mounting configuration. Random and sinusoidal vibration tests shall be performed at the levels specified below, which refer to both thrust and lateral axes. In the event of minor fixture resonances below 2000 Hz, either the resonances shall be damped or the input vibration amplitude adjusted to ensure testing at the levels specified in the table. During the test, the unit or subsystem shall operate in accordance with the requirements of the detailed component specification and with the conditions given in Table 4-X-1.

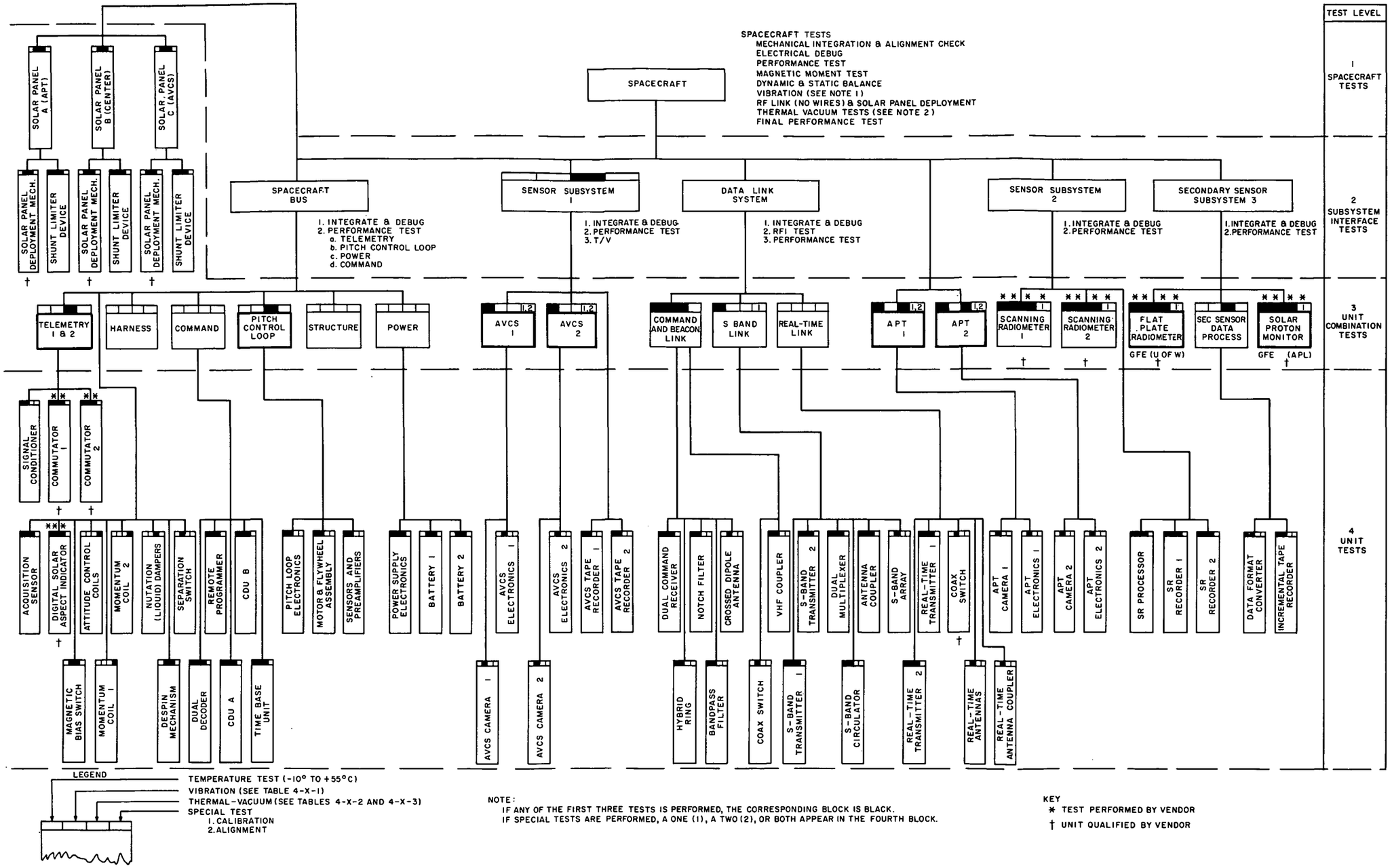

Figure 4-X-1. Spacecraft Test Sequence Diagram

TABLE 4-X-1. UNIT AND SUBSYSTEM VIBRATION TEST CONDITIONS

Vibration Type	Bandwidth (Hz)	Duration per axis	Sweep Rate (octaves/min)	Vibration Level	Spectral Density (g^2/Hz)
Random*	20-2000	2 min	------	10g-rms	0.05
Sinusoidal**	5-2000	---	4	5g (0 to pk)	----

* A 12 db/octave minimum rolloff shall be applied at both ends of the frequency bandwidth. Prior to testing, the flight component and vibration facility shall be equalized for a flat response within ±3 db with a low level vibration input (1.5 g-rms max) for each orthogonal axis. An equalization plot shall be obtained for each orthogonal axis and held on record.

**When the specified accelerations cannot be attained due to armature displacement limitations, the input may be a constant displacement not less than 0.5-inch double amplitude.

c. Thermal Vacuum Tests

The unit or subsystem shall be placed in a thermal vacuum chamber and operated in accordance with the detailed component specification and the applicable test procedure. The pressure within the thermal vacuum chamber shall be reduced to 5×10^{-5} mm Hg or less. The chamber temperature shall be stabilized at each of the temperature levels specified for the minimum periods indicated.

The period at each of the temperature levels shall be determined by the performance test requirements; the maximum period shall not exceed the minimum period by more than 6 hours. Pressure shall not exceed 5×10^{-5} mm Hg. Storage and/or operation in the thermal vacuum chamber for periods in excess of the minimum time shall not constitute disqualification under this specification.

The sequence and duration of temperature levels shall be in the order indicated in Table 4-X-2 for all units except tape recorders and cameras. The tape recorder and camera requirements are given in Table 4-X-3. Test interruption for external causes (other than failure of the component under test) shall void only that portion of the test

represented by the temperature level at the time of interruption. Upon resumption of testing, the pressure shall be restored to the specified level. Tests at those temperature levels not previously completed shall be performed, and the levels shall be maintained for at least the minimum times specified. Temperature shall be maintained within 2 degrees of the specified levels as measured at the interface between the surface of the heat sink in the thermal vacuum chamber and the mounting surface of the unit or subsystem under test. The rate of change of temperature between test levels must be controlled to obtain a rapid transition, but temperature may not exceed the desired test level by more than 2 degrees.

TABLE 4-X-2. UNIT AND SUBSYSTEM THERMAL-VACUUM TEST CONDITIONS*

Temperature (°C)	Duration (hours)	
	Minimum	Maximum
+55	12	18
-10	12	18
+55	6	12
-10	6	12

* These conditions do not apply for cameras and AVCS tape recorders. See Table 4-X-3.

TABLE 4-X-3. CAMERA AND AVCS TAPE-RECORDER THERMAL VACUUM TEST CONDITIONS

Temperature (°C)	Duration (hours)	
	Minimum	Maximum
+50	24	30
-10	8	14
-5	24	30
+45	8	14
+35	8	14
+25	8	14
+15	8	14
+5	8	14

3. Test Implementation

a. Unit Testing

The parallel testing sequence originates with the fourth-level, or unit, tests after the various component boards have been assembled to operate as specific spacecraft units. Testing at the fourth level is designed to ensure that the individual components meet the unit performance specification. At this test level, errors in workmanship and marginal or defective parts are discovered and corrected. Anomalies within the units are corrected, thus minimizing their impact on the overall schedule of testing and qualification.

b. Unit Combination Testing

At the third test level, units that operate together as major elements of a subsystem are mated and tested. For example, the AVCS camera is mated with its camera electronics unit. During the combination testing, interunit adjustments, such as optimized gain settings and threshold levels, are performed. Once specific units have been mated, tested, and adjusted, they form a functional combination that will be retained. In this manner, each unit of a functional group is optimized for operation with the other units of that combination. The performance criteria for the third-level tests are defined in the unit performance specifications.

c. Subsystem Interface Testing

The second level of testing is designed to detect interface problems between the functional elements of a subsystem. The major sources of these problems are the tolerances on interface signals between units. These tests can represent a major time saving, since such interface anomalies could only be found in one of two other ways: either the problem would be encountered on the integrated spacecraft and would impose a serial time delay on the spacecraft test program, or it could be discovered at the unit level, requiring that an exact duplicate of each interface circuit of the unit be provided in the unit test equipment. In this testing program, however, the subsystem test level generates the unit interfaces by employing the

actual interfaces with which the unit will operate on the spacecraft. Of prime interest during the second level of testing are the intrasubsystem interface signals; additional test equipment used during this test sequence provides the necessary power and signals to simulate these spacecraft-to-subsystem interfaces. The interunit harness approximates the line lengths anticipated in the actual spacecraft electrical harness. This harness is not an exact duplicate of the spacecraft harness, however, since the line-to-line crosstalk and coupling conditions of the actual flight harness cannot be duplicated.

C. SPACECRAFT QUALIFICATION TESTING

1. Test Philosophy

Spacecraft integration testing, the first test level, consists of (a) the mechanical and electrical integration of the qualified subsystems on the spacecraft assembly and (b) the calibration and environmental qualification of the integrated spacecraft as a complete system.

A detailed flow diagram of the spacecraft test program is presented in Figure 4-X-2.

All operations performed during integration, test, and calibration are designed to demonstrate the performance characteristics and capabilities of the spacecraft, while not compromising the flight equipment through severe overtesting. Parallel unit and subsystem testing reduces the time required to test equipment operating parameters on the assembled spacecraft to a minimum, and thus permits maximum test time for detection of system level problems, environmental simulation testing, and system calibration.

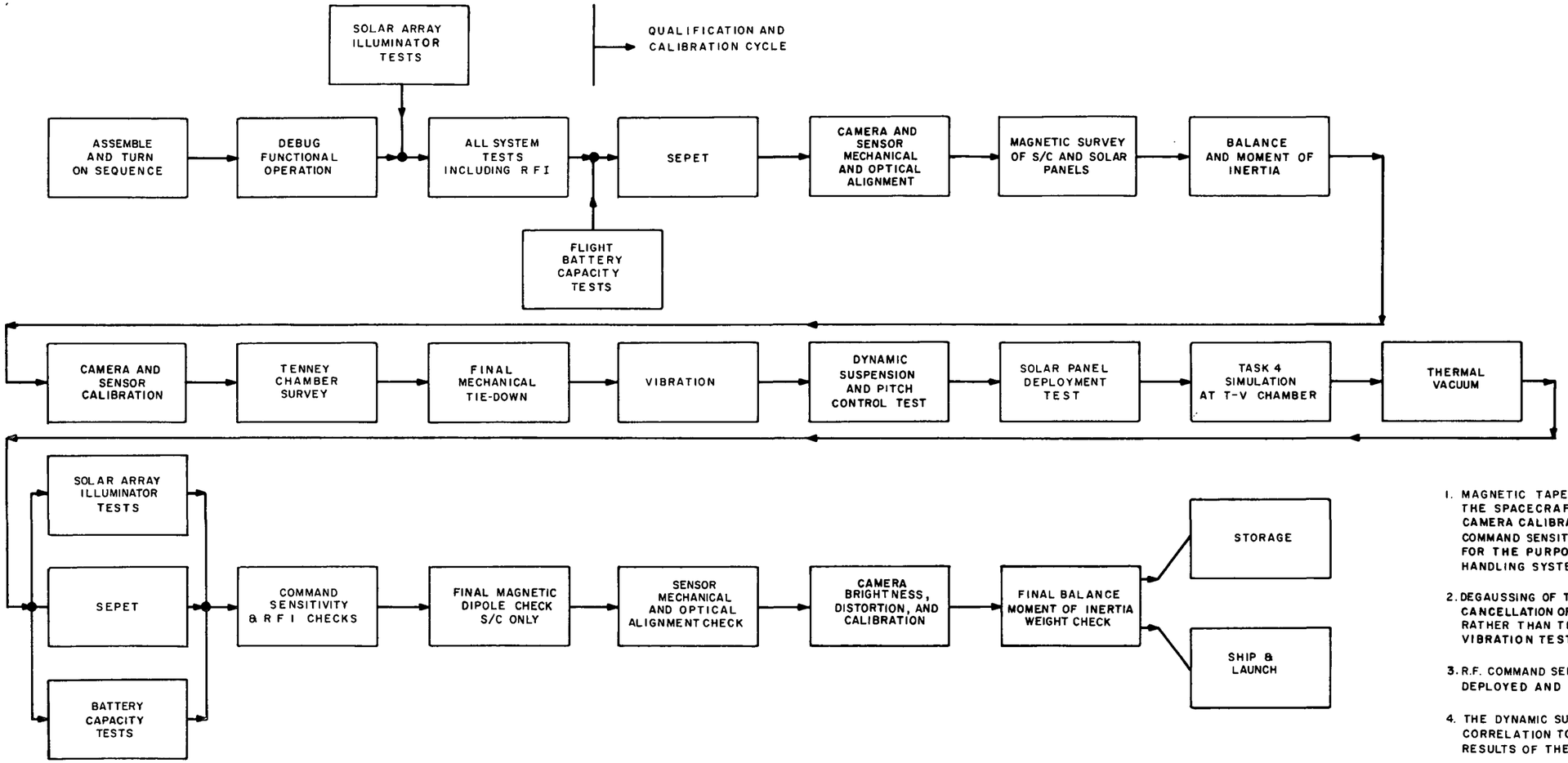

1. MAGNETIC TAPE RECORDINGS OF THE SELECTED DATA RECEIVED FROM THE SPACECRAFT DURING THE THERMAL VACUUM TEST PROGRAM, THE CAMERA CALIBRATIONS, THE DYNAMIC SUSPENSION TEST AND THE R.F. COMMAND SENSITIVITY TEST WILL BE SUPPLIED TO THE C.D.A. STATIONS FOR THE PURPOSE OF VERIFICATION OF THE "LONG LINE" DATA HANDLING SYSTEM.

2. DEGAUSSING OF THE SPACECRAFT IS PERFORMED TO PERMIT THE CANCELLATION OF THE TRUE RESIDUAL DIPOLE OF THE SPACECRAFT, RATHER THAN THOSE INDUCED BY TEST EQUIPMENT SUCH AS THE VIBRATION TEST FACILITY.

3. R.F. COMMAND SENSITIVITY WILL BE MEASURED WITH THE SOLAR PANELS DEPLOYED AND ALSO STOWED IN THE LAUNCH CONFIGURATION.

4. THE DYNAMIC SUSPENSION TEST WILL BE PERFORMED IN AIR ONLY. CORRELATION TO VACUUM OPERATION WILL BE OBTAINED FROM THE RESULTS OF THE TEST PROGRAM ON THE ELECTRICAL TEST MODEL.

Figure 4-X-2. Preliminary Flight Spacecraft Test and Calibration Plan

2. Test Conditions

a. Types of Tests

1. Mechanical integration and alignment check,
2. Electrical debugging,
3. Performance test,
4. Magnetic moment test,
5. Dynamic and static balance test,
6. Vibration test,
7. RF lines (no wires) and solar panel deployment test,
8. Thermal vacuum test, and
9. Final performance test.

b. Vibration Tests

The test conditions for the sinusoidal vibration test of the spacecraft are given in Table 4-X-4; for the random vibration test, in Table 4-X-5. These same conditions were used in the TOS flight acceptance test program.

TABLE 4-X-4. SPACECRAFT SINUSOIDAL VIBRATION TEST CONDITIONS

Axis	Frequency (Hz)	Duration (min)	Level* (g, 0 to peak)
Thrust	10-19	0.23	2.0
	20-24	0.10	3.0
	25-249	0.83	2.0
	250-399	0.17	3.0
	400-2000	0.58	5.0
Time: 1.91 minutes			
Laterals	5-249	1.42	1.5
	250-399	0.17	2.0
	400-2000	0.58	5.0
Time: 4.34 minutes (2.17 minutes per axis)			
Sweep rate: 4 octaves per minute			
Total Time: 6.25 minutes			
*When the specified accelerations cannot be attained due to armature displacement limitations, the input may be a constant displacement of not less than 0.5-inch double amplitude.			

TABLE 4-X-5. SPACECRAFT RANDOM VIBRATION TEST CONDITIONS

Frequency (Hz)	PSD (g^2/Hz)	Acceleration (g-rms)
20-149	0.01	6.15
150-299	*	6.15
300-2000	0.02	6.15
Time per axis: 2 minutes Total Time: 6 minutes		
*Increasing from 150 Hz at constant rate of 3 db per octave. With the spacecraft installed, the excitation spectrum, measured from the control accelerometer, shall be equalized such that the PSD is within ±3 db of the specified levels everywhere in the frequency band.		

c. Thermal Vacuum Tests

The vacuum pressure for spacecraft thermal vacuum tests shall not be greater than 5×10^{-5} mm Hg. The temperature levels to which the spacecraft shall be exposed are given in Table 4-X-6. These same conditions were used in the TOS flight acceptance test program.

TABLE 4-X-6. SPACECRAFT THERMAL VACUUM TEST CONDITIONS

Temperature (°C)	Duration (hours)
+50	24
-10	24
+35	48
- 5	48
+ 5	48
+15 (nominal orbital temperature)	24
+25 (nominal ambient temperature)	As required
Total Time: 216 hours +	

3. Test Implementation

a. General

The assimilation of qualified subsystems into the spacecraft system during the integration cycle is relatively simple since each subsystem has already proved its performance capabilities and compatibilities during the unit and subsystem qualification cycles. Obviously, noise and RF environmental conditions unique to the spacecraft configuration being integrated may generate problems that could not be detected during subsystem tests. Should such problems require modification of unit specifications, both the unit and subsystem test programs would also be revised to test the modification on subsequent units.

Following spacecraft integration and the elimination of subsystem interface problems, the calibration and environmental qualification cycle is initiated. The spacecraft is completely calibrated both before and after the environmental qualification cycle. Comparison of data from the two calibrations enables rapid detection of equipment degeneration and establishes the standards for evaluating the in-orbit performance of the spacecraft.

During the first-level test phase, the spacecraft is operated with standard Command and Data Acquisition station equipment in order to verify the compatibility of the ground stations and the spacecraft. Magnetic tapes of selected spacecraft data recorded during certain phases of the qualification and calibration cycle will be used to verify proper operation of the long line data transmission network between the facilities of the operational ground complex.

b. Flight Spacecraft Test and Calibration Plan

1) Spacecraft Integration

As shown in Figure 4-X-2, the first portion of the spacecraft test program is the mechanical and electrical integration of the qualified subsystems into the spacecraft assembly. Since each subsystem has been tested before integration, tests at the spacecraft level are designed to eliminate interface problems between the various subsystems.

The first phase of the integration cycle is the installation of the main electrical harness on the baseplate and the performance of a complete electrical continuity test. No spacecraft components will be connected to the main harness until the proper electrical continuity configuration is verified. Before any unit is connected to the harness, its complete interface is given a final check.

An orderly sequence of integration has been established to prevent catastrophic spacecraft malfunctions. The first electronic components connected to the main electrical harness are the units of the power supply subsystem. When installed and connected, a functional check of the power supply subsystem is performed to ensure that a safe and satisfactory power source is available for the units of the remaining subsystems of the spacecraft.

After the power supply subsystem has been checked and found to be operating satisfactorily, the command subsystem is integrated. Functional tests are performed on this subsystem to ensure that a safe and reliable command facility is

available. Next, the communications subsystem is connected, and the same functional checking process is performed. The vehicle dynamics subsystem is then integrated, followed by the primary and secondary sensor subsystems.

After the functional checks of the subsystems have been completed and the spacecraft is assembled, a thorough system-by-system check of the spacecraft in all operating modes is performed. After all subsystem interfaces are verified, a Spacecraft Electrical Performance Evaluation Test (SEPET) is performed. When the spacecraft passes this test, which indicates no system problems, electromagnetic interference (EMI) testing is performed. After all forms of interference have been eliminated, the spacecraft is subjected to the qualification and calibration cycle.

2) Prequalification Alignment and Calibration

The first test performed in this phase of spacecraft testing is an abbreviated SEPET, as shown in Figure 4-X-2. At this time, the flight battery packs, having satisfactorily completed capacity tests, are installed on the spacecraft. Mechanical and optical alignment of the sensors is then performed. Next, the spacecraft is subjected to magnetic testing and, at this time, corrective magnets are installed to cancel the residual dipole of the spacecraft. These measurements are performed on a degaussed spacecraft to ensure that the corrective magnets are canceling the true residual dipole. Following the installation of the magnets, the spacecraft is dynamically balanced and the moment of inertia is measured. A complete calibration of the camera subsystems is then performed, terminating the initial phase of the spacecraft calibration cycle.

To prepare for the environmental qualification cycle, the spacecraft is installed in a temperature chamber so that anomalies induced by thermal excursions can be detected. Functional checks of the spacecraft subsystems are performed at the

temperature extremes specified in the thermal vacuum test profile. Elimination of these potential thermal vacuum malfunctions during the temperature survey greatly reduces the amount of thermal vacuum retesting required on the spacecraft.

3) Environmental Qualification

Following completion of the preenvironmental calibration tests, final mechanical assembly of the spacecraft is completed in preparation for the environmental qualification test cycle indicated in Figure 4-X-2. Prior to initiation of the first environmental test, a complete SEPET is performed and the data from these tests establishes a standard for evaluating the effects of the environmental qualification phase on the overall performance characteristics of the spacecraft. In addition, an abbreviated SEPET is performed after each environmental exposure to ensure that no degradation of spacecraft performance is encountered.

Following the initial SEPET, the spacecraft is vibration tested to the levels indicated in Tables 4-X-4 and 4-X-5. System operation during vibration testing is limited to those units which operate during launch. After the vibration exposures, an abbreviated SEPET is performed. Following the SEPET, a dynamic suspension test and a solar panel deployment test is performed.

After satisfactorily completing these tests, the spacecraft is prepared for the thermal vacuum test cycle. Prior to initiation of chamber evacuation for the thermal vacuum tests, a launch simulation test is performed, essentially a duplication of the prelaunch tests on the spacecraft while it is mated to the launch vehicle. During evacuation of the thermal vacuum chamber, the spacecraft is operated in the launch configuration. During the thermal vacuum test cycle (see Table 4-X-6), specific spacecraft operating parameters are measured daily to ascertain performance in the simulated orbital environment. The main program of spacecraft operation

throughout the thermal vacuum profile duplicates orbital operation. The satisfactory completion of thermal vacuum testing terminates the environmental qualification phase of the spacecraft test program.

4) Final Spacecraft Calibration

After completion of the thermal vacuum tests, final calibration of the spacecraft is performed. The final calibration cycle is initiated with the performance of a complete SEPET. At this time, battery capacity tests are performed and the solar array panels are retested in the solar illuminator. Next, the RF command sensitivity and final RF interference are measured on the RF test range. Command sensitivity is measured with the solar array panels in both the stowed and deployed positions.

The spacecraft is then taken to the magnetic test site, and the magnetic dipole measurements are repeated. If these measurements indicate the presence of significant induced magnetic dipole from the vibration test equipment, the corrective magnets installed earlier will be removed; the spacecraft will again be degaussed, the magnets will be reinstalled, and the magnetic measurements will be rechecked. After the magnetic measurements are completed, sensor mechanical and optical alignment will be rechecked, and final calibration of the cameras will be performed. The final operations performed on the spacecraft prior to storage or preparation for shipment to the launch site are rechecks of the balance, moment of inertia, and spacecraft weight.

D. DESIGN VALIDITY TESTING

1. General

Two simulated spacecraft structures will be constructed to demonstrate, through testing, the design validity of the ITOS spacecraft. The first structure is the thermal test model (TTM), which, after completion of the thermal test program, will

be reconfigured as an RF test model (RFTM). The second structure will be a mechanical test model (MTM), which will be reconfigured as an electrical test model (ETM).

The test sequences which will be performed on these special spacecraft models are shown in Figure 4-X-3. Following completion of the design validity tests, the RF test model and electrical test model will be maintained in proper operating condition for subsequent special tests which may be required to support the flight spacecraft integration and qualification tests.

2. Thermal and RF Design Testing

To demonstrate the soundness of the ITOS thermal design, a thermal test model of the spacecraft will be constructed. This model will consist of a structure complemented with dummy units containing appropriate heat-generating elements. The thermal test model will be instrumented and placed in a thermal vacuum chamber to measure the thermal gradients which develop on the spacecraft as a function of subsystem operation, which is simulated by the dummy unit heaters. The ability to establish thermal balance within the desired temperature range will also be tested. The design of the spacecraft is such that thermal testing can be accomplished with infrared sources, thereby eliminating the need for solar illumination simulation.

When the thermal test cycle has been completed, the thermal test model will be reconfigured with RF equipment and antennas to become the RF test model. A complete series of tests will be performed at the RF range using this model to demonstrate the antenna patterns of the spacecraft. These tests will also demonstrate that no RF interference between the various RF subsystems is encountered in the flight configuration.

THERMAL TEST MODEL / RF TEST MODEL

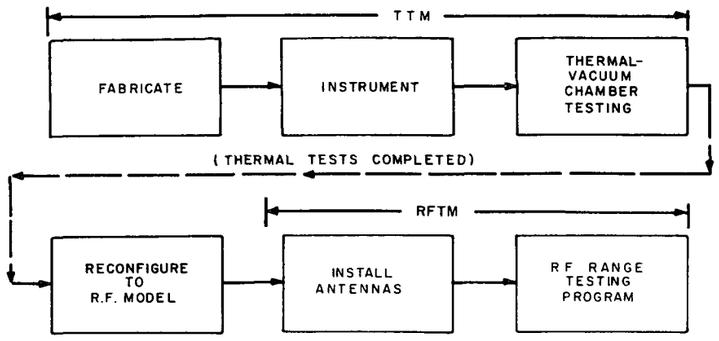

TTM TEST OBJECTIVES

1. THERMAL GRADIENT SURVEY WITH EXPECTED OPERATING MODE THERMAL PROFILES.
2. VERIFICATION OF THERMAL BALANCE WITH THERMAL CONTROL SUBSYSTEM.

RFTM TEST OBJECTIVES

1. DETERMINE OPERATING ANTENNA PATTERNS FOR "ON BOARD" TRANSMITTERS – SOLAR ARRAY EITHER STOWED OR DEPLOYED.
2. DETERMINE OPERATING ANTENNA PATTERNS FOR COMMAND RECEIVING SYSTEM – SOLAR ARRAY EITHER STOWED OR DEPLOYED.
3. VERIFICATION OF LACK OF RF INTERFERENCE BETWEEN ALL COMBINATIONS OF RF EQUIPMENT – SOLAR ARRAY EITHER STOWED OR DEPLOYED.

MECHANICAL TEST MODEL / ELECTRICAL TEST MODEL

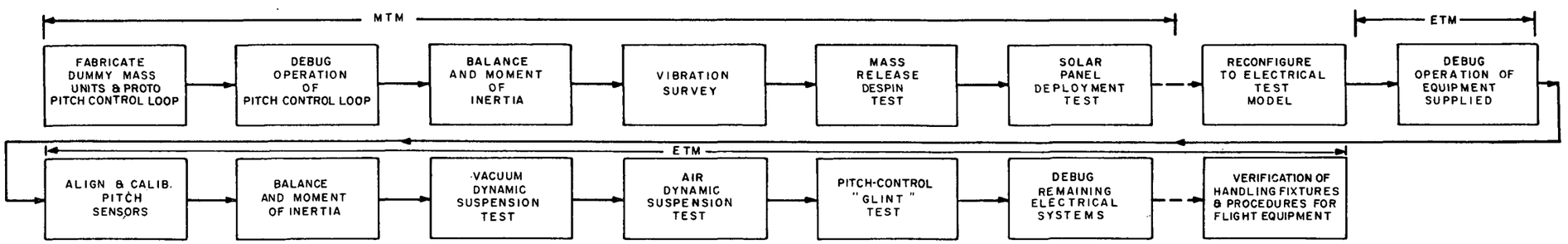

NOTES: 1. BOTH THE RF MODEL AND THE ELECTRICAL TEST MODEL WILL BE MAINTAINED IN PROPER OPERATING CONDITION TO SUPPORT SUBSEQUENT SPECIAL TESTING AS DICTATED BY THE FLIGHT SPACECRAFT INTEGRATION PROGRAM.

2. ALL TESTS AND OPERATIONS TO BE PERFORMED ON FLIGHT SPACECRAFT WILL FIRST BE PERFORMED ON THE ELECTRICAL TEST MODEL.

Figure 4-X-3. Preliminary Design Verification Test Program

3. Mechanical and Electrical Design Testing

A mechanical test model of the ITOS spacecraft will be constructed and used to demonstrate the integrity of the spacecraft mechanical design. The mechanical test model will consist of a structure, dummy mass units simulating the components of the spacecraft, a dummy harness, dummy solar panels, and an operating prototype of the pitch control subsystem. The mechanical test model will be balanced, and the balance axis, center of gravity, and the moment of inertia will be determined. Techniques for these operations will also be tested on this model, as will safe and secure operating procedures for the spacecraft handling equipment and test fixtures. Once balanced, the mechanical test model will be subjected to vibration tests. During vibration testing the test model will demonstrate the soundness of the spacecraft and its structure and unit configuration and measure the resonances and mechanical amplification of the structure and the mechanical configuration of the subsystem unit models.

The mechanical test model will then be used to verify the design of the mass release system (despin mechanism) through the performance of a despin test. The solar panel deployment mechanism will be similarly demonstrated, using dummy solar panels.

At completion of the mechanical design verification tests, the mechanical test model will be reconfigured to become the electrical test model. Sufficient prototype equipment (not environmentally qualified) to complete an electrical model of the spacecraft sufficient for the dynamics test will be mounted on this structure. The remaining dummy mechanical components will be retained in the assembly. This electronic equipment will be debugged and calibrated to the degree necessary to display satisfactory electrical operation. The model will be balanced, and the moment of inertia will be determined. The electrical test model will be placed in a thermal vacuum chamber, and the dynamic suspension test will be performed to demonstrate the satisfactory operation of the pitch control loop. Following the performance of this

test in the vacuum environment, it will be repeated under room ambient conditions to establish a correlation of air-to-vacuum data such that the dynamic suspension test for the flight spacecraft need only be performed in air. The air environment test is not designed to be a high resolution verification of the accuracy of the pitch control loop, but merely a functional demonstration to ensure that no gross errors exist. The accuracy is available from the calibration data of the specific units comprising the pitch control loop and will be arrived at by analysis of these data. A glint test may also be performed on the electrical test model to determine the effect of off axis heat sources on the pitch control sensors. After completion of these tests, the remainder of the prototype equipment allocated to the electrical test model will be integrated, and all other tests, handling procedures, and alignment procedures prescribed for the flight spacecraft will be exercised and demonstrated on the electrical test model. The safety of personnel and equipment, human engineering, and test effectiveness, both in time utilization and ability to generate the desired results, will be fully and carefully analyzed and evaluated.

RCA